Complexity

Control and Stability Analysis of Complex Dynamical Systems involved in Finance, Ecology and Engineering

Lead Guest Editor: Quanxin Zhu
Guest Editors: Hamid Reza Karimi, Xiaodi Li, Juan Carlos Cortés, and Ruofeng Rao

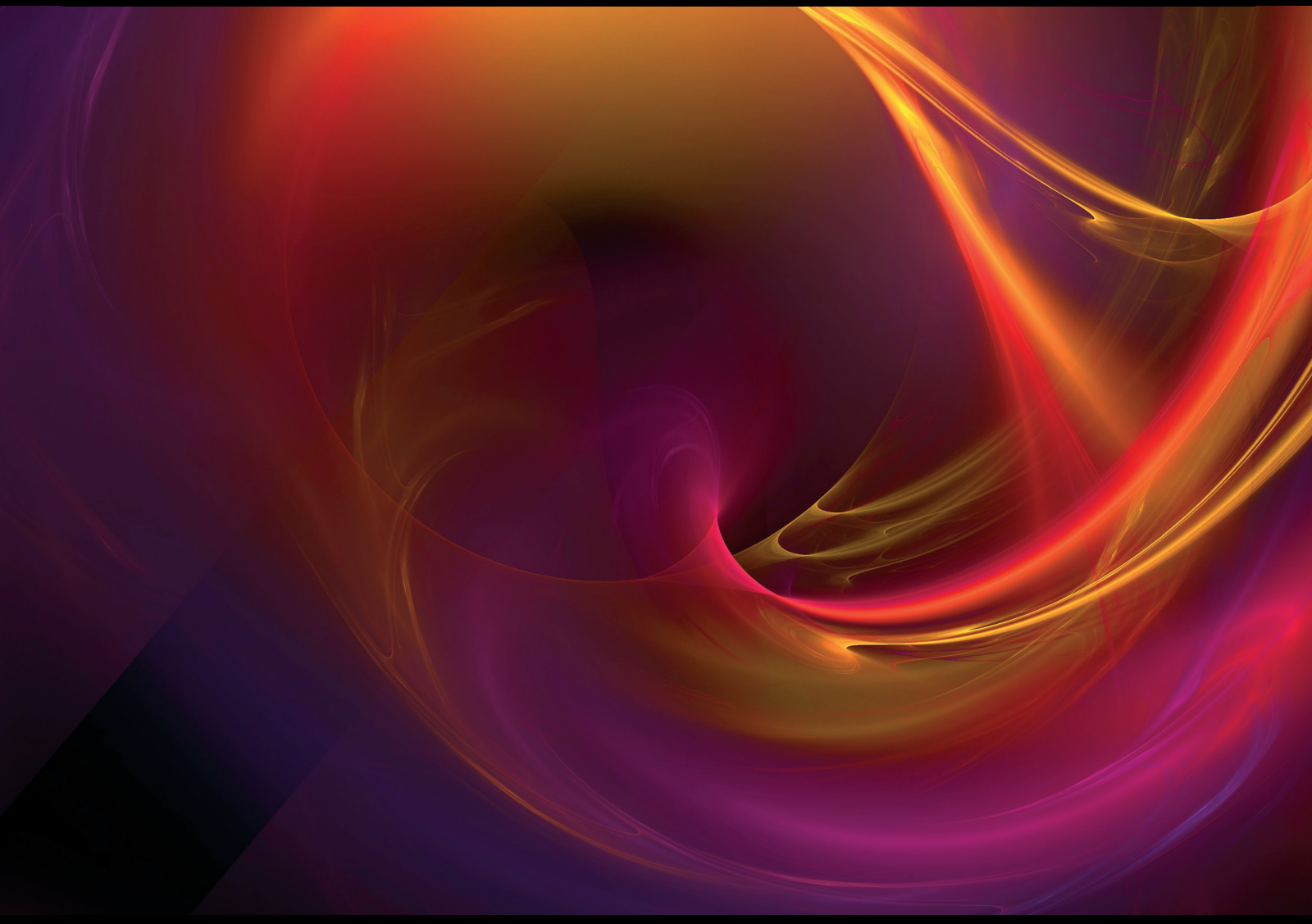

Control and Stability Analysis of Complex Dynamical Systems involved in Finance, Ecology and Engineering

Complexity

Control and Stability Analysis of Complex Dynamical Systems involved in Finance, Ecology and Engineering

Lead Guest Editor: Quanxin Zhu
Guest Editors: Hamid Reza Karimi, Xiaodi Li, Juan Carlos Cortés, and Ruofeng Rao

Contents

Extended Model on Structural Stability and Robustness to Bounded Rationality
Yi Liao, Lujiang Miao, Lei Wang, Fei Xu, and Chi Zhang
Research Article (6 pages), Article ID 4902786, Volume 2021 (2021)

Aperiodic Sampled-Data Control for Chaotic System Based on Takagi–Sugeno Fuzzy Model
Minjie Zheng, Shenhua Yang, and Lina Li
Research Article (8 pages), Article ID 6401231, Volume 2021 (2021)

Stabilization of Two Electricity Generators
Dany Ivan Martinez, José de Jesús Rubio, Arturo Aguilar, Jaime Pacheco, Guadalupe Juliana Gutierrez, Victor Garcia, Tomas Miguel Vargas, Genaro Ochoa, David Ricardo Cruz, and Cesar Felipe Juarez
Research Article (13 pages), Article ID 8683521, Volume 2020 (2020)

Research on How Human Intelligence, Consciousness, and Cognitive Computing Affect the Development of Artificial Intelligence
Yanyan Dong, Jie Hou, Ning Zhang, and Maocong Zhang
Research Article (10 pages), Article ID 1680845, Volume 2020 (2020)

Rich Dynamics of a Predator-Prey System with Different Kinds of Functional Responses
Kankan Sarkar, Subhas Khajanchi, Prakash Chandra Mali, and Juan J. Nieto
Research Article (19 pages), Article ID 4285294, Volume 2020 (2020)

Bogdanov–Takens Bifurcation in a Shape Memory Alloy Oscillator with Delayed Feedback
Jinbin Wang and Lifeng Ma
Research Article (10 pages), Article ID 9132501, Volume 2020 (2020)

A New Supply Chain System and Its Impulsive Synchronization
Yang Peng, Jiang Wu, Shiping Wen, Yuming Feng, Zhengwen Tu, and Limin Zou
Research Article (9 pages), Article ID 2414927, Volume 2020 (2020)

Rail Fastener Positioning Based on Double Template Matching
Yijin Qiu, Xingjie Chen, and Zhaomin Lv
Research Article (10 pages), Article ID 8316969, Volume 2020 (2020)

A Numerical Method for Time-Fractional Reaction-Diffusion and Integro Reaction-Diffusion Equation Based on Quasi-Wavelet
Sachin Kumar, Jinde Cao, and Xiaodi Li
Research Article (11 pages), Article ID 3291723, Volume 2020 (2020)

Nonparametric Range-Based Double Smoothing Spot Volatility Estimation for Diffusion Models
Jingwei Cai
Research Article (7 pages), Article ID 5048925, Volume 2020 (2020)

Construction of Regional Logistics Weighted Network Model and Its Robust optimization: Evidence from China
Lizhao Yan, Yi Wen, Kok Lay Teo, Jian Liu, and Fei Xu
Research Article (9 pages), Article ID 2109423, Volume 2020 (2020)

Adaptive Decentralized Control Scheme for a Stochastic Interconnected System
Xiaoli Jiang, Siqi Liu, Mingyue Liu, Li Yang, and Lina Liu
Research Article (11 pages), Article ID 6018398, Volume 2020 (2020)

Investigation of Droplets Distribution and Reaction Kinetics on SO_2 Removal in Flue Gas via Venturi Scrubber
Shuo Zhang, Wenyue Cui, Chen Wang, Tao Wu, and Xiaohang Zhao
Research Article (12 pages), Article ID 6107312, Volume 2020 (2020)

Decision and Coordination of Low-Carbon E-Commerce Supply Chain with Government Carbon Subsidies and Fairness Concerns
Qiang Han, Yuyan Wang, Liang Shen, and Wenquan Dong
Research Article (19 pages), Article ID 1974942, Volume 2020 (2020)

Global Stability for a Discrete Space-Time Lotka–Volterra System with Feedback Control
Li Xu and Ruiwen Han
Research Article (9 pages), Article ID 2960503, Volume 2020 (2020)

Independent Control of Temperature and Humidity in Air Conditioners by Using Fuzzy Sliding Mode Approach
Lijian Yang, Ziyang Li, Zhengtian Wu, Mingyang Xie, Baoping Jiang, and Baochuan Fu
Research Article (12 pages), Article ID 1976584, Volume 2020 (2020)

Learning-Based Dark and Blurred Underwater Image Restoration
Yifeng Xu, Huigang Wang, Garth Douglas Cooper, Shaowei Rong, and Weitao Sun
Research Article (14 pages), Article ID 6549410, Volume 2020 (2020)

Prediction of Air Quality Based on Hybrid Grey Double Exponential Smoothing Model
Zhicun Xu, Meng Dun, and Lifeng Wu
Research Article (13 pages), Article ID 9427102, Volume 2020 (2020)

New Controllability Results of Fractional Nonlocal Semilinear Evolution Systems with Finite Delay
Daliang Zhao and Juan Mao
Research Article (13 pages), Article ID 7652648, Volume 2020 (2020)

Hindawi
Complexity
Volume 2021, Article ID 4902786, 6 pages
https://doi.org/10.1155/2021/4902786

Research Article

Extended Model on Structural Stability and Robustness to Bounded Rationality

Yi Liao,[1] Lujiang Miao,[1] Lei Wang,[2] Fei Xu,[3] and Chi Zhang[4]

[1]*School of Business Administration, Faculty of Business Administration, Southwestern University of Finance and Economics, Chengdu, Sichuan 610074, China*
[2]*School of Economic Mathematics, Southwestern University of Finance and Economics, Chengdu, Sichuan 610074, China*
[3]*Department of Mathematics, Wilfrid Laurier University, Waterloo, Ontario N2L 3C5, Canada*
[4]*Graduate School, Shanghai Customs College, Shanghai 201201, China*

Correspondence should be addressed to Chi Zhang; zhangchi@shcc.edu.cn

Received 10 July 2020; Revised 21 November 2020; Accepted 28 April 2021; Published 17 May 2021

Academic Editor: Quanxin Zhu

In this article, we focus on an extended model $\overline{M}$ of bounded rationality. Based on a rationality function with lower semi-continuity, we analyze the relationship between structural stability and robustness of $\overline{\Omega}$. To further demonstrate the applicability of our theory, we introduce a model $\overline{\Omega}_0$ containing an abstract rationality function and generalize abstract fuzzy economies. We demonstrate the structural stability of the extended model $\overline{\Omega}_0$ at $(\bar{\xi}, \varepsilon)$. That is to say, $\overline{\Omega}_0$ is robust to the $(\bar{\xi}, \varepsilon)$-equilibria.

1. Introduction

Arrow and Debreu [1] studied the existence of equilibrium for a social competitive economy assuming that all participants are perfectly rational in the game in 1952. However, in reality, perfect rationality does not often occur. Hence, the assumption of perfect rationality restricted the application of the model. On the other hand, it is well known that the stability analysis is one of the significant topics in economic models. Anderlini and Canning [2] constructed an abstract framework Ω and derived necessary and sufficient conditions for the model being robust to ϵ-equilibria. Yu and Yu [3] extended the results in [2] under weaker conditions and proved the stability and robustness of the model. Wang et al. [4] generalized the model Ω [2] with abstract fuzzy economies. These authors studied the stability and showed its robustness. Miyazaki and Azuma [5] investigated the structural stability and robustness of the model introduced in [2]. They proved that if a system is (ξ, ε)-stable, then it is (ξ, ε)-robust. Loi and Matta [6] extended the model Ω introduced in [2] to a more general model $\overline{\Omega}$. They investigated a pure exchange economy using the abstract construction. Yu et al. [3] studied (ξ, ε)-stability and (ξ, ε)-robustness of model Ω introduced in [2]. In particular, they considered their relationship. Then, these results on stability and robustness in control and economy were further studied during the last decades [7–11].

Zadeh [12] initiated fuzzy set theory to describe scenarios with imprecise parameters. Kim and Lee [13] studied a fuzzy game and obtained corresponding equilibrium existence theorem. Huang [14, 15] studied a generalized abstract fuzzy model of economics and considered the existence of its equilibrium. Patriche [16, 17] presented a Bayesian abstract fuzzy economic model with a measure space of agents and demonstrated the existence of equilibrium of the constructed model. More recently, Cui et al. [18] studied the loss aversion level of a bimatrix game with payoff function described by fuzzy variables. These authors obtained synchronization conditions for the fuzzy stochastic complex networks.

Motivated by these existing studies, in this work, we study the extended model $\overline{\Omega}_0$ with generalized abstract fuzzy economies and an abstract rationality function. We are particularly interested in whether small deviations in the additional rationality of the extended model $\overline{\Omega}_0$ will cause only minor changes in bounded rational equilibria. When we extend the model Ω to a complex model $\overline{\Omega}$, it is difficult to obtain its structural stability. It is essential to derive the

relationship between the extended model $\overline{\Omega}$ and its structural stability. We mainly focus on the structure of Ω and how to extend Ω to $\overline{\Omega}$ in a natural way.

The rest of the paper is organized as follows. In section 2, we recall the notion of economic model Ω, structural stability, robustness to bounded rationality, and their connection. Moreover, we extend the model Ω to a complex model $\overline{\Omega}$. The relationship between $(\overline{\xi}, \varepsilon)$-stability and $(\overline{\xi}, \varepsilon)$-robustness of $\overline{\Omega}$ is discussed. In section 3, we prove a new theorem about the existence of equilibrium in $L\Gamma$-spaces for the generalized abstract fuzzy economic model. We further prove the structural stability of the extended model $\overline{\Omega}_0$ with a category of generalized abstract fuzzy economies at $(\overline{\xi}, \varepsilon)$. Finally, we present the conclusions of this article in section 4.

2. The Extended Model $\overline{\Omega}$

In this section, we introduce the following notation. Suppose that X and Y are topological spaces. For a subset D of topological space X, we use 2^D and $\langle D \rangle$ to denote, respectively, the set of all subsets of D and the family of all nonempty finite subset of D. If $G(x)$ is compact for all $x \in X$, we then say that $G\colon X \longrightarrow 2^Y$ is a compact valued correspondence. Assume X and Y are metric spaces. If for any $x_n \longrightarrow x$ and $y_n \in G(x_n)$, $y_n \longrightarrow y$, we have $y \in G(x)$, then G is upper semicontinuous at $x \in X$. If for any $x_n \longrightarrow x$ and $y \in G(x)$, we have $y_n \in G(x_n)$ such that $y_n \longrightarrow y$, then G is lower semicontinuous at x. If for any $x_n \longrightarrow x, h(G(x_n), G(x)) \longrightarrow 0$, where h is the Hausdorff distance defined on Y, then G is continuous at x.

Anderlini and Canning [2] studied an economic model of bounded rationality. The model Ω with a parameter space given by quadruple (Ψ, X, F, R): (Ψ, ϱ) is a parameter space and (X, d) is an action space, in which ϱ and d are metrics. Here, $F\colon \Psi \times X \longrightarrow 2^X$ represents the feasibility correspondence inducing a further correspondence $f(\xi) = \{x \in X\colon x \in F(\xi, x)\}$, for all $\xi \in \Psi$. The graph of f is denoted by $\mathrm{Graph}(f) = \{(\xi, x) \in \Psi \times X\colon x \in f(\xi)\}$ and $R\colon \mathrm{Graph}(f) \longrightarrow R^+$ is a rational function. When $R(\xi, x) = 0$, we say that the full rationality is realized. Given a model Ω, for all $\xi \in \Psi$, we define the ε-equilibria set at ξ as follows:

$$E(\xi, \varepsilon) = \{x \in f(\xi)\colon R(\xi, x) \le \varepsilon\}, \quad \forall \varepsilon \ge 0. \tag{1}$$

We use $E(\xi)$ to denote all equilibria set at ξ as

$$E(\xi) = E(\xi, 0) = \{x \in f(\xi)\colon R(\xi, x) = 0\}. \tag{2}$$

Here, we extend the model Ω proposed in [2] to a more complex model $\overline{\Omega}$. Using a rationality function with lower semicontinuity, we prove that $\overline{\Omega}$ is $(\overline{\xi}, \varepsilon)$-stable, which implies that $\overline{\Omega}$ is robust to $(\overline{\xi}, \varepsilon)$-equilibria.

Loi and Matta [6] studied the extended model $\overline{\Omega}$ as follows.

Definition 1 (see [6]). For a model $\Omega = \{\Psi, X, F, R\}$, its extended model $\overline{\Omega}$ is defined as a quadruple $\overline{\Omega} = \{\overline{\Psi}, \overline{X}, \overline{F}, \overline{R}\}$ satisfying the following:

(1) $(\overline{X}, \overline{d}) = (X, d)$;

(2) $\overline{\Psi} = (K(\Psi), h_\varrho)$, where $K(\Psi)$ is to be the set of all compact subsets of Ψ with the Hausdorff distance h_ϱ related to the metric ϱ of Ψ;

(3) $\overline{F}\colon \overline{\Psi} \times X \longrightarrow 2^X$ is denoted by $\overline{F} = \cup_{\mu \in \overline{\lambda}} F(\mu, x)$. We thus have $\overline{f}\colon \overline{\Psi} \longrightarrow 2^X, \overline{f}(\overline{\lambda}) = \{x \in X | x \in \overline{F}(\overline{\xi}, x)\}$;

(4) $\overline{R}\colon \mathrm{Graph}(\overline{f}) \longrightarrow R^+$ is an extended R. That is to say, for all $\xi \in \Psi, \overline{R}(\{\xi\}, x) = R(\xi, x)$ that satisfies

$$\overline{R}(\overline{\xi}, x) = \{0\} \Longleftrightarrow R(\xi, x) = 0, \quad \forall \xi \in \overline{\xi}. \tag{3}$$

Definition 2. Given an extended model $\overline{\Omega}$, for any $\overline{\xi} \in \overline{\Psi}$, the ϵ-equilibria set at $\overline{\xi}$ is given by

$$\overline{E}(\overline{\xi}, \varepsilon) = \{x \in \overline{f}(\overline{\xi}) | \overline{R}(\overline{\xi}, x) \subset [0, \varepsilon]\}, \quad \forall \varepsilon \ge 0. \tag{4}$$

We use $\overline{E}(\overline{\xi})$ to denote all equilibria set at $\overline{\xi}$ as

$$\overline{E}(\overline{\xi}) = \overline{E}(\overline{\xi}, 0) = \{x \in \overline{f}(\overline{\xi}) | \overline{R}(\overline{\xi}, x) = \{0\}\}. \tag{5}$$

Definition 3. The extended model $\overline{\Omega}$ is structurally stable at $(\overline{\xi}, \varepsilon)$ if $\overline{E}\colon \overline{\Psi} \times R^+ \longrightarrow 2^X$ is continuous at $(\overline{\xi}, \varepsilon)$.

Definition 4. The extended model $\overline{\Omega}$ is robust to $(\overline{\xi}, \varepsilon)$-equilibria if for all $\delta > 0$, we can find an $\overline{\varepsilon} > 0$ satisfying, for all $\varepsilon' > 0$ with $|\varepsilon - \varepsilon'| < \overline{\varepsilon}$ and for all $\xi' \in \overline{\Psi}$ with $h_\varrho(\xi, \xi') < \overline{\varepsilon}$ and $h_d(\overline{E}(\overline{\xi'}, \varepsilon), \overline{E}(\overline{\xi'}, \varepsilon')) < \delta$, where h_d is the Hausdorff distance defined on X.

Theorem 1. *Given a model $\Omega = (\Psi, X, F, R)$ and $\overline{\Omega} = \{\overline{\Psi}, \overline{X}, \overline{F}, \overline{R}\}$ is its corresponding extended model. If the model Ω satisfies the following assumptions:*

(1) (Ψ, ϱ) is a complete metric space and X is a compact metric space,

(2) $f\colon \Psi \longrightarrow 2^X$ is nonempty compact valued and upper semicontinuous,

(3) $R\colon \mathrm{Gragh}(f) \longrightarrow R^+$ is lower semicontinuous,

(4) for all $\xi \in \Psi$, $E(\xi) = \{x \in f(\xi)\colon R(\xi, x)\} \neq \varnothing$,

then $\overline{\Omega}$ being $(\overline{\xi}, \varepsilon)$-stable guarantees that $\overline{\Omega}$ is robust to $(\overline{\xi}, \varepsilon)$-equilibria.

Proof. Obviously, if (Ψ, ϱ) is a complete metric space, then it follows from Theorem 3.3 in Henrikson [19] that $(\overline{\Psi}, h_\varrho)$ is a complete metric space.

Suppose model $\overline{\Omega}$ is not robust to $(\overline{\xi}, \varepsilon)$-equilibria. Consequently, there exist $\overline{\xi} \longrightarrow \xi, \varepsilon_n \longrightarrow \varepsilon$, and $h_d(\overline{E}(\overline{\xi}_n, \varepsilon_n), \overline{E}(\overline{\xi}_n, \varepsilon)) \ge \delta_0$, where $\delta_0 > 0$, $\{\varepsilon_n\} \subset R^+$, and $\{\overline{\xi}\}$ is a sequence of compact subsets Ψ. Take the subsequence $\{\varepsilon_{n_k}\}$ of $\{\varepsilon_n\}$ such that $\varepsilon_{n_k} \ge \varepsilon_{n_{k+1}}$, $\varepsilon_{n_k} \ge \varepsilon$ or $\varepsilon_{n_k} \le \varepsilon_{n_{k+1}}$, $\varepsilon_{n_k} \le \varepsilon$.

First, consider the subsequence $\{\varepsilon_{n_k}\}$ satisfying $\varepsilon_{n_k} \ge \varepsilon_{n_{k+1}}$ and $\varepsilon_{n_k} \ge \varepsilon$. Then, we have $\overline{E}(\overline{\xi}_{n_k}, \varepsilon) \subset \overline{E}(\overline{\xi}_{n_k}, \varepsilon_{n_k})$. Thus, we can choose $x_{n_k} \in \overline{E}(\overline{\xi}_{n_k}, \varepsilon_{n_k})$ such that

$$\min_{y\in\overline{E}\left(\overline{\xi}_{n_k},\varepsilon\right)} d\left(x_{n_k}, y\right) > \frac{\delta_0}{2}. \tag{6}$$

Since $x_{n_k} \in \overline{E}(\overline{\xi}_{n_k}, \varepsilon_{n_k})$, then $x_{n_k} \in \overline{f}(\overline{\xi}_{n_k})$, and it follows from Definition 1 that $\overline{R}(\overline{\xi}_{n_k}, \varepsilon_{n_k}) \subset [0, \varepsilon_{n_k}]$. Moreover, since $f\colon \Psi \longrightarrow 2^X$ is nonempty compact valued and upper semicontinuous, it follows from Lemma 3.7 in [6] that the correspondence $\overline{f}\colon \overline{\Psi} \longrightarrow 2^X$ is nonempty compact valued and upper semicontinuous. Since $\xi_{n_k} \longrightarrow \xi$, without loss of generality, by Lemma 2.1 in [3], we can assume $x_{n_k} \longrightarrow x \in \overline{f}(\overline{\xi})$.

Because of the lower semicontinuity of $\overline{R}$, we obtain that $\overline{R}(\overline{\xi}_{n_k}, \varepsilon_{n_k}) \subset [0, \varepsilon_{n_k}], \varepsilon_{n_k} \longrightarrow \varepsilon$ which implies that $\overline{R}(\overline{\xi}, \varepsilon) \subset [0, \varepsilon]$. Therefore, $x \in \overline{E}(\overline{\xi}, \varepsilon)$. Since the extended model $\overline{\Omega}$ is $(\overline{\xi}, \varepsilon)$-stable, we have that $h_d(\overline{E}(\overline{\xi}_n, \varepsilon_n), \overline{E}(\overline{\xi}, \varepsilon)) \longrightarrow 0$. It follows from Lemma 2.5 in [20] and (6) that

$$\min_{y\in\overline{E}\left(\overline{\xi}_{n_k},\varepsilon\right)} d\left(x_{n_k}, y\right) \geq \frac{\delta_0}{2}. \tag{7}$$

However, this is in contradiction with $x \in \overline{E}(\overline{\xi}, \varepsilon)$.

Next, consider the subsequence $\left\{\varepsilon_{n_k}\right\}$ satisfying $\varepsilon_{n_k} \leq \varepsilon_{n_{k+1}}$ and $\varepsilon_{n_k} \leq \varepsilon$. We then have $\overline{E}(\overline{\xi}_{n_k}, \varepsilon_{n_k}) \subset \overline{E}(\overline{\xi}_{n_k}, \varepsilon)$. Therefore, we can choose $x_{n_k} \in \overline{E}(\overline{\xi}_{n_k}, \varepsilon)$ such that

$$\min_{y\in\overline{E}\left(\overline{\xi}_{n_k},\varepsilon_{n_k}\right)} d\left(x_{n_k}, y\right) > \frac{\delta_0}{2}. \tag{8}$$

Since $\overline{f}\colon \overline{\Psi} \longrightarrow 2^X$ is nonempty compact valued and upper semicontinuous and $\xi_{n_k} \longrightarrow \xi$, without loss of generality, it follows from Lemma 2.1 in [3] that we can assume $x_{n_k} \longrightarrow x \in \overline{f}(\overline{\xi})$.

Because of the lower semicontinuity of $\overline{R}$, we have that $\overline{R}(\overline{\xi}_{n_k}, \varepsilon_{n_k}) \subset [0, \varepsilon_{n_k}], \varepsilon_{n_k} \longrightarrow \varepsilon$. That is to say, $\overline{R}(\overline{\xi}, \varepsilon) \subset [0, \varepsilon]$. Therefore, $x \in \overline{E}(\overline{\xi}, \varepsilon)$. Since the extended model $\overline{\Omega}$ is $(\overline{\xi}, \varepsilon)$-stable, we have that $h_d(\overline{E}(\overline{\xi}_n, \varepsilon_n), \overline{E}(\overline{\xi}, \varepsilon)) \longrightarrow 0$. It follows from Lemma 2.5 in [20] and (8) that

$$\min_{y\in\overline{E}\left(\overline{\xi}_{n_k},\varepsilon\right)} d\left(x_{n_k}, y\right) \geq \frac{\delta_0}{2}. \tag{9}$$

However, this is in contradiction with $x \in \overline{E}(\overline{\xi}, \varepsilon)$, which completes the proof. □

Remark 1. Theorem 1 improves Theorem 4.6 in [5] and Theorem 3.4 in [3], where the extended model $\overline{\Omega}$ was extended. We also generalize Theorem 3.10 in [6] where the structurally stability at ξ and robustness to ϵ-equilibria are extended to the structurally stability at $(\overline{\xi}, \varepsilon)$ and the robustness to $(\overline{\xi}, \varepsilon)$-equilibria, respectively.

3. Application

Here, we propose a category of new generalized abstract fuzzy economies in an $L\Gamma$-space.

We then study the equilibrium existence theorem for the models. Furthermore, we establish an extended model $\overline{\Omega}_0$ with an abstract rationality function and a category of generalized abstract fuzzy economies. We demonstrate that $\overline{\Omega}_0$ is structurally stable at $(\overline{\xi}, \varepsilon)$. In other words, $\overline{\Omega}_0$ is robust to the $(\overline{\xi}, \varepsilon)$-equilibria.

3.1. The Equilibria of Generalized Abstract Fuzzy Economic Model in an $L\Gamma$-Space. The notions of abstract convex space and $L\Gamma$-space were introduced by Park [21, 22].

Definition 5 (see [21]). An abstract convex space $(E, D; \Gamma)$ consists of a topological space E, a nonempty set D, and a map $\Gamma\colon \langle D\rangle \longrightarrow E$ with nonempty values.

For any $A \in \langle D\rangle$, we denote $\Gamma_A = \Gamma(A)$. Let $co_\Gamma D' = \bigcup\{\Gamma_A | A \in \langle D\rangle\} \subset E$ be the Γ-convex hull of D', where $D' \subset D$. If for any $N \in \langle D\rangle$, we have $\Gamma_N \subset X$, i.e., $co_\Gamma D' \subset X$, then X is said to be a Γ-convex subset of $(E, D; \Gamma)$ related to D'. If $D \subset E$, the space is defined as $(E^{D;\Gamma})$. Here, if $co_\Gamma(X \cap D) \subset X$, then X is called Γ-convex. That is to say, X is Γ-convex related to $D' = X \cap D$. When $E = D$, we let $(E; \Gamma) = (E, E; \Gamma)$.

Definition 6 (see [22]). If an abstract convex space $(E, D; \Gamma)$ has a basis $\mathscr{B}$ of a uniformity of E, then it is said to be an abstract convex uniform space $(E, D; \Gamma; \mathscr{B})$. If D is dense in E and for any $U \in \mathscr{B}$ and for any Γ-convex subset $A \subset E$, the set $\{x \in E\colon A \cap U[x] \neq \varnothing\}$ is Γ-convex, then an abstract convex uniform space $(E^{D;\Gamma;\mathscr{B}})$ is said to be an $L\Gamma$-space.

Based on Proposition 5.1 and Theorem 8.5 in Park [22], we can obtain Lemma 1.

Lemma 1. *Let $(X, D; \Gamma)$ be a $L\Gamma$-space. Suppose that $G\colon X \longrightarrow 2^X$ is nonempty closed Γ_i-convex valued and compact upper semicontinuous. Then, we can find an $\widehat{x} \in X$ satisfying $\widehat{x} \in G(\widehat{x})$.*

Lemma 2. *Let $(X_i, D_i; \Gamma_i)_{i\in I}$ be a family of $L\Gamma$-spaces. For each $i \in I$, suppose that $G_i\colon X = \prod X_i \longrightarrow 2^{X_i}$ is nonempty closed Γ_i-convex valued and compact upper semicontinuous. Thus, for each $i \in I$, we can find an $\widehat{x} = (\widehat{x}_i)_{i\in I} \in X$ satisfying $\widehat{x}_i \in G_i(\widehat{x})$.*

Proof. Let $X = \prod_{i\in I} X_i$ and $D = \prod_{i\in I} D_i$. For each $i \in I$, let $\pi_i\colon X \longrightarrow X_i$ be the projection of X onto X_i. Then, for any $x \in X$, $G\colon X \longrightarrow 2^X$ is defined by $G(x) = \prod_{i\in I} G_i(x)$. We denote $\Gamma\colon \langle D\rangle \longrightarrow 2^X \backslash \{\varnothing\}$ as $\Gamma(A) = \prod_{i\in I} \Gamma_i(\pi_i(A))$, $\forall A \in \langle D\rangle$. It follows from Lemma 2 in [23] that (X, D, Γ) is a $L\Gamma$-space. Since each G_i is nonempty closed Γ_i-convex valued and compact upper semicontinuous, it follows from Lemma 3 of Fan [24] that G is also nonempty closed Γ_i-convex valued and compact upper semicontinuous. Next, we prove that, for any $x \in X$, $G(x)$ is Γ-convex. For every $A \in G(x)$ and $A \subset D$, we derive that for every $i \in I, \pi(A) \subset G_i(x) \cap D_i$. Since every $G_i(x)$ is Γ_i-convex, we have that $\Gamma_i(\pi_i(A)) \subset G_i(x)$ for each $i \in I$. Therefore, $\Gamma(A) = \prod_{i\in I} \Gamma_i(\pi_i(A)) \subset \prod_{i\in I} G_i(x) = G(x)$. Thus, we obtain that $G(x)$ is Γ-convex and $G\colon X \longrightarrow 2^X$ is nonempty closed Γ_i-convex valued and compact upper semicontinuous. It follows from Lemma 1, for each $i \in I$, we

can find an $\widehat{x} = (\widehat{x}_i)_{i\in I} \in X$ satisfying $\widehat{x} \in G(\widehat{x}) = \prod_{i\in I} G_i(\widehat{x})$, i.e., $\widehat{x}_i \in G_i(\widehat{x})$.

Let X and Y be two nonempty convex subsets of a Hausdorff topological vector space. In this article, we use $\mathrm{F}(X)$ to denote all the fuzzy sets on X. $F\colon X \longrightarrow \mathrm{F}(Y)$ is said to be a fuzzy mapping. Thus, we have that for each $x \in X, F(x)$(denote by F_x in the sequel) is a fuzzy set in $\mathrm{F}(Y)$. $F_x(y)$ is defined as the degree of membership of point y in F_x.

For every $q \in [0,1]$, we use $(A)_q = \{x \in X\colon A(x) \geq q\}$ to denote the q-cut set of $A \in \mathrm{F}(X)$. If I is a set of agents (finite or infinite), X_i is a nonempty topological space (a choice set), $A_i, B_i\colon X = \prod_{i\in I} X_i \longrightarrow \mathrm{F}(X_i)$ are fuzzy constraint mappings (fuzzy constraint correspondences), and $P_i\colon X \longrightarrow \mathrm{F}(X_i)$ is a fuzzy preference mapping (fuzzy preference correspondence), then $\Upsilon = (X_i, A_i, B_i, P_i)_{i\in I}$ is said to be a generalized abstract fuzzy economy. If, for every $i \in I, \widehat{x}_i \in (B_{i\widehat{x}})_{b_i(\widehat{x})}$ and $(A_{i\widehat{x}})_{a_i(\widehat{x})} \cap (P_{i\widehat{x}})_{p_i(\widehat{x})} = \varnothing$, where $a_i, b_i, p_i\colon X \longrightarrow (0,1]$, then the point $\widehat{x} \in X$ is said to be an equilibrium of Υ. □

Theorem 2. *Suppose that $\Upsilon = (X_i, A_i, B_i, P_i)_{i\in I}$ is an abstract fuzzy model of economics, $X = \prod_{i\in I} X_i$, and $a_i, b_i, p_i\colon X \longrightarrow (0,1]$. Suppose for every $i \in I$, $\Upsilon = (X_i, A_i, B_i, P_i)_{i\in I}$ satisfies the following conditions:*

(1) $(X_i, D_i; \Gamma_i)$ is a compact $L\Gamma$-space

(2) for every $x \in X, x \mapsto (A_{ix})_{a_i(x)}\colon X \longrightarrow 2^{X_i}$ and $x \mapsto (B_{ix})_{b_i(x)}\colon X \longrightarrow 2^{X_i}$ are compact and nonempty closed Γ_i-convex valued

(3) for every $x \in X, x \mapsto (P_{ix})_{p_i(x)}\colon X \longrightarrow 2^{X_i}$ is closed Γ_i-convex valued

(4) $E_i = \left\{x \in X\colon (A_{ix})_{a_i(x)} \cap (P_{ix})_{p_i(x)} \neq \varnothing\right\}$ is open in X

(5) for every $x \in X, x_i \notin (A_{ix})_{a_i(x)} \cap (P_{ix})_{p_i(x)}$

Then, for each $i \in I$, we can find an $\widehat{x} \in X$ satisfying $\widehat{x}_i \in (B_{i\widehat{x}})_{b_i(\widehat{x})}$ and $(A_{i\widehat{x}})_{a_i(\widehat{x})} \cap (P_{i\widehat{x}})_{p_i(\widehat{x})} = \varnothing$.

Proof. Let $X = \prod_{i\in I} X_i, D = \prod_{i\in I} D_i$, and $\Gamma(A) = \prod_{i\in I} \Gamma_i\ (\pi_i(A))$, where π_i is a projection of X onto X_i. By Lemma 2 in [23], we have that $(X, \mathcal{U}, \{\varphi_N\})$ is an $L\Gamma$-space. For each $i \in I$, $G_i\colon X \longrightarrow 2^{X_i}$ is defined as

$$G_i(x) = \begin{cases} (A_{ix})_{a_i(x)} \cap (P_{ix})_{p_i(x)}, & \text{if } x \in E_i, \\ (B_{ix})_{b_i(x)}, & \text{if } x \notin E_i. \end{cases} \tag{10}$$

From conditions (2) and (3) and Theorem 3.18 in [25], we have that $x \longrightarrow (A_{ix})_{a_i(x)} \cap (P_{ix})_{p_i(x)}$ is nonempty closed valued and compact upper semicontinuous. On the other hand, from conditions (2)–(4), Lemma 3 in [24], and Lemma 1 in [26], we have that G_i is nonempty closed Γ_i-convex valued and compact upper semicontinuous. From Lemma 2, for each $i \in I$, we can find an $\widehat{x} \in X$ satisfying $\widehat{x}_i \in G_i(\widehat{x})$. If, for some $j \in I, \widehat{x} \in E_j$, we obtain that $\widehat{x}_j \in (A_{j\widehat{x}})_{a_j(\widehat{x})} \cap (P_{j\widehat{x}})_{p_j(\widehat{x})}$. However, this is in contradiction with condition (5). Therefore, for each $i \in I, \widehat{x} \notin E_i$. By the definition of G_i, we have that for each $i \in I, \widehat{x}_i \in (B_{i\widehat{x}})_{b_i(\widehat{x})}$, and $(A_{i\widehat{x}})_{a_i(\widehat{x})} \cap (P_{i\widehat{x}})_{p_i(\widehat{x})} = \varnothing$. The proof is complete. □

Remark 2. Theorem 2 improves Theorem 2 in [14] and Theorem 2 in [15]. We also generalize the related results in [4] from generalized convex space to $L\Gamma$-space. Theorem 2 can be considered as an extended variant of Theorem 2 in [27] with respect to $L\Gamma$-spaces. We note that $L\Gamma$-spaces include a variety of topological spaces such as the LC-spaces and the LG-spaces (see [21, 22] and references therein).

3.2. Structural Stability and Robustness to Generalized Abstract Fuzzy Economies. Let $\Upsilon = (X_i, A_i, B_i, P_i)_{i\in I}$ be a generalized abstract fuzzy economic model satisfying all the conditions of Theorem 2. We introduce the definition $\Psi = \{\xi = \{G_i\}_{i\in I}\}$, where

$$G_i(x) = \begin{cases} (A_{ix})_{a_i(x)} \cap (P_{ix})_{p_i(x)}, & \text{if } x \in E_i, \\ (B_{ix})_{b_i(x)}, & \text{if } x \notin E_i. \end{cases} \tag{11}$$

By the proof of Theorem 2, we have that $G_i\colon X = \prod_{i\in I} X_i \longrightarrow 2^{X_i}$ is compact upper semicontinuous on X and there exists a point $x \in X$ such that $x_i \in G_i(x)$.

Let X_i be a metric space induced by a metric d_i. For each $\xi_1 = \{G_{1i}\}_{i\in I} \in \Psi$ and $\xi_2 = \{G_{2i}\}_{i\in I} \in \Psi$, we define

$$h_\varrho(\xi_1, \xi_2) = \sum_{i\in I} \sup_{x\in X} h_i(G_{1i}(x), G_{2i}(x)), \tag{12}$$

where h_i is the Hausdorff metric induced by d_i on X_i, for each $i \in I$.

Next, we consider the model $\Omega_0 = (\Psi, X, F, R)$, where $F(\xi, x) = G(x) = \prod_{i\in I} G_i(x)$, for all $\xi = \{G_i\}_{i\in I} \in \Psi$ and for any $x \in X$. Here, we denote $f\colon \Psi \longrightarrow 2^X$ by $f(\xi) = \{x \in X\colon x \in F(\xi, x)\} = \{x \in X\colon x_i \in G_i(x)\}$ and $R\colon \mathrm{Gragh}(f) \longrightarrow R^+$ is a rationality function, which is defined as

$$R(\xi, x) = \max_{i\in I} d_i(x_i, G_i(x)) = \max_{i\in I} \min_{y_i \in G_i(x)} d_i(x_i, y_i), \tag{13}$$

for any $x \in f(\xi)$. Here, for each $i \in I$, d_i is the distance on X_i.

For every $\xi \in \Psi$, the ϵ-equilibria set of the generalized abstract fuzzy model of economics Υ at ξ is defined as follows:

$$E(\xi, \varepsilon) = \{x \in f(\xi)\colon R(\xi, x) \leq \varepsilon\}. \tag{14}$$

We use $E(\xi)$ to denote all equilibria set of the generalized abstract fuzzy model of economics Υ at ξ as

$$E(\xi) = E(\xi, 0) = \{x \in f(\xi)\colon R(\xi, x) = 0\}. \tag{15}$$

We notice that for all $(\xi, \varepsilon) \in \Psi \times R^+$, $E(\xi, \varepsilon)$ is compact if R is lower semicontinuous. It follows from Theorem 1 that $E(\xi) \neq \varnothing$.

Obviously, if and only if for each $i \in I$, $x_i \in G_i(x)$, and $x \in E(\xi)$, $R(\xi, x) \geq 0$ and $R(\xi, x) = 0$.

Theorem 3. *Let $\overline{\Omega}_0 = \{\overline{\Psi}, \overline{X}, \overline{F}, \overline{R}\}$ be the extended model of Ω_0; if $\overline{\Omega}_0$ is structurally stable at $(\overline{\xi}, \varepsilon)$, then $\overline{\Omega}_0$ is robust to $(\overline{\xi}, \varepsilon)$-equilibria.*

Proof. First, we prove that (Ψ, ϱ) is a complete metric space. Let $\{\xi_m\}$ be any Cauchy sequence in Ψ. Consequently, for any $\varepsilon > 0$, we can find a positive integer $P(\varepsilon)$ such that

$$\varrho(\xi_m, \xi_p) = \sum_{i\in I} \sup_{x\in X} h_i(G_{mi}(x), G_{pi}(x)) < \varepsilon, \quad \forall m, p \geq P(\varepsilon). \tag{16}$$

Since X_i is compact, X_i is complete. As a result, $X = \prod_{i\in I} X_i$ is compact. Obviously, under the Hausdorff distance, the family of compact subsets of X_i is a complete metric space. We notice that $G_{mi}\colon X \longrightarrow 2^{X_i}$ is compact upper semicontinuous. Based on Proposition 3.1.11 in [25], for each $i \in I$, we can always find a compact set $G_i(x) \subset X_i$ satisfying $\lim_{p\longrightarrow\infty} G_{pi}(x) = G_i(x)$. From (16), we obtain that

$$\sum_{i\in I} \sup_{x\in X} h_i(G_{mi}(x), G_i(x)) \leq \varepsilon, \quad \forall m \geq P(\varepsilon). \tag{17}$$

Since $\xi_m = \{G_{mi}\}_{i\in I} \in \Psi$, we can always find an $x_m \in X$, such that $x_{mi} \in G_{mi}(x_m)$, for each $i \in I$. Because of the compactness of X, we can let $x_m \longrightarrow x$. Since G_i is upper semicontinuous on X, we can find a positive integer $m_0 \geq P(\varepsilon)$ satisfying

$$G_i(x_m) \subset U(\varepsilon, G_i(x)), \quad \forall m \geq m_0. \tag{18}$$

Therefore, we get

$$x_{mi} \in G_{mi}(x_m) \subset U(2\varepsilon, G_i(x_m)) \subset U(3\varepsilon, G_i(x)), \quad \forall m \geq m_0. \tag{19}$$

Let $m \longrightarrow \infty$, we thus have that $d_i(x_i, G_i(x)) \leq 3\varepsilon$. Because of the arbitrariness of ϵ, we obtain that $d_i(x_i, G_i(x)) = 0$ and as such $x_i \in G_i(x)$. That is to say, $\xi = \{G_i\}_{i\in I} \in \Psi$. Thus, (Ψ, ϱ) is a complete metric space.

In what follows, we aim to prove that $R(\xi, x)$ is lower semicontinuous at (ξ, x).

For every $\xi_n = \{G_{ni}\}_{i\in I} \in \Psi$ with $\varrho(\xi_n, \xi) \longrightarrow 0$, in which $\xi = \{G_i\}_{i\in I} \in \Psi$, and for any $x_n \in X$ with $x_n \longrightarrow x$, we obtain that

$$R(\xi_n, x_n) > R(\xi, x) - \varepsilon, \quad \forall \varepsilon > 0. \tag{20}$$

Since $G_i\colon X \longrightarrow 2^{X_i}$ is compact upper semicontinuous, it follows from Proposition 3.1.19 in [25] that $d_i(x_i, G_i(x)) = \min_{y_i\in G_i(x)} d_i(x_i, y_i)$ is a lower semicontinuous mapping at x_i. Hence, we can find a positive integer N_1 satisfying, for all $n \geq N_1$,

$$\min_{y_i\in G_i(x_n)} d_i(x_{ni}, y_i) > \min_{y_i\in G_i(x)} d_i(x_i, y_i) - \frac{\varepsilon}{2}, \quad \forall i \in I. \tag{21}$$

For any $n = 1, 2, \ldots$, since G_{ni} is compact, then we can find a $y_{ni} \in G_{ni}(x_n)$ satisfying

$$d_i(x_{ni}, y_{ni}) = \min_{y_i\in G_{ni}(x_n)} d_i(x_{ni}, y_i), \quad \forall i \in I. \tag{22}$$

From $h_i(G_{ni}(x_n), G_i(x_n)) \longrightarrow 0$ and $y_{ni} \in G_{ni}(x_n)$, there is always a positive integer N_2 such that, for all $n \geq N_2$, there exists $y'_{ni} \in G_i(x_n)$ with $d(y'_{ni}, y_{ni}) < (\varepsilon/2)$ for every $i \in I$. Let $N = \max\{N_1, N_2\}$. Then, for all $n \in N$, we have

$$\begin{aligned} R(\xi_n, x_n) &= \max_{i\in I} \min_{y_i\in G_{ni}(x_n)} d_i(x_{ni}, y_i) \\ &= \max_{i\in I} d_i(x_{ni}, y_{ni}) \\ &\geq \max_{i\in I} (d_i(x_{ni}, y'_{ni}) - d_i(y'_{ni}, y_{ni})) \\ &\geq \max_{i\in I} d_i(x_{ni}, y'_{ni}) - \max_{i\in I} d_i(y'_{ni}, y_{ni}) \\ &\geq \max_{i\in I} \min_{y_i\in G_i(x_n)} d_i(x_{ni}, y_i) - \frac{\varepsilon}{2} \\ &> \max_{i\in I} \min_{y_i\in G_i(x)} d_i(x_i, y_i) - \varepsilon \\ &= R(\xi, x) - \varepsilon. \end{aligned} \tag{23}$$

Now, we prove that $R(\xi, x)$ is lower semicontinuous at (ξ, x).

Consider the correspondence

$$f(\xi) = \{x \in X\colon x \in F(\xi, x)\} = \{x \in X\colon x_i \in G_i(x)\}. \tag{24}$$

It follows from Lemma 6 in [28] that $f\colon \Psi \longrightarrow 2^X$ is an upper semicontinuous mapping. Therefore, according to Theorem 2, we know that if $\overline{\Omega}_0$ is structurally stable at $(\overline{\xi}, \varepsilon)$, then $\overline{\Omega}_0$ is robust to $(\overline{\xi}, \varepsilon)$-equilibria. Thus, the proof is complete. □

Remark 3. Theorem 3 improves Theorem 2 of [2]. First, the compactness of Ψ is dropped. Second, f is upper semicontinuous weakened compared with the continuity. Third, F is lower semicontinuity weakened than the continuity. Compared with Theorem 2 in [4], we introduce a more general model in Theorem 3. The structural stability at ξ and robustness to ε-equilibria are extended to the structural stability at $(\overline{\xi}, \varepsilon)$ and the robustness to $(\overline{\xi}, \varepsilon)$-equilibria, respectively.

4. Conclusions

In this paper, we discuss the relationship between $(\overline{\xi}, \varepsilon)$-stability and $(\overline{\xi}, \varepsilon)$-robustness of $\overline{\Omega}$ using a lower semicontinuous rationality function. As an application, we introduce the model $\overline{\Omega}_0$ consisting of a category of the parameterized generalized abstract fuzzy economic model with related abstract rationality function. We prove that the model $\overline{\Omega}_0$ is structurally stable at $(\overline{\xi}, \varepsilon)$. Therefore, we can conclude the robustness of $\overline{\Omega}_0$ to $(\overline{\xi}, \varepsilon)$-equilibria. In short, our work generalizes the results in the extant literature.

For economic models, stability analysis is one of the most significant issues. Our assumptions and methods employed in this research can be adopted to solve other economic models. In summary, the results derived in this paper can help solve a variety of economic and financial problems. The conclusions drawn in this article are also helpful in solving optimal control problems, financial optimization problems, and Nash equilibrium problems. In our

future research, we will use the results obtained in this article to study various economic models.

Data Availability

No data were used to support this study.

Conflicts of Interest

The authors declare that they have no conflicts of interest regarding the publication of this paper.

Acknowledgments

This work was supported by the National Natural Science Foundation of China (11401484) and the Fundamental Research Funds for the Central Universities of China (JBK2102011). This research was also supported by Shanghai Social Sciences Planning Project (2020BJB013).

References

[1] K. J. Arrow and G. Debreu, "Existence of an equilibrium for a competitive economy," *Econometrica*, vol. 22, pp. 265–290, 1952.

[2] L. Anderini and D. Canning, "Structural stability implies robustness to bounded rationality," *Journal of Economic Theory*, vol. 101, pp. 395–442, 2001.

[3] C. Yu and J. Yu, "On structural stability and robustness to bounded rationality," *Nonlinear Analysis: Theory, Methods & Applications*, vol. 65, no. 3, pp. 583–592, 2006.

[4] L. Wang, Y. Je Cho, and N. J. Huang, "The robustness of generalized abstract fuzzy economies in generalized convex spaces," *Fuzzy Sets and Systems*, vol. 176, no. 1, pp. 56–63, 2011.

[5] Y. Miyazaki and H. Azuma, "(λ, ϵ)-stable model and essential equilibria," *Mathematical Social Sciences*, vol. 65, no. 2, pp. 85–91, 2013.

[6] A. Loi and S. Matta, "Increasing complexity in structurally stable models: an application to a pure exchange economy," *Journal of Mathematical Economics*, vol. 57, pp. 20–24, 2015.

[7] A. Al-khedhair, "Dynamics of a Cournot duopoly game with a generalized bounded rationality," *Complexity*, vol. 2020, Article ID 8903183, 10 pages, 2020.

[8] Z. Feng and C. Tan, "Subgame perfect equilibrium in the rubinstein bargaining game with loss aversion," *Complexity*, vol. 2019, Article ID 5108652, 23 pages, 2019.

[9] L. Liu, L. Zhang, S. Zhang, and S. Cao, "Multi-UUV cooperative dynamic maneuver decision-making algorithm using intuitionistic fuzzy game theory," *Complexity*, vol. 2020, Article ID 2815258, 11 pages, 2020.

[10] C. Oriol and M. Richard, "On the existence of Nash equilibrium in bayesian games," *Mathematics of Operations Research*, vol. 43, pp. 100–129, 2018.

[11] J. Zhang and X. Xi, "Complexity analysis of a 3-player game with bounded rationality participating in nitrogen emission reduction," *Complexity*, vol. 2020, pp. 2069614–16, 2020.

[12] L. A. Zadeh, "Fuzzy sets," *Information and Control*, vol. 8, no. 3, pp. 338–353, 1965.

[13] W. K. Kim and K. H. Lee, "Fuzzy fixed point and existence of equilibria of fuzzy games," *Journal of Fuzzy Mathematics*, vol. 6, pp. 193–202, 1998.

[14] N.-J. Huang, "A new equilibrium existence theorem for abstract fuzzy economies," *Applied Mathematics Letters*, vol. 12, no. 5, pp. 1–5, 1999.

[15] N.-J. Huang, "Existence of equilibrium for generalized abstract fuzzy economies," *Fuzzy Sets and Systems*, vol. 117, no. 1, pp. 151–156, 2001.

[16] M. Patriche, "Bayesian abstract economy with a measure space of agent," *Abstract and Applied Analysis*, vol. 2009, Article ID 523619, 11 pages, 2009.

[17] M. Patriche, "Bayesian abstract fuzzy economies, random quasi-variational inequalities with random fuzzy mappings and random fixed point theorems," *Fuzzy Sets and Systems*, vol. 245, pp. 125–136, 2014.

[18] C. Cui, Z. Feng, and C. Tan, "Credibilistic loss aversion Nash equilibrium for bimatrix games with triangular fuzzy payoffs," *Complexity*, vol. 2018, Article ID 7143586, 16 pages, 2018.

[19] J. Henrikson, "Completeness and total boundedness of the Hausdorff metric," *MIT Journal of Undergraduate Mathematics*, vol. 1, pp. 69–80, 1999.

[20] J. Yu, "Essential equilibria of n-person noncooperative games," *Journal of Mathematical Economics*, vol. 31, no. 3, pp. 361–372, 1999.

[21] S. Park, "On generalizations of the KKM principle on abstract convex spaces," *Nonlinear Analysis Forum*, vol. 11, pp. 67–77, 2006.

[22] S. Park, "Fixed point theory of multimaps in abstract convex uniform spaces," *Nonlinear Analysis: Theory, Methods & Applications*, vol. 71, no. 7-8, pp. 2468–2480, 2009.

[23] M. G. Yang, J. P. Xu, and N. J. Huang, "Systems of generalized quasivariational inclusion problems with applications in $L\Gamma$-spaces," *Fixed Point Theory and Applications*, vol. 2011, Article ID 561573, 12 pages, 2011.

[24] K. Fan, "Fixed-points and minimax theorems in locally convex topological linear spaces," *Proceedings of the National Academy of Sciences of the USA*, vol. 38, pp. 131–136, 1952.

[25] J. P. Aubin and I. Ekeland, *Applied Nonlinear Analysis*, Wiley, New York,NY, USA, 1984.

[26] X. Z. Yuan, *KKM Theory and Applications in Nonlinear Analysis*, Marcel Dekker, New York, NY, USA, 1999.

[27] X. P. Ding, "The generalized game and the system of generalized vector quasi-equilibrium problems in locally -uniform spaces," *Nonlinear Analysis: Theory, Methods & Applications*, vol. 68, no. 4, pp. 1028–1036, 2008.

[28] K.-K. Tan, J. Yu, and X.-Z. Yuan, "The stability of coincident points for multivalued mappings," *Nonlinear Analysis: Theory, Methods & Applications*, vol. 25, no. 2, pp. 163–168, 1995.

Hindawi
Complexity
Volume 2021, Article ID 6401231, 8 pages
https://doi.org/10.1155/2021/6401231

Research Article

Aperiodic Sampled-Data Control for Chaotic System Based on Takagi–Sugeno Fuzzy Model

Minjie Zheng, Shenhua Yang, and Lina Li

Navigation College, Jimei University, Jimei, Xiamen 361021, China

Correspondence should be addressed to Shenhua Yang; yangshh@163.com

Received 29 July 2020; Revised 9 December 2020; Accepted 16 April 2021; Published 27 April 2021

Academic Editor: Quanxin Zhu

This paper investigates the aperiodic sampled-data control for a chaotic system. Firstly, Takagi–Sugeno (T-S) fuzzy models for the chaotic systems are established. The lower and upper bounds of the sampling period are taken into consideration. Then, the criteria for mean square exponential stability analysis and aperiodic sampled-data controller synthesis are provided by means of linear matrix inequalities. And the real sampling patterns can be fully captured by constructing suitable Lyapunov functions. Finally, an illustrative example shows that the proposed method is effective to guarantee that the system's states are stable with aperiodic sampled data.

1. Introduction

Recently, the chaotic system has gradually become one of the hot topics in the field of nonlinear system. The chaotic system has wide application in several areas such as information processing, chemical reaction, power conversion, secure communication biological system, and other aspects. Thus, the control problem for the chaotic system has attracted considerable attention (see [1, 2]). Among these references, fuzzy control is an effective method to deal with chaotic systems, especially when the plant's knowledge is incomplete or the action cannot be accurately controlled. So far, many scholars have focused on the fuzzy chaotic systems (see [3–8]), and many methods have been developed, such as robust control [9], adaptive control [10], pulse control [11], and sliding mode control [12].

On the other hand, the chaotic system can be described with T-S fuzzy models (TSFM) [13–15], which can be analyzed by using mature linear system theory. Recently, considerable references have been reported about chaotic system with TSFM. In [16], the issue about asymptotic stability for the chaotic system with TSFM is studied, and an impulsive controller is designed. In [17], an adaptive synchronization method for the chaotic system with TSFM is proposed for solving the issue of parameter mismatch. In [18], the predictive control and synchronization for the chaotic system with TSFM is discussed. And the identical satellite systems are synchronized by the predictive control technique.

In the past few years, the sampled-data system has become an important topic because modern control systems widely used the digital computers to control continuous-time systems (see [19–21]). Compared with the analog controller, the digital controller has better reliability, lower installation, and easier maintenance, which are the advantages of the systems. The outstanding feature of the systems is the coexistence of continuous signal and discrete signal, which is difficult to be analyzed and designed. Until now, the system has attracted much attention of scholars, and considerable results have been reported for that system (see [22–25]). Besides, several sampled-data control approaches such as lifting technology and input delay approach have been used in the systems including many real systems such as the near-space hypersonic vehicles, autonomous airships, unmanned marine vehicles, and so on. Recently, the fuzzy sampled-data chaotic system has attracted considerable attention [26]. In [27], by adaptive event-triggered scheme, the issue about fault-tolerant synchronization for chaotic system is discussed. In [28], a new Lyapunov–Krasovskii function (LKF) method is introduced for the chaotic systems

with TSFM, and a sampled-data controller is produced to obtain a long sampling period. In [29], the exponential stabilization problem of the fuzzy semi-Markov chaotic system is discussed by establishing a new zero-value equation. In [30], the stochastic sampled-data controllers for the chaotic system are designed, and an improved LKF is constructed to fully exploit the sampling characteristics.

It is noted that the sampling periods of the existing references for the chaotic system are ideally assumed to be constant. However, the sampling period is aperiodic due to the aging of sensors and the interference of noise environment. Hence, to consider nonperiodicity sampling for designing sampled-data controller is practically significant. Besides, in these papers, the lower bound of the sampling period is often considered to be 0 which will lead to considerable conservatism because the value of the variable period may change in a range. Therefore, the lower bound and upper bound of the sampling period should be both considered. Finally, LKF has room for improving to fully capture the real sampling patterns.

Motivated by the above, in this paper, the issue about aperiodic fuzzy sampled-data control of the chaotic system is discussed. Firstly, TSFM is represented for chaotic systems. Then, both lower and upper bounds of the variable period are taken into consideration. In terms of LMI approach, Lyapunov theorem is involved for the stability analysis which can fully capture the sampling patterns. Then, the designed method of fuzzy sampled-data controller is introduced. Finally, a simulation of a chaotic system is conducted to verify the effectiveness of the given strategy.

Notations: Sym$\{M\}$ represents $M + M^T$. " $*$ " represents the symmetric term of a matrix.

2. Problem Formulation

Consider a chaotic system as follows:

$$\dot{x}(t) = f(x(t), u(t)), \tag{1}$$

where $x(t) \in R^n$ denotes the state vector, $u(t) \in R^m$ denotes the input vector, and $f(x(t))$ is a nonlinear function which satisfies $f(0,0) = 0$. Based on the TSFM, system (1) can be described as follows.

Mode Rule i: IF $z_1(t)$is χ_{i1}, and $\cdots z_n(t)$ is χ_{in}, THEN

$$\dot{x}(t) = A_i x(t) + B_i u(t), \quad i = 1, 2, \ldots, r, \tag{2}$$

where $\chi_{i1}, \chi_{i2}, \ldots, \chi_{in}$ denote the fuzzy sets, r denotes the number of rules, $z_1(t), z_2(t), \ldots, z_n(t)$ represent premise variables, and A_i, B_i denote the appropriated dimensioned matrices. Similar to [9], fuzzy system (2) is given by

$$\dot{x}(t) = \sum_{i=1}^{r} \mu_i(z(t))\left[A_i x(t) + B_i u(t)\right], \tag{3}$$

where

$$\begin{aligned} \mu_i(z(t)) &= \frac{v_i(z(t))}{\sum_{i=1}^{r} v_i(z(t))} \geq 0, \\ v_i(z(t)) &= \prod_{j=1}^{n} \chi_{ij}\left(z_j(t)\right), \\ \sum_{i=1}^{r} \mu_i(z(t)) &= 1, \quad z(t) = \left[z_1(t), z_2(t), \ldots, z_n(t)\right], \end{aligned} \tag{4}$$

with $\chi_{ij}(z_j(t))$ representing the membership grade of $z_j(t)$.

Assume that the state variables of chaotic systems are measured in $0 = t_0 < t_1 < t_2 < \cdots < t_k < \cdots \lim_{k\to\infty} t_k = +\infty$, where $t_k, k = 1, 2, \ldots$ is sampling instant. Moreover, the sampling period is aperiodic and satisfies

$$d_1 \leq t_{k+1} - t_k = d_k \leq d_2, \quad \forall k \geq 0, d_1 \geq 0, d_2 > 0. \tag{5}$$

The framework of the sampled-data chaotic system is given in Figure 1.

Then, based on parallel distributed compensation, the fuzzy sampled-data controller is designed.

Controller Rule i: IF $z_1(t)$ is χ_{i1}, and $\ldots z_n(t)$ is χ_{in}, THEN

$$u(t) = K_i x(t_k), \quad t_k \leq t < t_{k+1}, \tag{6}$$

where K is a controller matrix. Then, the overall fuzzy model is represented as follows:

$$u(t) = \sum_{j=1}^{r} \mu_j(z(t)) K_j x(t_k), \quad t_k \leq t < t_{k+1}, k = 0, 1, 2, \ldots. \tag{7}$$

Substituting (7) into equation (3), we obtain

$$\dot{x}(t) = \sum_{i=1}^{r}\sum_{j=1}^{r} \mu_i(z(t))\mu_j(z(t))\left[A_i x(t) + B_i K_j x(t_k)\right]. \tag{8}$$

The paper's purpose is designing a fuzzy sampled-data controller (FSDC) to satisfy that

(1) System (8) is mean square exponentially stable.

(2) A longer sampling period is achieved.

3. Main Results

In this section, the sufficient stability criteria for system (8) are exhibited by establishing LKF firstly. Then, the FSDC will be provided to analyze the stability criteria.

Theorem 1. *For scales $\varepsilon_1, \varepsilon_2$ and $d_2 > d_1 \geq 0$, system (8) is mean square exponentially stable, if there exist matrices $Y_{11}, Y_{22}, M, P > 0$, $\begin{bmatrix} Q_{11} & Q_{12} \\ * & Q_{22} \end{bmatrix} > 0$, such that*

$$\tilde{\Psi}_1^{ij}(d) = \Psi_1^{ij} + de^{-2\lambda d_2} I_3 Q_{22} I_3^T + dY_1 < 0, \tag{9}$$

$$\tilde{\Psi}_2^{ij}(d) = \begin{bmatrix} \Psi_1^{ij} & -de^{-2\lambda d_2}\Psi_3 \\ * & -de^{-2\lambda d_2} Q_{11} \end{bmatrix} < 0, \quad d \in \{d_1, d_2\}, \tag{10}$$

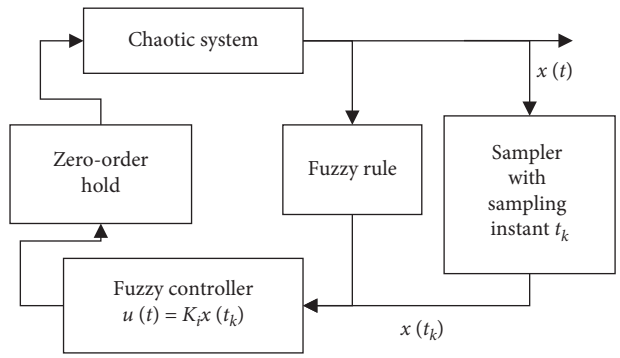

Figure 1: The framework of the sampled-data chaotic system.

$$\Theta = \begin{bmatrix} P + d_2\left(Y_{11} + Y_{11}^T\right) & -d_2\left(Y_{11} + Y_{22}\right) \\ * & d_2\left(Y_{22} + Y_{22}^T\right) \end{bmatrix} > 0, \tag{11}$$

where

$$\begin{aligned}
\Psi_1^{ij} &= \mathrm{Sym}\Big\{I_1 P I_2^T + \lambda I_1 P I_1^T - I_1 Y_{11} I_1^T + I_1 Y_{11} I_3^T + I_1 Y_{22} I_3^T - \varepsilon_1 I_1 M A_i I_1^T - I_1 \overline{A}_i^T M^T I_2^T - \varepsilon_1 I_1 M \overline{B}_i \theta K_j I_3^T \\
&\quad + I_2 M I_2^T - I_3 Y_{22} I_3^T + \varepsilon_1 I_1 M I_2^T - \varepsilon_1 I_1 \overline{A}_i^T M^T I_3^T - I_2 M \overline{B}_i \theta K_j I_3^T + \varepsilon_2 I_2 M^T I_3^T - \varepsilon_1 I_3 M \overline{B}_i \theta K_j I_3^T\Big\} + I - \mathrm{d}e^{-2\lambda d_2} I_3 Q_{22} I_3^T, \\
\Upsilon_1 &= \mathrm{Sym}\Big\{I_1\left(Y_{11} + Y_{11}^T\right) I_2^T - I_2\left(Y_{11} + Y_{22}\right) I_3^T + I_2 Q_{11} I_2^T\Big\} + I_2 Q_{12} I_3^T + \lambda I_1\left(Y_{11} + Y_{11}^T\right) I_1^T \\
&\quad - \lambda I_1\left(Y_{11} + Y_{22}\right) I_3^T + I_3 Q_{22} I_3^T + \lambda I_3\left(Y_{22} + Y_{22}^T\right) I_3^T\Big\}, \\
\Psi_3 &= \begin{bmatrix} 0 & 0 & Q_{12} \end{bmatrix}^T.
\end{aligned} \tag{12}$$

Proof. The novel LKF is proposed:

$$\begin{aligned}
V(t) &= \sum_{i=1}^{3} V_i(t), \quad t \in [t_k, t_{k+1}), \\
V_1(t) &= x(t)^T P x(t), \\
V_2(t) &= h_2(t) \int_{t_k}^{t} e^{2\lambda(s-t)} \begin{bmatrix} \dot{x}(s) \\ x(t_k) \end{bmatrix}^T \begin{bmatrix} Q_{11} & Q_{12} \\ * & Q_{22} \end{bmatrix} \begin{bmatrix} \dot{x}(s) \\ x(t_k) \end{bmatrix} \mathrm{d}s, \\
V_3(t) &= h_2(t) \begin{bmatrix} x(t) \\ x(t_k) \end{bmatrix}^T \begin{bmatrix} Y_{11} + Y_{11}^T & -Y_{11} - Y_{22} \\ * & Y_{22} + Y_{22}^T \end{bmatrix} \begin{bmatrix} x(t) \\ x(t_k) \end{bmatrix}.
\end{aligned} \tag{13}$$

It is noted that $\lim_{t \longrightarrow t_k^-} V_i(t) = \lim_{t \longrightarrow t_k^+} V_i(t) = V_i(t) = 0$, $i = 2, 3$, and hence $V(t)$is continuous on $[0, \infty)$. To reduce the conservatism, the matrix in $V_3(t)$ is free; then, according to condition (11), it can be obtained that

$$\begin{aligned}
V_1(t) + V_3(t) &= \frac{d_2 - h_2(t)}{d_2} x^T(t) P x(t) + \frac{h_2(t)}{d_2} x^T(t) P x(t) + \frac{h_2(t)}{d_2} d_2 \begin{bmatrix} x(t) \\ x(t_k) \end{bmatrix}^T \begin{bmatrix} Y_{11} + Y_{11}^T & -Y_{11} - Y_{22} \\ * & Y_{22} + Y_{22}^T \end{bmatrix} \begin{bmatrix} \dot{x}(t) \\ x(t_k) \end{bmatrix} \\
&= \frac{d_2 - h_2(t)}{d_2} x^T(t) P x(t) + \frac{h_2(t)}{d_2} \begin{bmatrix} x(t) \\ x(t_k) \end{bmatrix}^T \Theta \begin{bmatrix} \dot{x}(t) \\ x(t_k) \end{bmatrix} \geq 0.
\end{aligned} \tag{14}$$

Taking the derivative of $V(t)$, the following can be obtained:

$$\begin{aligned}
&\dot{V}_1(t)+2\lambda V_1(t)=2x^T(t)P\dot{x}(t)+2\lambda x^T(t)Px(t),\\
&\dot{V}_2(t)+2\lambda V_2(t)=h_2(t)\begin{bmatrix}\dot{x}(t)\\ x(t_k)\end{bmatrix}^T\begin{bmatrix}Q_{11} & Q_{12}\\ * & Q_{22}\end{bmatrix}\begin{bmatrix}\dot{x}(t)\\ x(t_k)\end{bmatrix}-e^{-2\lambda d_2}\int_{t_k}^{t}\begin{bmatrix}\dot{x}(s)\\ x(t_k)\end{bmatrix}^T\begin{bmatrix}Q_{11} & Q_{12}\\ * & Q_{22}\end{bmatrix}\begin{bmatrix}\dot{x}(s)\\ x(t_k)\end{bmatrix}\mathrm{d}s,\\
&\dot{V}_3(t)+2\lambda V_3(t)=2h_2(t)\begin{bmatrix}x(t)\\ x(t_k)\end{bmatrix}^T\begin{bmatrix}Y_{11}+Y_{11}^T & -Y_{11}-Y_{22}\\ * & Y_{22}+Y_{22}^T\end{bmatrix}\begin{bmatrix}\dot{x}(t)\\ 0\end{bmatrix}-\begin{bmatrix}x(t)\\ x(t_k)\end{bmatrix}^T\begin{bmatrix}Y_{11}+Y_{11}^T & -Y_{11}-Y_{22}\\ * & Y_{22}+Y_{22}^T\end{bmatrix}\begin{bmatrix}x(t)\\ x(t_k)\end{bmatrix}\\
&\qquad+2\lambda h_2(t)\begin{bmatrix}x(t)\\ x(t_k)\end{bmatrix}^T\begin{bmatrix}Y_{11}+Y_{11}^T & -Y_{11}-Y_{22}\\ * & Y_{22}+Y_{22}^T\end{bmatrix}\begin{bmatrix}x(t)\\ x(t_k)\end{bmatrix}.
\end{aligned}\tag{15}$$

For any free matrix M and scalars $\varepsilon_1, \varepsilon_2$, we can obtain the equation as follows:

$$2\sum_{i=1}^{3}\sum_{j=1}^{3}\mu_i(z(t))\mu_j(z(t))\left[\varepsilon_1 x^T(t)M+\dot{x}^T(t)M+\varepsilon_2 x^T(t_k)M\right]\times\left[\dot{x}(t)-\left(\overline{A}_i x(t)+\overline{B}_i K_j x(t_k)\right)\right]=0.\tag{16}$$

Then, combining (15) and (16), we have

$$\dot{V}(t)+2\lambda V(t)=2\sum_{i=1}^{3}\sum_{j=1}^{3}\mu_i(z(t))\mu_j(z(t))\left[\frac{h_2(t)}{\mathrm{d}_k}\zeta^T(t)\widetilde{\Psi}_1^{ij}(\mathrm{d}_k)\zeta(t)\frac{1}{\mathrm{d}_k}\int_{t_k}^{t}\zeta^T(t,s)\widetilde{\Psi}_2^{ij}(\mathrm{d}_k)\zeta(t,s)\mathrm{d}s\right],\tag{17}$$

where

$$\begin{aligned}
\zeta(t)&=\left[x^T(t)\ \ \dot{x}^T(t)\ \ x^T(t_k)\right]^T,\\
\zeta(t,s)&=\left[x^T(t)\ \ \dot{x}^T(t)\ \ x^T(t_k)\ \ \dot{x}^T(s)\right]^T.
\end{aligned}\tag{18}$$

From (9) and (10), the following can be obtained:

$$\begin{aligned}
\widetilde{\Psi}_1^{ij}(d_k)&=\frac{d_k-d_1}{d_2-d_1}\widetilde{\Psi}_1^{ij}(d_2)+\frac{d_2-d_k}{d_2-d_1}\widetilde{\Psi}_1^{ij}(d_1)<0,\\
\widetilde{\Psi}_2^{ij}(d_k)&=\frac{d_k-d_1}{d_2-d_1}\widetilde{\Psi}_2^{ij}(d_2)+\frac{d_2-d_k}{d_2-d_1}\widetilde{\Psi}_2^{ij}(d_1)<0,
\end{aligned}\tag{19}$$

which implies that

$$\dot{V}(t)+2\lambda V(t)<0,\tag{20}$$

and then we have

$$\begin{aligned}
\lambda_{\min}(P)\left\{\|x(t)\|^2\right\}&\le\{V(t)\}<e^{-2\lambda(t-t_k)}\{V(t_k)\}\\
&<e^{-2\lambda(t-t_{k-1})}\{V(t_{k-1})\}<\cdots<e^{-2\lambda t}\{V(0)\}\\
&\le\lambda_{\max}(P)e^{-2\lambda t}\left\|x(t_0)\right\|^2.
\end{aligned}\tag{21}$$

Then

$$\{\|x(t)\|\}\le\left(\frac{\sqrt{\lambda_{\max}(P)}}{\sqrt{\lambda_{\min}(P)}}\right)e^{-\lambda t}\left\|x(t_0)\right\|,\tag{22}$$

which implies that system (8) is mean square exponentially stable. This completed the proof. □

Remark 1. The mean square exponential stability criteria for system (8) are introduced in Theorem 1. To fully characterize the sampling pattern, a suitable time-dependent LKF (11) is constructed and a novel quadratic function$V_3(t)$ is added in LKF (11).

Remark 2. For the purpose of reducing the conservatism, more relaxed constraint matrices are introduced in LKF (13). The matrices are not required to be positive, which can effectively reduce conservatism.

Furthermore, the sampled-data controller (7) will be designed for stabilizing system (8) based on the following theorems.

Theorem 2. *For scales $\varepsilon_1, \varepsilon_2$ and $d_2>d_1\ge 0$, system (8) is mean square exponentially stable, if there exist matrices $\overline{Y}_{11}, \overline{Y}_{22}, \overline{M}, \overline{P}>0$, $\begin{bmatrix}\overline{Q}_{11} & \overline{Q}_{12}\\ * & \overline{Q}_{22}\end{bmatrix}>0$, satisfying*

$$\overline{\Psi}_1^{ij}(d) = \begin{bmatrix} \overline{\Psi}_1^{ij} + de^{-2\lambda d_2} I_3 \overline{Q}_{22} I_3^T + d\overline{Y}_1 & \overline{\Psi}_4 \\ * & -I \end{bmatrix} < 0, \quad (23)$$

$$\overline{\Psi}_2^{ij}(d) = \begin{bmatrix} \overline{\Psi}_1^{ij} & -de^{-2\lambda d_2}\overline{\Psi}_3 & \overline{\Psi}_4 \\ * & -de^{-2\lambda d_2}\overline{Q}_{11} & 0 \\ * & * & -I \end{bmatrix} < 0, \quad d \in \{d_1, d_2\}, \quad (24)$$

$$\overline{\Theta} = \begin{bmatrix} \overline{P} + d_2\left(\overline{Y}_{11} + \overline{Y}_{11}^T\right) & -d_2\left(\overline{Y}_{11} + \overline{Y}_{22}\right) \\ * & d_2\left(\overline{Y}_{22} + \overline{Y}_{22}^T\right) \end{bmatrix} > 0, \quad (25)$$

where

$$\begin{aligned}
\overline{\Psi}_1^{ij} &= \mathrm{Sym}\Big\{ I_1\overline{P}I_2^T + \lambda I_1\overline{P}I_1^T - I_1\overline{Y}_{11}I_1^T + I_1\overline{Y}_{11}I_3^T + I_1\overline{Y}_{22}I_3^T - \varepsilon_1 I_1\overline{A}_i\overline{M}I_1^T - I_1\overline{M}\overline{A}_i^T I_2^T \\
&\quad - \varepsilon_1 I_1\overline{B}_i\theta\overline{K}_j I_3^T + I_2\overline{M}I_2^T - I_3\overline{Y}_{22}I_3^T + \varepsilon_1 I_1\overline{M}I_2^T - \varepsilon_1 I_1\overline{M}\overline{A}_i^T I_3^T - I_2\overline{B}_i\theta\overline{K}_j I_3^T + \varepsilon_2 I_2\overline{M}^T I_3^T - \varepsilon_1 I_3\overline{B}_i\theta\overline{K}_j I_3^T \Big\} - \mathrm{d}e^{-2\lambda d_2} I_3\overline{Q}_{22}I_3^T, \\
\overline{Y}_1 &= \mathrm{Sym} I_1\Big\{\left(\overline{Y}_{11} + \overline{Y}_{11}^T\right)I_2^T - I_2\left(\overline{Y}_{11} + \overline{Y}_{22}\right)I_3^T + I_2\overline{Q}_{11}I_2^T + I_2\overline{Q}_{12}I_3^T + \lambda I_1\left(\overline{Y}_{11} + \overline{Y}_{11}^T\right)I_1^T \\
&\quad - \lambda I_1\left(\overline{Y}_{11} + \overline{Y}_{22}\right)I_3^T + I_3\overline{Q}_{22}I_3^T + \lambda I_3\left(\overline{Y}_{22} + \overline{Y}_{22}^T\right)I_3^T\Big\}, \\
\overline{\Psi}_3 &= \begin{bmatrix} 0 & 0 & \overline{Q}_{12} \end{bmatrix}^T, \\
\overline{\Psi}_4 &= \begin{bmatrix} \overline{M}^T & 0 & 0 \end{bmatrix}^T.
\end{aligned} \quad (26)$$

Then, the controller gain matrix Kcan be obtained as follows:

$$K = \overline{K}\overline{M}^{-T}. \quad (27)$$

Proof. Let

$$\begin{aligned}
\chi_1 &= \overline{M}, \\
\chi_2 &= \mathrm{diag}\{\overline{M}, \overline{M}\}, \\
\chi_3 &= \mathrm{diag}\{\chi_2, \overline{M}, I\}.
\end{aligned} \quad (28)$$

Define

$$\begin{aligned}
\overline{M} &= M^{-1}, \\
\overline{P} &= \overline{M}P\overline{M}^T, \\
Q_{11} &= \overline{M}Q_{11}\overline{M}^T, \\
Q_{12} &= \overline{M}Q_{12}\overline{M}^T, \\
Q_{22} &= \overline{M}Q_{22}\overline{M}^T, \\
Y_{11} &= \overline{M}Y_{11}\overline{M}^T, \\
Y_{22} &= \overline{M}Y_{22}\overline{M}^T, \\
\overline{K} &= K\overline{M}^T.
\end{aligned} \quad (29)$$

Pre- and post-multiply (9)–(11) by χ_1, χ_2, and $\chi_3$respectively; then, according to Schur complement, (23)–(25) can be obtained. This completed the proof. □

Remark 3. Note that the lower and upper bounds of the variable period are both considered in Theorem 1. If $d_1 = d_2 = d$, the periodic sampled-data issue for chaotic system can be solved, and the sampling period will reduce to be constant like [31], which have strict limitations on the lower bound of the delay and it will lead to considerable conservatism. So, the result in Theorem 1 covers [31] as a special case and has more significance than [31].

4. Numerical Examples

In the section, a simulation example for a chaotic system will be used to verify the effectiveness of given methods.

Consider a chaotic system as follows [15]:

$$\begin{cases} \dot{x}_1(t) = -ax_1(t) + ax_2(t), \\ \dot{x}_2(t) = cx_1(t) - x_2(t) - x_1(t)x_3(t) + u_1(t), \\ \dot{x}_3(t) = x_1(t)x_2(t) - bx_3(t) + u_2(t), \end{cases} \quad (30)$$

where

$$\begin{aligned} a &= 10, \\ b &= \frac{8}{3}, \\ c &= 28. \end{aligned} \quad (31)$$

Assume that $x_1(t) \in [m_1, m_2], \dot{x}_1(t) \in [-5, 5]$. According to [15], system (30) is represented with TSFM as follows.

Mode rule 1: IF $x_1(t)$ is ω_1, THEN

$$\dot{x}(t) = A_1x(t) + B_1u(t). \quad (32)$$

Mode rule 2: IF $x_1(t)$ is ω_2, THEN

$$\dot{x}(t) = A_2x(t) + B_2u(t), \quad (33)$$

where

$$A_1 = \begin{bmatrix} -a & a & 0 \\ c & -1 & m_1 \\ 0 & -m_1 & -b \end{bmatrix},$$
$$A_2 = \begin{bmatrix} -a & a & 0 \\ c & -1 & m_2 \\ 0 & -m_2 & -b \end{bmatrix}, \quad (34)$$
$$B_1 = B_2 = \begin{bmatrix} 0 & 0 \\ 1 & 0 \\ 0 & 1 \end{bmatrix}.$$

Then, the membership functions are

$$\mu_1(x(t)) = \frac{x_1(t) - m_1}{m_2 - m_1},$$
$$\mu_2(x_1(t)) = \frac{-x_1(t) - m_2}{m_2 - m_1}, \quad (35)$$

and the trajectories of system (30) are exhibited in Figure 2.

Let $m_1 = -25, m_2 = 25$. Firstly, we compare the results in Theorem 2 with the references which use different sampled-data control methods for chaotic systems. We suppose that $\tau_m = \tau_M$ and choose the same parameters; then, the maximum sampling period τ_M obtained by different references is shown in Table 1. It is obvious that Theorem 2 has longer sampling period than that in [15, 28, 31], which improves about 131.2%, 68.1%, and 19.35%, respectively. Hence, the result in the paper can reduce the conservatism to some extent. Besides, the lower and upper bounds of the sampling period are both considered in the paper, which has more significance than the previous work.

Then, we verify the effectiveness of the given method. The initial state is $x(t) = [-5 \;\; 3 \;\; 6]$. Assuming the sampling interval $\tau_m = 0.6$and $\varepsilon_1 = 1, \varepsilon_2 = 0.01$, then the maximum upper bound of sampling period is obtained as $\tau_M = 1.33$ by Theorem 2. Then, the related matrices by solving conditions (23)–(25) are obtained as

$$\overline{K}_1 = 10^{-9} \times [0.0028 \;\; 0.2369 \;\; 0.0174],$$
$$\overline{K}_2 = 10^{-9} \times [0.0028 \;\; 0.2369 \;\; 0.0174],$$
$$\overline{M} = 10^{-9} \times \begin{bmatrix} 0.3904 & 0.0219 & -0.0005 \\ -0.6132 & 0.1233 & 0.0023 \\ 0.0083 & -0.1864 & 0.0007 \end{bmatrix}. \quad (36)$$

Then, from (27), we can obtain the controller gain matrix.

$$K_1 = \overline{K}_1 M^{-T} = [13.5097 \;\; 8.6778 \;\; 6.0571],$$
$$K_2 = \overline{K}_2 M^{-T} = [13.5093 \;\; 8.6776 \;\; 6.0569]. \quad (37)$$

Under controller (37), the responses of the state are shown in Figures 3–5 , which indicate that the states are stable in a short time. It is easy to know that the designed FSDC achieves system's stabilization successfully, and a longer sampling period is obtained.

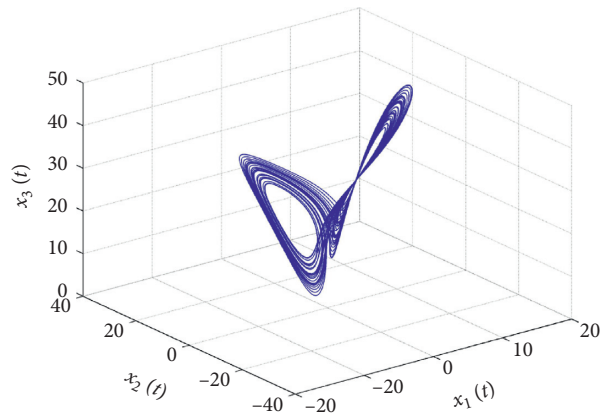

Figure 2: Trajectory of the chaotic system.

Table 1: The maximum upper bound for τ_M.

Method	[28]	[31]	[15]	Theorem 2
τ_M	0.0016	0.0022	0.0031	0.0037

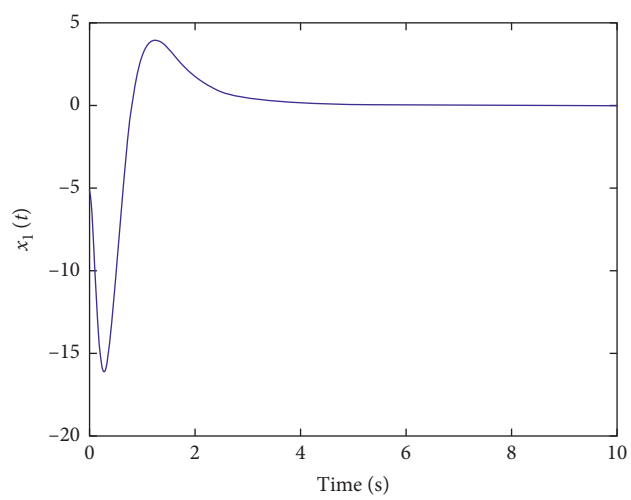

Figure 3: Responses of $x_1(t)$.

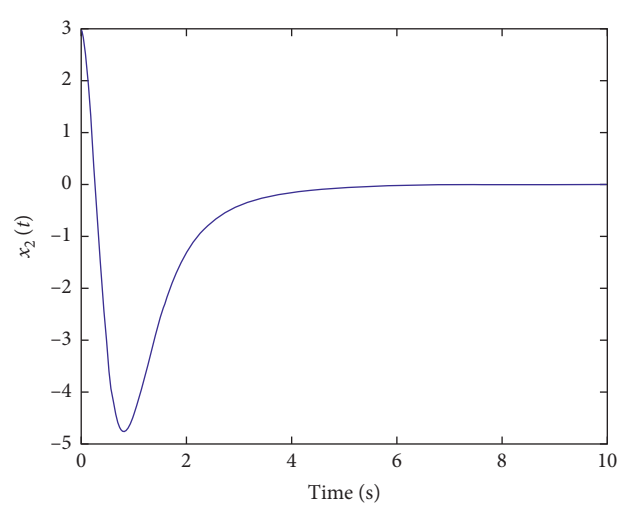

Figure 4: Responses of $x_2(t)$.

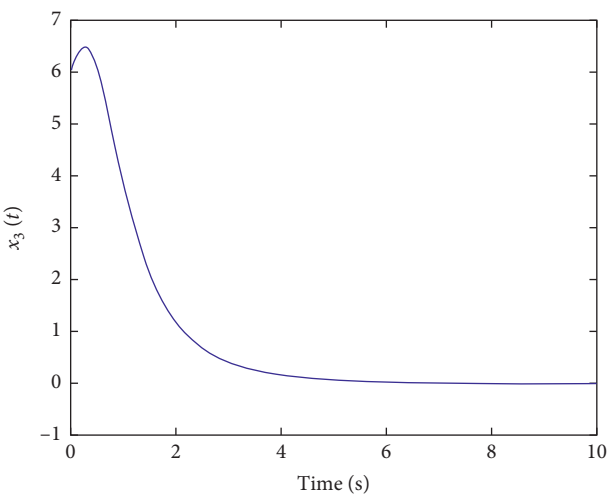

Figure 5: Responses of $x_3(t)$.

5. Conclusions

This paper discusses the aperiodic sampled-data control problem for a chaotic system with TSFM. And both lower and upper bounds of the sampling period are considered in the paper. Then, the criteria of mean square exponential stability are given. By constructing an appropriate LKF, the sampling patterns are fully captured and less conservative result is obtained. The simulation result is used to verify that the proposed fuzzy aperiodic sampled-data control strategy is effective.

Data Availability

No data were used to support this study.

Conflicts of Interest

The authors declare that they have no conflicts of interest.

Acknowledgments

This study was supported by the National Natural Science Foundation of China (51579114 and 51879119), Natural Science Foundation of Fujian Province (2018J01484 and 2020J01660), and Youth Innovation Foundation of Xiamen (3502Z20206019).

References

[1] S. Vaidyanathan and S. Sampath, "Anti-synchronization of four-wing chaotic systems via sliding mode control," *International Journal of Automation and Computing*, vol. 9, no. 3, pp. 274–279, 2012.

[2] D. H. Ji, S. C. Jeong, J. H. Park, and S. C. Won, "Robust adaptive backstepping synchronization for a class of uncertain chaotic systems using fuzzy disturbance observer," *Nonlinear Dynamics*, vol. 69, no. 3, pp. 1125–1136, 2012.

[3] N. Wang, M. J. Er, M. Han, and M. Han, "Large tanker motion model identification using generalized ellipsoidal basis function-based fuzzy neural networks," *IEEE Transactions on Cybernetics*, vol. 45, no. 12, pp. 2732–2743, 2015.

[4] R.-E. Precup and M. L. Tomescu, "Stable fuzzy logic control of a general class of chaotic systems," *Neural Computing and Applications*, vol. 26, no. 3, pp. 541–550, 2015.

[5] W. Xiang, Y. Sun, and H. Liu, "Fuzzy adaptive prescribed performance control for a class of uncertain chaotic systems with unknown control gains," *International Journal of Innovative Computing, Information and Control*, vol. 12, no. 2, pp. 603–613, 2016.

[6] Z. Liu and R. Guo, "Stabilization of a class of complex chaotic systems by the dynamic feedback control," *Complexity*, vol. 2020, Article ID 4938149, 10 pages, 2020.

[7] H. Medhaffar, M. Feki, and N. Derbel, "Adaptive fuzzy control for the stabilisation of chaotic systems," *International Journal of Automation and Control*, vol. 14, no. 2, pp. 115–137, 2020.

[8] H. K. Lam, W.-K. Ling, H. H.-C. Iu, and S. S. H. Ling, "Synchronization of chaotic systems using time-delayed fuzzy state-feedback controller," *IEEE Transactions on Circuits and Systems I: Regular Papers*, vol. 55, no. 3, pp. 893–903, Apr. 2008.

[9] S.-Y. Li and M. A. B. Hernández, "Robust synchronization of chaotic systems with novel fuzzy rule-based controllers," *Information Sciences*, vol. 481, pp. 604–615, 2019.

[10] J.-H. Kim, C.-H. Hyun, E. Kim, and M. Park, "Adaptive synchronization of uncertain chaotic systems based on T-S fuzzy model," *IEEE Transactions on Fuzzy Systems*, vol. 15, no. 3, pp. 359–369, Jun. 2007.

[11] C. Hu, H. Jiang, and Z. Teng, "General impulsive control of chaotic systems based on a TS fuzzy model," *Fuzzy Sets and Systems*, vol. 174, no. 1, pp. 66–82, Jul. 2011.

[12] S. M. A. Pahnehkolaei, A. Alfi, and J. T. Machado, "Fuzzy logic embedding of fractional order sliding mode and state feedback controllers for synchronization of uncertain fractional chaotic systems," *Computational and Applied Mathematics*, vol. 39, no. 3, pp. 1–16, 2020.

[13] T. Takagi and M. Sugeno, "Fuzzy identification of systems and its applications to modelling and control," *IEEE Transactions on Systems, Man, and Cybernetics*, vol. 15, no. 1, pp. 116–132, 1985.

[14] K. Tanaka and H. Wang, *Fuzzy Control Systems Design and Analysis: A Linear Matrix Inequality Approach*, John Wiely & Sons, New York, NY, USA, 2001.

[15] Y. Wang, Y. Xia, and P. Zhou, "Fuzzy-model-based sampled-data control of chaotic systems: a fuzzy time-dependent Lyapunov–Krasovskii functional approach," *IEEE Transactions on Fuzzy Systems*, vol. 25, no. 6, pp. 1672–1684, 2016.

[16] P. Shi, X. Su, and F. Li, "Dissipativity-based filtering for fuzzy switched systems with stochastic perturbation," *IEEE Transactions on Automatic Control*, vol. 61, no. 6, pp. 1694–1699, 2016.

[17] J.-H. Kim, C.-W. Park, E. Kim, and M. Park, "Fuzzy adaptive synchronization of uncertain chaotic systems," *Physics Letters A*, vol. 334, no. 4, pp. 295–305, 2005.

[18] A. Khan and S. Kumar, "T-S fuzzy modeling and predictive control and synchronization of chaotic satellite systems," *International Journal of Modelling and Simulation*, vol. 39, no. 3, pp. 203–213, 2019.

[19] K. Delchev, G. Boiadjiev, H. Kawasaki, and T. Mouri, "Iterative learning control with sampled-data feedback for robot manipulators," *Archives of Control Sciences*, vol. 24, no. 3, pp. 299–319, 2014.

[20] S. M. Abedi, "An optimal sample-data holds by using a Bi-objective criterion: trade-off between the phase delay and the

stability robustness," *Control Engineering and Applied Informatics*, vol. 17, no. 2, pp. 32–42, 2015.

[21] Y. Wang, H. R. Karimi, H.-K. Lam, and H. Shen, "An improved result on exponential stabilization of sampled-data fuzzy systems," *IEEE Transactions on Fuzzy Systems*, vol. 26, no. 6, pp. 3875–3883, 2018.

[22] E. Fridman, "Robust sampled-dataH_inftyControl of linear singularly perturbed systems," *IEEE Transactions on Automatic Control*, vol. 51, no. 3, pp. 470–475, 2006.

[23] H. J. Lee, M. H. Kim, S. Y. Lee, and T. Y. Kim, "Robust sampled-data fuzzy control of nonlinear systems with parametric uncertainties: its application to depth control of autonomous underwater vehicles," *International Journal of Control Automation and Systems*, vol. 10, no. 6, pp. 1164–1172, 2012.

[24] Z. G. Wu, P. Shi, and H. Y. Su, "Stochastic synchronization of markovian jump neural networks with time-varying delay using sampled data," *IEEE Transactions on Cybernetics*, vol. 43, no. 6, pp. 796–1806, 2013.

[25] M. Rubagotti, D. M. Raimondo, A. Ferrara, and L. Magni, "Robust model predictive control with integral sliding mode in continuous-time sampled-data nonlinear systems," *IEEE Transactions on Automatic Control*, vol. 56, no. 3, pp. 556–570, 2011.

[26] Y. Wang, Y. Zhu, H. R. Karimi, and X. Li, "Sampled-data exponential synchronization of chaotic Lur'e systems," *IEEE Access*, vol. 5, pp. 17834–17840, 2017.

[27] X. Li, D. Ma, X. Xie, and Q. Sun, "Fault-Tolerant synchronization of chaotic systems with fuzzy sampled data controller based on adaptive event-triggered scheme," *International Journal of Fuzzy Systems*, vol. 1–13, 2020.

[28] Z.-G. Wu, P. Shi, H. Su, and J. Chu, "Sampled-data fuzzy control of chaotic systems based on a T-S fuzzy model," *IEEE Transactions on Fuzzy Systems*, vol. 22, no. 1, pp. 153–163, 2014.

[29] T. Wu, J. Cao, L. Xiong, and H. Zhang, "New stabilization results for semi-markov chaotic systems with fuzzy sampled-data control," *Complexity*, vol. 2019, Article ID 7875305, 15 pages, 2019.

[30] N. Gunasekaran and Y. H. Joo, "Stochastic sampled-data controller for T-S fuzzy chaotic systems and its applications," *IET Control Theory & Applications*, vol. 13, no. 12, pp. 1834–1843, 2019.

[31] Z. P. Wang and H. N. Wu, "On fuzzy sampled-data control of chaotic systems via a time-dependent Lyapunov functional approach," *IEEE Trans. Cybern.*vol. 45, no. 4, pp. 819–829, 2015.

Hindawi
Complexity
Volume 2020, Article ID 8683521, 13 pages
https://doi.org/10.1155/2020/8683521

Research Article

Stabilization of Two Electricity Generators

Dany Ivan Martinez, José de Jesús Rubio, Arturo Aguilar, Jaime Pacheco, Guadalupe Juliana Gutierrez, Victor Garcia, Tomas Miguel Vargas, Genaro Ochoa, David Ricardo Cruz, and Cesar Felipe Juarez

Sección de Estudios de Posgrado e Investigación, ESIME Azcapotzalco, Instituto Politécnico Nacional, Av. De Las Granjas No. 682, Col. Santa Catarina, Ciudad de México 02250, Mexico

Correspondence should be addressed to José de Jesús Rubio; rubio.josedejesus@gmail.com

Received 2 July 2020; Revised 20 November 2020; Accepted 26 November 2020; Published 10 December 2020

Academic Editor: Hamid Reza Karimi

In this research, a sliding mode regulator with sine mapping is suggested for the stabilization of electricity generators being affected by magnet interaction nonlinearities and generator nonlinearities. To reach this goal, our suggested regulator has the following contributions: (a) it starts from the sliding mode regulator with the modifications that the saturation mapping is used to reach a smoother performance instead of the signum mapping, and the sine mapping is applied to reach an upper bound in the proportional gain error, (b) it is used to reach some chosen constant behaviors for the angle position, angle speed, and current in the electricity generators, and (c) its stabilization is ensured based on the Lyapunov approach. We show the simulation of the suggested regulator in two electricity generators.

1. Introduction

The term alternative energy is utilized in the electricity generation from the environment by the utilization of renewable fuels, evading the necessity of a no renewable fuel. Some of the most relevant alternative energies can be classified in electricity generators based on wind turbines, magnets, or solar panels. The electricity generator of this research uses the interactions between static and dynamic magnets for the electricity generation [1, 2]. The motivation of this research is the stabilization of electricity generators. A regulator is one technique for the stabilization of electricity generators which let us to reach some constant behaviors for the angle position, angle speed, and current [3–8].

There are many kinds of nonlinearities which impede to reach the stabilization of electricity generators, and some examples of these nonlinearities are the arbitrary switching [9–13], the time-delays [14–18], the impulse perturbations [19, 20], or the unknown nonlinearities [21–24]. The major issue is that in most of the cases, the mentioned nonlinearities are unknown. The challenge of this research is the stabilization of electricity generators being affected by unknown nonlinearities.

The magnet interaction nonlinearities and generator nonlinearities are two unknown nonlinearities of the electricity generators which can severely affect their performance [21–24]. Hence, the research about regulators for the stabilization of electricity generators where the magnet interaction nonlinearities and generator nonlinearities are unknown, which is of interest, and two alternatives are the proportional derivation regulator of [3–5] and the sliding mode regulator of [6–8].

In this research, a sliding mode regulator with sine mapping is suggested for the stabilization of electricity

generators being affected by magnet interaction nonlinearities and generator nonlinearities. To reach this goal, our suggested regulator has the following contributions:

(a) The sliding model regulator starts from the proportional derivation regulator with one additional term of the signum mapping used to reach the stabilization. The sliding mode regulator with sine mapping starts from the sliding mode regulator with the modifications that the saturation mapping is used to reach a smoother performance instead of the signum mapping, and the sine mapping is applied to reach an upper bound in the proportional gain error.

(b) Since the sliding mode technique is used in the suggested regulator instead of the magnet interaction nonlinearities and generator nonlinearities, the knowledge of these nonlinearities is not required in the electricity generators. Our suggested regulator is also used to reach some chosen constant behaviors for the angle position, angle speed, and current.

(c) We ensure the stabilization of the regulator error in our suggested regulator based on the Lyapunov approach. This research is focused on the asymptotic stabilization.

We organize the paper as follows: in Section 2, we present the mathematical model of electricity generators. In Section 3, we present the sliding mode regulator with sine mapping for the stabilization of electricity generator. In Section 4, we simulate the suggested regulator for the stabilization of two electricity generators. In Section 5 we present the conclusions and future research.

2. Mathematical Model and Regulators for the Electricity Generators

In Appendix A of this research, the descriptions of the electricity generator symbols are shown in Table 1 and the parameter values for mathematical models are shown in Table 2. The descriptions of the mathematical model symbols are shown in Table 3, and the descriptions of the regulator symbols are shown in Table 4.

In this section, we address some concepts such as the mathematical model and regulators for the electricity generators.

We consider the electricity generator with two static magnets and two dynamic magnets of Figure 1 via the utilization of two static magnets and two dynamic magnets.

We express the electricity generator with two static magnets and two dynamic magnets as [1, 2]

$$\begin{aligned}
\dot{z}_1 &= z_2,\\
\dot{z}_2 &= \left(\frac{1}{m_e\left(1/24a^2 + 1/24c^2 + r_g^2\right) + m_i\left(r_i^2 + 2r_g^2\right)}\right)\\
&\quad\cdot\left(v - \frac{\pi B^2 r_i^2 r_g^2 \sin z_1}{\mu\left[h^2 + 2r_g^2\left(1 - \cos z_1\right)\right]^{0.5}} + \frac{\pi B^2 r_i^2 r_g^2 \sin z_1}{\mu\left[h^2 + 2r_g^2\left(1 + \cos z_1\right)\right]^{0.5}} - bz_2\right),\\
\dot{z}_3 &= -\frac{\left(R + R_e\right)}{L}z_3 + \frac{K_m}{L}z_2.
\end{aligned} \tag{1}$$

Since all magnets are equal, $B_{11} = B_{12} = B$.

Table 1: Description of the electricity generator symbols.

Symbol	Description
m_e	The mass of the link 1
a	The width of the link 1
c	The length of the link 1
m_i	The mass of the dynamic magnet
r_i	The radius of the surface in the magnet
m	The mass
r_g	The radius of the body rotation
B_{11}	The magnet flux density produced by dynamic magnet 1 and static magnet 1
B_{12}	The magnet flux density produced by dynamic magnet 1 and static magnet 2
B_{21}	The magnet flux density produced by dynamic magnet 2 and static magnet 1
B_{22}	The magnet flux density produced by dynamic magnet 2 and static magnet 2
μ	The magnet permeability constant in magnets
h	The distance of a dynamic magnet and a static magnet on the axis z
K_m	The electromotive force constant
R	The resistance
i	The current
L	The inductance
R_e	The load resistance

We consider the electricity generator with four static magnets and four dynamic magnets of Figure 1 via the utilization of four static magnets and four dynamic magnets.

We express the electricity generator with four static magnets and four dynamic magnets as [1, 2]

$$\begin{aligned}
\dot{z}_1 &= z_2,\\
\dot{z}_2 &= \left(\frac{1}{m_e\left(1/24a^2 + 1/24c^2 + r_g^2\right) + m_i\left(r_i^2 + 2r_g^2\right)}\right)\left(v - \frac{\pi B^2 r_i^2 r_g^2 \sin z_1}{\mu\left[h^2 + 2r_g^2\left(1 - \cos z_1\right)\right]^{0.5}}\right.\\
&\quad - \frac{\pi B^2 r_i^2 r_g^2 \cos z_1}{\mu\left[h^2 + 2r_g^2\left(1 + \sin z_1\right)\right]^{0.5}} + \frac{\pi B^2 r_i^2 r_g^2 \sin z_1}{\mu\left[h^2 + 2r_g^2\left(1 + \cos z_1\right)\right]^{0.5}} + \frac{\pi B^2 r_i^2 r_g^2 \cos z_1}{\mu\left[h^2 + 2r_g^2\left(1 - \sin z_1\right)\right]^{0.5}} - \frac{\pi B^2 r_i^2 r_g^2 \sin\left(z_1 - \pi/4\right)}{\mu\left[h^2 + 2r_g^2\left(1 - \cos\left(z_1 - \pi/4\right)\right)\right]^{0.5}}\\
&\quad \left. - \frac{\pi B^2 r_i^2 r_g^2 \cos\left(z_1 - \pi/4\right)}{\mu\left[h^2 + 2r_g^2\left(1 + \sin\left(z_1 - \pi/4\right)\right)\right]^{0.5}} + \frac{\pi B^2 r_i^2 r_g^2 \sin\left(z_1 - \pi/4\right)}{\mu\left[h^2 + 2r_g^2\left(1 + \cos\left(z_1 - \pi/4\right)\right)\right]^{0.5}} + \frac{\pi B^2 r_i^2 r_g^2 \cos\left(z_1 - \pi/4\right)}{\mu\left[h^2 + 2r_g^2\left(1 - \sin\left(z_1 - \pi/4\right)\right)\right]^{0.5}} - bz_2\right),\\
\dot{z}_3 &= -\frac{\left(R + R_e\right)}{L} z_3 + \frac{K_m}{L} z_2.
\end{aligned} \tag{2}$$

Since all magnets are equal, $B_{11} = B_{12} = B_{21} = B_{22} = B$.

From the electricity generator with two static magnets and two dynamic magnets of equation (1) and the electricity generator with four static magnets and four dynamic magnets of equation (2), we express the mathematical model for the electricity generators as

Table 2: Parameters of electricity generators.

Parameter	Value	Parameter	Value
m_i	9.2×10^{-2} kg	R_e	30 Ω
μ	9.42×10^{-5} Hm^{-1}	r_g	7.5×10^{-2} m
B	8.4×10^{-1} T	r_i	2.9×10^{-2} m
L	6.03×10^{-1} H	a	1.5×10^{-1} m
K_m	45×10^{-2} Vsrad^{-1}	c	1.5×10^{-2} m
b	1×10^{-1} kgm^2 rads^{-1}	n_r	0.5
m_e	5×10^{-3} kg	n_l	0.5
h	4×10^{-2} m	w_r	0.5
R	6.96 Ω	w_l	−0.5

Table 3: Description of the mathematical model symbols.

Symbol	Description
$z_1 \in \mathfrak{R}$	The angle position
$z_2 \in \mathfrak{R}$	The angle speed
$z_3 \in \mathfrak{R}$	The current
$v \in \mathfrak{R}$	The fictitious input of torque produced by the magnets interaction
$O(z_1) \in \mathfrak{R}$	The magnets interaction nonlinearities
z_1, z_2, z_3	The states
Q, J, X, Y	Scalar constants
u	The input of the generator nonlinearities
n_r, n_l, w_r, w_l	Constant terms for the generator nonlinearities
$P(u)$	The generator nonlinearities

Table 4: Description of the regulators symbols.

Symbol	Description
$\tilde{z}_1 = z_1 - z_1^d \in \mathfrak{R}$	The position regulator error
$z_1^d \in \mathfrak{R}$	The constant reference position
$\tilde{z}_2 = z_2 \in \mathfrak{R}$	The speed regulator error
$K_1 \in \mathfrak{R}$	The proportional gain
$K_2 \in \mathfrak{R}$	The derivation gain
$\mathrm{sign}(\cdot)$	The signum mapping
$\mathrm{sat}(\cdot)$	The saturation mapping
$\sin(\cdot)$	The sine mapping
$\cos(\cdot)$	The cosine mapping
K	The sliding mode gain
$\tilde{z}_1^2 = (z_1 - z_1^d)^2$	The position regulator error
$\tilde{z}_2^2 = {z_2}^2$	The speed regulator error
$\tilde{z}_3^2 = {z_3}^2$	The current regulator error

$$\begin{aligned} \dot{z}_1 &= z_2, \\ Q\dot{z}_2 + Jz_2 + O(z_1) &= v, \\ \dot{z}_3 + Xz_3 + Yz_1 &= 0. \end{aligned} \tag{3}$$

The fictitious input v is affected by the generator nonlinearities, it is like a chattering movement presented in the electricity generator. We express the fictitious input v as [6]

$$v = \begin{cases} n_r(u - w_r), & u \geq w_r, \\ 0, & w_l < u < w_r, \\ n_l(u - w_l), & u \leq w_l. \end{cases} \tag{4}$$

We see that the model of equation (1) can be expressed as the model of equations (3) and (4) with

$$\begin{aligned} Q &= m_e\left(\frac{1}{24}a^2 + \frac{1}{24}c^2 + r_g^2\right) + m_i\left(r_i^2 + 2r_g^2\right), \\ J &= b, \\ X &= \frac{(R + R_e)}{L}, \\ Y &= -\frac{K_m}{L}, \\ O(z_1) &= \frac{\pi B^2 r_i^2 r_g^2 \sin z_1}{\mu\left[h^2 + 2r_g^2(1 - \cos z_1)\right]^{0.5}} \\ &\quad - \frac{\pi B^2 r_i^2 r_g^2 \sin z_1}{\mu\left[h^2 + 2r_g^2(1 + \cos z_1)\right]^{0.5}}. \end{aligned} \tag{5}$$

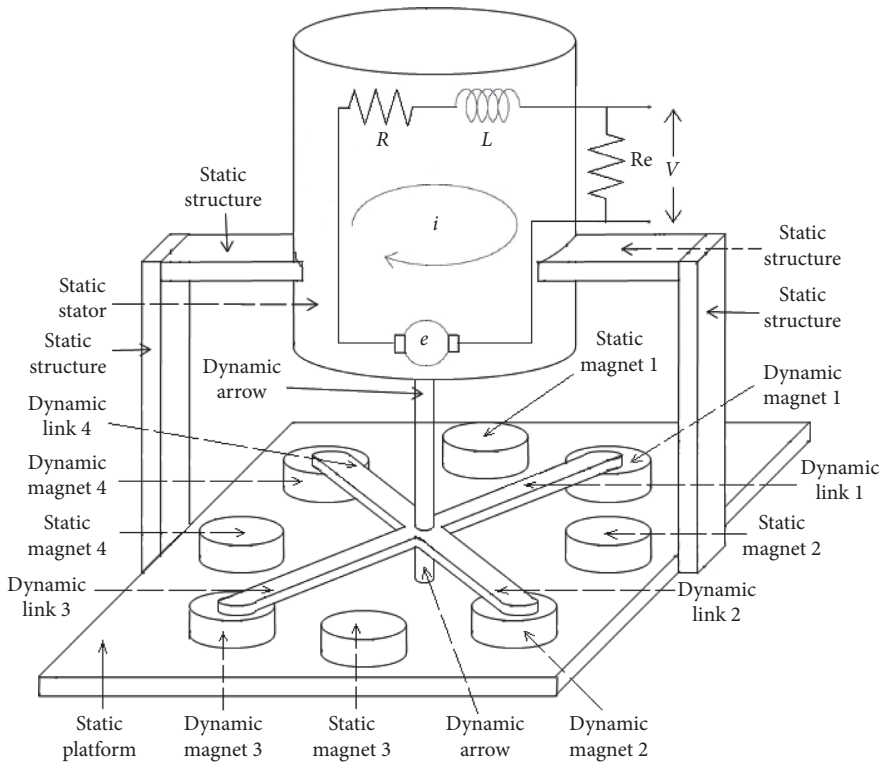

Figure 1: Electricity generator with static magnets and dynamic magnets.

We see that the model of equation (2) can be expressed as the model of equations (3) and (4) with

$$Q = m_e\left(\frac{1}{24}a^2 + \frac{1}{24}c^2 + r_g^2\right) + m_i\left(r_i^2 + 2r_g^2\right),$$

$$J = b,$$

$$X = \frac{(R + R_e)}{L},$$

$$Y = -\frac{K_m}{L},$$

$$\begin{aligned} O(z_1) = \Bigg(& \frac{\pi B^2 r_i^2 r_g^2 \sin z_1}{\mu\left[h^2 + 2r_g^2(1 - \cos z_1)\right]^{0.5}} + \frac{\pi B^2 r_i^2 r_g^2 \cos z_1}{\mu\left[h^2 + 2r_g^2(1 + \sin z_1)\right]^{0.5}} - \frac{\pi B^2 r_i^2 r_g^2 \sin z_1}{\mu\left[h^2 + 2r_g^2(1 + \cos z_1)\right]^{0.5}} - \frac{\pi B^2 r_i^2 r_g^2 \cos z_1}{\mu\left[h^2 + 2r_g^2(1 - \sin z_1)\right]^{0.5}} \\ & + \frac{\pi B^2 r_i^2 r_g^2 \sin(z_1 - (\pi/4))}{\mu\left[h^2 + 2r_g^2(1 - \cos(z_1 - (\pi/4)))\right]^{0.5}} + \frac{\pi B^2 r_i^2 r_g^2 \cos(z_1 - (\pi/4))}{\mu\left[h^2 + 2r_g^2(1 + \sin(z_1 - (\pi/4)))\right]^{0.5}} - \frac{\pi B^2 r_i^2 r_g^2 \sin(z_1 - (\pi/4))}{\mu\left[h^2 + 2r_g^2(1 + \cos(z_1 - (\pi/4)))\right]^{0.5}} \\ & - \frac{\pi B^2 r_i^2 r_g^2 \cos(z_1 - (\pi/4))}{\mu\left[h^2 + 2r_g^2(1 - \sin(z_1 - (\pi/4)))\right]^{0.5}} \Bigg). \end{aligned} \tag{6}$$

The generator nonlinearities of electricity generators are symmetric as $n_r = n_l$ in equation (4); consequently, we can express the fictitious input v of equation (4) as

$$v = \begin{cases} n_l u, & u \geq w_r, \\ n_l u, & w_l < u < w_r, \\ n_l u, & u \leq w_l, \end{cases} + \begin{cases} -n_l w_r, & u \geq w_r, \\ -n_l u, & w_l < u < w_r. \\ -n_l w_l, & u \leq w_l, \end{cases} \tag{7}$$

After some mathematical operations, the fictitious input v of equation (7) is expressed as

$$v = n_l u - P(u),$$
$$P(u) = \begin{cases} n_l w_r, & u \geq w_r, \\ n_l u, & w_l < u < w_r, \\ n_l w_l, & u \leq w_l. \end{cases} \tag{8}$$

We notice that the generator nonlinearities $P(u)$ are bounded as

$$|P(u)| \leq \overline{P}. \tag{9}$$

Remark 1. Even the mathematical model for the electricity generators of equations (3) and (4) seems to be simple, the complexity in this mathematical model is mainly focused on the magnets interaction nonlinearities $O(z_1) \in \mathfrak{R}$, such that the design and validation of this mathematical model resulted in two publications [1, 2].

Remark 2. From equations (5) and (6), it is observed that the magnet interaction nonlinearities $O(z_1) \in \mathfrak{R}$ are the most complex part in the mathematical model of equations (3) and (4), while Q, J, X, and Y are scalar constants corresponding to the electricity generators. Thus, these magnet interaction nonlinearities $O(z_1) \in \mathfrak{R}$ are mainly focused on this research.

Now, we express the proportional derivation and sliding mode regulators due to they will be utilized for the comparisons in a future section.

We express the proportional derivation regulator as [3–5]

$$u = \frac{1}{n_l}\{-K_1\tilde{z}_1 - K_2\tilde{z}_2\}. \tag{10}$$

We express the sliding mode regulator as [6–8]

$$u = \frac{1}{n_l}\{-K_1\tilde{z}_1 - K_2\tilde{z}_2 - K\operatorname{sign}(\tilde{z}_2)\},$$
$$\operatorname{sign}(\tilde{z}_2) = \begin{cases} 1, & \tilde{z}_2 > 0, \\ 0, & \tilde{z}_2 = 0, \\ -1, & \tilde{z}_2 < 0. \end{cases} \tag{11}$$

3. Sliding Mode Regulator with Sine Mapping

In this section, we address the design and stabilization of the sliding mode regulator with sine mapping.

We notice that the magnet interaction nonlinearities $O(z_1)$ of equation (3) are bounded as

$$|O(z_1)| \leq \overline{O}. \tag{12}$$

Since we use the reference speed states as $z_2^d = 0$, we consider the stabilization case, and the $z_1^d \in \mathfrak{R}$ reference position is a constant in this research. We express the sliding mode regulator with sine mapping u as

$$u = \frac{1}{n_l}\left\{-\cos(\tilde{z}_1)^T K_1 \sin(\tilde{z}_1) - K_2\tilde{z}_2 - K\operatorname{sat}(\tilde{z}_2)\right\},$$
$$\operatorname{sat}(\tilde{z}_2) = \begin{cases} 1, & \tilde{z}_2 > 1, \\ \tilde{z}_2, & |\tilde{z}_2| \leq 1, \\ -1, & \tilde{z}_2 < -1, \end{cases} \tag{13}$$

where K is a constant such as $\overline{O} + \overline{P} \leq K$, where $\overline{O}$ is in equation (12) and $\overline{P}$ is in equation (9). It is relevant to note that we do not know the behaviors of $O(z_1)$ and $P(u)$, and we use their upper bounds $\overline{O}$ and $\overline{P}$.

Remark 3. Since we consider the stabilization case, we do not require the application of the sine mapping to the term $K_2\tilde{z}_2$, i.e., since $z_2^d = 0$ and $\tilde{z}_2 = z_2$, we obtain small values in $\tilde{z}_2$. Since the state z_3 is dependent of the other states z_1, z_2, the stabilization of the states z_1, z_2 yields the stabilization of the state z_3 and we do not require the state z_3 in the regulator.

Remark 4. The convergence speed of the suggested regulator can be affected by choosing the gains K_1, K_2, and K. The complexity in the implementation of the suggested regulator is in the programming of the saturation mapping $\operatorname{sat}(\cdot)$; nevertheless, this complexity also is in all the regulators which use mappings.

In Figure 2, we show the sliding mode regulator with sine mapping of equations (13), (12), and (9) termed SMWS for the stabilization in the electricity generators of equations (3) and (4) termed EGM.

From Figure 3, it is shown that the proportional derivation regulator of equation (10) and [3–5] termed PD, the sliding model regulator of equations (11), (12,) and (9) and [6–8] termed SM, and the suggested sliding mode regulator with sine mapping of equations (13), (12), and (9) termed SMWS use the proportional gain K_1 and the derivation gain K_2. Furthermore, the existence, similarities, and differences between PD, SM, and SMWS are detailed as follows: the sliding model regulator starts from the proportional derivation regulator with one additional term of the signum mapping used to reach the stabilization, the sliding mode regulator with sine mapping starts from the sliding mode regulator with the modifications that the saturation mapping is used to reach a smoother performance instead of the signum mapping, and the sine mapping is applied to reach an upper bound of the proportional gain error.

Now, we will discuss the stabilization of the regulator.

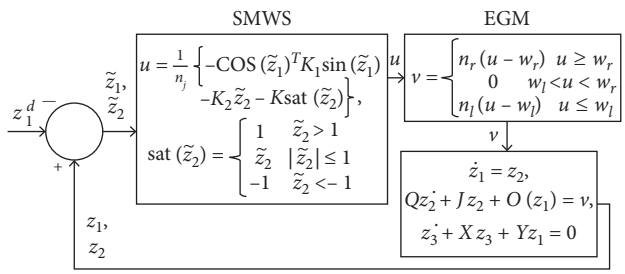

Figure 2: Sliding mode regulator with sine mapping.

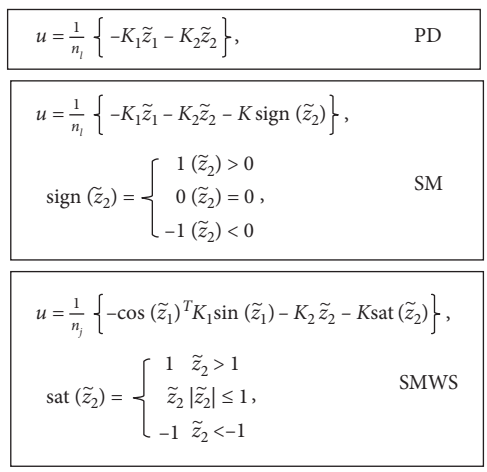

Figure 3: Relation between PD, SM, and SMWS.

Theorem 1. *The stabilization in the regulator error of the sliding mode regulator with sine mapping of equations (13), (12), and (9), and electricity generators of equations (3) and (4) are ensured, and the speed regulator error $\tilde{z}_2$ will converge to*

$$\limsup_{T \longrightarrow \infty} \left\|\tilde{z}_2\right\|^2 = 0, \tag{14}$$

with T as the final time, $\tilde{z}_2 = z_2$, the magnets interaction nonlinearities and generator nonlinearities are bounded as $|O(z_1)| \le \overline{O}$, $|P(u)| \le \overline{P}$, and $\overline{O} + \overline{P} \le K$.

Proof. We denote the candidate mapping as

$$V_1 = \frac{1}{2}\tilde{z}_2^T Q \tilde{z}_2 + \frac{1}{2}\sin(\tilde{z}_1)^T K_1 \sin(\tilde{z}_1), \tag{15}$$

with Q as the positive constant of equation (3) and K_1 as the positive constant of equation (13). We denote $\tilde{z}_2 = z_2$, we substitute equations (13) and (8) into equation (3), and we obtain the closed-loop model as

$$\begin{aligned} Q\dot{\tilde{z}}_2 + Jz_2 + O(z_1) &= v = n_l u - P(u) \\ &= n_l \frac{1}{n_l}\left\{-\cos(\tilde{z}_1)^T K_1 \sin(\tilde{z}_1) - K_2\tilde{z}_2 - K\mathrm{sat}(\tilde{z}_2)\right\} - P(u), \\ \Rightarrow Q\dot{\tilde{z}}_2 &= -\cos(\tilde{z}_1)^T K_1 \sin(\tilde{z}_1) - K_2\tilde{z}_2 - J\tilde{z}_2 - O(z_1) - P(u) - K\mathrm{sat}(\tilde{z}_2). \end{aligned} \tag{16}$$

We use the fact $\tilde{z}_2 = z_2$, and we obtain the derivation of equation (15) as

$$\dot{V}_1 = \tilde{z}_2^T Q \dot{\tilde{z}}_2 + \tilde{z}_2^T \cos(\tilde{z}_1)^T K_1 \sin(\tilde{z}_1), \tag{17}$$

with $\dot{\tilde{z}}_1 = \dot{z}_1 - \dot{z}_1^d = z_2 - z_2^d = z_2 = \tilde{z}_2$ and $\dot{\tilde{z}}_2 = \dot{z}_2$. We substitute last equation (16) into equation (17) as

$$\begin{aligned}
&\dot{V}_1 = \tilde{z}_2^T Q \dot{\tilde{z}}_2 + \tilde{z}_2^T \cos(\tilde{z}_1)^T K_1 \sin(\tilde{z}_1),\\
&\Rightarrow \dot{V}_1 = \tilde{z}_2^T \{-\cos(\tilde{z}_1)^T K_1 \sin(\tilde{z}_1) - K_2 \tilde{z}_2 - J\tilde{z}_2 - O(z_1) - P(u) - K\mathrm{sat}(\tilde{z}_2)\}\tilde{z}_2^T \cos(\tilde{z}_1)^T K_1 \sin(\tilde{z}_1),\\
&\Rightarrow \dot{V}_1 = -\tilde{z}_2^T K_2 z_2 - \tilde{z}_2^T J\tilde{z}_2 - \tilde{z}_2^T O(z_1) - \tilde{z}_2^T P(u) - \tilde{z}_2^T K\mathrm{sat}(\tilde{z}_2) - \tilde{z}_2^T \cos(\tilde{z}_1)^T K_1 \sin(\tilde{z}_1) + \tilde{z}_2^T \cos(\tilde{z}_1)^T K_1 \sin(\tilde{z}_1).
\end{aligned} \tag{18}$$

After some mathematical operations, $\dot{V}_1$ of equation (18) is as

$$\dot{V}_1 = -\tilde{z}_2^T K_2 \tilde{z}_2 - \tilde{z}_2^T J\tilde{z}_2 - \tilde{z}_2^T O(z_1) - \tilde{z}_2^T P(u) - \tilde{z}_2^T K\mathrm{sat}(\tilde{z}_2). \tag{19}$$

Equation (19) can be expressed as

$$\dot{V}_1 = -\tilde{z}_2^T [K_2 + J]\tilde{z}_2 - \tilde{z}_2^T O(z_1) - \tilde{z}_2^T P(u) - \tilde{z}_2^T K\mathrm{sat}(\tilde{z}_2). \tag{20}$$

Form equation (12), $O(z_1) \le |O(z_1)| + |P(u)| \le \overline{O} + \overline{P} \le K$, and from equation (13), $\mathrm{sat}(\tilde{z}_2) = \begin{cases} 1 & \tilde{z}_2 > 1 \\ \tilde{z}_2 & |\tilde{z}_2| \le 1 \\ -1 & \tilde{z}_2 < -1 \end{cases}$, we notice that there are three cases of the saturation mapping: (1) if $\tilde{z}_2 > 1$, then $\mathrm{sat}(\tilde{z}_2) = 1$ and $\tilde{z}_2 = |\tilde{z}_2|$, and we substitute into equation (20) as

$$\begin{aligned}
&\dot{V}_1 \le -\tilde{z}_2^T [K_2 + J]\tilde{z}_2 + |\tilde{z}_2|^T \overline{O} + |\tilde{z}_2|^T \overline{P} - |\tilde{z}_2|^T K,\\
&\Rightarrow \dot{V}_1 \le -\tilde{z}_2^T [K_2 + J]\tilde{z}_2.
\end{aligned} \tag{21}$$

(2) If $|\tilde{z}_2| \le 1$, then $\mathrm{sat}(\tilde{z}_2) = \tilde{z}_2$ and $\tilde{z}_2^T \tilde{z}_2 = |\tilde{z}_2|^T |\tilde{z}_2|$, and we substitute into equation (20) as

$$\begin{aligned}
&\dot{V}_1 = -\tilde{z}_2^T [K_2 + J]\tilde{z}_2 + |\tilde{z}_2|^T \overline{O} + |\tilde{z}_2|^T \overline{P} - \tilde{z}_2^T \tilde{z}_2 K,\\
&\Rightarrow \dot{V}_1 = -\tilde{z}_2^T [K_2 + J]\tilde{z}_2 + |\tilde{z}_2|^T \overline{O} + |\tilde{z}_2|^T \overline{P} - |\tilde{z}_2|^T |\tilde{z}_2| K,\\
&\Rightarrow \dot{V}_1 = -\tilde{z}_2^T [K_2 + J]\tilde{z}_2 - |\tilde{z}_2|^T \left[|\tilde{z}_2| K - \overline{O} - \overline{P}\right],\\
&\Rightarrow \dot{V}_1 = -\tilde{z}_2^T [K_2 + J]\tilde{z}_2,
\end{aligned} \tag{22}$$

since, in this case, $|\tilde{z}_2| \le 1$, $|\tilde{z}_2| K - \overline{O} - \overline{P} \ge 0 \Rightarrow \overline{O} + \overline{P} \le |\tilde{z}_2| K \le K$. (3) If $\tilde{z}_2 < -1$, then $\mathrm{sat}(\tilde{z}_2) = -1$ and $\tilde{z}_2 = -|\tilde{z}_2|$, and we substitute into equation (20) as

$$\begin{aligned}
&\dot{V}_1 = -\tilde{z}_2^T [K_2 + J]\tilde{z}_2 - \left(-|\tilde{z}_2|^T\right) O(z_1) - \left(-|\tilde{z}_2|^T\right) P(u) - \left(-|\tilde{z}_2|^T\right) K(-1),\\
&\Rightarrow \dot{V}_1 \le -\tilde{z}_2^T [K_2 + J]\tilde{z}_2 + |\tilde{z}_2|^T \overline{O} + |\tilde{z}_2|^T \overline{P} - |\tilde{z}_2|^T K,\\
&\Rightarrow \dot{V}_1 \le -\tilde{z}_2^T K_2 \tilde{z}_2.
\end{aligned} \tag{23}$$

From equations (21)–(23), the three cases have the same inequality expressed as

$$\dot{V}_1 \le -\tilde{z}_2^T [K_2 + J]\tilde{z}_2. \tag{24}$$

From the results of [5, 6], the stabilization of the regulator error is ensured. We integrate equation (24) from the initial time 0 to the final time T as

$$\begin{aligned}
&\int_0^T \tilde{z}_2^T [K_2 + J]\tilde{z}_2 \mathrm{d}t \le V_{1,0} - V_{1,T} \le V_{1,0},\\
&\Rightarrow \frac{[K_2 + J]}{T} \int_0^T \|\tilde{z}_2\|^2 \mathrm{d}t \le \frac{1}{T} \int_0^T \tilde{z}_2^T [K_2 + J]\tilde{z}_2 \mathrm{d}t \le \frac{1}{T} V_{1,0},
\end{aligned} \tag{25}$$

and we apply the limsup to both sides of the last inequality of equation (25) as $T \longrightarrow \infty$

$$\limsup_{T \longrightarrow \infty} \left(\frac{1}{T} \int_0^T \|\tilde{z}_2\|^2 \mathrm{d}t \right) \le \frac{V_{1,0}}{[K_2 + J]} \left[\limsup_{T \longrightarrow \infty} \left(\frac{1}{T} \right) \right] = 0. \tag{26}$$

If $T \longrightarrow \infty$, then $\|\tilde{z}_2\|^2 = 0$, and we comply with equation (14).

Remark 5. From equations (1) and (2), it can be seen that the angle speed behavior affects the angle position and current behaviors in the electricity generators. Then, the angle speed convergence of equation (14) is used to reach some chosen

constant behaviors for the angle position and current in the electricity generators.

Remark 6. This research focused on electricity generators. Nevertheless, our suggested regulator could be applied to other plants with similar structure to equations (3) and (4), such as are the motors, machines, robots, pendulums, or cranes.

Remark 7. There are several stabilization results such as the exponential stabilization [14, 17, 18, 20], the asymptotic stabilization [5, 6, 16, 22, 23], the uniformly ultimately boundedness [9–11], the feedback stabilization [15, 24], the stochastic stabilization [12, 21], or the mean square stabilization [13]. This research focused on the asymptotic stabilization.

4. Simulations

In this section, we compare the sliding mode regulator with sine mapping of equations (13), (12), and (9) termed SMWS, the proportional derivation regulator of equations (10), (12), and (9), and [3–5] termed PD, and the sliding mode regulator of equations (11), (12), and (9), and [6–8] termed SM for the stabilization of the two electricity generators of equations (3) and (4). The existence, similarities, and differences between PD, SM, and SMWS are detailed in Figure 3. Our goal in the regulators is that the angle position, angle speed, and current in electricity generators must reach some chosen constant references for the angle position, angle speed, and current as fast as possible in presence of the magnet interaction nonlinearities and generator nonlinearities. The chosen constant references in the angle position are higher or equal to zero, while the chosen constant references in the angle speed and current are equal to zero. We utilize the root mean square error (RMSE) for the comparisons as

$$\mathrm{RMSE} = \left(\frac{1}{T}\int_0^T \tilde{z}^2 \mathrm{d}t\right)^{1/2}, \tag{27}$$

with $\tilde{z}^2 = \tilde{z}_1^2 + \tilde{z}_2^2 + \tilde{z}_3^2$ for the states error or $\tilde{z}^2 = v^2$ for the fictitious input error.

Electricity generator with two static magnets and two dynamic magnets.

We express the electricity generator with two static magnets and two dynamic magnets in equations (1)–(5).

PD of [3–5] is expressed by equations (10), (12), and (9), with parameters $K_1 = 100$ and $K_2 = 0.1$.

SM of [6–8] is expressed by equations (11), (12), and (9), with parameters $K_1 = 100$, $K_2 = 0.1$, and $K = 0.5$.

SMWS is expressed by equations (13), (12), and (9), with parameters $K_1 = 100$, $K_2 = 0.1$, and $K = 0.5$.

We compare the fictitious input in Figure 4 and a zoom in Figure 5, we compare the states in Figure 6 and a zoom in Figure 7, and we show the RMSE of equation (27) in Figure 6 and Table 5 for the electricity generator with two static magnets and two dynamic magnets.

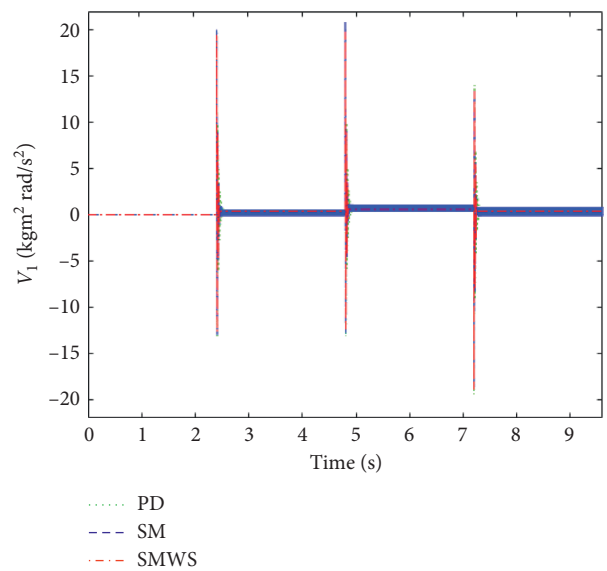

Figure 4: Fictitious input of the first electricity generator.

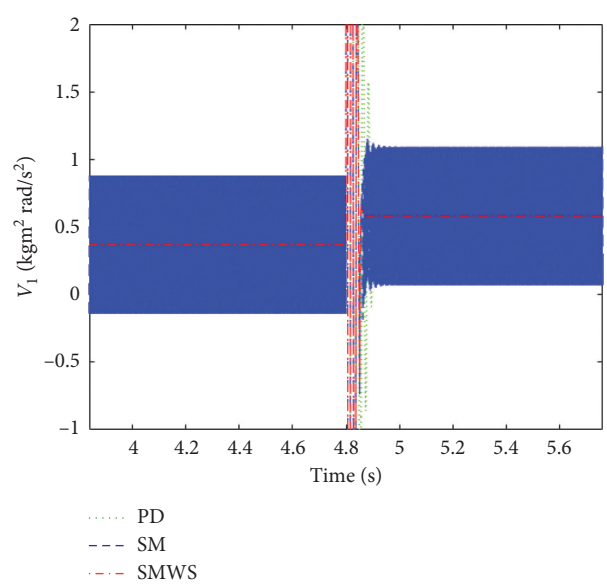

Figure 5: A zoom in the fictitious input of the first electricity generator.

In Figures 6 and 7, since the angle position, angle speed, and current of SMWS reach better the constant references in the angle position, angle speed, and current than the angle position, angle speed, and current of PD and SM, we can see that SMWS has the best performance. In Figures 4 and 5, the fictitious input for SMWS is smaller than for PD and SM. And in Figure 8 and Table 5, since the RMSE for the SMWS is smaller than for PD and SM, we can show that SMWS has the best performance.

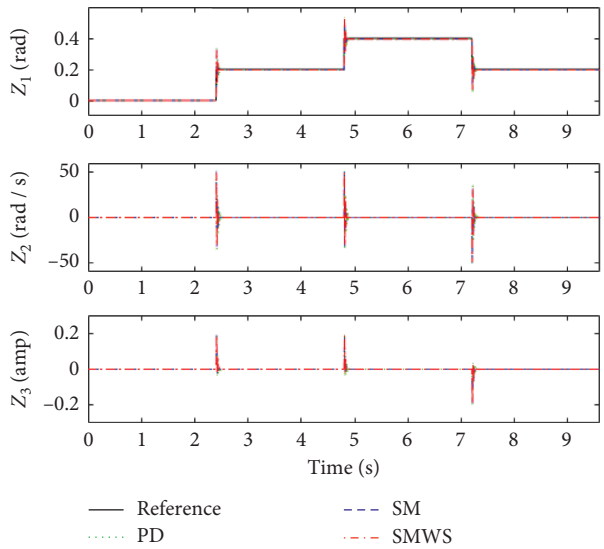

Figure 6: States of the first electricity generator.

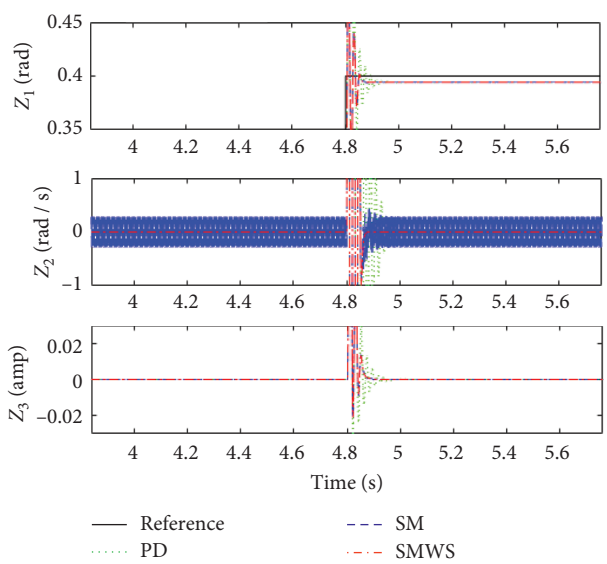

Figure 7: A zoom in the states of the first electricity generator.

Table 5: Comparisons for the first electricity generator.

	RMSE for $\tilde{z}$	RMSE for v
PD	2.0154	0.7386
SM	1.8226	0.7463
SMWS	1.7835	0.6656

Electricity generator with four static magnets and four dynamic magnets.

We express the electricity generator with four static magnets and four dynamic magnets in equations (2)–(6).

PD of [3–5] is expressed by equations (10), (12), and (9), with parameters $K_1 = 100$ and $K_2 = 0.1$.

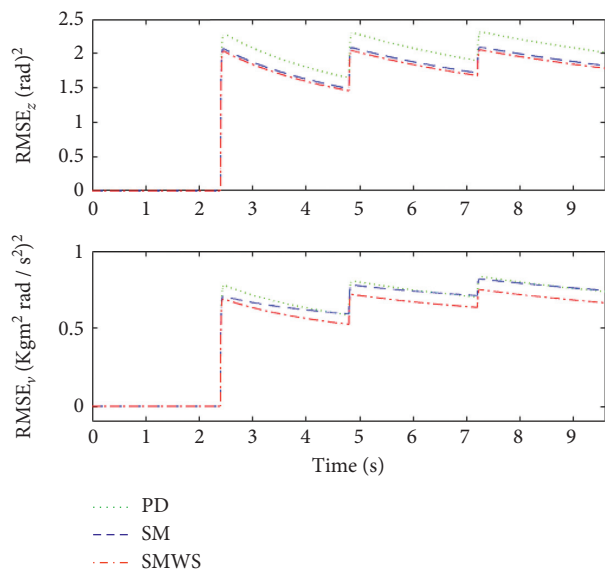

Figure 8: RMSE of the first electricity generator.

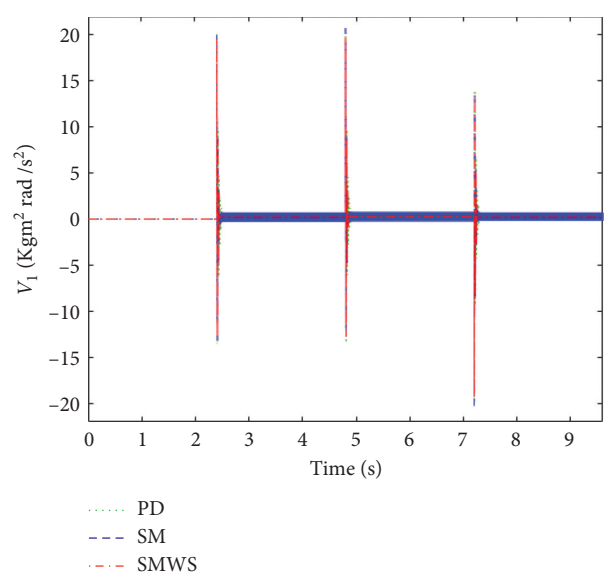

Figure 9: Fictitious input of the second electricity generator.

SM of [6–8] is expressed by equations (11), (12), and (9), with parameters $K_1 = 100$, $K_2 = 0.1$, and $K = 0.5$. SMWS is expressed by equations (13), (12), and (9), with parameters $K_1 = 100$, $K_2 = 0.1$, and $K = 0.5$.

We compare the fictitious inputs in Figure 9 and a zoom in Figure 10, we compare the states in Figure 11 and a zoom in Figure 12, and we show the RMSE of equation (27) in Figure 13 and Table 6 for the electricity generator with four static magnets and four dynamic magnets.

In Figures 11 and 12, since the angle position, angle speed, and current of SMWS reach better the constant references in the angle position, angle speed, and current than the angle position, angle speed, and current of PD and

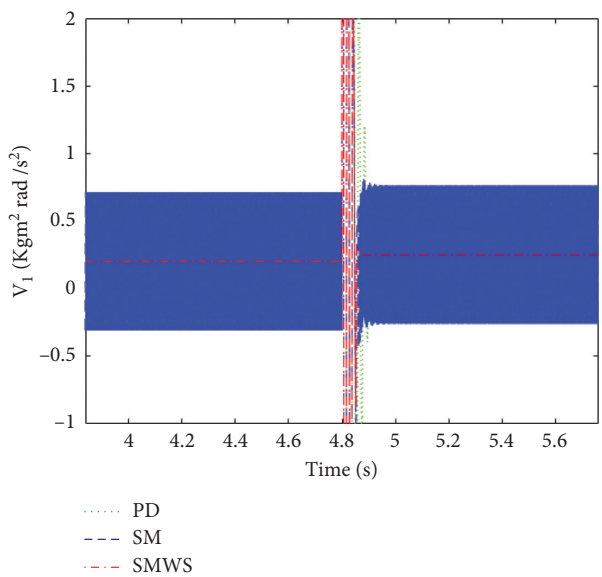

Figure 10: A zoom in the fictitious input of the second electricity generator.

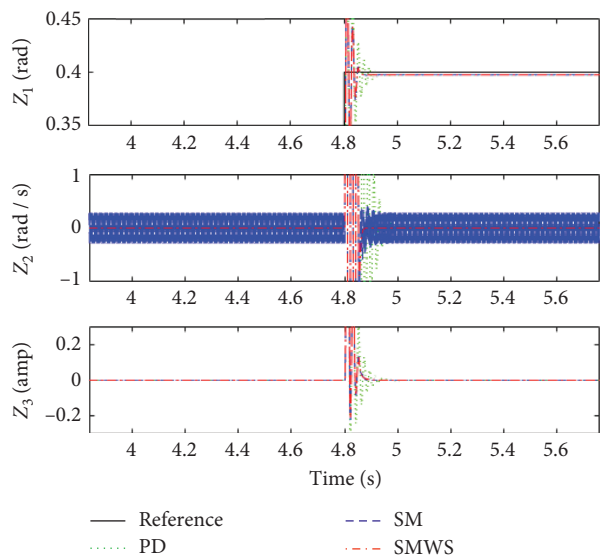

Figure 12: A zoom in the states of the second electricity generator.

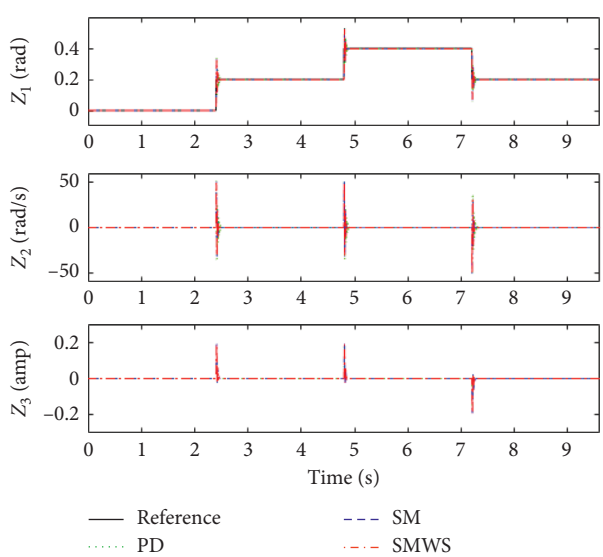

Figure 11: States of the second electricity generator.

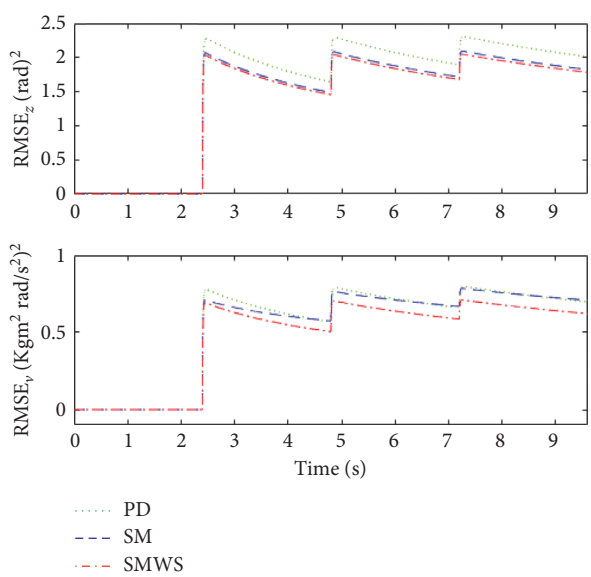

Figure 13: RMSE of the second electricity generator.

SM, we can see that SMWS has the best performance. In Figures 9 and 10, the fictitious input for SMWS is smaller than for PD and SM. And in Figure 13 and Table 6, since the RMSE for the SMWS is smaller than for PD and SM, we can show that SMWS has the best performance.

Remark 8. The course of RMSE is not monotonically increasing in Figures 8 and 13 even that it is indirectly suggested in equation (27) based on the following two reasons: (a) the final time T should increase for more simulation time, which is the denominator of equation (27), and (b) our goal is that the state error $\tilde{z}^2 = \tilde{z}_1^2 + \tilde{z}_2^2 + \tilde{z}_3^2$ or the fictitious input error $\tilde{z}^2 = v^2$ should decrease for more simulation time, which is the numerator of equation (27). The mentioned reasons result in the decreasing of RMSE.

Table 6: Comparisons for the second electricity generator.

	RMSE for $\tilde{z}$	RMSE for v
PD	2.0108	0.6995
SM	1.8230	0.7098
SMWS	1.7821	0.6224

Remark 9. Since Figures 4, 5, 9, and 10 describe the impulses used as the excitation to start moving these electricity generators and Figures 6, 7, 11, and 12 describe the angle position, angle speed, and current used as the responses of these electricity generators, the simulations could represent the real experiments.

5. Conclusions

In this research, we suggest a sliding mode regulator with sine mapping for the stabilization of two electricity generators being affected by unknown nonlinearities. In the simulations, we show that since angle position, angle speed, and current of our sliding mode regulator with sine mapping reach better the constant references of angle position, angle speed, and current than the angle position, angle speed, and current of the proportional derivation and sliding mode regulators, we can see that suggested regulator has the best performance in presence of the magnets interaction nonlinearities and generator nonlinearities. Our regulator illustrates the viability, efficiency, and potential of the approach especially relevant in electricity generators. Our suggested technique could also be applied to other mechatronic systems such as the electricity motors, machines, robots, pendulums, or cranes. The drawback of our regulator is that it is designed for models with structure of electricity generators, for models with other structures, the design should require modifications. In the future, we will apply our suggested regulator for the stabilization of robots or pendulums being affected by unknown nonlinearities.

Appendix

In this section, we express the tables used in this research.

Data Availability

The simulation data used to support this research are available from the second author upon request to the email rubio.josedejesus@gmail.com.

Conflicts of Interest

The authors declare that there are no conflicts of interest regarding the publication of this paper.

Acknowledgments

This research was financed by the Instituto Politécnico Nacional, Secretaría de Investigación y Posgrado, Comisión de Operación y Fomento de Actividades Académicas, and Consejo Nacional de Ciencia y Tecnología.

References

[1] J. J. Rubio, A. Aguilar, J. A. Meda-Campaña, G. Ochoa, R. Balcazar, and J. Lopez, "An electricity generator based on the interaction of static and dynamic magnets," *IEEE Transactions on Magnetics*, vol. 55, no. 8, Article ID 8204511, 2019.

[2] A. Aguilar, J. D. J. Rubio, J. A. Meda-Campaña et al., "Movable and immovable magnets for two machines," *International Journal of Applied Electromagnetics and Mechanics*, vol. 63, no. 2, pp. 229–248, 2020.

[3] J. O. Escobedo-Alva, E. C. Garcia-Estrada, L. A. Paramo-Carranza, J. A. Meda-Campaña, and R. Tapia-Herrera, "Theoretical application of a hybrid observer on altitude tracking of quadrotor losing GPS signal," *IEEE Access*, vol. 6, pp. 76900–76908, 2018.

[4] J. A. Meda-Campaña, "On the estimation and control of nonlinear systems with parametric uncertainties and noisy outputs," *IEEE Access*, vol. 6, pp. 31968–31973, 2018.

[5] J. D. J. Rubio, Z. Zamudio, J. Pacheco, and D. Mújica Vargas, "Proportional derivative control with inverse dead-zone for pendulum systems," *Mathematical Problems in Engineering*, vol. 2013, Article ID 173051, 9 pages, 2013.

[6] J. J. Rubio, "Sliding mode control of robotic arms with deadzone," *IET Control, Theory and Applications*, vol. 11, no. 8, pp. 1214–1221, 2017.

[7] C. Aguilar-Ibanez, H. Sira-Ramirez, M. S. Suarez-Castanon, and R. Garrido, "Robust trajectory-tracking control of a pvtol under crosswind," *Asian Journal of Control*, vol. 21, pp. 1293–1306, 2019.

[8] C. Aguilar-Ibanez and M. S. Suarez-Castanon, "A trajectory planning based controller to regulate an uncertain 3D overhead crane system," *International Journal of Applied Mathematics and Computer Science*, vol. 29, no. 4, pp. 693–702, 2019.

[9] Y. Chang, Y. Wang, F. E. Alsaadi, and G. Zong, "Adaptive fuzzy output-feedback tracking control for switched stochastic pure-feedback nonlinear systems," *International Journal of Adaptive Control and Signal Processing*, vol. 33, no. 10, pp. 1567–1582, 2019.

[10] Y. Chang, S. Zhang, N. D. Alotaibi, and A. F. Alkhateeb, "Observer-based adaptive finite-time tracking control for a class of switched nonlinear systems with unmodeled dynamics," *IEEE Access*, vol. 8, 2020.

[11] Y. Wang, Y. Chang, A. F. Alkhateeb, and N. D. Alotaibi, "Adaptive fuzzy output-feedback tracking control for switched nonstrict-feedback nonlinear systems with prescribed performance," *Circuits, Systems, and Signal Processing*, 2020.

[12] B. Jiang and H. R. Karimi, "Further criterion for stochastic stability analysis of semi-Markovian jump linear systems," *International Journal of Robust and Nonlinear Control*, vol. 30, no. 7, pp. 2689–2700, 2020.

[13] B. Wang and Q. Zhu, "Stability analysis of discrete time semi-markov jump linear systems," *IEEE Transactions on Automatic Control*, vol. 65, no. 12, pp. 5415–5421, 2020.

[14] W. Hu, Q. Zhu, and H. R. Karimi, "Some improved razumikhin stability criteria for impulsive stochastic delay differential systems," *IEEE Transactions on Automatic Control*, vol. 64, no. 12, pp. 5207–5213, 2019.

[15] H. Wang and Q. Zhu, "Global stabilization of a class of stochastic nonlinear time-delay systems with SISS inverse dynamics," *IEEE Transactions on Automatic Control*, vol. 65, no. 10, pp. 4448–4455, 2020.

[16] C. Yuan, S. Song, Q. Gao, H. R. Karimi, L. Pekar, and S. Guo, "A novel frequency-domain approach for the exact range of imaginary spectra and the stability analysis of LTI systems with two delays," *IEEE Access*, vol. 8, pp. 36595–36601, 2020.

[17] Q. Zhu, "Stability analysis of stochastic delay differential equations with Lévy noise," *Systems & Control Letters*, vol. 118, pp. 62–68, 2018.

[18] Q. Zhu and T. Huang, "Stability analysis for a class of stochastic delay nonlinear systems driven by G-Brownian motion," *Systems & Control Letters*, vol. 140, Article ID 104699, 2020.

[19] M. Li, H. Chen, and X. Li, "Synchronization analysis of complex dynamical networks subject to delayed impulsive disturbances," *Complexity*, vol. 2020, Article ID 5285046, 12 pages, 2020.

[20] Q. Zhu, "Stabilization of stochastic nonlinear delay systems with exogenous disturbances and the event-triggered feedback control," *IEEE Transactions on Automatic Control*, vol. 64, no. 9, pp. 3764–3771, 2019.

[21] A. Azizi, "A case study on computer-based analysis of the stochastic stability of mechanical structures driven by white and colored noise: utilizing artificial intelligence techniques to design an effective active suspension system," *Complexity*, vol. 2020, Article ID 9321928, 17 pages, 2020.

[22] W. Ji, J. Qiu, and H. R. Karimi, "Fuzzy-model-based output feedback sliding-mode control for discrete-time uncertain nonlinear systems," *IEEE Transactions on Fuzzy Systems*, vol. 28, no. 8, pp. 1519–1530, 2020.

[23] B. Xiao, X. Yang, H. R. Karimi, and J. Qiu, "Asymptotic tracking control for a more representative class of uncertain nonlinear systems with mismatched uncertainties," *IEEE Transactions on Industrial Electronics*, vol. 66, no. 12, pp. 9417–9427, 2019.

[24] Q. Zhu and H. Wang, "Output feedback stabilization of stochastic feedforward systems with unknown control coefficients and unknown output function," *Automatica*, vol. 87, pp. 166–175, 2018.

Hindawi
Complexity
Volume 2020, Article ID 1680845, 10 pages
https://doi.org/10.1155/2020/1680845

Research Article

Research on How Human Intelligence, Consciousness, and Cognitive Computing Affect the Development of Artificial Intelligence

Yanyan Dong,[1] Jie Hou,[2] Ning Zhang,[3] and Maocong Zhang[4]

[1]*Department of Education, Shandong Normal University, Jinan 250014, China*
[2]*Institute of Higher Education, Shandong Normal University, Jinan 250014, China*
[3]*Harris School of Public Policy, University of Chicago, Chicago 60601, USA*
[4]*Center of Educational Policy and Management, Shandong Normal University, Jinan 250014, China*

Correspondence should be addressed to Maocong Zhang; shd851@163.com

Received 15 July 2020; Revised 28 September 2020; Accepted 19 October 2020; Published 28 October 2020

Academic Editor: Ruofeng Rao

Artificial intelligence (AI) is essentially the simulation of human intelligence. Today's AI can only simulate, replace, extend, or expand part of human intelligence. In the future, the research and development of cutting-edge technologies such as brain-computer interface (BCI) together with the development of the human brain will eventually usher in a strong AI era, when AI can simulate and replace human's imagination, emotion, intuition, potential, tacit knowledge, and other kinds of personalized intelligence. Breakthroughs in algorithms represented by cognitive computing promote the continuous penetration of AI into fields such as education, commerce, and medical treatment to build up AI service space. As to human concern, namely, who controls whom between humankind and intelligent machines, the answer is that AI can only become a service provider for human beings, demonstrating the value rationality of following ethics.

1. Introduction

The term "artificial intelligence" was first used by John McCarthy at Dartmouth Conference in 1956. Since then, artificial intelligence (AI) has gone through three booms during decades of scientific and technological development. The first boom was from 1956 to 1976. Since the 1950s, humans had successively invented the first perception neural network software and chat software and proved some mathematical theorems, exclaiming that the "AI era is coming" and that "robots will surpass human beings in 10 years." During the second boom (1976–2006), Hopfield neural network [1] and BT training algorithm proposed in the 1980s made AI popular again, which led to the emergence of speech recognition, speech translation plan, and Japan's fifth-generation computer idea. However, these ideas fell through and the second boom broke up again. After data accumulated to a certain amount, some results would stop rising to some extent. During the third boom (2006 till now), AI broke out again as Hinton put forward deep learning technology in 2006 and ImageNet Competition made breakthroughs in image recognition in 2012. In 2016, AlphaGo defeated Lee Se-dol, once the world champion of Go, and that was regarded as the peak of AI development.

Now, humans have made great progress in various fields such as cognitive psychology, neuroscience, quantum physics, and brain science, and theories related to artificial intelligence have kept emerging. Without the integrated development of computer science with brain science, neuropsychology, linguistics, and other disciplines, the research and development of AI would not have made such great achievements. AI research has also presented some research highlights such as machine learning, neural network (NN), expert system, genetic algorithm (GA), fuzzy inference system (FIS), support vector machine (SVM), and particle swarm optimization (PSO) [2], as shown in Figure 1. AI has

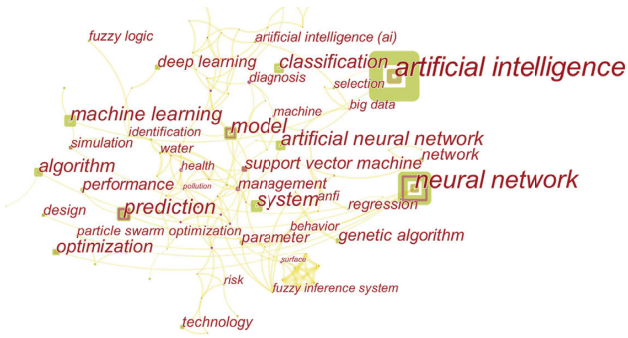

Figure 1: Knowledge graph of AI research hotspots.

been widely used in each aspect of human life, even surpassing human intelligence in some areas. AI can, to some extent, replace humans to complete the tasks of recognition, decision-making, and control. In terms of recognition, AI can distinguish, classify, and retrieve information. In the aspect of decision-making, AI can carry out numerical object evaluation and matching. Regarding control, AI can complete performance generation, design and action optimization, and operation automation.

However, scientific, technological, and social problems arisen from the development of AI are drawing more attention from the public. While promoting social progress, the widespread application of AI also has some prominent negative effects. For example, the application of robot has led to unemployment [3]; the application of AI has widened the gap of wealth; AI algorithms have caused bias; big data has resulted in privacy leakage and degeneration of human's spiritual life. All these are social problems brought about by the application of AI technologies. In his book *AI Future*, Kai-fu Lee analyzed the employment risks of manual and mental labor caused by AI. For manual workers, structured jobs with weak social interactions and low skills are facing higher risks, such as truck drivers, fast food cooks, and sewing workers. For mental workers, those engaged in weak social and low creative jobs are in greater danger of unemployment, such as radiologists and telemarketers. Therefore, in the AI era, it is inevitable for some occupations or jobs to be replaced. If your job does not require much talent and skills can be acquired through training, if what you need to do is a lot of repetitive work without too much thinking, and if you work in a narrow social network and have little communication with others, then you are highly likely to be replaced by AI.

The deconstruction and reconstruction of the occupational structure is just one aspect of what AI has brought about. Some people even put forward the "machine threat theory." Understanding AI is the prerequisite of applying it. AI is in essence the simulation of human intelligence and its development depends on breakthroughs of algorithms. Considering this relationship as well as human's confusion and concerns in understanding AI, this paper first analyzes the nature of AI, AI, and consciousness, as well as the features and advantages of cognitive computing, and further forecasts the future development of AI.

2. The Nature and Characteristics of AI

The difference between AI and ordinary computers lies in the new forms and technical means of AI, but they share the same nature. AI is still a tool of humans [4]. To accurately grasp AI, we can make an analysis from two aspects: hardware and software. From the hardware point of view, intelligent machines like computers and robots are physical and chemical entities separated from human brains. Although they are not physiological structures of human reflection and control systems, they are developed from the hardware of the system. The human brain is also hardware, but it is a physiological entity instead of a physical or chemical one. The human brain provides the material base of the reflection and control function. In this sense, the brain entity provides the structure and thinking offers the function. Intelligent machines have physical and chemical structures, in which electrons make a physical movement. This structure is a prerequisite for AI. The physiological structure of the human brain is different from the structure of intelligent machines, so they have no physiological or fixed hardware connections. Therefore, although intelligent machines are developed from the hardware of human's reflection and control system, their development is relatively independent. However, this does not mean that the hardware of intelligent machines can never be coupled with the human brain. Instead, it shows that strengthening the hardware connection between the human brain and intelligent machines is an attractive direction for intelligent development.

The intelligence of AI lies in its software. Why is AI possible? How is it related to human brain intelligence? To answer these questions, we need to carry out software analysis. Thinking is the function of the human brain. The analysis of thinking can be carried out through the functional structure method, hierarchical method, or the two approaches combined. From the hierarchy perspective, thinking has several layers: the first one is the layer of form, which is language; and the second one is the layer of content, which is the consciousness concept. These two layers are inward analysis of thinking itself. From the perspective of its interaction with its applied object, there is another layer of thinking, i.e., its outward function layer. When these three layers are divided according to a functional structure, language and consciousness concept are the internal structures, while the functional layer boasts the external function of thinking and consciousness, namely, intelligence. Consciousness concept, as the internal structure of thinking, refers to the structure of consciousness. Depending on the internal structure, reflection and control activities have corresponding manifestations at all internal levels of thinking. In the content level, it is shown as the activities of various consciousnesses and in the form level as corresponding language activities. Without the activities at all internal layers of thinking, there would be no overall intelligence or activity. Activities at the language layer are coding activities inside the human brain, which can be carried out directly by the bioelectrical movement.

Therefore, when people think of specific words, there are always corresponding specific electrical signals in the brain.

The fact that thinking activities have specific manifestations at the language level shows that thinking can be formalized through language. Language is not a conscious or conceptual thing. Instead, it has a corresponding movement of electrical signals in the brain, showing the characteristic of physical movement. As far as language and electrical signals are concerned, language is the content while electrical signals are the form. Language outside the brain refers to the sound that can be heard and words that can be seen. The internalization of language outside the brain is completed by the brain's thinking language, whose existence depends on the physiological, chemical, and physical movements of the brain. When dissecting a human brain, there is no language entity inside. Instead, only corresponding brain structures and movement can be found. Therefore, the role of the language inside the brain is highlighted as the coding rules of electronic movement. Only when there is a specific movement of electrical signals in the brain can there be language movement and further consciousness activities. These serial relationships lay a foundation for formalizing thinking activities, namely, linguisticization, and then for the electronic movement. This is the most fundamental reason why electronic computers are able to simulate the intelligence of the human brain.

In short, AI is not independent. It is within the scope of human intelligence and part of it. The reason why AI belongs to human intelligence is that it is a product of human intelligence developed to a certain historical stage, a tool of the human brain, and an expansion of human intelligence [5]. All AI is extending along the direction of human intelligence, and all their functions in various fields of social life are within the scope of reflection and control. With the development of humankind, all aspects of social life today are increasingly complex, which makes it more and more difficult for the human brain to make direct adjustment and control and increasingly unable for mankind to meet the requirements in both magnitude and precision. As a result, the activities in many fields of society cannot be regulated and controlled only by human intelligence. Of course, this is not the limitation of the human brain in quality, but in quantity. Therefore, the development of human intelligence can be achieved by brain expansion in a certain way, so as to meet the requirements of social life.

3. AI and Human Consciousness

In the coming years, machines will get smarter. If we cannot distinguish a machine from a human, then we have reason to think that this machine is intelligent [6]. Therefore, the question we are going to face is as follows: can an intelligent machine be considered as having consciousness? This requires us to understand the relationship between AI and human consciousness.

3.1. AI Promotes the Development of Human Intelligence. As a necessary supplement to human intelligence, AI effectively extends the human brain and enlarges its intelligence. AI and the human brain are correlated and have been supporting each other forward. All these make human cognition scope continuously expand to the micro- and macropoles, enabling people to have a deeper understanding of the essence of things indirectly, and greatly enriching the content of consciousness.

AI, which simulates human operational intelligence, is far superior to human beings in computing speed, capacity, and accuracy. It indeed can liberate mental labor. With the support of the Internet and big data technology, AI will help humans in more fields and more profoundly, even conducting rescue operations in extreme environments. In the field of medical practice, brain stimulation is helpful to restore the damaged brain nerve. In terms of transportation, with the application of data, connection, real-time sensing, and traffic prediction, humans will experience shared riding and automatic driving for the first time. The revolution of the third-generation culture carrier represented by AI will promote the great change of human memory and learning style. AI is our brain assist device, which stores a lot of information in an intact manner. The undertaker of memory and thinking is gradually separating from the human body and tends to become objectified. Portable computers have replicated what we call as cognition, and even our human rationality also faces challenges. However, human beings can use their dynamic intuition and give play to their innovation abilities [5]. The printing carrier once ushered in a period of flourishing human culture. Now, we should keep an open mind on the promotion role of AI in human consciousness. AI technology has put forward new requirements for human data observing and processing ability. The workers who receive information technology (IT) vocational training will better adapt to the changes, so we can be one step forward in the transformation to an intelligence-intensive society. With the help of intelligent machines, humans could become new-type, creative, and reliable cognitive subjects.

3.2. Human Consciousness Restricts the Development of AI. The nature of consciousness affects the development of AI. Consciousness can be introspective, which reveals what cannot be reached by the objective research on consciousness. Human consciousness is not a passive or negative reflection of reality; instead, it is a positive and active one. When determining the behavior of the subject, the external experience must be reflected through the inner world as well as the thinking and feeling system of the subject. The so-called animal consciousness is a statement untested, because animals cannot distinguish themselves from their activities. They are integral. The same is true of artificial consciousness. Although AI can complete part of human thinking activities, it does not understand the meaning of doing this. It operates mechanically and aimlessly. Even if AI has a purpose, it is all instilled by humans to achieve goals of themselves. After 70 years, the movement of logical functionalism ended in a dismal way, while the structuralism of consciousness points out a new direction for AI. Structuralism has a successively experienced semantic network and neural network. The latter one argues that connections among things in the world

are all the same, while the differences lie in their frequencies of occurrence. The neural network cannot distinguish the "White" as a name and the "White" as a color. This kind of AI, in essence, is a program or function that makes similar reflex responses to specific stimuli. AlphaGo is weak AI, and programming is not an effective way to achieve a machine's consciousness.

The change and development of consciousness bring about corresponding changes in AI. Under the consciousness theory system of a subject-object dichotomy, abstract operational rules promote the R&D of algorithms. This theory argues that human consciousness can be simply summarized as the brain's symbolic operation, while the characteristics of consciousness in intuition, common sense, and external environment are ignored. In fact, the change in AI development level is indeed related to the development of human consciousness. Behaviorism and structuralism, which are similar to the human brain neural network, are simulations of human adaptive mechanisms and not restricted by forms. Subject-object integration, a philosophical trend focusing on the interaction with the real world, provides ideological inspiration for AI. Human consciousness theory criticizes principles of form. Deep learning represented by AlphaGo has gotten rid of structural restrictions and acquired problem-solving strategies through learning human's experiences. In 2016, by adopting Monte-Carlo Tree Search (MCTS) and deep learning (DL) to think from the whole picture and make the optimal choice, AlphaGo, a program developed by DeepMind, won the Go game, getting rid of the restrictions of brute force method [7]. When embodiment philosophy arose, AI began to imitate the human body's movement and gestures, such as simulating the rules of facial movement. To some extent, the fact that AI began to shift its focus to the human body and external environment is inseparable from the exposition of consciousness by phenomenologists [8]. We can tell that although the philosophical theory of consciousness cannot directly improve the technical essence of AI, its development and change will provide foresight for the exploration of AI.

4. AI and Cognitive Computing Technology

AI is a broad concept. From the perspective of ultimate goals, cognitive computing is an important way to realize AI. Cognitive computing refers to cognition and effective expression of the internal meaning of the objective world as well as of various pieces of information and data that can be observed and measured at present. It is the expression of AI toward specific problems to be solved.

4.1. The Concept of Cognitive Computing. Cognitive computing is a technique that enables humans to cooperate with machines. This term comes from cognitive science and artificial intelligence. It builds algorithms with theories of cognitive science to simulate human's objective cognition and psychological cognition process, so as to enable machines to reach a certain degree of "brain-like" cognitive intelligence [9]. Cognitive computing uses technology and algorithm to automatically extract concepts and relationships from data, understand their meanings, learn independently from data patterns and prior experience, and ultimately extend what people or machines could do on their own. Based on this, Roma further put forward three main applications of cognitive computing: robotic and cognitive automation to automate repeatable tasks to improve efficiency, quality, and accuracy; cognitive insights to uncover hidden patterns and relationships to identify new opportunities for innovation; and cognitive engagement to drive customer actions by delivering hyper-personalization at scale [10]. Cognitive computing is a synthesis of technologies where each of them contributes a distinct methodology for addressing problems in its domain. Artificial Neural Network (ANN) uses the interactions of biological neurons as a model for pattern recognition, decision, modeling, and forecasting. Fuzzy logic uses approximate information in a manner similar to the human decision process and is useful in control and decision-making applications. Evolutionary computation adopts natural selection and evolution theory and is useful in optimization. Cognitive computing provides an effective way to analyze technological processes and human activities [11].

Based on the above concepts, cognitive computing can be simply understood as a technical field that integrates multiple technologies and aims to use artificial mechanisms based on computing technology to realize the human cognitive function. It is the core technical field of cognitive science. In essence, cognitive computing is expected to understand the internal relationships among various kinds of data and phenomena in the real world through technologies, such as AI, pattern recognition, and machine learning, and further develop tools and systems to improve productivity, protect the environment, and contribute to social governance.

4.2. Characteristics and Advantages of Cognitive Computing. After tabular computing and programming computing, now the era of cognitive computing is coming. Generally speaking, cognitive computing has a wide range of applications, including participation, decision-making, discovery, and other aspects, centering the improvement of human's "cognitive" ability. Leslie G. Valiant from Harvard University thought that compared with other approaches, cognitive computing has three main characters: each act of memorization, learning, or recall is an algorithmically simple process executed on a network laden with information previously acquired; the system learns continuously as a background activity; in more complex cognitive processes such as analyzing complex scenes or reasoning, the internal computations have an important time domain and state information needs to be retained [12]. The cognitive computing system has a strong comprehension ability. Through natural language comprehension technology and its superior ability to process structured and unstructured data, it can interact with users in various industries and then understand and respond to their problems. The cognitive computing system has an intelligent logical thinking ability.

It can reveal insights, patterns, and relations through data and hypothesis and connect scattered pieces of knowledge for reasoning, analysis, comparison, induction, summary, demonstration, and obtainment of deep insights and evidence for decision-making. The cognitive computing system has excellent learning ability. Through evidence-based learning ability, it can rapidly extract key information from big data and learn like a human. It can gain feedback through expert training and experience learning in the interaction to optimize models and make improvements. In addition, a cognitive computing system also has elaborated personalized analysis ability. Using text analysis and psycholinguistic models, it can conduct an in-depth analysis of massive social media data and business data, grasp users' personalities, and portray individuals in an all-around way. This system is not a simple collection of all these technologies. Instead, it integrates these technologies in an unprecedented way, profoundly changing the means and efficiency of solving business problems.

Compared with previous computing paradigms, cognitive computing has significant characters in adaptability, interaction, iteration, and context sensing. It can perceive the surrounding environment and context and make the corresponding self-adaptation. Cognitive computing requires dynamic programming and must understand, identify, and extract context elements, such as connotation, grammar, time, location, regulation, user profile, process, tasks, and targets. They might use multiple information sources, including structured and unstructured digital information, and sensorial inputs, such as vision, gesture, hearing, or information of the sensors. Cognitive computing also has the "memory" function and is able to conduct an iterative operation. The cognitive computing system must be able to remember previous interactive information to make rational reasoning and aid decision-making through the superposition of information and semantics. For instance, as a digital medical aid, when a user communicates with it about the personal situation of "chest distress or insomnia" at 1:00 a.m., the medical aid must "recognize" the current time and the user's situation, make comprehensive judgments combining user's previous conditions, and offer a reasonable suggestion.

At present, there are four key technologies of cognitive computing recognized by researchers: first, machine learning, natural language understanding, and human-computer interaction techniques which are on the top floor; second, big data technologies, including how to store, organize, manage, and analyze big data; third, computer architecture (the computing ability required by the cognitive system is far more than what we can provide today; therefore, how to realize the design of a data-centered system is also a challenge facing us today); fourth, at the bottom level breakthroughs of atomic and nanotechnologies which are required [13]. There are two main tasks of cognitive computing: one is to study and simulate a human's understanding of the objective world through a computer; the other is to take the cognition and value discovery of information and data as the main goal. Compared with AI, the research of cognitive computing is deeper and more specific. "Deeper" means that it does not only study the simulation of human brain behavior but also focus on the understanding of the operation law of the objective world as well as the internal law and external expression of the data generated in the world; "more specific" means that it has more direct expressions in the applied business area, which can offer direct decision-making suggestions to corporate leaders.

5. Forecast of Future Development of AI

What kind of role will AI play in the future? Professor Jiang from Stanford University said, "I hope young people can understand the difference between the working mode of AI and that of humans, and then develop the abilities that can distinguish them from AI." [14]. From the perspective of core technologies, breakthroughs in three levels are expected to advance further development of AI. The breakthroughs in platforms, algorithms, and interfaces will promote AI to achieve leapfrog development. Building an intelligent platform that can serve various enterprises and meet different demands will be a major trend of future technological development.

5.1. Making Innovations of Intelligent Technologies and Realizing Reproduction of Human's Personalized Intelligence. At present, AI is still in the "weak AI" phase and can only simulate, extend, and expand low-end human intelligence, namely, human's feelings, perceptions, and conventional and programmed logical reasoning. As for human's high-end creative intelligence, imagination, intuition, potential, and unconventional and nonprogrammed personalized intelligence such as tacit knowledge, experience, and skills which can only be expressed through behavior, "weak AI" is not able to simulate them, let alone extension or expansion. This high-end and unconventional intelligence can only be simulated, extended, and expanded when we enter into a "strong AI" phase.

The development of AI is, in varying degrees, based on the research of brain science. The inexplicable "black box" characteristics of its operation are closely related to the fact that brain science has not yet fully grasped the operation rules and mechanisms of human brain intelligence. The cracking of AI's "black box" characteristic depends on the further development of brain science. Will AI surpass man's biological intelligence in the future? This kind of judgment actually presupposes that machine intelligence has great development potential, but it ignores the fact that brain science has already revealed that human brain intelligence is also far from being fully exploited and released and also enjoys great potential. In terms of AI, the proportion of human intelligence that can be simulated or extended is just the tip of the iceberg above the water, only including the conventional, logical, explicit, and universal consciousness and intelligence. The vast number of unconventional, illogical, and personalized consciousnesses hidden in the water is still difficult to be simulated or extended. As is pointed out by the "Iceberg Theory" of the psychoanalyst Freud, the human psychological structure is composed of consciousness, preconsciousness, and subconsciousness.

Consciousness is only the tip of the iceberg above the water, while subconsciousness occupies most of the psychological structure and hides below the water surface [15]. This is mainly because humans have little cognition and development of this part of consciousness and intelligence, not to mention the artificial intelligence of it. Of course, with the continuous development of the brain, human potential, and AI itself, it is possible for AI to simulate and extend human's personalized and fuzzy consciousness and intelligence. American futurist Ray Kurzweil once predicted that the year 2045 will be a time of profound and divisive transformation, "abiotic intelligence in this year will be a billion times the wisdom of all human beings today" [16].

How to realize strong AI? This requires a "brain-computer interface" (BCI), a cutting-edge research area. It studies the means of establishing a direct connection between human or animal brains and external devices to translate consciousness in real time and ultimately transfer and download thoughts freely among humans or between humans and machines. Astonishingly, Neuralink, a brain-computer interface research company founded by Elon Musk, released a groundbreaking "brain-machine interface" technology, which utilizes threads 4 to 6 μm thick, less than a tenth of that of hair, to transmit brain signals fetched by chips. Tiny electronic devices are implanted in the brain so that thoughts can be transmitted through wireless devices and even interact with iPhone apps. Brain-computer interface technology can realize four functions. By manipulating machines through the mind, machines can replace some functions of the human body and repair the physical defects of the persons with disabilities. Anything can be controlled through the mind. Brain operation can be improved through BCIs, making us feel like we have just had a good sleep and feel energized, focused, and quick on the trigger so that we can work soberly and efficiently. In 2014, ABM, an American company, trained testers through an EEG brain-computer interface, making novices learn 2.3 times faster than before. Through the brain-computer interface, we can acquire a lot of knowledge and skills in a short time and even acquire superpowers that ordinary humans cannot possess. With a brain-computer interface, human beings can communicate with each other without using language and only rely on neural signals in the brain, thus realizing "lossless" brain information transmission. Musk crazily envisions that human-computer combination can help realize faster and more accurate communication, and this nonverbal communication is better. However, we believe that communication is a basic human behavior and also the basis of human cooperation. In a virtual digital space, the human language will evolve rather than be replaced entirely. The future development of AI is to enhance, not to replace, the overall intelligence of human beings and promote the complementation of AI and human intelligence, giving play to their respective advantages to realize the "coevolution" of human and AI machines.

5.2. Making Breakthroughs in Specialized Algorithms and Building Intelligence Service Space. AI is expected to soon obtain an almost infinite information storage space, quantum computing ability 100 times or even 10,000 times more than that of humans, and breakthroughs in various specialized algorithms. Even if an AI system is equipped with the most advanced current computing platform, without effective algorithms, it will only be like a person with well-developed limbs but the head of a moron, which cannot be regarded as having real intelligence. The enhancement of algorithm capability will further promote the continuous breakthroughs of AI. In many consumption scenarios in life, people's demand for personalized experience is increasing, and personalized and scene-based services will gradually become the main direction of AI-driven innovation. With the help of the Internet, a professional-level knowledge base together with program settings is expected to "answer" most professional or scientific questions in the near future. Their professional abilities are equivalent to those of senior doctors, architects, engineers, math professors, and so on.

In the field of education, AI can become an important driver for the education of students. It has unique advantages in creating large-scale personalized learning environments and building smart campuses. With the deep integration of education with cloud computing, big data, VR/AR, and other technologies, the application of AI in the field of education has infinite potential and possibility in the future [17]. At present, BCI technology is applied to measure students' implicit data, including their learning status, attention level, cognitive load, and learning style [18, 19]. Brain measurement can reveal the brain differences among students and enhance our understanding of learning [20]. Based on the attention data collected when different learners watched, listened, read, wrote, or operated learning materials, the SVM learning algorithm was used to identify their learning styles. Its average recognition rate was 75.8%, and the highest accuracy of a single time was 83.3% [21]. In the future, cognitive computing will be mainly used to customize personalized learning assistants for students to improve their overall learning experience. Through collecting and analyzing students' learning data, AI gradually outlines each student's learning style and characteristics and then automatically adjusts teaching content, method, and pace, so that students can have access to the most suitable education for themselves. Not only does an intelligent learning system easily provide personalized teaching for students, but also real-time data and automatic analysis provide teachers with a lot of information so that they can have a deeper understanding of each student. Meanwhile, data can guide teachers to constantly improve their teaching content and make more accurate teaching planning based on the problems of each student, so that their teaching could be more targeted. However, it should be noted that everything will become different in the future. Only the ability to solve new problems remains unchanged [21]. 98 percent of our genetic make-up is the same as that of chimpanzees, but our language, values, artistic expression, understanding of science, and research of technologies make us distinctive. This is the result of creativity, which is credited with most of the interesting, important, and humanized things. Creative people tend to be more independent in thinking and operations. They tend to be imaginative, curious, and willing to

try and take risks. In its competition with the Go genius Jie Ke, AlphaGo was like a martial arts master who could absorb the opponent's power. Each manual and game could be an effective source driving its power growth. It was so powerful that even one of the smartest humans felt "cold." Moreover, robots never get angry or tired, so it is impossible for humans to win the competition with machines. Therefore, "we cannot just instill our children with knowledge, because machines can learn faster [22]."

In the health care area, many companies are developing AI technologies that can be used in the medical field. Classification and identification capabilities are the primary goals of these devices. It can be very helpful in identifying carcinogens because it can help inspectors interpret countless documents in less time. In addition, it can evaluate relevant information of patients, go through all the medical records thoroughly, find clues that may cause the problems of patients, and assist diagnosis. Through the analysis of the medical history of patients based on lots of medical textbooks and related data, AI can provide some diagnostic bases for doctors. Sometimes, they may offer disease diagnosis that doctors have never considered or even do not know. In the business area, combined with big data and algorithms which can meet the demands of customers, AI can play an important role in the economic decision-making process. Companies can use AI to incorporate various risk factors into their decision-making process and then offer effective suggestions on investment or site selection of branches. In the field of finance, AI promotes the rise of humanized fin-tech, which can be widely adopted by banks and financial institutions to serve growing numbers of customers more effectively. Besides automatically performing back-end and administrative tasks, it can also take the initiative in activities toward customers. In the manufacturing industry, AI can assist designers to complete the design of products. Ideally, it can largely make up for the shortage of medium and high-end designers, thus greatly improving the product design capabilities of the industry. Meanwhile, by mining and studying a large amount of production and supply chain data, AI is expected to help optimize the allocation of resources and improve the efficiency of enterprises. In an ideal situation, AI can provide enterprises with whole-process support including product design, raw material procurement plan and distribution, production and manufacturing, and user's feedback data collection and analysis, so as to promote the transformation and upgrading of China's manufacturing industry.

5.3. Demonstrating Value Rationality and Avoiding Ethics Risks. Understanding the trend of technological and ethical risks of AI is a part of the research on the development trend of AI. And how to effectively avoid these risks is also a very popular research topic in the field of AI.

In various AI application scenarios such as data analysis, content recommendation, and face recognition, human identity and behavior are directly involved and affected. The harm and negative impact of abusing related technologies will be far greater than that of traditional networks and digital technologies [23]. Specifically, there is algorithmic bias in AI applications. An algorithm is essentially an objective mathematical expression, but modeling and data input are completed by humans. In this process, human's inherent bias and discrimination will affect the decision-making of the algorithm and then lead to ethical problems such as algorithmic bias. There are social ethical problems with AI. The application of AI in human life makes the relationship between humans and machines increasingly complicated, further leading to a series of social-ethical problems. Among them, the most primary one is whether AI can replace humans to work? From the perspective of operational effectiveness and economic efficiency, a large number of white-collar or blue-collar jobs will be occupied by AI in the future, which will inevitably lead to large-scale technical unemployment and, to a certain extent, lead to the antagonism between human and AI. There are responsibilities and emotional ethical problems with AI. The widespread application of AI brings about the difficulty in judging subjects in many events or cases. For example, during the sudden braking of driverless automobiles in case of emergency, each step adopted by AI is stipulated by algorithms, which are set by human beings. Therefore, ethical problems are bound to arise in the judgment of liability subjects in scenarios like this. If we stick to the position of optimism and pragmatism without introspection, the potential threats of AI to society and individuals will be overlooked or ignored and the ethical risks will not be prevented in advance or corrected afterward. It will inevitably not only lead to serious consequences but also destroy the trust of the whole society in AI, which will inevitably bring on huge risks and losses to the institutions and enterprises within the innovation ecosystem.

In order to standardize the development of AI, the UK Government Office for Science published the report "Artificial Intelligence: opportunities and Implications for the Future of Decision Making" in 2015, which pointed out the serious consequences of algorithmic bias, nontransparency, and improper accountability and stressed that further development of AI should be based on the premise of enabling innovation, building trust among citizens, establishing a stable environment, and fostering appropriate access to the data necessary [24]. In December 2016, the Institute of Electrical and Electronics Engineers released "Ethically Aligned Design: A Vision for Prioritizing Human Wellbeing with Artificial Intelligence and Autonomous Systems, First Edition," which suggested that "human benefit," "responsibility," "transparency," and "education and awareness" should be the general principles in the research and development process of products [25]. In June 2019, the "G20 AI principles" were issued in the communique of the G20 Ministerial Meeting on Trade and Digital Economy, which made it clear that AI systems should be "stable and secure" in the whole life cycle and put forward five principles for responsible stewardship of trustworthy AI [26]. In the same month, the "Governance Principles for the New Generation Artificial Intelligence—Developing Responsible Artificial Intelligence" was released by the National Governance Committee for the New Generation Artificial Intelligence of

China, proposing eight principles of "harmony and human-friendly," "fairness and justice," "inclusion and sharing," "respect for privacy," "safety and controllability," "shared responsibility," "openness and collaboration," and "agile governance" [27].

Most of the above documents consider the possible impact of AI technology applications on society from the perspective of national development strategy. Science is a powerful instrument. How it is used, whether it is a blessing or a curse to mankind, depends on mankind and not on the instrument [28]. Generally speaking, the ethical norm of AI aims to equip AI with a "good core (conscientiousness)." This means that, different from other technologies, the ethical research of AI should be carried out centering "machine's core" and "human conscientiousness." "Machine's core" mainly refers to the moral algorithm of AI, which aims to instill "good ethics" into AI so as to generate moral AI or machines. "Human conscientiousness" mainly refers to the design and application ethics of AI, which aims to enable the developers and users of AI to have "conscientiousness," ensuring the design of AI conform to morality, avoiding malicious design, and making sure that AI is used rationally to benefit human society. Whether AI is a "blessing" or a "curse" to mankind depends on what kind of value human holds. Only by highlighting the value rationality in the design of AI and avoiding the distortion of its development, we can realize the sustainable development of human beings and finally achieve human liberation.

6. Conclusion

Based on the above analysis, the following conclusions are drawn:

(1) In the future, the human-computer combination can help realize faster and more accurate communication, and this nonverbal communication is better. However, we believe that communication is a basic human behavior and also the basis of human cooperation. In a virtual digital space, the human language will evolve rather than be replaced entirely. The future development of AI is to enhance, not to replace, the overall intelligence of human beings and promote the complementation of AI and human intelligence, giving play to their respective advantages to realize the "coevolution" of human and AI machines. Breakthroughs in algorithms represented by cognitive computing promote the continuous penetration of AI into fields such as education, commerce, and medical treatment to build up AI service space. As to human's concern, namely, who controls whom between humankind and intelligent machines, the answer is that AI can only become a service provider for human beings, demonstrating the value rationality of following ethics

(2) If we view the emergence of AI from the historical process of human inventing, manufacturing, and using tools, we will find that AI is an intelligent tool. Though it has qualitative differences from previous physical tools, based on their nature as tools, they have some same characteristics. In the competition between man and AI, AlphaGo's victory, in fact, is not the victory of intelligent robots but the victory of many present and past Go experts. Therefore, we cannot simply draw the conclusion that the intelligence of robots is higher than that of humans or that robots can replace or dominate humans. We should view AI from the history of human inventing and using tools and from the relationship between humans and tools. From the perspective of tool theory, the earliest tools of mankind are stone implements made by the primitive ancestors. After entering the agricultural civilization, farmers invented, manufactured, and used various farm tools. After entering the industrial civilization, engineers invented and manufactured a variety of automated machines. Stone implement, farm tools, and machines are all the replacement, extension, and expansion of human physical ability. Every qualitative leap of physical tools is a huge liberation of human physical fitness, improving productivity and promoting social development and progress. In the postindustrial civilization era, most of the original artificial physical fitness has been transformed and replaced by artificial intelligence. The birth of AI is another revolution in human tools' history. AI is not only automated but also intelligent. It can replace, extend, and expand not only most of the human physical fitness but also part of human intelligence. It frees humans from not only burdensome and tedious physical labor but also part of the mental labor, once again rapidly improving productivity and promoting human development and social progress

(3) Intellectualization is the inexorable trend of the future whether seen from the maturity of the technology or seen from the development of human intelligence. As Kurzweil said, we could neither prevent the acceleration of change nor prevent AI from surpassing humans in various fields [17]. The most unique feature of AI technology is that it can endow "machine" with "intelligence." Technologies were invented by "human intelligence" before. However, from now on, technologies can also be invented by "the machine's intelligence." An important mark of the coming of AI singularity is "producing intelligence with machine's intelligence" [29]. By 2050, AI will be infinitely close to human intelligence. However, mankind "still has the right to determine future technologies and life." In other words, many advanced abilities of human beings are irreplaceable by AI. AI can only be a service provider for human beings. Although from the fractional and individual level, AI can replace, expand, and surpass humans; its position as a subject is stronger than that

of a human, namely, it can dominate and control individuals, and humans serve AI. However, from the perspective of the whole and mankind, AI is an electronic machine, not an animate individual, having no life form or movement. It has no independent needs, attributes, nature, consciousness, or social behavior like human beings. Therefore, it is impossible for AI to become a subject like a human. On the contrary, it can only be a machine used by people, being tools and accessories in human production and life. If we excessively rely on AI, we will have a dependence tendency, and this tendency (for example, we think that the data provided by advanced instruments are the most perfect and reliable) will not only make people lose their critical thinking skills but also cause irreversible mistakes or disasters. Therefore, for human beings and society, many key abilities, such as the ability to promote social and human progress, can only rely on ourselves

In human history, all major technological revolutions have brought about shocks to humankind and even the whole society. The invention of ironware and the beginning of traditional agricultural society sparked a war in the cold weapon era. In China, this war lasted from the Spring and Autumn Period and the Warring States Period to the Han Dynasty. The invention of electricity and the arising of industrial society incurred World War I and World War II, staining the first half of the 20th century with blood. Now, while delivering technological benefits, the advancement of technologies such as AI, nanotechnology, brain-computer interface, and biotechnology will also start a new storm of social change. As what Charles Dickens said in *A Tale of Two Cities*, "it was the best of times, it was the worst of times, it was the age of wisdom, it was the age of foolishness, it was the epoch of belief, it was the epoch of incredulity, it was the season of Light, it was the season of Darkness, it was the spring of hope, it was the winter of despair, we had everything before us, we had nothing before us, we were all going direct to Heaven, we were all going direct the other way" [30].

Data Availability

No data were used to support this study.

Conflicts of Interest

The authors declare that there are no conflicts of interest regarding the publication of this paper.

References

[1] J. Chen, X. D. Li, and D. Q. Wang, "Asymptotic stability and exponential stability of impulsive delayed hopfield neural networks," *Abstract and Applied Analysis*, vol. 2013, Article ID 638496, 10 pages, 2013.

[2] M. C. Zhang, K. Y. Liu, and Y. Y. Dong, "The hotspot dynamics and development tendency of artificial intelligence research—mirror scanning of mapping knowledge domain based on Chinese and foreign journal papers recent 10 years," *Journal of Shandong Normal University (Natural Science)*, vol. 34, no. 1, pp. 1–12, 2019, in Chinese.

[3] M. Liu, S. Li, X. D. Li, L. Jin, and C. F. Yi, "Intelligent controllers for multirobot competitive and dynamic tracking," *Complexity*, vol. 2018, Article ID 4573631, 12 pages, 2018.

[4] S. H. Ji, "Research on the tool nature of artificial intelligence: a reflection inspired by the world's first AI inventor," *China Invention and Patent*, vol. 17, no. 6, pp. 54–61, 2020, in Chinese.

[5] L. R. Wang, "Relationship between artificial intelligence and human intelligence," *Technology Innovation and Application*, vol. 31, p. 76, 2016, in Chinese.

[6] A. M. Turing, "Computing machinery and intelligence," *Mind*, vol. 59, no. 236, pp. 433–460, 1950.

[7] D. Silver, A. Huang, C. J. Maddison et al., "Mastering the game of go with deep neural networks and tree search," *Nature*, vol. 529, no. 7587, p. 484, 2016.

[8] S. M. Cheng, "Paradigm shift and development prospect of artificial intelligence," *Philosophical Trends*, vol. 12, pp. 15–21, 2017, in Chinese.

[9] M. Chen, *Introduction to Cognitive Computing*, Huazhong University of Science and Technology, Wuhan, China, 2017.

[10] B. Violino, "What is cognitive computing? Here's what you should know," 2019, https://www.infoworld.com/article/3198633/primer-make-sense-of cognitive-computing.html.

[11] M. B. Lourdes, M. A. Fernando, M. B. Jorge et al., "Complexity and cognitive computing," in *Proceedings of the 11th International Conference on Industrial and Engineering Applications of Artificial Intelligence and Expert Systems: Methodology and Tools in Knowledge-Based Systems*, pp. 408–417, Springer-Verlag, London, UK, 1998.

[12] L. G. Valiant, "Cognitive computation," in *Proceedings of the 1995 36th Annual Foundations of Computer Science*, pp. 2-3, Milwaukee, WI, USA, 1995.

[13] X. W. Shen, "Cognitive computing leads industry in intelligence," *Journal of the Chongqing University*, vol. 2910, pp. 5-6, 2015.

[14] L. Jiang, H. Zhang, L. Zhang, C. Wu, Q. C. Sun, and H. Li, "Mapping knowledge domains analysis on evolution of BCI and potential application in educational field: based on journals of SCI and SSCI from 1985 to 2018," *Journal of Distance Education*, vol. 36, no. 4, pp. 27–38, 2018, in Chinese.

[15] S. Freud, *The Interpretation of Dreams*, Shanghai Sanlian Press, Shanghai, China, 2008.

[16] R. Kurzweil, *How to Create a Mind: The Secret of Human Thought Revealed*, Zhejiang People's Publishing House, Hangzhou, China, 2013.

[17] Y. Shen and Q. Wang, "Ethic arguments of AI in education: an analysis of the EU's ethics guidelines for trustworthy AI from an educational perspective," *Peking University Education Review*, vol. 17, no. 4, pp. 18–34, 2019, in Chinese.

[18] Y. B. Chen and W. L. Zhang, "Hotspot, trend, and enlightenment of educational artificial intelligence research abroad," *Open Education Research*, vol. 25, no. 4, pp. 43–58, 2019, in Chinese.

[19] Q. C. Ke and P. L. Wang, "Research progress on the application of brain-computer interface technology in education," *China Educational Technology*, vol. 10, pp. 14–22, 2019, in Chinese.

[20] J. D. E. Gabrieli, "The promise of educational neuroscience: comment on Bowers (2016)," *Psychological Review*, vol. 123, no. 5, pp. 613–619, 2016.

[21] I. Joi and H. J. Whiplash, *How to Survive Our Faster Future*, Grand Central Publishing, New York, NY, USA, 2016.
[22] J. Ma, "Many jobs are disappearing. What should we teach our children?," 2017, https://www.sohu.com/a/13%201544213_229818.
[23] W. W. Duan, *New Trend of Humanistic Reflection on Artificial Intelligence*, Chinese Academy of Social Sciences, Beijing, China, 2020, http://www.gmw.cn/xueshu/2020-02/04/content_33523867.htm.
[24] M. Hancock, *Artificial Intelligence: Opportunities and Implications for the Future of Decision Making*, The UK Government Office for Science, London, UK, 2015, http://assets.publishing.service.gov.uk/government/uploads/system/uploads/attachment_data/file/566075/gs-16-19-artificial-intelligence-ai-report.
[25] IEEE Global Initiative, "Ethically aligned design: a vision for prioritizing human well-being with autonomous and intelligent systems," 2016, https://standards.ieee.org/content/dam/ieee-standards/standards/web/documents/other/ead1e.
[26] G20, *G20 AI Principles*, https://www.g20-insights.org/wp-content/uploads/2019/07/G20-Japan-AI-Principles, 2019.
[27] National Governance Committee for the New Generation Artificial Intelligence, "Governance principles for the new generation artificial intelligence—developing responsible artificial intelligence," 2019, http://www.gov.cn/xinwen/2019-06/17/content_5401006.htm.
[28] A. Einstein, *Collected Works of Einstein*, The Commercial Press, Beijing, China, 1979.
[29] B. James, *Our Final Invention: Artificial Intelligence and the End of the Human Era*, St. Martin's Griffin, New York, NY, USA, 2015.
[30] D. Charles, *A Tale of Two Cities*, Wordsworth Editions Limited, Hertfordshire, UK, 1993.

Hindawi
Complexity
Volume 2020, Article ID 4285294, 19 pages
https://doi.org/10.1155/2020/4285294

Research Article

Rich Dynamics of a Predator-Prey System with Different Kinds of Functional Responses

Kankan Sarkar,[1,2] **Subhas Khajanchi**,[3] **Prakash Chandra Mali**,[2] **and Juan J. Nieto**[4]

[1]*Department of Mathematics, Malda College, Malda 732101, India*
[2]*Department of Mathematics, Jadavpur University, Kolkata 700032, India*
[3]*Department of Mathematics, Presidency University, 86/1 College Street, Kolkata 700073, India*
[4]*Instituto de Matemáticas, Universidade de Santiago de Compostela, Santiago de Compostela, Spain*

Correspondence should be addressed to Subhas Khajanchi; subhaskhajanchi@gmail.com

Received 17 June 2020; Revised 2 September 2020; Accepted 4 September 2020; Published 28 October 2020

Academic Editor: Hamid Reza Karimi

In this study, we investigate a mathematical model that describes the interactive dynamics of a predator-prey system with different kinds of response function. The positivity, boundedness, and uniform persistence of the system are established. We investigate the biologically feasible singular points and their stability analysis. We perform a comparative study by considering different kinds of functional responses, which suggest that the dynamical behavior of the system remains unaltered, but the position of the bifurcation points altered. Our model system undergoes Hopf bifurcation with respect to the growth rate of the prey population, which indicates that a periodic solution occurs around a fixed point. Also, we observed that our predator-prey system experiences transcritical bifurcation for the prey population growth rate. By using normal form theory and center manifold theorem, we investigate the direction and stability of Hopf bifurcation. The biological implications of the analytical and numerical findings are also discussed in this study.

1. Introduction

The interaction between prey species and predator species constitutes biological processes of major ecological importance that are ubiquitous in nature. The dynamical interaction between prey-predator models with different kinds of response function is a dominant theme in applied mathematics and theoretical ecology [1]. Mathematical modeling for prey-predator interplays has drawn attention to the mathematicians and scientists since the pioneering worked by Lotka and Volterra in the year 1920s, and there has been a large investigation for their rich dynamics [2–6]. When we go through the interaction between prey-predator system through mathematical modeling, initially it appears to be very straightforward, but at the end, it becomes very challenging tasks from the view point of mathematicians. The investigation and validation for the proper ecological behavior of the proposed model under consideration becomes most challenging and crucial. Since the complicated and rich dynamics for the interactive populations are usual throughout the world, many ecologists have studied the processes that influence the kinetics of predator-prey system and are interested to know which model would be best to represent the interaction among species.

The dynamical behavior for the prey-predator system takes part in a significant role in theoretical ecology. There are many ecologists feeling that the unique nonnegative steady state for a predator-prey model is globally asymptotically stable if it becomes stable asymptotically although it is not always true. It can be shown that, under suitable condition, a unique nonnegative locally asymptotically stable steady state has at least one limit cycle around the steady state. Therefore, many mathematicians attempt to utilize some well-studied methods to obtain situations of global stability of the steady state for the prey-predator model [5–10].

Generally, the prey-predator system obeys two basic principles: (i) prey species has natural birth rate and both the

species has natural death rate; (ii) predator species can only grow by consuming the prey species [11]. In order to explain the predation phenomenon, Holling [12] has proposed different types of functional responses such as type-I, type-II, and type-III. The response functions are the rate of prey consumption by the predator per unit time. The functional responses proposed by Holling [12] are the functions of prey density only. The response functions are independent of predator density. One of the widely studied functional responses is Holling type-II response function, which is characterized by decelerating intake rate. The rate of predation rises as prey density increases, but after a certain stage, the rate of predation remains constant although prey density increases. In the nature, predator population death rate is likely to be maximum when the prey population is minimum due to the lack of food. Later, it is recognized that the response function is also dependent on predator density. In the year 1975, Beddington and DeAngelis [13, 14] introduce a response function, which is alike to Holling type-II response function but holds an additional term, which represents the mutual interaction between the predators. Hence, Beddington–DeAngelis-type response function is a function of both prey and predator density; that is, the rate of predation is function of both prey and predator density. However, depending upon the structural complexity of the prey habitat, the response function for the prey-predator interaction may be different [15].

Recently, a series of mathematical models has been developed to better understand the dynamics of the predator-prey system with different kinds of functional responses [6, 16–24]. Dalziel et al. [16] studied a modified Holling type-II predator-prey model, based on the premise that the search rate of predators is dependent on the prey density, rather than constant. They performed a complete analysis of the global behavior of their model and the dichotomy properties. Wang et al. [17] investigated an improved predator-prey model that incorporates seasonality and a predator maturation delay, leading to a system of periodic differential equations with a time delay. They also defined the basic reproduction number R_0 and show that it is a threshold parameter determining whether the predators can coexist with the prey species. Kohnke et al. [18] studied a predator-prey model and developed a functional response using timescale separation. In their study, they showed that the resulting functional response contains a single parameter that controls whether the group defense functional response is saturating or dome-shaped. Their model exhibits bifurcation analysis. Antwi-Fordjour et al. [19] investigated the interplay of the mutual interference exponent, and prey refuge, on the behavior of a predator-prey model with a generalized Holling-type functional response considering in particular the "nonsmooth" case. The authors studied the dynamical properties of their model and derived conditions for the occurrence of saddle-node, transcritical, and Hopf bifurcations. Also, they derived the sufficient condition for finite time extinction of the prey population.

When we look through literature review for the published research papers on the dynamics of the prey-predator model, we notice that there are multiple numbers of good research works on the dynamics of prey and predators with different kinds of functional responses. Some researchers investigated and elevated some open quires of various kinds of response function. Seo and Kot [2] have compared two prey-predator models with Holling type-I response function. In [25], the author investigated a predator-prey model with different kinds of functional responses by incorporating the role of constant prey refuge. Aiello and Freedman [26] studied a single species model with the effect of discrete time lag, in which the species was divided into mature and immature. Their model demonstrates nonnegative equilibria as the global attractor. Kon et al. [27] established the criteria for the permanence of stage structure prey-predator interactions. These are some existing articles which focused on Beddington–DeAngelis-type functional responses [28–31]. Beddington–DeAngelis-type response function confesses plentiful and biologically relevant prey-predator dynamics [29], which attract researchers to further study the predator-prey model including Beddington–DeAngelis response function. Khajanchi [28] studied a predator-prey model with age-structured incorporating Beddington–DeAngelis-type response function, in which the author performed global stability analysis. Xie et al. [20] studied a predator-prey system by using a system of fractional order differential equations with Holling type-III response function and incorporate the effect of discontinuous harvesting. Predator-prey system has been investigated by introducing discrete time delay with disease in the predator by Huang et al. [21]. Also, nonautonomous Leslie–Gower predator-prey system with nonlinear prey harvesting was studied by Alam et al. [22]. Sarkar and Khajanchi [23] studied a predator-prey system by incorporating the effect of fear with Holling type-II response function, where the authors preformed the bifurcation analysis of the system to better understand the dynamics of the model. Seasonally, varying prey-predator system with the Allee effect model was investigated by Rebelo and Soresina [24], and they studied the coexistence of all the species. Time delay plays an important role in stability switching and may change drastically the qualitative behavior of solutions for the model system under consideration [32–35].

The main aim of this manuscript is to study a very simple two-tier continuous predator-prey model with different kinds of functional responses. Although the model is very simple, it gives rich and biologically meaningful dynamics. A comparative study of the stability property was done by considering Holling type-I, Holling type-II, and Beddington–DeAngelis-type response functions. Our predator-prey system experiences Hopf bifurcation with respect to the prey birth rate r_0, which gives more complicated dynamics of the system. The predator-prey system also experiences transcritical bifurcation with respect to the prey birth rate r_0. The biological implications of the theoretical and numerical results are also investigated.

This article is organized in the following way: we present a predator-prey model with different kinds of functional responses in the next section. In Section 3, we discuss the qualitative behavior for the model, and positivity for the model, boundedness for the solutions, and the position of all

possible feasible equilibria and the existence criteria of the equilibria are presented. The criteria for stability of the predator-prey system around those equilibria are studied. In the same section, we performed a comparative study by considering different kinds of functional responses. We performed global stability analysis by constructing suitable Lyapunov function. By using normal form theory and center manifold theorem, we investigate direction and stability of Hopf bifurcation in Section 4. In the next section, we give some numerical simulations to support our analytical findings. Section 6 presents the discussion about key findings for our problem.

2. The Model

The interaction between prey and predator species in simplest form is represented by the following system of coupled differential equations [2, 36]:

$$\begin{aligned} \frac{\mathrm{d}u}{\mathrm{d}t} &= uf(u) - g(u,v)v, \\ \frac{\mathrm{d}v}{\mathrm{d}t} &= v\left(-\delta_2 + \theta g(u,v)\right), \end{aligned} \tag{1}$$

where $v(t)$ and $u(t)$ represent the predator and prey populations, respectively, at any time t and $f(u)$ stands the birth rate of prey species in exclusion of any predator population as well as death rate and the intraspecific competition between the prey species. Here, δ_2 denotes the natural death rate for predator species and θ stands the conversion coefficient of prey's biomass to predator's biomass, and $g(u,v)$ indicates the prey-dependent response function.

Our proposed model consists of two population, namely, prey population and predator population. Concentration of prey and predator species at time t can be represented by $u(t)$ and $v(t)$, respectively. Both the prey and predator populations are continuous in time t. The predator-prey interaction with response function $g(u,v)$ can be expressed by the system of coupled differential equations:

$$\left.\begin{aligned} \frac{\mathrm{d}u}{\mathrm{d}t} &= r_0 u - \delta_1 u - \gamma u^2 - g(u,v)v, \\ \frac{\mathrm{d}v}{\mathrm{d}t} &= v\left(-\delta_2 + \theta g(u,v)\right). \end{aligned}\right\} \tag{2}$$

With initial values $u(0) = u_0 \geq 0$ and $v(0) = v_0 \geq 0$, all the model parameters r_0, δ_1, γ, δ_2, and θ are positive constants and can be interpreted as follows: r_0 represents the birth rate of prey species in absence of predators, δ_1 represents the death rate for prey population, γ denotes the intraspecific competition of prey species, δ_2 represents the death rate for predator population, and θ represents the conversion coefficient of prey's biomass to predator's biomass. The dimension of prey and predator biomass is Mass. Also, the dimensions of r_0, δ_1, γ, and δ_2 are Time^{-1}, Time^{-1}, $\mathrm{Mass}^{-1}\cdot\mathrm{Time}^{-1}$, and Time^{-1}, respectively, and the parameter θ is dimensionless. In exclusion of predator species, the prey population obeys the logistic growth with an intrinsic growth rate $(r_0 - \delta_1) > 0$.

2.1. Functional Response. In ecology, the functional responses are the intake rate of predator population as a function of prey population. Holling [12] proposed three types of response function, namely, Holling types-I, II, and III. In our model formulation, we consider Holling Type-II response function in the following form:

$$g(u,v) = \frac{\alpha u}{1+\beta u}, \tag{3}$$

where α represents the attack rate and β is the handling time to capture the prey population; both α and β are positive constants. The dimensions of α and β are $\mathrm{Mass}^{-1}\,\mathrm{Time}^{-1}$ and Mass^{-1}, respectively. The predation rate increases as prey density increases, but after a certain stage, rate of predation becomes constant although prey density increases. The functional response depends on prey density but not on predator density. By using the functional form of $g(u,v)$ given by (3), system (2) becomes

$$\left.\begin{aligned} \frac{\mathrm{d}u}{\mathrm{d}t} &= r_0 u - \delta_1 u - \gamma u^2 - \frac{\alpha u v}{1+\beta u} \equiv F_1(u,v), \\ \frac{\mathrm{d}v}{\mathrm{d}t} &= \frac{\alpha\theta u v}{1+\beta u} - \delta_2 v \equiv F_2(u,v). \end{aligned}\right\} \tag{4}$$

3. Qualitative Behavior of the Model

3.1. Positivity, Boundedness, and Uniform Persistence. Right side of the system (4) is a continuous function for dependent variable t. Hence, after integration on both sides of each equation of system (4), we get

$$\begin{aligned} u(t) &= u(0)\exp\left(\int_0^t \left[r_0 - \delta_1 - \gamma u(s) - \frac{\alpha v(s)}{1+\beta u(s)}\right]\mathrm{d}s\right) > 0, \quad \forall t \geq 0, \\ v(t) &= v(0)\exp\left(\int_0^t \left[\frac{\alpha\theta u(s)}{1+\beta u(s)} - \delta_2\right]\mathrm{d}s\right) > 0, \quad \forall t \geq 0. \end{aligned} \tag{5}$$

From the above expressions of $u(t)$ and $v(t)$, it is clear that both $u(t)$ and $v(t)$ remain nonnegative for all finite time, that is, $t \geq 0$. Hence, $\mathfrak{R}_2^+ = \{(u(t), v(t)) : u(t) \geq 0, v(t) \geq 0\}$ is positively invariant of system (4). In order to prove the boundedness of the prey-predator model (4), we consider the function

$$\phi(t) = u(t) + \frac{1}{\theta} v(t). \tag{6}$$

Differentiation with respect to t gives

$$\frac{d\phi(t)}{dt} = \frac{du(t)}{dt} + \frac{1}{\theta}\frac{dv(t)}{dt} = (r_0 - \delta_1)u(t) - \gamma u^2 - \frac{\delta_2}{\theta} v(t). \tag{7}$$

Now, for each $\phi(t) > 0$, we get

$$\frac{\phi(t)}{dt} + \rho\phi(t) \le r_0 u - \gamma u^2, \tag{8}$$

where $\rho = \min\{\delta_1, (\delta_2/\theta)\}$. The maximum value of $r_0 u - \gamma u^2$ is $(r_0^2/4\gamma)$. Therefore,

$$\frac{\phi(t)}{dt} + \rho\phi(t) \le \frac{r_0^2}{4\gamma} = m\,(\text{say}). \tag{9}$$

Due to the theory of differential inequality, we have

$$0 \le \phi(t) \le \frac{m}{\rho}\left(1 - e^{-\rho t}\right) + \phi(0)e^{-\rho t} \tag{10}$$

for $t \longrightarrow \infty$, and we have $0 \le \phi(t) \le (m/\rho)$. Therefore, $\phi(t)$ is bounded. Thus, all the solution of (4) are confined in

$$\Omega = \left\{(u, v)\colon 0 \le u(t) + \frac{1}{\theta} v(t) \le \frac{m}{\rho} + \varepsilon, \quad \forall \varepsilon \ge 0\right\}. \tag{11}$$

This implies that the solution of system (4) is bounded. Thus, we have the following theorem.

Theorem 1. *For any initial value $(u_0, v_0) \in \mathfrak{R}_2^+$, all the solutions for (4) are nonnegative and bounded.*

From the ecological perspective, the positivity of the prey-predator system (4) interprets that prey and the predators biologically well-behaved. The boundedness for the solutions of the prey-predator model (4) implies that neither the prey population nor the predator population will grow unboundedly or abruptly for a large period.

Definition 1. System (4) is said to be uniformly persistent if there exist two constants κ and τ, where $0 \le \kappa \le \tau$ such that $\max\{\limsup_{t\longrightarrow\infty} u(t), \limsup_{t\longrightarrow\infty} v(t)\} \le \tau$ and $\min\{\liminf_{t\longrightarrow\infty} u(t), \liminf_{t\longrightarrow\infty} v(t)\} \ge \kappa$, where κ and τ are independent of the initial conditions.

Theorem 2. *System (4) is uniformly persistent if $r_0 > \delta_1 + \alpha\overline{v}$, where $\overline{v}$ is the upper bound of $v(t)$.*

Proof. From the proof of Theorem 1, we have $\limsup_{t\longrightarrow\infty} u(t) \le (m/\rho)$ and $\limsup_{t\longrightarrow\infty} v(t) \le (m\theta/\rho)$. We choose $\tau = \max\{(m/\rho), (m\theta/\rho)\}$. Hence, there exists $\tau > 0$ such that $\max\{\limsup_{t\longrightarrow\infty} u(t), \limsup_{t\longrightarrow\infty} v(t)\} \le \tau$.

Now, from the first equation of system (4), we have

$$\begin{aligned}\frac{du}{dt} &= r_0 u - \delta_1 u - \gamma u^2 - \frac{\alpha u v}{1 + \beta u} \ge r_0 u - \delta_1 u - \gamma u^2 - \alpha u \overline{v} \\ &= (r_0 - \delta_1 - \alpha\overline{v})u - \gamma u^2,\end{aligned} \tag{12}$$

where $\overline{v}$ is the upper limit of v in Ω.

Thus, we can conclude that $\liminf_{t\longrightarrow\infty} u(t) \ge ((r_0 - \delta_1 - \alpha\overline{v})/\gamma)$ with $r_0 > \delta_1 + \alpha\overline{v}$. Again, from the second equation of (4), we have

$$\frac{dv}{dt} = \frac{\alpha\theta u v}{1 + \beta u} - \delta_2 v \ge -\delta_2 v. \tag{13}$$

Hence, we have $\liminf_{t\longrightarrow\infty} v(t) \ge 0$. Thus, if we choose $\kappa = \min\{0, ((r_0 - \delta_1 - \alpha\overline{v})/\gamma)\} = 0$ with $r_0 > \delta_1 + \alpha\overline{v}$, then $\min\{\liminf_{t\longrightarrow\infty} u(t), \liminf_{t\longrightarrow\infty} v(t)\} \ge \kappa$. Therefore, system (4) will be uniformly persistent if $r_0 > \delta_1 + \alpha\overline{v}$. □

3.2. Equilibria and Their Existence. The singular points for the model (4) are nonnegative solutions for $F_1(u, v) = 0$ and $F_2(u, v) = 0$ in $\mathfrak{R}_+^2$; that is, the equilibrium points of system (4) are the positive point of intersection for zero growth of prey and predator isoclines. The prey isoclines are given by $u = 0$, and $v = ((r_0 - \delta_1 - \gamma u)(1 + \beta u)/\alpha)$ with predator isoclines is stated as $v = 0$ and the vertical straight line $u = (\delta_2/(\alpha\theta - \beta\delta_2))$. System (4) possesses three biologically meaningful singular points, as follows:

(i) Trivial steady state $E_0(0, 0)$.

(ii) Boundary singular point $E_1(\overline{u}, 0)$, where $\overline{u} = (r_0 - \delta_1)/\gamma$, which is feasible only when $r_0 > \delta_1$; that is, growth of prey population is higher than the death rate for prey population.

(iii) The positive interior equilibrium point $E^*(u^*, v^*)$, where $u^* = \delta_2/(\alpha\theta - \beta\delta_2)$ and $v^* = (r_0 - \delta_1 - \gamma u^*)((1/\alpha) + (\beta/\alpha)u^*)$.

The shape and position of the curve $v = (r_0 - \delta_1 - \gamma u)(1 + \beta u)/\alpha$ depends upon multiple parameters. For different values of β, the zero growth prey isoclines are convex curve joining the boundary equilibrium $E_1(\overline{u}, 0)$ and $(0, ((r_0 - \delta_1)/\alpha))$ (see Figure 1(a)). As β increases, the vertical predator isocline shifted towards increasing u. For different values of α, zero growth prey isocline becomes a convex curve, which meets at boundary equilibrium $E_1(\overline{u}, 0)$ (see Figure 1(b)). As α increases, the vertical predator isocline shifted towards decreasing u and the prey isocline shifted towards decreasing v. Also, for different values of r_0, the zero growth prey isoclines are convex curve, but the zero growth predator isoclines do not change position. As r_0 increases, the zero growth prey isocline shifted towards v increasing. In all these situations, the interior equilibrium point $E^*(u^*, v^*)$ exists only if $\alpha\theta - \beta\delta_2 > 0$ (see Figure 1(c)).

3.3. Local Stability Analysis. In this section, we analyzed the linear stability for the predator-prey system (4). Using linearization techniques, the local behavior of the nonlinear predator-prey system can be investigated. Generally, the

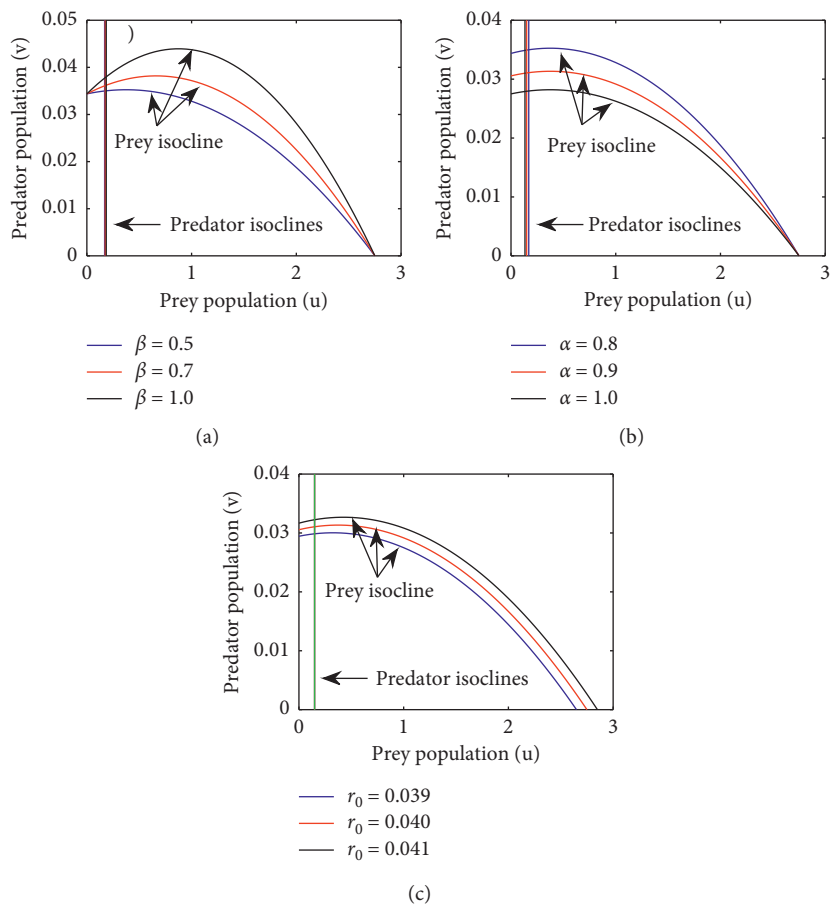

Figure 1: Isoclines of the predator-prey system (4) for three different cases with the following set of parameter values: $r_0 = 0.04, \delta_1 = 0.0125, \gamma = 0.01, \alpha = 0.8, \beta = 0.5, \theta = 0.4$, and $\delta_2 = 0.05$. (a) For different β; (b) for different α; (c) for different values of r_0, as shown in the inset.

predator-prey system is linearized around every biologically feasible singular point, and the model is perturbed by a small quantity and observed whether the model returns to that state of singular point converges to another state of singular point. Analysis of local stability leads to investigate qualitative dynamics for the model system under consideration. For local stability analysis of the considered model (4) around every singular point, first calculate the Jacobian matrix obtained from each of the equilibrium point. The variational matrix of the model (4) at (u, v) is

$$J = \begin{bmatrix} F_u & F_v \\ G_u & G_v \end{bmatrix}, \tag{14}$$

where

$$\begin{aligned} F_u &= r_0 - \delta_1 - 2\gamma u - \frac{\alpha v}{(1+\beta u)^2}, \\ F_v &= -\frac{\alpha u}{1+\beta u}, \\ G_u &= \frac{\alpha\theta v}{(1+\beta u)^2}, \\ G_v &= \frac{\alpha\theta u}{1+\beta u} - \delta_2. \end{aligned} \tag{15}$$

Theorem 3. *If $r_0 < \delta_1$, then the trivial singular point $E_0(0,0)$ of (4) is locally asymptotically stable and otherwise unstable.*

Proof. The eigenvalues of the Jacobian matrix (14) of the system (4) at the trivial equilibrium point $E_0(0,0)$ are $r_0 - \delta_1$ and $-\delta_2$. Here, $\delta_2 > 0$; therefore, the trivial equilibrium point $E_0(0,0)$ of the model (4) will be locally asymptotically stable if $r_0 < \delta_1$; that is, the growth rate of prey species is less than the natural death rate of prey species. It can be noted that if the trivial equilibrium point $E_0(0,0)$ is asymptotically stable, then the boundary singular point $E_1(\overline{u}, 0)$ does not exist. For $r_0 = \delta_1$, the trivial equilibrium point $E_0(0,0)$ has eigenvalues 0 and $-\delta_2$. So $E_0(0,0)$ is a nonhyperbolic equilibrium point [6]. □

Theorem 4. *If $\delta_1 < r_0 < \delta_1 + \gamma\delta_2/(\alpha\theta - \beta\delta_2)$, then the boundary equilibrium point $E_1(\overline{u}, 0)$ of the model (4) is locally asymptotically stable and otherwise unstable.*

Proof. The eigenvalues of the Jacobian matrix (14) of the system (4) at the equilibrium point $E_1(\overline{u}, 0)$ are $\lambda_1 = -(r_0 - \delta_1)$ and $\lambda_2 = ((\alpha\theta(r_0 - \delta_1))/(\gamma + \beta(r_0 - \delta_1))) - \delta_2$. The boundary equilibrium point $E_1(\overline{u}, 0)$ will be locally

asymptotically stable if $\lambda_1 < 0$ and $\lambda_2 < 0$, and this condition implies $\delta_1 < r_0 < \delta_1 + (\gamma\delta_2/\alpha\theta - \beta\delta_2)$. Biologically, $r_0 > \delta_1$ implies that the rate of growth of prey population is higher than the natural rate of death of the prey. Also, $r_0 < \delta_1 + (\gamma\delta_2/\alpha\theta - \beta\delta_2)$ implies that the prey growth rate cannot be unbounded. It is to be noted that if the boundary equilibrium state $E_1(\overline{u}, 0)$ is locally asymptotically stable, then the trivial equilibrium state $E_0(0,0)$ is unstable. □

Theorem 5. *If $r_0 - \delta_1 - 2\gamma u^* - (\alpha v^*/(1+\beta u^*)^2) < 0$, then the positive interior singular point $E^*(u^*, v^*)$ of (4) will be asymptotically stable and otherwise unstable.*

Proof. The variational matrix around the coexisting singular point $E^*(u^*, v^*)$ for the system (4) is given by

$$J^* = \begin{bmatrix} r_0 - \delta_1 - 2\gamma u^* - \dfrac{\alpha v^*}{(1+\beta u^*)^2} & -\dfrac{\alpha u^*}{1+\beta u^*} \\ \dfrac{\alpha\theta v^*}{(1+\beta u^*)^2} & 0 \end{bmatrix}. \quad (16)$$

The characteristic equation of the above matrix J^* can be expressed as

$$\lambda^2 - \left[r_0 - \delta_1 - 2\gamma u^* - \frac{\alpha v^*}{(1+\beta u^*)^2}\right]\lambda + \frac{\alpha\delta_2 v^*}{(1+\beta u^*)^2} = 0,$$
$$\text{or } \lambda^2 - K_{11}\lambda + K_{22} = 0, \quad (17)$$

where $K_{11} = r_0 - \delta_1 - 2\gamma u^* - (\alpha v^*/(1+\beta u^*)^2)$ and $K_{22} = (\alpha\delta_2 v^*/(1+\beta u^*)^2)$.

Due to well-known Routh-Hurwitz criterion, the characteristic (17) will have negative real roots if $K_{11} < 0$ and $K_{22} > 0$. Hence, $r_0 - \delta_1 - 2\gamma u^* - (\alpha v^*/(1+\beta u^*)^2) < 0$ and $(\alpha\delta_2 v^*/(1+\beta u^*)^2) > 0 \Longrightarrow v^* > 0$ since $\alpha, \delta_2, (1+\beta u^*)^2 > 0$. It is obvious that $v^* > 0$ because $E^*(u^*, v^*)$ will be positive interior singular point of (4). Therefore, the positive interior steady state $E^*(u^*, v^*)$ of (4) will be asymptotically stable if $r_0 - \delta_1 - 2\gamma u^* - (\alpha v^*/(1+\beta u^*)^2) < 0$ and otherwise unstable.

Figure 2 shows the stability region of different singular points of (4) in $r_0 - \beta$ parameter-space. The growth rate of prey species r_0 varies from 0 to 0.1, and the half saturation constant β varies from 0 to 1; the other parameters are fixed as $\delta_1 = 0.0125$, $\gamma = 0.01$, $\alpha = 0.8$, $\theta = 0.4$, and $\delta_2 = 0.05$. For a very small value of r_0, that is, when $r_0 < \delta_1$, the trivial equilibrium E_0 is locally asymptotically stable. The stability region of E_0 is shown by blue-shaded region in the $r_0 - \beta$ plane. In this blue-shaded region, the boundary equilibrium E_1 and the interior equilibrium E^* are unstable. The boundary equilibrium E_1 is locally asymptotically stable in the green-shaded region. But the trivial equilibrium E_0 and the interior equilibrium E^* are unstable in this green-shaded region. The red-shaded region of Figure 2 shows the locally asymptotically stable behavior of the interior equilibrium E^*; that is, both the prey and predator populations can exist together in the red-shaded region. For higher value of r_0 (such as $r_0 > 0.06$) and for higher value of β (such as $\beta > 0.5$), the coexisting equilibrium E^* loses stability. The trivial equilibrium E_0 and the boundary equilibrium E_1 are unstable in the red-shaded region. All the equilibria lose stability in the white-shaded region. □

3.4. Comparative Study with Different Kinds of Functional Responses. Mainly, three types of response functions (Holling types-I, II, and III) and Beddington–DeAngelis are widely investigated by the researchers in the predator-prey system [29, 37, 38]. Here, we also investigate the role of different kinds of functional responses on the dynamics for the predator-prey system (2). To exemplify this matter, we performed a relative study for (2) with reference to three kinds of response functions, namely, Beddington–DeAngelis, Holling type-I, and Holling type-II (already used in the model (4)). Holling-type response functions are the function of prey population only; that is, the response functions are independent of predator population. But, in the nature, response functions are also the function of predator population. Widely studied Beddington–DeAngelis [13, 14] response function considered the density of predators also. In our study, we have also studied stability of the system by considering Beddington–DeAngelis functional responses and two types of response function. The Beddington–DeAngelis response function is of the following form:

$$g(u, v) = \frac{\alpha u}{1 + \beta u + \xi v}, \quad (18)$$

where the parameters α, β, and ξ are nonnegative and have their usual biological meanings. The Beddington–DeAngelis response function is a similar kind of Holling type-II response function but contains an additional term ξv at the denominator. The term ξv indicates the mutual interaction between the predator population. Thus, when the prey density $u(t)$ is constant and predator density $v(t)$ is minimum, then the value of the response function $g(u, v)$ is maximum; when predator density $v(t)$ is maximum, then the value of the response function $g(u, v)$ is minimum. This is more realistic because when the number of predator species are less than their prey, consumption due to predators per unit time will be more, but when predator density is more, then the prey consumption due to predators per unit time will be less due to mutual interaction of predator population. But, when $\xi = 0$, then the Beddington–DeAngelis functional response is the same as Holling type-II functional response. Again, for $\beta = 0$ and $\xi = 0$, then Beddington–DeAngelis response function is the same as Holling type-I response function. Hence, we may conclude that Beddington–DeAngelis response function is a more generalized form of Holling type-II and type-I functional

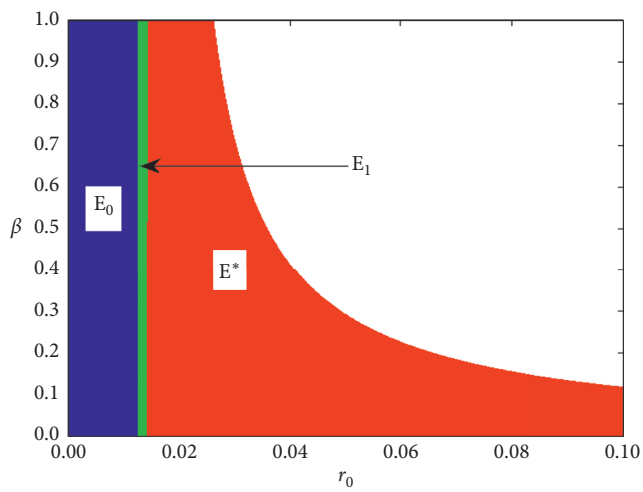

FIGURE 2: The stability region of the trivial singular state E_0, boundary singular state E_1, and the coexisting singular state E^* of (4), in the $(r_0 - \beta)$ parameter-space where $r_0 \in (0, 0.1)$ and $\beta \in (0, 1.0)$. Other parameter values are $\delta_1 = 0.0125$, $\gamma = 0.01$, $\alpha = 0.8$, $\theta = 0.4$, and $\delta_2 = 0.05$. In the figure, (i) within the blue colored region, the equilibrium point E_0 is locally asymptotically stable, but boundary singular point E_1 and the interior equilibrium E^* are unstable; (ii) within the green colored region, the equilibrium point E_1 is locally asymptotically stable, but trivial equilibria E_0 and interior equilibrium E^* are unstable; and (iii) within the red colored region, the interior equilibrium point E^* is locally asymptotically stable, but the trivial equilibrium E_0 and boundary equilibrium E_1 are unstable.

responses. By considering Beddington–DeAngelis response function, the system (2) becomes

$$\left.\begin{aligned} \frac{du}{dt} &= r_0 u - \delta_1 u - \gamma u^2 - \frac{\alpha u v}{1 + \beta u + \xi v}, \\ \frac{dv}{dt} &= \frac{\alpha \theta u v}{1 + \beta u + \xi v} - \delta_2 v. \end{aligned}\right\} \tag{19}$$

The predator-prey system (19) with Beddington–DeAngelis functional response has three ecologically relevant singular points, namely, trivial singular point $E^0(0,0)$, boundary singular point $E^1(\hat{u}, 0)$, and an interior steady state $E^*(\hat{u}^*, \hat{v}^*)$. Here, $\hat{u} = (r_0 - \delta_1/\gamma)$, and $\hat{u}^*$ is the positive root for the following second-degree equation:

$$\begin{aligned} &\theta\gamma\xi\hat{u}^{*2} - [(r_0 - \delta_1)\theta\xi - (\alpha\theta - \beta\delta_2)]\hat{u}^* - \delta_2 = 0, \\ &\hat{v}^* = \frac{1}{\xi\delta_2}[(\alpha\theta - \beta\delta_2)\hat{u}^* - \delta_2]. \end{aligned} \tag{20}$$

We have made a relative investigation of the predator-prey model (2), by considering three different functional responses, which are type-I (model (19) with $\beta = 0, \xi = 0$), Holling type-II (already used in model (4) with $\xi = 0$), and Beddington–DeAngelis. We are not showing detailed analysis of the model (2) for the different functional responses; rather, we have presented the stability scenarios for these three types of response function in Table 1. The parameters r_0, θ, and γ are varied to observed the stability behavior of the system. The detailed numerical study and graphical illustrations have been shown in numerical Section 5.

3.5. Global Stability Analysis around $E^*(u^*, v^*)$. In this subsection, we investigate the sufficient condition for global asymptotic stability of the positive coexisting singular point $E^*(u^*, v^*)$ by establishing appropriate Lyapunov function.

Theorem 6. *The positive interior steady state $E^*(u^*, v^*)$ of the system (4) is globally asymptotically stable if $(\gamma/\alpha\beta) > v^*$.*

Proof. The interior steady state $E^*(u^*, v^*)$ of the prey-predator model (4) fulfills the following conditions:

$$\begin{aligned} r_0 - \delta_1 &= \gamma u^* + \frac{\alpha v^*}{1 + \beta u^*}, \\ \delta_2 &= \frac{\alpha\theta u^*}{1 + \beta u^*}. \end{aligned} \tag{21}$$

With the help of these above two equations, the model (4) leads to

$$\left.\begin{aligned} \frac{du}{dt} &= u\left(-\gamma(u - u^*) + \frac{\alpha v^*}{1 + \beta u^*} - \frac{\alpha v}{1 + \beta u}\right), \\ \frac{dv}{dt} &= v\left(\frac{\alpha\theta u}{1 + \beta u} - \frac{\alpha\theta u^*}{1 + \beta u^*}\right). \end{aligned}\right\} \tag{22}$$

We define the Lyapunov functional $V(u, v)$: $\mathfrak{R}_2^+ \longrightarrow \mathfrak{R}$ such that

$$V(u, v) = V_1(u, v) + V_2(u, v), \tag{23}$$

where $V_1(u, v) = u - u^* - u^* \ln(u/u^*)$ and $V_2(u, v) = K(v - v^* - v^* \ln(v/v^*))$. Here, K is a positive constant and is defined as $K = (1/\theta)(1 + \beta u^*)$. This particular type of Lyapunov function to study the stability of the interior equilibrium has been used widely [29, 30, 39, 40]. The Lyapunov function $V(u, v)$ is continuous on $\mathrm{Int}(\mathfrak{R}_2^+)$ and vanishes at $E^*(u^*, v^*)$. Also, $V(u, v)$ is positive definite in

Table 1: Stability conditions for different equilibrium points of system (19).

Equilibria	Holling type-I ($\beta = 0, \xi = 0$)	Holling type-II ($\xi = 0$)	Beddington–DeAngelis
$E^0(0,0)$	$r_0 < \delta_1$	$r_0 < \delta_1$	$r_0 < \delta_1$
$E^1(\widehat{u},0)$	$r_0 > \delta_1$ and $\alpha\theta(r_0 - \delta_1) < \delta_2$	$r_0 > \delta_1$ and $(\alpha\theta\gamma(r_0 - \delta_1)/\{\gamma + \beta(r_0 - \delta_1)\}^2) < \delta_2$	$r_0 > \delta_1$ and $(\alpha\theta\gamma(r_0 - \delta_1)/\{\gamma + \beta(r_0 - \delta_1)\}^2) < \delta_2$
$E^*(\widehat{u}^*, \widehat{v}^*)$	$M_1 + M_4 < 0$ and $M_1M_4 - M_2M_3 > 0$ with $\beta = 0$ and $\xi = 0$	$M_1 + M_4 < 0$ and $M_1M_4 - M_2M_3 > 0$ with $\xi = 0$	$M_1 + M_4 < 0$ and $M_1M_4 - M_2M_3 > 0$

M_1, M_2, M_3, and M_4 are the elements of the variational matrix around interior singular point $E^*(\widehat{u}^*, \widehat{v}^*)$, where $M_1 = -\gamma\widehat{u}^* - (\alpha\beta\widehat{u}^*\widehat{v}^*/(1 + \beta\widehat{u}^* + \xi\widehat{v}^*)^2)$, $M_2 = -(\alpha\widehat{u}^*(1 - \xi\widehat{v}^*)/(1 + \beta\widehat{u}^* + \xi\widehat{v}^*)^2)$, $M_3 = (\alpha\theta\widehat{v}^*(1 - \beta\widehat{u}^*)/(1 + \beta\widehat{u}^* + \xi\widehat{v}^*)^2)$, and $M_4 = (\alpha\theta\widehat{u}^*(1 - \xi\widehat{v}^*)/(1 + \beta\widehat{u}^* + \xi\widehat{v}^*)^2) - \delta_2$.

$\mathrm{Int}(\mathfrak{R}_2^+)$. Furthermore, $(\partial V_1/\partial u) > 0$ when $u > u^*$, $(\partial V_1/\partial u) < 0$ when $u < u^*$, $(\partial V_2/\partial u) > 0$ when $v > v^*$, and $(\partial V_2/\partial v) < 0$ when $v < v^*$. Hence, $E^*(u^*, v^*)$ is a global minimum of $V(u,v)$. The time derivative of $V_1(u,v)$ and $V_2(u,v)$ along the solution for (4) is

$$\frac{\mathrm{d}V_1}{\mathrm{d}t} = \frac{u - u^*}{u}\frac{\mathrm{d}u}{\mathrm{d}t} = (u - u^*)\left[-\gamma(u - u^*) + \frac{\alpha v^*}{1 + \beta u^*} - \frac{\alpha v}{1 + \beta u}\right],$$
$$\frac{\mathrm{d}V_2}{\mathrm{d}t} = K\frac{v - v^*}{v}\frac{\mathrm{d}v}{\mathrm{d}t} = K\alpha\theta(v - v^*)\left[\frac{u}{1 + \beta u} - \frac{u^*}{1 + \beta u^*}\right]. \tag{24}$$

Now, differentiating (23) with respect to time t and using the values of $(\mathrm{d}V_1/\mathrm{d}t)$ and $(\mathrm{d}V_2/\mathrm{d}t)$, we obtain

$$\begin{aligned}\frac{\mathrm{d}V}{\mathrm{d}t} &= \frac{\mathrm{d}V_1}{\mathrm{d}t} + \frac{\mathrm{d}V_2}{\mathrm{d}t}\\ &= -\gamma(u - u^*)^2 - \frac{\alpha(u - u^*)\{(v - v^*) + \beta(u^*v - uv^*)\}}{(1 + \beta u)(1 + \beta u^*)}\\ &\quad + \frac{K\alpha\theta(u - u^*)(v - v^*)}{(1 + \beta u)(1 + \beta u^*)}.\end{aligned} \tag{25}$$

Using the relation $u^*v - uv^* = u^*(v - v^*) - v^*(u - u^*)$, we obtain

$$\begin{aligned}\frac{\mathrm{d}V}{\mathrm{d}t} &= -\gamma(u - u^*)^2 + \frac{\alpha\beta v^*(u - u^*)^2}{(1 + \beta u)(1 + \beta u^*)}\\ &\quad - \frac{\alpha(1 + \beta u^* - K\theta)}{(1 + \beta u)(1 + \beta u^*)}(u - u^*)(v - v^*).\end{aligned} \tag{26}$$

Putting the value of K, we obtain

$$\begin{aligned}\frac{\mathrm{d}V}{\mathrm{d}t} &= -\gamma(u - u^*)^2 + \frac{\alpha\beta v^*(u - u^*)^2}{(1 + \beta u)(1 + \beta u^*)}\\ &\le -(\gamma - \alpha\beta v^*)(u - u^*)^2.\end{aligned} \tag{27}$$

Hence, $(\mathrm{d}V/\mathrm{d}t) < 0$ along the trajectories in $\mathfrak{R}_2^+$ excluding at $E^*(u^*, v^*)$ if $\gamma - \alpha\beta v^* > 0$, that is, if $(\gamma/\alpha\beta) > v^*$. Thus, if $(\gamma/\alpha\beta) > v^*$, then the coexisting singular point $E^*(u^*, v^*)$ is globally asymptotically stable. □

3.6. Hopf Bifurcation Analysis. In our study, the growth rate r_0 of prey population is one of the most important parameters. In this section, we investigate how predator-prey model behavior alters with respect to r_0 by using the analysis of Hopf bifurcation. We start with a theorem to study the analysis of Hopf bifurcation.

Theorem 7. *When the prey birth rate r_0 crosses a threshold value $r_0 = r_0^* = (\delta_1 + 2\gamma u^*)(1 + (1/\beta u^*)) - (1/\beta u^*)(\delta_1 + \gamma u^*)$, the predator-prey model (4) experiences Hopf bifurcation around the interior singular point E^*. Necessary and sufficient conditions of Hopf bifurcation to occur are that there exists $r_0 = r_0{}^*$ such that the transversality condition holds:*

$$\frac{\mathrm{d}}{\mathrm{d}r_0}(\mathrm{Re}(\lambda(r_0)))\Big|_{r_0 = r_0^*} = \frac{\beta u^*}{1 + \beta u^*} \neq 0. \tag{28}$$

Proof. A necessary condition for the change in dynamics of the coexisting singular point $E^*(u^*, v^*)$ of the prey-predator model (4) is that the characteristic polynomial (17) should have purely complex eigenvalues. The characteristic roots of the equation (17) will have purely complex roots if and only if $K_{11} = 0$ and $K_{22} > 0$. For $K_{11} = 0$ gives, $r_0 = r_0^* = (\delta_1 + 2\gamma u^*)(1 + (1/\beta u^*)) - (1/\beta u^*)(\delta_1 + \gamma u^*)$, where $u^* = \delta_2/(\alpha\theta - \beta\delta_2)$. Due to Theorem 5, we can conclude that the positive coexisting singular point $E^*(u^*, v^*)$ of the predator-prey model (4) will be stable asymptotically if $r_0 - \delta_1 - 2\gamma u^* - (\alpha v^*/(1 + \beta u^*)^2) < 0$ and the model (4) experiences Hopf bifurcation at $r_0 = r_0{}^*$.

Let the roots of the characteristic (17) are of the form $\lambda_{1,2} = \phi(r_0) \pm i\psi(r_0)$. Then, $\lambda_1 + \lambda_2 = 2\phi(r_0) = K_{11}$; that is, $\mathrm{Re}(\lambda(r_0)) = \phi(r_0) = (1/2)K_{11}$. To prove the transversality condition, we need to verify the following condition:

$$\frac{\mathrm{d}}{\mathrm{d}r_0}(\mathrm{Re}(\lambda(r_0)))\Big|_{r_0 = r_0^*} = \frac{\beta u^*}{1 + \beta u^*} \neq 0, \quad \text{if } \beta \neq 0. \tag{29}$$

Hence, the transversality condition holds, and the system (4) experiences Hopf bifurcation at $r_0 = r_0{}^*$. □

4. Direction and Stability of Hopf Bifurcation

To study the stability of bifurcating limit cycle appearing through Hopf bifurcation, we use the theorem of center manifold. Center manifold theorem is an essential tool to reduce the dimension of a differential equation system in a neighborhood of a coexisting steady state (see the book by Guckenheimer and Holmes, 1983, [41]). For the predator-prey system (4), we obtain the variational matrix J^* has a pair of complex conjugate eigenvalues for Hopf bifurcation

[42]. Thus, we can investigate the model on a 2-dimensional center manifold [43].

To determine center manifold and investigate the flow here, first interpret the origin for the coordinate system to an interior singular point $E^*(u^*, v^*)$ by expressing $\hat{u} = u - u^*$ and $\hat{v} = v - v^*$. For simplicity $\hat{u}$ and $\hat{v}$ denoted by u and v, respectively, the system (4) leads to

$$\left.\begin{aligned} \frac{\mathrm{d}u}{\mathrm{d}t} &= (r_0 - \delta_1)(u + u^*) - \gamma(u + u^*)^2 - \frac{\alpha(u + u^*)(v + v^*)}{1 + \beta(u + u^*)}, \\ \frac{\mathrm{d}v}{\mathrm{d}t} &= \frac{\alpha\theta(u + u^*)(v + v^*)}{1 + \beta(u + u^*)} - \delta_2(v + v^*). \end{aligned}\right\} \tag{30}$$

The system of (30) can be rewritten as

$$\begin{bmatrix} u_t \\ v_t \end{bmatrix} = J^*(r_0)\begin{bmatrix} u \\ v \end{bmatrix} + \begin{bmatrix} f_1(u, v, r_0) \\ f_2(u, v, r_0) \end{bmatrix}, \tag{31}$$

where $J^*(r_0)$ defined in (16), and

$$\begin{aligned} f_1(u, v, r_0) &= a_1 u^2 + a_2 uv + a_3 v^2 + \ldots, \\ f_2(u, v, r_0) &= -(a_1 + \gamma)\theta u^2 - a_2 \theta uv + a_3 v^2 + \ldots, \end{aligned} \tag{32}$$

where $a_1 = -\gamma + (\alpha\beta v^*/(1 + \beta u^*)^3)$, $a_2 = -(\alpha/(1 + \beta u^*)^2)$, and $a_3 = 0$.

Let the characteristic roots of the Jacobian matrix $J^*(r_0)$ are of the form $\lambda_{1,2} = \phi(r_0) \pm i\psi(r_0)$, where $\phi(r_0) = (1/2)\mathrm{tr}(J^*)$ and $\psi(r_0) = \sqrt{\det(J^*) - \phi^2(r_0)}$. Here, the characteristics roots $\lambda_{1,2}$ are complex conjugate if $\det(J^*) - \phi^2(r_0) > 0$ and the characteristic roots $\lambda_{1,2}$ are purely imaginary; that is, $\lambda_{1,2} = \pm i\psi(r_0)$ when $\phi(r_0) = 0$; that is, when $r_0 = r_0^*$. Now set the following matrix to get the normal form of the predator-prey system (4):

$$D = \begin{bmatrix} 1 & 0 \\ P & Q \end{bmatrix}, \tag{33}$$

where $\begin{bmatrix} 1 \\ P - iQ \end{bmatrix}$ is the eigenvector corresponding to $\lambda = \phi(r_0) + i\psi(r_0)$ with $P = (1 + \beta u^*/\alpha u^*)[(\alpha\beta u^* v^*/(1 + \beta u^*)^2) - \gamma u^* - \phi]$ and $Q = ((1 + \beta u^*)\psi/\alpha u^*)$. Then, we have

$$D^{-1} = \begin{bmatrix} 1 & 0 \\ -\dfrac{Q}{P} & \dfrac{1}{Q} \end{bmatrix}. \tag{34}$$

By using the transformation

$$\begin{bmatrix} u \\ v \end{bmatrix} = D\begin{bmatrix} x \\ y \end{bmatrix}, \tag{35}$$

System (30) becomes

$$\begin{bmatrix} x_t \\ y_t \end{bmatrix} = L_0(r_0)\begin{bmatrix} x \\ y \end{bmatrix} + \begin{bmatrix} G(x, y, r_0) \\ H(x, y, r_0) \end{bmatrix}, \tag{36}$$

where

$$L_0(r_0) = \begin{bmatrix} \phi & -\psi \\ \psi & \phi \end{bmatrix}, \tag{37}$$

with

$$\begin{aligned} G(x, y, r_0) &= \frac{\phi - \beta\gamma u^{*2}}{(1 + \beta u^*)u^*}x^2 - \frac{\phi}{(1 + \beta u^*)u^*}xy + 0 \times y^2 - \frac{\beta(\gamma u^* + \phi)}{(1 + \beta u^*)^2 u^*}x^3 + \frac{\beta\phi}{(1 + \beta u^*)^2 u^*}x^2 y + 0 \times xy^2 + 0 \times y^3 + \ldots, \\ H(x, y, r_0) &= -\frac{P}{Q}G(x, y, r_0) + \frac{1}{Q}g_2(x, y, r_0), \\ g_2(x, y, r_0) &= \alpha\theta\left[\frac{P}{(1 + \beta u^*)^2} - \frac{\beta v^*}{(1 + \beta u^*)^3}\right]x^2 + 0 \times y^2 + \frac{\alpha\theta Q}{(1 + \beta u^*)^2}xy \\ &\quad - \alpha\beta\theta\left[\frac{P}{(1 + \beta u^*)^3} - \frac{\beta v^*}{(1 + \beta u^*)^4}\right]x^3 - \frac{\alpha\beta\theta Q}{(1 + \beta u^*)^3}x^2 y + 0 \times xy^2 + 0 \times y^3 + \ldots. \end{aligned} \tag{38}$$

Now, rewriting the expression (36) in polar coordinate (r, ζ) and then expanding in the Taylor series expansion at $r_0 = r_0^*$, we obtain

$$\left.\begin{aligned} \zeta_t &= \psi(r_0) + c(r_0)r^2 + \ldots = \psi(r_0^*) + \psi'(r_0)(r_0 - r_0^*) + c(r_0^*)r^2 + \ldots, \\ r_t &= \phi(r_0)r + a(r_0)r^3 + \ldots = \phi'(r_0^*)(r_0 - r_0^*)r + a(r_0^*)r^3 + \ldots. \end{aligned}\right\} \tag{39}$$

To investigate the stability of Hopf bifurcating periodic solution, we must have to compute the sign of the coefficient of $a(r_0)$, where $a(r_0)$ is given by

$$\begin{aligned} a(r_0^*) = {} & \frac{1}{16}\left[G_{xxx} + G_{xyy} + H_{xxy} + H_{yyy}\right]\Big|_{(0,0,r_0^*)} \\ & + \frac{1}{16\psi(r_0^*)}\left[G_{xy}\left(G_{xx} + G_{yy}\right) - H_{xy}\left(H_{xx} + H_{yy}\right)\right. \\ & \left. - G_{xx}H_{xx} + G_{yy}H_{yy}\right]\Big|_{(0,0,r_0^*)}. \end{aligned} \tag{40}$$

The above expression of $a(r_0^*)$ is obtained by well-known Hopf bifurcation formula to transform (36) into Jordan form [41]. Here, the subscript denotes partial derivative, and we have

$$\begin{aligned} G_{xxx}(0,0,r_0^*) &= -\frac{3\beta(\gamma u^* + \phi)}{(1+\beta u^*)^2}, \\ G_{xyy}(0,0,r_0^*) &= H_{yyy}(0,0,r_0^*) = G_{yy}(0,0,r_0^*) \\ &= H_{yy}(0,0,r_0^*) = 0, \\ H_{xxy}(0,0,r_0^*) &= -\frac{2P\beta\phi}{Qu^*(1+\beta u^*)^2} - \frac{2\alpha\beta\theta}{(1+\beta u^*)^3}, \\ G_{xy}(0,0,r_0^*) &= -\frac{\phi}{(1+\beta u^*)u^*}, \\ G_{xx}(0,0,r_0^*) &= \frac{2\left(\phi - \beta\gamma u^{*2}\right)}{(1+\beta u^*)u^*}, \\ H_{xy}(0,0,r_0^*) &= \frac{P\phi}{Q(1+\beta u^*)u^*} + \frac{\alpha\theta}{(1+\beta u^*)^2}, \\ H_{xx}(0,0,r_0^*) &= -\frac{2P\left(\phi - \beta\gamma u^{*2}\right)}{Qu^*(1+\beta u^*)} \\ &\quad + \frac{2\alpha\theta}{Q}\left[\frac{P}{(1+\beta u^*)^2} - \frac{\beta v^*}{(1+\beta u^*)^3}\right]. \end{aligned} \tag{41}$$

Here, $\phi(r_0) = (1/2)\mathrm{tr}(J^*) = (1/2)[(\alpha\beta u^* v^*/(1+\beta u^*)^2) - \gamma u^*]$ and $(\mathrm{d}\phi/\mathrm{d}r_0) = (\beta u^*/2(1+\beta u^*)) > 0$.

We obtain that $\Lambda = -(a(r_0)/\phi'(r_0))$.

From the above computation of $a(r_0^*)$, the following theorem can be stated

Theorem 8

(i) The direction of Hopf bifurcation is supercritical, and bifurcating periodic solutions are stable if $a(r_0^*) < 0$.

(ii) The direction of Hopf bifurcation is subcritical, and bifurcating periodic solutions are unstable if $a(r_0^*) > 0$.

5. Numerical Simulations

In this section, we compute some numerical simulations regarding stability and bifurcation for the predator-prey model (4) in the vicinity of the coexisting singular point $E^*(u^*, v^*)$. It is quite difficult to verify the mathematical model simulations with realistic parameter values. We have taken a hypothetical set of parameter values to illustrate our analytical findings. The set of model parameters is as follows: $r_0 = 0.01$, $\delta_1 = 0.02$, $\gamma = 0.01$, $\alpha = 0.9$, $\beta = 0.5$, $\theta = 0.4$, and $\delta_2 = 0.05$. For this parameter, set the stability condition $r_0 < \delta_1$ for the trivial singular point E_0 is satisfied, and hence, $E_0(0,0)$ is locally asymptotically stable. From the time series solution shown in Figure 3(a), it can be noticed that both prey and predator populations $u(t)$ and $v(t)$ initiate from the initial values $(0.5, 0.3)$ and goes to extinct; hence, the trivial steady state E_0 is stable asymptotically. Again, we have chosen the parameter values as $r_0 = 0.03$, $\delta_1 = 0.01$, $\gamma = 0.15$, $\alpha = 0.9$, $\beta = 0.5$, $\theta = 0.4$, and $\delta_2 = 0.05$. The condition of locally asymptotic stability $\delta_1 < r_0 < \delta_1 + (\gamma\delta_2/(\alpha\theta - \beta\delta_2))$ of the boundary equilibrium point $E_1(\overline{u}, 0)$ is satisfied, and hence, $E_1(\overline{u}, 0)$ is locally asymptotically stable. Time series solution demonstrated in Figure 3(b) represents that both predator and prey populations $u(t)$ and $v(t)$ initiate from an initial value $(0.5, 0.3)$ and go to their boundary equilibrium state, and hence, the boundary steady state $E_1(0.1333, 0)$ is stable asymptotically. Also, we have chosen the parameter set as $r_0 = 0.03$, $\delta_1 = 0.02$, $\gamma = 0.01$, $\alpha = 0.9$, $\beta = 0.5$, $\theta = 0.4$, and $\delta_2 = 0.05$. The condition of locally asymptotic stability $r_0 - \delta_1 - 2\gamma u^* - (\alpha v^*/(1+\beta u^*)^2) = -0.0009 < 0$ of the coexisting singular point $E^*(u^*, v^*)$ is satisfied, and hence, $E^*(u^*, v^*)$ is locally asymptotically stable. From the time series analysis shown in Figure 3(c), it can be demonstrated that both prey and predators $u(t)$ and $v(t)$ initiate from the

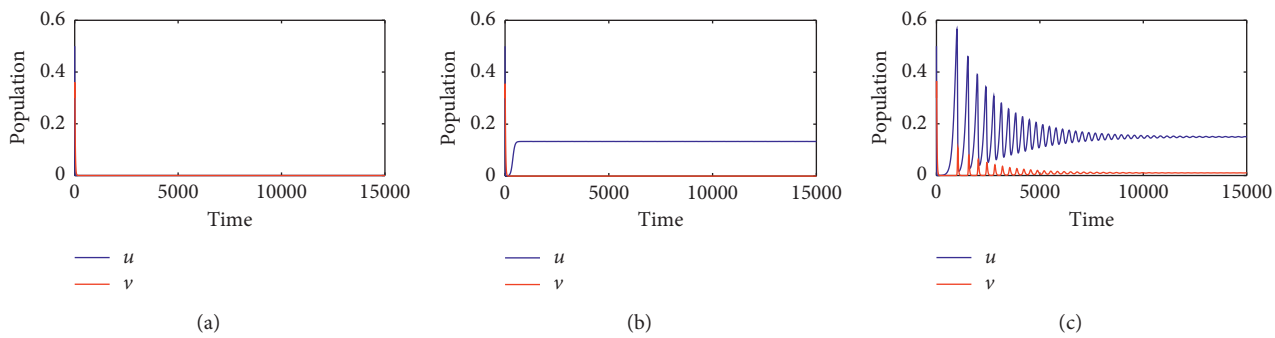

Figure 3: The time series evolution of prey population $u(t)$ and predator population $v(t)$ for the model system (4) with parameters is defined in numerical section. The subplot (a) shows that trivial singular point $E_0(0,0)$ is locally asymptotically stable, (b) boundary singular point $E_1(0.1333,0)$ is locally asymptotically stable, and (c) the coexisting steady state $E^*(0.1493,0.0102)$ is stable asymptotically.

initial value $(0.5,0.3)$ and go to their interior singular point; hence, the coexisting steady state $E^*(0.1493,0.0102)$ is locally asymptotically stable.

The dynamical behavior around the coexisting steady state $E^*(u^*,v^*)$ of the system (4) has been shown in the phase diagram (Figure 4). The system (4) is integrated by using fourth-order Runge–Kutta scheme with the parameter set $\delta_1 = 0.01$, $\gamma = 0.01$, $\alpha = 0.9$, $\beta = 0.5$, $\delta_2 = 0.05$, and $\theta = 0.4$ and varies the prey birth rate r_0. For $r_0 = 0.018$, the positive interior singular point is given by $E^*(0.1493, 0.0078)$. To verify Theorem 5, we find $K_{11} = r_0 - \delta_1 - 2\gamma u^* - (\alpha v^*/(1+\beta u^*)^2) = -0.1113 < 0$ and $K_{22} = 0.0003 > 0$, which ensure that the asymptotic stability of coexisting state $E^*(u^*,v^*)$. Phase portrait diagram (see Figure 4(a)) demonstrates that the predator-prey model (4) is stable asymptotically at coexisting equilibrium state $E^*(u^*,v^*)$ as we have chosen an initial point $E(0.5,0.3)$ and both the species move around interior steady state $E^*(0.1493,0.0078)$ and ultimately go to E^*. The system (4) enters into the limit cycle behavior from stable one, for the value of prey birth rate r_0 gradually increases, which means that, for increasing the size of prey population, the predator has taken more time to handle the prey species. Thus, the magnitude of the prey oscillation increases due to increasing size of the prey species. Figure 4(b) demonstrates the limit cycle oscillations around coexisting state $E^*(0.1493,0.0400)$ for $r_0 = 0.045$, and the other parameter values are the same as in Figure 4(a). In this case, the values of the coefficients of the characteristic (17) are $K_{11} = 0.000834 > 0$ and $K_{22} = 0.001559 > 0$, which does not satisfy the conditions for locally asymptotically stability of E^* in Theorem 5. As the values of K_{11} and K_{22} are both positive for $r_0 = 0.045$, the solutions of the system (4) are unstable, and this ensures the limit cycle oscillation around the coexisting equilibrium $E^*(0.1493,0.0400)$.

Analytically, we have shown that the coexisting state $E^*(u^*,v^*)$ for the system (4) experiences Hopf bifurcation with respect to the prey birth rate r_0. By numerical simulations, Figure 5 exhibits that the predator-prey system (4) experiences Hopf bifurcation around the threshold values $r_0^* = 0.0330$. For the set of parameter values specified in this section, we obtain $(\mathrm{d}/\mathrm{d}r_0)(\mathrm{Re}(\lambda(r_0)))|_{r_0=r_0^*} = 0.0694 > 0$. This indicates that the transversality condition for Hopf bifurcation is verified. Hence, the coexistence steady state $E^*(u^*,v^*)$ of the predator-prey system (4) is asymptotically stable for $r_0 < r_0^*$ and unstable for $r_0 > r_0^*$. It can also be noticed that the system (4) exhibits oscillatory behavior from the stable one, when the value of prey birth rate r_0 is increased gradually, and the high amplitude oscillation may lead to the crash of the species [44, 45]. Hence, the prey growth rate (r_0) has a critical role for the stability of the system (4).

In our study, we have not shown analytically the bifurcation for the predator-prey system (4) with respect to the conversion coefficient θ and the intraspecific coefficient γ; here, we have numerically plotted the bifurcation figure for (4) with reference to the parameters θ and γ. The bifurcation figure for (4) with respect to θ is shown in Figure 6. Here, r_0 is predetermined at 0.07, and the rest of parameters are the same as in Figure 5. The system (4) shows the limit cycle oscillation from equilibrium state as the bifurcation parameter θ increases. The system (4) experiences Hopf bifurcation around $\theta \approx 0.055$. The bifurcation diagram for the system (4) with reference to the intraspecific competition coefficient γ is shown in Figure 7. Here, r_0 is predetermined at 0.07, and the rest of parameters are the same as in Figure 5. This bifurcation diagram shows that the model alters the stability from limit cycle behavior to equilibrium state as bifurcation parameter γ increases.

Again, the dynamics around the interior singular point of the Beddington–DeAngelis-type predator-prey system (19) is shown in Figure 8. The system (19) is integrated using the Runge–Kutta scheme with parameter set $\delta_1 = 0.01$, $\gamma = 0.01$, $\alpha = 0.9$, $\beta = 0.5$, $\delta_2 = 0.05$, $\theta = 0.4$, $\xi = 0.3$, and varies the prey birth rate r_0. For $r_0 = 0.018$, the predator-prey system (19) has one interior positive singular point $E^*(0.1496,0.0078)$. As shown in Table 1, we compute the value of $M_1 + M_4 = -0.0056$ and $M_1M_4 - M_2M_3 = 0.0002659$; therefore, $M_1 + M_4 < 0$ and $M_1M_4 - M_2M_3 > 0$. This ensures the stability for the interior singular point for the predator-prey system (19). The phase portrait diagram for Beddington–DeAngelis-type prey-predator system (19) shown in Figure 8(a) demonstrates that the coexisting steady state is locally asymptotically stable. The Beddington–DeAngelis-type prey-predator system (19) enters into the limit cycle behavior from stable one for increasing value

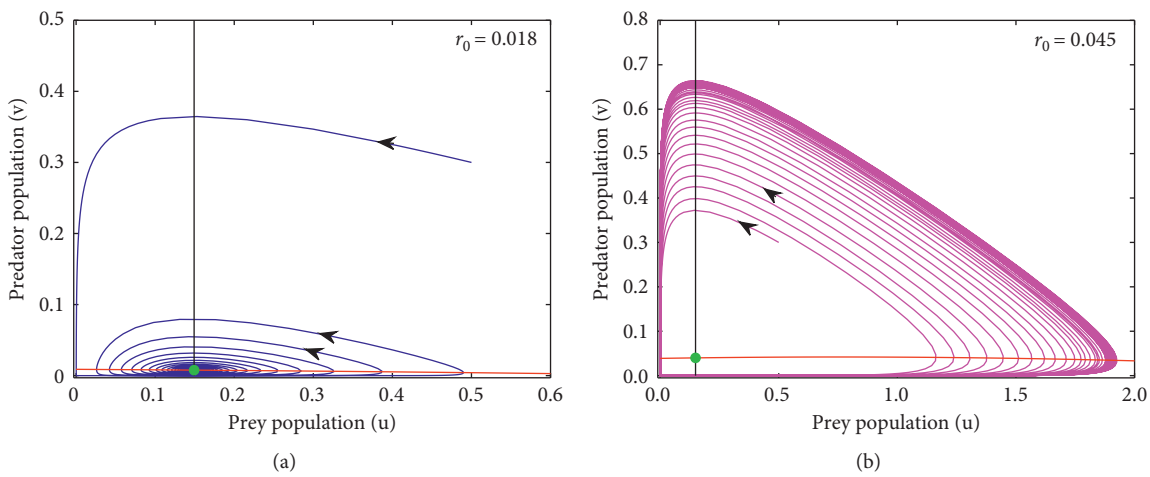

Figure 4: The phase portrait diagram of (4) around the coexisting singular point E^*(green filled circle) with initial values $[x(0), y(0)] = [0.5, 0.3]$. Black vertical line represents the predator isocline, and the red curve represents the prey isocline. The subplot (a) shows the phase portrait diagram is stable asymptotically at E^* $(0.1493, 0.0078)$ for $r_0 = 0.018$, and (b) the phase portrait diagram shows the limit cycle oscillation around E^* $(0.1493, 0.0400)$ for $r_0 = 0.018$; the other parameter values are $\delta_1 = 0.01$, $\gamma = 0.01$, $\alpha = 0.9$, $\beta = 0.5$, $\theta = 0.4$, and $\delta_2 = 0.5$.

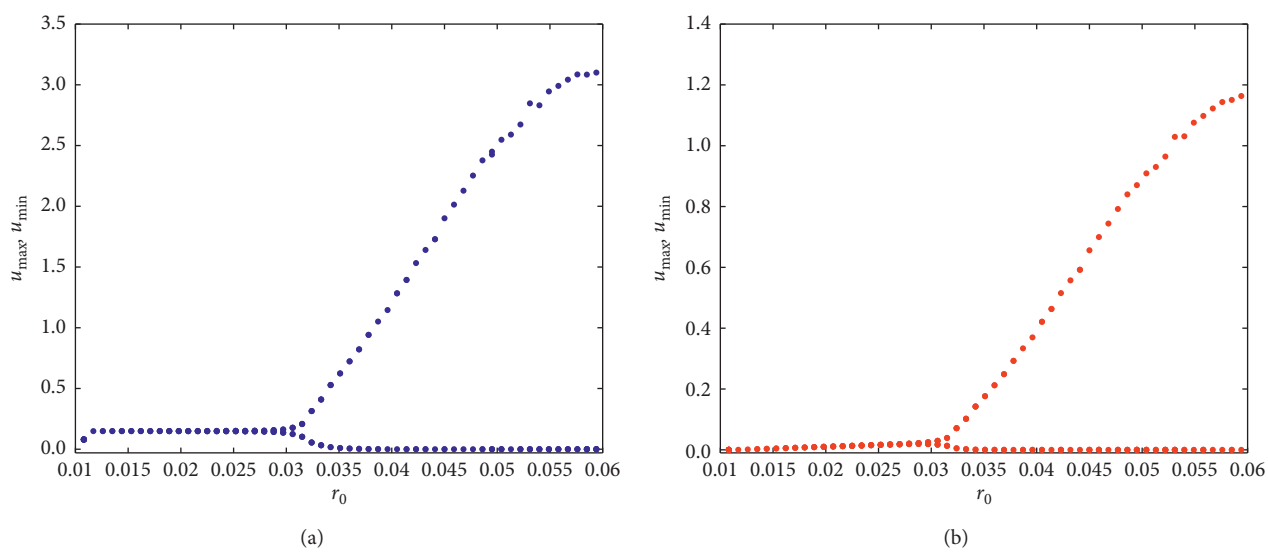

Figure 5: Bifurcation diagram with respect to the prey birth rate r_0 of the predator-prey system (4) with Holling type-II response function. Other parameter values are $\delta_1 = 0.01$, $\gamma = 0.01$, $\alpha = 0.9$, $\beta = 0.5$, $\delta_2 = 0.05$, and $\theta = 0.4$.

of r_0. Also, the phase portrait (Figure 8(b)) shows the limit cycle oscillation at an interior singular state $E^*(0.1511, 0.0405)$ for $r_0 = 0.045$.

The bifurcation diagram of the Beddington–DeAngelis-type predator-prey system (19) with respect to growth rate r_0 for prey species, the conversion rate θ of prey biomass to predator biomass, and the intraspecific competition rate γ are plotted numerically in Figures 9–11, respectively. From the bifurcation diagram of the Holling Type-II predator-prey system (4) and Beddington–DeAngelis-type predator-prey system (19), it can be observed that we obtained the similar kind of dynamics of the prey and predator species except the changes in the bifurcation point. The bifurcation in Figure 9 represents that the predator-prey system (19) is asymptotically stable for lower critical values of prey birth rate r_0, and if r_0 crosses threshold value $r_0^c \approx 0.035$, the Beddington–DeAngelis-type predator-prey system (19) shows limit cycle behavior or oscillating behavior. The bifurcation diagram for the Beddington–DeAngelis-type predator-prey system (19) is shown in Figure 10 with respect to conversion parameter θ. Figure 10 exhibits that the system alters the stability from equilibrium state to limit cycle behavior as the bifurcation parameter θ increases. The bifurcation diagram shown in Figure 11 of the Beddington–DeAngelis-type predator-prey system (19) with respect to the intraspecific competition rate γ shows that the model alters the stability

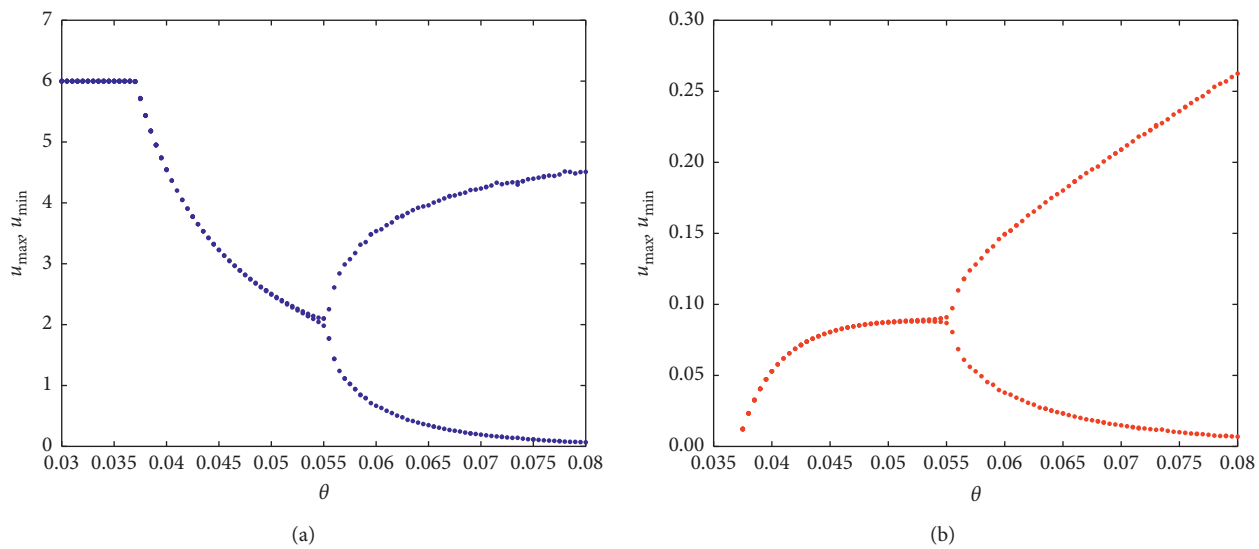

Figure 6: Bifurcation diagram with respect to conversion term θ for the predator-prey model (4) with Holling type-II response function. Rest of parameters: $r_0 = 0.07$, $\delta_1 = 0.01$, $\gamma = 0.01$, $\alpha = 0.9$, $\beta = 0.5$, and $\delta_2 = 0.05$.

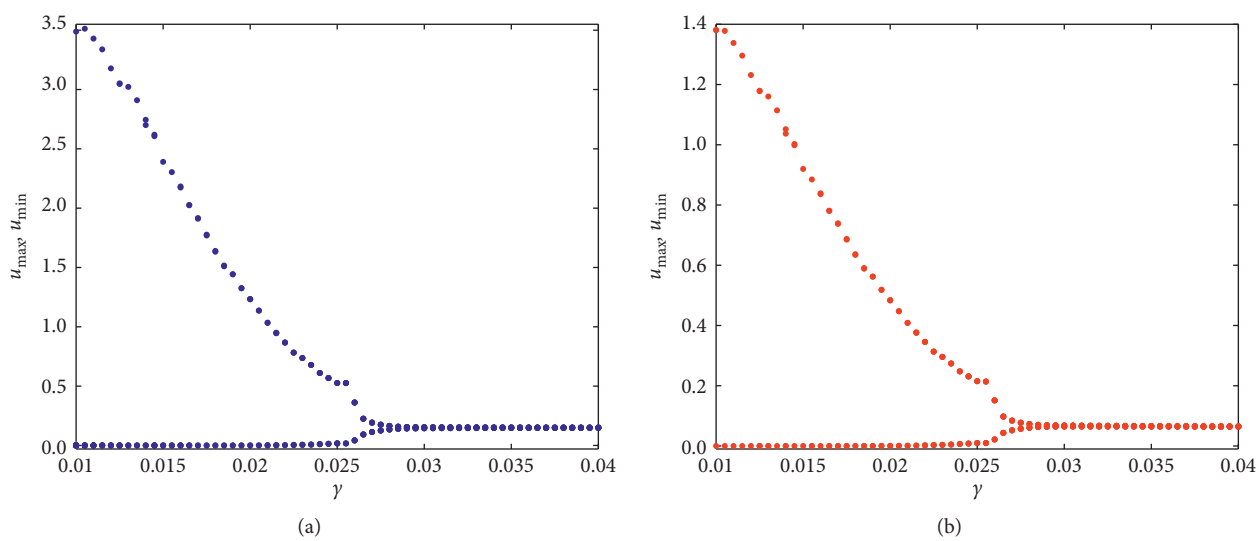

Figure 7: Bifurcation diagram with respect to intraspecific competition between prey species γ for predator-prey system (4) with Holling type-II response function. Rest of the parameters $r_0 = 0.07$, $\delta_1 = 0.01$, $\alpha = 0.9$, $\beta = 0.5$, $\theta = 0.4$, $\delta_2 = 0.05$.

from limit cycle behavior to equilibrium state for increasing bifurcation term γ.

Our predator-prey system (4) with Holling type-II response function undergoes transcritical bifurcation with respect to the prey growth rate r_0, which is plotted in the bifurcation diagram in Figure 12, and the other parameter values are $\delta_1 = 0.01$, $\gamma = 0.01$, $\alpha = 0.9$, $\beta = 0.5$, $\theta = 0.4$, and $\delta_2 = 0.05$. The bifurcating parameter r_0 varied from 0 to 0.04 and is plotted r_0 along the $x-$axis and equilibrium prey (left panel in Figure 12) and predator (right panel in Figure 12) density along the $y-$axis . Black line represents the stable branch of the trivial equilibrium point $E_0(0,0)$, blue-dotted line represents the stable branch of the boundary equilibrium point $E_1(\overline{u},0)$, and the green line represents the unstable branch of the boundary equilibrium point $E_1(\overline{u},0)$. The red horizontal line (left panel) and the red oblique line (right panel) indicate the stable branch of the interior equilibrium point $E^*(u^*,v^*)$, and the magenta line indicates the unstable branch of the interior steady state $E^*(u^*,v^*)$. There is no stable branch of the boundary steady state $E_1(\overline{u},0)$ in the plot of predator density (right panel in Figure 12) as there is no predator density in the boundary equilibrium $E_1(\overline{u},0)$. Both the prey and predator populations oscillate in the blue-shaded region.

Our predator-prey system (19) with Beddington–DeAngelis response function also undergoes transcritical bifurcation with respect to the prey growth rate r_0, which is plotted in the bifurcation diagram in Figure 13, and

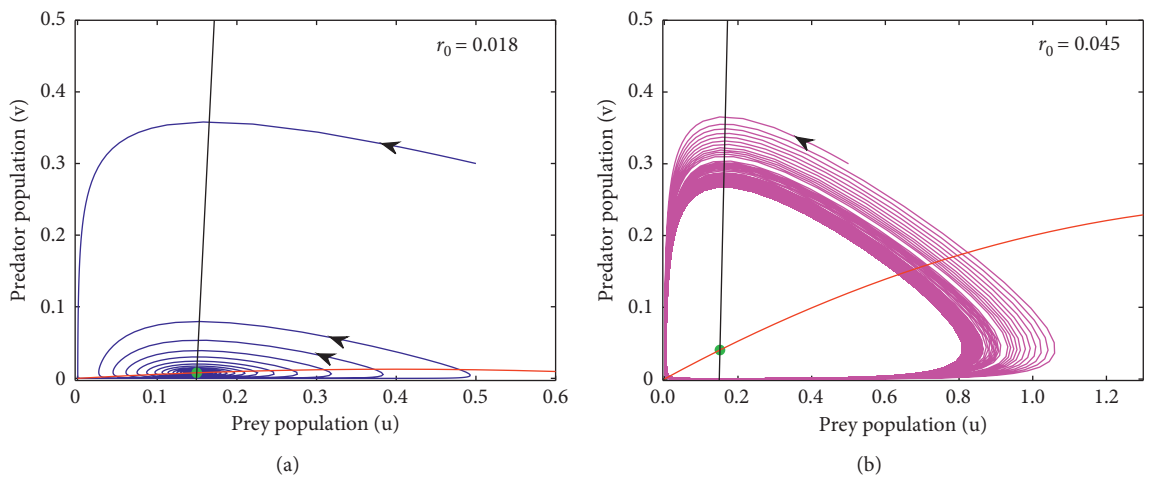

Figure 8: Phase portrait diagram of the predator-prey system (19) with Beddington–DeAngelis-type response function at the coexisting singular point E^* (green filled circle) with initial values $[x(0), y(0)] = [0.5, 0.3]$. Black line is the predator isocline, and the red curve is the prey isocline. (a)$r_0 = 0.018$; (b)$r_0 = 0.045$, and rest of the parameters are specified as $\delta_1 = 0.01$, $\gamma = 0.01$, $\alpha = 0.9$, $\beta = 0.5$, $\theta = 0.4$, $\delta_2 = 0.05$, and $\xi = 0.30$.

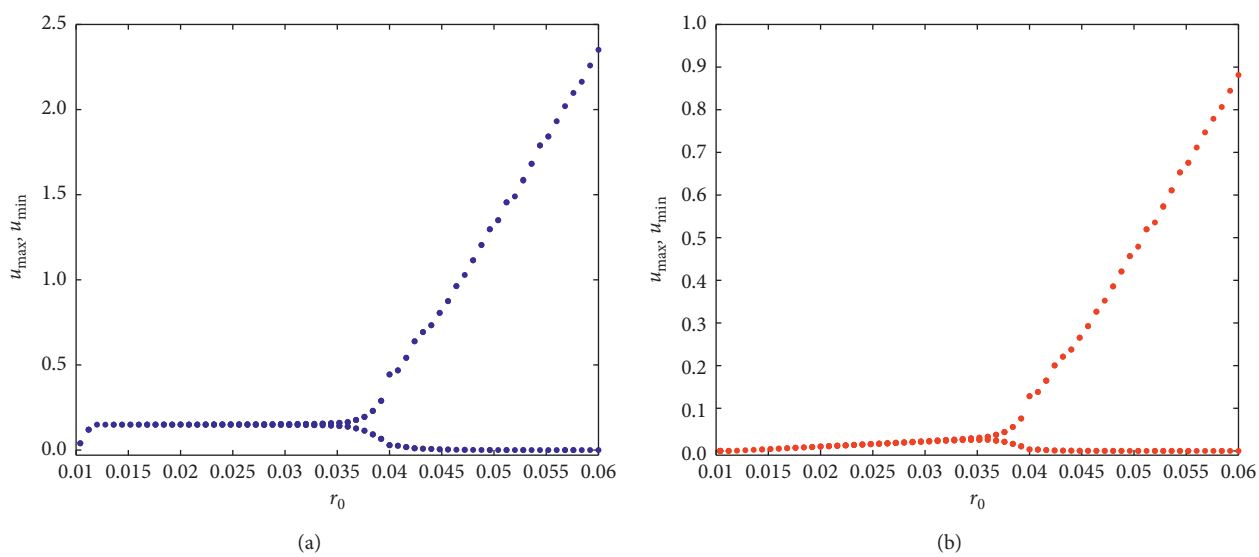

Figure 9: Bifurcation diagram with respect to birth rate of prey species r_0 of the predator-prey system (19) with Beddington–DeAngelis-type response function. Other parameter values are specified as $\delta_1 = 0.01$, $\gamma = 0.01$, $\alpha = 0.9$, $\beta = 0.5$, $\delta_2 = 0.05$, $\theta = 0.4$, and $\xi = 0.30$.

the other parameter values are $\delta_1 = 0.01$, $\gamma = 0.01$, $\alpha = 0.9$, $\beta = 0.5$, $\theta = 0.4$, $\delta_2 = 0.05$, and $\xi = 0.30$. The bifurcating parameter r_0 varied from 0 to 0.04 and is plotted r_0 along the $x-$axis and equilibrium prey (left panel in Figure 13) and predator (right panel in Figure 13) density along the $y-$axis. Black line represents the stable branch of the trivial equilibrium point $E^0(0,0)$, blue-dotted curve represents the stable branch of the boundary equilibrium point $E^1(\hat{u},0)$, and the green line represents the unstable branch of the boundary equilibrium point $E^1(\hat{u},0)$. Red curve indicates the stable branch of the interior equilibrium point $E^*(\hat{u}^*,\hat{v}^*)$, and the magenta line indicates the unstable branch of the interior steady state $E^*(\hat{u}^*,\hat{v}^*)$. There is no stable branch of the boundary steady state $E^1(\hat{u},0)$ in the plot of the predator density (right panel in Figure 13) as there is no predator density in the boundary equilibrium $E^1(\hat{u},0)$. Both the prey and predator populations oscillate in the blue-shaded region. From the transcritical bifurcation for Holling type-II and Beddington–DeAngelis-type response function, we can conclude that density of prey species increases (see the read curve of Figures 12 and 13) for Beddington–DeAngelis-type response function. The red curve (left panel in Figure 13) is increasing as the value of r_0 is increasing; that is, the density of prey species is increasing as the prey growth rate r_0 is increasing. To better understand the increasing pattern of prey species for Beddington–DeAngelis-type response function, we put a portion of the red curve in the dash-dotted box, which has been zoomed and plotted in the inset (left panel of Figure 13).

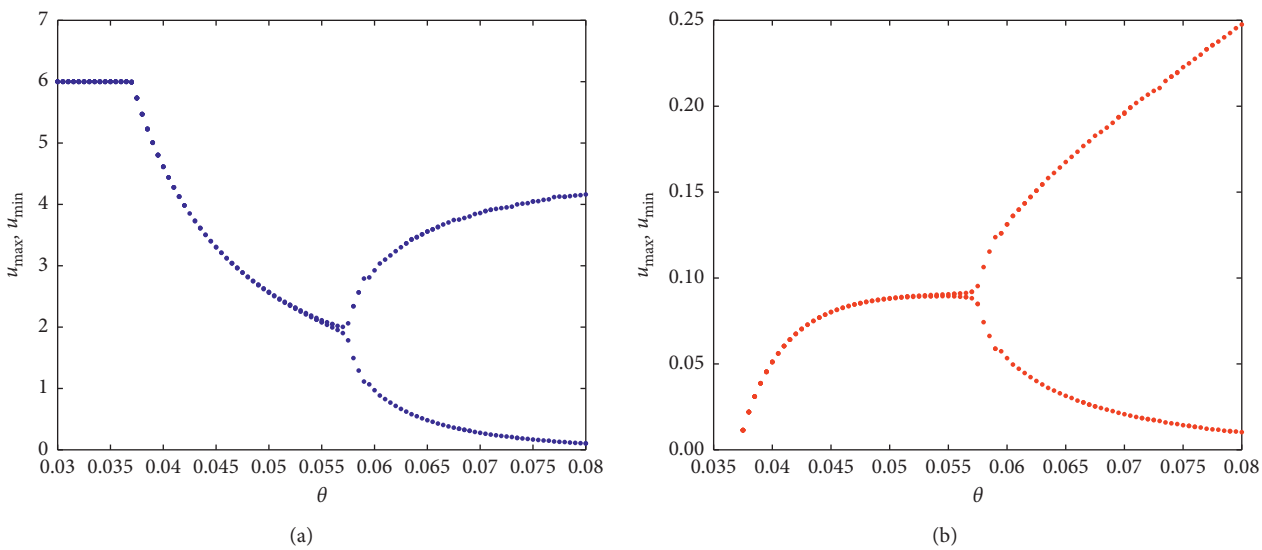

Figure 10: Bifurcation diagram with respect to conversion term θ for predator-prey system (19) with Beddington–DeAngelis-type response function. Rest of parameters are $r_0 = 0.07$, $\delta_1 = 0.01$, $\gamma = 0.01$, $\alpha = 0.9$, $\beta = 0.5$, $\delta_2 = 0.05$, and $\xi = 0.30$.

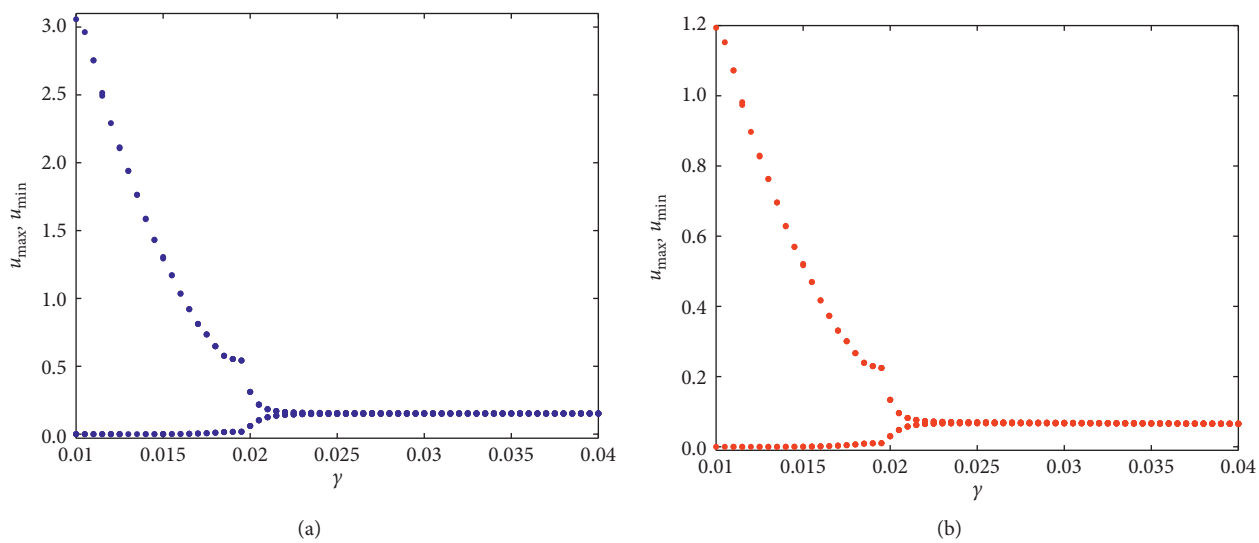

Figure 11: Bifurcation diagram with respect to intraspecific competition between prey species γ for predator-prey system (19) with Beddington–DeAngelis response function. Rest of parameters are specified as $r_0 = 0.07$, $\delta_1 = 0.01$, $\alpha = 0.9$, $\beta = 0.5$, $\theta = 0.4$, $\delta_2 = 0.05$, and $\xi = 0.30$.

By constructing suitable Lyapunov function, we have analytically shown that (see the Section 3.5) the coexisting steady state $E^*(u^*, v^*)$ for the predator-prey system (4) is globally asymptotically stable for $(\gamma/\alpha\beta) > v^*$. For the following parameter values $r_0 = 0.045$, $\delta_1 = 0.01$, $\gamma = 0.15$, $\alpha = 0.9$, $\beta = 0.5$, $\theta = 0.4$, and $\delta_2 = 0.05$, we obtain the interior equilibrium is $E^*(0.1493, 0.0151)$. Here, $(\gamma/\alpha\beta) = 0.3333$ and $v^* = 0.0151$, so it can be verified that $(\gamma/\alpha\beta) > v^*$ for the assumed set of parameter value. Therefore, the interior steady state $E^*(0.1493, 0.0151)$ is globally asymptotically stable. Now, we have numerically integrated the predator-prey system (4) using the Runge–Kutta scheme with the assumed parameter values and considered different initial values $(0.4, 0.1)$, $(0.2, 0.2)$, $(0.4, 0.1)$, and $(0.1, 0.3)$. The phase diagram of this solution is plotted in Figure 14. All the solution trajectories for different initial values converge to an interior singular point $E^*(0.1493, 0.0151)$. This numerically ensures that the interior steady state E^* for the model (4) is globally asymptotically stable.

6. Discussion

Mathematical modeling is an important powerful tool to better understand the interplays between various species that allow us to continue biodiversity and ecosystem in essence.

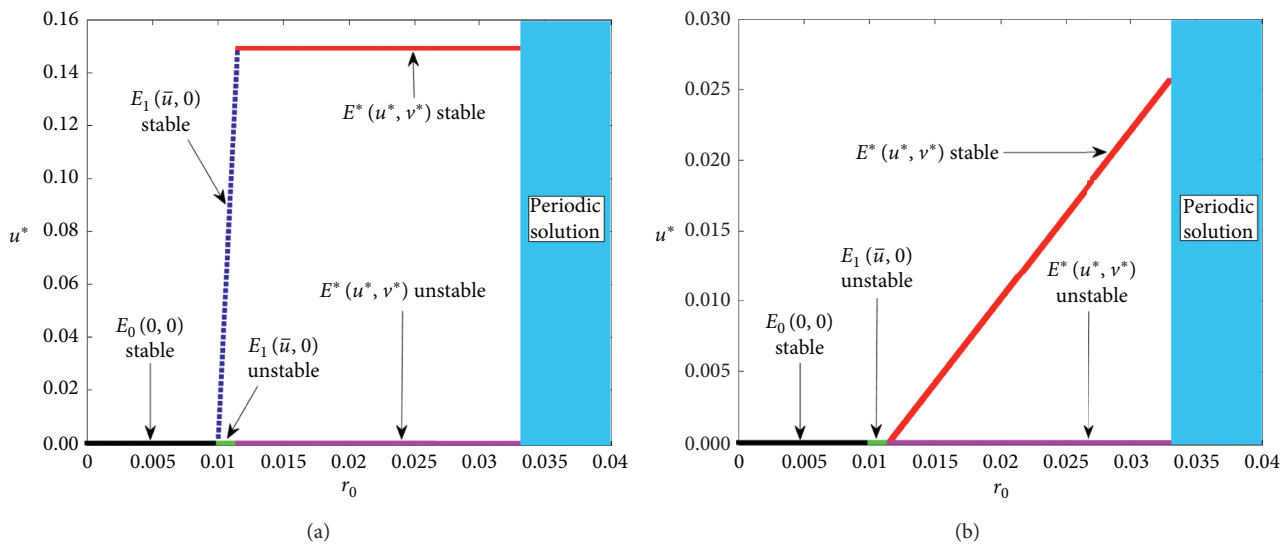

Figure 12: The transcritical bifurcation diagram with respect to the prey birth rate r_0 for the predator-prey system (4) with Holling type-II response function. Other parameter values are specified as $\delta_1 = 0.01$, $\gamma = 0.01$, $\alpha = 0.9$, $\beta = 0.5$, $\theta = 0.4$, and $\delta_2 = 0.05$.

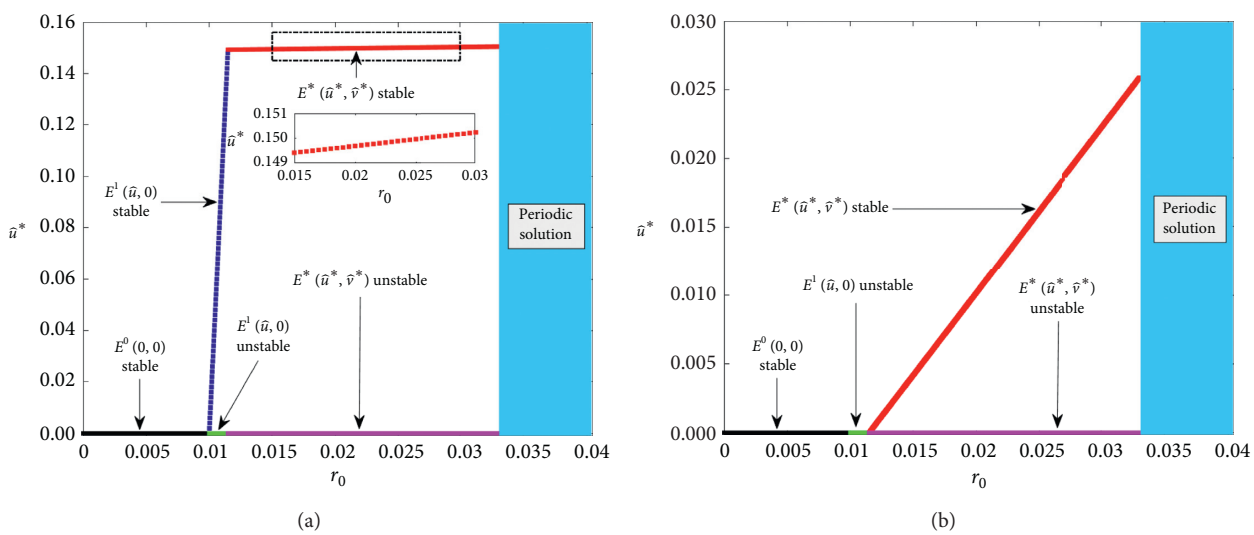

Figure 13: Bifurcation diagram with respect to the growth rate r_0 of the prey species for predator-prey model system (19) with Beddington–DeAngelis response function. Other parameter values are specified as $\delta_1 = 0.01$, $\gamma = 0.01$, $\alpha = 0.9$, $\beta = 0.5$, $\theta = 0.4$, $\delta_2 = 0.05$, and $\xi = 0.30$. The dash-dotted box is zoomed in the inset, which shows the increasing trend of the stable branch of the interior steady state $E^*(\hat{u}^*, \hat{v}^*)$.

In literature, a series of mathematical models has been explored to understand the dynamics for prey-predator model with different kinds of functional responses [12]. In this paper, we investigate a very simple mathematical model for predator-prey system with rich dynamics. Here, we consider a prey-predator system with Holling type-II functional response. The present investigation has been done in three folds. First, we study a prey-predator model with Holling type-II response function, and then, we perform a comparative study of different kinds of functional responses including Beddington–DeAngelis-type response function. Then, we confirm our analytical calculations with numerical illustrations for the hypothetical parameter set.

The solutions of the appraised predator-prey model are showed to be bounded, which indicate none of the species would go at its infinite. To study the kinetics of (4), we discussed the existence of biologically meaningful singular points and their stability including global asymptotic stability. The singular points are identified using prey and predator isocline and found three biologically meaningful steady states of the system (4). The boundary steady state $E_1(\overline{u}, 0)$ shows oscillatory dynamics to the present system (4) as the stability for the model around E_1 indicates the infeasibility for the trivial equilibrium point E_0. The boundary steady state $E_1(\overline{u}, 0)$ is feasible if $r_0 > \delta_1$; that is, growth rate of the prey species is higher than the decay rate

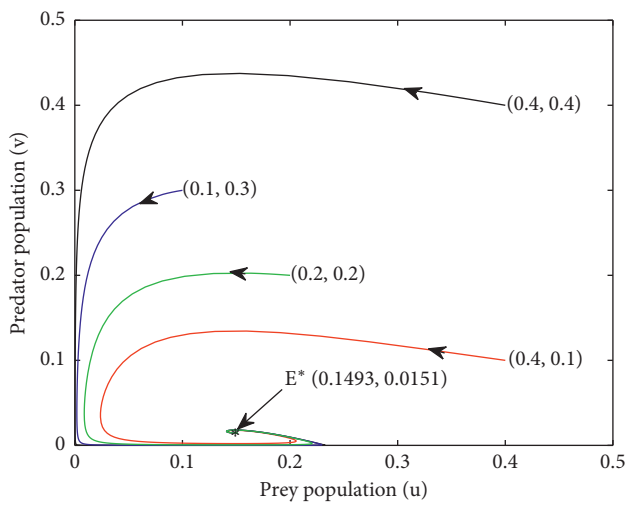

Figure 14: Interior singular point E^* (0.1493, 0.0151) for predator-prey system (4) is globally asymptotically stable with the parameters specified as $r_0 = 0.045$, $\delta_1 = 0.01$, $\gamma = 0.15$, $\alpha = 0.9$, $\beta = 0.5$, $\theta = 0.4$, and $\delta_2 = 0.05$. The initial values are shown within the bracket.

for the prey population. We find the stability region for all the three singular points, namely, trivial, boundary, and interior steady states. In the $r_0 - \beta$ plane, the trivial equilibrium is stable in the blue-shaded region, boundary equilibrium is stable in the green-shaded region, and the interior equilibrium is stable in the red-shaded region (see Figure 2). The equilibrium points of the system (4) are stable in mutually disjoint regions.

A comparative study has been made in this study by considering Holling type-I, Holling type-II, and Beddington–DeAngelis-type response functions of the predator-prey system (4). The stability conditions for different biologically feasible equilibrium points by considering three different types of response functions are presented in Table 1. Our results demonstrate that birth suppression of prey population by predator population lowers the density of equilibrium point of predator population. Moreover, we notice that, above the critical value of prey birth rate r_0^* of the interplay between prey and predator populations, the system produces limit cycle oscillations. Thus, the prey growth rate plays a critical role to destabilize the predator-prey dynamics through Hopf bifurcation (see Figure 5). Analytically, we have computed the global asymptotic stability condition for the interior equilibrium point of the prey-predator system (4) by formulating an appropriate Lyapunov functional. The coexisting singular point is globally asymptotically stable if $(\gamma/\alpha\beta) > v^*$; that is, the predator species is lower than the ratio of intraspecific competition between prey population and the product of attack rate and handling time to capture the prey population by predator population. For the hypothetical parameter set, we have shown numerically the condition for global asymptotic stability of the coexisting singular point E^*. Thus, Theorem 6 is verified numerically.

The phase portrait diagram (Figure 4) for the system (4) indicates that the dynamical behavior of (4) changes as the birth rate r_0 of prey species increases. For increasing the birth rate r_0 for prey species, the amplitude of limit cycle increases, which mean that the predator population will take more time to capture the prey population. We have explored the bifurcation scenario of the systems (4) and (19) by varying the birth rate r_0 of prey species, the conversion coefficient θ of prey biomass to predator biomass, and the intraspecific competition γ between prey species. Analytically, we have shown that the system (4) experiences a Hopf bifurcation around E^* (u^*, v^*) with respect to the prey birth rate at $r_0 = r_0^*$. Bifurcation diagram with respect to another two parameters θ and γ have been plotted by numerical simulations and found that both the systems (4) and (19) undergo from limit cycle oscillations to equilibrium state situation as the parameter γ increases. Again both the systems (4) and (19) undergo equilibrium state to limit cycle oscillation as the conversion coefficient (θ) increases. Thus, the dynamical behavior of (19) remains the same as system (4) as only the position of the bifurcation points has been changed.

We performed direction and stability for Hopf bifurcation of the predator-prey system (4). The main result of the direction of Hopf bifurcation is presented in Theorem 8. The sign of $a(r_0^*)$ governs the stability of Hopf bifurcating periodic solution. When the bifurcating periodic solutions are stable, the direction for Hopf bifurcation becomes supercritical, and when the bifurcating periodic solutions are unstable, the direction for Hopf bifurcation becomes subcritical. Theoretical and numerical illustrations for our present paper describe that a simple predator-prey system can have rich dynamics which can be observed in the ecological system. Numeric simulations are employed for the complexity of theoretical findings, where achievable. For the aptitude suggestions of our investigation, there is a permanent need for observational work to test these forecasts. It can also be observed that the illustrations represented in our manuscript should be examined from qualitative, preferably, than quantitative view point. Our study is based on hypothetical set of parameter values and not based on any particular case as we have no experimental data in our hand, but this investigation might be useful for ecologists who are performing their observation in similar field on the basis of experimental data.

Data Availability

All relevant data are included within the paper.

Conflicts of Interest

The authors declare that they have no conflicts of interest.

Acknowledgments

The work of J. J. Nieto has been partially supported by the Agencia Estatal de Investigación (AEI) of Spain, cofinanced by the European Fund for Regional Development (FEDER) corresponding to the 2014–2020 multiyear financial framework (project MTM2016-75140-P) and Xunta de Galicia (grant ED431C 2019-02). The work of Subhas Khajanchi was supported by the Science and Engineering

Research Board (SERB) (file no. ECR/2017/000234), Department of Science and Technology, Government of India.

References

[1] A. A. Berryman, "The orgins and evolution of predator-prey theory," *Ecology*, vol. 73, no. 5, pp. 1530–1535, 1992.

[2] G. Seo and M. Kot, "A comparison of two predator-prey models with Holling's type I functional response," *Mathematical Biosciences*, vol. 212, no. 2, pp. 161–179, 2008.

[3] P. Turchin, *Complex Population Dynamics: A Theoretical/empirical Synthesis*, Princeton University Press, Princeton, NJ, USA, 2003.

[4] D. Xiao and S. Ruan, "Global dynamics of a ratio-dependent predator-prey system," *Journal of Mathematical Biology*, vol. 43, no. 3, pp. 268–290, 2001.

[5] R. Arditi and L. R. Ginzburg, "Coupling in predator-prey dynamics: ratio-dependence," *Journal of Theoretical Biology*, vol. 139, no. 3, pp. 311–326, 1989.

[6] Y. Lv, L. Chen, and F. Chen, "Stability and bifurcation in a single species logistic model with additive Allee effect and feedback control," *Applied Mathematics and Computation*, vol. 129, p. 2020, 2020.

[7] W. Wang, G. Mulone, F. Salemi, and V. Salone, "Permanence and stability of a stage-structured predator-prey model," *Journal of Mathematical Analysis and Applications*, vol. 262, no. 2, pp. 499–528, 2001.

[8] B. Leard and J. Rebaza, "Analysis of predator-prey models with continuous threshold harvesting," *Applied Mathematics and Computation*, vol. 217, no. 12, pp. 5265–5278, 2011.

[9] S. Khajanchi, "Uniform persistence and global stability for a brain tumor and immune system interaction," *Biophysical Reviews and Letters*, vol. 12, no. 4, pp. 187–208, 2017.

[10] S. Khajanchi and S. Banerjee, "Quantifying the role of immunotherapeutic drug T11 target structure in progression of malignant gliomas: mathematical modeling and dynamical perspective," *Mathematical Biosciences*, vol. 289, pp. 69–77, 2017.

[11] L. R. Ginzburg, "Assuming reproduction to be a function of consumption raises doubts about some popular predator-prey models," *Journal of Animal Ecology*, vol. 67, no. 2, pp. 325–327, 1998.

[12] C. S. Holling, "The functional response of predators to prey density and its role in mimicry and population regulation," *Memoirs of the Entomological Society of Canada*, vol. 97, no. S45, pp. 5–60, 1965.

[13] J. R. Beddington, "Mutual interference between parasites or predators and its effect on searching efficiency," *The Journal of Animal Ecology*, vol. 44, no. 1, pp. 331–340, 1975.

[14] D. L. DeAngelis, R. A. Goldstein, and R. V. O'Neill, "A model for tropic interaction," *Ecology*, vol. 56, no. 4, pp. 881–892, 1975.

[15] T. W. Anderson, "Predator responses, prey refuges, and density-dependent mortality of a marine fish," *Ecology*, vol. 82, no. 1, pp. 245–257, 2001.

[16] B. D. Dalziel, E. Thomann, J. Medlock, and P. De Leenheer, "Global analysis of a predator-prey model with variable predator search rate," *Journal of Mathematical Biology*, vol. 81, no. 1, pp. 159–183, 2020.

[17] X. Wang, H. Wang, and M. Y. Li, "R_0 and sensitivity analysis of a predator-prey model with seasonality and maturation delay," *Mathematical Biosciences*, vol. 315, 2019.

[18] M. C. Köhnke, I. Siekmann, H. Seno, and H. Malchow, "A type IV functional response with different shapes in a predator-prey model," *Journal of Theoretical Biology*, vol. 505, 2020.

[19] K. Antwi-Fordjour, R. D. Parshad, and M. A. Beauregard, "Dynamics of a predator.prey model with generalized Holling type functional response and mutual interference," *Mathematical Biosciences*, vol. 326, 2020.

[20] Y. Xie, Z. Wang, B. Meng, and X. Huang, "Dynamical analysis for a fractional-order prey-predator model with Holling III type functional response and discontinuous harvest," *Applied Mathematics Letters*, vol. 106, 2020.

[21] C. Huang, H. Zhang, J. Cao, and H. Hu, "Stability and Hopf bifurcation of a delayed prey-predator model with disease in the predator," *International Journal of Bifurcation and Chaos*, vol. 29, no. 7, 2019.

[22] S. Alam, S. Abbas, and J. J. Nieto, "Periodic solutions of a nonautonomous leslie-gower predator-prey model with nonlinear type prey harvesting on time scales," *Differential Equations and Dynamical Systems*, vol. 27, no. 4, pp. 357–367, 2019.

[23] K. Sarkar and S. Khajanchi, "Impact of fear effect on the growth of prey in a predator-prey interaction model," *Ecological Complexity*, vol. 42, 2020.

[24] C. Rebelo and C. Soresina, "Coexistence in seasonally varying predator-prey systems with Allee effect," *Nonlinear Analysis: Real World Applications*, vol. 55, 2020.

[25] S. Khajanchi and S. Banerjee, "Role of constant prey refuge on stage structure predator-prey model with ratio dependent functional respons," *Nonlinear Analysis: Real World Applications*, vol. 314, pp. 193–198, 2017.

[26] W. G. Aiello, H. I. Freedman, and J. Wu, "Analysis of a model representing stage-structured population growth with state-dependent time delay," *SIAM Journal on Applied Mathematics*, vol. 52, no. 3, pp. 855–869, 1992.

[27] R. Kon, Y. Saito, and Y. Takeuchi, "Permanence of single-species stage-structured models," *Journal of Mathematical Biology*, vol. 48, no. 5, pp. 515–528, 2004.

[28] S. Khajanchi, "Dynamic behavior of a beddington-deangelis type stage structured predator-prey model," *Applied Mathematics and Computation*, vol. 244, pp. 344–360, 2014.

[29] R. S. Cantrell and C. Cosner, "On the dynamics of predator-prey models with the Beddington-DeAngelis functional response," *Journal of Mathematical Analysis and Applications*, vol. 257, no. 1, pp. 206–222, 2001.

[30] S. Khajanchi, "Modeling the dynamics of glioma-immune surveillance," *Chaos, Solitons & Fractals*, vol. 114, 2018.

[31] S. Liu and E. Beretta, "A stage-structured predator-prey model of Beddington-DeAngelis type," *SIAM Journal on Applied Mathematics*, vol. 66, no. 4, pp. 1101–1129, 2006.

[32] S. Khajanchi and J. J. Nieto, "Mathematical modeling of tumor-immune competitive system, considering the role of time delay," *Applied Mathematics and Computation*, vol. 340, 2019.

[33] S. Khajanchi, "Chaotic dynamics of a delayed tumor-immune interaction model," *International Journal of Biomathematics*, vol. 13, no. 2, 2020.

[34] A. K. Misra, R. K. Singh, P. K. Tiwari, S. Khajanchi, and Y. Kang, "Dynamics of algae blooming: effects of budget allocation and time delay," *Nonlinear Dynamics*, vol. 100, 2020.

[35] S. Khajanchi, "Bifurcation analysis of a delayed mathematical model for tumor growth," *Chaos, Solitons & Fractals*, vol. 77, p. 264, 2015.

[36] S.-B. Hsu, T.-W. Hwang, and Y. Kuang, "Global analysis of the Michaelis-Menten-type ratio-dependent predator-prey

system," *Journal of Mathematical Biology*, vol. 42, no. 6, pp. 489–506, 2001.

[37] L. Chen, F. Chen, and L. Chen, "Qualitative analysis of a predator-prey model with Holling type II functional response incorporating a constant prey refuge," *Nonlinear Analysis: Real World Applications*, vol. 11, no. 1, pp. 246–252, 2010.

[38] S. Khajanchi, "Modeling the dynamics of stage-structure predator-prey system with Monod-Haldane type response function," *Applied Mathematics and Computation*, vol. 302, p. 122, 2017.

[39] H. Li and Y. Takeuchi, "Dynamics of the density dependent predator-prey system with Beddington-DeAngelis functional response," *Journal of Mathematical Analysis and Applications*, vol. 374, no. 2, pp. 644–654, 2011.

[40] S. Khajanchi, "Stability analysis of a mathematical model for glioma-immune interaction under optimal therapy," *International Journal of Nonlinear Sciences and Numerical Simulation*, vol. 20, no. 3-4, pp. 269–285, 2019.

[41] J. Guckenheimer and P. Holmes, "Nonlinear oscillations, dynarnical systems, and bifurcation of vector fields," *Applied Mathematics and Science*, vol. 42, 1983.

[42] S. Khajanchi and S. Baneerjee, "Influence of multiple delays in brain tumor and immune system interaction with T11 target structure as a potent stimulator," *Mathematical Biosciences*, vol. 302, 2018.

[43] M. Sambath, K. Balachandran, and M. Suvinthra, "Stability and Hopf bifurcation of a diffusive predator-prey model with hyperbolic mortality," *Complexity*, vol. 21, no. S1, pp. 34–43, 2016.

[44] M. L. Rosenzweig, "Paradox of enrichment: destabilization of exploitation ecosystems in ecological time," *Science*, vol. 171, no. 3969, pp. 385–387, 1971.

[45] M. E. Gilpin and M. L. Rosenzweig, "Enriched predator-prey systems: theoretical stability," *Science*, vol. 177, no. 4052, pp. 902–904, 1972.

Hindawi
Complexity
Volume 2020, Article ID 9132501, 10 pages
https://doi.org/10.1155/2020/9132501

Research Article

Bogdanov–Takens Bifurcation in a Shape Memory Alloy Oscillator with Delayed Feedback

Jinbin Wang[1,2] **and Lifeng Ma**[1,2]

[1]*Engineering Research Center Heavy Machinery Ministry of Education, Taiyuan University of Science and Technology, Taiyuan, China*
[2]*College of Mechanical Engineering, Taiyuan University of Science and Technology, Taiyuan 030024, Shanxi, China*

Correspondence should be addressed to Jinbin Wang; wangjinbin@tyust.edu.cn

Received 20 July 2020; Revised 14 September 2020; Accepted 18 September 2020; Published 24 October 2020

Academic Editor: J.-C. Cortés

This work is focused on a shape memory alloy oscillator with delayed feedback. The main attention is to investigate the Bogdanov–Takens (B-T) bifurcation by choosing feedback parameters $A_{1,2}$ and time delay τ. The conditions for the occurrence of the B-T bifurcation are derived, and the versal unfolding of the norm forms near the B-T bifurcation point is obtained by using center manifold reduction and normal form. Moreover, it is demonstrated that the system also undergoes different codimension-1 bifurcations, such as saddle-node bifurcation, Hopf bifurcation, and saddle homoclinic bifurcation. Finally, some numerical simulations are given to verify the analytic results.

1. Introduction

In recent years, smart materials have been widely used in many fields such as aircraft manufacturing [1, 2], control field [3], energy [4, 5], and medical [6] due to their special properties. The discovery and application of shape memory alloys [7–9] is an important part of smart materials. The so-called shape memory alloy (SMA) [10] is a new type of smart material with special shape memory effect and pseudo-elasticity, which can restore the previously defined shape when subjected to an appropriate thermomechanical loading process.

SMA spring oscillators can exhibit rich dynamic behaviors based on their pseudo-elasticity, thus promoting the study of nonlinear dynamics and bifurcation of shape memory oscillators [11–15]. Savi et al. [16] studied the nonlinear dynamics of shape memory alloy systems and established the constitutive model of the SMA. Fu and Lu [17] investigated the nonlinear dynamics and vibration damping of dry friction oscillators with SMA restraints. Costa et al. [18] applied the extended time-delayed feedback approach to investigate the chaos control of an SMA two-bar truss. de Paula et al. [19] controlled a shape memory alloy two-bar truss by the delayed feedback method.

The governing equation of motion of a shape memory oscillator [20, 21] is given by

$$m\ddot{x} + c\dot{x} + K(x,T) = F\cos(\omega t), \tag{1}$$

where $\overline{q} = (qA/L)$, $\overline{b} = (bA/L^3)$, and $\overline{e} = (eA/L^5)$. m is the mass of the oscillator. $F\cos(\omega t)$ is a periodic external force, and $K(x,T) = \overline{q}(T - T_m)x - \overline{b}x^3 + \overline{e}x^5$ is the restoring force of the spring. L and A, respectively, denote a shape memory element of length and cross-section area. b, e, c, and q are constants of the material. T_M corresponds to the temperature where the martensitic phase is stable.

In 2016, Yu et al. [22] considered a typical dimensionless system of the SMA oscillator based on equation (1) as follows:

$$\ddot{x} + \alpha_1\dot{x} + \alpha_2 x - \alpha_3 x^3 + \alpha_4 x^5 = k\cos(\theta t), \tag{2}$$

and they added a time-delayed feedback to control equation (2), and equation (2) can be rewritten as

$$\ddot{x} + \alpha_1\dot{x} + \alpha_2 x - \alpha_3 x^3 + \alpha_4 x^5 = k\cos(\theta t) + A_1 x_\tau + A_2 x_\tau^3, \tag{3}$$

where $x_\tau = x(t-\tau)$, τ is denoted as delay, and $A_{1,2}$ is the delay position feedback parameter.

If $k\cos(\theta t)$ is considered as the control parameter δ, equation (3) can be rewritten as

$$\ddot{x} + \alpha_1\dot{x} + \alpha_2 x - \alpha_3 x^3 + \alpha_4 x^5 = \delta + A_1 x_\tau + A_2 x_\tau^3. \tag{4}$$

They used the normal form theory (NFT) and center manifold theorem (CMT) to calculate the conditions of the Hopf bifurcation and stability of equation (4).

The deep insight of the system dynamics is helpful to understand the nonlinear dynamics of shape memory alloy systems. However, many studies on time-delay systems have focused on analyzing the bifurcations of codimension-1, such as Hopf bifurcation [23]. Actually, the time-delay system may have more complicated dynamics when two separate parameters or many parameters are changed simultaneously. B-T bifurcation, which is a typical codimension-2 bifurcation, is studied in [24–28].

Motivated by the above works, we consider system (4) and investigate the B-T bifurcation under some critical conditions. The main contributions of this paper are as follows:

(1) The feedback parameters $A_{1,2}$ and time delay τ are selected to analyze their impact on codimension-2 bifurcations of system (4)

(2) The bifurcation diagram and topological classification of the trajectory of a universal unfolding are given

(3) The second-order terms of the normal form on a center manifold of the SMA system are obtained

The layout of this work is organized as follows: in Section 2, we, respectively, give conditions for the occurrence of the B-T bifurcation and mainly discuss the normal forms for the B-T bifurcation. In Section 3, some numerical simulations are implemented to validate the above analysis. We give some conclusions in Section 4, respectively.

2. Stability and B-T Bifurcation

In this section, we mainly establish the existence of the B-T bifurcation under some critical conditions.

Firstly, let $\dot{x} = y$; then, system (4) can be equivalent to

$$\begin{cases} \dot{x} = y, \\ \dot{y} = -\alpha_1 y - \alpha_2 x + \alpha_3 x^3 - \alpha_4 x^5 + \delta + A_1 x_\tau + A_2 x_\tau^3. \end{cases} \tag{5}$$

Denoting the equilibrium of system (4) as $E_0 = (x_0, 0)$, x_0 satisfies an algebraic equation as follows:

$$g(x) = e_1 x^5 + e_2 x^3 + e_3 x + e_4 = 0, \tag{6}$$

where $e_1 = \alpha_4$, $e_2 = -(\alpha_3 + A_2)$, $e_3 = \alpha_2 - A_1$, and $e_4 = -\delta$.

Next, we discuss the existence conditions of the root of equation (6).

Lemma 1. *For the roots of equation (6), the following results hold:*

(i) If $e_1 < 0$, $e_3 > 0$, and $e_4 = 0$, then equation (6) has tree roots, and they are $x_1 = 0$ and $x_{2,3} = \pm\sqrt{((-e_2 - \sqrt{e_2^2 - 4e_1e_3})/2e_1)}$

(ii) If $e_1 > 0$, $e_3 < 0$, and $e_4 = 0$, then equation (6) has tree roots, and they are $x_1 = 0$ and $x_{2,3} = \pm\sqrt{((-e_2 - \sqrt{e_2^2 - 4e_1e_3})/2e_1)}$

(iii) If $(e_2/e_1) < 0$, $(e_3/e_1) > 0$, $\triangle = e_2^2 - 4e_1e_3 > 0$, and $e_4 = 0$, then equation (6) has five roots, and they are $x_1 = 0$, $x_{2,3} = \pm\sqrt{((-e_2 - \sqrt{e_2^2 - 4e_1e_3})/2e_1)}$, and $x_{4,5} = \pm\sqrt{((-e_2 - \sqrt{e_2^2 - 4e_1e_3})/2e_1)}$

(iv) If $e_i > 0\,(i = 1, 2, 3, 4)$, then equation (6) has no real root

(v) If $e_1 > 0$ and $e_4 < 0$, then equation (6) has at least one positive real root

(vi) If $e_1 > 0$ and $e_4 > 0$ and there exists $\xi > 0$ such that $g(\xi) < 0$, then equation (6) has at least two positive real roots

(vii) If $x > 0$, $e_1 > 0$, $e_2 > 0$, $e_3 < 0$, and $e_4 > 0$ and there exists $\xi > 0$ such that $g(\xi) < 0$, then equation (6) has two positive real roots

Proof

(i), (ii), and (iii) are easy to prove, and we do not show the process of proof.

(iv) If $e_i > 0\,(i = 1, 2, 3, 4)$, then $g(0) = e_4 > 0$ and $g'(x) > 0$. Thus, we can obtain that equation (6) has no real root.

(v) If $e_1 > 0$ and $e_4 < 0$, then $g(0) = e_4 < 0$ and $\lim_{x\longrightarrow+\infty} g(x) = +\infty$, and we can obtain that equation (6) has at least one positive real root.

(vi) If $e_1 > 0$ and $e_4 > 0$ and there exists $\xi > 0$ such that $g(\xi) < 0$, we can obtain $g(0) = e_4 > 0$ and $\lim_{x\longrightarrow+\infty} g'(x) = +\infty$, and there exists $x_1 \in (0, \xi)$ and $x_2 \in (\xi, +\infty)$ such that $g(x_1) = g(x_2) = 0$. Thus, equation (6) has at least two positive real roots.

(vi) If $x > 0$, $e_1 > 0$, $e_2 > 0$, $e_3 < 0$, and $e_4 > 0$ and there exists $\xi > 0$ such that $g(\xi) < 0$, we can obtain that $g'(0) = e_3 < 0$, $g''(x) = 20e_1x^3 + 6e_2x > 0$, $\lim_{x\longrightarrow+\infty} g'(x) = +\infty$, and $g'(x) = 0$ have only one positive real root. Furthermore, from $g(0) = e_4 > 0$ and $\lim_{x\longrightarrow+\infty} g(x) = +\infty$, we get that equation (6) has two positive real roots. This completes the proof.

Let $\tilde{x} = x - x_0$ and $\tilde{y} = y$. Omitting the tilde, then system (5) can be rewritten as

$$\begin{cases} \dot{x} = y, \\ \dot{y} = -\alpha_1 y + c_1 x + c_2 x^2 + c_3 x^3 + c_4 x^4 + c_5 x^5 + d_1 x_\tau + d_2 x_\tau^2 + d_3 x_\tau^3, \end{cases} \tag{7}$$

where

$$\begin{aligned} c_1 &= -\alpha_2 + 3\alpha_3 x_0 + 5\alpha_4 x_0^4, \\ c_2 &= 3\alpha_3 x_0 - 10\alpha_4 x_0^3, \\ c_3 &= \alpha_3 + 10\alpha_4 x_0^2, \\ c_4 &= -5\alpha_4 x_0, \\ c_5 &= -\alpha_4, \\ d_1 &= A_1 + 3x_0^2 A_2, \\ d_2 &= 3A_2 x_0, \\ d_3 &= A_2. \end{aligned} \tag{8}$$

The characteristic equation of system (7) at the zero equilibrium $E_0 = (0,0)^T$ is

$$F(\lambda, \tau) = \lambda^2 + \alpha_1 \lambda - c_1 - d_1 e^{-\lambda\tau} = 0. \tag{9}$$

Next, we give the conditions for the existence of the B-T bifurcation and investigate the dynamical classification near the B-T bifurcation point. □

Lemma 2. *If $d_0 < 0$, then the following is obtained:*

(i) If $d_1 = d_0$ and $\tau \neq \tau_0$, $\lambda = 0$ is a single root of equation (9)

(ii) If $\lambda = 0, d_1 = d_0$, and $\tau = \tau_0$, $\lambda = 0$ is a double root of equation (9)

(iii) If $d_1 = d_0$, all the roots of equation (9) have negative real parts except for the zero roots

Here, $\tau_0 = -(\alpha_1/d_0)$ and $d_0 = -c_1$.

Proof. Clearly, $F(0,\tau) = d_1 + c_1 = 0$. By calculating, we can obtain the following result:

$$\begin{aligned} \frac{\partial F(\lambda,\tau)}{\partial \lambda} &= 2\lambda + \alpha_1 + d_0 \tau e^{-\lambda\tau}, \\ \frac{\partial^2 F(\lambda,\tau)}{\partial \lambda^2} &= 2 - d_0 \tau^2 e^{-\lambda\tau}. \end{aligned} \tag{10}$$

It is easy to obtain if $\lambda = 0$ and $\tau \neq \tau_0$, then $(\partial F(\lambda,\tau)/\partial\lambda)|_{\lambda=0,\tau\neq\tau_0} \neq 0$. Thus, (i) holds.

If $\lambda = 0$ and $\tau = \tau_0$, then $(\partial F(\lambda,\tau)/\partial\lambda)|_{\lambda=0,\tau=\tau_0} = 0$ and $(\partial^2 F(\lambda,\tau)/\partial\lambda^2)|_{\lambda=0,\tau=\tau_0} = 2 - (\alpha_1^2/d_0) > 0$. Thus, (ii) holds.

If $\tau = 0, \alpha_1 > 0$, and $d_1 = d_0$, equation (9) has roots $\lambda_1 = 0$ and $\lambda_2 = -\alpha_1 < 0$. When $\tau \neq 0$, let $\lambda = i\omega\,(\omega > 0)$ be a root of equation (9); then, we have

$$\begin{aligned} -\omega^2 + d_0 - d_0 \cos\omega\tau &= 0, \\ \alpha_1 \omega + d_0 \sin\omega\tau &= 0. \end{aligned} \tag{11}$$

$$\omega^4 + \left(\alpha_1^2 - 2d_0\right)\omega^2 = 0. \tag{12}$$

Let $\omega^2 = t > 0$; then, equation (12) can be rewritten as

$$t^2 + pt = 0, \tag{13}$$

where $p = \alpha_1^2 - 2d_0$. If $d_0 < 0$, it results in $p > 0$. Clearly, equation (13) has no positive roots. Thus, (iii) holds. This completes the proof.

Next, we will investigate the B-T bifurcation of system (7) near (d_0, τ_0) by choosing d_1 and τas bifurcation parameters.

Taking $t = (t/\tau)$, $d_1 = d_0 + \mu_1$, and $\tau = \tau_0 + \mu_2$, system (5) can be rewritten as

$$\begin{cases} \dot{x} = (\tau_0 + \mu_2) y, \\ \dot{y} = (\tau_0 + \mu_2)\big[-\alpha_1 y + c_1 x + c_2 x^2 + c_3 x^3 + c_4 x^4 + c_5 x^5 \\ \qquad + (d_0 + \mu_1) x(t-1) + d_2 x^2(t-1) + d_3 x^3(t-1)\big], \end{cases} \tag{14}$$

where μ_1 and μ_2 are perturbation parameters.

The phase space $C = C([0,1]; R^2)$ is chosen as the Banach space of the continuous mappings from [0,1] toR^2. For $\forall x \in C$, we define $x_t(t+\theta)$ and $\|x\| = \sup_{-1<\theta<0}|x(\theta)|$. System (14) becomes

$$\dot{x}(t) = Ex_t + Fx_t, \tag{15}$$

where E and F are operators, given by

$$\begin{aligned} &E\varphi = \dot{\varphi}, D(E) = \varphi \in C^1\big([0,1]; R^2\big): \dot{\varphi}(0) = \int_{-1}^{0} \mathrm{d}\eta(\theta)\varphi(-\theta), \\ &\mathrm{d}\eta(\theta) = \big(A_0\delta(\theta) + B_0\delta(\theta+1)\big)\mathrm{d}\theta, \\ &F\varphi = \begin{cases} 0, & \theta \in [-1,0), \\ L_1(\mu)x_t + G(x_t,\mu), & \theta = 0, \end{cases} \end{aligned} \tag{16}$$

where $\delta(\theta)$ is the Dirac delta function, $A_0 = \begin{pmatrix} 0 & \tau_0 \\ c_1\tau_0 & -\alpha_1\tau_0 \end{pmatrix}$, and $B_0 = \begin{pmatrix} 0 & 0 \\ d_0\tau_0 & 0 \end{pmatrix}$.

$$\begin{aligned} L_1(\mu)x_t &= \begin{pmatrix} \mu_2 y(0) \\ -\mu_2\alpha_1 y(0) + c_1\mu_2 x(0) + d_0\mu_2 x(-1) + \tau_0\mu_1 x(-1) \end{pmatrix}, \\ G(x_t,\mu) &= \begin{pmatrix} 0 \\ c_2\tau_0 x^2(0) + c_3\tau_0 x^3(0) + c_4\tau_0 x^4(0) + c_5\tau_0 x^5(0) \\ +\tau_0 d_2 x^2(-1) + \tau_0 d_3 x^3(-1) \end{pmatrix}. \end{aligned} \tag{17}$$

From Lemma 1, equation (6) has a double-zero root, and all other eigenvalues have negative real parts. Let Λ be the set of eigenvalues with zero real part; C can be decomposed as $C = A \oplus B$, where A is the generalized eigenspace associated with Λ which has two zero eigenvalues and A^* is the space adjoint with A, and $B = \{\varphi \in C: \langle\varphi,\psi\rangle = 0, \forall\varphi \in A^*\}$. Next, we define

$$\begin{aligned} E^*\psi = -\dot{\psi}, D(E^*) = \psi \in C^1\big([0,1]; R^{2*}\big): \dot{\psi}(0) \\ = -\int_{-1}^{0} \mathrm{d}\eta(\theta)\psi(-\theta), \end{aligned} \tag{18}$$

and the bilinear form on $C \times C^*$ is

$$\langle \psi, \varphi \rangle = \psi(0)\varphi(0) - \int_{-1}^{0}\int_{0}^{\theta} \psi(\xi-\theta)\mathrm{d}\eta(\theta)\varphi(\xi)\mathrm{d}\xi. \quad (19)$$

□

Lemma 3 (see [24, 28, 29]). *The bases Φ and Ψ for A and A^* can be chosen such that $\langle \Psi, \Phi \rangle = I$, $\dot{\Phi} = \Phi\begin{pmatrix} 0 & 1 \\ 0 & 0 \end{pmatrix}$, and $\dot{\Psi} = -\begin{pmatrix} 0 & 1 \\ 0 & 0 \end{pmatrix}\Psi$, where $\Phi(\theta) = (\varphi_1(\theta), \varphi_2(\theta))(\theta \in [-1,0])$, $\psi(s) = col(\psi_1(s), \psi_2(s))(s \in [0,1])$, $\varphi_1(\theta) = \varphi_1^0 \in R^n\backslash\{0\}$, $\varphi_2(\theta) = \varphi_2^0 + \varphi_1^0\theta$, $\varphi_2^0 \in R^n$, and $\psi_2(s) = \psi_2^0 \in R^{n*}\backslash\{0\}$, $\psi_1(s) = \psi_1^0 - s\psi_2^0$, $\psi_1^0 \in R^{n*}$, which satisfy*

(i) $(A_0 + B_0)\varphi_1^0 = 0$.

(ii) $(A_0 + B_0)\varphi_2^0 = (B_0 + I)\varphi_1^0$.

(iii) $\psi_2^0(A_0 + B_0) = 0$.

(iv) $\psi_1^0(A_0 + B_0) = \psi_2^0(B_0 + I)$.

(v) $\psi_2^0\varphi_2^0 - (1/2)\psi_2^0 B_0\varphi_1^0 + \psi_2^0 B_0\varphi_2^0 = 1$.

(vi) $\psi_1^0\varphi_2^0 - (1/2)\psi_1^0 B_0\varphi_1^0 + \psi_1^0 B_0\varphi_2^0 + (1/6)\ \psi_2^0 B_0\varphi_1^0 - (1/2)\ \psi_2^0 B_0\varphi_2^0 = 0$.

By calculating, we can obtain

$$\Phi(\theta) = \begin{pmatrix} 1 & b^* + \theta \\ 0 & \dfrac{1}{\tau_0} \end{pmatrix},$$
$$\Psi(s) = \begin{pmatrix} -s\alpha_1 d^* & -sd^* - \dfrac{d^*}{\alpha_1\tau_0} \\ \alpha_1 d^* & d^* \end{pmatrix}, \quad (20)$$

where $b^* = (\alpha_1^2\tau_0^2 + 6 + 3\alpha_1\tau_0/6\alpha_1\tau_0 + 3\alpha_1^2\tau_0^2)$ and $d^* = (2\tau_0/2 + \alpha_1\tau_0)$.

Let $X = \Phi Z + W$, where $Z \in R^2$ and $W \in B$, namely,

$$\begin{cases} x_1(\theta) = Z_1 + (b^* + \theta)Z_2 + w_1(\theta), \\ x_2(\theta) = \dfrac{1}{\tau_0}Z_2 + w_2(\theta), \end{cases}$$
$$\begin{cases} x_1(0) = Z_1 + b^* Z_2 + w_1(0), \\ x_2(0) = \dfrac{1}{\tau_0}Z_2 + w_2(0), \\ x_1(-1) = Z_1 + (b^* - 1)Z_2 + w_1(-1). \end{cases} \quad (21)$$

From [30, 31], system (14) can be written as

$$\begin{cases} \dot{Z}_1 = Z_2 - \dfrac{d^*}{a_1\tau_0}F_2^2, \\ \dot{Z}_2 = a_1 d^* F_2^1 + d^* F_2^2, \end{cases} \quad (22)$$

where

$$F_2^1 = \frac{\mu_2}{\tau_0}Z_2,$$
$$F_2^2 = (c_2\tau_0 + \tau_0 d_2)Z_1^2 + (2c_2\tau_0 b + 2\tau_0 d_2(b^* - 1))Z_1 Z_2 + \left(c_2\tau_0 b^{*2} + \tau_0 d_2(b^* - 1)^2\right)Z_2^2 + \tau_0\mu_1 Z_1 + \tau_0(b^* - 1)\mu_1 Z_2 + \left(-\frac{\alpha_1}{\tau_0} + c_1 x^* - d_0\right)\mu_2 Z_2. \quad (23)$$

From [26], we can obtain the following result:

$$f_{2(Z,0,\mu)}^1 = \begin{pmatrix} h_1 Z_1^2 + h_2 Z_1 Z_2 + h_3 Z_2^2 + h_4\mu_1 Z_1 + h_5\mu_2 Z_1 + h_6\mu_1 Z_2 + h_7\mu_2 Z_2 \\ f_1 Z_1^2 + f_2 Z_1 Z_2 + f_3 Z_2^2 + f_4\mu_1 Z_1 + f_5\mu_2 Z_1 + f_6\mu_1 Z_2 + f_7\mu_2 Z_2 \end{pmatrix}, \quad (24)$$

where

$$h_1 = -\frac{d^*}{\alpha_1}(c_2 + d_2), h_2 = -\frac{d^*}{\alpha_1}(2c_2 b^* + 2d_2(b^* - 1)),$$
$$h_3 = -\frac{d^*}{\alpha_1}\left(c_2 b^{*2} + d_2(b^* - 1)^2\right), h_4 = -\frac{d^*}{\alpha_1},$$
$$h_5 = 0, h_6 = -\frac{d^*}{\alpha_1}(b^* - 1), h_7 = -\frac{d^*}{\tau_0\alpha_1}\left(-\frac{\alpha_1}{\tau_0} - d_0\right),$$
$$f_1 = d^*\tau_0(c_2 + d_2), f_2 = d^*\tau_0(2c_2 b^* + 2d_2(b^* - 1)),$$
$$f_3 = d^*\tau_0\left(c_2 b^{*2} + d_2(b^* - 1)^2\right),$$
$$f_4 = d^*\tau_0, f_5 = 0, f_6 = d^*\tau_0(b^* - 1), f_7 = -d_0 d^*. \quad (25)$$

The following normal form with versal unfolding on the center manifold can be obtained by some calculations:

$$\begin{cases} \dot{Z}_1 = Z_2, \\ \dot{Z}_2 = \lambda_1 Z_1 + \lambda_2 Z_2 + \eta_1 Z_1^2 + \eta_2 Z_1 Z_2, \end{cases} \quad (26)$$

where $\lambda_1 = d^*\tau_0\mu_1$, $\lambda_2 = \tau_0(b^* - 1)d^*\mu_1 - d_0 d^*\mu_2$, $\eta_1 = d^*\tau_0(c_2 + d_2)$, and $\eta_2 = -(2d^*/\alpha_1)(c_2 + d_2) + d^*\tau_0(2c_2 b^* + 2d_2\ (b^* - 1))$. The detailed calculations can be found in Appendix.

By calculating, we can get

$$\left(\frac{\partial(\lambda_1, \lambda_2)}{\partial(\mu_1, \mu_2)}\right)\Big|_{\mu=0} = -d_0(d^*)^2\tau_0 \neq 0. \quad (27)$$

Thus, the map $(\mu_1, \mu_2) \longrightarrow (\lambda_1, \lambda_2)$ is regular, and system (14) is equivalent to the normal form (26), where $\eta_1 \cdot \eta_2 > 0$.

Let $Z_1 \longrightarrow (\eta_1/\eta_2^2)(Z_1 - \lambda_1(\eta_2^2/2\eta_1^2))$, $Z_2 \longrightarrow -(\eta_1^2/\eta_2^3)Z_2$, and $t \longrightarrow -(\eta_2/\eta_1)t$; system (26) can be rewritten as

$$\begin{cases} \dot{Z}_1 = Z_2, \\ \dot{Z}_2 = v_1 + v_2 Z_2 + Z_1^2 - Z_1 Z_2, \end{cases} \tag{28}$$

where $v_1 = -(\lambda_1^2\eta_2^4/4\eta_1^4)$ and $v_2 = -\lambda_2(\eta_2/\eta_1) - \lambda_1(\eta_2^2/2\eta_1^2)$.

System (28) as a universal unfolding [30, 31] with codimension-2 has been well studied. We can acquire the complete bifurcation diagram and topological classification of the trajectory of system (28), and the bifurcation diagram of system (28) on the perturbation parameter v_1 and v_2 planes is shown in Figure 1 [17, 21]. Furthermore, we give a concise form to list the conclusion as follows:

(1) System (28) undergoes a saddle-node bifurcation on the set

$$\begin{aligned} \mathrm{SN} &= \{(v_1, v_2)\colon v_1 = 0, v_2 \neq 0\} \\ &= \left\{(\mu_1, \mu_2)\colon \mu_1 = 0, -[\tau_0(b^* - 1)d^*\mu_1 - d_0 d^*\mu_2]\frac{\eta_2}{\eta_1} - d^*\tau_0\mu_1\frac{\eta_2^2}{2\eta_1^2} \neq 0\right\}. \end{aligned} \tag{29}$$

(2) System (28) undergoes a stable Hopf bifurcation on the set

$$\begin{aligned} H &= \left\{(v_1, v_2)\colon v_1 = -v_2^2, v_2 > 0\right\} \\ &= \left\{(\mu_1, \mu_2)\colon \frac{(d^*\tau_0\mu_1)^2\eta_2^4}{4\eta_1^4} = -\left[(\tau_0(b^* - 1)d^*\mu_1 - d_0 d^*\mu_2)\frac{\eta_2}{\eta_1} + (d^*\tau_0\mu_1)\frac{\eta_2^2}{2\eta_1^2}\right]^2\right\}. \end{aligned} \tag{30}$$

(3) System (28) undergoes a saddle homoclinic bifurcation on the set

$$\begin{aligned} T &= \left\{(v_1, v_2)\colon v_1 = -\frac{49}{25}v_2^2\right\} \\ &= \left\{(\mu_1, \mu_2)\colon \frac{(d^*\tau_0\mu_1)^2\eta_2^4}{4\eta_1^4} = -\frac{49}{25}\left[(\tau_0(b^* - 1)d^*\mu_1 - d_0 d^*\mu_2)\frac{\eta_2}{\eta_1} + (d^*\tau_0\mu_1)\frac{\eta_2^2}{2\eta_1^2}\right]^2\right\}. \end{aligned} \tag{31}$$

3. Numerical Simulation

In this section, we use the dde23 method in MATLAB and show some numerical simulations to illustrate the analysis results given in the previous sections.

In order to easily verify the obtained results, we choose parameters $\alpha_1 = 1$, $\alpha_2 = 0.1$, $\alpha_3 = 1$, $\alpha_4 = 1$, $\delta = 0.8$, $A_1 = -1$, and $A_2 = -1$. Furthermore, based on results of Lemmas 1 and 2, we can calculate$x_0 = 0.634$, $\tau_0 = 0.344$, $d_0 = -2.902$, $c_2 = -0.646$, $c_3 = 5.02$, $c_4 = -3.17$, $c_5 = -1$, $d_2 = -1.902$, and $d_3 = -1$. In Figure 1, the bifurcation diagrams of system (16) are composed of codimension-2 bifurcation point $(v_1, v_2) = (0, 0)$ and three codimension-1 curves (saddle-node bifurcation curve, Hopf bifurcation curve, and saddle homoclinic bifurcation curve). When the parameters v_1 and v_2 change in different regions, system (16) will produce different dynamic properties.

To easily analyze the dynamics of system (7), we fix $\mu_1 = -0.001$ and only choose the value of μ_2 to change. From Lemma 2, the B-T bifurcation point $(d_0, \tau_0) = (-2.902, 0.344)$ is obtained. Thus, we give some numerical examples as follows:

(i) If setting $(\mu_1, \mu_2) = (-0.001, 0.006)$, there exist a saddle and a stable focus in region A_2 (see Figure 1), as shown in Figures 2 and 3

(ii) Fix $(\mu_1, \mu_2) = (-0.001, 0.026)$; Figures 4 and 5 show that a stable periodic solution occurs when bifurcation parameters pass through the Hopf bifurcation line H in region A_3 (see Figure 1)

(iii) Fix $(\mu_1, \mu_2) = (-0.001, 0.1664)$; Figures 6–8 show that a closed orbit exists through the homoclinic bifurcation line $T \in$ ③ (see Figure 1)

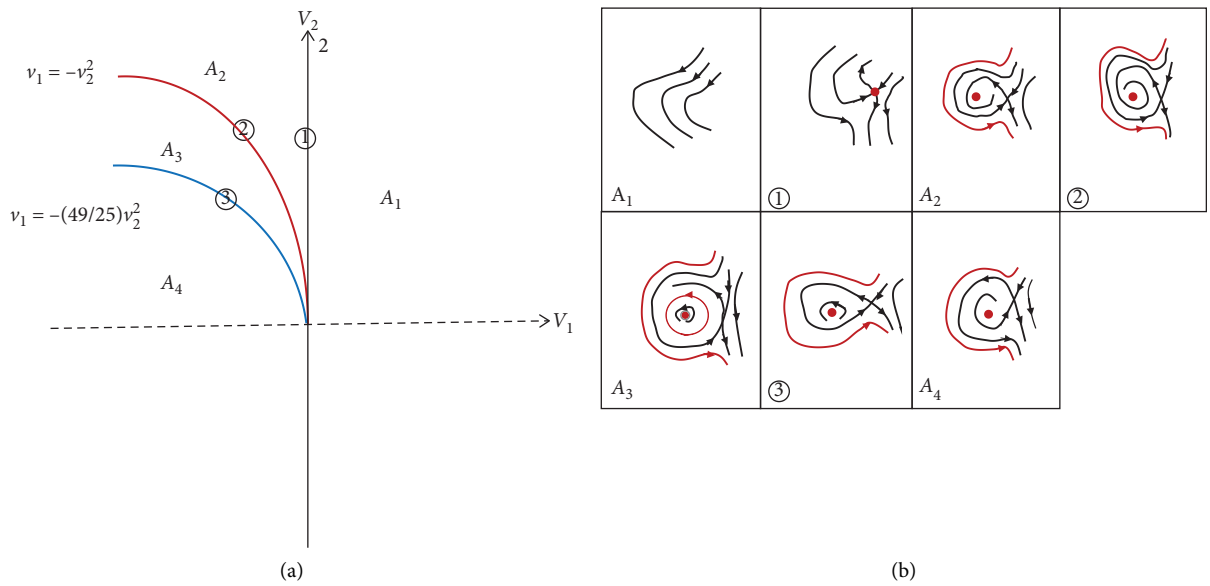

FIGURE 1: The bifurcation diagram (a) and phase portraits (b) of system (15) on the perturbation parameter v_1 and v_2 planes.

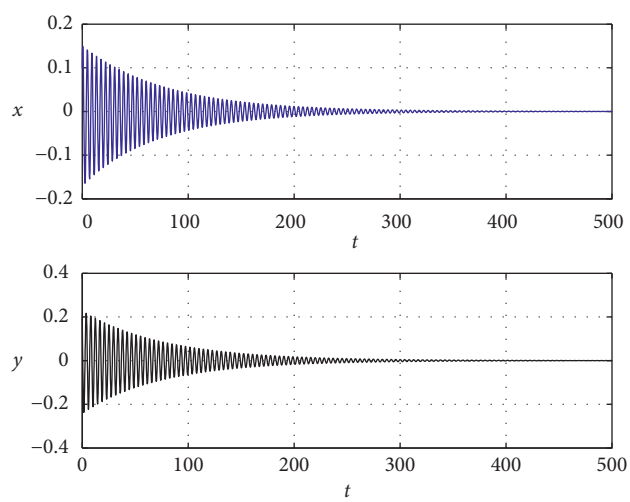

FIGURE 2: Waveform plot of system (7) near $(d_0, \tau_0) = (-2.902, 0.344)$ with parameters $(\mu_1, \mu_2) = (-0.001, 0.006)$, $\tau = 0.35$, tspan $= [0, 500]$, and $(x_0, y_0) = (0.1, 0.2)$.

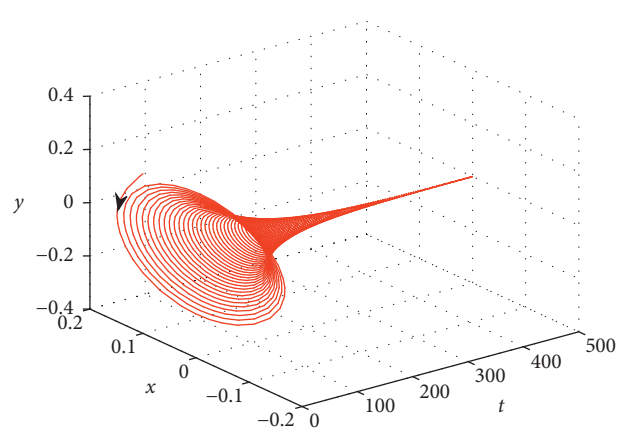

FIGURE 3: State trajectory of system (7) near $(d_0, \tau_0) = (-2.902, 0.344)$ with parameters $(\mu_1, \mu_2) = (-0.001, 0.006)$, $\tau = 0.35$, tspan $= [0, 500]$, and $(x_0, y_0) = (0.1, 0.2)$.

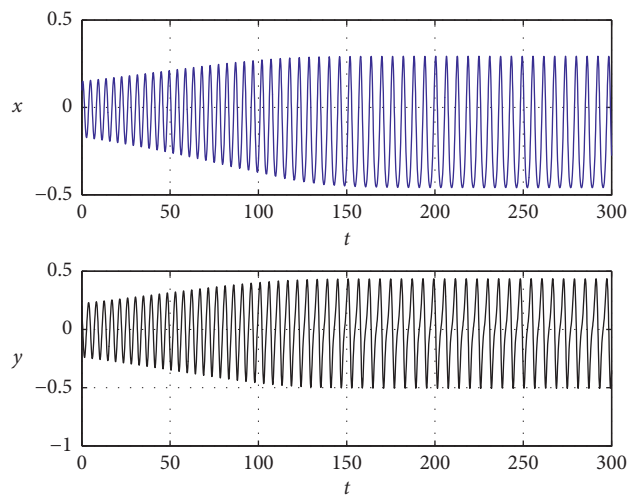

Figure 4: Waveform plot of system (7) near $(d_0, \tau_0) = (-2.902, 0.344)$ with parameters $(\mu_1, \mu_2) = (-0.001, 0.026)$, $\tau = 0.37$, tspan $= [0, 300]$, and $(x_0, y_0) = (0.1, 0.2)$.

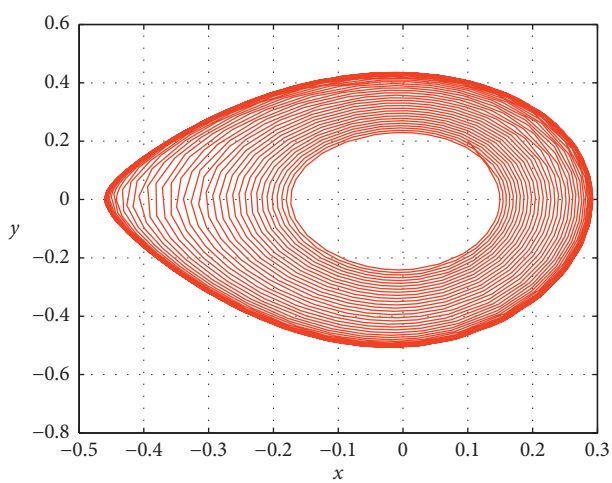

Figure 5: Phase portraits of system (7) near $(d_0, \tau_0) = (-2.902, 0.344)$ with parameters $(\mu_1, \mu_2) = (-0.001, 0.026)$, $\tau = 0.37$, tspan $= [0, 300]$, and $(x_0, y_0) = (0.1, 0.2)$.

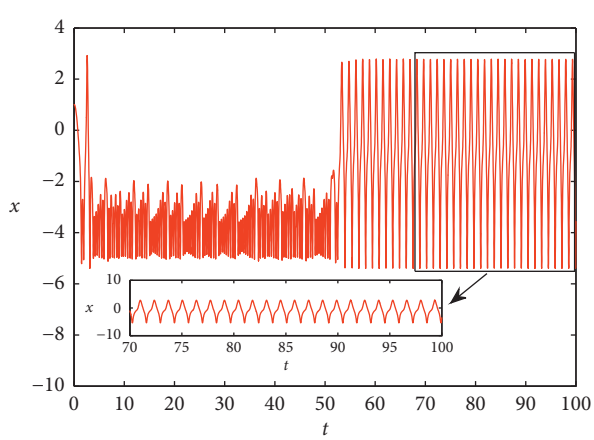

Figure 6: Waveform plot of system (7) near $(d_0, \tau_0) = (-2.902, 0.344)$ with parameters $(\mu_1, \mu_2) = (-0.001, 0.1664)$, $\tau = 0.5104$, tspan $= [0, 100]$, and $(x_0, y_0) = (0.1, 0.2)$.

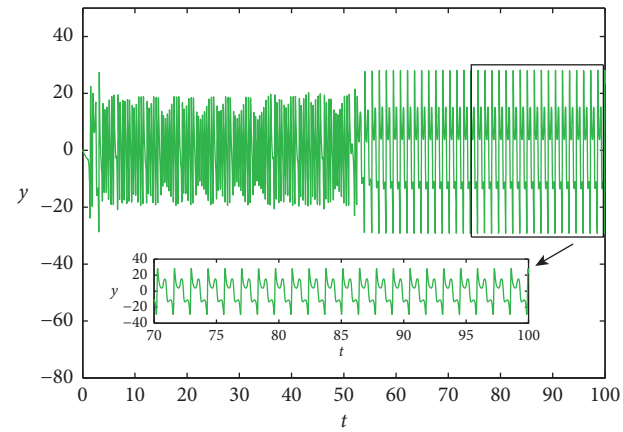

Figure 7: Waveform plot of system (7) near $(d_0, \tau_0) = (-2.902, 0.344)$ with parameters $(\mu_1, \mu_2) = (-0.001, 0.1664)$, $\tau = 0.5104$, tspan $= [0, 100]$, and $(x_0, y_0) = (0.1, 0.2)$.

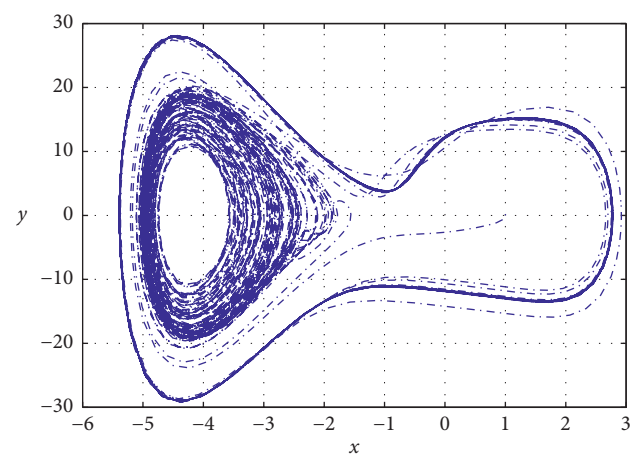

Figure 8: Phase portraits of system (7) near $(d_0, \tau_0) = (-2.902, 0.344)$ with parameters $(\mu_1, \mu_2) = (-0.001, 0.1664)$, $\tau = 0.5104$, tspan $= [0, 100]$, and $(x_0, y_0) = (0.1, 0.2)$.

4. Conclusions

In this work, a shape memory alloy oscillator with delayed feedback has been analyzed. We mainly choose the two parameters $d_1 = A_1 + 3x_0^2 A_2$ and τ to investigate the B-T bifurcation of system (6). It is demonstrated that the feedback parameters $A_{1,2}$ and time delay τ have an important influence on the shape memory alloy oscillator. As the two parameters of the SMA oscillator change, the conditions for the occurrence of B-T bifurcation and some phase portraits and bifurcation diagrams are given. By using the CMT and NFT of functional differential equations, we investigate some typical codimension-1 bifurcations such as saddle-node bifurcation, Hopf bifurcation, and saddle homoclinic bifurcation. Some numerical simulations further verify the obtained analytic results.

In our paper, second-order terms of the normal form on a center manifold are given, but the higher order is not investigated. System (2) or (3) is only discussed by considering $k\cos(\theta t)$ as the control parameter δ (see [22]).

However, the periodic force $k\cos(\theta t)$ has an important effect on the vibration and memory characteristics of the SMA system. Therefore, further discussion and analysis of the SMA system will be our future work.

Appendix

The following calculations of the norm forms of the equation are based on [25, 26, 32, 33].

Let $x = \Phi z + w$. Then, system $\dot{x}(t) = Ex_t + Fx_t$ can be decomposed into the following form:

$$\begin{cases} \dot{z} = Bz + \psi(0)F(\Phi z + w, \mu), \\ \dot{w} = A_{Q^1} w + (I - \pi)x_0 F(\Phi z + w, \mu), \end{cases} \tag{A.1}$$

where A_{Q^1} is the restriction of A_0 as an operator from Q^1 to the Banach space $\ker\pi$. Employing Taylor expansion, system (A.1) becomes

$$\begin{cases} \dot{z} = Bz + \sum_{j\geq 2} \frac{1}{j!} f\left(j_1(z, w, \mu),\right. \\ \dot{w} = A_{Q^1} w + \sum_{j\geq 2} \frac{1}{j!} f_j^2(z, w, \mu), \end{cases} \tag{A.2}$$

where $f_j^1(z, w, \mu)(j = 1, 2)$ denote the homogeneous polynomials of degree j in (z, w, μ). Then, we can obtain the following form:

$$\dot{z} = Bz + \frac{1}{2} g_2^1(z, 0, \mu) + h.o.t. \tag{A.3}$$

Denote $V_j^4(z)$ as the linear space of homogeneous polynomials and M_j^1 as the operator on $V_j^4(R^2)$ with $M_j^1 \begin{pmatrix} p_1 \\ p_2 \end{pmatrix} = \begin{pmatrix} (\partial p_1 & /\partial z_1) z_2 - p_2 \\ (\partial p_2 & /\partial z_1) z_2 \end{pmatrix}$, where $\begin{pmatrix} p_1 \\ p_2 \end{pmatrix} \in V_j^4\ (R^2)$. $V_2^4(R^2)$ can be decomposed as $V_2^4(R^2) = \mathrm{Im}(M_2^1) \oplus \mathrm{Im}(M_2^1)^c$.

Then, $(1/2) g_2^1(z, 0, \mu)$ can be written as

$$g_2^1(z, 0, \mu) = \mathrm{Project}_{\mathrm{Im}(M_2^1)^c} f_2^1(z, 0, \mu). \tag{A.4}$$

The base of $V_2^4(R^2 \times \ker\pi)$ can be chosen as follows:

$$\begin{pmatrix} 0 \\ z_1^2 \end{pmatrix}, \begin{pmatrix} 0 \\ z_1 z_2 \end{pmatrix}, \begin{pmatrix} 0 \\ \mu_1 z_1 \end{pmatrix}, \begin{pmatrix} 0 \\ \mu_2 z_1 \end{pmatrix}, \begin{pmatrix} 0 \\ \mu_2 z_1 \end{pmatrix}, \begin{pmatrix} 0 \\ \mu_2 z_2 \end{pmatrix}, \begin{pmatrix} 0 \\ \mu_1^2 \end{pmatrix}, \begin{pmatrix} 0 \\ \mu_1 \mu_2 \end{pmatrix}, \begin{pmatrix} 0 \\ \mu_2^2 \end{pmatrix}, \begin{pmatrix} -z_1^2 \\ 2z_1 z_2 \end{pmatrix}, \begin{pmatrix} z_1 z_2 \\ 0 \end{pmatrix}, \begin{pmatrix} z_2^2 \\ 0 \end{pmatrix}, \begin{pmatrix} \mu_1 z_1 \\ -\mu_1 z_2 \end{pmatrix}, \begin{pmatrix} \mu_2 z_1 \\ -\mu_2 z_2 \end{pmatrix}, \begin{pmatrix} \mu_1 z_2 \\ 0 \end{pmatrix}, \begin{pmatrix} \mu_2 z_2 \\ 0 \end{pmatrix}, \begin{pmatrix} \mu_1^2 \\ 0 \end{pmatrix}, \begin{pmatrix} \mu_1 \mu_2 \\ 0 \end{pmatrix}, \begin{pmatrix} \mu_2^2 \\ 0 \end{pmatrix}, \begin{pmatrix} 0 \\ z_2^2 \end{pmatrix}. \tag{A.5}$$

The base of $\mathrm{Im}(M_2^1)$ can be chosen as follows:

$$\begin{pmatrix} -z_1^2 \\ 2z_1 z_2 \end{pmatrix}, \begin{pmatrix} z_1 z_2 \\ 0 \end{pmatrix}, \begin{pmatrix} z_2^2 \\ 0 \end{pmatrix}, \begin{pmatrix} \mu_1 z_1 \\ -\mu_1 z_2 \end{pmatrix}, \begin{pmatrix} \mu_2 z_1 \\ -\mu_2 z_2 \end{pmatrix}, \begin{pmatrix} \mu_1 z_2 \\ 0 \end{pmatrix}, \begin{pmatrix} \mu_2 z_2 \\ 0 \end{pmatrix}, \begin{pmatrix} \mu_1^2 \\ 0 \end{pmatrix}, \begin{pmatrix} \mu_1 \mu_2 \\ 0 \end{pmatrix}, \begin{pmatrix} \mu_2^2 \\ 0 \end{pmatrix}, \begin{pmatrix} 0 \\ z_2^2 \end{pmatrix}. \tag{A.6}$$

The base of $\mathrm{Im}(M_2^1)^c$ can be chosen as follows:

$$\begin{pmatrix} 0 \\ z_1^2 \end{pmatrix}, \begin{pmatrix} 0 \\ z_1 z_2 \end{pmatrix}, \begin{pmatrix} 0 \\ \mu_1 z_1 \end{pmatrix}, \begin{pmatrix} 0 \\ \mu_2 z_1 \end{pmatrix}, \begin{pmatrix} 0 \\ \mu_2 z_1 \end{pmatrix}, \begin{pmatrix} 0 \\ \mu_2 z_2 \end{pmatrix}, \begin{pmatrix} 0 \\ \mu_1^2 \end{pmatrix}, \begin{pmatrix} 0 \\ \mu_1 \mu_2 \end{pmatrix}, \begin{pmatrix} 0 \\ \mu_2^2 \end{pmatrix}. \tag{A.7}$$

Then, we can get the following result:

$$f_{2(z,0,\mu)}^1 = \begin{pmatrix} e_1 z_1^2 + e_2 z_1 z_2 + e_3 z_2^2 + e_4 \mu_1 z_1 + e_5 \mu_2 z_1 + e_6 \mu_1 z_2 + e_7 \mu_2 z_2 \\ f_1 z_1^2 + f_2 z_1 z_2 + f_3 z_2^2 + f_4 \mu_1 z_1 + f_5 \mu_2 z_1 + f_6 \mu_1 z_2 + f_7 \mu_2 z_2 \end{pmatrix}, \tag{A.8}$$

where

$$e_1 = -\frac{d^*}{\alpha_1}(c_2 + d_2), e_2 = -\frac{d^*}{\alpha_1}(2c_2b^* + 2d_2(b^* - 1)), e_3 = -\frac{d^*}{\alpha_1}\left(c_2b^{*2} + d_2(b^* - 1)^2\right),$$
$$e_4 = -\frac{d^*}{\alpha_1}, e_5 = 0, e_6 = -\frac{d^*}{\alpha_1}(b^* - 1), e_7 = -\frac{d^*}{\tau_0\alpha_1}\left(-\frac{\alpha_1}{\tau_0} - d_0\right), \tag{A.9}$$
$$f_1 = d^*\tau_0(c_2 + d_2), f_2 = d^*\tau_0(2c_2b^* + 2d_2(b^* - 1)), f_3 = d^*\tau_0\left(c_2b^{*2} + d_2(b^* - 1)^2\right),$$
$$f_4 = d^*\tau_0, f_5 = 0, f_6 = d^*\tau_0(b^* - 1), f_7 = -d_0d^*.$$

Thus, the following normal form with versal unfolding on the center manifold can be obtained by some calculations:

$$\begin{cases} \dot{Z}_1 = Z_2, \\ \dot{Z}_2 = \lambda_1 Z_1 + \lambda_2 Z_2 + \eta_1 Z_1^2 + \eta_2 Z_1 Z_2, \end{cases} \tag{A.10}$$

where $\lambda_1 = d^*\tau_0\mu_1$, $\lambda_2 = \tau_0(b^* - 1)d^*\mu_1 - d_0d^*\mu_2$, $\eta_1 = d^*\tau_0(c_2 + d_2)$, and $\eta_2 = -(2d^*/\alpha_1)(c_2 + d_2) + d^*\tau_0(2c_2b^* + 2d_2(b^* - 1))$.

Data Availability

The data used to support the findings of this study are included within the article.

Conflicts of Interest

The authors declare that they have no conflicts of interest.

Authors' Contributions

J. B. Wang carried out the study. L. F. Ma supervised the work and provided the support of funds. All authors read and approved the final manuscript.

Acknowledgments

This work was supported by the National Natural Science Foundation of China (no. U1610253), the Key Research and Development Program of Shanxi Province (no. 201603D111004), and the Fund for Shanxi "1331 Project" Key Subjects Construction.

References

[1] K. K. Denoyer, R. S. Erwin, and R. R. Ninneman, "Advanced smart structures flight experiments for precision spacecraft," *Acta Astronautica*, vol. 47, no. 2–9, pp. 389–397, 2000.

[2] P. M. C. L. Pacheco and M. A. Savi, "A non-explosive release device for aerospace applications using shape memory alloys," in *Proceedings of XIV the Brazilian Congress of Mechanical Engineering (COBEM 1997-ABCM)*, Bauru, Brazil, November 1997.

[3] W. M. Bessa, A. S. de Paula, and M. A. Savi, "Adaptive fuzzy sliding mode control of smart structures," *The European Physical Journal Special Topics*, vol. 222, no. 7, pp. 1541–1551, 2013.

[4] G. A. Lebedev, B. V. Gusarov, B. Viala et al., "Thermal energy harvesting using shape memory/piezoelectric composites," in *Proceedings of the Solid-State Sensors, Actuators and Microsystems Conference (TRANSDUCERS), 2011 16th International*, pp. 669-670, Beijing, China, June 2011.

[5] L. L. SilvaS. A. Oliveira et al., "Synergistic use of smart materials for vibration-based energy harvesting," *European Physical Journal: Special Topics*, vol. 224, no. 14-15, pp. 3005–3021, 2015.

[6] L. G. Machado and M. A. Savi, "Medical applications of shape memory alloys," *Brazilian Journal of Medical and Biological Research*, vol. 36, no. 6, pp. 683–691, 2003.

[7] K. Otsuka and C. M. Wayman, *Shape Memory Materials*, Cambridge University Press, Cambridge, U.K, 1998.

[8] X. Xu, W. Ito, R. Y. Umetsu, R. Kainuma, and K. Ishida, "Anomaly of critical stress in stress-induced transformation of NiCoMnIn metamagnetic shape memory alloy," *Applied Physics Letters*, vol. 95, no. 18, Article ID 181905, 2009.

[9] X. Wang, B. Verlinden, and J. Van Humbeeck, "Effect of post-deformation annealing on the R-phase transformation temperatures in NiTi shape memory alloys," *Intermetallics*, vol. 62, pp. 43–49, 2015.

[10] M. A. Savi, "Nonlinear dynamics and chaos in shape memory alloy systems," *International Journal of Non-linear Mechanics*, vol. 70, pp. 2–19, 2015.

[11] G. M. Luciano, A. S. Marcelo, and M. C. L. P. Pedro, "Nonlinear dynamics and chaos in coupled shape memory oscillators," *International Journal of Solids*, vol. 40, pp. 5139–5156, 2003.

[12] A. S. Marcelo, A. N. S. Milton, P. Alberto, and M. C. L. P. Pedro, "Tensile-compressive asymmetry influence on shape memory alloy system dynamics," *Chaos Solitons Fractals*, vol. 36, pp. 828–842, 2008.

[13] S. Elena, P. Ekaterina, W. Marian, and A. S. Marcelo, "Vibration reduction of the impact system by an SMA restraint: numerical studies," *International Journal of Non-Linear Mechanics*, vol. 45, pp. 837–849, 2010.

[14] C. S. dos Bruno and A. S. Marcelo, "Nonlinear dynamics of a nonsmooth shape memory alloy oscillator," *Chaos Solitons Fractals*, vol. 40, pp. 197–209, 2009.

[15] M. A. Savi, P. M. C. L. Pacheco, M. S. Garcia et al., "Nonlinear geometric influence on the mechanical behavior of shape memory alloy helical springs," *Smart Materials and Structures*, vol. 24, p. 35012, 2014.

[16] M. A. Savi, M. A. N. Sá, A. Paiva, and P. M. C. L. Pacheco, "Tensile-compressive asymmetry influence on shape memory

alloy system dynamics," *Chaos, Solitons & Fractals*, vol. 36, no. 4, pp. 828–842, 2008.

[17] S. Fu and Q. Lu, "Nonlinear dynamics and vibration reduction of a dry friction oscillator with SMA restraints," *Nonlinear Dynamics*, vol. 69, no. 3, pp. 1365–1381, 2012.

[18] D. D. A. Costa, M. A. Savi, A. S. de Paula, and D. Bernardini, "Chaos control of a shape memory alloy structure using thermal constrained actuation," *International Journal of Nonlinear Mechanics*, vol. 111, pp. 106–118, 2019.

[19] A. S. de Paula, M. V. S. dos Santos, M. A. Savi, and W. M. Bessa, "Controlling a shape memory alloy two-bar truss using delayed feedback method," *International Journal of Structural Stability and Dynamics*, vol. 14, no. 8, Article ID 1440032, 2014.

[20] V. Piccirillo, J. M. Balthazar, and B. R. Pontes, "Analytical study of the nonlinear behavior of a shape memory oscillator: Part I-primary resonance and free response at low temperatures," *Nonlinear Dynamics*, vol. 59, no. 4, pp. 733–746, 2009.

[21] V. Piccirillo, J. M. Balthazar, and B. R. Pontes, "Analytical study of the nonlinear behavior of a shape memory oscillator: Part II-resonance secondary," *Nonlinear Dynamics*, vol. 60, no. 4, pp. 513–524, 2009.

[22] Y. Yu, Z. Zhang, Q. Bi, and Y. Gao, "Bifurcation analysis on delay-induced bursting in a shape memory alloy oscillator with time delay feedback," *Applied Mathematical Modelling*, vol. 40, no. 3, pp. 1816–1824, 2016.

[23] J. Wang, L. Ma, and Y. Wang, "Hopf bifurcation control for the main drive delay system of rolling mill," *Advances in Difference Equations*, vol. 2020, p. 211, 2020.

[24] X. He, C. Li, T. Huang et al., "Codimension two bifurcation in a simple delayed neuron model," *Neural Computing and Applications*, vol. 23, no. 7-8, pp. 2295–2300, 2013.

[25] X. Peng, C. Li, and Y. Shu, "Bogdanov-Takens bifurcation in a single inertial neuron model with delay," *Neurocomputing*, vol. 89, pp. 193–201, 2012.

[26] C. Zhang and B. Zheng, "Explicit formulas for computing the normal form of Bogdanov-Takens bifurcation in delay differential equations," *Nonlinear Dynamics*, vol. 89, no. 2, pp. 1187–1194, 2017.

[27] J. Guckenheimer and P. Holmes, *Nonlinear Oscillations, Dynamical Systems, and Bifurcations of Vector Fields*, Springer, Berlin, Germany, 1983.

[28] Y. Li, Z. Wei, W. Zhang et al., "Bogdanov-Takens singularity in the Hindmarsh-Rose neuron with time delay," *Applied Mathematics and Computation*, vol. 354, pp. 180–188, 2019.

[29] Y. Perc and M. Huang, "Homoclinic orbits and Hopf bifurcations in delay differential systems with T-B singularity," *Journal of Differential Equations*, vol. 244, no. 3, pp. 582–598, 2008.

[30] S. N. Chow, C. Li, and D. Wang, *Normal Forms and Bifurcation of Planar Vector Fields*, Cambridge University Press, Cambridge, UK, 1994.

[31] J. Guckenheimer and P. Holmes, *Nonlinear Oscillations, Dynamical Systems, and Bifurcations of Vector Fields*, Springer, New York, NY, USA, 1983.

[32] J. Wang, X. Liu, and J. Liang, "Bogdanov-Takens bifurcation in an oscillator with positive damping and multiple delays," *Nonlinear Dynamics*, vol. 87, no. 1, pp. 255–269, 2017.

[33] T. Faria and L. T. Magalhaes, "Normal forms for retarded functional differential equations and applications to Bogdanov-Takens singularity," *Journal of Differential Equations*, vol. 122, no. 2, pp. 201–224, 1995.

Hindawi
Complexity
Volume 2020, Article ID 2414927, 9 pages
https://doi.org/10.1155/2020/2414927

Research Article

A New Supply Chain System and Its Impulsive Synchronization

Yang Peng,[1] Jiang Wu,[1] Shiping Wen,[2] Yuming Feng,[3] Zhengwen Tu,[3] and Limin Zou[3]

[1]*School of Statistics, Southwestern University of Finance and Economics, Chengdu 611130, China*
[2]*Centre for Artificial Intelligence, University of Technology Sydney, Ultimo, NSW 2007, Australia*
[3]*Key Laboratory of Intelligent Information Processing and Control, Chongqing Three Gorges University, Chongqing 404100, China*

Correspondence should be addressed to Yang Peng; peng_yang2011@163.com

Received 23 July 2020; Revised 10 September 2020; Accepted 17 September 2020; Published 13 October 2020

Academic Editor: Quanxin Zhu

The purpose of this paper is to discuss modelling and synchronization of nonlinear supply chain system. Firstly, we present a new supply chain system which is sensitive to various uncertainties along with exogenous disturbances. Synchronization is an important method to reduce the negative impact of uncertainties and disturbances on the supply chain. Since impulsive control can reduce control cost and the amount of transmitted information drastically, we discuss impulsive synchronization behavior of two supply chain systems with the same structure. Finally, simulation experiments are given to show the effectiveness of our analytical results.

1. Introduction

Supply chain globalization is conducive to increasing the competitiveness of enterprises, but it also makes the supply chain face various uncertainties more frequently, such as demand uncertainty, supply uncertainty, and operational uncertainty. These uncertainties lead to the supply chain system showing complex dynamic characteristics, such as bullwhip effect [1, 2].

In recent years, academia and industry are actively studying the complexity of the supply chain system. For example, Anne et al. [3] presented a three-echelon supply chain model which can be stated as follows:

$$\begin{cases} \dot{x}_1 = mx_2 - (n+1)x_1, \\ \dot{x}_2 = x_1(r - x_3) - x_2, \\ \dot{x}_3 = x_1x_2 + (b-1)x_3, \end{cases} \tag{1}$$

where x_1 is the quantity demanded by retailer in current period, x_2 is the quantity distributors can supply in current period, and x_3 is the quantity produced in the current period depend on the order, m is the coefficient of distributor delivery, n is rate of customer demand satisfaction at retailer, r is production threshold, and b is manufacturer's safety stock factor. Supply chain system (1) has complex dynamic behavior. For example, if we choose $m = 10, n = 3, r = 18$, and $b = 3/7$, then system (1) is chaotic and Figure 1 shows the chaotic phenomenon of system (1) with the initial condition $(x_1, x_2, x_3)^T = (10, 10, 10)^T$.

Chaotic supply chain system (1) is very sensitive to disturbances. When a node in the supply chain changes, then the change will spread to the other two nodes quickly and cause the supply chain to deviate from the original state. For example, suppose that $m = 10, n = 3, r = 18$, and $b = 3/7$, if the state variables $X(t_0) = (10, 10, 10)$ becomes $Y(t_0) = (10.1, 10, 10)$ at some point, that is to say, the retailer's demand will increase by 0.1 unit, then the operation state of the supply chain will be changed, as shown in Figure 2.

From Figure 2, it can be seen that the small change of retailer's demand has little impact on the operation state of the supply chain at the beginning, but with the passage of time, the operation state of the supply chain will change greatly, resulting in the operation of the supply chain deviating from the preset state. Therefore, the general idea is to restore the deviated operation state to the expected track through appropriate control strategies, so as to reduce the impact of uncertainty factors.

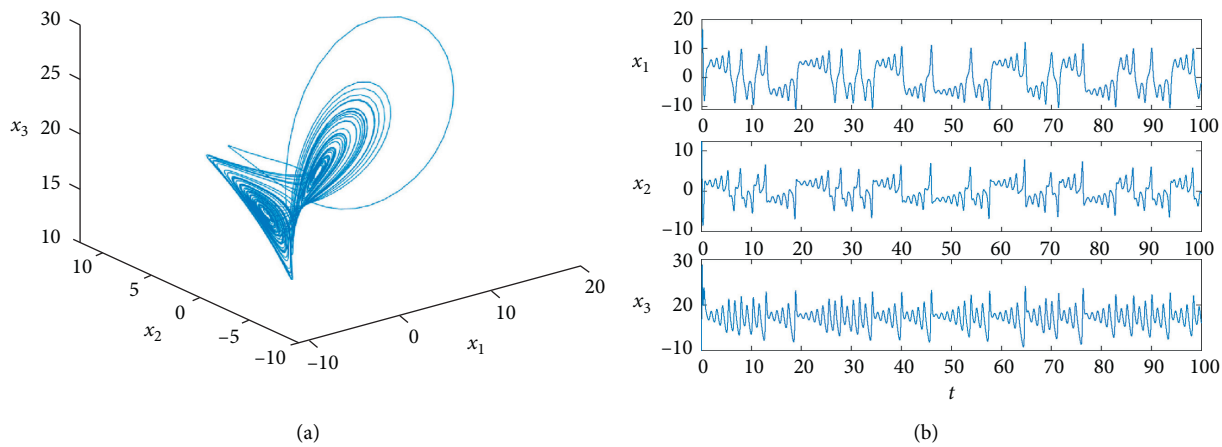

Figure 1: The chaotic phenomenon of system (1) with the initial condition $(x_1, x_2, x_3)^T = (10, 10, 10)^T$. (a) 3D phase portraits. (b) Time series of x_i, $i = 1, 2, 3$.

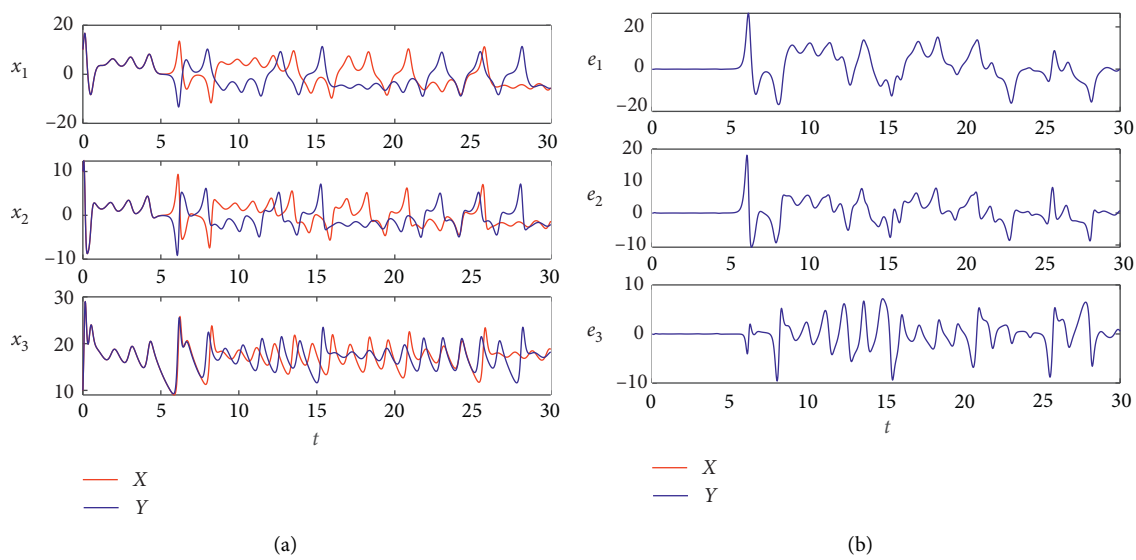

Figure 2: The influence of uncertain factors on system (1). (a) Time series with different initial values. (b) Errors of each node.

Synchronization is an important method to reduce the negative impacts of uncertainties and disturbances on the supply chain. Göksu et al. [4] discussed the synchronization of two identical chaotic supply chain systems, and active and linear feedback controllers are applied for the system. Kocamaz et al. [5] presented the control of chaotic supply chain with Artificial Neural Network-based controllers and the synchronization of two identical chaotic supply chains. Tirandaz [6, 7] discussed adaptive modified projective synchronization and adaptive integral sliding mode control synchronization of supply chain system (1), respectively. Geng and Xiao [8] discussed the outer synchronization and parameter identification approach to the resilient recovery of supply network with uncertainty. Xu et al. [9] designed the adaptive super-twisting sliding mode control algorithm for chaos suppression and synchronization of the supply chain system.

Considering the fact that the demand of a product does not increase monotonically with the increase of inventory, Mondal [10] proposed a new supply chain model as follows:

$$\begin{cases} \dot{x}_1 = \dfrac{mx_2}{1 + ax_2} - (n+1)x_1, \\ \dot{x}_2 = x_1(r - x_3) - \dfrac{px_2}{1 + ax_2}, \\ \dot{x}_3 = x_1x_2 + (b-1)x_3, \end{cases} \tag{2}$$

where a determines the saturation rate of demand with the increase of inventory and p denotes the effect of demand variation of the inventory. The author also discussed synchronization behavior of two coupled identical supply chain models under both unidirectional and bidirectional coupling.

However, system (2) has a singularity when $x_2 = -(1/a)$ and the second equation is unreasonable according to the analysis of Anne et al. [3]. Therefore, in this paper, following the idea of Mondal, in which demand has a saturation level and it does not increase monotonically with the inventory, we will propose a new supply chain system which does not have

singularity. In addition, considering the feasibility of the control strategy, we use the impulsive control method to realize the synchronization of the new system. For more information on impulsive control method and its advantages, the reader can refer to [11–22] and the references therein.

2. A New Supply Chain System and Its Impulsive Synchronization

Combining system (1) with (2), we propose a new supply chain system as follows:

$$\begin{cases} \dot{x}_1 = \dfrac{mx_2}{\sqrt{1+a^2x_2^2}} - (n+1)x_1, \\ \dot{x}_2 = x_1(r - x_3) - x_2, \\ \dot{x}_3 = x_1x_2 + (b-1)x_3. \end{cases} \tag{3}$$

Putting $a = 0$ in system (3), we obtain system (1). The function $f(x_2) = (x_2/(\sqrt{1+a^2x_2^2}))$ is used to describe the saturation degree of retailer's demand with respect to supply. It is easy to see that f is odd function and $\lim_{x_2 \longrightarrow +\infty} f(x_2) = (1/a)$. The graph of function f is shown in Figure 3.

By decomposing the linear and nonlinear parts of system in (3), we can rewrite it as follows:

$$\dot{X} = \mathrm{AX} + \phi(X), \tag{4}$$

where

$$A = \begin{pmatrix} -n-1 & 0 & 0 \\ r & -1 & 0 \\ 0 & 0 & b-1 \end{pmatrix}, \quad X = \begin{pmatrix} x_1 \\ x_2 \\ x_3 \end{pmatrix}, \quad \phi(X) = \begin{pmatrix} \dfrac{mx_2}{\sqrt{1+a^2x_2^2}} \\ -x_1x_3 \\ x_1x_2 \end{pmatrix}. \tag{5}$$

If we choose $m = 10, n = 3, r = 18, b = 3/7$, and $a = 0.3$, then system (3) is chaotic and Figure 4 shows the chaotic phenomenon of system (3) with the initial condition $(x_1, x_2, x_3)^T = (10, 10, 10)^T$.

Next, we investigate impulsive synchronization of two supply chain systems with the same structure. System (3) is the driving system and the driven system is defined as

$$\begin{cases} \dfrac{\mathrm{d}Y}{\mathrm{d}t} = \mathrm{AY} + \phi(Y), & t \neq \tau_k, \\ \Delta Y = \mathrm{Be}, & t = \tau_k,\ k = 1, 2, \ldots, \end{cases} \tag{6}$$

where $Y = (y_1, y_2, y_3)^T$ and B is impulsive control gain matrix. The symbol e denotes system errors and

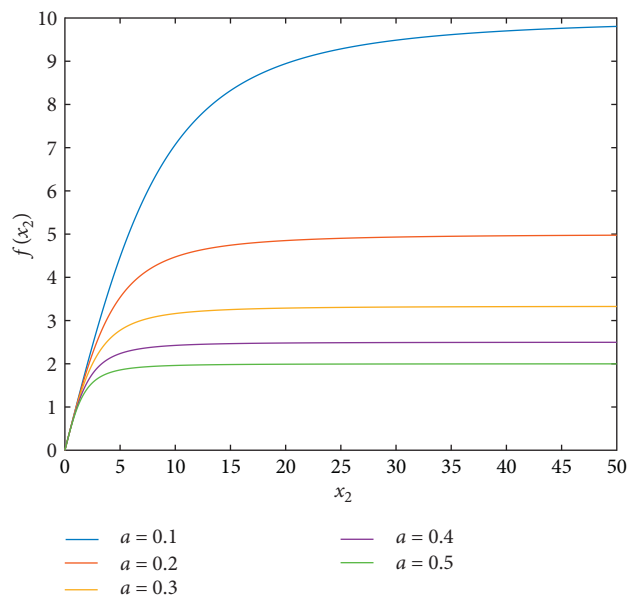

Figure 3: The graph of function f for different values of a.

$e = (e_1, e_2, e_3)^T = (y_1 - x_1, y_2 - x_2, y_3 - x_3)^T$. There will be a jump in system (6) when $t = \tau_k$ and $t_0 = \tau_0 < \tau_1 < \tau_2 < , \ldots, \lim_{k \longrightarrow \infty} \tau_k = \infty$. Through, system (6) minus system (3), we obtain

$$\begin{cases} \dfrac{\mathrm{d}e}{\mathrm{d}t} = \mathrm{Ae} + \psi(X, Y), & t \neq \tau_k, \\ \Delta e = \mathrm{Be}, & t = \tau_k,\ k = 1, 2, \ldots, \end{cases} \tag{7}$$

where $\psi(X, Y) = \phi(Y) - \phi(X)$.

Due to the boundedness of the chaotic system (3), we suppose that $|x_i| \leq M$, $i = 1, 2, 3$. In the following theorem, we present a sufficient condition for the stability of error system (7).

Theorem 1. *Let α and λ be the largest eigenvalues of $A^T + A$ and $(I + B^T)(I + B)$, respectively. If*

$$\log\lambda + (\alpha + 2M + 3m)(\tau_k - \tau_{k-1}) < 0 \tag{8}$$

holds for all $k = 1, 2, \ldots$, then the origin of impulsive synchronization error system (7) is asymptotically stable.

Proof. Let

$$V(e(t)) = e^T(t)e(t). \tag{9}$$

For $t \in [t_0, \tau_1)$, we have

$$\begin{aligned} \frac{\mathrm{d}V(e(t))}{\mathrm{d}t} &= (Ae + \psi(X, Y))^T e + e^T(Ae + \psi(X, Y)) \\ &= e^T A^T e + \psi(X, Y)^T e + e^T Ae + e^T \psi(X, Y) \\ &= e^T\left(A^T + A\right)e + 2e^T\psi(X, Y). \end{aligned} \tag{10}$$

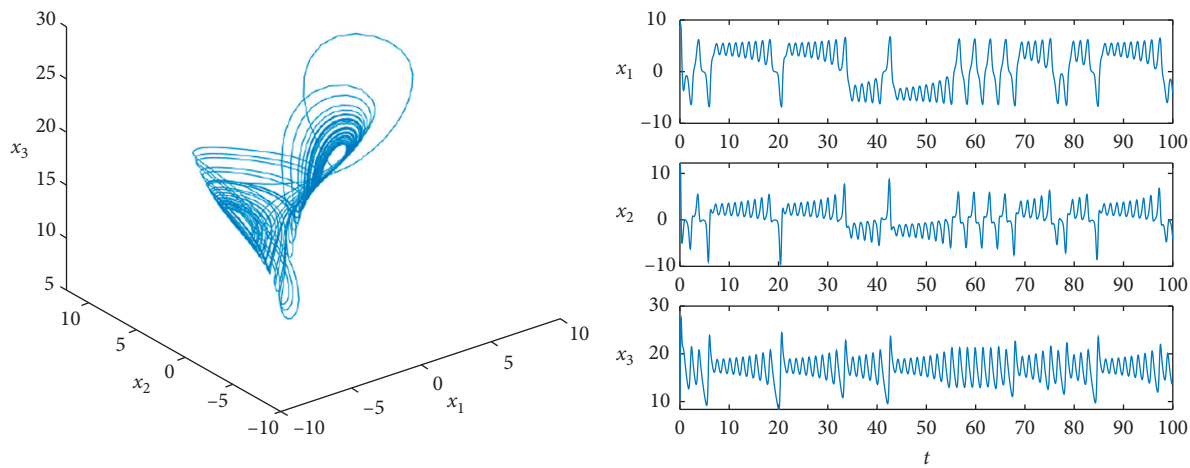

(a) (b)

FIGURE 4: The chaotic phenomenon of system (3) with the initial condition $(x_1, x_2, x_3)^T = (10, 10, 10)^T$. (a) 3D phase portraits. (b) Time series of x_i, $i = 1, 2, 3$.

By the arithmetic-geometric mean inequality, we have

$$
\begin{aligned}
e^T\psi(X,Y) &= (y_1 - x_1, y_2 - x_2, y_3 - x_3)\left(\frac{my_2}{\sqrt{1+a^2y_2^2}} - \frac{mx_2}{\sqrt{1+a^2x_2^2}}, -y_1y_3 + x_1x_3, y_1y_2 - x_1x_2\right)^T \\
&= e_1\left(\frac{my_2}{\sqrt{1+a^2y_2^2}} - \frac{mx_2}{\sqrt{1+a^2y_2^2}} + \frac{mx_2}{\sqrt{1+a^2y_2^2}} - \frac{mx_2}{\sqrt{1+a^2x_2^2}}\right) + x_1x_3y_2 + x_2y_1y_3 - y_3x_1x_2 - x_3y_1y_2 \\
&= e_1\left(\frac{me_2}{\sqrt{1+a^2y_2^2}} + mx_2\left(\frac{1}{\sqrt{1+a^2y_2^2}} - \frac{1}{\sqrt{1+a^2x_2^2}}\right)\right) + x_2e_1e_3 - x_3e_1e_2 \\
&= e_1\left(\frac{me_2}{\sqrt{1+a^2y_2^2}} + mx_2\left(\frac{a^2(x_2-y_2)(x_2+y_2)}{\sqrt{1+a^2y_2^2}\sqrt{1+a^2x_2^2}\left(\sqrt{1+a^2x_2^2}+\sqrt{1+a^2y_2^2}\right)}\right)\right) + x_2e_1e_3 - x_3e_1e_2 \\
&= \frac{me_1e_2}{\sqrt{1+a^2y_2^2}}\left(1 - a^2\left(\frac{x_2}{\sqrt{1+a^2x_2^2}}\,\frac{x_2+y_2}{\sqrt{1+a^2x_2^2}+\sqrt{1+a^2y_2^2}}\right)\right) + x_2e_1e_3 - x_3e_1e_2 \\
&\le \frac{me_1e_2}{\sqrt{1+a^2y_2^2}}\left(1 + a^2\left(\left|\frac{x_2}{\sqrt{1+a^2x_2^2}}\right|\left|\frac{x_2+y_2}{\sqrt{1+a^2x_2^2}+\sqrt{1+a^2y_2^2}}\right|\right)\right) + |x_2e_1e_3| + |x_3e_1e_2| \\
&\le \frac{me_1e_2}{\sqrt{1+a^2y_2^2}}\left(1 + a^2\left(\left|\frac{1}{a}\right|\left|\frac{2}{a}\right|\right)\right) + M\left(|e_1e_3| + |e_1e_2|\right) \\
&\le \frac{3me_1e_2}{\sqrt{1+a^2y_2^2}} + M\left(|e_1e_3| + |e_1e_2|\right) \\
&\le \frac{3}{2}m\left(e_1^2 + e_2^2\right) + M\left(|e_1e_3| + |e_1e_2|\right) \\
&\le \frac{3m + 2M}{2}e^Te.
\end{aligned}
\tag{11}
$$

It follows from (10) and (11) that

$$\frac{\mathrm{d}V(e(t))}{\mathrm{d}t} \leq (\alpha + 2M + 3m)V(e(t)). \tag{12}$$

Let

$$g(t) = \frac{\mathrm{d}V(e(t))}{\mathrm{d}t} - (\alpha + 2M + 3m)V(e(t)). \tag{13}$$

Then, we obtain

$$V(e(t)) = e^{(\alpha+2M+3m)(t-t_0)}\left(\int_{t_0}^{t} e^{-(\alpha+2M+3m)\tau} g(\tau)d\tau + V(e(t_0))\right). \tag{14}$$

Since $g(t) \leq 0$, we have

$$V(e(t)) \leq V(e(t_0))e^{(\alpha+2M+3m)(t-t_0)}, \tag{15}$$

for $t \in [t_0, \tau_1)$.

When $t = \tau_1$, we have

$$\begin{aligned} V(e(\tau_1)) &= ((I+B)e(\tau_1^-))^T (I+B)e(\tau_1^-) \\ &= e^T(\tau_1^-)\left(I + B^T\right)(I+B)e(\tau_1^-) \\ &\leq \lambda e^T(\tau_1^-)e(\tau_1^-) \\ &= \lambda V(e(\tau_1^-)). \end{aligned} \tag{16}$$

If $t \in [\tau_1, \tau_2)$, then repeating the process of deriving inequality (15), we obtain

$$V(e(t)) \leq V(e(\tau_1))e^{(\alpha+2M+3m)(t-\tau_1)}. \tag{17}$$

It follows from (16) and (17) that

$$V(e(t)) \leq \lambda V(e(\tau_1^-))e^{(\alpha+2M+3m)(t-\tau_1)}. \tag{18}$$

By inequality (18) and local order preserving of function limit, we obtain

$$V(e(\tau_1^-)) \leq V(e(t_0))e^{(\alpha+2M+3m)(\tau_1-t_0)}. \tag{19}$$

Combining with inequalities (18) and (19), we have

$$V(e(t)) \leq \lambda V(e(t_0))e^{(\alpha+2M+3m)(t-t_0)}, \tag{20}$$

for $t \in [\tau_1, \tau_2)$.

When $t = \tau_2$, by the same method which is used to deduce inequality (16), we obtain

$$V(e(\tau_2)) \leq \lambda V(e(\tau_2^-)), \tag{21}$$

and so

$$\begin{aligned} V(e(t)) &\leq V(e(\tau_2))e^{(\alpha+2M+3m)(t-\tau_2)} \\ &\leq \lambda V(e(\tau_2^-))e^{(\alpha+2M+3m)(t-\tau_2)} \\ &\leq \lambda\left(\lambda V(e(t_0))e^{(\alpha+2M+3m)(\tau_2-t_0)}\right)e^{(\alpha+2M+3m)(t-\tau_2)} \\ &= \lambda^2 V(e(t_0))e^{(\alpha+2M+3m)(t-t_0)}, \end{aligned} \tag{22}$$

for $t \in [\tau_2, \tau_3)$.

Therefore, by the repeatability of the proof process and inequalities (15), (20), and (22), we know that

$$\begin{aligned} V(e(t)) &\leq \lambda^{k-1} V(e(t_0))e^{(\alpha+2M+3m)(t-t_0)} \\ &= V(e(t_0))e^{(\alpha+2M+3m)(t-t_0)}e^{(k-1)\log\lambda} \\ &= V(e(t_0))e^{\log\lambda+(\alpha+2M+3m)(\tau_1-t_0)}e^{\log\lambda+(\alpha+2M+3m)(\tau_2-\tau_1)}\cdots e^{(\alpha+2M+3m)(t-\tau_{k-1})} \\ &= \lambda^{-1}V(e(t_0))e^{\log\lambda+(\alpha+2M+3m)(\tau_1-t_0)}e^{\log\lambda+(\alpha+2M+3m)(\tau_2-\tau_1)}\cdots e^{\log\lambda+(\alpha+2M+3m)(t-\tau_{k-1})}, \end{aligned} \tag{23}$$

for $t \in [\tau_{k-1}, \tau_k)$.

So, if $\alpha + 2M + 3m < 0$, then

$$V(e(t)) \leq V(e(t_0))e^{\sum_{i=1}^{k-1}(\log\lambda+(\alpha+2M+3m)(\tau_i-\tau_{i-1}))}. \tag{24}$$

On the other hand, if $\alpha + 2M + 3m \geq 0$, then

$$V(e(t)) \leq \lambda^{-1}V(e(t_0))e^{\sum_{i=1}^{k}(\log\lambda+(\alpha+2M+3m)(\tau_i-\tau_{i-1}))}. \tag{25}$$

Hence, if $\log\lambda + (\alpha + 2M + 3m)(\tau_k - \tau_{k-1}) < 0$, $k = 1, 2, \ldots$, then $V(e(t)) \longrightarrow 0$ when $k \longrightarrow +\infty$, that is, $t \longrightarrow +\infty$. This completes the proof.

In generally, the intensity of each impulsive may not be the same, in view of this, we have the following result. □

Theorem 2. *Let α and λ_k be the largest eigenvalues of $A^T + A$ and $(I + B_k^T)(I + B_k)$, respectively. If*

$$\log\lambda_k + (\alpha + 2M + 3m)(\tau_k - \tau_{k-1}) < 0, \tag{26}$$

holds for all $k = 1, 2, \ldots,$ then the origin of impulsive synchronization error system (7) is asymptotically stable. The proof of this result is the same as Theorem 1.

Recently, Hu et al. considered the effect of noise disturbances and provided some new methods [23–26]. Now, following the ideas of these authors, we consider system (3) with parameter uncertainty and state variables perturbation. The corresponding system can be described as follows:

$$\frac{\mathrm{d}X}{\mathrm{d}t} = (A + \Delta A)X + \phi(X) + f(X), \tag{27}$$

where $f(X) = (a\sin(x_1), b\cos(x_2), c\sin(x_3))^T$ and

$$\Delta A = \begin{pmatrix} \delta n & 0 & 0 \\ \delta r & 0 & 0 \\ 0 & 0 & \delta b \end{pmatrix}. \tag{28}$$

Similarly, we can obtain the error system as follows:

$$\begin{cases} \dfrac{\mathrm{d}e}{\mathrm{d}t} = (A + \Delta A)e + \psi(X,Y) + g(X,Y), & t \neq \tau_k, \\ \Delta e = Be, & t = \tau_k,\ k = 1, 2, \ldots, \end{cases} \tag{29}$$

where $g(X,Y) = f(Y) - f(X)$.

Theorem 3. *Let α and λ be the largest eigenvalues of $A^T + A$ and $(I + B^T)(I + B)$, respectively. Let $\gamma = \max\{\delta_1, \delta_2\}$ with $\delta_1 = 2\delta_b, \delta_2 = \delta_n + \sqrt{\delta_n^2 + \delta_r^2}$, and $\rho = 2\max\{|a|, |b|, |c|\}$. If*

$$\ln\lambda + (\alpha + \gamma + 2M + 3m + \rho)(\tau_i - \tau_{i-1}) < 0 \tag{30}$$

holds for all $k = 1, 2, \ldots,$, then the origin of impulsive synchronization error system (29) is asymptotically stable.

Proof. Note that

$$\Delta A + (\Delta A)^T = \begin{pmatrix} 2\delta_n & \delta_r & 0 \\ \delta_r & 0 & 0 \\ 0 & 0 & 2\delta_b \end{pmatrix}. \tag{31}$$

Then, we have

$$\begin{aligned} \left|xI - \Delta A + (\Delta A)^T\right| &= \begin{vmatrix} x - 2\delta_n & \delta_r & 0 \\ \delta_r & x & 0 \\ 0 & 0 & x - 2\delta_b \end{vmatrix} \\ &= (x - 2\delta_b)\left[x(x - 2\delta_n) - \delta_r^2\right] \\ &= (x - 2\delta_b)\left(x^2 - 2\delta_n x - \delta_r^2\right). \end{aligned} \tag{32}$$

So, the eigenvalues of $\Delta A + (\Delta A)^T$ are

$$\begin{aligned} \delta_1 &= 2\delta_b, \\ \delta_{2,3} &= \delta_n \pm \sqrt{\delta_n^2 + \delta_r^2}. \end{aligned} \tag{33}$$

Meanwhile, simple calculations show that

$$\begin{aligned} e^T g(X,Y) &= \left(ae_1(\sin(Y_1) - \sin(X_1)) + be_2(\cos(Y_2) - \cos(X_2)) + ce_3(\sin(Y_3) - \sin(X_3))\right) \\ &\leq \left(|a|e_1(Y_1 - X_1) + |b|e_2(Y_2 - X_2) + |c|e_3(Y_3 - X_3)\right) \\ &= \left(|a|e_1^2 + |b|e_2^2 + |c|e_3^2\right) \\ &\leq \max\{|a|, |b|, |c|\}e^T e. \end{aligned} \tag{34}$$

Let us construct the following Lyapunov function:

$$V(e(t)) = e^T e. \tag{35}$$

For $t \in [t_0, \tau_1)$, we have

$$\begin{aligned} \frac{\mathrm{d}V(e(t))}{\mathrm{d}t} &= \left((A + \Delta A)e + \psi(X,Y) + g(X,Y)^T\right)e + e^T\left((A + \Delta A)e + \psi(X,Y) + g(X,Y)\right)e \\ &= e^T\left(A + A^T + \Delta A + \Delta A^T\right)e + 2e^T\psi(X,Y) + 2e^T g(X,Y). \end{aligned} \tag{36}$$

It follows from (11) and (34) that

$$\begin{aligned} \frac{\mathrm{d}V(e(t))}{\mathrm{d}t} &\leq e^T\left(A + A^T + \Delta A + \Delta A^T\right)e + (2M + 3m)e^T e + \rho e^T e \\ &\leq (\alpha + \gamma)e^T e + (2M + 3m)e^T e + \rho e^T e \\ &= (\alpha + \gamma + 2M + 3m + \rho). \end{aligned} \tag{37}$$

The rest of proof is the same as Theorem 1. This completes the proof. □

3. Simulation Experiments

In this section, we will use some numerical simulation experiments to illustrate how to use the strategies presented in Section 2 to eliminate or suppress the negative impacts of uncertain factors on the supply chain system.

Experiment 1. This example simulates the impact of the change of retailer demand on the system operation in supply chain system (3) and restores the operation state of supply chain to the expected track through impulsive control strategy. As mentioned above, if we choose $m = 10, n = 3, r = 18, b = 3/7$, and $a = 0.3$, then system (3) is chaotic.

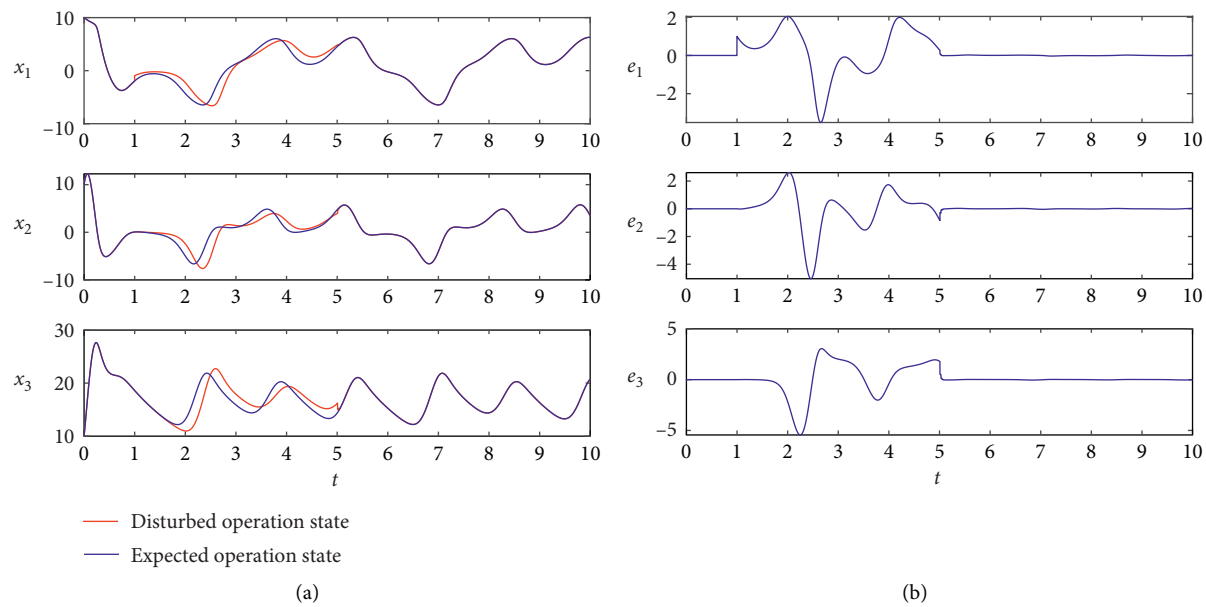

FIGURE 5: Impulsive synchronization of supply chain system (3). (a) Time series of x_i, $i = 1, 2, 3$. (b) Errors of each node.

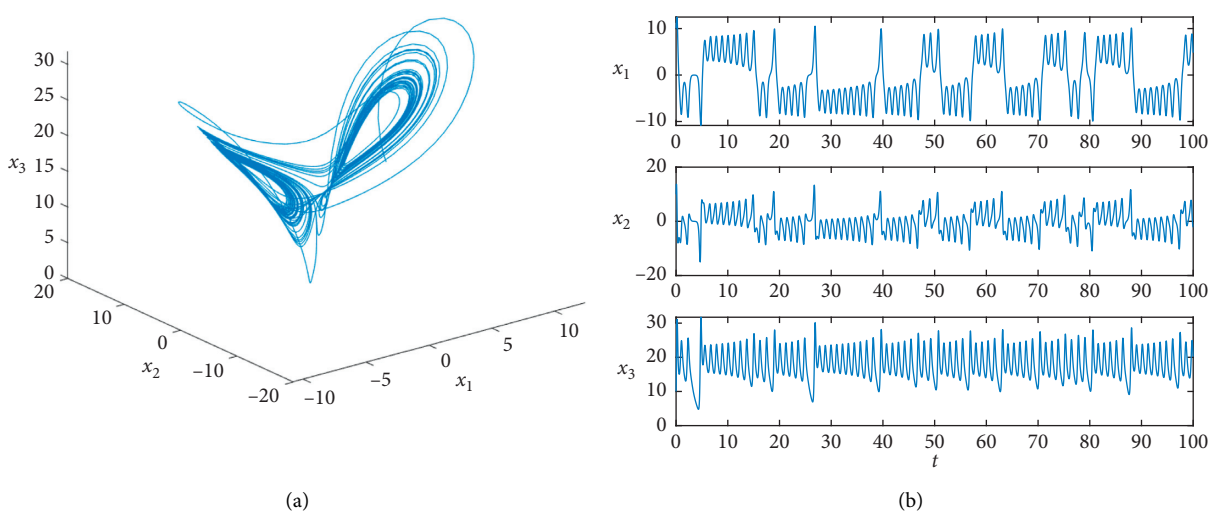

FIGURE 6: The chaotic phenomenon of system (27) with the initial condition $X(t_0) = (10, 10, 10)$. (a) 3D phase portraits. (b) Time series of x_i, $i = 1, 2, 3$.

Small calculations show that $\alpha = 13.2483$ and $M = 27.5293$. When $t = 1$, the retailer's demand is reduced by one unit. We find that the operation of the supply chain is seriously deviated from the expected state soon afterwards. We hope that the supply chain system can return to its original state by itself after a period. Unfortunately, the two tracks have not come together. We start to implement impulsive control when $t = 5$ and assume that the intensity of each regulation is the same. According to Theorem 1, by simple calculations, we know that if the intensity and time interval of impulsive control satisfy the following inequality

$$\log \lambda + 98.3069 (\tau_k - \tau_{k-1}) < 0, \tag{38}$$

then, the disturbed operation state will return to the expected orbit after appropriate impulsive control. In order to satisfy inequality (38), we choose impulsive control gain matrix $B = -0.7I$, that is, the value of each node in the supply chain Y_{i+1} becomes $0.7X_i + 0.3Y_i$. So, the time interval of regulation should meet $\tau_k - \tau_{k-1} < 0.0245$. Suppose that $\tau_k - \tau_{k-1} = 0.0200$, which means that the time interval of impulsive regulation is 20 unit time (the unit time is taken as 0.001 in the experiment). The numerical simulation results are shown in Figure 5.

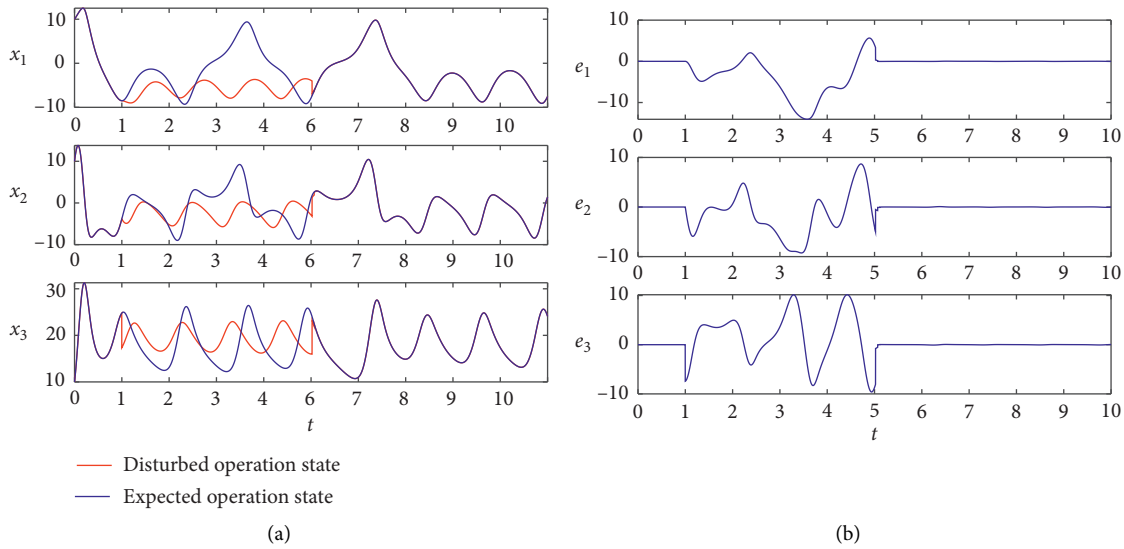

Figure 7: Impulsive synchronization of supply chain system (27). (a) Time series of x_i, $i = 1, 2, 3$. (b) Errors of each node.

Experiment 2. In this example, we simulate the impact of the change of the manufacturer's output on the system operation in the supply chain system (27), and through impulsive control strategy, the supply chain operation state is restored to the expected track. Let $m = 5, n = 1, r = 20, b = 0.3, a = 0.1, \delta_m = \delta_n = 0.1, \delta_r = 0.2$, and $\delta_b = -0.1$ and $f(t, X) = (0.01\sin(x_1), 0.02\cos(x_2), 0.03\sin(x_3))^T$ be input disturbance. Suppose that $X(t_0) = (10, 10, 10)$, the phase diagram of the system and state trajectory of each node are shown in Figure 6.

Small calculations show that $\alpha = 17.0250, M = 31.7329, \gamma = 0.3236$, and $\rho = 0.06$. When $t = 1$, the produced quantity of the manufacturer is reduced, say, 0.7 times of the original for some reason. We find that the operation of the supply chain is seriously deviated from the expected state soon afterwards. We start to implement impulsive control when $t = 15$ and assume that the intensity of each regulation is the same. According to Theorem 3, by simple calculations we know that if the intensity and time interval of impulsive control satisfy the following inequality

$$\log\lambda + 96.1744(\tau_k - \tau_{k-1}) < 0, \tag{39}$$

then, the disturbed operation state will return to the expected orbit after appropriate impulsive control. In order to satisfy inequality (39), we choose impulsive control gain matrix $B = -0.9I$, that is, the value of each node in the supply chain Y_{i+1} becomes $0.9X_i + 0.1Y_i$. So, the time interval of regulation should meet $\tau_k - \tau_{k-1} < 0.0479$ and suppose that $\tau_k - \tau_{k-1} = 0.0450$ which means that the time interval of impulsive regulation is 45 unit time (the unit time is taken as 0.001 in the experiment). The numerical simulation results are shown in Figure 7.

It can be seen from Figure 7 that the operation state of the system quickly returns to the expected orbit.

4. Conclusion

As pointed out in [3], in today's global marketplace, the supply chain is dynamic and unstable. This dynamic and unstable properties produce a variety of uncertainties in the supply chain, such as demand uncertainty, supply uncertainty, delivery uncertainty, and forecast uncertainty. These uncertainties make the upstream and downstream transmission of the supply chain complex and nonlinear. In this paper, we propose a new supply chain system which is more in line with the actual situation. As stated earlier, synchronization is an important way to avoid uncertainty in supply chains, and impulsive control is an effective method to realize synchronization. So, we also discuss impulsive synchronization of supply chain system and some impulsive synchronization strategies are obtained. These results may be useful to the management of the supply chain.

Data Availability

The Matlab code data used to support the findings of this study are available from the corresponding author upon request.

Conflicts of Interest

The authors declare that they have no conflicts of interest.

Authors' Contributions

All authors contributed equally to the writing of this paper. All authors read and approved the final version of this paper.

Acknowledgments

This research was supported by the Fundamental Research Funds for the Central Universities (Grant no. JBK2002011) and Science and Technology Research Program of

Chongqing Municipal Education Commission (Grant no. KJQN201800811).

References

[1] Q. Hu, "Bullwhip effect in a supply chain model with multiple delivery delays," *Operations Research Letters*, vol. 47, no. 1, pp. 36–40, 2019.

[2] E. Pastore, A. Alfieri, G. Zotteri, and J. E. Boylan, "The impact of demand parameter uncertainty on the bullwhip effect," *European Journal of Operational Research*, vol. 283, no. 1, pp. 94–107, 2020.

[3] K. R. Anne, J. C. Chedjou, and K. Kyamakya, "Bifurcation analysis and synchronisation issues in a three-echelon supply chain," *International Journal of Logistics Research and Applications*, vol. 12, no. 5, pp. 347–362, 2009.

[4] A. Göksu, U. E. Kocamaz, and Y. Uyaroğlu, "Synchronization and control of chaos in supply chain management," *Computers & Industrial Engineering*, vol. 86, pp. 107–115, 2015.

[5] U. E. Kocamaz, H. Taşkın, Y. Uyaroğlu, and A. Göksu, "Control and synchronization of chaotic supply chains using intelligent approaches," *Computers & Industrial Engineering*, vol. 102, pp. 476–487, 2016.

[6] H. Tirandaz, "On adaptive modified projective synchronization of a supply chain management system," *Pramana-Journal of Physics*, vol. 89, no. 6, p. 85, 2017.

[7] H. Tirandaz, "Adaptive integral sliding mode control method for synchronization of supply chain system," *WSEAS Transactions on Systems and Control*, vol. 13, pp. 54–62, 2018.

[8] L. Geng and R. Xiao, "Outer synchronization and parameter identification approach to the resilient recovery of supply network with uncertainty," *Physica A: Statistical Mechanics and Its Applications*, vol. 482, pp. 407–421, 2017.

[9] X. Xu, S.-D. Lee, H.-S. Kim, and S.-S. You, "Management and optimisation of chaotic supply chain system using adaptive sliding mode control algorithm," *International Journal of Production Research*, pp. 1–7, 2020, In press.

[10] S. Mondal, "A new supply chain model and its synchronization behaviour," *Chaos, Solitons & Fractals*, vol. 123, pp. 140–148, 2019.

[11] C. Li, X. Liao, and X. Zhang, "Impulsive synchronization of chaotic systems," *Chaos: An Interdisciplinary Journal of Nonlinear Science*, vol. 15, no. 2, Article ID 023104, 2005.

[12] X. Li and J. Wu, "Stability of nonlinear differential systems with state-dependent delayed impulses," *Automatica*, vol. 64, pp. 63–69, 2016.

[13] X. Li and J. Cao, "An impulsive delay inequality involving unbounded time-varying delay and applications," *IEEE Transactions on Automatic Control*, vol. 62, no. 7, pp. 3618–3625, 2017.

[14] X. Li and S. Song, "Stabilization of delay systems: delay-dependent impulsive control," *IEEE Transactions on Automatic Control*, vol. 62, no. 1, pp. 406–411, 2017.

[15] Q. Song, H. Yan, Z. Zhao, and Y. Liu, "Global exponential stability of complex-valued neural networks with both time-varying delays and impulsive effects," *Neural Networks*, vol. 79, pp. 108–116, 2016.

[16] Q. Song, H. Yan, Z. Zhao, and Y. Liu, "Global exponential stability of impulsive complex-valued neural networks with both asynchronous time-varying and continuously distributed delays," *Neural Networks*, vol. 81, pp. 1–10, 2016.

[17] W. Xiong, D. Zhang, and J. Cao, "Impulsive synchronisation of singular hybrid coupled networks with time-varying nonlinear perturbation," *International Journal of Systems Science*, vol. 48, no. 2, pp. 417–424, 2017.

[18] F. Yao, J. Cao, P. Cheng, and L. Qiu, "Generalized average dwell time approach to stability and input-to-state stability of hybrid impulsive stochastic differential systems," *Nonlinear Analysis: Hybrid Systems*, vol. 22, pp. 147–160, 2016.

[19] X. Yang and J. Cao, "Hybrid adaptive and impulsive synchronization of uncertain complex networks with delays and general uncertain perturbations," *Applied Mathematics and Computation*, vol. 227, pp. 480–493, 2014.

[20] X. Yang, J. Cao, and Z. Yang, "Synchronization of coupled reaction-diffusion neural networks with time-varying delays via pinning-impulsive controller," *SIAM Journal on Control and Optimization*, vol. 51, no. 5, pp. 3486–3510, 2013.

[21] X. Yang, J. Lam, D. W. C. Ho, and Z. Feng, "Fixed-time synchronization of complex networks with impulsive effects via nonchattering control," *IEEE Transactions on Automatic Control*, vol. 62, no. 11, pp. 5511–5521, 2017.

[22] X. Yang, D. Peng, X. Lv, and X. Li, "Recent progress in impulsive control systems," *Mathematics and Computers in Simulation*, vol. 155, pp. 244–268, 2019.

[23] W. Hu, H. R. Q. Zhu, and H. R. Karimi, "Some improved Razumikhin stability criteria for impulsive stochastic delay differential systems," *IEEE Transactions on Automatic Control*, vol. 64, no. 12, pp. 5207–5213, 2019.

[24] W. Hu and Q. Zhu, "Stability analysis of impulsive stochastic delayed differential systems with unbounded delays," *Systems & Control Letters*, vol. 136, Article ID 104606, 2020.

[25] W. Hu, H. R. Q. Zhu, and H. R. Karimi, "On the *p*th moment integral input-to-state stability and input-to-state stability criteria for impulsive stochastic functional differential equations," *International Journal of Robust and Nonlinear Control*, vol. 29, no. 16, pp. 5609–5620, 2019.

[26] Q. Zhu, "*p*th moment exponential stability of impulsive stochastic functional differential equations with Markovian switching," *Journal of the Franklin Institute*, vol. 351, no. 7, pp. 3965–3986, 2014.

Hindawi
Complexity
Volume 2020, Article ID 8316969, 10 pages
https://doi.org/10.1155/2020/8316969

Research Article

Rail Fastener Positioning Based on Double Template Matching

Yijin Qiu, Xingjie Chen, and Zhaomin Lv

School of Urban Railway Transportation, Shanghai University of Engineering Science, Shanghai 201620, China

Correspondence should be addressed to Xingjie Chen; xj_chen975@163.com

Received 6 July 2020; Revised 3 September 2020; Accepted 22 September 2020; Published 6 October 2020

Academic Editor: Hamid Reza Karimi

For global template matching (GTM), which is commonly used in the positioning of rail fasteners, only the fastener template is used to search the global image in both two dimensions, which will result in errors in two dimensions, and the lower positioning accuracy will be caused. A positioning method for rail fasteners based on double template matching (DTM) is proposed in this paper, in which the double template contains the rail template and the fastener template. First, the rail template is used to scan the original image in horizontal dimension, and the squared Euclidean distance (SED) is used to obtain the rail positioning in the original image. Combining with the prior knowledge of the fastener template image, the image composed of the rail and the fastener can be obtained, which is called the Rail Area Map (RAM) in this paper. Then, after preprocessing the RAM and the fastener template image, the fastener template image is used to scan the RAM in vertical dimension, and the normalized correlation coefficient (NCC) is used to calculate the similarity between the template and the subgraph of the RAM to achieve precise positioning of the fastener. The proposed DTM method adopts a positioning strategy from coarse to fine, and two templates are used to complete different positioning tasks in their own dimension, respectively. Due to the rail can be precise positioned in horizontal dimension, the error of the fastener positioning in the horizontal dimension can be avoided, and thus, the positioning accuracy can be improved. Experiments on the on-site line fastener images prove that the proposed method can effectively achieve the precise positioning of fasteners.

1. Introduction

As one of the most important modern transportation modes, rail transit has been greatly developed all over the world, especially in China, and the total mileage of rail lines has reached the world's first, besides rail fasteners play a vital role in the safety of trains. According to the research, many train derailment events are caused by the lack of rail fasteners; so, it is necessary to frequently detect rail fasteners [1]. With the rapid growth of China's railway operating mileage, the problems of high cost, low efficiency, and various safety hazards caused by ordinary manual inspections [2–4] have been unable to meet the needs of frequent inspections of the railway network. Therefore, the realization of automatic detection of railway fasteners [5–7] has become particularly important.

In recent years, artificial intelligence technology has made great progress [8–17], and many technologies based on computer vision have been applied into the detection task of railway fasteners [3, 18–21]. However, if the entire image obtained from the line is detected, not only will it fail to meet the real-time requirements of fastener detection due to the long recognition time but also the complex background in the entire railway line image will inevitably cause the detection accuracy decline. In order to improve the detection efficiency and reduce the interference of complex backgrounds, the precisely positioning of rail fasteners has become an indispensable prerequisite for fastener detection [22]. At present, positioning methods based on edge contours [23–25], positioning methods based on pixel statistics (PS) [26], positioning methods based on GTM [27], and improved methods based on the above methods [28] are the main methods which are used in fastener positioning.

Feng et al. [29] used the line segment detector (LSD) to determine the edge positions of rails and sleepers by detecting straight lines, and then, the fastener positioning can be realized based on the geometric relationship of sleepers, rails, and fasteners. In the literature [30], the edge

density feature is combined with the Random Sample Consensus (RANSAC) to locate the rail and sleeper areas, and then, the positioning of the fastener can also be realized based on the geometric position relationship of the rail, sleeper, and fastener. However, the above two methods are mainly applied to ballasted track, which have sleepers. For ballastless track, in which the sleepers are replaced by monolithic track bed and the fasteners are installed directly on the monolithic track bed, the above methods are not applicable. In addition, ballastless track is gradually replacing the traditional ballasted track.

Aiming at the positioning of ballastless track fasteners, Wei et al. [26] used PS to calculate the vertical gray value characteristics of the fastener and horizontal gray value characteristics of the rail, and then, the appropriate thresholds are selected to locate the rail and fastener backing plates, respectively; finally, the location of the fastener area is indirectly located according to the geometric positional relationship between the fastener backing plates and the rail. However, the pixel gray level between the fastener backing plates and the monolithic track bed is very similar, which makes it difficult to determine the threshold for dividing these two areas.

In response to the above problems, Yang et al. [31] extract the directional field as the feature descriptor of the fastener, and then, the positioning of the fastener can be achieved by GTM; Fan et al. [32] used the improved local binary pattern algorithm to obtain the fastener target feature and reconstruct the fastener template image and original image, and then, GTM is used to achieve fastener positioning. The GTM can be effectively applied to ballastless track. However, GTM uses a single fastener template to match in the whole image in two dimensions (vertical and horizontal dimensions), so there will be errors in two dimensions, and the fastener positioning accuracy will be reduced.

Therefore, a fastener positioning method based on DTM is proposed in this paper. According to prior knowledge, the entire image is vertically penetrated by the rail. Therefore, first, the rail template is used to scan the original image horizontally, and the SED is used to measure the similarity between the rail template and the subgraph of the original image to obtain the rail positioning in the original image. Due to the obvious difference between the gray level of rail and other regions, only one dimension (horizontal direction) is searched, which effectively ensures that there is no horizontal error in rail positioning. According to the width of the fastener template, the RAM including the rail and the fastener can be divided from the original track image, and it can ensure that the width of the RAM image is equal to the width of the fastener template image. Then, the image preprocessing can suppress noise and improve the contrast between the fastener area and other areas, which is beneficial to improve the accuracy of fastener positioning. Finally, the NCC [33–35] is used to measure the similarity between the fastener template image and the subgraph in the RAM to realize the accurate positioning of the fastener. The matching of one dimension on the RAM can avoid errors in the other dimension. Therefore, the proposed DTM can improve the accuracy of fastener positioning.

The main innovations of this article are as follows: (1) when the GTM is used to locate the rail fasteners, the only fastener template needs to be scanned and matched in two dimensions of the whole original image at the same time, which will cause errors in both two dimensions. In theory, the DTM method in this paper only has errors in the vertical direction, which improves the accuracy of fastener positioning. (2) Through the experiment of fastener positioning based on DTM, the accuracy of fastener positioning is improved, and the effectiveness of the method is verified.

The remainder of this paper is organized as follows. Section 2 introduces the theory of GTM. Section 3 describes the theory of the proposed DTM rail fastener positioning method. Section 4 introduces the experimental results of DTM theory, and the improvement of the accuracy of the DTM method compared to the GTM method is verified, besides the accuracy of the DTM method, and the existing common methods have been compared. Section 5 summarizes and prospects the full text.

2. Basic Introduction of GTM

The method of GTM is mainly to use the template image to perform the similarity calculations from left to right and top to bottom on the original image, and finally, a correlation coefficient matrix can be obtained: the parameter values in the coefficient matrix are used to compare the similarity between the template image and the subgraph of the original image. The principle is shown in Figure 1; the searched image is $S(W, H)$, where W is the width of the image, and H is the height of the image; the template is $T(N, M)$, where N is the width of the image, and M is the height of the image. The area covered by the template image in the searched image is called the subgraph S_{ij}, i and j are the coordinate positions of the subgraph's upper left corner in the searched graph, and the search range is $0 \le i < W - N$, $0 \le j < H - M$. By using the similarity calculation method, the similarity degree between the template and subgraph is calculated. When the similarity degree between the template graph and subgraph is the maximum, the corresponding subgraph S_{ij} is the matching target.

3. Fastener Positioning Based on DTM

A detailed description of the DTM fastener positioning method proposed in this paper will be provided in this section. The flow chart consists of two modules: template matching in horizontal direction for positioning rail and template matching in vertical direction for positioning fasteners. The comprehensive flow chart is shown in Figure 2, and the details are described in the following contents.

3.1. Rail Positioning. In order to reduce the amount of calculation, the grayscale processing is used to process the image [36]. Since the color image of the original image is three channels, the data are relatively large, and the calculation is time-consuming. The gray image will be changed from three channels to a single channel, and the data of single channel are relatively small, so it will be easier to

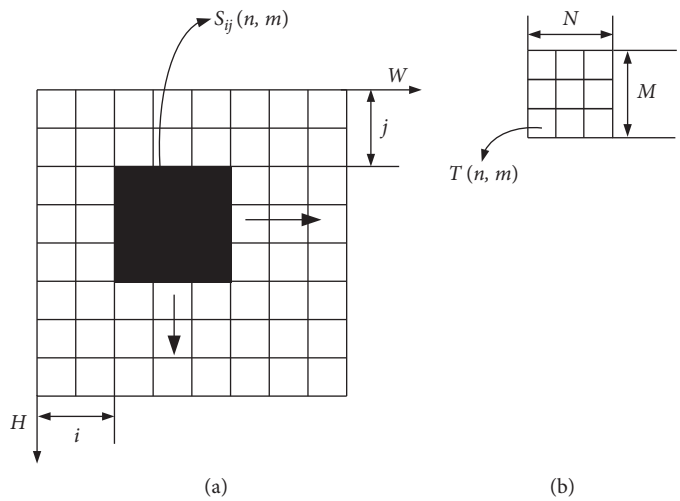

Figure 1: The principle of GTM. (a) Searched image S S (W, H). (b) Template image T T (N, M).

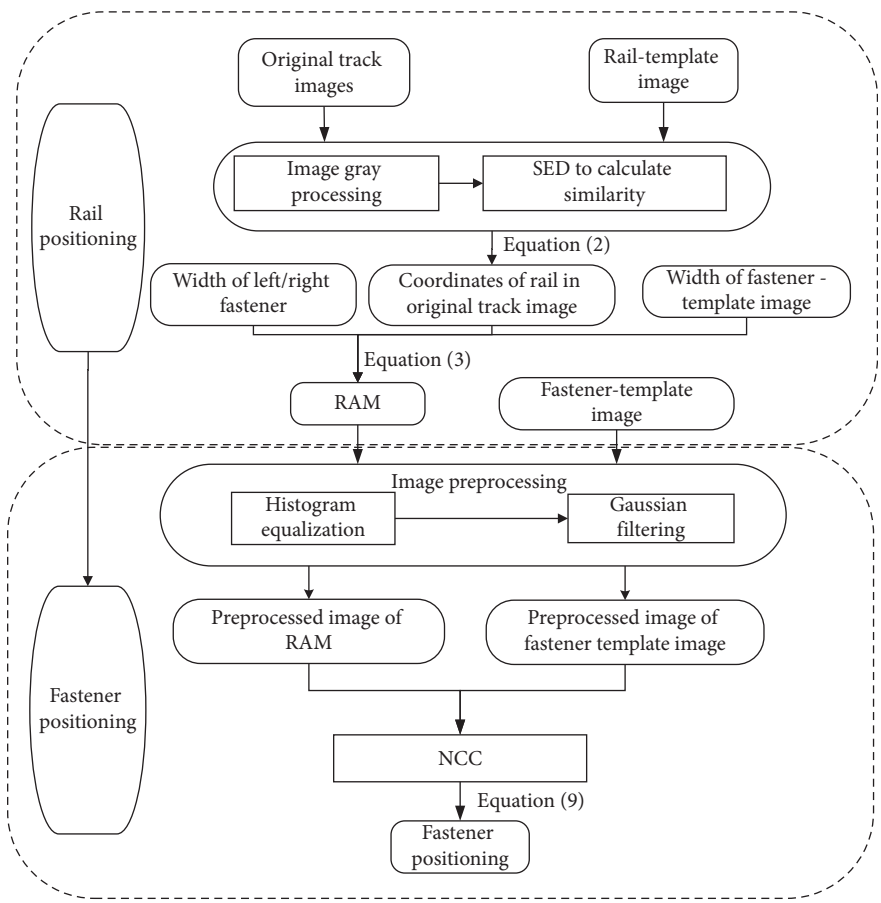

Figure 2: Flow chart of fastener positioning based on DTM.

process. The equation of the weighted average method is as follows:

$$V_{\text{gray}}(x, y) = 0.299 \times V_R(x, y) + 0.587 \times V_G(x, y) + 0.114 \times V_B(x, y), \quad (1)$$

where $V_{\text{gray}}(x, y)$ is the gray value obtained after weighted average, and $V_R(x, y)$, $V_G(x, y)$, and $V_B(x, y)$ are the pixel values of the red channel, green channel, and blue channel, respectively.

According to the prior knowledge, each original track image contains at least the following three features: (1) the rail runs through the original track image in the vertical direction, the fastener area is horizontally distributed on both sides of the rail in the track image [37], and the size of the fastener area remains the same. (2) The location of the

rail is basically fixed in all rail maps, and the horizontal offset is small, that is, the horizontal offset of the rail in the continuously captured images can be ignored. (3) Due to the repeated friction between the wheel and rail, the rail is obviously white and bright, and its average gray value is obviously different from other areas in the image.

First, the rail template is made offline where the number of rows in the rail template is equal to the original image, that is, $H = M$ as shown in Figure 3. Then, the template image is used to slide in the horizontal direction in step = 1 in the original image, and the similarity value between the template image and the area (subgraph) covered by it will be calculated. According to the prior knowledge, the gray value of the rail is significantly different from other regions. Therefore, the similarity degree between the rail template image and the original image can be measured by using the SED. The calculation formula is shown in the following equation:

$$R(i) = \sum_{m=1}^{M} \sum_{n=1}^{N} \left[T(n,m) - S_i(n,m)\right]^2, \tag{2}$$

where $R(i)$ refers to the similarity value between the template image $T(N, M)$ and the subgraph at coordinates $(i, 0)$ in track original image S, $T(n, m)$ is the gray value at coordinates (n, m) in the template T, and $S_i(n, m)$ is the gray value at coordinates (n, m) in subgraph S_i. When the template and subgraph are exactly the same, the correlation coefficient is 0. After the original image is completely searched, $R_{\min}(i)$ is found, and its corresponding subgraph S_i is the rail position in the original image.

After positioning to the rail, the column coordinates of the RAM containing the fasteners and rail in the original image can be obtained by the following equation:

$$\begin{aligned} C_l &= c_l - \alpha, \\ \beta &= w_t - \alpha - (c_r - c_l), \\ C_r &= c_r + \beta, \end{aligned} \tag{3}$$

where C_l is the column coordinate of the left edge of the located RAM in the original image; C_r is the column coordinate of the right edge of the located RAM in the original image; c_l is the column coordinate of the left edge of the rail in the original image obtained by template matching in the horizontal direction; c_r is the column coordinates of the right edge of the rail in the original image; w_t is the width of the fastener template image which is known by prior knowledge; α is the width of the left fastener in the fastener template image which is known by prior knowledge; and β is the parameter that controls the width of the RAM to equal the width of the fastener template image, and it is also the width of the right fastener in the fastener template image.

3.2. Fastener Positioning. In this section, the image preprocessing involved in this paper will be first introduced, which includes image enhancement [38] and image denoising [39], and then, the principle of how to use vertical template matching to achieve accurate fastener positioning will be explained.

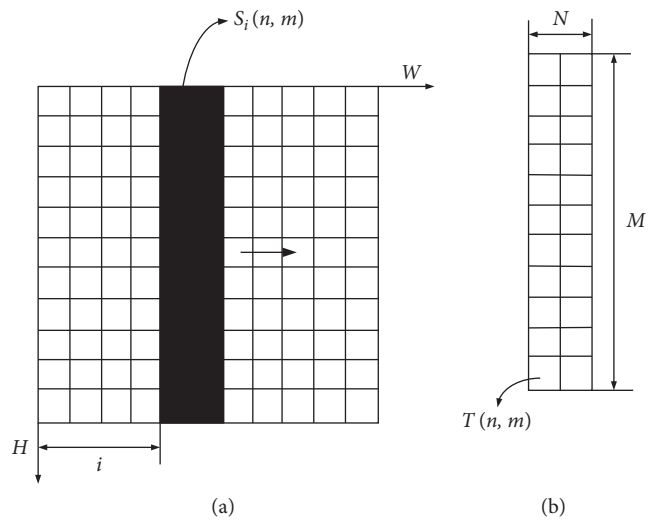

Figure 3: Schematic diagram of template matching in horizontal direction. (a) Searched image S S (W, H). (b) Template image T T (N, M).

3.2.1. Image Enhancement Based on Histogram Equalization. The distribution probability of each gray level in the image is shown by the gray histogram of the image. Therefore, histogram equalization method can be used to reconstruct the original image into a new image whose gray value conforms to the balanced distribution by adjusting the gray distribution of an image from nonuniform distribution to uniform distribution. And the histogram equalization has been proved to be effective in track image preprocessing [40]. The pixel value of an image is $u \geq 0$, the probability density function is $p_u(u_k)$, and its value can be obtained by the following equation:

$$p_u(u_k) = \frac{h(u_k)}{\sum_{k=0}^{L-1} h(u_k)}, \quad k = 0, 1, \ldots, L-1. \tag{4}$$

The input u contains L gray levels, and its probability is $p_u(u_k)$, $k = 0, 1, \ldots, L-1$. $p_u(u_k)$ is determined by the histogram $h(u_k)$, and $h(u_k)$ represents the number of pixels whose gray value is equal to u_k. The output $v(u_k)$ has L gray levels, and $v(u_k)$ can be obtained by the following equation:

$$v(u_k) = \sum_{0}^{k} p_u(u_k), \tag{5}$$

where $v(u_k)$ is the cumulative distribution probability value of the pixel value u_k in the original image, and the rounded $g(u_k)$ of the gray value of the new image can be obtained by the following equation:

$$g(u_k) = \text{round}(255 \times v(u_k)). \tag{6}$$

3.2.2. Image Denoising Based on the Gaussian Filter. Gaussian filtering can effectively suppress noise and smooth the image. The function expression is as follows:

$$G(x, y, \sigma) = \frac{1}{2\pi\sigma^2} e^{-(x^2+y^2/2\sigma^2)}. \tag{7}$$

After the gray value $f(x, y)$ of the original image at (x, y) is processed by the Gaussian filter, the gray value of the new image $g(x, y)$ can be obtained by the following equation:

$$g(x, y) = f(x, y) * G(x, y, \sigma). \tag{8}$$

3.2.3. Accurate Positioning of Fasteners. Symmetry is a basic geometric attribute. Image symmetry and feature symmetry are widely used in image processing, and the effect is remarkable [41]. According to the analysis of fastener image characteristics, fastener is a kind of standard axisymmetric object. Therefore, a pair of complete normal fasteners are selected as the fastener template, and according to the control of equation (3), the width of the fastener template is consistent with the width of the RAM; this limits that the RAM can only be scanned from top to bottom by the symmetrical fastener template, and finally, the precise positioning of the fastener will be obtained. The schematic diagram is shown in Figure 4. Due to the complex grayscale characteristics of the fastener and the influence of illumination, if the simple Euclidean distance is used to calculate the similarity here, only the size relationship between pixels will be considered, a larger error will occur, and affect the accuracy. Therefore, considering the accurate positioning of fasteners, the NCC is used to measure the similarity between the template and the rail area map, and the calculation formula is shown in the following equation:

$$\begin{cases} R(j) = \dfrac{\sum_{m=1}^{M}\sum_{n=1}^{N}\left[T'(n,m) \times S'_j(n,m)\right]}{\sqrt{\sum_{m=1}^{M}\sum_{n=1}^{N}T'(n,m)^2 \sum_{m=1}^{M}\sum_{n=1}^{N}S'_j(n,m)^2}}, \\ T' = T - \dfrac{1}{w \times h}\sum_{m=1}^{M}\sum_{n=1}^{N}T(n,m), \\ S'_j = S_j - \dfrac{1}{w \times h}\sum_{m=1}^{M}\sum_{n=1}^{N}S_j(n,m), \end{cases} \tag{9}$$

where $R(j)$ refers to the similarity value between the fastener template image T and RAM S at coordinates $(0, j)$, $T(n, m)$ is the gray value at coordinates (n, m) in the template T, $S_j(n, m)$ is the gray value at coordinates (n, m) in subgraph S_j, and correlation coefficient is 1 for perfect matching, -1 for poor matching, and 0 for no correlation. Find $R_{\max}(j)$, and its corresponding subimage S_j is the precise positioning of fastener position.

According to equation (9), the coordinates of a pair of fasteners can be accurately located, and then, the images of left fastener and right fastener can be obtained by combining the width of the rail template $(c_r - c_l)$, the width of left fastener α, the width of right fastener β, and the height of the fastener template h_t. The upper left corner coordinates of the left fastener in the RAM is $(0, j)$, its height is h_t, and its width is α. The upper left corner coordinates of the right fastener in the RAM is $(\alpha + c_r - c_l, j)$, its height is h_t, and its width is β.

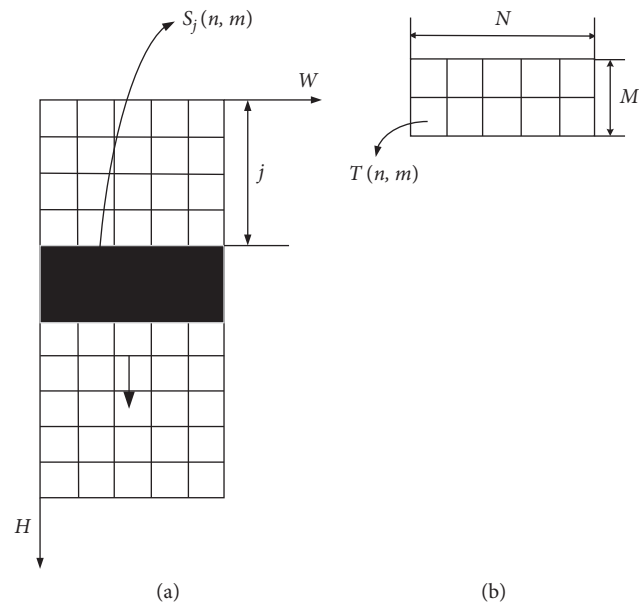

Figure 4: 3Schematic diagram of template matching in vertical direction. (a) Searched image S S (W, H). (b) Template image T T (N, M).

4. Experimental Result

In this paper, the real application scenario has been considered, and the resolution of the image captured by the line-scan camera is 2048×4096. A total of 631 pieces of fasteners from the Shijiazhuang-Taiyuan railway line were collected. Each image is composed by a pair of left and right fasteners, as shown in Figure 5, where in the original image of the ballastless track (i) is the fastener and (ii) is the rail. The templates are shown in Figure 6, where (a) is the rail template, (b) is the symmetrical fastener template, and (c) is the fastener template after image preprocessing.

4.1. Analysis of Experimental Results. In order to improve the accuracy of fastener positioning, the coarse to the fine positioning method is adopted in this paper. First, the SED is used to measure the similarity between the rail template image and the subgraph of the original track image. The results are shown in Figure 7, where the x-axis indicates the column coordinates of the subgraph in the original image, and the y-axis represents the similarity value between the rail template image and each subgraph. As can be seen from the figure, there is a value extremely close to 0 at the column coordinate of about 2200, that is, the most similar area between the rail template image and the original track image. The subgraph determined by this value can realize the positioning of the rail, and then, the column coordinate of the RAM can be calculated by equation (3). It also can be seen that the matching times of the rail are less than 4000 times/frame. The divided RAM shown in Figures 8(a) and 8(b) is the RAM after image preprocessing.

After the segmentation of the RAM, the similarity value between the fastener template map and the subgraphs in the

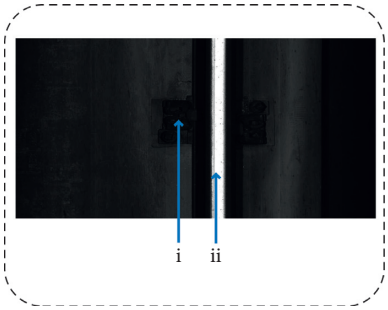

Figure 5: Original track image: (i) fastener and (ii) rail.

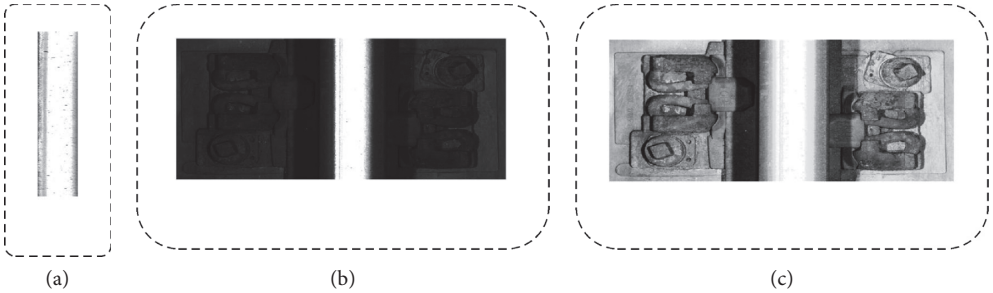

Figure 6: Template images. (a) The rail template. (b) The symmetrical fastener template. (c) The fastener template after image preprocessing.

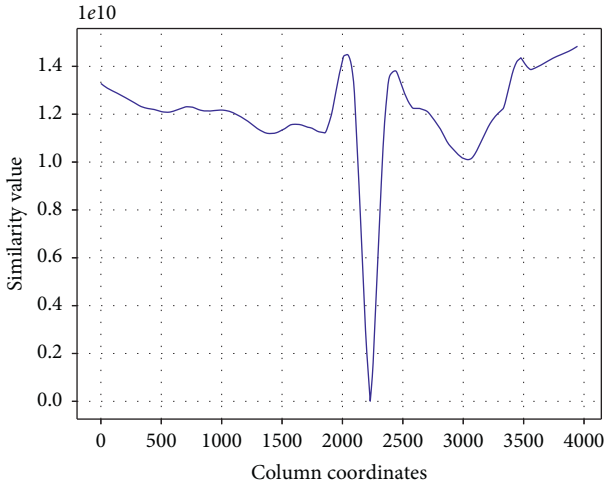

Figure 7: Similarity between the rail template and each subpicture.

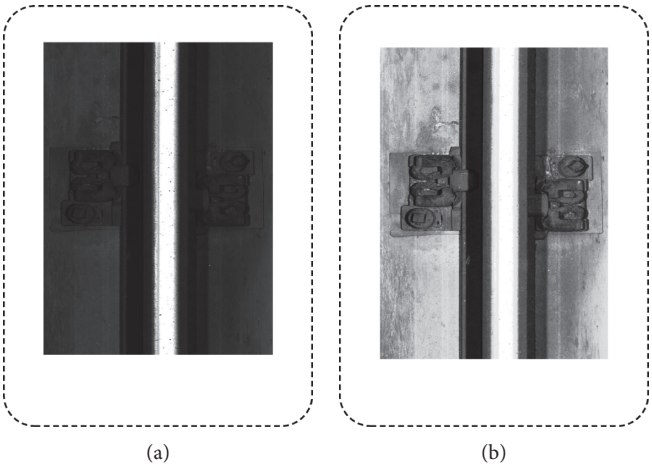

Figure 8: RAM. (a) The RAM segmented from the original image. (b) The RAM after image preprocessing.

RAM can be measured by using the NCC, and the results are shown in Figure 9. The row coordinate of the upper edge of the subgraph in the RAM is represented by x-axis, and the similarity value between the fastener template image and the subgraph is represented by y-axis. The experimental result of DTM algorithm in this paper is represented by the red curve, and the experimental result of using the method in this paper but skipping the image preprocessing step is represented by the blue curve. Since the NCC is used to measure the similarity between the template and subgraph in fastener positioning, the closer the similarity value between the fastener template image and the subgraph is 1, the more similar they are. As can be seen from the figure, there is a maximum value 0.871 at the column coordinate of 1008. Comparing the template matching similarity curve before and after image preprocessing, the blue curve has no obvious maximum value, which indicates that the gray feature of fastener is not obvious in the RAM when the image is not preprocessed, but the maximum value of the red curve is obvious, which indicates that the gray feature of fastener is obvious in the RAM when the image is preprocessed. In this experiment, the fastener positioning is realized on the preprocessed image, while the fastener positioning is lost on the non-preprocessed image. At the same time, it can be seen from the figure that the matching times for accurate positioning of fasteners are less than 1400 times/frame.

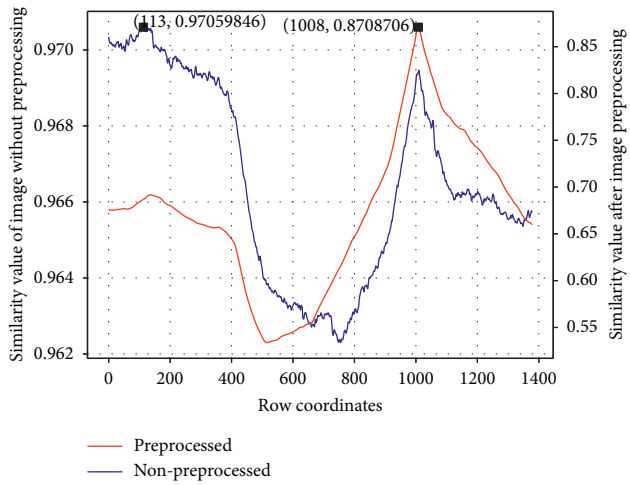

Figure 9: Similarity between the fastener template and each subgraph.

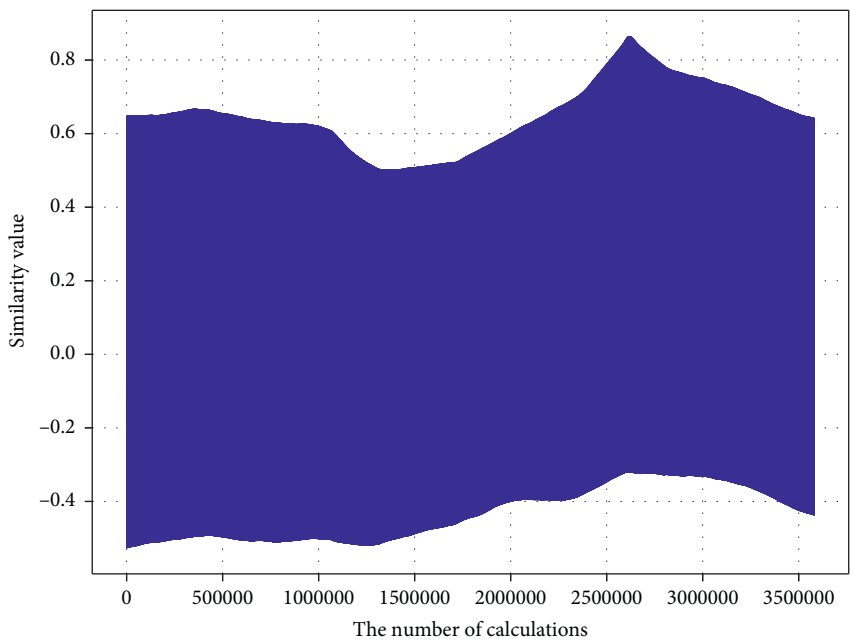

Figure 10: Similarity curve of GTM.

The similarity curve of the template matching using the global two dimensions is shown in Figure 10, where the number of calculations is represented by x-axis, and the similarity value between the fastener template image and the subgraph of the original image is represented by y-axis. Compared with the DTM method, the number of matches of DTM is less than 5400 times/frame, but the template matching times of the global two dimensions are more than 3.5 million times/frame. The more matching times, the greater the calculation of the method, and the more time will be consumed.

And as shown in Figure 11, the different similarity measurement algorithms are represented by x-axis, the number of fasteners with wrong positioning is represented by y-axis, the number of wrong positioning using DTM algorithm in this paper is counted by the blue histogram, and the number of wrong positioning using the global two-dimensions template matching is counted by the orange histogram. With the optimization of the algorithm, the number of wrong fastener position decreases significantly. Second, the number of wrong fastener position located by using DTM algorithm is significantly less than the number of wrong fastener position located by using the GTM algorithm. Third, when using the SED to measure the similarity, only the distance between the template and the corresponding gray value of the original image is calculated, which will not achieve the precise fastener positioning. However, in the normalized correlation matching [42] and NCC method, after adding the similarity measurement of the change trend and direction of the image content, the number of wrong positioning was significantly reduced.

The difficulty of precise positioning fasteners is increased in the actual rail line such as broken fasteners, lost

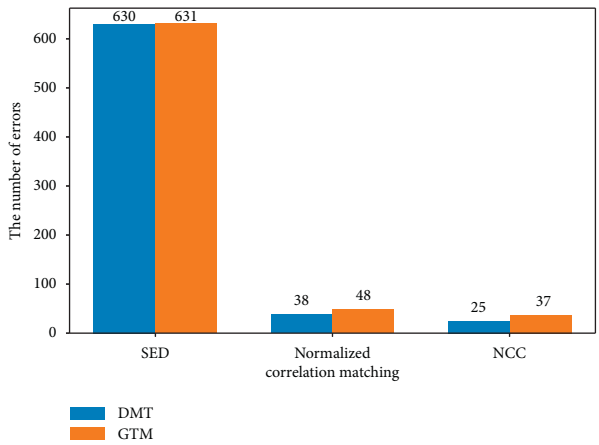

Figure 11: Comparison of the number of wrong positioning between DTM and GTM.

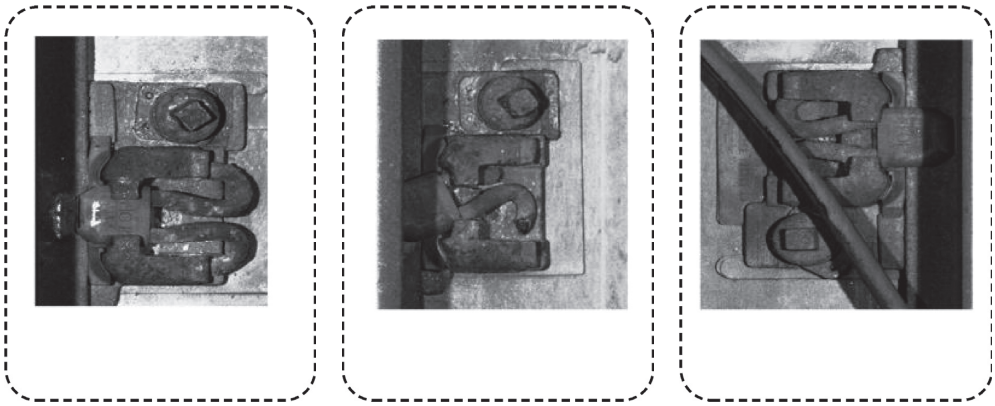

(a) (b) (c)

Figure 12: Position of the damaged rail fasteners. (a) The image of loose fastener. (b) The image of broken fastener. (c) The image of fastener obscured by cables.

fasteners, and fasteners covered by foreign matters. The results of fastener position based on the DTM method in this paper are shown in Figure 12, where (a) is the image of loose fastener, (b) is the image of broken fastener, and (c) is the image of fastener obscured by cables. It can be seen that the above interference problems have been effectively solved.

4.2. Evaluation of Experimental Methods. In order to evaluate the performance of this method, the accuracy rate (AR) of positioning is used as the evaluation standard. O is represented as the number of original image s, and S is represented as the number of images successfully segmented.

$$\mathrm{AR} = \frac{S}{O} \times 100\%. \tag{10}$$

As can be seen from Table 1, the accuracy rate of rail positioning is 100%, which proves that in the entire fastener positioning process, the horizontal error is reduced.

As can be seen from Table 2, since there is no sleeper in ballastless track, the edge contour method is not compared. And the threshold value of the fastener backing plates in ballastless track is difficult to be determined by the PS method, so the accuracy rate of fastener positioning is only 86.05%. In addition, if the image is not preprocessed, the grayscale features of the fasteners are not obvious in the whole image, which also leads to inaccurate positioning of the fasteners. Therefore, the DTM method in this article is used but without preprocessing the image, and the accuracy of fastener positioning is only 82.09%. Since the matching in global two dimensions, the calculation amount is large, and it will cause errors in both two dimensions; the DTM method is proposed in this paper, and the positioning accuracy of the fastener is significantly improved. The accuracy of DTM is 1.9% higher than GTM, and its accuracy rate is higher than other methods.

Table 1: The accuracy rate of rail positioning.

Track line type	O (piece)	S (piece)	AR (%)
Ballastless track	631	631	100

Table 2: Comparison of positioning accuracy.

Track line type	Method	O (piece)	S (piece)	AR (%)
Ballastless track	PS	631	543	86.05
	Without image preprocessed DTM	631	518	82.09
	GTM	631	594	94.14
	DTM	**631**	**606**	**96.04**

5. Conclusion

In this paper, a fastener positioning method based on DTM is proposed to solve the problem of low positioning accuracy caused by GTM scanning in global two directions in the existing fastener positioning methods. First, the rail template is used to scan the whole image in the horizontal direction, and the SED is used to measure the similarity; then, combined with the prior knowledge of the fastener template image, the RAM can be located from the original image, which reduces the complexity of the fastener positioning. Second, through image preprocessing, the image quality is improved, and the gray characteristics of the fastener are more significant. Finally, the symmetric fastener template is used to scan the RAM only in the vertical direction, which reduces the positioning error caused by the two directions in the GTM, and the NCC is used to measure the similarity between the fastener template image and the subgraph in the RAM, through that the precise positioning of the fasteners will be achieved. It has been verified by experiments that this method can be effectively applied to ballastless tracks in practice.

When the track fastener positioning is carried out through the original track images, since the original images used in this article only contain a pair of complete fasteners, the method does not discuss how to realize the positioning of multiple fasteners when an original track image contains multiple fasteners. In the future, the team will try to further optimize the proposed method DTM and effectively use the position information, which is obtained by measuring the distance between adjacent fasteners, to realize multiple fastener positioning.

Data Availability

The data used to support the findings of this study are currently under embargo, while the research findings are commercialized and are made available from the corresponding author upon request 12 months after publication of this article.

Conflicts of Interest

The authors declare that there are no conflicts of interest regarding the publication of this paper.

Acknowledgments

This work was supported by the National Natural Science Foundation of China (51975347), Shanghai Science and Technology Committee (18030501300), Shanghai Sailing Program (18YF1409200), talent program of Shanghai University of Engineering Science, and Opening Project of Shanghai Trusted Industrial Control Platform (TICPSH202003021-ZC).

References

[1] L. Zuwen, "Overall comments on track technology of high-speed railway," *Journal of Railway Engineering Society*, vol. 1, pp. 41–54, 2007.

[2] R. Montero, J. G. Victores, S. Jardón, and C. Balaguer, "Past, present and future of robotic tunnel inspection," *Automation in Construction*, vol. 59, pp. 99–112, 2015.

[3] C. Aytekin, Y. Rezaeitabar, S. Dogru, and I. Ulusoy, "Railway fastener inspection by real-time machine vision," *IEEE Transactions on Systems, Man, and Cybernetics: Systems*, vol. 45, no. 7, pp. 1101–1107, 2015.

[4] X. Gibert, V. M. Patel, and R. Chellappa, "Robust fastener detection for autonomous visual railway track inspection," in *Proceedings of the 2015 IEEE Winter Conference on Applications of Computer Vision*, pp. 694–701, IEEE, Waikoloa, HI, USA, January 2015.

[5] Y. Ou, J. Luo, B. Li, and B. He, "A classification model of railway fasteners based on computer vision," *Neural Computing and Applications*, vol. 31, no. 12, pp. 9307–9319, 2019.

[6] H. Zhang, J. Yang, W. Tao, and H. Zhao, "Vision method of inspecting missing fastening components in high-speed railway," *Applied Optics*, vol. 50, no. 20, pp. 3658–3665, 2011.

[7] F. Marino, A. Distante, P. L. Mazzeo, and E. Stella, "A real-time visual inspection system for railway maintenance: automatic hexagonal-headed bolts detection," *IEEE Transactions on Systems, Man and Cybernetics, Part C*, vol. 37, no. 3, pp. 418–428, 2007.

[8] H. R. Karimi, B. Lohmann, P. J. Maralani, and B. Moshiri, "A computational method for solving optimal control and parameter estimation of linear systems using Haar wavelets," *International Journal of Computer Mathematics*, vol. 81, no. 9, pp. 1121–1132, 2004.

[9] K. Yu, J. J. Liang, B. Y. Qu, X. Chen, and H. Wang, "Parameters identification of photovoltaic models using an improved JAYA optimization algorithm," *Energy Conversion and Management*, vol. 150, pp. 742–753, 2017.

[10] Z. Lv, X. Yan, Q. Jiang et al., "Just-in-time learning-multiple subspace support vector data description used for non-Gaussian dynamic batch process monitoring," *Journal of Chemometrics*, vol. 33, no. 6, 2019.

[11] K. Yu, B. Qu, C. Yue, S. Ge, X. Chen, and J. Liang, "A performance-guided JAYA algorithm for parameters identification of photovoltaic cell and module," *Applied Energy*, vol. 237, pp. 241–257, 2019.

[12] B. Song, X. Zhou, H. Shi, and Y. Tao, "Performance-indicator-oriented concurrent subspace process monitoring method," *IEEE Transactions on Industrial Electronics*, vol. 66, no. 7, pp. 5535–5545, 2019.

[13] Z. Lv, X. Yan, and Q. Jiang, "Batch process monitoring based on self-adaptive subspace support vector data description," *Chemometrics and Intelligent Laboratory Systems*, vol. 170, pp. 25–31, 2017.

[14] K. Yu, J. J. Liang, B. Y. Qu, Z. Cheng, and H. Wang, "Multiple learning backtracking search algorithm for estimating parameters of photovoltaic models," *Applied Energy*, vol. 226, pp. 408–422, 2018.

[15] B. Song, H. Yan, H. Shi, and S. Tan, "Multisubspace elastic network for multimode quality-related process monitoring," *IEEE Transactions on Industrial Informatics*, vol. 16, no. 9, pp. 5874–5883, 2020.

[16] Y. Li, H. R. Karimi, Q. Zhang, D. Zhao, and Y. Li, "Fault detection for linear discrete time-varying systems subject to random sensor delay: a riccati equation Approach," *IEEE Transactions on Circuits and Systems I: Regular Papers*, vol. 65, no. 5, pp. 1707–1716, 2018.

[17] B. Song, H. B. Shi, S. Tan et al., "Multi-Subspace orthogonal canonical correlation analysis for quality related plant wide process monitoring," *IEEE Transactions on Industrial Informatics*, 2020.

[18] E. Resendiz, L. F. Molina, J. M. Hart et al., "Development of a machine-vision system for inspection of railway track components," in *Proceedings of the 12th World on Transport Research*, pp. 1–22, Lisbon, Portugal, 2010.

[19] A. Berry, B. Nejikovsky, X. Gibert et al., "High speed video inspection of joint bars using advanced image collection and processing techniques," *World Congress on Railway Research*, vol. 290, pp. 619–622, 2008.

[20] E. Resendiz, J. Hart, and N. Ahuja, "Automated visual inspection of railroad tracks," *Intelligent Transportation Systems, IEEE Transactions on*, vol. 14, no. 2, pp. 751–760, 2013.

[21] L. Scarlett, W. Quandong, and L. Yiping, "A review of applications of visual inspection technology based on image processing in the railway industry," *Transportation Safety and Environment*, vol. 1, pp. 185–204, 2019.

[22] B. Dong, Q. Li, J. Wang et al., "An end-to-end abnormal fastener detection method based on data synthesis," in *Proceedings of the 2019 IEEE 31st International Conference on Tools with Artificial Intelligence (ICTAI)*, pp. 149–156, Portland, OR, USA, June 2019.

[23] L. Jiajia, X. Ying, L. Bailin et al., "Research on automatic inspection algorithm for railway fastener defects based on computer vision," *Journal of the China Railway Society*, vol. 38, pp. 73–80, 2016.

[24] Y. Li, H. Trinh, N. Haas et al., "Rail component detection, optimization, and assessment for automatic rail track inspection," *IEEE Transactions on Intelligent Transportation Systems*, vol. 15, no. 2, pp. 760–770, 2014.

[25] Y. Li, C. Otto, N. Haas et al., "Component-based track inspection using machine-vision technology," in *Proceedings of the 1st ACM International Conference on Multimedia Retrieval*, vol. 60, Trento, Italy, April 2011.

[26] X. Wei, Z. Yang, Y. Liu, D. Wei, L. Jia, and Y. Li, "Railway track fastener defect detection based on image processing and deep learning techniques: a comparative study," *Engineering Applications of Artificial Intelligence*, vol. 80, pp. 66–81, 2019.

[27] Y. Xia, F. Xie, and Z. Jiang, "Broken railway fastener detection based on adaboost algorithm," in *Proceedings of the 2010 International Conference on Optoelectronics and Image Processing*, pp. 313–316, Haikou, China, November 2011.

[28] X. Dai, Y. Peng, K. C. P. Wang et al., "Railway fastener detection method based on 3D images," in *Proceedings of the First International Conference on Rail Transportation 2017*, SW Jiaotong University, Chengdu, China, pp. 938–946, 2018.

[29] H. Feng, Z. Jiang, F. Xie, P. Yang, J. Shi, and L. Chen, "Automatic fastener classification and defect detection in vision-based railway inspection systems," *IEEE Transactions on Instrumentation and Measurement*, vol. 63, no. 4, pp. 877–888, 2014.

[30] T. Prasongpongchai, T. H. Chalidabhongse, and S. Leelhapantu, "A vision-based method for the detection of missing rail fasteners," in *Proceedings of the 2017 IEEE International Conference on Signal and Image Processing Applications (ICSIPA)*, pp. 419–424, Kuching, Malaysia, March 2017.

[31] J. Yang, W. Tao, M. Liu, Y. Zhang, H. Zhang, and H. Zhao, "An efficient direction field-based method for the detection of fasteners on high-speed railways," *Sensors*, vol. 11, no. 8, pp. 7364–7381, 2011.

[32] H. Fan, P. C. Cosman, Y. Hou, and B. Li, "High-Speed railway fastener detection based on a line local binary pattern," *IEEE Signal Processing Letters*, vol. 25, no. 6, pp. 788–792, 2018.

[33] M. Debella-Gilo and A. Kääb, "Sub-pixel precision image matching for measuring surface displacements on mass movements using normalized cross-correlation," *Remote Sensing of Environment*, vol. 115, no. 1, pp. 130–142, 2011.

[34] C. Yang, W. Gui, Z. Chen et al., "Voltage difference residual-based open-circuit fault diagnosis approach for three-level converters in electric traction systems," *IEEE Transactions on Power Electronics*, vol. 35, no. 99, pp. 3012–3028, 2020.

[35] Z. Chen, X. Li, C. Yang et al., "A data-driven ground fault detection and isolation method for main circuit in railway electrical traction system," *ISA Transactions*, vol. 87, pp. 264–271, 2019.

[36] C. Kanan and G. W. Cottrell, "Color-to-Grayscale: does the method matter in image recognition," *Plos One*, vol. 7, no. 1, pp. 133–139, Article ID e29740, 2012.

[37] J. Liu, Y. Huang, Q. Zou et al., "Learning visual similarity for inspecting defective railway fasteners," *IEEE Sensors Journal*, vol. 19, no. 16, pp. 6844–6857, 2019.

[38] T. Celik, "Two-dimensional histogram equalization and contrast enhancement," *Pattern Recognition*, vol. 45, no. 10, pp. 3810–3824, 2012.

[39] B. Pan, "Bias error reduction of digital image correlation using Gaussian pre-filtering," *Optics and Lasers in Engineering*, vol. 51, no. 10, pp. 1161–1167, 2013.

[40] Z. Anzhong, H. Xinyang, J. Minyu et al., "Multi-target defect detection of railway track based on image processing," in *Proceedings of the 2020 Chinese Control and Decision Conference (CCDC)*, pp. 3377–3382, Hefei, China, 2020.

[41] Y. Xu, X. Li, J. Yang, and D. Zhang, "Integrate the original face image and its mirror image for face recognition," *Neurocomputing*, vol. 131, pp. 191–199, 2014.

[42] N. N. Dawoud, B. B. Samir, and J. Janier, "N-mean kernel filter and normalized correlation for face localization," in *Proceedings of the 2011 IEEE 7th International Colloquium on Signal Processing and its Applications (CSPA)*, IEEE, Penang, Malaysia, March 2011.

Hindawi
Complexity
Volume 2020, Article ID 3291723, 11 pages
https://doi.org/10.1155/2020/3291723

Research Article

A Numerical Method for Time-Fractional Reaction-Diffusion and Integro Reaction-Diffusion Equation Based on Quasi-Wavelet

Sachin Kumar,[1] Jinde Cao,[2] and Xiaodi Li[3]

[1]*Department of Mathematics, Govt. MGM PG College, Itarsi 461111, India*
[2]*School of Mathematics, Southeast University, Nanjing 210096, China*
[3]*School of Mathematics and Statistics, Shandong Normal University, Ji'nan 250014, China*

Correspondence should be addressed to Jinde Cao; jdcao@seu.edu.cn

Received 16 May 2020; Accepted 4 August 2020; Published 26 September 2020

Academic Editor: Honglei Xu

In this research work, we focused on finding the numerical solution of time-fractional reaction-diffusion and another class of integro-differential equation known as the integro reaction-diffusion equation. For this, we developed a numerical scheme with the help of quasi-wavelets. The fractional term in the time direction is approximated by using the Crank–Nicolson scheme. The spatial term and the integral term present in integro reaction-diffusion are discretized and approximated with the help of quasi-wavelets. We study this model with Dirichlet boundary conditions. The discretization of these initial and boundary conditions is done with a different approach by the quasi-wavelet-based numerical method. The validity of this proposed method is tested by taking some numerical examples having an exact analytical solution. The accuracy of this method can be seen by error tables which we have drawn between the exact solution and the approximate solution. The effectiveness and validity can be seen by the graphs of the exact and numerical solutions. We conclude that this method has the desired accuracy and has a distinctive local property.

1. Introduction

Differential and integral calculus is a vital and broad branch of mathematics [1, 2]. First of all, the integer-order differential and integer calculus came into existence. About a few decades ago, the concept of fractional calculus came into existence. Day by day the new concept, new definitions, and new terminology are emerging. The concepts and ideas of fractional calculus were evolved by Liouville and Abel. The more basic fundamentals and concepts are available in the literature [3, 4]. This branch of mathematics allows us to generalize the order of derivatives from the integer order to the real and arbitrary order. There are so many types available in the literature of fractional calculus. Some of them are Caputo, Hadamard, Riemann–Liouville, and Grunwald–Letnikov. As time passes, in the development of this branch, the variable-order derivative concepts are introduced in which orders of derivatives are functions of variables. The most prevailing derivatives are power law kernel derivatives. But, in recent few years, the derivatives with nonsingular kernel are introduced. Derivatives with the Mittag–Leffler kernel are known as Atangana–Baleanu derivatives, and derivatives with the exponential kernel are known as the Caputo–Fabrizio derivative. The fractional differential equations are in trends to study. There are so many physical phenomena in which fractional differential equations depict and represent the behavior and dynamics of the phenomena in a more accurate way than integer-order differential equations. To find out the solution of the fractional differential equation and fractional partial differential equations is a tough task as it is not possible always to find out the exact solution. The researchers started to develop the methods and schemes for finding the numerical solution of fractional differential equations. Many numerical methods are developed and available in the literature. Some of them are the fractional differential transform method [5], predictor-corrector method [6], Adomian decomposition method [7], homotopy perturbation method [8], and generalized block pulse operational matrix method [9]. The operational matrix method is a spectral method which is

easy to be applicable for many types of fractional differential equations whether they are of integer, fractional, and variable type. Its results are so accurate, and it is easy to apply. Some of them are Gegenbauer wavelet [9], Haar wavelets [10], Chebyshev wavelets [11], and Legendre wavelets [12]. The stability of discrete-time delayed switched systems and time delayed systems is given in the literature [13, 14].

FDEs, FPDEs, and fractional integro-differential equations are used to model many physical phenomena [15–17], which have arisen in physics, chemistry, biology, electrical engineering, nuclear reactor, viscoelastic, fluid dynamics, population dynamics, and medical science. To show the memory effect of the system, in the branch of nuclear reactor and thermo elasticity, we use the fractional differential equations. But, while modeling, the effect of history is being ignored. This can be taken into account by adding a term of integration in these fractional PDEs. The integro-differential equations have so many applications in control theory, financial market, fluid dynamics, aerospace systems, and viscoelastic mechanism. The most occurring physical process in nature is the diffusion process. In this process of diffusion, the molecules or energy or any physical quantity is transferred to the low concentration area from the high concentration area. If another process known as reaction is added to the process of diffusion, then it is called the reaction-diffusion process. In this process, molecules react with the fluids. This phenomenon of diffusion can be depicted by the following PDE known as the reaction-diffusion partial differential equation:

$$\frac{\partial \Psi(\zeta,\eta)}{\partial \eta} = D\nabla^2\Psi(\zeta,\eta) + P(\Psi,\zeta,\eta), \tag{1}$$

where $P(\Psi,\eta)$ represents the reaction term and the first term on the right-hand side of the equation represents the diffusion process with D as the diffusion coefficient.

We divided our article into many sections as follows: Section 1 contains the preliminary definitions which will be used throughout the article. This section contains the theory and methods of the quasi-wavelet to find out an approximation of an unknown function. The taken model of integro reaction-diffusion and reaction-diffusion is given in Section 3. How to deal with discretization of spatial and time-fractional terms with Dirichlet boundary conditions is also given in Section 3. The numerical results which depict the effectiveness and accuracy of our proposed method are present in Section 4. The conclusion of this paper is contained in Section 5.

2. Preliminary Definition about Fractional Derivative and Quasi-Wavelets

In this section, we described the definitions of fractional derivatives which will be used throughout the article. There are two types of definitions available in the literature of the fractional derivative, i.e., Riemann–Liouville and Caputo definitions. We have taken Caputo's one because it is more reliable in modeling.

2.1. Integration and Differentiation of Riemann–Liouville Type. The R-L-type definition of fractional integration is given as follows [18]:

$$I^{\varrho}\zeta(\theta) = \frac{1}{\Gamma(\varrho)}\int_0^{\theta}(\theta-\Omega)^{\varrho-1}\zeta(\Omega)\mathrm{d}\Omega, \quad \theta>0,\ \varrho\in R^{+}. \tag{2}$$

The definition of fractional differentiation in the R-L sense is given by the following definition:

$$D_l^{\varrho}\zeta(\theta) = \left(\frac{\mathrm{d}}{\mathrm{d}\theta}\right)^m \left(I^{m-\varrho}\zeta\right)(\theta),\ (\varrho>0, m-1<\varrho<m). \tag{3}$$

2.2. Definition of Fractional Derivative in Caputo Sense. The following equation represents the definition of fractional differentiation in Caputo sense:

$$D_c^{\varrho}\zeta(\theta) = \begin{cases} \dfrac{\mathrm{d}^q\zeta(\theta)}{\mathrm{d}\theta^q}, & \varrho = q\in N, \\[2ex] \dfrac{1}{\Gamma(\varrho)}\displaystyle\int_0^{\theta}(\theta-\eta)^{q-\varrho-1}\zeta^q(\eta)\mathrm{d}\eta, & q-1<\varrho<q, \end{cases} \tag{4}$$

where the parameter q represents the integer. A resemblance of the Caputo definition with the integer-order derivative is as follows:

$$D_c^{\varrho}M = 0, \tag{5}$$

with M being a constant.

$$D_c^{\varrho}\theta^{\sigma} = \begin{cases} 0, & \sigma\in N\cup 0 \text{ and } \sigma<\lceil\varrho\rceil, \\[2ex] \dfrac{\Gamma(1+\sigma)}{\Gamma(1-\varrho+\sigma)}\theta^{-\varrho+\sigma}, & \sigma\in N\cup 0 \text{ and } \sigma\geq\lceil\varrho\rceil \text{ or } \sigma\notin N \text{ and } \sigma>\lceil\varrho\rceil, \end{cases} \tag{6}$$

where $\lfloor\varrho\rfloor$ represents the floor function. All these types of fractional operators follow the linear property:

$$D_c^{\varrho}\left(C_1h_1(\theta)+C_2h_2(\theta)\right) = C_1D_c^{\varrho}h_1(\theta)+C_2D_c^{\varrho}h_2(\theta), \tag{7}$$

with C_1 and C_2 being constants. A useful relation between the R-L definition and Caputo is given as follows:

$$\left(I^{\vartheta}D_c^{\vartheta}\varsigma\right)(\eta) = \varsigma(\eta) - \sum_{k=0}^{l-1}\varsigma^k(0^+)\frac{\eta^k}{k!}, \quad l-1<\vartheta\leq l. \tag{8}$$

2.3. Approximation of Functions with the Help of Quasi-Wavelets. The method based upon quasi-wavelets nowadays is developing in the form of the local spectral collocation method. It is used for seeking the numerical solution of the fractional-order partial differential equation and integral equations. The singular convolution used in this method is a significant transformation. We define this transformation as follows:

$$\varpi(\theta) = (R^* p)(\theta) = \int_{-\infty}^{\infty} R(\theta - \zeta) p(\zeta) \mathrm{d}\zeta, \tag{9}$$

where $p(\theta)$ is known as the test function and R is a singular kernel. We know that the construction of the family of wavelets is done with the help of a function known as the mother wavelet φ. We use the operations of dilation and transformation to form the family of wavelets:

$$\varphi_{\vartheta,\gamma}(\zeta) = \vartheta^{-1/2} \varphi\left(\frac{\zeta - \gamma}{\vartheta}\right). \tag{10}$$

We have used two parameters here. The parameter ϑ is the dilation parameter, and γ is the translation parameter. The kernel known as Shannon's delta sequence is used in the construction of quasi-wavelets. It is defined as

$$\delta_\theta(\eta) = \frac{1}{\pi} \int_0^{\pi} \cos(\eta y) \mathrm{d}y = \frac{\sin(\theta\eta)}{\pi\eta}, \tag{11}$$

where $\lim_{\theta \longrightarrow \theta_0} \delta_\theta(\eta) = \delta(\eta)$ and δ is a well-known Dirac delta function. Shannon's delta sequence kernel produces the basis for the Paley–Wiener reproducing kernel Hilbert space $\mathbf{B}_\theta^2$ [19] for a given $\theta > 0$ which is a subspace of $\mathbf{L}^2(R)$. We can produce uniquely a function $\varsigma(\zeta) \in \mathbf{B}_\theta^2$ as follows:

$$\varsigma(\zeta) = \int_{-\infty}^{\infty} \varsigma(\zeta) \delta_\theta(\zeta - \eta) \mathrm{d}t = \int_{-\infty}^{\infty} \varsigma(\zeta) \frac{\sin(\theta(\zeta - \eta))}{\pi(\zeta - \eta)} \mathrm{d}\eta, \quad \forall \varsigma \in \mathbf{B}_\theta^2. \tag{12}$$

The sampling scaling function can be written in another form as follows:

$$\delta_{\theta,p} = \delta_\theta(\zeta - \zeta_p) = \frac{\sin((\zeta - \zeta_p)\theta)}{(\zeta - \zeta_p)\pi}. \tag{13}$$

We have denoted the sampling points around the space ζ by $\{\zeta_p\}$ which are sampling points centered around ζ. The discrete form of function $\varsigma(\zeta)$ which belongs to the space $\mathbf{B}_\theta^2$ is presented by the following infinite series expansion:

$$\varsigma(\zeta) = \sum_{p=-\infty}^{\infty} \varsigma(\zeta_p) \delta_\theta(\zeta - \zeta_p). \tag{14}$$

The above approximation can be rewritten with the help of Shannon sampling theorem at the Nyquist frequency θ in the band-limited signal in B_θ^2:

$$\varsigma(\zeta) = \sum_{p=-\infty}^{\infty} \varsigma(\zeta_p) \delta_\theta(\zeta - \zeta_p) = \sum_{p=-\infty}^{\infty} \varsigma(\zeta_p) \frac{\sin(\pi(\zeta - \zeta_p)/\Delta)}{(\pi(\zeta - \zeta_p)/\Delta)}, \tag{15}$$

where the value of parameter θ is π/Δ and the grid size in spatial direction is denoted by Δ. We improved the localized asymptotic behavior of Dirichlet's delta sequence kernel by using the regularizer $R_\sigma(\zeta)$. In the literature, many regularizers are introduced, and we use here the following Gaussian type regularizer:

$$R_\sigma(\zeta) = \exp\left(\frac{-\zeta^2}{2\sigma^2}\right), \quad \sigma > 0, \tag{16}$$

where σ represents the width parameter of the Gaussian envelope. The parameters Δ and σ are related by the expression $\sigma = r \times \Delta$, with r as the computation parameter. The sampling scaling function is modified as follows by using the Gaussian regularizer:

$$\delta_{\Delta,\sigma}(\zeta) = \frac{\sin(\pi\zeta/\Delta)}{\pi\zeta/\Delta} \exp\left(\frac{-\zeta^2}{2\sigma^2}\right), \tag{17}$$

where

$$\lim_{\sigma \longrightarrow \infty} \delta_{\Delta,\sigma}(\zeta) = \frac{\sin(\pi\zeta/\Delta)}{(\pi\zeta/\Delta)}, \tag{18}$$

where the Gaussian-regularized sampling scaling function follows the property of the quasi-scaling function. So, we can approximate an unknown function $\varsigma(\zeta)$ belonging to the space textbf B_θ^2 with the help of the quasi-scaling function:

$$\varsigma(\zeta) = \sum_{p=-\infty}^{\infty} \varsigma(\zeta_p) \delta_\theta(\zeta - \zeta_p) = \sum_{p=-\infty}^{\infty} \varsigma(\zeta_p) \delta_\theta(\zeta - \zeta_p) R_\theta(\zeta - \zeta_p). \tag{19}$$

Here, the infinite sampling points have been used, but while commutating in practical manner, we cannot use these infinite points. By seeing this problem, the domain of computation is restricted to the finite sampling points. For this purpose, we select $(2W + 1)$. The simplified form of the above equation is as follows:

$$\varsigma(\zeta) = \sum_{p=-W}^{W} \varsigma(\zeta_p) \delta_{\Delta,\sigma}(\zeta - \zeta_p). \tag{20}$$

Now, for the approximation of integer-order derivatives of order n of the function $f(\zeta)$,

$$\varsigma^n(\zeta) = \sum_{p=-W}^{W} \varsigma(\zeta_p) \delta_{\Delta,\sigma}^n(\zeta - \zeta_p), \quad n = 1, 2, \ldots. \tag{21}$$

The sampling points vary from $p = -W$ to $p = +W$, i.e., there are $2W + 1$ sampling points. We give some of the formula of $\delta_{\Delta,\sigma}, \delta_{\Delta,\sigma}^1$, and $\delta_{\Delta,\sigma}^2$ [20] for the calculation purpose:

$$\delta_{\Delta,\sigma}(\zeta)=\begin{cases}\dfrac{\exp\left\{-\zeta^2/2\sigma^2\right\}\sin(\zeta\pi/\Delta)}{(\pi\zeta/\Delta)}, & \zeta\neq 0\\ 1, & \zeta=0,\end{cases}$$

$$\delta^1_{\Delta,\sigma}(\zeta)=\begin{cases}\left(-\dfrac{\sin(\pi\zeta/\Delta)}{\left(\pi\zeta^2/\Delta\right)}-\dfrac{\Delta\sin(\pi\zeta/\Delta)}{\left(\pi\sigma^2/\Delta\right)}+\dfrac{\cos(\pi\zeta/\Delta)}{\zeta}\right)\exp\left(-\dfrac{\zeta^2}{2\sigma^2}\right), & \zeta\neq 0,\\ 0, & \zeta=0,\end{cases}$$

$$\delta^2_{\Delta,\sigma}(\zeta)=\begin{cases}\left(\dfrac{2\Delta\sin(\zeta\pi/\Delta)}{\pi\zeta^3}-\dfrac{2\cos(\pi\zeta/\Delta)}{\zeta^2}+\dfrac{\Delta\zeta\sin(\zeta\pi/\Delta)}{\pi\sigma^4}+\dfrac{\Delta\sin(\pi\zeta/\Delta)}{\pi\sigma^2\zeta}-\dfrac{2\cos(\pi\zeta/\Delta)}{\sigma^2}-\dfrac{\pi\sin(\zeta\pi/\Delta)}{\zeta\Delta}\right)\exp\left(-\dfrac{\zeta^2}{2\sigma^2}\right), & \zeta\neq 0,\\ 0, & \zeta=0.\end{cases} \tag{22}$$

3. Mathematical Model and Used Proposed Method

In this section, we propose the integrated mathematical model of the reaction-diffusion and integro reaction-diffusion equation. In this section, we develop the Crank–Nicolson scheme with the combination of the quasi-wavelet-based numerical method to find the numerical solution of the taken model:

$$\frac{\partial^{\vartheta}\varsigma}{\partial\eta^{\vartheta}}=\frac{\partial^2\varsigma}{\partial\zeta^2}+a\varsigma(\eta,\zeta)(1-\varsigma(\eta,\zeta))+b\varsigma(\eta,\zeta)\int_0^{\eta}\kappa(\eta-s,\zeta)\varsigma(s,\zeta)\mathrm{d}s+f(\zeta,\eta). \tag{23}$$

We have taken the following Dirichlet boundary conditions and initial conditions:

$$\varsigma(0,\eta)=g_1(\eta),\varsigma(1,\eta)=g_2(\eta),\varsigma(\zeta,0)=g_3(\zeta), \tag{24}$$

where the term $f(\zeta,\eta)$ denotes the forced function and $\kappa(\zeta,\eta)$ is known as a kernel.

3.1. Using Crank–Nicolson Scheme for the Time Discretization. To discretize the time derivatives present in model, we will use the Crank–Nicolson scheme. We divided the time interval into discrete points as $\eta_n=n\times\Delta\eta$ where $n=0,1,\ldots,M$ and time length is noted by $\Delta\eta$. The notations ς^n and f^n represent the values of $\varsigma(\zeta,\eta)$ and $f(\zeta,\eta)$ at time $\eta_n=n\times\Delta\eta$. The term $\partial^{\vartheta}\varsigma(\zeta,\eta)/\partial\eta^{\vartheta}$ from the model is approximated as at the grid point $(\zeta,\eta_{n+(1/2)})$:

$$\begin{aligned}\frac{\partial^{\vartheta}\varsigma\left(\zeta,\eta_{n+(1/2)}\right)}{\partial\eta^{\vartheta}}&=\frac{1}{\Gamma(1-\vartheta)}\int_0^{\eta_{n+(1/2)}}\left(\eta_{n+(1/2)}-s\right)^{-\vartheta}\times\frac{\partial\varsigma(\zeta,s)}{\partial s}\mathrm{d}s\\
&=\frac{1}{\Gamma(1-\vartheta)}\left[\int_0^{\eta_n}\left(\left(n+\frac{1}{2}\right)\Delta\eta-s\right)^{-\vartheta}\times\frac{\partial\varsigma(x_i,s)}{\partial s}\mathrm{d}s+\int_{\eta_n}^{\eta_{\eta_{n+(1/2)}}}\left[\left(\frac{\varsigma^{n+1}-\varsigma^n}{\Delta\eta}\right)+O(\Delta\eta)\right]\left(\left(n+\frac{1}{2}\right)\Delta\eta-s\right)^{-\vartheta}\mathrm{d}s\right]\\
&=\frac{1}{\Gamma(1-\vartheta)}\sum_{m=1}^{n}\int_{(m-1)\Delta\eta}^{m\Delta\eta}\left(\left(\left(n+\frac{1}{2}\right)\Delta\eta-s\right)^{-\vartheta}\right)\times\left[\frac{\varsigma^{m+1}-\varsigma^m}{\Delta\eta}+\left(s-\eta_{m-(1/2)}\right)u_{tt}(c_m,\zeta)\right]\mathrm{d}s\\
&\quad+\frac{1}{\Gamma(1-\vartheta)}\int_{n\Delta\eta}^{(n+(1/2))\Delta\eta}\left[\left(\frac{\varsigma^{n+1}-\varsigma^n}{\Delta\eta}\right)+O(\Delta\eta)\right]\left(\left(n+\frac{1}{2}\right)\Delta\eta-s\right)^{-\vartheta}\mathrm{d}s.\end{aligned} \tag{25}$$

In aberration form, we can rewrite as

$$\frac{\partial^{\vartheta}\varsigma\left(\zeta,\eta_{n+(1/2)}\right)}{\partial\eta^{\vartheta}}=\frac{\Delta\eta^{-\vartheta}}{\Gamma(2-\vartheta)}\sum_{m=1}^{n}\left(\varsigma^{m+1}-\varsigma^{m}\right)\left(\left(n+\frac{3}{2}-m\right)^{1-\vartheta}+\left(n+\frac{1}{2}-m\right)^{1-\vartheta}\right)+\frac{\Delta\eta^{-\vartheta}}{\Gamma(2-\vartheta)}\frac{\varsigma^{n+1}-\varsigma^{n}}{2^{1-\vartheta}}+\frac{1}{\Gamma(1-\vartheta)}\sum_{m=1}^{n}\int_{(m-1)\Delta\eta}^{m\Delta\eta}$$
$$\cdot\left(\left(n+\frac{1}{2}\right)\Delta\eta-s\right)^{-\vartheta}\times\left(s-\eta_{m-(1/2)}\right)u_{tt}\left(c_m,\zeta\right)\mathrm{d}s+\frac{\Delta\eta^{-\vartheta}}{\Gamma(2-\vartheta)}\frac{1}{2^{1-\vartheta}}O\left((\Delta\eta)^{2-\vartheta}\right). \tag{26}$$

Hence, we obtain

$$\frac{\partial^{\vartheta}\varsigma\left(x_i,\eta_{n+(1/2)}\right)}{\partial\eta^{\vartheta}}=\frac{\Delta\eta^{-\vartheta}}{\Gamma(2-\vartheta)}\left[\sum_{m=1}^{n}\left(u_i^{m+1}-u_i^{m}\right)\left(\left(n+\frac{3}{2}-m\right)^{1-\vartheta}+\left(n+\frac{1}{2}-m\right)^{1-\vartheta}\right)+\frac{u_i^{n+1}-u_i^{n}}{2^{1-\vartheta}}\right]+R_1+R_2, \tag{27}$$

where

$$\begin{aligned}R_1&=\frac{1}{\Gamma(1-\vartheta)}\sum_{m=1}^{n}\int_{(m-1)\Delta\eta}^{m\Delta\eta}\left(\left(\left(n+\frac{1}{2}\right)\Delta\eta-s\right)^{-\vartheta}\right)\times\left[\left(s-\eta_{m-(1/2)}\right)u_{tt}\left(c_m,x_i\right)\right]\mathrm{d}s,\\R_2&=\frac{2^{\vartheta-1}}{\Gamma(2-\vartheta)}O\left((\Delta\eta)^{2-\vartheta}\right).\end{aligned} \tag{28}$$

The bound of R_1 is as follows after simplifying:

$$R_1\leq\frac{\max_{0\leq\zeta\leq1}\left|u_{tt}\left(c_m,\zeta\right)\right|}{\Gamma(1-\vartheta)}\Delta\eta^{2-\vartheta}. \tag{29}$$

The trapezoidal technique is implemented to deal with the integral term $\int_0^{\eta}\kappa(\eta-s,\zeta)\varsigma(s,\zeta)\mathrm{d}s$:

$$\int_0^{\eta_{n+(1/2)}}\kappa(\zeta,\eta-s)\varsigma(\zeta,s)\mathrm{d}s=\frac{1}{2}\left\{\int_0^{\eta_n}\kappa(\zeta,\eta-s)\varsigma(\zeta,s)\mathrm{d}s+\int_0^{\eta_{n+1}}\kappa(\zeta,\eta-s)\varsigma(\zeta,s)\mathrm{d}s\right\}. \tag{30}$$

Taking the exponential form of the kernel as $\kappa(\eta-s,\zeta)=e^{\{-(\eta-s)\}}$, then

$$\begin{aligned}\int_0^{\eta_n}\kappa(\zeta,\eta-s)\varsigma(\zeta,s)\mathrm{d}s&=\sum_{j=0}^{n-1}\int_{\eta_j}^{\eta_{j+1}}\exp\{-(\eta_n-s)\}\varsigma(\zeta,s)\mathrm{d}s\\&=\sum_{j=0}^{n-1}\int_{\eta_j}^{\eta_{j+1}}\exp\{-(\eta_n-s)\}\left\{\varsigma\left(\zeta,\eta_{j+1}\right)\frac{s-\eta_j}{\Delta\eta}+\varsigma\left(\zeta,\eta_j\right)\frac{\eta_{j+1}-s}{\Delta\eta}\right\}\mathrm{d}s\\&=\frac{e^{-\eta_n}}{\Delta\eta}\sum_{j=0}^{n-1}\left\{\varsigma^{j+1}\left(e^{\eta_{j+1}}\Delta\eta-e^{\eta_{j+1}}+e^{\eta_j}\right)+\varsigma^{j}\left(-e^{\eta_j}\Delta\eta+e^{\eta_{j+1}}-e^{\eta_j}\right)\right\}.\end{aligned} \tag{31}$$

Similarly,

$$\int_0^{\eta_{n+1}} \kappa(\zeta,\eta-s)\varsigma(\zeta,s)\mathrm{d}s = \frac{e^{-\eta_{n+1}}}{\Delta\eta}\left\{\varsigma^{n+1}\left(e^{\eta_{n+1}}\Delta\eta - e^{\eta_{n+1}} + e^{\eta_n}\right) + \varsigma^n\left(-e^{\eta_n}\Delta\eta + e^{\eta_{n+1}} - e^{\eta_n}\right)\right\} + \frac{e^{-\eta_{n+1}}}{\Delta\eta}\sum_{j=0}^{n-1}\left\{\varsigma^{j+1}\left(e^{\eta_{j+1}}\Delta\eta - e^{\eta_{j+1}} + e^{\eta_j}\right) + \varsigma^j\left(-e^{\eta_j}\Delta\eta + e^{\eta_{j+1}} - e^{\eta_j}\right)\right\}. \tag{32}$$

The temporal semidiscrete form is obtained with the help of equations (32)–(34):

$$\frac{\Delta\eta^{-\vartheta}}{\Gamma(2-\vartheta)}\left[\sum_{m=1}^{n}\left(\varsigma^{m+1}-\varsigma^m\right)\left(\left(n+\frac{3}{2}-m\right)^{1-\vartheta}+\left(n+\frac{1}{2}-m\right)^{1-\vartheta}\right)+\frac{\varsigma^{n+1}-\varsigma^n}{2^{1-\vartheta}}\right] = b\varsigma^n(\zeta)\frac{e^{-\eta_n}+e^{-\eta_{n+1}}}{2\Delta\eta}\sum_{j=0}^{n-1}\left\{\varsigma^{j+1}\left(e^{\eta_{j+1}}\Delta\eta - e^{\eta_{j+1}} + e^{\eta_j}\right) + \varsigma^j\left(-e^{\eta_j}\Delta\eta + e^{\eta_{j+1}} - e^{\eta_j}\right)\right\} + b\varsigma^n(\zeta)\frac{e^{-\eta_{n+1}}}{2\Delta\eta}\left\{\varsigma^{n+1}\left(e^{\eta_{n+1}}\Delta\eta - e^{\eta_{n+1}} + e^{\eta_n}\right) + \varsigma^n\left(-e^{\eta_n}\Delta\eta + e^{\eta_{n+1}} - e^{\eta_n}\right)\right\} + \frac{\partial^2\varsigma^n(\zeta)}{\partial\zeta^2} + a\varsigma^n(\zeta)\left(1-\varsigma^n(\zeta)\right). \tag{33}$$

3.2. Use of Quasi-Wavelet-Based Approximation for the Discretization of Spatial Derivatives. By using the approximation by quasi-wavelets given in Section 2, we discretize the unknown function and its spatial derivatives. The spatial step is chosen as $\Delta\zeta = 1/N$. We denote the value of the unknown function $\varsigma(\zeta,\eta)$ at spatial point ζ_i and time $\eta = t_i$ by ς_i^n with $i = 0,1,\ldots,N$ and $n = 0,1,\ldots,M$. By using the approximation from equation (21), we have

$$\varsigma^n(x_i) = \sum_{p=i-W}^{i+W}\varsigma(\zeta_k,\eta_n)\delta_{\Delta,\sigma}^n(\zeta_i-\zeta_k), \quad n = 0,1,2,\ldots,\ i = 0,1,\ldots,N-1. \tag{34}$$

With the help of equation (33), we can rewrite equation (34) as follows:

$$\begin{aligned}\frac{\Delta\eta^{-\vartheta}}{\Gamma(2-\vartheta)}&\left[\sum_{m=1}^{n}\left(\varsigma^{m+1}-\varsigma^m\right)\left(\left(n+\frac{3}{2}-m\right)^{1-\vartheta}+\left(n+\frac{1}{2}-m\right)^{1-\vartheta}\right)+\frac{\varsigma^{n+1}-\varsigma^n}{2^{1-\vartheta}}\right]\\ &= b\sum_{k=i-W}^{i+W}\varsigma(\zeta_k,\eta_n)\delta_{\Delta,\sigma}(\zeta_i-\zeta_k)\frac{e^{-t\eta_n}+e^{-\eta_{n+1}}}{2\Delta\eta}\sum_{j=0}^{n-1}\left\{\varsigma^{j+1}\left(e^{\eta_{j+1}}\Delta\eta - e^{\eta_{j+1}} + e^{\eta_j}\right) + \varsigma^j\left(-e^{\eta_j}\Delta\eta + e^{\eta_{j+1}} - e^{\eta_j}\right)\right\}\\ &\quad + b\sum_{p=i-W}^{i+W}\varsigma(\zeta_k,\eta_n)\delta_{\Delta,\sigma}(\zeta_i-\zeta_k)\frac{e^{-\eta_{n+1}}}{2\Delta\eta}\\ &\quad\left\{\varsigma^{n+1}\left(e^{\eta_{n+1}}\Delta\eta - e^{\eta_{n+1}} + e^{\eta_n}\right) + \varsigma^n\left(-e^{\eta_n}\Delta\eta + e^{\eta_{n+1}} - e^{\eta_n}\right)\right\} + \sum_{p=i-W}^{i+W}\varsigma(\zeta_k,\eta_n)\delta_{\Delta,\sigma}^2(\zeta_i-\zeta_k) + a\sum_{p=i-W}^{i+W}\varsigma(\zeta_k,\eta_n)\delta_{\Delta,\sigma}(\zeta_i-\zeta_k)\\ &\quad\cdot\left(1-\sum_{p=i-W}^{i+W}\varsigma(\zeta_k,\eta_n)\delta_{\Delta,\sigma}(\zeta_i-\zeta_k)\right).\end{aligned} \tag{35}$$

Considering $x_p - x_i = x_k$, we have the following:

$$\begin{aligned}
&\frac{\Delta\eta^{-\vartheta}}{\Gamma(2-\vartheta)}\left[\sum_{m=1}^{n}\left(\varsigma_i^{m+1}-\varsigma_i^{m}\right)\left(\left(n+\frac{3}{2}-m\right)^{1-\vartheta}+\left(n+\frac{1}{2}-m\right)^{1-\vartheta}\right)+\frac{\varsigma_i^{n+1}-\varsigma_i^{n}}{2^{1-\vartheta}}\right]\\
&\quad= b\sum_{k=-W}^{+W}u_{k+i}^{n}\delta_{\Delta,\sigma}(-k\Delta\zeta)\times\frac{e^{-\eta_n}+e^{-\eta_{n+1}}}{2\Delta\eta}\sum_{j=0}^{n-1}\left\{\varsigma_i^{j+1}\left(e^{\eta_{j+1}}\Delta\eta-e^{\eta_{j+1}}+e^{\eta_j}\right)+\varsigma_i^{j}\left(-e^{\eta_j}\Delta\eta+e^{\eta_{j+1}}-e^{\eta_j}\right)\right\}\\
&\quad+ b\sum_{k=-W}^{+W}u_{k+i}^{n}\delta_{\Delta,\sigma}(-k\Delta\zeta)\times\frac{e^{-\eta_{n+1}}}{2\Delta\eta}\left\{\varsigma_i^{n+1}\left(e^{\eta_{n+1}}\Delta\eta-e^{\eta_{n+1}}+e^{\eta_n}\right)+\varsigma_i^{n}\left(-e^{\eta_n}\Delta\eta+e^{\eta_{n+1}}-e^{\eta_n}\right)\right\}+\\
&\sum_{k=-W}^{+W}u_{k+i}^{n}\delta_{\Delta,\sigma}^{2}(\zeta_i-\zeta_k)+a\sum_{k=-W}^{i+W}u_{k+i}^{n}\delta_{\Delta,\sigma}(-k\Delta\zeta)\left(1-\sum_{k=-W}^{+W}u_{k+i}^{n}\delta_{\Delta,\sigma}(-k\Delta\zeta)\right).
\end{aligned}\tag{36}$$

This is the full discrete form of the taken model in case of the kernel $\kappa(\zeta,\eta)=e^{-\eta}$. For other kernels $\kappa(\zeta,\eta)=1$ and $\kappa(\zeta,\eta)=e^{-\zeta^2 t}$, the discrete form is obtained as follows:

$$\begin{aligned}
&\frac{\Delta\eta^{-\vartheta}}{\Gamma(2-\vartheta)}\left[\sum_{m=1}^{n}\left(\varsigma_i^{m+1}-\varsigma_i^{m}\right)\left(\left(n+\frac{3}{2}-m\right)^{1-\vartheta}+\left(n+\frac{1}{2}-m\right)^{1-\vartheta}\right)+\frac{\varsigma_i^{n+1}-\varsigma_i^{n}}{2^{1-\vartheta}}\right]\\
&\quad= b\left(\frac{\Delta\eta}{4}\sum_{j=0}^{n-1}\left(u_i^{j}+\varsigma_i^{j+1}\right)+\frac{\Delta\eta}{4}\sum_{j=0}^{n}\left(u_i^{j}+\varsigma_i^{j+1}\right)\right)+\sum_{k=-W}^{+W}u_{k+i}^{n}\delta_{\Delta,\sigma}^{2}(\zeta_i-\zeta_k)+a\sum_{k=-W}^{i+W}u_{k+i}^{n}\delta_{\Delta,\sigma}(-k\Delta\zeta)\left(1-\sum_{k=-W}^{+W}u_{k+i}^{n}\delta_{\Delta,\sigma}(-k\Delta\zeta)\right),\\
&\quad\cdot\frac{\Delta\eta^{-\vartheta}}{\Gamma(2-\vartheta)}\left[\sum_{m=1}^{n}\left(\varsigma_i^{m+1}-\varsigma_i^{m}\right)\left(\left(n+\frac{3}{2}-m\right)^{1-\vartheta}+\left(n+\frac{1}{2}-m\right)^{1-\vartheta}\right)+\frac{\varsigma_i^{n+1}-\varsigma_i^{n}}{2^{1-\vartheta}}\right]\\
&\quad= b\sum_{k=-W}^{+W}u_{k+i}^{n}\delta_{\Delta,\sigma}(-k\Delta\zeta)\times\frac{e^{-\eta_{n+1}x_i^2}}{2\Delta\eta}\sum_{j=0}^{n-1}\left\{\varsigma_i^{j+1}\left(\frac{e^{\eta_{j+1}x_i^2}}{x_i^2}\Delta\eta-\frac{e^{\eta_{j+1}x_i^2}}{x_i^4}+\frac{e^{\eta_j x_i^2}}{x_i^4}\right)+u_i^{j}\left(\frac{-e^{\eta_{j+1}x_i^2}}{x_i^2}\Delta\eta+\frac{e^{\eta_{j+1}x_i^2}}{x_i^4}-\frac{e^{\eta_j x_i^2}}{x_i^4}\right)\right\}\\
&\quad+\sum_{k=-W}^{+W}u_{k+i}^{n}\delta_{\Delta,\sigma}^{2}(\zeta_i-\zeta_k)+a\sum_{k=-W}^{i+W}u_{k+i}^{n}\delta_{\Delta,\sigma}(-k\Delta\zeta)\left(1-\sum_{k=-W}^{+W}u_{k+i}^{n}\delta_{\Delta,\sigma}(-k\Delta\zeta)\right).
\end{aligned}\tag{37}$$

The discretization of initial and boundary conditions is performed by adopting a technique because the value of $\varsigma(\zeta_k)$ is not defined outside the domain $[0,1]$:

$$\begin{aligned}
\varsigma(i,n)&=\varsigma_i^{n}=0,\quad i>M, i<0, n=0,1,\ldots,N,\\
u_i^{0}&=f_3(\zeta_i),\quad i=0,1,\ldots,M.
\end{aligned}\tag{38}$$

3.3. Theorem (see [21]). Considering the function $f(\zeta)$ which is a member of the space $L_\infty\cap L_2(\Omega)\cap C^s(\Omega)$ and band limited to B, $s\in Z^+$, $\sigma=\Delta r$, $W\in N$, $W\geq rs/\sqrt{2}$. Then, we have the following required result:

$$\left\|f^s-\sum_{k=-W}^{W}\delta_{\sigma,\Delta}^{s}(\zeta-\zeta_k)f(\zeta_k)\right\|\leq\beta\times\exp\left(\frac{-\gamma^2}{2r^2}\right),\tag{39}$$

where

$$\begin{aligned}
\gamma&=\min\left(r^2(\pi-B\Delta),W\right),\\
\beta&=\left(\sqrt{2B}\,\|f\|_{L_s(\Omega)}+2r\|f\|_{L_\infty(\Omega)}\right)\times\frac{e^{\pi}(s+1)!r}{\gamma\pi\Delta^s}.
\end{aligned}\tag{40}$$

4. Numerical Results and Validation

In this section, we take some numerical examples of the reaction-diffusion equation and the integro reaction-diffusion equation. We show the validity and feasibility by showing the absolute error tables. The formula of finding errors E_r between exact and numerical solutions is as follows:

$$E_r = \left|\varsigma\left(\zeta_i, \eta_j\right) - \tilde{\varsigma}\left(\zeta_i, \eta_j\right)\right|, \tag{41}$$

where $\tilde{\varsigma}(\zeta_i, \eta_j)$ denotes the numerical solution at point (ζ_i, η_j). We do all numerical computation in Wolfram Mathematica version-11.3.

Example 1. We take the following particular case of our model with parameters $a = 1$, $\vartheta = 0.9$, and $b = 0$:

$$\frac{\partial^{\vartheta}\varsigma(\eta,\zeta)}{\partial\eta^{\vartheta}} = \frac{\partial^2\varsigma(\eta,\zeta)}{\partial\zeta^2} + \varsigma(\eta,\zeta)(1-\varsigma(\eta,\zeta)) + f(\zeta,\eta). \tag{42}$$

The initial and boundary conditions are taken as follows:

$$\begin{aligned} \varsigma(\zeta,0) &= \sin(2\pi\zeta), \\ \varsigma(0,\eta) &= 0, \varsigma(1,\eta) = 0. \end{aligned} \tag{43}$$

We determine the force function $f(\zeta,\eta)$ by putting the value of the exact solution $\varsigma(\zeta,\eta) = \sin(2\pi\zeta)/\sqrt{\eta+1}$ in the taken particular case of the model. The graph is plotted for the exact and approximate solutions with parameters' value $M = 30, \Delta\eta = 0.0001$, and $N = 10$ which can be seen in Figure 1. The variation of absolute errors between exact and numerical solutions is depicted in Table 1.

Example 2. Taking the following integro diffusion equation as a particular case of our model with parametric value $\kappa(\zeta,\eta) = 1, a = 0$, $\vartheta = 1$, and $b = 1$:

$$\frac{\partial\varsigma(\eta,\zeta)}{\partial\eta} = \frac{\partial^2\varsigma(\eta,\zeta)}{\partial\zeta^2} - \int_0^{\eta}\varsigma(s,\zeta)\mathrm{d}s + f(\zeta,\eta). \tag{44}$$

The boundary and initial conditions are taken as follows:

$$\begin{aligned} \varsigma(0,\zeta) &= \frac{1}{2}\left(1-\zeta^2\right), \\ \varsigma(\eta,0) &= \frac{\cosh(\eta)}{\sinh^2(\eta)+2}, \\ \varsigma(\eta,1) &= 0. \end{aligned} \tag{45}$$

The exact solution of the above problem is taken as $\varsigma(\zeta,\eta) = (1-\zeta^2)\cosh(\eta)/\sinh^2(\eta) + 2$ while force function $f(\zeta,\eta)$ is chosen with the help of exact solutions and the given problem. The graph is plotted for the numerical and exact solutions with parameters' value $N = 10, M = 30$, and $\Delta\eta = 0.0001$ which can be seen in Figure 2. The variation of absolute errors between exact and numerical solutions is depicted in Table 2.

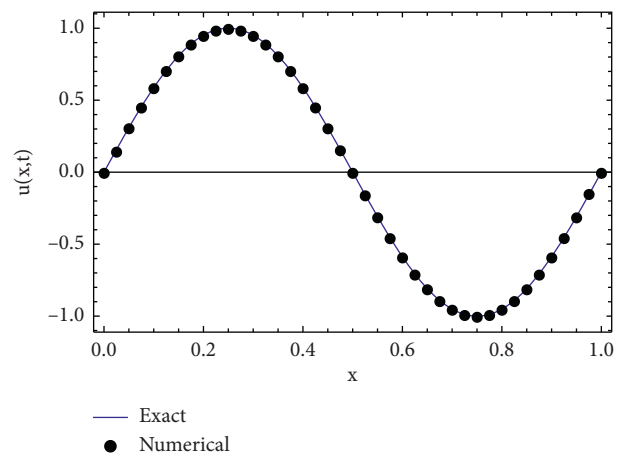

Figure 1: Graph of exact and numerical solutions with parametric value $\varsigma(\zeta,\eta)$ for $M = 30$, $\vartheta = 0.9$, $W = 30$, $\Delta\eta = 0.00001$, and $r = 3.2$.

Table 1: Representation of absolute errors for different M and $\Delta\eta$.

M ↓	$\Delta\eta = 0.0001$	$\Delta\eta = 0.000001$
10	6.50×10^{-2}	3.6×10^{-3}
15	4.5×10^{-2}	1.1×10^{-3}
20	7.60×10^{-3}	1.15×10^{-4}
30	9.10×10^{-4}	2.2×10^{-5}

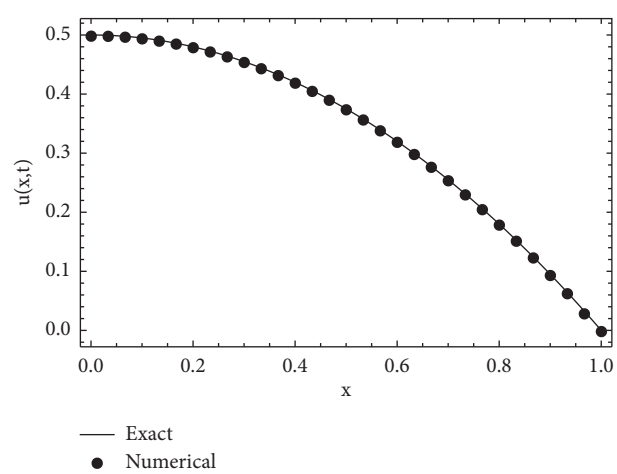

Figure 2: Graph of approximate and exact and numerical solutions with parametric value $\varsigma(\zeta,\eta)$ for $M = 30$, $\vartheta = 1$, $W = 30$, $\Delta\eta = 0.00001$, and $r = 3.2$.

Table 2: Representation of absolute errors for different M and $\Delta\eta$.

M ↓	$\Delta\eta = 0.0001$	$\Delta\eta = 0.000001$
10	9.40×10^{-4}	3.4×10^{-5}
15	7.1×10^{-4}	2.4×10^{-5}
20	4.6×10^{-4}	1.9×10^{-5}
30	4.0×10^{-4}	1.3×10^{-5}

Example 3. If we take $a = 1$, $\vartheta = 1$, $b = 1$, and kernel $\kappa(\eta, \zeta) = e^{-\zeta^2 t}$, then we get

$$\frac{\partial \varsigma(\eta,\zeta)}{\partial \eta} = \frac{\partial^2 \varsigma(\eta,\zeta)}{\partial \zeta^2} + \varsigma(\eta,\zeta)(1-\varsigma(\eta,\zeta)) + \varsigma(\eta,\zeta) \int_0^{\eta} e^{-\zeta^2(\eta,\zeta)} \varsigma(\eta,\zeta) \mathrm{d}s + f(\eta,\zeta). \tag{46}$$

With the following initial and boundary conditions:

$$\varsigma(\zeta,0) = 0, \varsigma(0,\eta) = \sin\eta, \varsigma(1,\eta) = \frac{\sin\eta}{2}. \tag{47}$$

The function $\varsigma(\zeta,\eta) = \sin\eta/1+\zeta^2$ is an exact solution of the problem. The graph is plotted for the numerical and exact solutions with parameters' value $N = 10, M = 30$, and $\Delta\eta = 0.0001$ which can be seen in Figure 3. The variation of absolute errors between exact and numerical solutions is depicted in Table 3.

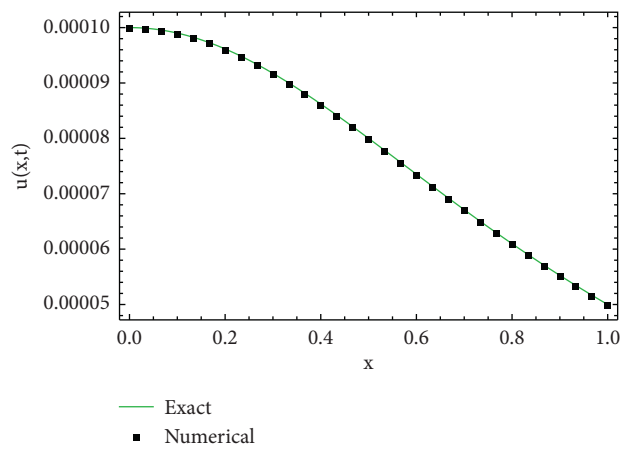

Figure 3: Graph of approximate and exact solutions with parametric value $\varsigma(\zeta,\eta)$ for $\vartheta = 1$, $W = 30$, $\Delta\eta = 0.00001$, $M = 30$, and $r = 3.2$.

Table 3: Representation of absolute errors for different M and $\Delta\eta$.

M ↓	$\Delta\eta = 0.0001$	$\Delta\eta = 0.000001$
10	1.97×10^{-7}	7.4×10^{-13}
15	1.90×10^{-7}	4.8×10^{-13}
20	1.84×10^{-7}	3.5×10^{-13}
30	1.7×10^{-7}	2.2×10^{-13}

Example 4. If we take $\kappa(\eta,\zeta) = e^{-\eta}$, $a = 1$, $\vartheta = 0.9$, and $b = 1$, then our model (42) is reduced to

$$\frac{\partial^{0.9} \varsigma(\eta,\zeta)}{\partial \eta^{0.9}} = \frac{\partial^2 \varsigma(\eta,\zeta)}{\partial \zeta^2} + \varsigma(\eta,\zeta)(1-\varsigma(\eta,\zeta)) + \varsigma(\eta,\zeta) \int_0^{\eta} e^{-(\eta-s)} \varsigma(s,\zeta) \mathrm{d}s + f(\zeta,\eta). \tag{48}$$

The following equations are chosen as initial and boundary conditions:

$$\begin{aligned} \varsigma(\zeta,0) &= \left(1-\zeta^4\right)\sin(\zeta), \\ \varsigma(0,\eta) &= \sin\eta, \\ \varsigma(1,\eta) &= 0, \end{aligned} \tag{49}$$

with the exact solution $\varsigma(\zeta,\eta) = \sin(\eta+\zeta)(1-\zeta^4)$.

The graph is plotted for the exact and approximate solutions with parameters' value $N = 10, M = 30$, and $\Delta\eta = 0.0001$ which can be seen in Figure 4. The variation of absolute errors between exact and numerical solutions is depicted in Table 4. The graphs and error tables clearly show that our numerical results are in feasible and desirable accuracy.

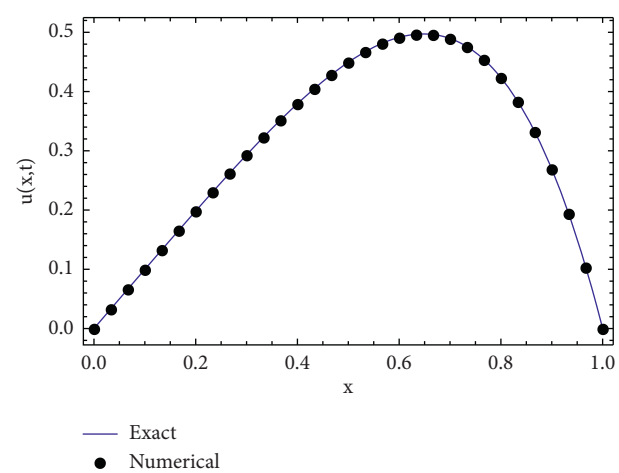

Figure 4: Graph of approximate and exact solutions with parametric value $\varsigma(\zeta,\eta)$ for $M = 30$, $\vartheta = 0.9$, $W = 30$, $\Delta\eta = 0.00001$, and $r = 3.2$.

Table 4: Representation of absolute errors for different M and $\Delta\eta$.

M ↓	$\Delta\eta = 0.0001$	$\Delta\eta = 0.000001$
10	9.80×10^{-4}	4.9×10^{-5}
15	5.5×10^{-4}	3.3×10^{-5}
20	2.90×10^{-4}	2.5×10^{-5}
30	1.50×10^{-4}	1.7×10^{-5}

Example 5. Let us take another example of the Burger–Fisher equation:

$$\frac{\partial \varsigma(\zeta,\eta)}{\partial \eta} = \frac{\partial^2 \varsigma(\zeta,\eta)}{\partial \zeta^2} + \varsigma\frac{\partial \varsigma(\zeta,\eta)}{\partial \zeta} + \varsigma(1-\varsigma), \quad 0 < \zeta < 1,\ \eta > 0, \tag{50}$$

with following initial and boundary conditions:

Table 5: Comparison of absolute errors for our proposed method and the method given in [22].

$(\zeta,\eta)\downarrow$	Our method with $\Delta\eta = 10^{-7}$	Method given in literature
(0.1,1)	$6,9\times10^{-8}$	2.51×10^{-7}
(0.2,1)	5.9×10^{-8}	1.07×10^{-6}
(0.3,1)	3.5×10^{-8}	2.13×10^{-6}
(0.4,1)	6.5×10^{-8}	3.21×10^{-6}
(0.5,1)	5.7×10^{-8}	4.13×10^{-6}
(0.6,1)	4.9×10^{-8}	4.74×10^{-6}
(0.7,1)	8.2×10^{-7}	4.89×10^{-6}
(0.8,1)	1.5×10^{-8}	4.37×10^{-6}
(0.9,1)	4.40×10^{-7}	2.8×10^{-6}

$$\begin{aligned}\varsigma(\zeta,0) &= \frac{1}{2}+\frac{1}{2}\tanh\left(\frac{\zeta}{4}\right),\\ \varsigma(0,\eta) &= \frac{1}{2}+\frac{1}{2}\tanh\left(\frac{5\eta}{8}\right),\\ \varsigma(1,\eta) &= \frac{1}{2}+\frac{1}{2}\tanh\left(\frac{1}{4}\left(1+\frac{5\eta}{2}\right)\right),\end{aligned} \tag{51}$$

where the exact solution of the above problem is $(1/2)+(1/2)\tanh((1/4)(\zeta+5\eta/2))$. Now, our obtained numerical results are compared with the results given in [22].

5. Conclusion

In this research work, we developed a numerical scheme for time-fractional partial differential equations and integro fractional partial differential equations. The discretization of the time-fractional derivative is done by using the Crank–Nicolson scheme, and the discretization of the unknown function and its spatial derivatives is performed with the help of the quasi-wavelet-based numerical method. For different kernels, we show the validity and effectiveness of our method. Our method has a good accuracy for both fractional PDEs and fractional integro PDEs as seen from the error tables. The same can be seen by the plotted graph for the existing exact solution and numerical solution.

Data Availability

No data were used to support this study.

Conflicts of Interest

The authors declare that there are no conflicts of interest.

Acknowledgments

This work was supported by the National Natural Science Foundation of China (61673247) and the Research Fund for Distinguished Young Scholars and Excellent Young Scholars of Shandong Province (JQ201719).

References

[1] X. Lv, R. Rakkiyappan, R. Rakkiyappan, and X. Li, "m-stability criteria for nonlinear differential systems with additive leakage and transmission time-varying delays," *Nonlinear Analysis: Modelling and Control*, vol. 23, no. 3, pp. 380–400, 2018.

[2] A. Vinodkumar, T. Senthilkumar, and X. Li, "Robust exponential stability results for uncertain infinite delay differential systems with random impulsive moments," *Advances in Difference Equations*, no. 1, p. 39, 2018.

[3] A. Kilbas, H. Srivastava, and J. J. Trujillo, *Theory and Applications of the Fractional Differential Equations*, Vol. 204, Elsevier, Amsterdam, Netherlands, 2006.

[4] I. Podlubny, *Fractional Differential Equations, to Methods of Their Solution and Some of Their Applications, Fractional Differential Equations: An Introduction to Fractional Derivatives*, Academic Press, San Diego, CA, USA, 1998.

[5] P. Darania and A. Ebadian, "A method for the numerical solution of the integro-differential equations," *Applied Mathematics and Computation*, vol. 188, no. 1, pp. 657–668, 2007.

[6] K. Diethelm, N. J. Ford, and A. D. Freed, "A predictor-corrector approach for the numerical solution of fractional differential equations," *Nonlinear Dynamics*, vol. 29, no. 1–4, pp. 3–22, 2002.

[7] L. Suarez and A. Shokooh, "An eigenvector expansion method for the solution of motion containing fractional derivatives," *Journal of Applied Mechanics*, vol. 64, p. 9, 1997.

[8] S. Kumar and D. Baleanu, "Numerical solution of two-dimensional time fractional cable equation with mittag-leffler kernel," *Mathematical Methods in the Applied Sciences*, vol. 43, no. 15, pp. 8348–8362, 2020.

[9] S. Kumar, P. Pandey, and S. Das, "Gegenbauer wavelet operational matrix method for solving variable-order non-linear reaction–diffusion and galilei invariant advection–diffusion equations," *Computational and Applied Mathematics*, vol. 38, no. 4, p. 162, 2019.

[10] Y. Li and W. Zhao, "Haar wavelet operational matrix of fractional order integration and its applications in solving the fractional order differential equations," *Applied Mathematics and Computation*, vol. 216, no. 8, pp. 2276–2285, 2010.

[11] L. Yuanlu, "Solving a nonlinear fractional differential equation using Chebyshev wavelets," *Communications in Nonlinear Science and Numerical Simulation*, vol. 15, no. 9, pp. 2284–2292, 2010.

[12] H. Jafari, S. A. Yousefi, M. A. Firoozjaee, S. Momani, and C. M. Khalique, "Application of legendre wavelets for solving fractional differential equations," *Computers & Mathematics with Applications*, vol. 62, no. 3, pp. 1038–1045, 2011.

[13] B. Liu and D. J. Hill, "Stability via hybrid-event-time Lyapunov function and impulsive stabilization for discrete-time delayed switched systems," *SIAM Journal on Control and Optimization*, vol. 52, no. 2, pp. 1338–1365, 2014.

[14] B. Liu, D. J. Hill, Z. Sun, and J. Huang, "Event-triggered control via impulses for exponential stabilization of discrete-time delayed systems and networks," *International Journal of Robust and Nonlinear Control*, vol. 29, no. 6, pp. 1613–1638, 2019.

[15] X. Li, X. Yang, and T. Huang, "Persistence of delayed cooperative models: impulsive control method," *Applied Mathematics and Computation*, vol. 342, pp. 130–146, 2019.

[16] D. Yang, X. Li, J. Shen, and Z. Zhou, "State-dependent switching control of delayed switched systems with stable and

unstable modes," *Mathematical Methods in the Applied Sciences*, vol. 41, no. 16, pp. 6968–6983, 2018.

[17] X. Zhang, X. Li, and X. Han, "Design of hybrid controller for synchronization control of chen chaotic system," *The Journal of Nonlinear Sciences and Applications*, vol. 10, no. 6, pp. 3320–3327, 2017.

[18] D. Tavares, R. Almeida, and D. F. M. Torres, "Caputo derivatives of fractional variable order: numerical approximations," *Communications in Nonlinear Science and Numerical Simulation*, vol. 35, pp. 69–87, 2016.

[19] G. W. Wei, "Discrete singular convolution for the solution of the Fokker-Planck equation," *The Journal of Chemical Physics*, vol. 110, no. 18, pp. 8930–8942, 1999.

[20] X. Yang, D. Xu, and H. Zhang, "Quasi-wavelet based numerical method for fourth-order partial integro-differential equations with a weakly singular kernel," *International Journal of Computer Mathematics*, vol. 88, no. 15, pp. 3236–3254, 2011.

[21] L. Qian, "On the regularized Whittaker-Kotel'nikov-Shannon sampling formula," *Proceedings of the American Mathematical Society*, vol. 131, no. 4, pp. 1169–1176, 2003.

[22] S. Kumar, P. Pandey, and S. Das, "Operational matrix method for solving nonlinear space-time fractional order reaction-diffusion equation based on genocchi polynomial," *Special Topics & Reviews in Porous Media: An International Journal*, vol. 11, no. 1, pp. 33–47, 2020.

Hindawi
Complexity
Volume 2020, Article ID 5048925, 7 pages
https://doi.org/10.1155/2020/5048925

Research Article

Nonparametric Range-Based Double Smoothing Spot Volatility Estimation for Diffusion Models

Jingwei Cai

School of Science, Jinling Institute of Technology, Nanjing 211169, China

Correspondence should be addressed to Jingwei Cai; jingwei_cai@126.com

Received 16 June 2020; Accepted 29 August 2020; Published 21 September 2020

Academic Editor: Ruofeng Rao

We consider nonparametric spot volatility estimation for diffusion models with discrete high frequency observations. Our estimator is carried out in two steps. First, using the local average of the range-based variance, we propose a crude estimator of the spot volatility. Second, we use usual nonparametric kernel smoothing to reconstruct the volatility function from the crude estimator. By inference, we find such a double smoothing operation can effectively reduce the estimation error.

1. Introduction

In recent years, stochastic differential equations have been widely studied by many researchers and some interesting results have appeared in the literature (see [1–5] and references therein). In particular, as a kind of stochastic differential equations, diffusion processes are usually involved in many popular models in financial mathematics, statistics, and econometrics. These models are widely used in option pricing, hedging, interest rate (exchange rate) modelling, and engineering management.

We consider a class of diffusion process as follows:

$$X_t = X_0 + \int_0^t \alpha_u \mathrm{d}u + \int_0^t \beta_u \mathrm{d}W_u, t \in [0, T], \tag{1}$$

with an initial condition X_0, where $\{X_t\}_{t\geq 0}$ solves the equation and is often used to describe the logarithmic price of a security. $\{W_t\}_{t\geq 0}$ is a standard Brownian motion. The continuous process $\{\alpha_t\}_{t\geq 0}$ and $\{\beta_t\}_{t\geq 0}$ are the drift term and the diffusion term (spot volatility) of the process $\{X_t\}_{t\geq 0}$.

Consider an arbitrary partition: $0 = t_0 < t_1 < t_2 < \cdots < t_n = T$. For any nonnegative integer $i\,(0 \leq i \leq n)$, we define $\delta_i = t_i - t_{i-1}$. For the sake of discussion, it is assumed that sample observations are selected at equal time interval, and the time interval between adjacent sample observations can be denoted as $\delta = T/n$; hence, $t_i = iT/n$. For the case of unequal time interval, it is enough to define $\delta = \max_{0\leq i\leq n}\{t_i - t_{i-1}\}$.

As it is known to all, volatility is very important in the derivative securities pricing, its correct estimation is the basis of reasonable pricing derivatives. In view of the robustness and accuracy of the nonparametric approach in modelling, many scholars use this approach to estimate volatility (see [6–8]). However, most of the nonparametric volatility estimation works were conducted around integral volatility (see [9, 10]).

Constraining a kernel function and choosing appropriate bandwidth parameters, Kristensen [11] proposed a filtered kernel-based spot volatility estimator for time-dependent diffusion models:

$$\widehat{\beta}_\tau^2 = \frac{1}{h}\sum_{i=1}^{n} K\left(\frac{t_i - \tau}{h}\right)\left(X_{t_i} - X_{t_{i-1}}\right)^2, \tag{2}$$

where $K(\cdot)$ and h were the kernel function and its bandwidth, respectively. Under certain conditions, they showed the following central limit theorem:

$$\sqrt{\frac{h}{\delta}}\left(\widehat{\beta}_\tau^2 - \beta_\tau^2\right) \xrightarrow{d} N\left(0, 2\beta_\tau^4 \int_R K^2(s)\mathrm{d}s\right). \tag{3}$$

Similar to Kristensen [11], Renault et al. [12] proposed a spot volatility estimator which can approach the

nonparametric bound arbitrarily with unevenly spaced data at hand. By using multiple observations, Liu et al. [13] provided an "ideal" preaveraging estimator, established its asymptotic distribution, and considered the asymptotic efficiency of the proposed estimator. Recently, more and more scholars began to consider estimating spot volatility (see [14–16]), and spot volatility inference has become a hot issue in the field of regression dynamic research. Under microstructure noise or Poisson jumps, based on delta sequences, Mancini et al. [17] prevented a nonparametric estimation method of spot volatility. Taking into account fixed time-horizon and infill asymptotics, they obtained the full limit theory under unequally sample observation. Under the coexistence of market microstructure noise and multiple transactions, with high frequency data, Liu et al. [18] gave a spot volatility estimation procedure by taking the sum from the local range increments and discussed the estimator's consistency and asymptotic normality. Similar literatures include [19], among others.

Range-based volatility estimation technique is an effective method; Alizadeh et al. [20] revealed this theoretically, practically, and numerically. Christensen and Podolskij [21] defined the range in $[t_{i-1}, t_i]$ as

$$r_{X_{t_i,\delta}} = \sup_{t_{i-1}\le\varsigma,\tau\le t_i} \left\{X_\varsigma - X_\tau\right\}. \tag{4}$$

They replaced realized return-based variance with range-based variance, and they found that the latter had higher accuracy. For a scaled Brownian motion $X_t = \beta W_t$, Parkinson [22] proposed the pth moment generating function of its range in $[t_{i-1}, t_i]$ as

$$E\left[r^p_{X_{t_i,\delta}}\right] = \lambda_p \delta_i^{p/2} \beta^p \ (p \ge 1), \tag{5}$$

where $\lambda_p = E[r^p_{W_{1,1}}]$.

Christensen and Podolskij [23] provided a range-based multipower variation theory for diffusion models with jumps and showed that their theory was more efficient than returned-based estimators. Recent literatures included but not limited to [24–27].

If we substitute $r^2_{X_{t_i,\delta}}/\lambda_2$ for the square increment $(X_{t_i} - X_{t_{i-1}})^2$ in equation (2), we may propose a range-based spot volatility:

$$\widehat{\beta}^2_\tau = \frac{1}{h\lambda_2} \sum_{i=1}^{n} K\left(\frac{t_i - \tau}{h}\right) r^2_{X_{t_i,\delta}}. \tag{6}$$

Accordingly, we also may provide the following central limit theorem:

$$\sqrt{\frac{h}{\delta}}\left(\widehat{\beta}^2_\tau - \beta^2_\tau\right) \xrightarrow{d} N\left(0, \Lambda_2 \beta^4_\tau \int_R K^2(s)\mathrm{d}s\right), \tag{7}$$

where $\Lambda_2 = (\lambda_4 - \lambda_2^2)/\lambda_2^2$.

Bandi and Phillips [28] used double smoothing technique to estimate drift and diffusion function and proposed their robust and reliable spot volatility estimator in which they took both infill asymptotics and long span one into account. Song [29] expanded this technique to the diffusion models with jumps and illustrated that this two-step smoothing estimator could narrow mean-squared error effectively. It is not difficult to find that the diffusion models in the above three literatures are both homogeneous. As far as we know, so far, few scholars have applied the double smoothing method to time-dependent diffusion models.

In this paper, the double smoothing technique is used to estimate the spot volatility of time-dependent diffusion models, and the consistency and asymptotic normality of the estimator are obtained. Compared with single smoothing, the double smoothing method has less error and less information loss. Our consideration is twofold. First, in the first step smoothing, we estimate the spot volatility at any time point by calculating local average of square of the range within a suitable time interval. This allows us to replicate as much as possible the actual features of the volatility function. Using the crude estimator obtained from the first smoothing, we then re-estimate the volatility function by means of usual kernel smoothing. Second, the inferiority on choosing moderate frequency data can be effectively overcome by using the range-based technique. Indeed, the return-based technique is a simple and convenient method to estimate volatility function; however, its disadvantages cannot be ignored either. When the sampling frequency is increased, the high frequency data is easily affected by microscopic noise. With high frequency data at hand, the range-based estimator is more precise than the return-based one.

2. Nonparametric Range-Based Double Smoothing Spot Volatility Estimation

Define

$$\begin{aligned} t_{i,1} &= \inf\left\{t \ge 0\colon \left|t - t_i\right| \le \varepsilon\right\}, \\ t_{i,(j+1)} &= \inf\left\{t \ge t_{i,j} + \delta\colon \left|t - t_i\right| \le \varepsilon\right\}, \end{aligned} \tag{8}$$

where ε satisfies $\varepsilon = o_P(1)$ and $\delta/\varepsilon = o_P(1)$. For any $i\,(0 \le i \le n)$, define

$$m_i = \sum_{j=1}^{n} I_{\left\{\left|t_{i,j} - t_i\right| \le \varepsilon\right\}} = \left\lfloor \frac{2\varepsilon}{\delta} \right\rfloor + 1, \tag{9}$$

where $I_{\{\cdot\}}$ and $\lfloor\cdot\rfloor$ denote indicative function and rounding function, respectively.

Remark 1. As a matter of fact, when $i < \lfloor \varepsilon/\delta \rfloor$ or $i > n - \lfloor \varepsilon/\delta \rfloor$, it has $m_i < \lfloor 2\varepsilon/\delta \rfloor + 1$. Fortunately, this is only a small number of cases. Therefore, without loss of generality, for any $i\,(0 \le i \le n)$, we suppose $m_i = \lfloor 2\varepsilon/\delta \rfloor + 1$ and $2\varepsilon/\delta$ is an integer, then $m_i = 2\varepsilon/\delta + 1$ ($m = 2\varepsilon/\delta + 1$ for short).

Some of the technical conditions necessary are given below, which are common in estimating volatility.

T1 The process $\{\alpha_t\}_{t\ge 0}$ satisfies

$$\sup_{0<t<T} \left|\alpha_t\right| < \infty. \tag{10}$$

T2 The process $\{\beta_t\}_{t\geq 0}$ is differentiable and satisfies

$$\sup\left\{\left|\beta_s-\beta_t\right|, s,t\in[0,T], |s-t|\leq\xi\right\}=O_P\left(\xi^{1/2}|\log\xi|^{1/2}\right)\quad \sup_{0\leq t\leq T}\beta_t^2<\infty. \tag{11}$$

T3 The bandwidth h satisfies

$$h\sim\frac{\delta^{1/2}}{\log(1/\delta)}. \tag{12}$$

T4 Kernel function $K(\cdot)$ is differentiable with support $[-1,1]$ and satisfies

$$\begin{aligned}&\text{(i)}\ \int_{-1}^{1}K(c)\mathrm{d}c=1,\\&\text{(ii)}\ \int_{-1}^{1}K'(c)\mathrm{d}c<\infty,\\&\text{(iii)}\ \int_{-1}^{1}K^2(c)\mathrm{d}c<\infty,\\&\text{(iv)}\ \int_{-1}^{1}K^3(c)\mathrm{d}c<\infty.\end{aligned} \tag{13}$$

Remark 2. As we know, the drift parameter is not important in volatility estimation, so we restrict it simply and indispensably in condition T1.

Remark 3. Condition T2 is a common assumption about the diffusion parameter. The same or similar assumptions are used in [16, 30].

Remark 4. Bandwidth selection is very important in kernel-based estimators. Condition T3 chooses the same bandwidth as [30].

Now, we denote the nonparametric range-based double smoothing spot volatility estimator of β_t^2 as

$$\widehat{\beta}_t^2=\frac{\delta}{h}\sum_{i=1}^{n}K\left(\frac{t_i-t}{h}\right)\cdot\breve{\beta}_{t_i}^2, \tag{14}$$

where

$$\breve{\beta}_{t_i}^2=\frac{1}{\delta m\lambda_2}\sum_{j=1}^{m}r_{X_{t_{i,j},\delta}}^2. \tag{15}$$

Remark 5. In equation (15), we take a certain point as the midpoint and set a reasonable period, during which the volatility is only a function of state variables and has nothing to do with time. By calculating a local average of the range square in the time period and supposing it as the initial value of the spot volatility estimator at the time point, the real characteristics of volatility can be reproduced as much as possible. At the same time, the complete sample data are used in ranges to ensure the integrity of information.

3. The Consistency and the Asymptotic Normality of the Estimator

Theorem 1. *Assume that the process $\{X_t\}_{t\geq 0}$ satisfies the model in equation (1) and conditions T1–T4 hold; then, as $\delta\longrightarrow 0$,*

$$\widehat{\beta}_t^2\xrightarrow{P}\beta_t^2. \tag{16}$$

Proof. $\widehat{\beta}_t^2$ can be decomposed into $A+B$, where

$$\begin{aligned}A&=\frac{\delta}{h}\sum_{i=1}^{n}K\left(\frac{t_i-t}{h}\right)\cdot\left(\breve{\beta}_{t_i}^2-\beta_{t_i}^2\right),\\B&=\frac{\delta}{h}\sum_{i=1}^{n}K\left(\frac{t_i-t}{h}\right)\cdot\beta_{t_i}^2.\end{aligned} \tag{17}$$

We discuss the term B first. It can be further decomposed into $B_1+B_2+B_3$, where

$$\begin{aligned}B_1&=\frac{1}{h}\sum_{i=1}^{n}\beta_{t_i}^2\int_{t_{i-1}}^{t_i}\left(K\left(\frac{t_i-t}{h}\right)-K\left(\frac{u-t}{h}\right)\right)\mathrm{d}u,\\B_2&=\frac{1}{h}\sum_{i=1}^{n}\int_{t_{i-1}}^{t_i}K\left(\frac{u-t}{h}\right)\left(\beta_{t_i}^2-\beta_u^2\right)\mathrm{d}u,\\B_3&=\frac{1}{h}\sum_{i=1}^{n}\int_{t_{i-1}}^{t_i}K\left(\frac{u-t}{h}\right)\beta_u^2\mathrm{d}u.\end{aligned} \tag{18}$$

For B_1, using Tylor's formula, we can obtain

$$\begin{aligned}B_1&=\frac{1}{h}\sum_{i=1}^{n}\beta_{t_i}^2\int_{t_{i-1}}^{t_i}\left(K'\left(\frac{u-t}{h}\right)\cdot\frac{t_i-u}{h}+o\left(\frac{t_i-u}{h}\right)\right)\mathrm{d}u\\&=O_P\left(\frac{\delta}{h^2}\int_0^T K'\left(\frac{u-t}{h}\right)\mathrm{d}u\right)\\&=O_P\left(\frac{\delta}{h}\int_{-1}^{1}K'(s)\mathrm{d}s\right).\end{aligned} \tag{19}$$

By the conditions of T3 and T4 (ii), we can get $B_1=O_P(\delta/h)=O_P=(1)$. From the conditions of T2 and T4 (i), it is obvious that $B_2=\delta^{1/2}|\log\delta|^{1/2}=o_P(1)$. Consider B_3 term below. Let

$$\frac{u-t}{h}=s. \tag{20}$$

Then,

$$\begin{aligned} B_3 &= \int_{-1}^{1} K(s)\beta_{sh+t}^2 \mathrm{d}s \\ &= \int_{-1}^{1} K(s)\left(\beta_t^2 + O_P\left(h^{1/2}|\log h|^{1/2}\right)\right)\mathrm{d}s \\ &= \beta_t^2 + O_P\left(h^{1/2}|\log h|^{1/2}\right). \end{aligned} \tag{21}$$

Combining B_1, B_2 with B_3, we have $B \longrightarrow^P \beta_t^2$. In order to prove Theorem 1, we just have to prove $A \longrightarrow^P 0$, namely, $\breve{\beta}_{t_i}^2 \longrightarrow^P \beta_{t_i}^2$. Let

$$\omega_{i,j} = \frac{1}{\delta m \lambda_2}\beta_{t_i}^2 r_{W_{i,j},\delta}^2. \tag{22}$$

It can be known from equation (5) that

$$\sum_{j=1}^{m} E\left[\omega_{i,j}\right] = \beta_{t_i}^2. \tag{23}$$

Now, suppose

$$\theta_{i,j} = \omega_{i,j} - E\left[\omega_{i,j}\right], \tag{24}$$

we can obtain

$$E\left[\theta_{i,j}^2\right] = \frac{\Lambda}{m^2}\beta_{t_i}^4, \tag{25}$$

where $\Lambda = (\lambda_4 - \lambda_2^2)/\lambda_2^2$. Furthermore,

$$\sum_{j=1}^{m} E\left[\theta_{i,j}^2\right] \xrightarrow{P} 0. \tag{26}$$

Therefore,

$$\sum_{j=1}^{m} \omega_{i,j} \xrightarrow{P} \beta_{t_i}^2. \tag{27}$$

Next, we prove $\breve{\beta}_{t_i}^2 \longrightarrow^P \sum_{j=1}^{m} \omega_{i,j}$. Notice that

$$\begin{aligned} \breve{\beta}_{t_i}^2 - \sum_{j=1}^{m} \omega_{i,j} &= \frac{1}{\delta m \lambda_2}\sum_{j=1}^{m}\left(r_{X_{t_{i,j},\delta}} + \beta_{t_i} r_{W_{t_{i,j},\delta}}\right)\left(r_{X_{t_{i,j},\delta}} - \beta_{t_i} r_{W_{t_{i,j},\delta}}\right) \\ &= D_1 + D_2, \end{aligned} \tag{28}$$

where

$$\begin{aligned} D_1 &= \frac{1}{\delta m \lambda_2}\sum_{j=1}^{m}\left(r_{X_{t_{i,j},\delta}} - \beta_{t_i} r_{W_{t_{i,j},\delta}}\right)^2, \\ D_2 &= \frac{2}{\delta m \lambda_2}\sum_{j=1}^{m}\left(r_{X_{t_{i,j},\delta}} - \beta_{t_i} r_{W_{t_{i,j},\delta}}\right)\beta_{t_i} r_{W_{t_{i,j},\delta}}. \end{aligned} \tag{29}$$

For D_1, we further decompose it as follows:

$$\begin{aligned} D_1 &\le \frac{1}{\delta m \lambda_2}\sum_{j=1}^{m}\left(\sup_{t_{i,(j-1)}\le \varsigma, \tau \le t_{i,j}}\left|\int_{\varsigma}^{\tau}\alpha_u \mathrm{d}u + \int_{\varsigma}^{\tau}\left(\beta_u - \beta_{t_i}\right)\mathrm{d}W_u\right|\right)^2 \\ &\le \frac{2}{\delta m \lambda_2}\sum_{j=1}^{m}\left(\sup_{t_{i,(j-1)}\le \varsigma, \tau \le t_{i,j}}\left|\int_{\varsigma}^{\tau}\alpha_u \mathrm{d}u\right|\right)^2 \\ &\quad + \frac{2}{\delta m \lambda_2}\sum_{j=1}^{m}\left(\sup_{t_{i,(j-1)}\le \varsigma, \tau \le t_{i,j}}\left|\int_{\varsigma}^{\tau}\left(\beta_u - \beta_{t_i}\right)\mathrm{d}W_u\right|\right)^2 \\ &= D_{1,1} + D_{1,2}. \end{aligned} \tag{30}$$

From condition T1, it is obvious that $D_{1,1} = O_P(\delta)$. For $D_{1,2}$, by the Burkholder–Davis–Gundy inequality (BDG inequality for short), there exists a constant $C(>0)$ to make

$$E\left[D_{1,2}\right] \le \frac{2C}{\delta m \lambda_2}\sum_{j=1}^{m} E\left[\int_{t_{i,(j-1)}}^{t_{i,j}}\left(\beta_u - \beta_{t_i}\right)^2 \mathrm{d}u\right]. \tag{31}$$

By the condition of T2 and the definition of $t_{i,j}$, we can obtain

$$E\left[D_{1,2}\right] = O_P(\varepsilon \log|\varepsilon|). \tag{32}$$

Therefore, $D_1 = o_P(1)$. For D_2, using the decomposition similar to D_1, it holds that

$$D_2 \le \frac{2}{\delta m \lambda_2}\sum_{j=1}^{m}\beta_{t_i} r_{W_{t_{i,j},\delta}}\left(\sup_{t_{i,(j-1)}\le \varsigma, \tau \le t_{i,j}}\left|\int_{\varsigma}^{\tau}\alpha_u du + \int_{\varsigma}^{\tau}\left(\beta_u - \beta_{t_i}\right)\mathrm{d}W_u\right|\right). \tag{33}$$

Using Hölder's inequality, we obtain

$$\begin{aligned} D_2 &\le 2\left(\frac{1}{\delta m \lambda_2}\sum_{j=1}^{m}\left(\beta_{t_i} r_{W_{t_{i,j},\delta}}\right)^2\right)^{1/2} \\ &\quad \cdot \left(\frac{1}{\delta m \lambda_2}\sum_{j=1}^{m}\left(\sup_{t_{i,(j-1)}\le \varsigma, \tau \le t_{i,j}}\left|\int_{\varsigma}^{\tau}\alpha_u \mathrm{d}u + \int_{\varsigma}^{\tau}\left(\beta_u - \beta_{t_i}\right)\mathrm{d}W_u\right|\right)^2\right)^{1/2}. \end{aligned} \tag{34}$$

Using Hölder's inequality again, we may further obtain

$$\begin{aligned} E[D_2] &\le 2\left(E\left[\frac{1}{\delta m \lambda_2}\sum_{j=1}^{m}\left(\beta_{t_i} r_{W_{t_{i,j},\delta}}\right)^2\right]\right)^{1/2} \\ &\quad \cdot \left(E\left[\frac{1}{\delta m \lambda_2}\sum_{j=1}^{m}\left(\sup_{t_{i,(j-1)}\le \varsigma, \tau \le t_{i,j}}\left|\int_{\varsigma}^{\tau}\alpha_u \mathrm{d}u + \int_{\varsigma}^{\tau}\left(\beta_u - \beta_{t_i}\right)\mathrm{d}W_u\right|\right)^2\right]\right)^{1/2}. \end{aligned} \tag{35}$$

From the discussion of D_1, it is true that $E[D_2] = O_P(\varepsilon^{1/2}|\log \varepsilon|^{1/2})$. So, $\breve{\beta}_{t_i}^2 - \sum_{j=1}^{m}\omega_{i,j} \longrightarrow^P 0$, and these complete the proof. □

Theorem 2. *Assume that the process $\{X_t\}_{t\geq 0}$ satisfies the model in equation (1) and the condition T1–T4 hold, given $\delta \longrightarrow 0$, such that*

$$\frac{\varepsilon h^2|\log h|}{\delta^2} = o_P(1). \tag{36}$$

$$\frac{h\varepsilon^2|\log \varepsilon|}{\delta^2} = o_P(1). \tag{37}$$

Then,

$$\frac{\sqrt{\varepsilon h}}{\delta}\left(\widehat{\beta}_t^2 - \beta_t^2\right) \xrightarrow{P} N\left(0, \frac{\Lambda_2\beta_t^4}{2}\int_{-1}^{1} K^2(s)\mathrm{d}s\right), \tag{38}$$

where $\Lambda_2 = (\lambda_4 - \lambda_2^2)/\lambda_2^2$.

Proof. Decompose $(\widehat{\beta}_t^2 - \beta_t^2)$ as follows:

$$\begin{aligned}\widehat{\beta}_t^2 - \beta_t^2 &= \left(\widehat{\beta}_t^2 - \frac{\delta}{h}\sum_{i=1}^{n} K\left(\frac{t_i - t}{h}\right)\cdot\sum_{j=1}^{m}\omega_{i,j}\right)\\ &\quad + \frac{\delta}{h}\sum_{i=1}^{n} K\left(\frac{t_i - t}{h}\right)\cdot\sum_{j=1}^{m}\theta_{i,j}\\ &\quad + \left(\frac{\delta}{h}\sum_{i=1}^{n} K\left(\frac{t_i - t}{h}\right)\cdot\sum_{j=1}^{m}E\left[\omega_{i,j}\right] - \beta_t^2\right)\\ &= F_1 + F_2 + F_3.\end{aligned} \tag{39}$$

By the proof of Theorem 1, we know

$$\begin{aligned}F_1 &= O_P\left(\varepsilon^{1/2}|\log\varepsilon|^{1/2}\right),\\ F_3 &= O_P\left(h^{1/2}|\log h|^{1/2}\right).\end{aligned} \tag{40}$$

It can be seen from equations (36) and (37) that

$$\begin{aligned}\frac{\sqrt{\varepsilon h}}{\delta}F_1 &= o_P(1),\\ \frac{\sqrt{\varepsilon h}}{\delta}F_3 &= o_P(1).\end{aligned} \tag{41}$$

Now, we discuss

$$\frac{\sqrt{\varepsilon h}}{\delta}F_2 = \sqrt{\frac{\varepsilon}{h}}\sum_{i=1}^{n} K\left(\frac{t_i - t}{h}\right)\sum_{j=1}^{m}\theta_{i,j}. \tag{42}$$

Let

$$\rho_i = \sqrt{\frac{\varepsilon}{h}}K\left(\frac{t_i - t}{h}\right)\sum_{j=1}^{m}\theta_{i,j}. \tag{43}$$

For $\forall i(=1,2,\ldots,n)$, $j,k(=1,2,\ldots,m)$, as $j\neq k$, $\theta_{i,j}$ and $\theta_{i,k}$ are independent of each other, so

$$\begin{aligned}E\left[\rho_i^2\right] &= \frac{\varepsilon}{h}K^2\left(\frac{t_i - t}{h}\right)\sum_{j=1}^{m}E\left[\theta_{i,j}^2\right]\\ &= \frac{\varepsilon\Lambda}{mh}K^2\left(\frac{t_i - t}{h}\right)\beta_{t_i}^4.\end{aligned} \tag{44}$$

Furthermore,

$$\begin{aligned}\sum_{i=1}^{n}E\left[\rho_i^2\right] &= \frac{\varepsilon\Lambda}{mh}\sum_{i=1}^{n}K^2\left(\frac{t_i - t}{h}\right)\beta_{t_i}^4\\ &= \frac{\varepsilon\Lambda}{mh}\sum_{i=1}^{n}K^2\left(\frac{t_i - t}{h}\right)\left(\left(\beta_{t_i}^4 - \beta_t^4\right) + \beta_t^4\right)\\ &= \frac{\varepsilon\Lambda}{m\delta}\left(\beta_t^4\int_{-1}^{1}K^2(s)\mathrm{d}s + O_P(h|\log h|)\right)\\ &\xrightarrow{P} \frac{\Lambda\beta_t^4}{2}\int_{-1}^{1}K^2(s)\mathrm{d}s.\end{aligned} \tag{45}$$

Similarly,

$$\begin{aligned}\sum_{i=1}^{n}E\left[\rho_i^3\right] &= \frac{\varepsilon^{3/2}}{h^{3/2}}\sum_{i=1}^{n}K^3\left(\frac{t_i - t}{h}\right)\sum_{j=1}^{m}E\left[\theta_{i,j}^3\right]\\ &= \frac{\varepsilon^{3/2}}{h^{3/2}}\sum_{i=1}^{n}K^3\left(\frac{t_i - t}{h}\right)\frac{\beta_{t_i}^6}{m^2}\frac{\lambda_6 - 3\lambda_4\lambda_2 + 2\lambda_2^3}{\lambda_2^3}\\ &= \frac{\lambda_6 - 3\lambda_4\lambda_2 + 2\lambda_2^3}{\lambda_2^3}\\ &\quad\cdot\frac{\varepsilon^{3/2}}{m^2h^{1/2}\delta}\left(\beta_t^6\int_{-1}^{1}K^3(s)\mathrm{d}s + O_P(h|\log h|)\right).\end{aligned} \tag{46}$$

From Remark 1 and condition T4 (iv), it holds that

$$\sum_{i=1}^{n}E\left[\rho_i^3\right] = O\left(\frac{\delta}{\varepsilon^{1/2}h^{1/2}}\right) = o_P(1). \tag{47}$$

It can be obtained from Lyapunov's central limit theorem that

$$\frac{\sqrt{\varepsilon h}}{\delta}F_2 \xrightarrow{d} N\left(0, \frac{\Lambda\beta_t^4}{2}\int_{-1}^{1}K^2(s)\mathrm{d}s\right). \tag{48}$$

Remark 6. When we choose $\varepsilon = \delta|\log\delta|$, equations (36) and (37) are both satisfied. Then, it holds that $m = 2\lfloor|\log\delta|\rfloor + 1$. From equation (38), we can find that the greater the ε you choose, the higher the accuracy of the estimator you will obtain. Therefore, the optimal ε is its maximum, satisfying equations (36) and (37).

Remark 7. In equation (3), the constant in front of $\beta_\tau^4\int_R K^2(s)\mathrm{d}s$ is 2 while the constant at the corresponding position in equation (7) is $\Lambda_2 \approx 0.4$ (see [21]), so the precision of the range-based single smoothing estimator is

better than the return-based single smoothing estimator. By comparing equations (7) and (38), we find that the range-based double smoothing estimator is more accurate than the single one because $\delta/\sqrt{\varepsilon h} = o_P(\sqrt{\delta/h})$.

4. Conclusions

Using the entire sample data, range-based estimator not only guarantees the integrity of information but also reduces influence of microstructure noise. Compared with single smoothing, the double smoothing method can replicate the actual features of the volatility function more. In this paper, combining the range technique with the double smoothing method, we propose a range-based double smoothing spot volatility estimator and prove its consistency and asymptotic normality. We also find that the range-based single smoothing estimator is better than the return-based single smoothing one, while the range-based double smoothing one is the best.

Data Availability

No data were used to support this study.

Conflicts of Interest

The authors declare that they have no conflicts of interests.

Acknowledgments

This work was jointly supported by Start-up Fund for Scientific Research of High-level Talents of Jinling Institute of Technology (Grant no. jit-b-202028) and Advanced Study and Training of Professional Leaders of Higher Vocational Colleges in Jiangsu (Grant no. 2017GRFX019).

References

[1] W. Hu, Q. Zhu, and H. R. Karimi, "Some improved Razumikhin stability criteria for impulsive stochastic delay differential systems," *IEEE Transactions on Automatic Control*, vol. 64, no. 12, pp. 5207–5213, 2019.

[2] B. Wang and Q. Zhu, "Stability analysis of semi-Markov switched stochastic systems," *Automatica*, vol. 94, pp. 72–80, 2018.

[3] H. Wang and Q. Zhu, "Adaptive output feedback control of stochastic nonholonomic systems with nonlinear parameterization," *Automatica*, vol. 98, pp. 247–255, 2018.

[4] Q. Zhu, "Stabilization of stochastic nonlinear delay systems with exogenous disturbances and the event-triggered feedback control," *IEEE Transactions on Automatic Control*, vol. 64, no. 9, pp. 3764–3771, 2019.

[5] Q. Zhu and H. Wang, "Output feedback stabilization of stochastic feedforward systems with unknown control coefficients and unknown output function," *Automatica*, vol. 87, pp. 166–175, 2018.

[6] Y. Aït-Sahalia, P. A. Mykland, and L. Zhang, "Ultra high frequency volatility estimation with dependent microstructure noise," *Journal of Econometrics*, vol. 160, no. 1, pp. 160–175, 2011.

[7] T. G. Andersen, T. Bollerslev, F. X. Diebold, and P. Labys, "Modeling and forecasting realized volatility," *Econometrica*, vol. 71, no. 2, pp. 579–625, 2003.

[8] J. W. Cai, Q. X. Zhu, and P. Chen, "Nonparametric threshold estimation of spot volatility based on high-frequency data for time-dependent diffusion models with jumps," *Advances in Difference Equations*, vol. 2020, no. 1, 2020.

[9] J. Fan and Y. Wang, "Multi-scale jump and volatility analysis for high-frequency financial data," *Journal of the American Statistical Association*, vol. 102, no. 480, pp. 1349–1362, 2007.

[10] L. Zhang, P. A. Mykland, and Y. Aït-Sahalia, "A tale of two time scales," *Journal of the American Statistical Association*, vol. 100, no. 472, pp. 1394–1411, 2005.

[11] D. Kristensen, "Nonparametric filtering of the realized spot volatility: A kernel-based approach," *Econometric Theory*, vol. 26, no. 1, pp. 60–93, 2010.

[12] E. Renault, C. Sarisoy, and B. J. M. Werker, "Efficient estimation of integrated volatility and related processes," *Econometric Theory*, vol. 33, no. 2, pp. 439–478, 2017.

[13] Z. Liu, X.-B. Kong, and B.-Y. Jing, "Estimating the integrated volatility using high-frequency data with zero durations," *Journal of Econometrics*, vol. 204, no. 1, pp. 18–32, 2018.

[14] A. Alvarez, F. Panloup, M. Pontier, and N. Savy, "Estimation of the instantaneous volatility," *Statistical Inference for Stochastic Processes*, vol. 15, no. 1, pp. 27–59, 2012.

[15] P. A. Mykland and L. Zhang, "Inference for volatility-type objects and implications for hedging," *Statistics and its Interface*, vol. 1, no. 2, pp. 255–278, 2008.

[16] Y. Zu and H. Peter Boswijk, "Estimating spot volatility with high-frequency financial data," *Journal of Econometrics*, vol. 181, no. 2, pp. 117–135, 2014.

[17] C. Mancini, V. Mattiussi, and R. Renò, "Spot volatility estimation using delta sequences," *Finance and Stochastics*, vol. 19, no. 2, pp. 261–293, 2015.

[18] Q. Liu, Y. Liu, Z. Liu, and L. Wang, "Estimation of spot volatility with superposed noisy data," *The North American Journal of Economics and Finance*, vol. 44, pp. 62–79, 2018.

[19] Q. Liu, Y. Liu, and Z. Liu, "Estimating spot volatility in the presence of infinite variation jumps," *Stochastic Processes and their Applications*, vol. 128, no. 6, pp. 1958–1987, 2018.

[20] S. Alizadeh, M. W. Brandt, and F. X. Diebold, "Range-based estimation of stochastic volatility models," *The Journal of Finance*, vol. 57, no. 3, pp. 1047–1091, 2002.

[21] K. Christensen and M. Podolskij, "Realized range-based estimation of integrated variance," *Journal of Econometrics*, vol. 141, no. 2, pp. 323–349, 2007.

[22] M. Parkinson, "The extreme value method for estimating the variance of the rate of return," *The Journal of Business*, vol. 53, no. 1, pp. 61–65, 1980.

[23] K. Christensen and M. Podolskij, "Asymptotic theory of range-based multipower variation," *Journal of Financial Econometrics*, vol. 10, no. 3, pp. 417–456, 2012.

[24] J. Liu, Y. Wei, F. Ma, and M. I. M. Wahab, "Forecasting the realized range-based volatility using dynamic model averaging approach," *Economic Modelling*, vol. 61, pp. 12–26, 2017.

[25] N. K. Haur, S. Peiris, J. S.-K. Chan, N. K. Huat, and D. Allen, "Efficient modelling and forecasting with range based volatility models and its application," *North American Journal of Economics and Finance*, vol. 42, pp. 448–460, 2017.

[26] J. Cai, Q. Zhu, P. Chen, and X. Mei, "Central limit theorems of range-based estimators for diffusion models," *Communications in Statistics - Theory and Methods*, vol. 48, no. 24, pp. 5969–5984, 2019.

[27] J. W. Cai, P. Chen, and X. Mei, "Range-based threshold spot volatility estimation for jump diffusion models," *IAENG International Journal of Applied Mathematics*, vol. 47, no. 1, pp. 43–48, 2017.
[28] F. M. Bandi and P. C. B. Phillips, "Fully nonparametric estimation of scalar diffusion models," *Econometrica*, vol. 71, no. 1, pp. 241–283, 2003.
[29] Y. P. Song, "On double smoothed volatility estimation of potentially nonstationary jump-diffusion model," 2018.
[30] J. Fan and Y. Wang, "Spot volatility estimation for high-frequency data," *Statistics and its Interface*, vol. 1, no. 2, pp. 279–288, 2008.

Hindawi
Complexity
Volume 2020, Article ID 2109423, 9 pages
https://doi.org/10.1155/2020/2109423

Research Article

Construction of Regional Logistics Weighted Network Model and Its Robust optimization: Evidence from China

Lizhao Yan,[1] Yi Wen,[1] Kok Lay Teo,[2,3] Jian Liu,[4] and Fei Xu[5]

[1]*College of Business, Hunan Normal University, Changsha, Hunan 410081, China*
[2]*School of Mathematical Sciences, Sunway University, Subang Jaya, Selangor 47500, Malaysia*
[3]*Coordinated Innovation Center for Computable Modeling in Management Science, Tianjin University of Finance and Economics, Tianjin 300222, China*
[4]*School of Economics and Management, Changsha University of Science and Technology, Changsha, Hunan 410004, China*
[5]*Department of Mathematics, Wilfrid Laurier University, Ontario N2L 3C5, Canada*

Correspondence should be addressed to Jian Liu; ljorg@126.com

Received 2 May 2020; Revised 24 August 2020; Accepted 2 September 2020; Published 14 September 2020

Academic Editor: Ruofeng Rao

In this paper, we construct a regional logistics model from a macroperspective. First, based on the gravity model, the index of logistics attraction between cities is established as the weight of the model, and hence the regional logistics weighted model is constructed. Next, we use the social network analysis method to analyze its structure and make specific recommendations for the construction of logistics networks. Finally, we analyze the model's response to random attacks and deliberate attacks. From our study, it is found that when the failure nodes or edges reach a certain percentage, the regional logistics network will collapse on a large scale. Therefore, it is important to optimization the threshold of the regional logistics network. This clearly provides a new perspective for the study of the regional logistics networks.

1. Introduction

With the rapid development of e-commerce and the increasing close cooperation between enterprises, the logistics industry has become the focus of attention from all walks of life. On the other hand, the demand for regional logistics network is also increasing. At present, the study of regional logistics network mainly focuses on the allocation and coordination of logistics resources among enterprises, which include (i) the location of the logistics distribution center; (ii) the layout of the regional logistics network; and (iii) the emergency response capability and regional logistics network optimization, for example, the P-median problem [1] which considers the location of the logistics center [2–5] from the viewpoint of the shortest distance from all logistics nodes to the logistics center. On the other hand, the location of the logistics center problem has been studied from the perspective of covering problem [6–9] and fixed-charge facility location problem [10–13]. The layout of the regional logistics network is mainly modeled as a hub-and-spoke network, where the logistics center is the "axis" and the logistics connections with other nodes are the "spokes". Such networks are studied to achieve minimum cost or optimal transportation efficiency [14–18]. In the existing literature, the emergency response capabilities of regional logistics networks (such as extreme weather) are also being discussed. For example, Wang and Xiao [19] proposes a chain failure recovery method for supply chain network based on ant colony algorithm. Hu et al. [20] proposes a multitask model to study the impact of road congestion on the regional logistics network and develops an optimization strategy. We have noticed that the current research on regional logistics network is mainly from a microperspective, using econometric analysis method to analyze a certain aspect of the logistics industry. However, such research does not provide enough results to reflect macrocharacteristics. The complex network theory developed in recent years provides a tool for regional economics from a macroperspective [21–23]. For

example, Meepetchdee and Shah [24] discuss the growth, robustness, and benefits of logistics networks and uses the complex networks to simulate logistics networks. Viljoen and Joubert [25] uses complex networks to discuss stability. In addition, many scholars use the complex network theory to explore the structural characteristics of urban traffic networks and aviation networks [26–29]. However, the weights of network connections are not considered in the above studies. Some of the weights being chosen are unreasonable, which leads to a large gap between the established regional logistics network and the actual situation. Therefore, it is necessary to construct a more realistic regional logistics network and propose specific logistics network optimization strategies.

When studying the regional logistics network on a complex network, we usually simulate the regional logistics network based on theoretical knowledge by considering the interaction between nodes and the influence of the network on the nodes. In this paper, we establish the index of an urban logistics linkage based on the gravity model and the self-selection characteristics of logistics nodes. Then, the intercity logistics linkages are introduced into the regional logistics network as the connection weight, and the regional logistics weighted network is established. Such an investigation provides a new approach to construct the regional logistics weighted network model. On this basis, combined with complex network theory, the statistical properties and topological structure of the regional logistics weighted network are discussed, the stability and robustness of the network are analyzed, and a more stable topological structure model of the regional logistics network is found. Compared with the previous research, we use the failure area to describe the response of the regional logistics network under random attacks and deliberate attacks. The consideration is comprehensive. Then, we improve the comprehensive robustness optimization model, discuss how to maximize the comprehensive robustness of the regional logistics network at a limited cost, and search for the optimal solution through Python.

The reminder of the paper is organized as follows. In Section 2, we describe the mechanism of building a regional logistics weighted network model. In Section 3, we take Jiangsu-Zhejiang-Shanghai region, the most developed e-commerce region in China, as an example to establish a regional logistics weighted network. Then, we analyze the statistical characteristics of the system using complex network theory. In Section 4, we discuss the robustness of the regional logistics weighted network, develop the optimization strategy of the model and consider its robustness, and seek the optimal solution of the model at a limited cost. Conclusions are drawn in Section 5.

2. Regional Logistics Weighted Network

Regional logistics network is mainly composed of nodes and edges, in which nodes denote different cities and edges mainly represent transportation routes between cities. Since the focus of this paper is on the study of logistics in a small area, the nodes represent county-level cities within the region and the edges represent transportation roads.

We use Z to denote all nodes i in the regional logistics network, N the node connection matrix, and $n(i, j)$ the connection between nodes i and j. Thus, N is given by

$$N = \{(i, j) \mid n(i, j) = 1, \quad (i, j) \in Z, n \in N\}. \tag{1}$$

For $n(i, j) = 1$, it implies that there is a logistics connection between node i and node j, and $n(i, j) = 0$ means that there is no logistics connection between node i and node j. Based on formula (1), we establish a weighted regional logistics network model which has weighted information of all edges between nodes. Thus,

$$W = \left\{(i, j) \mid w(i, j) = H_{ij}, \quad (i, j) \in Z, h \in U\right\}, \tag{2}$$

where $w(i, j)$ denotes the logistics connection weight between node i and node j and U denotes the connection weight matrix between nodes. The construction method of H_{ij} is described below.

According to the gravity model, the index of intercity logistics linkages is established and hence the weight index of regional logistics network. Based on the autonomous selectivity and preference of nodes in the regional logistics network and the joining of the regional logistics network, new nodes often establish logistic linkages with nodes having strong logistics competitiveness. From a market perspective, the supply-demand relationship of logistics industry directly reflects the logistics competitiveness of nodes, while the freight volume of the node directly reflects the demand of the node logistics industry. The logistics supply capacity of the node is determined by the logistics cost. The logistics cost mainly refers to the transportation cost and labor cost, which is proportional to distance. The greater the distance between two nodes, the greater the cost of forming a logistics connection. In summary, we select two indices from the logistics evaluation system: the freight volume of the node and the road distance between two nodes. Nodes with large freight volumes have high logistics demands and are more attractive to surrounding nodes. On the other hand, the shorter the distance between two nodes, the lower the cost of forming logistics connection. The regional logistics system is expressed as the abovementioned supply and demand model. Through the construction of the gravity model, we take the intercity logistics linkage index R_{ij} as the influencing factors of the system, which is positively correlated with the freight volume and negatively correlated with the distance between two nodes. Thus,

$$\begin{aligned} R_{ij} &= \frac{\sqrt{M_I} * \sqrt{M_j}}{D_{ij}}, \\ H_{ij} &= \frac{R_{ij}}{\sum_{i=1}^{n} R_{ij}}, \end{aligned} \tag{3}$$

where M_i and M_j are freight volumes of node i and node j, respectively, D_{ij} is the distance between i and j, and H_{ij} denotes the degree of node i and node j. We use H_{ij} to denote the weight between node i and node j in (2), i.e.,

$h = H_{ij}$. The regional logistics weighted network can be described as

$$R = (Z, N, U), \tag{4}$$

where Z is the set of all nodes, N is the connection state between nodes, and U is the connection weight between nodes.

3. Case Study: Regional Logistics Weighted Network in Jiangsu-Zhejiang-Shanghai Region

Taking Jiangsu-Zhejiang-Shanghai region as an example, we establish a regional logistics weighted network. In this model, each node represents a city. The connection weight is the degree of logistics membership between nodes. We get the latest freight volume from the 2017 Statistical Yearbook of China. The shortest road distance between cities is obtained from the map of China. According to formula (3), we get the attraction of intercity logistics linkages among 118 nodes. After further processing, we get the membership degree of nodes and then construct the regional logistics weighted network in this area. The results of the regional logistics weighted network obtained by Ucinet are shown in Figure 1. As shown in the Figure 1, the cities with large freight volumes, such as Shanghai, Hangzhou, and Ningbo, are more attractive to the surrounding cities, and as such, it is easy for these cities to generate contacts with nodes. These cities are in network-intensive areas. The cities far away from the surrounding cities with small freight volume are difficult to generate contacts with the network. These cities are in the marginal area of the regional logistics network. The situation shown in Figure 1 is basically consistent with the reality. Based on the complex network theory, we analyze the network structure of the regional logistics weighted network from the statistical characteristics.

3.1. Degree and Degree Distribution. The degree of a node refers to the number of other nodes connected to the node, which is often used to describe the capacity of the node. We use k_i to represent the degree of node i, $k_i = \sum_{i \neq j} n(i, j)$. The average degree k of the network is 9.8136, and the degree distribution of the logistics network is shown in Figure 2. From Figure 2, we see that Suzhou is the node with the largest degree, up to 43, followed by Wuxi (32), Shaoxing (30), Jiande (28), Hangzhou (21), Shanghai (19), and Nanjing (18). We note that although Shanghai's GDP is much higher than its surrounding cities such as Hangzhou, it is not the most important logistics node in the network. Therefore, we should not only consider regional GDP to select the central node of the regional logistics network. The location factor should also be taken into consideration as a reference index.

As shown in Figure 3, we find that only a few nodes in the regional logistics weighted network have high degree. Most nodes have degrees distributed between 0 and 15. The regional logistics weighted network is very uneven having the characteristics of scale-free network. This kind of network has obvious weaknesses. Attacks on key nodes in the network can easily lead to large-scale paralysis. On the other hand, the uneven structure of network model can easily cause network congestion. Based on the above discussion, since it is easy for the nodes in Suzhou, Wuxi, Shaoxing, Jiande, and Hangzhou to produce logistics links with their surrounding nodes, it is more reasonable, from the perspective of the construction of the whole regional logistics network, to choose these nodes as the central locations of the regional logistics network.

Through the above analysis on the degree distribution, we find that a small number of nodes in the regional logistics network are hub nodes, and the degrees of most of the nodes are relatively small. Furthermore, we measure the degree distribution characteristics of the regional logistics network by the cumulative distribution function $P > k$, as shown in Figure 4. We assume that there is a constant C and a power exponent γ, which satisfy $P \sim \mathrm{C}k^{-\gamma}$. Then, we can infer that the processed data approximately conform to the power-law distribution. We use SPSS for exponential fitting and use the nonparametric KolmogorovSmirnov test to verify the hypothesis. The results are shown in Tables 1 and 2. Therefore, we believe that the regional logistics weighted network has scale-free network characteristics and thus is a scale-free network.

3.2. Average Shortest Path Length. The shortest path length L_c refers to the path connecting the two nodes with the least number of edges in the network. The average shortest path length L is the average of the shortest path lengths of all nodes in the network. The average shortest path length L of the regional logistics weighted network is 3.069. Although the structure of the network seems complex and huge, the distance between nodes is not far away, which further shows that the network has the characteristics of small world network according to complex network theory.

3.3. Betweenness Centrality. Betweenness centrality is an index to describe the importance of a node by the number of the shortest paths of the node. The distribution of the betweenness centrality of the regional logistics weighted network is shown in Figure 5, which shows that there are five distinct peaks corresponding to Jiande, Dongyang, Changzhou, Suzhou, and Yizheng. The above nodes have significant influences on the connectivity of the network. In addition, we also find that the nodes of Yongjia, Pingyang, Pujiang, Kaihua, Daishan, Qixian, Xianju, Longquan, Qingyuan, Suichang, Jingning, Pei, Kunshan, Taicang, Qidong, Jurong, Jingjiang, Taixing, Shuyang, and Sihong have betweenness centrality 0. These nodes contribute little to network connectivity, and hence they can almost be ignored.

3.4. Clustering Coefficient. The clustering coefficient C_i refers to the connection between other nodes connected to i. The higher the clustering coefficient C_i is, the closer the relationship between the neighbors of i is. The clustering coefficient C_i is defined as

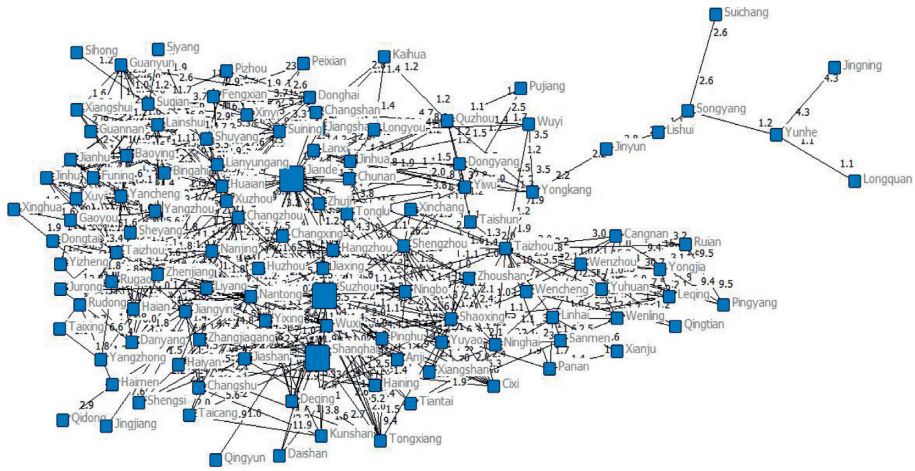

Figure 1: The regional logistics weighted network of Jiangsu-Zhejiang-Shanghai area.

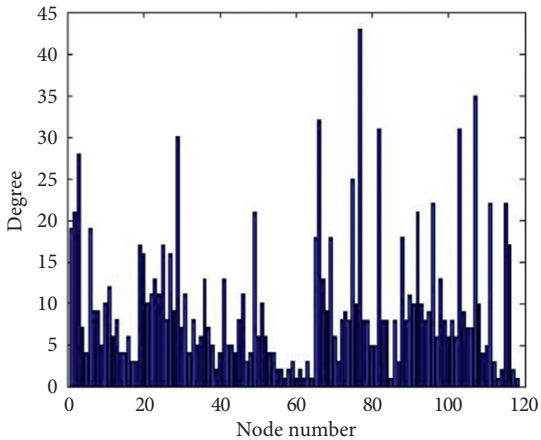

Figure 2: The degree of nodes.

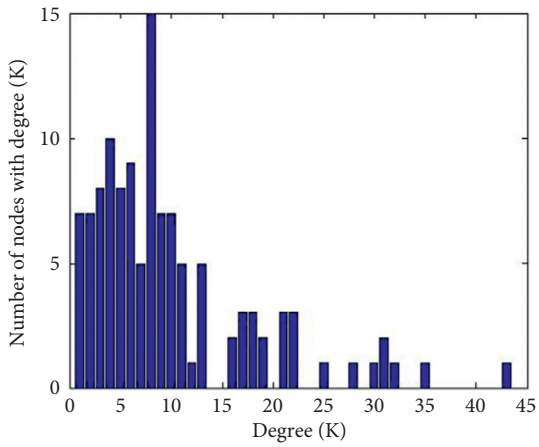

Figure 3: The degree distribution.

$$C_i = \frac{2E_i}{k_i(k_i - 1)}. \tag{5}$$

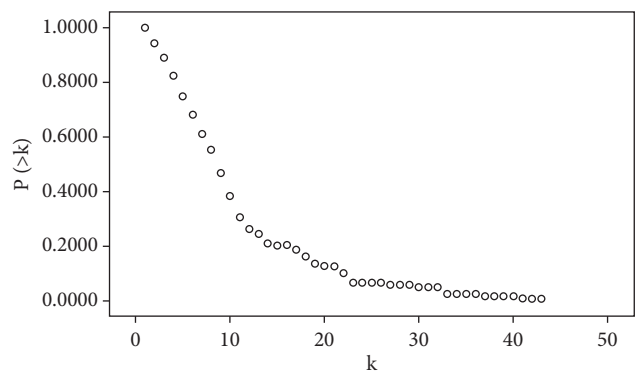

Figure 4: The cumulative distribution.

The average clustering coefficient C refers to the average of the clustering coefficients of all nodes in the network. The average clustering coefficient C of the regional logistics weighted network of Jiangsu-Zhejiang-Shanghai region is obtained as 0.5868 using MATLAB. There are many nodes in the regional logistics weighted network, these nodes are actually closely linked through the connection, and the distance between nodes is much smaller than imagined. The clustering coefficients of each node are shown in Figure 6.

According to Figures 1 and 6, the clustering coefficients of Yongjia, Pingyang, Pujiang, Kaihua, Daishan, Shengsi, Xianju, Peixian, Kunshan, Taicang, Jurong, Taixing, and Siyang counties are 1, which indicate that the other nodes connected with these cities are fully connected. The above nodes are in a very stable network structure. The clustering coefficients of Wencheng, Taishun, Lishui, Longquan, Qingtian, Yunhe, Qingyun, Jinyun, Suichang, Songyang, Jingning, Qidong, Jingjiang, and Sihong are 0, implying that these nodes are totally disconnected. If such nodes are in the bridge position in the network model, they will easily cause network paralysis when attacked. Figure 1 shows that this kind of nodes either have only one connection node, or the nodes connected to them are disconnected. If such nodes are in the bridge position in the network, they will easily cause network paralysis when attacked.

Table 1: Summary of statistical analysis.

	Coefficient				
	Coefficient of nonstandardization		Standard coefficient	t	Significance
	B	Standard error	β		
Degree	−0.112	0.002	−0.994	−57.093	0.000
(Constant)	1.205	0.060		20.181	0.000

Table 2: Summary of hypothesis tests.

Original hypothesis	Test	Significance	Decision
The cumulative distribution is exponential distribution with an average of 0.200	Single-sample KolmogorovSmirnov test	0.062	Keep the original hypothesis

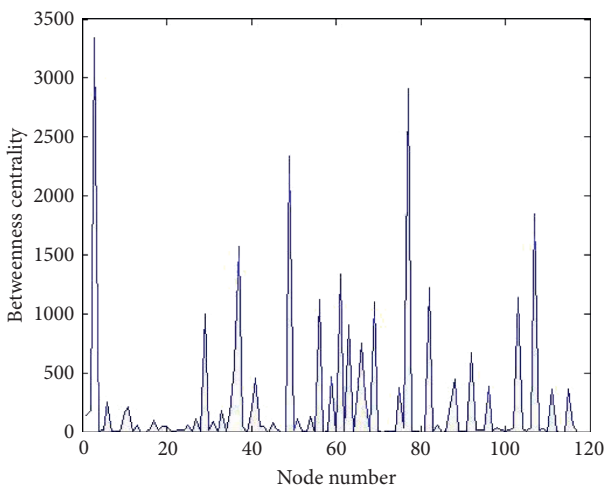

Figure 5: Betweenness centrality.

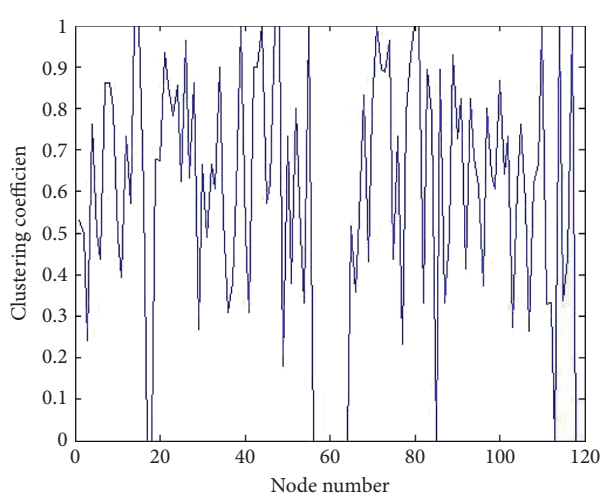

Figure 6: Clustering coefficient.

4. Robustness of Regional Logistics Weighted Network

The regional logistics network is the basis of interregional economic cooperation and an important guarantee for the coordinated development of regional economies. Through the above analysis of the statistical characteristics of the regional logistics weighted network, it is found that the network has an extremely uneven network structure. For this kind of network structure, the failure of logistics nodes or edges caused by traffic jams, traffic accidents, natural disasters, bad weather, or major incidents may lead to large-scale failure of the logistics network. Therefore, it is of great significance to discuss how to improve the ability of the regional logistics network to respond to various emergencies. We further analyze the robustness of regional logistics network model and discuss methods to optimize the robustness of the network at a limited cost.

4.1. Robustness Analysis of the Network. The robustness analysis of a complex network refers to the analysis of the connection state between nodes and the change of the whole network connection state when the network is attacked intentionally or randomly. Intentional attack refers to the failure of a certain percentage of important nodes or edges in the network. Random attack refers to completely random failures of nodes or edges in the network. In this paper, we choose the relative scale of the maximum connected subgraph Q to measure the robustness of the network after being attacked.

$$Q = \frac{s}{S}, \tag{6}$$

where s is the maximum connected subgraph range of the network when the network is attacked and S is the initial scale of the network. The smaller the relative scale of the maximum connected subgraph, the more serious the damage of the regional logistics network is. Simulate the above situation by Python, the results are shown in Figures 7 and 8. Figure 7 shows the trend of Q under various node failure strategies. Figure 8 shows the trend of Q under various edge failure strategies. From Figure 7, we can see that in the case of random attack on nodes in the regional logistics weighted network, Q shows a linear trend and slowly decreases as the number of nodes being attacked increases. Under random attack, the effect of each node being attacked is not much different, so it will only reduce Q by a very small value. This clearly shows that the regional logistics weighted

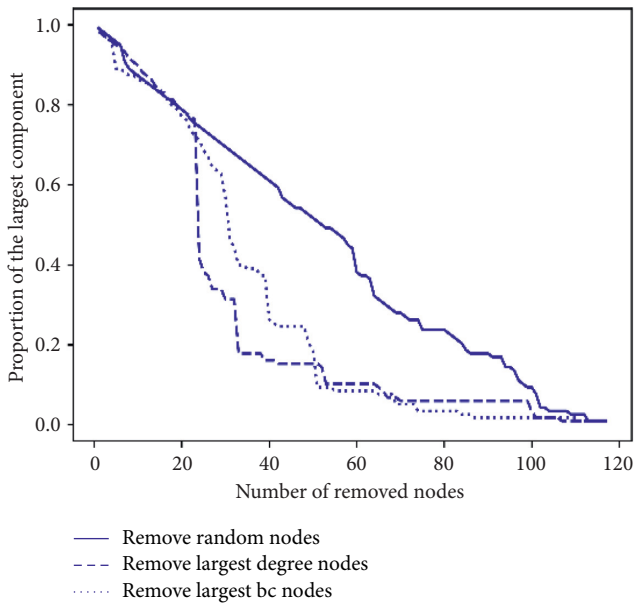

Figure 7: Robustness analysis under node failure.

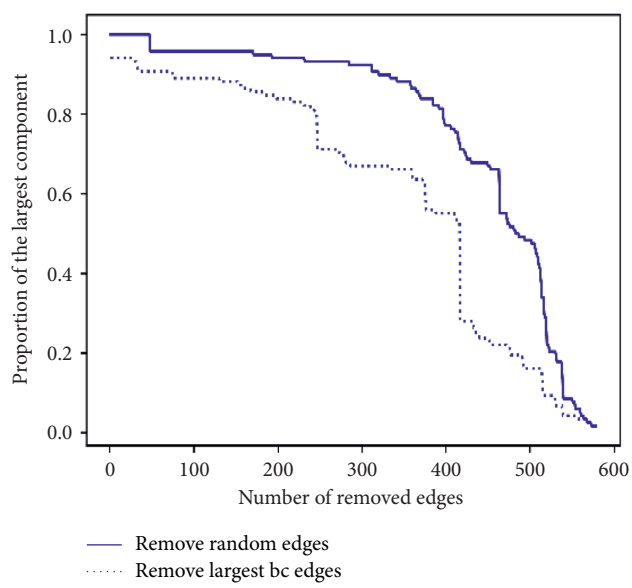

Figure 8: Robustness analysis under edge failure.

network has strong robustness under random attack. Under intentional attacks, Q decreases as the number of failed nodes increases. When the number of failed nodes reaches 20, the relative scale of the maximum connected subgraph Q of the regional logistics weighted network shows a rapid shrinking trend, indicating that the regional logistics weighted network is no longer robust. This phenomenon is consistent with the characteristics of scale-free networks, which is robust to random failures but is vulnerable to intentional attacks. Figure 8 shows that under random attack, when the number of failed edges of the regional logistics weighted network is less than 300, the Q *value* of the network will not change significantly and basically remains at about 0.95. Under intentional attacks, the robustness of the network is obviously weaker than that under random attacks. When the number of failed edges in the network exceeds 100, the decline rate of the Q *value* increases significantly. When the number of failed edges exceeds 200, the Q *value* will decrease linearly and the regional logistics weighted network will be paralyzed in a large area. The regional logistics weighted network is not very robust to the intentional attack strategy of nodes or edges. Therefore, we propose a robust optimization model based on the existing robustness research and discuss how to maximize the robustness of the regional logistics weighted networks under a limited cost.

4.2. Robustness Optimization of the Network. At present, there are few studies on the robust optimization of scale-free networks. In [30, 31], an in-depth study of the phase transition characteristics of the scale-free networks is carried out, where criteria for determining the existence of the largest interconnected group in the network are derived, and the threshold P^c is established for scale-free networks in response to intentional and random attacks. When the one-time failure ratio of scale-free network $P > P^c$, scale-free network will fall into a large area of failure [30, 31]. On this basis, by combining the penetration theory and an optimization method, an optimization model of scale-free networks under random and intentional attacks is proposed in [32]. More specifically, based on the percolation theory and an optimization method, it can quantify the robustness index of the regional logistics network in response to random attacks and intentional attacks, Then, it will be able to establish a comprehensive robust optimization model of the regional logistics system under the cost constraints and to find the optimal solution of the robust optimization model under a limited cost.

The aim of this paper is to maximize the threshold P^c of the network subject to the constraints on the cost. When scale-free networks are attacked randomly, the threshold P^c_{random} is

$$P^c_{\text{random}} = 1 - \frac{1}{k_0 - 1}, \tag{7}$$

where k_0 can be obtained as

$$k_0 = \frac{\sum_{k=m}^{K} k^2}{\sum_{k=m}^{K} k}, \tag{8}$$

while m is the minimum node degree and K is the maximum node degree. When scale-free network is attacked intentionally, the threshold P^c_{target} is given by

$$P^c_{\text{target}} = \left(\frac{K^*}{m}\right)^{1-\gamma} - \frac{1}{n}, \tag{9}$$

where n is the number of network nodes, K^* is the maximum node degree after the node is inactivated, and γ is the exponential value of the degree distribution of the network. Here, K^* is given by

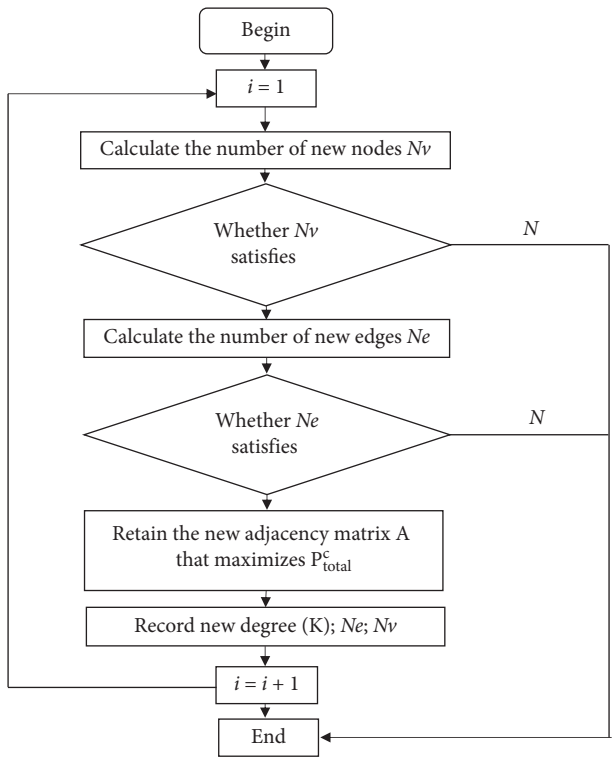

Figure 9: Flow chart of robust optimization.

Table 3: Regional logistics network optimization results.

(Chunan, Pujiang)	(Tonglu, Tongxiang)	(Tonglu, Zhenjiang)	(Tonglu, Leqing)
(Chunan, Deqing)	(Shanghai, Jinhua)	(Chunan, Longyou)	(Yuyao, Wenchen)
(Ruian, Shaoxing)	(Shanghai, Yiwu)	(Yuyao, Zhenjiang)	(Cixi, Suining)
(Yongjia, Cangnan)	(Xiangshan, Zhenjiang)	(Shaoxing, Nantong)	(Shaoxing, Yangzhou)
(Shaoxing, Zhenjiang)	(Jiande, Shaoxing)	(Hnagzhou, Zhenjiang)	(Shaoxing, Changzhou)

$$\left(\frac{K^*}{m}\right)^{2-\alpha} - 2 = \frac{2-\alpha}{3-\alpha} m \left[\left(\frac{K^*}{m}\right)^{3-\alpha} - 1\right]. \tag{10}$$

Therefore, the comprehensive threshold of robustness can be expressed as

$$P^c_{\text{total}} = \alpha P^c_{\text{random}} + \beta P^c_{\text{target}}, \tag{11}$$

where α and $\beta = (1-\alpha)$ are weights of random attack and intentional attack thresholds, respectively. It is known that the robustness of the logistics network will be enhanced when new nodes or connections are introduced. However, the cost of establishing new logistics nodes or links is high. Based on the above theory, we design the robust optimization model for the regional logistics network under fixed cost.

To enhance the robustness of regional logistics network, new logistics warehouses can be added between current logistics nodes and new logistics links can be established between nodes. We assume that the total cost is C, the cost of introducing a new logistics node is a, and the cost of establishing a new logistics connection is b. The robust optimization model of the regional logistics network can be expressed as

$$\begin{aligned} &\max P^c_{\text{total}} = \alpha P^c_{\text{random}} + \beta P^c_{\text{target}} \\ &\text{s.t.:} \quad \mathrm{aN}_V + \mathrm{bN}_e \le \mathrm{C} \\ &0 \le N_v < \frac{C}{a} \\ &0 < N_e \le \frac{C}{b}, \end{aligned} \tag{12}$$

where N_V is the number of newly introduced nodes and N_e is the number of newly established logistics connections. The design procedures of the optimization program are as follows:

(i) Introduce new nodes or edges to the regional logistics network. Then, test whether or not the cost constraints in the optimization model are met.

(ii) If the restrictions are not met, the cost has been used up and the result is obtained. If the constraints are satisfied, calculate the P^c_{total} of the regional logistics network with the new nodes or edges having introduced to all its possible locations. The maximum value of P^c_{total} is retained.

(iii) Record the location of the newly introduced nodes and edges, output P^c_{total}, and the new connection matrix.

The logic diagram of the optimization program is shown in Figure 9, which is implemented by Python.

For the regional logistics weighted networks, the ability to resist intentional attacks is more important than the ability to resist random attacks. Therefore, we assume that the weight of random attack $\alpha = 0.3$ and the weight of intentional attack robustness $\beta = 0.7$. The P^c_{random} of the initial logistics network is 0.93522, the P^c_{target} of the initial logistics network is 0.001162, and the comprehensive threshold P^c_{total} is 0.281379. Assume that the cost of establishing new logistics nodes N_V is 20, the cost of establishing new logistics connections N_e is 10, and the total cost C is 200. Through the above optimization program, the output result is $N_V = 0$ and $N_e = 20$; the locations of including new nodes and connections are listed in Table 1. The P^c_{random} of the optimized regional network is 0.93792, and the P^c_{target} of the optimized regional network is 0.041338. The comprehensive robustness threshold $P^c_{\text{total}} = 0.31031$ is 8.8% higher than that of the original network robustness.

Based on the above discussion, we believe that when we optimize the robustness of the regional logistics weighted network of Jiangsu-Zhejiang-Shanghai region under a limited cost, adding the above connections as shown in Table 3 can maximize the comprehensive robustness of regional logistics.

5. Conclusion

In this work, our study was mainly focused on the construction of regional logistics network and the development of robust optimization. We established the regional logistics weighted network from a macroperspective. Through the discussion and analysis of this paper, the summary is as follows:

(1) Compared with previous studies from the single node location [2–5] or hub model [14], we studied the logistics activities of a region from the perspective of macronetwork. According to the relevant economic research, we believe that the logistics nodes have self-selection capabilities and constructed the attractiveness index of logistics nodes as the weight of the regional logistics network. It is found that the economically developed cities are located in dense areas of logistics networks. For economically underdeveloped cities, they are located in sparse areas of logistics network. The results obtained are in line with the actual situation. This also verifies the feasibility of our modeling ideas.

(2) We analyze the regional logistics network model of Jiangsu-Zhejiang-Shanghai through the social network method. The average shortest path length is 3.069 and the aggregation coefficient is 0.5868. Although there are many nodes in a single regional logistics weighted network model, the average degree and average path length are not large, which shows that it has obvious small world characteristics. On this basis, we can provide more economic insights for the construction of regional logistics networks.

(3) Through robustness analysis, it is found that the Jiangsu-Zhejiang-Shanghai region logistics network model is robust in the face of random attacks and is prone to large-scale failures when facing deliberate attacks. This is also a common feature of scale-free networks. When $\alpha = 1$ and $\beta = 0$, the robust optimization model can resist random attacks which is in line with the results obtained in [28]. When $\alpha = 0$ and $\beta = 1$, the robust optimization model can resist deliberate attacks which agrees with the results reported in [29]. We comprehensively considered the response of the regional logistics network to the two kinds of attacks. Then, we established a comprehensive robustness index for the critical value of large-area failures and discussed how to maximize performance under fixed costs. Finally, taking Jiangsu-Zhejiang-Shanghai region logistics network model as an example, specific experimental results are given.

When establishing a robust optimization model, this paper simplifies the actual situation by ignoring the difference in connection costs between different nodes. We only discuss static models. In future research, various practical factors should be taken into account in the investigation of the regional logistics networks.

Data Availability

Some or all data, models, or code generated or used during the study are available from the corresponding author by request.

Conflicts of Interest

The authors declare that there are no conflicts of interest regarding the publication of this paper.

Acknowledgments

This work was partially supported by the National Natural Science Foundation of China (Nos. 71501069, 71420107027, and 71871030), Humanities and Social Sciences Project of the Ministry of Education of China (No. 19YJAZH132), Scientific Research Project of Hunan Provincial Education Department in China (No.18A037), Hunan Key Laboratory of Macroeconomic Big Data Mining and its Application, and a Discovery Grant from Australian Research Council.

References

[1] C. S. Revelle and R. W. Swain, "Central facilities location," *Geographical Analysis*, vol. 2, no. 1, pp. 30–42, 2010.

[2] R. Tadei, N. Ricciardi, and G. Perboli, "The stochastic -median problem with unknown cost probability distribution," *Operations Research Letters*, vol. 37, no. 2, pp. 135–141, 2009.

[3] S. Elloumi, "A tighter formulation of the p-median problem," *Journal of Combinatorial Optimization*, vol. 19, no. 1, pp. 69–83, 2010.

[4] Y. An, B. Zeng, Y. Zhang, and L. Zhao, "Reliable p-median facility location problem: two-stage robust models and algorithms," *Transportation Research Part B: Methodological*, vol. 64, pp. 54–72, 2014.

[5] M. Albareda-Sambola, Y. Hinojosa, and J. Puerto, "The reliable p -median problem with at-facility service," *European Journal of Operational Research*, vol. 245, no. 3, pp. 656–666, 2015.

[6] A. Saxena, V. Goyal, and M. A. Lejeune, "MIP reformulations of the probabilistic set covering problem," *Mathematical Programming*, vol. 121, no. 1, pp. 1–31, 2010.

[7] O. Baron, O. Berman, S. Kim, and D. Krass, "Ensuring feasibility in location problems with stochastic demands and congestion," *IIE Transactions*, vol. 41, no. 5, pp. 467–481, 2009.

[8] O. Berman and J. Wang, "The minmax regret gradual covering location problem on a network with incomplete information of demand weights," *European Journal of Operational Research*, vol. 208, no. 3, pp. 233–238, 2011.

[9] G. Alexandris and I. Giannikos, "A new model for maximal coverage exploiting GIS capabilities," *European Journal of Operational Research*, vol. 202, no. 2, pp. 328–338, 2010.

[10] L. Yan, F. Xu, J. Liu, K. L. Teo, and M. Lai, "Stability strategies of demand-driven supply networks with transportation delay," *Applied Mathematical Modelling*, vol. 76, pp. 109–121, 2019.

[11] S. Xie, X. Li, and Y. Ouyang, "Decomposition of general facility disruption correlations via augmentation of virtual supporting stations," *Transportation Research Part B: Methodological*, vol. 80, pp. 64–81, 2015.

[12] L. Yan, J. Liu, and Z. Luo, "Existence and multiplicity of solutions for second-order impulsive differential equations on the half-line," *Advances in Difference Equations*, vol. 63, pp. 1–12, 2013.

[13] Z. Yu-Feng, M. A. Zu-Jun, and W. Ke-Ming, "Reliability capacitated fixed-charge location problem," *Operations Research and Management Science*, vol. 11, pp. 677–686, 2015.

[14] C. S. Sung and H. W. Jin, "Dual-based approach for a hub network design problem under non-restrictive policy," *European Journal of Operational Research*, vol. 132, no. 1, pp. 88–105, 2001.

[15] R. Ishfaq and C. R. Sox, "Hub location-allocation in intermodal logistic networks," *European Journal of Operational Research*, vol. 210, no. 2, pp. 213–230, 2011.

[16] S. A. Alumur, B. Y. Kara, and O. E. Karasan, "Multimodal hub location and hub network design," *Omega*, vol. 40, no. 6, pp. 927–939, 2012.

[17] J. T. Bowen, "A spatial analysis of FedEx and UPS: hubs, spokes, and network structure," *Journal of Transport Geography*, vol. 24, pp. 419–431, 2012.

[18] N. Gallego, C. Llano, T. De La Mata, and J. DÍaz-Lanchas, "Intranational home bias in the presence of wholesalers, hub-spoke structures and multimodal transport deliveries," *Spatial Economic Analysis*, vol. 10, no. 3, pp. 369–399, 2015.

[19] Y. Wang and R. Xiao, "An ant colony based resilience approach to cascading failures in cluster supply network," *Physica A: Statistical Mechanics and Its Applications*, vol. 462, pp. 150–166, 2016.

[20] L. Hu, J. X. Zhu, Y. Wang and L. H. Lee, Joint design of fleet size, hub locations, and hub capacities for third-party logistics networks with road congestion constraints," *Transportation Research Part E: Logistics and Transportation Review*, vol. 118, no. 10, pp. 568–588, 2018.

[21] T. Broekel, "The Co-evolution of proximities - a network level study," *Regional Studies*, vol. 49, no. 6, pp. 921–935, 2015.

[22] B. Derudder and P. J. Taylor, "Central flow theory: comparative connectivities in the world-city network," *Regional Studies*, vol. 52, no. 2, pp. 1–14, 2017.

[23] B. D. Vos, B. Raa, and S. D. Vuyst, "A savings analysis of horizontal collaboration among VMI suppliers," *Journal of Industrial and Management Optimization*, vol. 13, no. 5, pp. 1–19, 2017.

[24] Y. Meepetchdee and N. Shah, "Logistical network design with robustness and complexity considerations," *International Journal of Physical Distribution & Logistics Management*, vol. 37, no. 3, pp. 201–222, 2007.

[25] N. M. Viljoen and J. W. Joubert, "The vulnerability of the global container shipping network to targeted link disruption," *Physica A: Statistical Mechanics and Its Applications*, vol. 16, pp. 785–792, 2016.

[26] J. Liu, Y. Huang, and C.-P. Chang, "Leverage analysis of carbon market price fluctuation in China," *Journal of Cleaner Production*, vol. 245, p. 118557, 2020.

[27] J. Liu, C. Cheng, X. Yang, L. Yan, and Y. Lai, "Analysis of the efficiency of Hong Kong REITs market based on Hurst exponent," *Physica A: Statistical Mechanics and Its Applications*, vol. 534, p. 122035, 2019.

[28] A. T. Buba and L. S. Lee, "Differential evolution with improved sub-route reversal repair mechanism for multi-objective urban transit routing problem," *Numerical Algebra*, vol. 8, no. 3, pp. 361–386, 2018.

[29] M. E. O'Kelly, "Global airline networks: comparative nodal access measures," *Spatial Economic Analysis*, vol. 11, no. 3, pp. 253–275, 2016.

[30] R. Cohen, K. Erez, D. Benavraham et al., "Breakdown of the internet under intentional attack," *Physical Review Letters*, vol. 86, no. 16, pp. 36–82, 2001.

[31] G. Paul, T. Tanizawa, S. Havlin, and H. E. Stanley, "Optimization of robustness of complex networks," *The European Physical Journal B*, vol. 38, no. 2, pp. 187–191, 2004.

[32] J. G. Liu, Z. T. Wang, and Y. Z. Dang, "Optimization of robustion of scale-free network to random and targeted attacks," *Modern Physics Letters B*, vol. 19, no. 16, pp. 785–792, 2008.

Hindawi
Complexity
Volume 2020, Article ID 6018398, 11 pages
https://doi.org/10.1155/2020/6018398

Research Article

Adaptive Decentralized Control Scheme for a Stochastic Interconnected System

Xiaoli Jiang,[1] Siqi Liu,[1] Mingyue Liu,[1] Li Yang,[1] and Lina Liu[2]

[1]*College of Mathematics and Physics, Bohai University, Jinzhou 121013, Liaoning, China*
[2]*School of Electronic and Information Engineering, Soochow University, Suzhou, Jiangsu 215006, China*

Correspondence should be addressed to Xiaoli Jiang; jxls309@163.com and Lina Liu; lln@suda.edu.cn

Received 17 April 2020; Revised 28 June 2020; Accepted 30 July 2020; Published 29 August 2020

Academic Editor: Quanxin Zhu

This work investigates a decentralized state feedback scheme of neural network control for an interconnected system. The completely unknown associated terms are estimated directly by the neural structure. A modified approach is proposed to deal with the state feedback format. By combining the Lyapunov function and backstepping technology together, an adaptive decentralized controller is established, and we can construct the boundedness of all signals in the closed-loop structure through the controller, which can drive the formation of a given reference signal. In the end, the effectiveness of the presented strategy is referred to a simulation example.

1. Introduction

Interconnected systems are a race of large-scale systems, which contain some related subsystems. Interactions among subsystems often exist in interconnected systems, such as aerospace systems and electric power and computer systems. Decentralized control method is effective to solve stability of the interconnected structure. Its main principle is to use local information to form local controllers and achieve to control the entire system. The advantage is that it is simpler and more effective than the centralized control. Some important achievements have been made in this field, especially the stabilization and tracking control issues, see [1–7]. Planting parameters and interactions among subsystems are often unknown; the decentralized control technique via Nussbaum gain function can solve the difficulty, which only depends on local measurements [8]. In [9–11], the authors discussed some decentralized ideas to deal with the dimensional uncertainty of interconnected systems.

Recently, research on decentralized control using backstepping approach has also received considerable attention, such as improving transient performance [12]. This control strategy only uses local signals to design local controllers for each subsystem, which not only simplifies the controller structure but also improves the stability and performance analysis of the whole closed-loop system when there is uncertain interaction between subsystems. In the early stage of research, decentralized adaptive control was mainly based on the traditional deterministic equivalence principle, which usually requires some conservative assumptions on the structure and interaction of subsystems. By means of the linear state observer, several different controllers were developed by Ji et al. and Liu et al. [13, 14]. Some feedback control approaches have been presented for different systems in [13, 15, 16]. The authors in [17] solved the exponential stability criteria for interval-delayed neural networks. A filter was constructed to eliminate interference signals in [18]. The event-triggered feedback control was studied for an exogenous disturbance system [19]. In fact, stochastic disturbances often exist in the practical systems; it should be noted that the aforementioned adaptive algorithms were only limited to the uncertain ones, and they cannot be directly used in those interconnected ones with stochastic forms; this kind of problem has not been studied in depth. In addition, the control format for stochastic systems involves Itô formula which contains gradient terms and also includes higher-order Hessian terms. Therefore, how to design a stable scheme for interconnected stochastic systems is our main purpose.

It is common knowledge that fuzzy logic or neural network structure is valid to settle the indeterminacy. Its basic conception is to select controllers by backstepping technique and then choose a system to approximate the indeterminate functions. This function estimation technique has been developed for the completely unknown nonlinearities, which has been applied to single input or output models in [20–27], and multiple input and output models were established in [28–31]. As a specialized approximator, a fuzzy logic structure was employed to estimate the unknown functions, and an output controller was established in [28]. In [29, 30], the controllers of multiple input and output models were established. Combining with the radial basis function, an adaptive feedback algorithm was proposed in [31]. The aforementioned conclusions have been extended to output feedback cases in [22, 23]. In [32], adaptive dynamics and higher and lower powers were introduced to construct the controller, and the state feedback stabilization was obtained by using the Lyapunov function and the backstepping method. Neural networks solved the unmeasured states, and decentralized controllers were discussed in [33, 34]. Therefore, a natural idea is that we can control interconnected systems with various uncertainties by the above methods. Although many results have been listed on various models with nonlinearities, the interaction among subsystems is unknown and satisfies the high-order nonlinear boundary, numerous actual problems cannot be converted into the ideal state, and the approximation-based inversion technology is hindered. When the system is considered as an interconnection type and wants to achieve a steady state, the existing control methods cannot deal with this type of problem. In fact, few results were reported on the stabilization for stochastic interconnect systems. In most of research studies, adaptive controllers were constructed in traditional backstepping design. Whether this method can be directly applied to obtain controllers for stochastic and interconnected characteristics, and what improvements are needed are the issues to be discussed in this work.

Inspired by the above works, this paper investigates an adaptive neural decentralized scheme for an uncertain interconnected system with unknown terms. It is supposed that only the output state can be measured, and there exist uncertain nonlinear functions, unknown associated terms, and stochastic disturbance. We design a neural controller via a modified backstepping approach. The proposed scheme is independent of the prior knowledge of the basis functions. Compared with the existing design methods, the innovation points of this paper are stated as follows:

(1) When the completely unknown associated terms exist and the state variable information is unknown, a modified adaptive neural scheme is proposed to deal with the distributed large-scale systems. It is different from the above works that the whole system needs only one virtual control signal. It is not necessary to repeatedly distinguish the virtual signals in each subsystem. The reliability can be improved when the random phenomenon occurs.

(2) Only one adaptive parameter is needed in the design process, so the proposed control method has fewer parameters and less calculation.

The rest of this work is composed of the following: we introduced some assumptions and preliminaries and described problem statements in Section 2, as well as adaptive neural controller design and stability analysis are listed Section 3. Simulation results can been found in Section 4, with conclusion in Section 5.

2. Problem Statements and Preliminaries

2.1. System Description. Now, let us first give our system and some related assumptions. Consider an interconnected system that is composed of N subsystems; the ith subsystem is given as

$$\begin{cases} dx_{i,1} = \left(x_{i,2} + h_{i,1}\left(\overline{x}_{i,1}\right) + \Phi_{i,1}\left(\overline{y}\right)\right)\mathrm{d}t + \psi_{i,1}^{T}\left(y_i\right)\mathrm{d}\omega_i, \\ dx_{i,2} = \left(x_{i,3} + h_{i,2}\left(\overline{x}_{i,2}\right) + \Phi_{i,2}\left(\overline{y}\right)\right)\mathrm{d}t + \psi_{i,2}^{T}\left(y_i\right)\mathrm{d}\omega_i, \\ \vdots \\ dx_{i,n_i} = \left(u_i + h_{i,n_i}\left(\overline{x}_{i,n_i}\right) + \Phi_{i,n_i}\left(\overline{y}\right)\right)\mathrm{d}t + \psi_{i,n_i}^{T}\left(y_i\right)\mathrm{d}\omega_i, \\ y_i = x_{i,1}, \end{cases} \tag{1}$$

where $\overline{x}_{i,j} = [x_{i,1}, \ldots, x_{i,j}]^T$, $\overline{y} = [y_1, y_2, \ldots, y_N]^T$, $x_i = [x_{i,1}, x_{i,2}, \ldots, x_{i,n_i}]^T \in R^{n_i}$, and $u_i \in R$ and $y_i \in R$ are the input and output of the system, respectively. $\psi_{i,j}(y_i)$ is the smooth function with $\psi_{i,j}(0) = 0$, and ω_i denotes an r-dimensional standard Brownian motion defined on the complete probability space $(\Delta, F, \{F_t\}_{t\geq 0}, P)$, with Δ being the sample space, F being $\sigma-$filed, $\{F_t\}_{t\geq 0}$ being the filtration, and P being the probability measure. $h_{i,j}(\overline{x}_{i,j})$, $1 \leq i \leq N$, is an unknown nonlinear smooth function with $h_{i,j}(0) = 0$, and $\Phi_{i,j}(\overline{y})$ is a nonlinear uncertainty, which represents the ith interconnection between the subsystem and other subsystems.

Assumption 1. Since $\Phi_{i,j}(\overline{y})$ and $\psi_{i,j}(\overline{y})$ are smooth functions, unknown smooth functions $\Phi_{i,j,l}(y_l)$ and $\psi_{i,j,l}(y_l)$ satisfy the following inequalities:

$$\begin{aligned} \left|\Phi_{i,j}\left(\overline{y}\right)\right|^2 &\leq \sum_{l=1}^{N} \Phi_{i,j,l}^2\left(y_l\right), \\ \left\|\psi_{i,j}\left(\overline{y}\right)\right\|^2 &\leq \sum_{l=1}^{N} \psi_{i,j,l}^2\left(y_l\right), \end{aligned} \tag{2}$$

with $\Phi_{i,j,l}(0) = \psi_{i,j,l}(0) = 0$, $l = 1, 2, \ldots, N$.

Remark 1. Note that $\Phi_{i,j,l}(y_l)$ and $\psi_{i,j,l}(y_l)$ are smooth functions and $\Phi_{i,j,l}(0) = \psi_{i,j,l}(0)$; there exist unknown functions $\overline{\Phi}_{i,j,l}(y_l)$ and $\overline{\psi}_{i,j,l}(y_l)$ which can be expressed as

$$\left|\Phi_{i,j}(\overline{y})\right|^2 \le \sum_{l=1}^{N} y_l^2 \overline{\Phi}_{i,j,l}^2(y_l),$$
$$\left\|\psi_{i,j}(\overline{y}_i)\right\|^2 \le \sum_{l=1}^{N} y_l^2 \overline{\psi}_{i,j,l}^2(y_l). \tag{3}$$

2.2. Preliminaries' Description. We will present some lemmas, definitions, and basic knowledge in this part; they will be used in the subsequent developments. Consider the stochastic structure

$$dx(t) = f(x(t))\mathrm{d}t + g(x(t))\mathrm{d}\omega, \tag{4}$$

where x and ω are the same as defined in (1) and $f(\cdot)$ and $g(\cdot)$ are local Lipschitz functions and satisfy $f(0) = g(0)$.

Lemma 1 (see [35]). *For each pair $(x, y) \in R^2$, Young's inequality holds*

$$xy \le \frac{\varepsilon^a}{a}|x|^a + \frac{1}{b\varepsilon^b}|y|^b, \tag{5}$$

where $\varepsilon > 0, a > 1, b > 1$, and $(a-1)(b-1) = 1$.

Definition 1. (see [36]). For any given $V(x) \in C^2$, which is associated with (4), the infinitesimal generator $\mathscr{L}$ is defined as

$$\mathscr{L}V(x) = \frac{\partial V}{\partial x} f(x) + \frac{1}{2}\mathrm{Tr}\left\{g(x)^T \frac{\partial^2 V}{\partial x^2} g(x)\right\}. \tag{6}$$

$\mathrm{Tr}(A)$ is the trace of a matrix.

Lemma 2. *Consider system (4); if there exists a Lyapunov function $V(x) \in C^2$, $\overline{\mu}_1$ and $\overline{\mu}_2$ are class kappa functions, and two constants $p_0 > 0$ and $q_0 > 0$ such that*

$$\overline{\mu}_1(x) \le V(x) \le \overline{\mu}_2(x),$$
$$\mathscr{L}V(x) \le -p_0 V(x) + q_0. \tag{7}$$

Therefore, one conclusion that can be drawn is for (4) and each $x_0 \in R^n$, the solution satisfies

$$E[V(x)] \le V(x_0)e^{-p_0 t} + \frac{p_0}{q_0}, \quad \forall t > t_0. \tag{8}$$

Definition 2. For any continuous unknown smooth nonlinear function $h_{i,j}(Z)$ over a compact set $\Delta_Z \subset R^q$, there exist neural networks $W_{i,j}^{*T}\phi(Z)$ such that, for a desired level of accuracy $\varepsilon_{i,j}$,

$$h_{i,j}(Z) = W_{i,j}^{*T}\phi(Z) + \delta_{i,j}(Z), \quad \left|\delta_{i,j}(Z)\right| \le \varepsilon, \tag{9}$$

$$\psi_{i,j}\left(Z_{i,j}\right) = W_{i,j}^T \phi_{i,j}\left(Z_{i,j}\right) + \delta_{i,j}\left(Z_{i,j}\right)\left|\delta_{i,j}\left(Z_{i,j}\right)\right| < \varepsilon_{i,j}, \tag{10}$$

where $W_{i,j}^*$ is the ideal constant weight vector and is defined by

$$W_{i,j}^* = \arg\min_{W \in R^N}\left\{\sup_{Z \in \Delta_Z}\left|h_{i,j}(Z) - W^T\phi_{i,j}(Z)\right|\right\}. \tag{11}$$

$\delta_{i,j}(Z)$ is the approximation error, $W_{i,j} = [w_1, \ldots, w_N]^T$ is the weight vector, and $\phi_{i,j}(Z) = [\phi_1(Z), \ldots, \phi_N(Z)]^T$ is the basis function vector with N being the number of the networks nodes and $N > 1$. Radial basis function $\phi_i(Z) = \exp[-((Z-\varsigma_i)^T(Z-\varsigma_i)/\eta_i^2)], i = 1, 2, \ldots, N$, where $\varsigma_i = [\varsigma_{i1}, \varsigma_{i2}, \ldots, \varsigma_{in}]^T$, is the center of the receptive field, and η_i is the width of the Gaussian function. For the ith subsystem, $W_{i,j}^T\phi(Z)$ will be used to construct unknown function $\overline{h}_{i,j}(Z_{i,j})$ at step j. At last, we design achievable virtual control signals and adaptive laws in the following form:

$$\alpha_{i,j}\left(Z_{i,j}\right) = -k_{i,j}z_{i,j} - \frac{1}{2p_{i,j}^2}z_{i,j}^3\widehat{\theta}_i\phi_{i,j}^T\left(Z_{i,j}\right)\phi_{i,j}\left(Z_{i,j}\right), \tag{12}$$

$$\dot{\widehat{\theta}}_i = \sum_{j=1}^{n_i}\frac{\varpi_i}{2p_{i,j}^2}z_{i,j}^6\phi_{i,j}^T\left(Z_{i,j}\right)\phi_{i,j}\left(Z_{i,j}\right) - \gamma_i\widehat{\theta}_i, \tag{13}$$

where $i = 1, 2, \ldots, N$, $j = 1, 2, \ldots, n_i$, $k_{i,j}, p_{i,j}, \varpi_i$, and γ_i are positive design parameters, and $Z_{i,1} = x_{i,1}, Z_{i,j} = [\overline{x}_{i,j}^T, \widehat{\theta}_i]^T$ $(j = 2, \ldots, n_i)$ with $\overline{x}_{i,j} = [x_{i,1}, x_{i,2}, \ldots, x_{i,j}]^T$. Now, we introduce a change of coordinates as

$$z_{i,j} = x_{i,j} - \alpha_{i,j-1}, \tag{14}$$

with $\alpha_{i,0} = 0$. To begin with the backstepping design procedure, let us define constant θ_i which will be written as

$$\theta_i = \max\left\{\left\|W_{i,j}\right\|^2, \quad j = 1, 2, \ldots, n_i\right\}, \tag{15}$$

where $\widehat{\theta}_i$ is the estimate of θ_i.

3. Adaptive Neural Control Design

A neural controller will be constructed for interconnected system (1). At the same time, the adaptive laws will be given in this section.

Step 1. It follows from $z_{i,1} = x_{i,1}, z_{i,2} = x_{i,2} - \alpha_{i,1}$ that

$$dz_{i,1} = \left(z_{i,2} + \alpha_{i,1} + h_{i,1} + \Phi_{i,1}(\overline{y})\right)\mathrm{d}t + \psi_{i,1}^T(y_i)\mathrm{d}\omega_i. \tag{16}$$

Establish a Lyapunov candidate $V_{i,1}$ as

$$V_{i,1} = \frac{1}{4}z_{i,1}^4 + \frac{1}{2\varpi_i}\widetilde{\theta}_i^2, \tag{17}$$

where $\varpi_i > 0$ are design parameters.

By taking (6) and (16) into account, we have

$$\mathscr{L}V_{i,1} = z_{i,1}^3\left(z_{i,2} + \alpha_{i,1} + h_{i,1} + \Phi_{i,1}(\overline{y})\right) + \frac{3}{2}z_{i,1}^2\psi_{i,1}^T(y_i)\psi_{i,1}(y_i) - \frac{1}{\varpi_i}\widetilde{\theta}_i\dot{\theta}_i. \tag{18}$$

By Lemma 1, it can be obtained that

$$z_{i,1}^3 z_{i,2} \le \frac{3}{4} z_{i,1}^4 + \frac{1}{4} z_{i,2}^4, \tag{19}$$

$$\begin{aligned} z_{i,1}^3 \Phi_{i,1}(\overline{y}) &\le \frac{3}{4} z_{i,1}^4 + \frac{1}{4} \Phi_{i,1}^4(\overline{y}), \\ &\le \frac{3}{4} z_{i,1}^4 + \frac{1}{4} N \left(\sum_{l=1}^{N} y_l^4 \overline{\Phi}_{i,j,l}^4(y_l) \right), \end{aligned} \tag{20}$$

$$\frac{3}{2} z_{i,1}^2 \psi_{i,1}^T(y_i) \psi_{i,1}(y_i) \le \frac{3}{4} z_{i,1}^4 + \frac{3}{4} N \sum_{l=1}^{N} y_l^4 \overline{\psi}_{i,1,l}^4(y_l). \tag{21}$$

Substituting (19)–(21) into (18), it follows that

$$\begin{aligned} \mathscr{L} V_{i,1} \le{}& \frac{3}{4} z_{i,1}^4 + \frac{1}{4} z_{i,2}^4 + \frac{3}{4} z_{i,1}^4 + z_{i,1}^3 \left(\alpha_{i,1} + h_{i,1} \right) \\ &+ \frac{1}{4} N \sum_{l=1}^{N} y_l^4 \overline{\Phi}_{i,j,l}^4(y_l) + \frac{3}{4} z_{i,1}^4 \\ &+ \frac{3}{4} N \sum_{l=1}^{N} y_l^4 \overline{P}_{i,1,l}^4(y_l) - \frac{1}{\varpi_i} \tilde{\theta}_i \dot{\theta}_i. \end{aligned} \tag{22}$$

Step $m (2 \le m \le n_i)$. According to the coordinate transformation, one has

$$\begin{aligned} dz_{i,m} ={}& \left(z_{i,m+1} + \alpha_{i,m} + h_{i,m} + \Phi_{i,m}(\overline{y}) - \mathscr{L} \alpha_{i,m-1} \right) dt \\ &+ \left(\psi_{i,m}(y_i) - \sum_{k=1}^{m-1} \frac{\partial \alpha_{i,m-1}}{\partial x_{i,k}} \psi_{i,m-1}^T(y_i) \right) d\omega_i, \end{aligned} \tag{23}$$

where

$$\begin{aligned} \mathscr{L} \alpha_{i,m-1} ={}& \sum_{k=1}^{m-1} \frac{\partial \alpha_{i,m-1}}{\partial x_{i,k}} \left(x_{i,k+1} + h_{i,k} + \Phi_{i,k}(\overline{y}) \right) \\ &+ \frac{1}{2} \sum_{p,q=1}^{m-1} \frac{\partial^2 \alpha_{i,m-1}}{\partial x_{i,p} \partial x_{i,q}} \psi_{i,p}^T(y_i) \psi_{i,q}(y_i) + \frac{\partial \alpha_{i,m-1}}{\partial \hat{\theta}_i} \dot{\hat{\theta}}_i. \end{aligned} \tag{24}$$

Construct a stochastic Lyapunov candidate:

$$\begin{aligned} V_m &= \frac{1}{4} z_{i,m}^4 + \frac{1}{2\varpi_i} \tilde{\theta}_i^2, \\ \mathscr{L} V_{i,m} &= z_{i,m}^3 \Bigg(z_{i,m+1} - \sum_{k=1}^{m-1} \frac{\partial \alpha_{i,m-1}}{\partial x_{i,k}} \left(x_{i,k+1} + h_{i,k} \right) \\ &\quad - \frac{\partial \alpha_{i,m-1}}{\partial \hat{\theta}_i} \dot{\hat{\theta}}_i - \sum_{k=1}^{m-1} \frac{\partial \alpha_{i,m-1}}{\partial x_{i,k}} \Phi_{i,k}(\overline{y}) + \alpha_{i,m}(\overline{y}) \\ &\quad + h_{i,m} + \Phi_{i,m} - \frac{1}{2} \sum_{p,q=1}^{m-1} \frac{\partial^2 \alpha_{i,m-1}}{\partial x_{i,p} \partial x_{i,q}} \psi_{i,p}^T(y_i) \psi_{i,q}(y_i) \Bigg) \\ &\quad + \frac{3}{2} z_{i,m}^2 \left(\psi_{i,m}(y_i) - \sum_{k=1}^{m-1} \frac{\partial \alpha_{i,m-1}}{\partial x_{i,k}} \psi_{i,k}(y_i) \right)^T \\ &\quad \cdot \left(\psi_{i,m}(y_i) - \sum_{k=1}^{m-1} \frac{\partial \alpha_{i,m-1}}{\partial x_{i,k}} \psi_{i,k}(y_i) \right) - \frac{1}{\varpi_i} \tilde{\theta}_i \dot{\theta}_i. \end{aligned} \tag{25}$$

Furthermore, similar to the derivations from (19) to (21), the following inequalities can be verified easily:

$$z_{i,m}^3 z_{i,m+1} \le \frac{3}{4} z_{i,m}^4 + \frac{1}{4} z_{i,m+1}^4, \tag{26}$$

$$-z_{i,m}^3 \sum_{k=1}^{m-1} \frac{\partial \alpha_{i,m-1}}{\partial x_{i,k}} \Phi_{i,k}(\overline{y}) \le \frac{3}{4} z_{i,m}^4 \sum_{k=1}^{m-1} \left(\frac{\partial \alpha_{i,m-1}}{\partial x_{i,k}} \right)^{(3/4)} + \frac{1}{4} N \sum_{k=1}^{m-1} \sum_{l=1}^{N} y_l^4 \overline{\Phi}_{i,j,l}^4(y_l), \tag{27}$$

$$z_{i,m}^3 \Phi_{i,k}(\overline{y}) \le \frac{3}{4} z_{i,m}^4 + \frac{1}{4} N \sum_{l=1}^{N} y_l^4 \overline{\Phi}_{i,m,l}^4(y_l), \tag{28}$$

$$-\frac{1}{2} z_{i,m}^3 \sum_{p,q=1}^{m-1} \frac{\partial^2 \alpha_{i,m-1}}{\partial x_{i,p} \partial x_{i,q}} \psi_{i,p}^T(y_i) \psi_{i,q}(y_i) \le \frac{1}{4} z_{i,m}^6 \sum_{p=1}^{m-1} \sum_{q=1}^{m-1} \left(\frac{\partial^2 \alpha_{i,m-1}}{\partial x_{i,p} \partial x_{i,q}} \right)^2 + \frac{1}{4} (m-1) N \sum_{p=1}^{m-1} \sum_{l=1}^{N} y_l^4 \overline{\psi}_{i,p,l}^4(y_l), \tag{29}$$

$$\frac{3}{2} z_{i,m}^2 \left\| \psi_{i,m}(y_i) - \sum_{k=1}^{m-1} \frac{\partial \alpha_{i,m-1}}{\partial x_{i,k}} \psi_{i,k}(y_i) \right\|^2 \le \frac{3}{4} m z_{i,m}^4 \left(1 + \sum_{k=1}^{m-1} \left(\frac{\partial \alpha_{i,m-1}}{\partial x_{i,k}} \right)^4 \right) + \frac{3}{4} m N \sum_{k=1}^{m} \sum_{k=1}^{N} y_l^4 \overline{\psi}_{i,p,l}^4(y_i). \tag{30}$$

Substituting (26)–(30) into (25), it shows the result

$$\begin{aligned}\mathscr{L}V_{i,m} \le z_{i,m}^3 \Bigg(& \alpha_{i,m} + h_{i,m} - \sum_{k=1}^{m-1} \frac{\partial \alpha_{i,m-1}}{\partial x_{i,k}} \left(x_{i,k+1} + h_{i,k} \right) + \frac{3}{2} z_{i,m} + \frac{3}{4} m z_{i,m} + \frac{3}{4} z_{i,m} \sum_{k=1}^{m-1} \left(\frac{\partial \alpha_{i,m-1}}{\partial x_{i,k}} \right)^{\frac{3}{4}} \frac{1}{4} z_{i,m}^3 \sum_{p=1}^{m-1} \sum_{q=1}^{m-1} \left(\frac{\partial^2 \alpha_{i,m-1}}{\partial x_{i,p} \partial x_{i,q}} \right)^2 \\ & - \frac{\partial \alpha_{i,m-1}}{\partial \widehat{\theta}_i} \dot{\widehat{\theta}}_i + + \frac{3}{4} m z_{i,m} \sum_{k=1}^{m-1} \left(\frac{\partial \alpha_{i,m-1}}{\partial x_{i,k}} \right)^4 \Bigg) \\ & + \frac{1}{4} m z_{i,m+1}^4 + \frac{1}{4} (m-1) N \sum_{p=1}^{m-1} \sum_{l=1}^{N} y_l^4 \overline{\Phi}_{i,j,l}^4 (y_l) + \frac{1}{4} N \sum_{k=1}^{m} \sum_{k=1}^{N} y_l^4 \overline{\Phi}_{i,k,l}^4 (y_l) - \frac{1}{\varpi_i} \widetilde{\theta}_i \dot{\theta}_i + \frac{3}{4} m N \sum_{k=1}^{m} \sum_{l=1}^{N} y_l^4 \overline{\Phi}_{i,k,l}^4 (y_l).\end{aligned} \tag{31}$$

Step n_i. By using (5) and the Itô formula, we have

$$\begin{aligned} dz_{i,n_i} = & \left(u_i + h_{i,n_i} + \Phi_{i,n_i}(\overline{y}) - \mathscr{L}\alpha_{i,n_i-1} \right) dt \\ & + \left(\psi_{i,n_i}(y_i) - \sum_{k=1}^{n_i-1} \frac{\partial \alpha_{i,n_i-1}}{\partial x_{i,k}} \psi_{i,k}^T (y_i) \right) d\omega_i, \end{aligned} \tag{32}$$

where $\mathscr{L}\alpha_{i,n_i-1}$ is given in (18). Define a stochastic Lyapunov function V_{i,n_i} as

$$V_{i,n_i} = \frac{1}{4} z_{i,n_i}^4 + \frac{1}{2\varpi_i} \widetilde{\theta}_i^2. \tag{33}$$

Then, by means of (6), we can derive

$$\begin{aligned}\mathscr{L}V_{i,n_i} = z_{i,n_i}^3 \Bigg(& u_i + h_{i,n_i} - \sum_{k=1}^{n_i-1} \frac{\partial \alpha_{i,n_i-1}}{\partial x_{i,k}} \left(x_{i,k+1} + h_{i,k} \right) - \frac{\partial \alpha_{i,n_i-1}}{\partial \widehat{\theta}_i} \dot{\widehat{\theta}}_i + \Phi_{i,n_i}(\overline{y}) - \sum_{k=1}^{n_i-1} \frac{\partial \alpha_{i,n_i-1}}{\partial x_{i,k}} (\overline{y}) \\ & - \frac{1}{2} \sum_{p,q=1}^{n_i-1} \frac{\partial^2 \alpha_{i,n_i-1}}{\partial x_{i,p} \partial x_{i,q}} \psi_i^T \left(y_{i,p} \right) \psi_i \left(y_{i,p} \right) \Bigg) - \frac{1}{\varpi_i} \widetilde{\theta}_i \dot{\theta}_i \\ & + \frac{3}{2} z_{i,n_i}^2 \left\| \psi_{i,n_i}(y_i) - \sum_{k=1}^{n_i-1} \frac{\partial \alpha_{i,n_i-1}}{\partial x_{i,k}} \psi_{i,k}(y_i) \right\|^2 .\end{aligned} \tag{34}$$

Repeating similar methods used in the above procedure, we have

$$\begin{aligned}\mathscr{L}V_{i,n_i} \le z_{i,n_i}^3 \Bigg(& u_i + h_{i,n_i} - \sum_{k=1}^{n_i-1} \frac{\partial \alpha_{i,n_i-1}}{\partial x_{i,k}} \left(x_{i,k+1} + h_{i,k} \right) - \frac{\partial \alpha_{i,n_i-1}}{\partial \widehat{\theta}_i} \dot{\widehat{\theta}}_i + \frac{3}{4} z_{i,m} \sum_{k=1}^{m-1} \left(\frac{\partial \alpha_{i,m-1}}{\partial x_{i,k}} \right)^{3/4} + \frac{1}{4} z_{i,m}^3 \sum_{p=1}^{m-1} \sum_{q=1}^{m-1} \left(\frac{\partial^2 \alpha_{i,m-1}}{\partial x_{i,p} \partial x_{i,q}} \right)^2 \\ & + \frac{3}{4} z_{i,n_i} + \frac{3}{4} n_i z_{i,n_i} \sum_{k=1}^{n_i-1} \frac{\partial \alpha_{i,n_i-1}}{\partial x_{i,k}} \left(x_{i,k+1} + h_{i,k} \right)^4 \Bigg) \\ & + \frac{1}{4} N \sum_{k=1}^{n_i} \sum_{l=1}^{N} y_l^4 \overline{\Phi}_{i,j,l}^4 (y_l) + \frac{3}{4} n_i z_{i,n_i} - \frac{1}{\varpi_i} \widetilde{\theta}_i \dot{\theta}_i + \frac{1}{4} (n_i - 1) N \sum_{p=1}^{n_i-1} \sum_{l=1}^{N} y_l^4 \overline{\Psi}_{i,p,l}^4 (y_l) + \frac{3}{4} n_i N \sum_{k=1}^{n_i} \sum_{l=1}^{N} y_l^4 \overline{\Psi}_{i,p,l}^4 (y_l).\end{aligned} \tag{35}$$

Choose V as a Lyapunov function for the whole system:

$$V = \sum_{i=1}^{N}\sum_{j=1}^{n_i} V_{i,j} = \sum_{i=1}^{N}\left(\frac{1}{4}\sum_{j=1}^{n_i} z_{i,j}^4 + \frac{1}{2\varpi_i}\tilde{\theta}_i^2\right). \tag{36}$$

Combining inequalities (22) and (31) with (32), it follows that

$$\begin{aligned}
\mathscr{L}V \le{}& \sum_{i=1}^{N} z_{i,1}^3\Bigg(\alpha_{i,1} + h_{i,1} + \frac{1}{4}Nz_{i,1}\sum_{l=1}^{N}\sum_{s=1}^{n_l}\sum_{k=1}^{s}\overline{\Phi}_{l,k,i}^4(\overline{y}) + \frac{9}{4}z_{i,1} + \frac{1}{4}Nz_{i,1}\sum_{l=1}^{N}\sum_{s=1}^{n_i-1} s\sum_{p=1}^{s}\overline{\psi}_{l,p,i}^4(\overline{y}) \\
&+ \frac{3}{4}Nz_{i,1}\sum_{l=1}^{N}\sum_{s=1}^{n_i-1} s\sum_{p=1}^{s}\overline{\psi}_{l,k,i}^4(\overline{y})\Bigg) + \frac{3}{4}\left(j+\frac{7}{3}\right)z_{i,j} \\
&+ \sum_{i=1}^{N}\sum_{j=2}^{n_i-1} z_{i,j}^3\left(\alpha_{i,j} + \frac{1}{4}z_{i,j}^3\sum_{p=1}^{j-1}\sum_{q=1}^{j-1}\left(\frac{\partial^2\alpha_{i,j-1}}{\partial x_{i,p}\partial x_{i,q}}\right)^2\right) + h_{i,1} + \frac{3}{4}z_{i,j} + \frac{3}{4}z_{i,j}\sum_{k=1}^{j-1}\left(\frac{\partial\alpha_{i,j-1}}{\partial x_{i,k}}\right)^{3/4} \\
&- \sum_{i=1}^{N}\frac{1}{\varpi_i}\tilde{\theta}_i\dot{\hat{\theta}}_i - \sum_{k=1}^{j-1}\frac{\partial\alpha_{i,j-1}}{\alpha x_{i,k}}\left(x_{i,k+1} + h_{i,k}\right) + \frac{3}{4}jz_{i,j}\sum_{k=1}^{j-1}\left(\frac{\partial\alpha_{i,j-1}}{\partial x_{i,k}}\right)^4,
\end{aligned} \tag{37}$$

$$\frac{1}{4}N\sum_{i=1}^{N}\sum_{s=1}^{n_i} s\sum_{k=1}^{s}\sum_{l=1}^{N} y_l^4\overline{\Phi}_{i.k.l}^4(y_l) = \frac{1}{4}N\sum_{i=1}^{N}\sum_{l=1}^{N}\sum_{s=1}^{n_i} s\sum_{k=1}^{s} y_i^4\overline{\Phi}_{l,k,i}^4(y_i),$$

$$\frac{3}{4}N\sum_{i=1}^{N}\sum_{s=1}^{n_i} s\sum_{k=1}^{s}\sum_{l=1}^{N} y_l^4\overline{\psi}_{i.k.l}^4(y_l) = \frac{3}{4}N\sum_{i=1}^{N}\sum_{l=1}^{N}\sum_{s=1}^{n_i} s\sum_{k=1}^{s} y_i^4\overline{\psi}_{l,k,i}^4(y_i),$$

$$\frac{1}{4}N\sum_{i=1}^{N}\sum_{s=1}^{n_i-1} s\sum_{p=1}^{s}\sum_{l=1}^{N} y_l^4\overline{\psi}_{i,p,l}^4(y_l) = \frac{1}{4}N\sum_{i=1}^{N}\sum_{l=1}^{N}\sum_{s=1}^{n_i-1} s\sum_{p=1}^{s} y_i^4\overline{\psi}_{l,p,i}^4(y_i).$$

By (12) and rearranging the sequence, it follows that

$$\begin{aligned}
-\sum_{i=1}^{N}\sum_{j=2}^{n_i} z_{i,j}^3\frac{\partial\alpha_{i,j-1}}{\partial\hat{\theta}_i}\dot{\hat{\theta}}_i &= -\sum_{i=1}^{N}\sum_{j=2}^{n_i} z_{i,j}^3\frac{\partial\alpha_{i,j-1}}{\partial\hat{\theta}_i}\left(\sum_{k=1}^{n_i}\frac{\varpi_i}{2p_{i,k}^2}z_{i,k}^6\phi_{i,k}^T\phi_{i,k} - \gamma_i\hat{\theta}_i\right) \\
&= \sum_{k=1}^{j-1}\frac{\varpi_i}{2p_{i,k}^2}z_{i,k}^6\phi_{i,k}^T\phi_{i,k} - \sum_{i=1}^{N}\sum_{j=2}^{n_i} z_{i,j}^3\frac{\partial\alpha_{i,j-1}}{\partial\hat{\theta}_i}\sum_{k=j}^{n_i}\frac{\varpi_i}{2p_{i,k}^2}z_{i,k}^6\phi_{i,k}^T\phi_{i,k}
\end{aligned} \tag{38}$$

$$\begin{aligned}
\sum_{i=1}^{N}\sum_{j=2}^{n_i} z_{i,j}^3\frac{\partial\alpha_{i,j-1}}{\partial\hat{\theta}_i}\gamma_i\hat{\theta}_i - \sum_{i=1}^{N}\sum_{j=2}^{n_i} z_{i,j}^3\frac{\partial\alpha_{i,j-1}}{\partial\hat{\theta}_i} &\le \sum_{i=1}^{N}\sum_{j=2}^{n_i} z_{i,j}^3\frac{\partial\alpha_{i,j-1}}{\partial\hat{\theta}_i}\gamma_i\hat{\theta}_i - \sum_{i=1}^{N}\sum_{j=2}^{n_i} z_{i,j}^3\frac{\partial\alpha_{i,j-1}}{\partial\hat{\theta}_i}\sum_{k=1}^{j-1}\frac{\varpi_i}{2p_{i,k}^2}z_{i,k}^6\phi_{i,k}^T\phi_{i,k} \\
&\quad + \sum_{i=1}^{N}\sum_{j=2}^{n_i}\frac{\varpi_i}{2p_{i,j}^2}z_{i,j}^6\left(\sum_{k=2}^{j}\left|z_{i,k}^3\frac{\partial\alpha_{i,k-1}}{\partial\hat{\theta}_i}\right|\right).
\end{aligned}$$

Substituting (38) into (36) yields

$$\mathscr{L}V \le \sum_{i=1}^{N} z_i^3\left(\alpha_{i,1} + \overline{h}_{i,1}\left(Z_{i,1}\right)\right) + \sum_{i=1}^{N}\sum_{j=2}^{n_i-1} z_{i,j}^3\left(\alpha_{i,j} + \overline{h}_{i,j}\left(Z_{i,j}\right)\right) + \sum_{i=1}^{N} z_{i,n_i}^3\left(u_i + \overline{h}_{i,n_i}\left(Z_{i,n_i}\right)\right) - \frac{3}{4}\sum_{i=1}^{N}\sum_{j=1}^{n_i} z_{i,j}^4 - \sum_{i=1}^{N}\frac{1}{\varpi_i}\widetilde{\theta}_i\dot{\widehat{\theta}}_i. \tag{39}$$

The function $\overline{h}_{i,j}(Z_{i,j}), i = 1, 2, \ldots, N$, is defined as

$$\begin{aligned}
\overline{h}_{i,1}\left(Z_{i,1}\right) &= h_{i,1} + 3y_i + \frac{1}{4}Ny_i\sum_{l=1}^{N}\sum_{s=1}^{n_i}\sum_{k=1}^{s}\overline{h}_{l,k,i}^4(y_i) + \frac{3}{4}Ny_i\sum_{i=1}^{N}\sum_{s=1}^{n_i}s\sum_{k=1}^{s}\overline{\psi}_{l,k,i}^4(y_i) + \frac{1}{4}Ny_i\sum_{l=1}^{N}\sum_{s=1}^{n_i}s\sum_{p=1}^{s}\overline{\psi}_{l,p,i}^4(y_i),\\
\overline{h}_{i,j}\left(Z_{i,j}\right) &= h_{i,j} - \sum_{k=1}^{j-1}\frac{\partial\alpha_{i,j-1}}{\partial x_{i,k}}\left(x_{i,k+1} + h_{i,k}\right) + \frac{3}{4}z_{i,j} + \frac{3}{4}z_{i,j}\sum_{k=1}^{j-1}\left(\frac{\partial\alpha_{i,j-1}}{\partial x_{i,k}}\right)^{3/4} + \frac{3}{4}jz_{i,j}\sum_{k=1}^{j-1}\left(\frac{\partial\alpha_{i,j-1}}{\partial x_{i,k}}\right)^4\\
&\quad + \frac{1}{4}z_{i,j}^3\sum_{p=1}^{j-1}\sum_{q=1}^{j-1}\left(\frac{\partial^2\alpha_{i,j-1}}{\partial x_{i,p}\partial x_{i,q}}\right)^2 + \frac{3}{4}(j+2)z_{i,j}\\
&\quad + \frac{\partial\alpha_{i,j-1}}{\partial\widehat{\theta}_i}\gamma_i\widehat{\theta}_i - \sum_{k=1}^{j-1}\frac{\lambda_i}{2p_{i,k}^2}z_{i,k}^6\phi_{i,k}^T\phi_{i,k} + \frac{1}{4}z_{i,j} + \frac{\varpi_i}{2p_{i,j}^2}z_{i,j}^3\left(\sum_{k=2}^{j}\left|z_{i,k}^3\frac{\partial\alpha_{i,k-1}}{\partial\widehat{\theta}_i}\right|\right), \quad j = 2, \ldots, n_i - 1,\\
\overline{h}_{i,n_i}\left(Z_{i,n_i}\right) &= h_{i,n_i} - \sum_{k=1}^{n_i-1}\frac{\partial\alpha_{i,n_i-1}}{\partial x_{i,k}}\left(x_{i,k+1} + h_{i,k}\right) + \frac{\varpi_i}{2p_{i,n_i}^2}z_{i,n_i}^3\left(\sum_{k=2}^{n_i}\left|z_{i,k}^3\frac{\partial\alpha_{i,k-1}}{\partial\widehat{\theta}_i}\right|\right) + \frac{3}{4}z_{i,n_i}\sum_{k=1}^{n_i-1}\left(\frac{\partial\alpha_{i,n_i-1}}{\partial x_{i,k}}\right)^{3/4}\\
&\quad + \frac{1}{4}z_{i,n_i} + \frac{1}{4}z_{i,n_i}^3\sum_{p=1}^{n_i-1}\sum_{q=1}^{n_i-1}\left(\frac{\partial^2\alpha_{i,n_i-1}}{\partial x_{i,p}\partial x_{i,q}}\right)^2\\
&\quad + \frac{3}{4}(n_i+2)z_{i,n_i} + \frac{\partial\alpha_{i,n_i-1}}{\partial\widehat{\theta}_i}\gamma_i\widehat{\theta}_i - \frac{\partial\alpha_{i,n_i-1}}{\partial\widehat{\theta}_i}\sum_{k=1}^{n_i-1}\frac{\varpi_i}{2p_{i,k}^2}z_{i,k}^6S_{i,k}^T\phi_{i,k} + \frac{3}{4}n_iz_{i,n_i}\sum_{k=1}^{n_i-1}\left(\frac{\partial\alpha_{i,n_i-1}}{\partial x_{i,k}}\right)^4.
\end{aligned} \tag{40}$$

Furthermore, by (10) and Young's inequality, we have

$$\begin{aligned}
z_{i,j}^3\overline{h}_{i,j}\left(Z_{i,j}\right) &= z_{i,j}^3\frac{W_{i,j}^T}{\left\|W_{i,j}\right\|}\phi_{i,j}\left\|W_{i,j}\right\| + z_{i,j}^3\delta_{i,j}\left(Z_{i,j}\right) \le \frac{1}{2p_{i,j}^2}z_{i,j}^6\left\|W_{i,j}\right\|^2\phi_{i,j}^T\phi_{i,j} + \frac{1}{2}p_{i,j}^2 + \frac{3}{4}z_{i,j}^4 + \frac{1}{4}\varepsilon_{i,j}^4 \le \frac{1}{2p_{i,j}^2}z_{i,j}^6\theta_i\phi_{i,j}^T\phi_{i,j}\\
&\quad + \frac{1}{2}p_{i,j}^2 + \frac{3}{4}z_{i,j}^4 + \frac{1}{4}\varepsilon_{i,j}^4,\\
\mathscr{L}V &\le \sum_{i=1}^{N} z_{i,1}^3\left(\alpha_{i,1} + \frac{1}{2p_{i,1}^2}z_{i,1}^3\theta_i\phi_{i,1}^T\phi_{i,1}\right) + \sum_{i=1}^{N}\sum_{j=2}^{n_i-1} z_{i,j}^3\left(\alpha_{i,j} + \frac{1}{2p_{i,j}^2}z_{i,j}^3\theta_i\phi_{i,j}^T\phi_{i,j}\right) + \sum_{i=1}^{N} z_{i,n_i}^3\left(u_i + \frac{1}{2p_{i,n_i}^2}z_{i,n_i}^3\theta_i\phi_{i,n_i}^T\phi_{i,n_i}\right)\\
&\quad + \sum_{i=1}^{N}\sum_{j=1}^{n_i}\left(\frac{1}{2}p_{i,j}^2 + \frac{1}{4}\varepsilon_{i,j}^4\right) - \sum_{i=1}^{N}\frac{1}{\varpi_i}\widetilde{\theta}_i\dot{\widehat{\theta}}_i.
\end{aligned} \tag{41}$$

Furthermore, by taking (8) and (9) into account and using the following inequality,

$$z_{i,j}^3\alpha_{i,j} \le -a_{i,j}z_{i,j}^4 - \frac{1}{2p_{i,j}^2}z_{i,j}^6\widehat{\theta}_i\phi_{i,j}^T\phi_{i,j}, \quad i = 1,2,\ldots,N, \quad j = 1,2,\ldots,n_i, \tag{42}$$

(41) can be rewritten as

$$\mathscr{L}V \le -\sum_{i=1}^{N}\left(\sum_{j=1}^{n_i} a_{i,j}z_{i,j}^4 + \frac{\gamma_i}{2\varpi_i}\widetilde{\theta}_i^2\right) + \sum_{i=1}^{N}\sum_{j=1}^{n_i}\left(\frac{1}{2}p_{i,j}^2 + \frac{1}{4}\varepsilon_{i,j}^4 + \frac{\gamma_i}{2\varpi_i}\theta_i^2\right). \tag{43}$$

The inequalities $z_{i,1}^3\alpha_{i,1} \le -k_{i,j}z_{i,j}^4 - (1/2p_{i,j}^2)z_{i,n_i}^3\widehat{\theta}_i\phi_{i,j}^T\phi_{i,j}$, $i = 1,2,\ldots,N$, $j = 1,2,\ldots,n_i$, and $\widetilde{\theta}_i\widehat{\theta}_i \le -(1/2)\widetilde{\theta}_i^2 + (1/2)\theta_i^2$ have been used in (43).

According to the above design stage, we introduce our main result in the following theorem.

Theorem 1. *Under Assumption 1, the closed-loop structure consists of controller (11) and the adaptive law (12), which are designed from system (1). Suppose that, for $1 \le i \le N$ and $1 \le j \le n_i$, all the unknown nonlinear functions can be estimated by the neural network structure with the bounded approximation errors $\varepsilon_{i,j}(Z_{i,j})$ in probability. Then, all signals are bounded with the suitable parameter. The error signals $z_{i,j}$ and $\widetilde{\theta}_i$ eventually converge to the compact set Δ_s defined by*

$$\Delta_s = \left\{ z_{i,j}, \widetilde{\theta}_i \,\middle|\, \sum_{i=1}^{N}\sum_{j=1}^{n_i} E\left[\left|z_{i,j}\right|^4\right] \le \frac{4p_0}{q_0}, \quad \left|\widetilde{\theta}_i\right| \le \sqrt{\frac{2\varpi_i p_0}{q_0}}, \ 1 \le i \le N \right\}. \tag{44}$$

Proof. Let $p_0 = \min\{4k_{i,j}, \gamma_i, i = 1,2,\ldots,N, j = 1,2,\ldots,n_i\}$ and $q_0 = \sum_{i=1}^{N}\sum_{j=1}^{n_i}((1/2)p_{i,j}^2 + (1/4)\varepsilon_{i,j}^4 + (\gamma_i/2\varpi_i)\theta_i^2)$; then, (43) can be rewritten as

$$\mathscr{L}V \le -p_0V + q_0, \quad t \ge 0. \tag{45}$$

According to Lemma 1, it is easy to obtain that $z_{i,j}$ and $\widetilde{\theta}$ are bounded. Moreover, in terms of θ_i is a constant, thus $\widehat{\theta}_i$ is bounded. It can be derived that $z_{i,j}$ and $\widehat{\theta}_i$ are bounded variables. So, $\alpha_{i,j}$ is also bounded in probability. As a result, all signals $x_{i,j} = z_{i,j} + \alpha_{i,j-1}$ are also bounded. Furthermore, from (45), the following inequality holds:

$$\frac{\mathrm{d}E[V(t)]}{\mathrm{d}t} \le -p_0E[V(t)] + q_0, \tag{46}$$

which implies that

$$E[V(t)] \le e^{-p_0t}[V(0)] + \frac{q_0}{p_0}, \quad \forall t > 0. \tag{47}$$

Then, it is easily to obtain that

$$E[V(t)] \le \frac{q_0}{p_0}, \quad t \longrightarrow +\infty. \tag{48}$$

Therefore, based on the definition of V in (36), the signals $z_{i,j}$ and $\widetilde{\theta}_i$ eventually converge to the compact set Δ_s specified in (44). Now, it can be shown that all the signals are semiglobally, uniformly, and ultimately bounded, which are the desired results, and it completes the proof. □

4. Simulation Example

We will construct a numerical simulation example to verify the effectiveness of the proposed controllers. The stochastic large-scale system with nonlinear uncertainty is defined as follows:

$$\begin{aligned} dx_{1,1} &= \left(x_{1,2} + h_{1,1} + \Phi_{1,1}\right)\mathrm{d}t + \psi_{1,1}^T dw_i, \\ dx_{1,2} &= \left(u_1 + h_{1,2} + \Phi_{1,2}\right)\mathrm{d}t + \psi_{1,2}^T dw_i, \\ y_1 &= x_{1,1}, \\ dx_{2,1} &= \left(x_{2,2} + h_{2,1} + \Phi_{2,1}\right)\mathrm{d}t + \psi_{2,1}^T dw_i, \\ dx_{2,2} &= \left(u_2 + h_{2,2} + \Phi_{2,2}\right)\mathrm{d}t + \psi_{2,2}^T dw_i, \\ y_2 &= x_{2,1}, \end{aligned} \tag{49}$$

where the nonlinear functions are $h_{1,1} = (3/5)x_{1,1}$, $h_{1,2} = 3x_{1,2}^2$, $h_{2,1} = x_{2,1}$, and $h_{2,2} = (2/3)x_{2,2}^2$, the interconnection functions are $\Phi_{1,1} = (1/10)_1^3\sin(x_1x_2)$, $\Phi_{1,2} = 2\sin(x_1x_2)$, $\Phi_{2,1} = 15\sin(x_1x_2)$, and $\Phi_{2,2} = (1/100)x_1^3\sin(x_2^2)$, the stochastic disturbance functions are $\psi_{1,1} = (1/15)x_1, \psi_{1,2} = (1/8)x_1$, $\psi_{2,1} = (1/12)x_1$, and $\psi_{2,2} = (1/8)x_1$, and the initial states are chosen as $x_{1,1}(0) = 0.2$, $x_{1,2}(0) = 0.3$, $x_{2,1}(0) = 0.5$, $x_{2,2}(0) = 0.4$.

According to Theorem 1, the virtual controls $\alpha_{1,1}$, $\alpha_{2,1}$ and the true control laws u_1, u_2 are chosen, respectively, as

$$\begin{aligned} \alpha_{1,1} &= -k_{1,1}z_{1,1} - \frac{1}{2p_{1,1}^2}z_{1,1}^3\widehat{\theta}_1\phi_{1,1}^T\phi_{1,1}, \\ u_1 &= -k_{1,2}z_{1,2} - \frac{1}{2p_{1,2}^2}z_{1,2}^3\widehat{\theta}_1\phi_{1,2}^T\phi_{1,2}, \\ \alpha_{2,1} &= -k_{2,1}z_{2,1} - \frac{1}{2p_{2,1}^2}z_{2,1}^3\widehat{\theta}_2\phi_{2,1}^T\phi_{2,1}, \\ u_2 &= -k_{2,2}z_{2,2} - \frac{1}{2p_{2,2}^2}z_{2,2}^3\widehat{\theta}_2\phi_{2,2}^T\phi_{2,2}, \end{aligned} \tag{50}$$

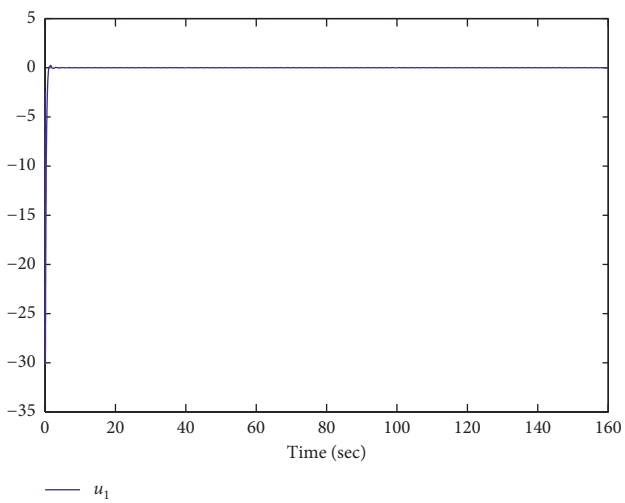

Figure 1: The control input u_1.

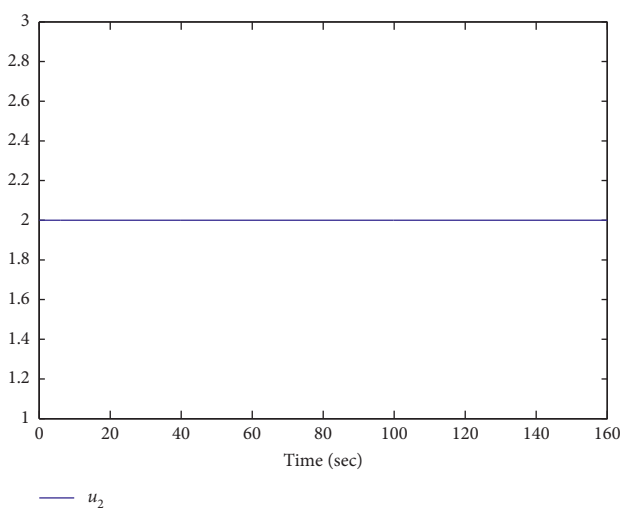

Figure 2: The control input u_2.

where $z_{1,1} = x_{1,1}$, $z_{1,2} = x_{1,2} - \alpha_{1,1}$, $z_{2,1} = x_{2,1}$, and $z_{2,2} = x_{2,2} - \alpha_{2,1}$. The adaptive laws are given as

$$\dot{\widehat{\theta}}_1 = \sum_{j=1}^{2} \frac{\varpi_1}{2k_{1,j}^2} z_{1,j}^6 \phi_{1,j}^T \phi_{1,j} - \gamma_1 \widehat{\theta}_1,$$
$$\dot{\widehat{\theta}}_2 = \sum_{j=1}^{2} \frac{\varpi_2}{2k_{2,j}^2} z_{2,j}^6 \phi_{2,j}^T \phi_{2,j} - \gamma_2 \widehat{\theta}_2. \tag{51}$$

In the simulation, the design parameters are chosen as $k_{1,1} = k_{1,2} = k_{2,1} = k_{2,2} = 1.5$, $\varpi_1 = \varpi_2 = 1$, and $\gamma_1 = \gamma_2 = 2$.

The simulation results are illustrated in Figures 1–5, respectively. Figures 1 and 2 demonstrate the control inputs. Figures 3 and 4 illustrate the system states. Figure 5 gives the trajectories of adaptive parameters θ_1 and θ_2. From Figures 1–5, it can be seen that all signals in the closed-loop structure are bounded, and the states can track the given

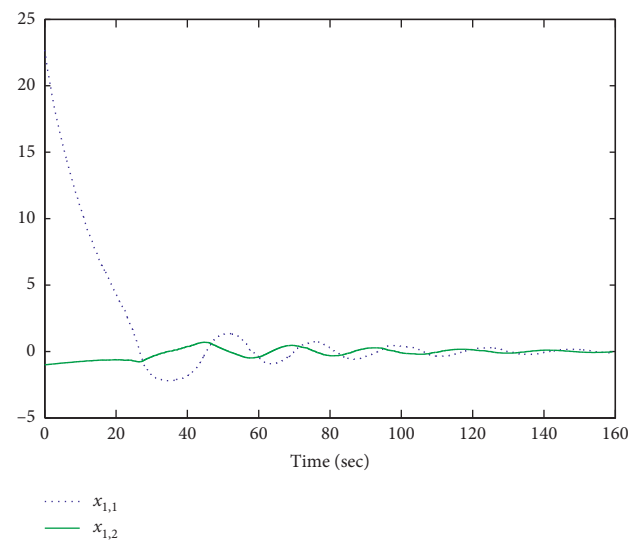

Figure 3: The state profile of $x_{1,1}$ and $x_{1,2}$.

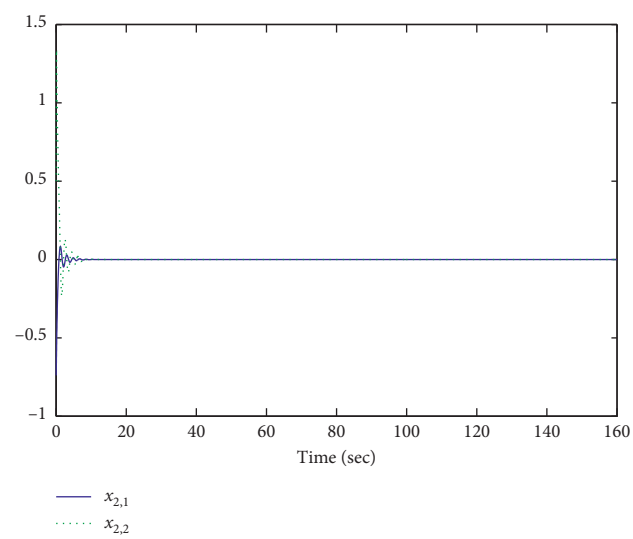

Figure 4: The state profile of $x_{2,1}$ and $x_{2,2}$.

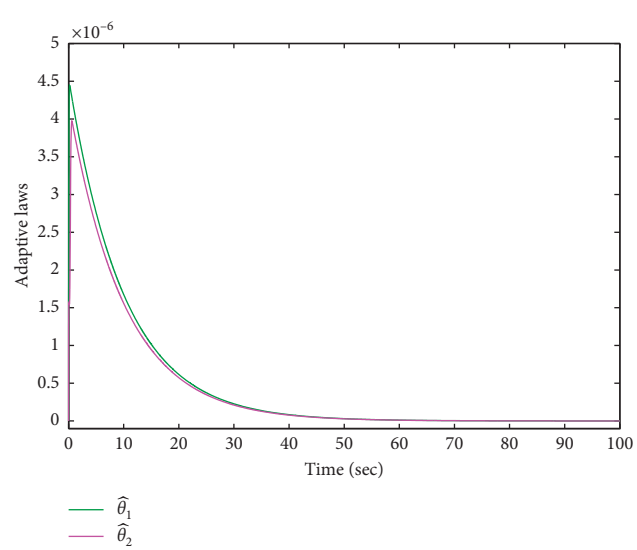

Figure 5: The time profile of $\widehat{\theta}_1$ and $\widehat{\theta}_2$.

reference signals. Based on the simulation results, we can conclude that the proposed decentralized control scheme is effective for the large-scale stochastic system.

5. Conclusions

Different from the related literature studies, we investigated the control problem for an uncertain interconnected system and designed a state feedback decentralized scheme. There are two difficulties in this paper: one is that the associated terms are completely unknown, and a neural network system is an effective function approximator at present. Therefore, we chose it to estimate these functions. The other is that how to design a decentralized controller to resist the impact among interconnected systems; to deal with this problem, we introduced a neural controller into the control scheme to track the variation of the error. The controller is constructed based on the improved backstepping technique. It is proved that all the signals of the whole closed-loop system are semiglobally, uniformly, and ultimately bounded. The numerical simulations showed that the controller can effectively and steadily drive the original signal. The main novelty is that this work gives a universal formula for establishing a neural state feedback scheme with only one adaptive parameter. Of course, there are still many questions to be further studied. For example, when the solvability of individual subsystems is not assumed, how to find a sufficient condition to make systems stable is an open problem. For another example, we ignored the external disturbance in the system, which is difficult to avoid in the actual control. Therefore, our future work will be devoted to investigating the control method with perturbation terms. Also, we will focus on the control for interconnected systems with output constraints based on the results of this paper.

Data Availability

The data used to support the findings of this study are included within the article.

Conflicts of Interest

The authors declare that they have no conflicts of interest.

Acknowledgments

This work was supported in part by the National Natural Science Foundation of China (Grant nos. 11871117 and 61976027) and the Natural Science Foundation of Liaoning Province of China (Grant nos. 20180551262 and LQ2019008).

References

[1] C. Wen, "Decentralized adaptive regulation," *IEEE Transactions on Automatic Control*, vol. 39, no. 10, pp. 2163–2166, 1994.

[2] S. Jain and F. Khorrami, "Decentralized adaptive control of a class of large-scale interconnected nonlinear systems," *IEEE Transactions on Automatic Control*, vol. 42, no. 2, pp. 136–154, 1997.

[3] S. Jain and F. Khorrami, "Decentralized adaptive output feedback design for large-scale nonlinear systems," *IEEE Transactions on Automatic Control*, vol. 42, no. 5, pp. 729–735, May 1997.

[4] X. Ye and J. Huang, "Decentralized adaptive output regulation for a class of large-scale nonlinear systems," *IEEE Transactions on Automatic Control*, vol. 48, no. 2, pp. 276–281, 2003.

[5] Z. P. Jiang, "Decentralized and adaptive nonlinear tracking of large-scale systems via output feedback," *IEEE Transactions on Automatic Control*, vol. 45, no. 11, pp. 2122–2128, 2000.

[6] Z. P. Jiang, D. W. Repperger, and D. J. Hill, "Decentralized nonlinear output-feedback stabilization with disturbance attenuation," *IEEE Transactions on Automatic Control*, vol. 46, no. 10, pp. 1623–1629, 2001.

[7] Z.-P. Jiang, "Decentralized disturbance attenuating output-feedback trackers for large-scale nonlinear systems," *Automatica*, vol. 38, no. 8, pp. 1407–1415, 2002.

[8] S. Tong, C. Liu, Y. Li, and H. Zhang, "Adaptive fuzzy decentralized control for large-scale nonlinear systems with time-varying delays and unknown high-frequency gain sign," *IEEE Transactions on Systems, Man, and Cybernetics. Part B (Cybernetics)*, vol. 41, no. 2, pp. 474–485, 2011.

[9] D. Siljak, "Decentralized control and computations: status and prospects," *Annual Review in Automatic Programming*, vol. 20, pp. 131–141, 1996.

[10] D. D. Siljak and A. I. Zecevic, "Control of large-scale systems: beyond decentralized feed-back," *Annual Reviews in Control*, vol. 29, no. 2, pp. 169–179, 2005.

[11] L. Bakule, "Decentralized control: an overview," *Annual Reviews in Control*, vol. 32, no. 1, pp. 87–98, 2008.

[12] M. Krstic, I. Kanellakopoulos, and P. V. Kokotovic, *Nonlinear and Adaptive Control Design*, Wiley, New York, NY, USA, 1995.

[13] H.-B. Ji and H.-S. Xi, "Adaptive output-feedback tracking of stochastic nonlinear systems," *IEEE Transactions on Automatic Control*, vol. 51, no. 2, pp. 355–360, 2006.

[14] S.-J. Liu, S. S. Ge, and J.-F. Zhang, "Adaptive output-feedback control for a class of uncertain stochastic non-linear systems with time delays," *International Journal of Control*, vol. 81, no. 8, pp. 1210–1220, 2008.

[15] Y.-G. Liu and J.-F. Zhang, "Practical output-feedback risk-sensitive control for stochastic nonlinear systems with stable zero-dynamics," *SIAM Journal on Control and Optimization*, vol. 45, no. 3, pp. 885–926, 2006.

[16] S.-J. Liu, J.-F. Zhang, and Z.-P. Jiang, "Decentralized adaptive output-feedback stabilization for large-scale stochastic nonlinear systems," *Automatica*, vol. 43, no. 2, pp. 238–251, 2007.

[17] X. Su, Z. Li, Y. Feng, and L. Wu, "New global exponential stability criteria for interval-delayed neural networks," *Proceedings of the Institution of Mechanical Engineers, Part I: Journal of Systems and Control Engineering*, vol. 225, no. 1, pp. 125–136, 2011.

[18] X. Su, P. Shi, L. Wu, and Y. Song, "A novel approach to filter design for T-S fuzzy discrete-time systems with time-varying delay," *IEEE Transactions on Fuzzy Systems*, vol. 20, no. 6, pp. 1114–1129, 2012.

[19] Q. Zhu, "Stabilization of stochastic nonlinear delay systems with exogenous disturbances and the event-triggered feedback control," *IEEE Transactions on Automatic Control*, vol. 64, no. 9, pp. 3764–3771, 2019.

[20] B. Chen, X. Liu, K. Liu, and C. Lin, "Direct adaptive fuzzy control of nonlinear strict-feedback systems," *Automatica*, vol. 45, no. 6, pp. 1530–1535, 2009.

[21] S. Tong and Y. Li, "Observer-based fuzzy adaptive control for strict-feedback nonlinear systems," *Fuzzy Sets and Systems*, vol. 160, no. 12, pp. 1749–1764, 2009.
[22] S. Tong, X. He, and H. Zhang, "A combined backstepping and small-gain approach to robust adaptive fuzzy output feedback control," *IEEE Transactions on Fuzzy Systems*, vol. 17, no. 5, pp. 1059–1069, 2009.
[23] B. Chen, X. Liu, K. Liu, and C. Lin, "Fuzzy-approximation-based adaptive control of strict-feedback nonlinear systems with time delays," *IEEE Transactions on Fuzzy Systems*, vol. 18, no. 5, pp. 883–892, 2010.
[24] Q. Zhou, P. Shi, J. Lu, and S. Xu, "Adaptive output feedback fuzzy tracking control for a class of nonlinear systems," *IEEE Transactions on Fuzzy Systems*, vol. 19, no. 5, pp. 972–982, 2011.
[25] H. Zhang, Z. Wang, and D. Liu, "Global asymptotic stability of recurrent neural networks with multiple time-varying delays," *IEEE Transactions on Neural Networks*, vol. 19, no. 5, pp. 855–873, 2008.
[26] H. Zhang and Y. Quan, "Modeling, identification and control of a class of nonlinear system," *IEEE Transactions on Fuzzy Systems*, vol. 9, no. 2, pp. 349–354, 2001.
[27] W. Chen, L. Jiao, J. Li, and R. Li, "Adaptive nn backstepping output-feedback control for stochastic nonlinear stict-feedback systems with time-varying delays," *IEEE Transactions on Systems, Man, and Cybernetics, Part B (Cybernetics)*, vol. 40, no. 3, pp. 939–950, 2010.
[28] B. Chen and X. Liu, "Fuzzy approximate disturbance decoupling of MIMO nonlinear systems by backstepping and application to chemical processes," *IEEE Transactions on Fuzzy Systems*, vol. 13, no. 6, pp. 832–847, 2005.
[29] B. Chen, S. Tong, and X. Liu, "Fuzzy approximate disturbance decoupling of MIMO nonlinear systems by backstepping approach," *Fuzzy Sets and Systems*, vol. 158, no. 10, pp. 1097–1125, 2007.
[30] Y. Li, C. Yang, S. Ge, and T. Lee, "Adaptive output feedback nn control of a class of discrete-time mimo nonlinear systems with unknown control directions," *IEEE Transactions on Systems, Man, and Cybernetics. Part B (Cybernetics)*, vol. 41, no. 2, pp. 507–517, 2011.
[31] S. Tong, Y. Li, G. Feng, and T. Li, "Observer-based adaptive fuzzy backstepping dynamic surface control for a class of mimo nonlinear systems," *IEEE Transactions on Systems, Man, and Cybernetics. Part B (Cybernetics)*, vol. 41, no. 4, pp. 1124–1135, 2011.
[32] H. Wang and Q. X. Zhu, "Global stabilization of a class of stochastic nonlinear time-delay systems with SISS inverse dynamics," *IEEE Transactions on Automatic Control*, 2020.
[33] J. Li, W. Chen, J. Li, and Y. Fang, "Adaptive NN output-feedback stabilization for a class of stochastic nonlinear strict-feedback systems," *ISA Transactions*, vol. 48, no. 4, pp. 468–475, Oct. 2009.
[34] J. Li, W. S. Chen, and J. M. Li, "Adaptive NN output-feedback decentralized stabilization for a class of large-scale stochastic nonlinear strict-feedback systems," *International Journal of Robust and Nonlinear Control*, vol. 21, no. 4, pp. 452–472, 2011.
[35] H. Deng and M. Krstić, "Stochastic nonlinear stabilization-I: a backstepping design," *Systems & Control Letters*, vol. 32, no. 3, pp. 143–150, 1997.
[36] Y. Li, Z. Ma, and S. Tong, "Adaptive fuzzy output-constrained fault-tolerant control of nonlinear stochastic large-scale systems with actuator faults," *IEEE Transactions on Cybernetics*, vol. 47, no. 9, pp. 2362–2376, 2017.

Hindawi
Complexity
Volume 2020, Article ID 6107312, 12 pages
https://doi.org/10.1155/2020/6107312

Research Article

Investigation of Droplets Distribution and Reaction Kinetics on SO_2 Removal in Flue Gas via Venturi Scrubber

Shuo Zhang,[1] Wenyue Cui,[1] Chen Wang,[1] Tao Wu,[2] and Xiaohang Zhao[2]

[1]*Key Laboratory of Intelligent Control and Optimization for Industrial Equipment of Ministry of Education, Dalian University of Technology, Dalian, China*
[2]*Process Department, CNPC Northeast Refining & Chemical Engineering Co. Ltd., Dalian, China*

Correspondence should be addressed to Shuo Zhang; zhangshuo_arbeit@126.com

Received 21 April 2020; Revised 9 June 2020; Accepted 23 June 2020; Published 24 August 2020

Guest Editor: Hamid Reza Karimi

This paper investigates the problem of gas-liquid flow SO_2 removal in nonquiescent flue gas. Using venturi scrubber as the prototype, the population balance model (PBM) combined with the CFD is implemented to characterize the droplets behaviors. Discrete methods as class model (CM) and various quadrature-based moment models (QBMMs) are applied to numerically solve the population balance equations (PBEs). Taking NaOH solution as the reaction kinetics, the sulfur removal efficiency simulation with CM and different QBMMs methods is validated through the operation measurements. The comparison results show that the CM can achieve better accuracy with more bins, which showed the minimal error 3.6%, consisting 30 bins. However, the computational time of the CM is approximately 19.3 times as long as QBMMS. Among the QBMMs, the ECQMOM approach enjoys the best balance between the simulation efficiency and accuracy, while EQMOM shows the least computational load and CQMOM wins the minimal calculation precision. This result will provide sufficient reference for engineers working in the field of the droplets distribution in the venturi scrubber design.

1. Introduction

As the main pollutant in the petroleum industry, exhaust gas from fuel contains a significant amount of SO_2 owing to the sulfur contained in fossil fuels [1]. The emissions of SO_2 severely cause atmosphere pollution and ecosystem damage, which significantly threatens the human life. Also, the increase of the emission is one of the principal causes of the acid rain [2]. With the stringent emission standards of SO_2, the improvement of currently used methods is essential. Currently, wet flue gas desulfurization coupled with selective catalytic reduction is popular for the simultaneous SO_2 removal [3, 4].

The venturi that is investigated in this paper is a device used to absorb sulfur dioxide, which is installed at the end of production line as an equipment to clean the flue gas. Venturi scrubber is a two-phase reactor with low-energy input and good-mixing effect. Now most of the relevant studies are based on experiments, which require a long time and a lot of cost to verify the correctness of the designs. The flow field inside venturi is complex, and the fluid velocity is fast, which make the experiment difficult to observe. These above make numerical simulation indispensable in venturi's research. So this paper aims at finding the most suitable simulation method of the venturi. Due to the high ratio of gas to liquid, the result of CFD with multiphase model cannot meet the rate measured in factory. Thus, PBM is needed to compute a correct result. And most reactors use low-density medium as the discrete phase to study the dynamics characteristics of particles. Besides, the discrete phase of the venturi selected in this paper is liquid. In this case, the behavior of particles such as growth, breakup, and aggregation is more affected by its own stress, which is different from the situation of gas as the discrete phase. So the paper studies the condition of the internal flow field and adaptability of different discrete methods to the venturi firstly. The condition of the flow can show the process of the mass and energy transfer, which could indicate the direction

of redesigns. And the choices of the discrete methods should consider both accuracy and time cost, which could provide the basement with subsequent investigations and designs.

As for energy transfer between two phases, Bhutada et al. [5] investigated the relationship between throat structure and the change of pressure and velocity. Dopkin et al. [6] considered that longer multiphase-mixed tube could make consumption of momentum increased due to friction force. In contrast, shorter tube which cannot meet requirement of complete exchange of energy is also averse to mixture. Sun et al. [7] presented an analysis model to optimize venturi based on constant pressure mixing theory. Galanis et al. [8] proposed a thermodynamic mode to calculate critical pressure and structure parameters of venturi. To study the process of reaction happening in venturi, Guerra et al. [9] thought that there is a strong dependence of the dispersed phase distribution on the parameter values used in the droplet size distribution model. Majid et al. [7] studied gas velocity in throat, volume faction, and removal efficiency to analyze performance of venturi scrubber. As for the multiphase flow model, Lehr et al. [10] fully characterized and described the behavior of the discrete phase. Ishii et al. [11] studied the interaction of discrete phases with surrounding media. Ameras et al. [12] discussed turbulence and mixing caused by discrete phases. Due to a series of studies on multiphase flow, numerical simulations can be used for satisfactory simulation work in many cases. The volumetric mass transfer coefficient $k_l a$ is the key parameter in mass transfer model in venturi scrubber. However, there are some deficiencies in the direct prediction of $k_l a$, since its theoretical correlation of the microscale hydrodynamics and microscale interfacial phenomena is very complex.

The mass transfer coefficient k_l is commonly predicted by the penetration model [10] and eddy cell model [11]. a depends on the behavior of dispersed phase, such as breakup and aggregation, which will change the area between two phases and the transfer of mass and energy. As shown in Figure 1, the liquid in the venturi reactor atomizes small particles under pressure after injection into the concentration. The particles will grow, break up, and aggregate due to the influences by internal and external factors. The external stress of continuous phase leads to deformation to particles. Nevertheless, the surface stress of particles and viscous stresses result in a stable shape of particles [13]. In multiphase, the particles would grow by adsorbing deposited liquid and spreading itself [14]. At the same time, the collision of droplets and vortex in flow field would make droplets breaking under turbulent conditions. And the viscous stress of continuous phase can cause the velocity gradient at the interface around the particles, which would also lead to deformation and even breakage. As for aggregation, the eddy will cause the collision of particles less than 8 mm in size. The difference in speed on particles and wake eddy of big droplets would also cause aggregation happening (Figure 1).

In the simulation of the multiphase flow, the population balance model (PBM) have a good performance to describe the process of reaction and the Sauter Mean Diameter (SMD) of droplets, which can be used to analyze the

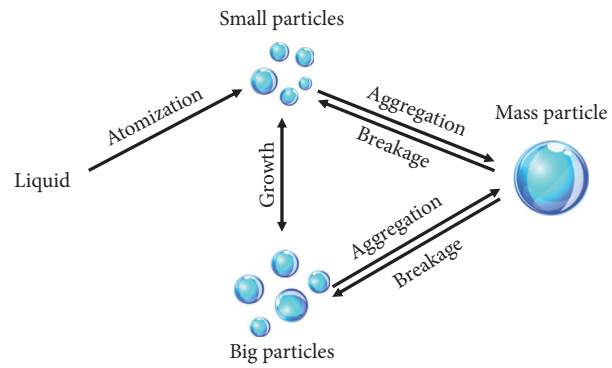

Figure 1: Schematic of dynamic evaluation of particles.

behavior of the population of droplets from the single droplet in their local environment [15–17]. Danckwerts [18] first used population balance theory to describe the residence time distribution (RTD) of the process of flowing and mixing. Hulburt et al. [19] built PBM matrix equations, used to show the behaviors of particle about nucleating, growing, and aggregating in chemical engineering. Coulaloglou [20] set up phenomenological model about breakup and aggregation of droplets. Lee et al. [21] presented functions of breakup and aggregation, which made probability density distribution replaced by number density distribution. On the basis of this, Lehr et al. [22] investigated the distribution of particle size in bubble-bed reactor and presented aggregation function basing on the experiment. Olmos [23] used bubble-bed reactor to study SMD and gas volume fraction. Venneker et al. [24] researched local gas holdup and volume mass transfer coefficient in stirred tank reactors by PBM.

To simulate the discrete phase distribution, the population balance equation (PBE) is used to describe the particles behaviors as breakage and aggregation. Several numerical methods are commonly applied, such as the class method (CM) [25, 26] and method of moments (MOM) [27, 28]. The CM can descript the description of the particles with a highly computational resource demanding. It needs a number of bins as the amount of discretized sections, which is larger leading to a more accurate model with a longer calculate time. The MOM is able to predict the SMD as accurately as the CM, which cannot drawback the description about diameters of particles. The MOM calculates the PBE by tracking the time dependence of the lower-order moments of the SMD rather than the distribution of particle size. Because of the balance between complexity of calculation and accuracy, the simulation methods that are based on the MOM are very popular, of which the methods that used Gaussian quadrature to close the source terms are grouped into the so-called quadrature-based moment methods (QBMMs).

To extend the area adopted by the MOM, McGraw [29] proposed the quadrature method of moments (QMOM) to solve the problems in simulation by PBE. In the QMOM, the moments of the SMD are approximated by the n-point Gaussian quadrature, which converts the integral form of the number density function to the sum of characteristic abscissas and weights that can be computed by product-

difference (PD) algorithm [30]. And the SMD can be approximated by the abscissas with a delta function [30]. However, there are some restrictions in use of the QMOM; for example, it is only applicable to univariate distributions due to the limitations of Gaussian quadrature. As the result, the conditional quadrature method of moments (CQMOM) was came up to solving the multivariate system. It uses conditional probability function theory to calculate the multivariate SMD. In the CQMOM, the velocity of particles is treated as a separate "internal coordinate," and the quadrature approximation is used to overcome the closure problem, which consists of different abscissas or nodes that can be considered as separate particle classes. This method was mainly used to predict particle trajectory crossing [31]. Another method is the extended quadrature method of moments (EQMOM), which was developed by Yuan et al. [32]. The QBMMs that were referenced above only predict a discontinuous value of SMD, which would lead to problems in the situation where the PBE cannot explain the loss of particles of zero-size well. To evaluate the problem, the value of the particle size for a zero-size particle is required [33]. One possible solution is to increase substantially the number of abscissas so that the phase space is adequately discretized. Besides, the EQMOM was presented to simulate the distribution of the particles from a moment set using continuous kernel density functions, which has heavier computation compared to QMOM and CQMOM [34]. The ECQMOM was presented by Chalons [35] et al., of which calculations of the source terms and the moment transport equations are similar to the CQMOM and the EQMOM.

In this contribution, four type of QBMMs, as QMOM, CQMOM, EQMOM and ECQMOM as well as the CM, have been presented to solve the multiphase reaction with multivariate SMD and mass transfer, which are described in Section 2. In Section 3, the apparatus setup and the numerical strategy are introduced about the proposed venturi scrubber. In Section 4, the experiment and the CFD-PBM simulation results are compared with CM and QBMMs, which the balance between the calculation efficiency and model accuracy are analyzed. Finally, conclusions are drawn in Section 5.

2. Numerical Methods

The sulfur dioxide content before and after the flue gas passes through the venturi scrubber with the NaOH solution injection, where the mass transfer efficiency of wet desulfurization is simulated throughout the venturi scrubber chamber [36]. The CM and QBMMs are adopted in the simulation of this paper to simulate the change of droplets size inside the venturi scrubber, so as to calculate the average specific surface area of droplets and mass transfer efficiency and compare with the measured data to calculate the error and measure the accuracy of the model in this work.

The population balance model is adopted for modeling the droplets behaviors in the venturi scrubber, which describes the processes of the natural growth and decrease of droplets and the birth and death of particles occur due to aggregation and breakage. And the breakup kernel which was presented by Hengel et al. [36] and aggregation kernel which was presented by Vigil and Ziff [37] was applied in the simulation. The governing equations for PBM model [38, 39] are shown in Table 1.

After the procedure given above, the SMD is worked out by the simulation, which is used to calculate the contact surface between gas and liquid phases. Then the removal rate of sulfur dioxide is reckoned based on the mass transfer equation, which are shown in Table 2 [44–47].

3. Experiment and Simulation

This section may be divided into subheadings. It should provide a concise and precise description of the experimental results and their interpretation as well as the experimental conclusions that can be drawn.

3.1. Apparatus Setup. In this work, a sulfur removal scrubber with a capacity of 4000 tons/year is taken as the prototype (refer to Figure 2). In venturi, sodium hydroxide solution is used to absorb sulfur dioxide from the flue gas, thus achieving the purpose of cleaning the gas. And at the same time, the liquid transmits some energy to the gas by crashing. The venturi scrubber is composed of gas-liquid two-phase inlet, receiving chamber, throat, and diffusion section. The inlet diameter of gas that the device involved in this work is d_1, which is 750 mm. The diameter of the liquid sparger is d_2, which is designed by requirement of spray. The convergence has a diameter of dcon, which is 1.3 times as long as d_1, with a length of l2 ($1.9d_1$). The throat has a diameter of dthroat ($0.85d_1$), and a length of l4 ($0.48d_1$). The diameter of the outlet of the diffusion section is dout, which is the same length as d_1. The contraction angle from the convergence to the throat is θ_1, and the expansion angle after the throat is θ_2.

In field equipment, SGA94-SO_2 flue gas analyzer made by KANE corporation (refer to Figure 3) is used to measure sulfur dioxide concentration at the gas phase inlet and outlet of the scrubber respectively, refer to Figure 3. After the analyzer is calibrated in normal air, the probe of the analyzer is dipped into the venturi through the three holes on the wall at the monitoring locations (inlet, throat, and outlet) marked in Figure 2(a). The sensor measures the concentration of sulfur dioxide through the degree of oxidation reaction on the electrode, and converts it into a current signal and demonstrates the result on the portable device. Field data measured by sensors are shown in Table 3 (refer to Table 3).

3.2. Numerical Strategy. In this section, the model in the previous section is simulated and verified. Three-dimensional transient and steady simulations are carried out with the commercial CFD software Ansys FLUENT 18.0. The iteration time step is set to be $1e-5$ s. In this study, Tomiyama's model is chosen to describe the drag force [48] between the multiphase. The Universal-drag model is used to the lift force [49]. The wall lubrication force [50] chose Antal et al model. And the turbulent dispersion force [51] chose Burn et al model. The realizable k-epsilon model is added to simulate the turbulence kinetics [52]. Besides, the stagey of convergence adopts a

Table 1: The equations for PBM model.

Name	Equations	Equ. num.
Bubble source equation	$\partial/\partial t\,[n(V,t)] + \nabla\cdot[\overrightarrow{\mu}\,n(V,t)] + \nabla_v\cdot[G_v n(V,t)] = D,$	(1)
	$D = (\mathrm{Br}_{\mathrm{ag}} - \mathrm{Dr}_{\mathrm{ag}}) + (\mathrm{Br}_{\mathrm{br}} - \mathrm{Dr}_{\mathrm{br}}),$	(2)
Bubble growth equation	$G_v = 3K_v L^2 G,$	(3)
	$K_v = L_3/V,$	(4)
Aggregation equation [40] (ω_{ij} is the distance ratio of the bubble and its turbulence path length; ε refers to the turbulent energy)	$\mathrm{Br}_{\mathrm{ag}} = 1/2\int_0^V \beta(V_i - V_j, V_j)n(V_i - V_j, t)n(V_j, t)\mathrm{d}V_j,$	(5)
	$\mathrm{Dr}_{\mathrm{ag}} = \int_0^\infty \beta(V_i - V_j)n(V_i, t)n(V_j, t)\mathrm{d}V_j,$	(6)
	$\beta(V_i, V_j) = \omega_d(V_i, V_j)\cdot p_d(L_i, L_j),$	(7)
	$\omega_d(V_i, V_j) = \pi/4\omega_{ij}(d_i^2 + d_j^2)n_i n_j(d_i^{2/3} d_j^{2/3})^{1/2}\varepsilon^{1/3},$	(8)
	$P_d = (2k_B T/3\mu)((L_i + L_j)^2/L_i L_j),$	(9)
Breakage equation [40] (λ_e is particle eddy size; ϵ is the energy dissipation)	$\mathrm{Br}_{\mathrm{br}} = \int_{\Omega_v} p g_d(V_j)\gamma(V_i \mid V_j)n(V_j, t)\mathrm{d}V_j,$	(10)
	$\mathrm{Dr}_{\mathrm{br}} = g_d(V_i)n(V_i, t),$	(11)
	$g_d(V_j) = 0.923(1 - \alpha_g)n_B\varepsilon^{1/3}((d_B + \lambda_e)^2/\lambda_e^{11/3}),$	(12)
QMOM model equation [41]	$m_k = \sum_{i=1}^N \varphi_i L_i^k,$	(13)
CQMOM [42]	$\mathrm{Br}_{a,\mathrm{QM}} = (1/2)\sum_{i=1}^N \varphi_i \sum_{j=1}^N \varphi_j (L_i^3 + L_j^3)^{k/3}\beta(L_i, L_j),$	(14)
	$\mathrm{Dr}_{a,\mathrm{QM}} = \sum_{i=1}^N L_i^k \varphi_i \sum_{j=1}^N \varphi_j \beta(L_i, L_j),$	(15)
	$\mathrm{Br}_{b,\mathrm{QM}} = \sum_{i=1}^N \varphi_i \int_0^\infty L_k g(L_i)\gamma(L \mid L_i)\mathrm{d}L,$	(16)
	$\mathrm{Dr}_{b,\mathrm{QM}} = \sum_{i=1}^N \varphi_i L_i^k g(L_i),$	(17)
	$m(L, w) = m(w \mid L)m(L),$	(18)
	$\mathrm{Br}_{a,\mathrm{CQM}} = (L^2/2)\int_0^L\int_0^W (a((d^3 - d'^3)^{1/3}, d\prime))/(d^3 - d'^3)^{2/3} n(d, w_L)L\,dw_L,$	(19)
	$\mathrm{Dr}_{a,\mathrm{CQM}} = \sum_{i=1}^N L_a^i g(L_a)\varphi_a(\sum_{j=1} w_{a,\gamma}^i \varphi_{a,\gamma}),$	(20)
	$\mathrm{Br}_{b,\mathrm{CQM}} = \int_0^L\int_0^w g(d)\beta(d, w \mid L, w_L)n(d, w_L)L\,dw_L,$	(21)
	$\mathrm{Dr}_{b,\mathrm{CQM}} = g(L_i)m(L, w),$	(22)
EQMOM [42]	$m_k = \sum_{i=1}^N \varphi_i \beta(L, L_i),$	(23)
	$\mathrm{Br}_{a,\mathrm{EQM}} = (1/2)\sum_{i_1=1}^N \sum_{j_1=1}^N \varphi_{i_1}\varphi_{i_1 j_1} \sum_{i_2=1}^N \sum_{j_2=1}^N \varphi_{i_2}\varphi_{i_2 j_2}(L_{i_1 j_1}^3 + L_{i_2 j_2}^3)^{k/3}\beta(L_{i_1 j_1}, L_{i_2 j_2}),$	(24)
	$\mathrm{Dr}_{a,\mathrm{EQM}} = \sum_{i_1=1}^N \sum_{j_1=1}^N L_{i_1}^k \varphi_{i_1}\varphi_{i_1 j_1} \sum_{i_2=1}^N \sum_{j_2=1}^N L_{i_2}^k \varphi_{i_2}\varphi_{i_2 j_2}\beta(L_{i_1 j_1}, L_{i_2 j_2}),$	(25)
	$\mathrm{Br}_{b,\mathrm{EQM}} = \sum_{i=1}^N \sum_{j=1}^N \varphi_i \varphi_{ij} \int_0^\infty L_{ij}^k g(L_{\mathrm{ij}})\gamma(L \mid L_{ij})\mathrm{d}L,$	(26)
	$\mathrm{Dr}_{b,\mathrm{EQM}} = \sum_{i=1}^N \sum_{j=1}^N \varphi_i \varphi_{ij} L_{ij}^k,$	(27)
ECQMOM [43]	$m_k = \sum_{i=1}^N \sum_{j=2}^N \varphi_i \varphi_{ij} m_{\forall,k}^{(i)} S_{ij}^l,$	(28)
	$\mathrm{Br}_{\mathrm{ECQM}} = \int_0^\infty\int_0^\infty V^k S^l \beta(V - V', V'S - S', S')n(V - V', S - S')n(V', S')\mathrm{d}V\mathrm{d}S,$	(29)
	$\mathrm{Dr}_{\mathrm{ECQM}} = \int_0^\infty\int_0^\infty \beta(V, V', S, S')n(V, S)n(V', S')\mathrm{d}V\mathrm{d}S.$	(30)

Table 2: The equations for mass transfer.

Name	Equations	Eq. Number
Mass transfer equation (V_l and V_g are the volume flow rate of liquid and gas respectively; $c_{s,l}$ and $e_{s,g}$ are the molarity concentrations; $c_{h,l}$ is the molarity concentration of sodium hydroxide; ε_1 is the volume fraction of the liquid phase; $E_{s,l}$ and $E_{s,g}$ are eddy current diffusion coefficients of sulfur dioxide in liquid and gas; $E_{h,l}$ is the eddy current diffusion coefficient of sodium hydroxide in liquid phase; $c_{s,g}^*$ for the equilibrium concentration of sulfur dioxide in liquid phase interface)	$(\mathrm{d}V_g c_{s,g}/\mathrm{d}x) - S(1 - \varepsilon_l)E_{s,g}(\mathrm{d}^2 c_{s,g}/\mathrm{d}x^2) + Sk_l a(c_{s,g} - c_{s,g}^*) = 0,$	(31)
	$-(\mathrm{d}c_{s,l}V_l/\mathrm{d}x) + \varepsilon_l E_{s,l}(\mathrm{d}^2 c_{s,l}/\mathrm{d}x^2)S + K_l aS(c_{s,l}^* - c_{s,l}) - SK_{\varepsilon_l c_{s,l} c_{h,l}} = 0,$	(32)
	$-(\mathrm{d}c_{h,l}V_l/\mathrm{d}x) + S\varepsilon_1 E_{h,l}(\mathrm{d}^2 c_{h,l}/\mathrm{d}x^2) - 2SK_{\varepsilon_l c_{s,l} c_{h,l}} = 0,$	(33)
	$d = (0.0422 + 5.776\times 10^{-3}(V_l/V_g)^{1.932})/u_{g0}^{1.602},$	(34)
	$k_l = 2c_p\sqrt{D_{s,g}(V_l/V_g)/\pi\mathrm{d}},$	(35)
	$\alpha = ((V_l/(1/6)\pi d_d^3)\pi d^2/(V_l + V_g)) = (6V_l/d(V_l + V_g)).$	(36)

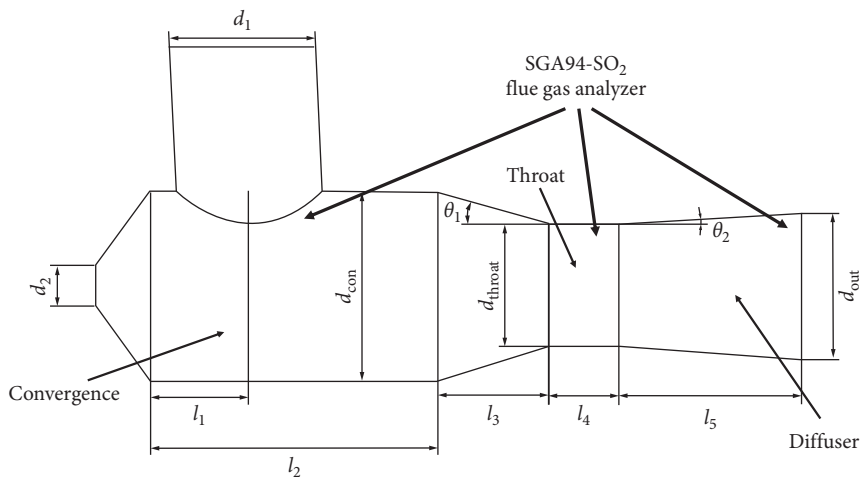

(a)

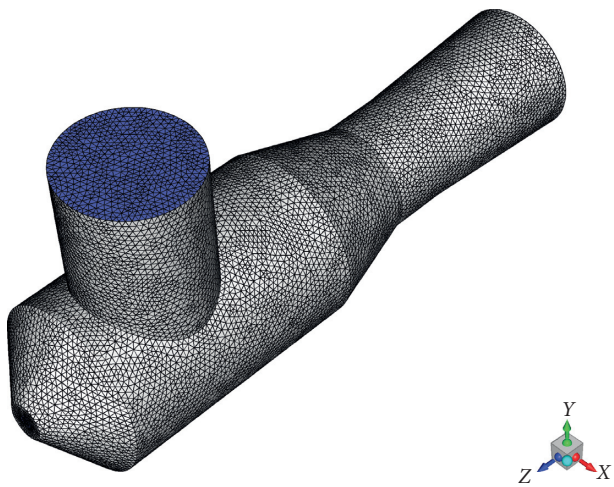

(b)

Figure 2: (a) Schematic diagram. (b) Meshing diagram.

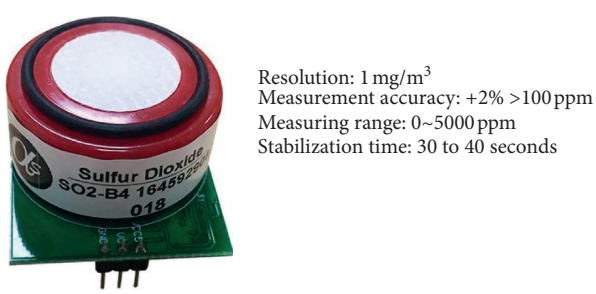

Figure 3: SGA94-SO_2 flue gas analyzer.

Table 3: Field data of the venturi scrubber.

Venturi scrubber measurement data			
Liquid flow rate	33 m^3/h	Gas flow rate	4000 Nm^3/h
Liquid temperature	58.3°C	Gas temperature	155°C
Liquid pressure	0.72 MPa	SO_2 concentration	765 mg/Nm^3
NaOH concentration	0.125 mol/l	Sulfur removal efficiency	48.76%

logarithmic descent direction algorithm, which was presented by Wu et al. [53]. The proposed algorithm is based on the Karush–Kuhn–Tucker necessary optimality condition and the damped Newton method. At last, the iteration residual errors are set to be $1e-5$.

On the basis of the simulation, the PBM model is adopted to use the CM. According to Kazakis et al. [54], the mean Sauter diameter of droplets performances at the liquid sparger is initialed as equation (37), and the distribution is compiled in UDF. In the process of CM simulation, different numbers of bins and different ratio exponents are set to change the diameter range and accuracy of droplets calculated by simulation, so as to find the most suitable simulation parameters for the reactors and reaction conditions involved in this paper. The QBMMs are implemented for the case comparison study. The maximum and minimum particle sizes of the inlet droplets are set as 2 mm and 0.05 mm, respectively. And the calculation results of the above model are compared for simulation accuracy of different QBMM models.

$$d_{32} = 7.35 d_s \left[W_e^{-1.7} R_e^{0.1} F_r^{1.8} \left(\frac{d_p}{d_d} \right)^{1.7} \right]^{1/5}, \tag{1}$$

where d_{32} is the mean Sauter diameter and d_s is the diameter of sparger. And the distribution of particle is calculated as follows:

$$d = \frac{d_{32}}{k R_e^{-a} W_e^{-b} f^h}. \tag{2}$$

When the atomized medium is water, $a = -0.097$, $b = 0.392$, and $h = -0.177$.

In the above simulation model, sodium hydroxide is added to absorb sulfur dioxide, and the reaction model proposed by Uchida [55] is used:

$$\begin{gathered} SO_2\,(A) + 2NaOH\,(B) \rightleftharpoons Na_2SO_3\,(C) + H_2O\,(D), \\ K = 1 \times 10^6 m^3/(mol{\cdot}s). \end{gathered} \tag{3}$$

As the results of simulation, the concentration of sulfur dioxide is compared with the measure value of experiment to obtain the errors of different models and the simulation model of venturi reactor which is the most suitable for the working environment mentioned in the paper is found by the comprehensive consideration of calculation time and calculation accuracy.

4. Results and Discussion

In this section, the results of above experimental and simulation are introduced, and the results are compared and analyzed to draw relevant conclusions.

4.1. Mesh Size Analyze. Firstly, this paper discusses the influence on the results by mesh size, which compares the simulation results of velocity under different sizes of mesh. In the simulation, more accurate results need the smaller mesh, which would increase the computation and prolong the simulation time. Bhutani et al. firstly applied mesh adaptivity to population balance equation for modeling the multiphase flow and presented the mesh at two-phase mixing area should be smaller [56]. This paper adopts a fixed mesh strategy. Because the process of transfer mainly occurs at the injection area, the mesh of the venturi central area is set to half of the maximum mesh size. When smaller size does not improve accuracy, the size should be chosen. The velocity distribution at the outlet of venturi is studied when the size of mesh is 8, 10, 15, and 20 mm, respectively. It can be seen from the results of simulation that when the size of mesh is 15 mm and 20 mm, the velocity at center of the outlet is larger and the circumference is smaller, which has more errors. When the mesh size is less than 10 mm, there is no significant fluctuation in the simulation results. So, 10 mm is adopted as the diameter of mesh in the subsequent simulation in this paper (refer to Figure 4).

4.2. Velocity Distribution. After determining the mesh size, the process of reaction mass transfer is added on the basis of the cold mode flow field to calculate the concentration of sulfur dioxide, and the PBM is also added to investigate the distribution of droplet size. The velocity and pressure distribution of the flow field in the reactor is shown in Figure 5, which shows the velocity at the top, middle, and bottom parts of the reactor and the pressure distribution on the axis. The change of liquid pressure and velocity reflects the change of liquid energy. It can be seen that on the central axis of the reactor, the liquid entrances convergence at a high speed to atomize into droplets, and the speed gradually decreased during the mixing process with the gas. The speed on the top line is a little faster than the speed on the bottom line due to the gas that flows into convergence from top inlet. In convergence, the pressure of liquid drops slightly due to diffusion and friction with the gas. When the flow passes the contraction section, the pressure decreases due to the narrowing pipe with the liquid accelerating. In this section, the pressure drops nearly 300 kPa, and the velocity changes to 19.8 m/s from 9.5 m/s. According to the Bernoulli equation, nearly 50% of pressure decrease does work to accelerate. Wu et al. [57] thought that reduction in pressure due to friction with the pipe is 40% of that resulting in acceleration. So the remaining 30% of the pressure loss works to transfer energy to the gas. And there is sudden change of pressure decrease and velocity increase at the entrance of the throat because of the geometrical mutation between the tail of convergent and throat entrance, which was also mentioned by Wu et al. [57]. Near the exit of throat, the velocity begins to decrease because of backflow, which is made by negative pressure. In the diffuser, the velocity of the mixed phase decreases gradually and the pressure increase due to the wider pipe. The process of change about energy of gas and liquid can be seen by the change of pressure and velocity from Figure 5. The loss of liquid energy is partly due to the conversion of its energy. As the pipe narrows, the pressure drops with an increased velocity. At the same time, the work done by the liquid in the process of collision with the gas also causes the drop of liquid pressure and the increase of gas energy (refer to Figure 5).

4.3. Phase Volume Faction. Figure 6 shows the concentration distribution of liquid and SO_2 in venturi, which can directly

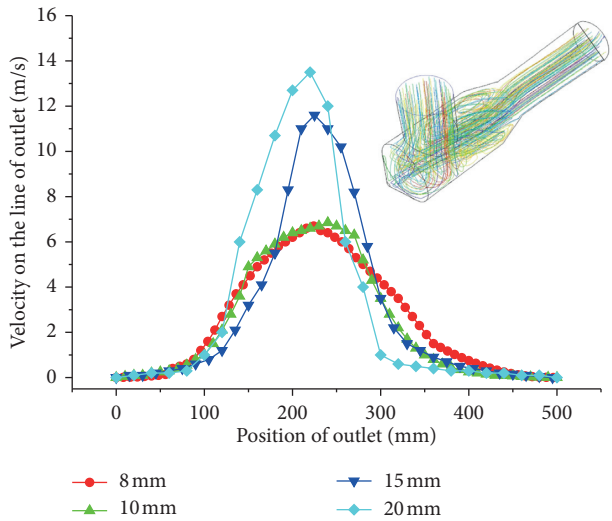

Figure 4: The results of velocity in different mesh size.

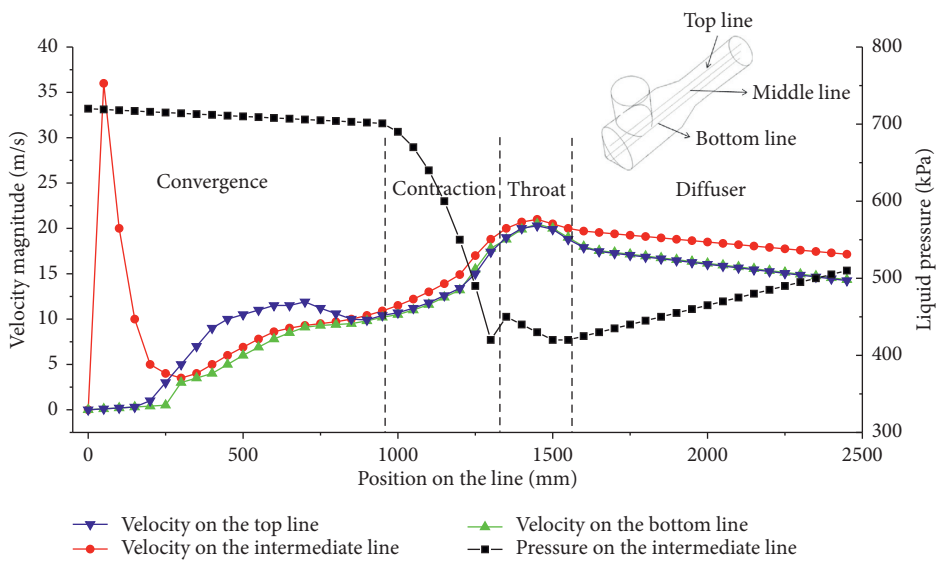

Figure 5: The velocity of different part in the venturi scrubber.

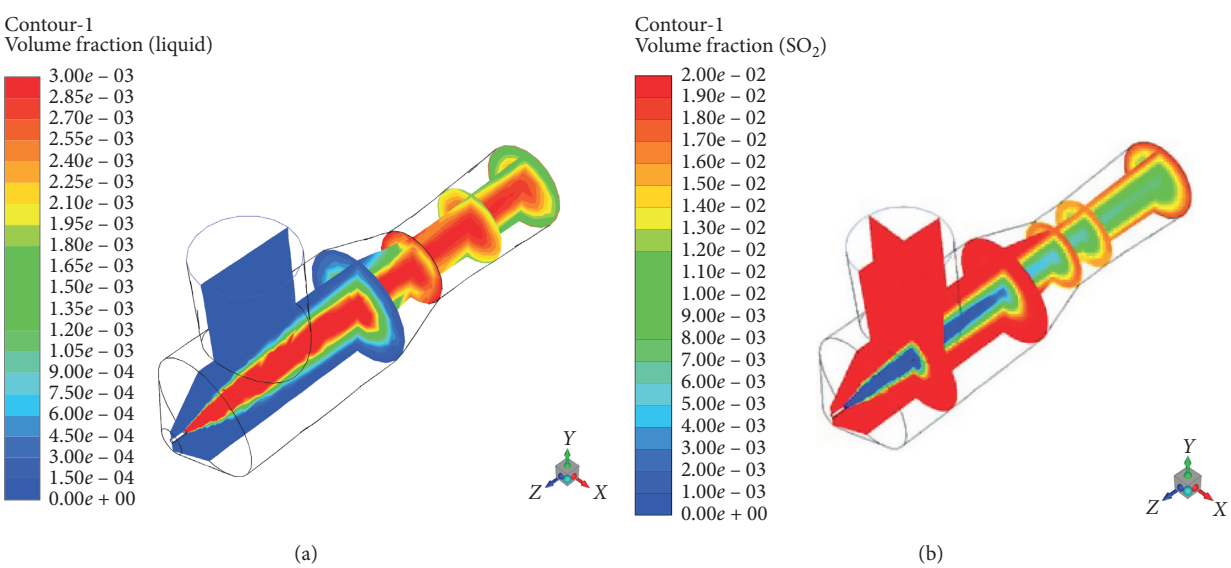

Figure 6: (a) concentration of liquid in venturi; (b) concentration of SO_2 in venturi.

reflect the simulation of mixing. It can be seen that the liquid is atomized and vaporized under high pressure after entering venturi and the mixing begins to occur at the interface of gas-liquid. In the contraction section, due to the dramatic change of pressure and velocity, the gas distribution tends to be uniform rapidly. When the liquid accelerates, the break frequency of droplets would increase. It is easier to mix the gas with dispersed droplets. So, there is only a little difference in concentration because of the reaction. In the throat, the fastest speed and the effect of negative pressure make the turbulence intensity stronger and the flow field more complex. And under the influence of the above reasons, the droplets are broken more violently and dispersed more evenly. So the throat is where most of the reaction happens in venturi. Finally, the flow entrances the diffuser. In the process of pressure and velocity change, the velocity around the pipeline decreases fast and the velocity in the center decreases slowly due to the influence of friction on the reactor wall. The difference in velocity would create the difference in pressure, which was called collapse pressure by Zhang [58] et al. Also, the collapse pressure makes the cloud of droplets moving inward, which can be seen from Figure 6(a). On the whole, when the gas enters venturi, the concentration of sulfur dioxide is 2 v%. The reaction is basically balanced when the multiphase is mixed. As a result, the concentration of sulfur dioxide at the outlet is 1.097 v%. According to the simulation results, it can be seen that the reaction mainly occurred in the throat section. After entering the diffuser section, the concentration of sulfur dioxide basically does not change, so the throat should be the focus of venturi reactor research (refer to Figure 6).

4.4. Experimental Verification of Different Methods. In the experiment, because the venturi reactor mentioned in this paper is a working equipment, it is impossible to directly obtain the state of the internal flow field by using PIV and other devices. Therefore, only the measured value of sulfur dioxide can be used to verify the correctness of the simulation. So sulfur dioxide concentrations at different locations in the reactor are measured using the sensors mentioned in Figure 3. During normal operation of venturi, the concentration of SO_2 is measured on the inlet, throat, and outlet sections of the venturi scrubber in 10 groups. Each group is measured for 10 minutes, and the average value of the meter reading is calculated within 10 minutes as the measurement result. According to the results, the amounts of mean concentration at inlet, throat, and outlet are 633,550 and 392 mg/Nm^3, respectively. It indicates that the removal reaction of sulfur dioxide mainly occurs in the convergence and throat, while the interaction between the two phases in the contraction section is mainly dominated by collision and mixing. In the convergence, the concentration of sulfur dioxide decreases by 132 mg/Nm^3, which may be because the two phases have higher concentrations of sulfur dioxide and sodium hydroxide at the beginning of the reactor entry, so the reaction happening is larger. In the contraction section, the concentration of sulfur dioxide dropped by 83 mg/Nm^3, but the mixture is more uniform. In the throat, where the reaction is most concentrated due to the degree of mixing and the intensity of turbulence, the concentration of SO_2 drops by 158 mg/Nm^3. Because of the other component in the gas (e.g., H_2S and CO) and the accuracy of sensor, there is a 5% error in the measurement. The removal rate by measurement is 48.76%. And the sulfur dioxide is removed 20.66% during the throat (refer Figure 7).

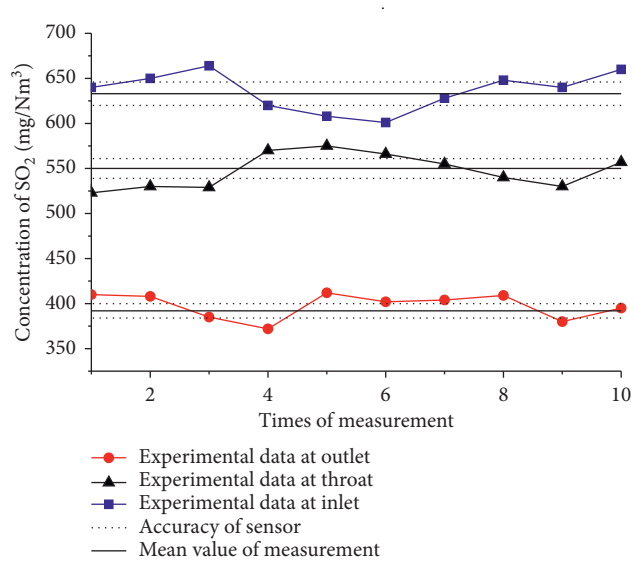

Figure 7: The value of measurement.

In this paper, venturi is simulated by CM and QBMMs, respectively. And the results of simulation are compared with those of experiment to obtain the most suitable method (refer to Figure 8).

As for the CM, the quantity of bins would influent on the accuracy and time cost consumption. Bannari [59] et al. studied the relation between bins and simulation about gas hold-up and liquid velocity. And Bannari thought 25 bins would a good choice for simulating gas-liquid flow, because using more than 25 bins gave also good results but the computational efforts became prohibitive. But Laakkonen [46] et al. found that more than 80 bins should be used to minimize errors. In this case, the CM method in 5, 10, 20, and 30 bins are used to simulate the flow in venturi. The results of simulation are shown in Figure 8(a). It can be seen that the more the bins, the more accurate the result of simulation is. But a more accurate result could cost more time, which can be seen from Table 4. When the number of bins is chosen as 30, the error is 3.2% (removal rate is 45.59%). However, the simulation by 30 bins spends nearly 10 times as much as that by 5 bins (error of 14.99%) (refer to Table 4).

As for the QBMMs, the most significant advantage is the fast and accurate potential, which becomes more important as the number of bins used in the CM is increased [60]. The QMOM served as the simplest of QBMMs only need few abscissas, which can change the weights to minimize the committed error [61]. And the error of QMOM is 7.75%. Compared with the QMOM, the EQMOM could be slower than QBMMs [62], because an additional parameter is

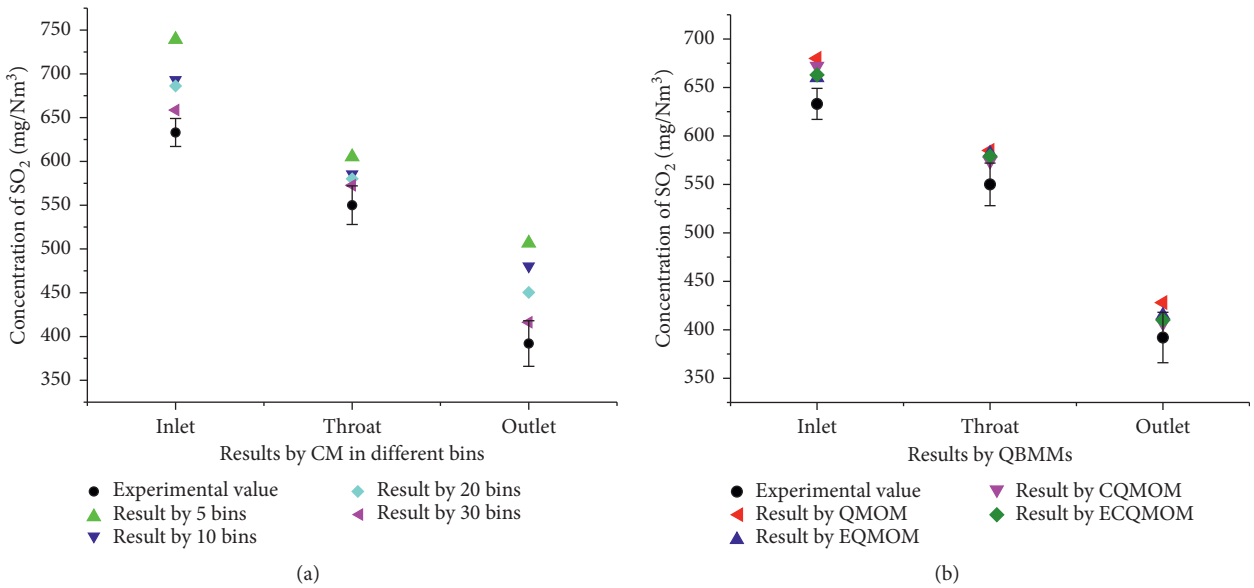

Figure 8: (a) The results of simulation by CM in different bins. (b) The results of simulation by QBMMs.

Table 4: Computational time and error of simulation in different models.

Model	CM (5 bins)	10 bins	20 bins	30 bins
Error (%)	14.99	11.54	7.63	3.2
Cost	3.2	8.7	12.3	19.3

Table 5: Computational time and error of simulation in different models.

Model	CM (30 bins)	QMOM	EQMOM	CQMOM	ECQMOM
Error (%)	3.2	7.75	4.05	6.34	5.28
Cost	19.3	1	1.5	0.8	1.2

calculated to reconstruct a continuous number density function, and most of the computational resources are spent on the calculation of the source terms. So the EQMOM spends 1.5 times as much as the QMOM with the error of 4.35%, with is the most arcuate method among QBMMS. The distinctive advantage of CQMOM is the speed of computation, which is suitable for simulating the multiphase system with mass transfer [63, 64]. The time, the CQMOM costs, is eight-tenths of what QMOM does with the error of 6.34%. Finally, the ECQMOM has a balance between accuracy and consumption, of which the result is 43.48%, with an error of 5.28% (refer to Table 5).

5. Conclusion

The SMD of droplets plays a fundamental role in the CFD study of multiphase flow via venturi scrubber under industrial operating conditions. PBM is coupled with CFD simulations to account for dispersed phase behavior. The results of velocity, pressure, and volume faction can illustrate the accuracy of the simulation. And it also can be seen that the CM and QBMMs approaches can predict the gas/liquid flow dynamics, mass transfer, and the SO_2 removal rate in the venturi scrubber.

The CM can compute SMD of droplets in venturi and describe the distribution about diameter of droplets. And the accuracy of CM heavily depends on the quantity of bins. There is 3.2% gap between the results of experiment and simulation by the CM with 30 bins, while the simulation by CM with 5 bins has an error of 14.99%.

However, the QBMMs do not pay attention to the process of aggregation and breakage of each droplet, which are effectively able to save the time consumed in the simulation of multiphase, which only costs about 5% of time spent by CM. Among the various QBMMs, the CQMOM computes the result of simulation in a shortest time and the EQMOM adapts venturi most satisfactorily. The ECQMOM can calculate the result of simulation fast under a higher accuracy (5.28%). So the ECQMOM can become the best choice for the optimization design.

The application of QBMMs to simulate the condition of flow in the venturi could be an important evolution of investigation in this work. And the QBMMs methods could calculate an accurate result under a faster speed, especially ECQMOM. But this method cannot calculate the distribution of the particle size. So if you want to study quantitatively the size of particles, such as the size of the daughter particle after breakup or the proportion of small particles in the discrete phase, it could not be used. And the error of the QBMMs can be accepted in engineering projects. However, if a higher accuracy is required in the experimental study, the CM method with a large number of bins would be the only choice. In this paper, the PBM-CFD is proved to predict the flow field in venturi at different methods and provide a basis for optimization. A comparison on cost and accuracy between CM and QBMMs in this paper and the reduction of high gas-liquid ratio flow field would be useful, in order to highlight advantages and drawbacks.

Data Availability

(1) The data used to support the findings of Table 3 have been deposited in the figshare repository (https://figshare.com/articles/work_environment_xlsx/12171741). (2) The data used to support the findings of Figure 4 have been deposited in the figshare repository (https://figshare.com/articles/results_in_differnet_mish_size/12172314). (3) The data used to support the findings of Figure 5 have been deposited in the figshare repository (https://figshare.com/articles/Untitled_Item/12173205). (4) The data used to support the findings of Figure 6 have been deposited in the figshare repository (https://figshare.com/articles/concentration_distribution/12173367). (5) The data used to support the findings of Figure 7 have been deposited in the figshare repository (https://figshare.com/articles/measure/12173361). (6) The data used to support the findings of Figure 8 have been deposited in the figshare repository (https://figshare.com/articles/simulation_results/12173220). (7) The data used to support the findings of Tables 4 and 5 have been deposited in the figshare repository (https://figshare.com/articles/simulation_accuracy_and_cost_xlsx/12173328).

Conflicts of Interest

The authors declare that they have no conflicts of interest.

Authors' Contributions

All authors have read and agreed to the published version of the manuscript. Shuo Zhang and Wenyue Cui were responsible for numerical model. Shuo Zhang and Wenyue Cui provided the experimental device. Shuo Zhang and Wenyue Cui performed simulation. Shuo Zhang and Wenyue Cui performed validation. Tao Wu and Xiaohang Zhao performed data analysis. Shuo Zhang performed investigation. Wenyue Cui wrote the original draft. Shuo Zhang reviewed and edited the article. Shuo Zhang supervised the study. Wenyue Cui performed project administration. Shuo Zhang was responsible for funding acquisition.

Acknowledgments

The validation measurements were provided by CNPC Northeast Refining & Chemical Engineering Co. Ltd in a certain CNPC refinery plant CFF boiler. This research was funded by National Natural Science Foundation of China (Grant no. 61803071), China Postdoctoral Science Foundation (Grant nos. 2018M631786 and 2019T120205).

References

[1] D. W. Kwon, K. H. Park, H. P. Ha, and S. C. Hong, "The role of molybdenum on the enhanced performance and SO_2 resistance of V/Mo-Ti catalysts for NH_3-SCR," *Applied Surface Science*, vol. 481, no. 1, pp. 1167–1177, 2019.

[2] J. Chen, B. Li, J. Zheng, and J. Chen, "Control of H_2S generation in simultaneous removal of NO and SO_2 by rotating drum biofilter coupled with FeII (EDTA)," *Environmental Technology*, pp. 1–35, 2018.

[3] J. Chen, S. Gu, J. Zheng, and J. Chen, "Simultaneous removal of SO_2 and NO in a rotating drum biofilter coupled with complexing absorption by FeII (EDTA)," *Biochemical Engineering Journal*, vol. 114, pp. 87–93, 2016.

[4] K. Liu, Q. Yu, B. Wang, J. San, W. Duan, and Q. Qin, "Binary copper-manganese based catalysts with urea for low-temperature selective catalytic reduction of NO: performance, characterization and mechanism," *Applied Surface Science*, vol. 508, p. 144755, 2020.

[5] G. Bhutani and P. R. Brito-Parada, "Analytical solution for a three-dimensional non-homogeneous bivariate population balance equation-a special case," *International Journal of Multiphase Flow*, vol. 89, pp. 413–416, 2017.

[6] R. G. Cunningham and R. J. Dopkin, "Jet breakup and mixing throat lengths for the liquid Jet gas pump," *Journal of Fluids Engineering*, vol. 96, no. 3, pp. 216–226, 1974.

[7] M. Ali, C. Yan, Z. Sun, H. Gu, and K. Mehboob, "Dust particle removal efficiency of a venturi scrubber," *Annals of Nuclear Energy*, vol. 54, pp. 178–183, 2013.

[8] N. Galanis and M. Sorin, "Ejector design and performance prediction," *International Journal of Thermal Sciences*, vol. 104, pp. 315–329, 2016.

[9] V. G. Guerra, A. E. Achiles, and R. Béttega, "Influence of droplet size distribution on liquid dispersion in a venturi scrubber: experimental measurements and CFD Simulation," *Industrial & Engineering Chemistry Research*, vol. 56, no. 8, pp. 2177–2187, 2017.

[10] F. Lehr, M. Millies, and D. Mewes, "Bubble-size distribution and flow fields in bubble columns," *AIChE Journal*, vol. 48, no. 11, pp. 2426–2443, 2010.

[11] M. Ishii and K. Mishima, "Two-fluid model and hydrodynamic constitutive relations," *Nuclear Engineering & Design*, vol. 82, no. 2-3, pp. 107–126, 1984.

[12] E. Alméras, F. Risso, V. Roig, S. Cazin, and C. Plais, "Mixing by bubble-induced turbulence," *Journal of Fluid Mechanics*, vol. 776, pp. 458–474, 2015.

[13] G. Augier and M. Ishii, "Foundation of the interfacial area transport equation and its closure relations," *International Journal of Heat and Mass Transfer*, vol. 38, no. 3, pp. 481–493, 1995.

[14] J. W. Mullin, *Crystallization*, Butterworth Heinemann, Oxford, UK, 4th edition, 2001.

[15] V. V. Buwa and V. V. Ranade, "Dynamics of gas-liquid flow in a rectangular bubble column: experiments and single/multi-group CFD simulations," *Chemical Engineering Science*, vol. 57, no. 22-23, pp. 4715–4736, 2002.

[16] M. R. Bhole, J. B. Joshi, and D. Ramkrishna, "CFD simulation of bubble columns incorporating population balance modeling," *Chemical Engineering Science*, vol. 63, no. 8, pp. 2267–2282, 2008.

[17] A. Buffo, M. Vanni, D. L. Marchisio, and R. O. Fox, "Multivariate quadrature-based moments methods for turbulent polydisperse gas-liquid systems," *International Journal of Multiphase Flow*, vol. 50, pp. 41–57, 2013.

[18] P. V. Danckwerts, "Continuous flow systems," *Chemical Engineering Science*, vol. 2, no. 1, pp. 1–13, 1953.

[19] H. M. Hulburt and S. Katz, "Some problems in particle technology," *Chemical Engineering Science*, vol. 19, no. 8, pp. 555–574, 1964.

[20] C. A. Coulaloglou and L. L. Tavlarides, "Description of interaction processes in agitated liquid-liquid dispersions," *Chemical Engineering Science*, vol. 32, no. 11, pp. 1289–1297, 1977.

[21] C.-H. Lee, L. E. Erickson, and L. A. Glasgow, "Bubble breakup and coalescence in turbulent gas-liquid dispersions," *Chemical Engineering Communications*, vol. 59, no. 1-6, pp. 65–84, 1987.

[22] F. Lehr and D. Mewes, *A Transport Equation for the Interfacial Area in Bubble Columns Using a Population Balance Approach*, Springer, Heidelberg, Germany, 2004.

[23] E. Olmos, C. Gentric, C. Vial, G. Wild, and N. Midoux, "Numerical simulation of multiphase flow in bubble column reactors. Influence of bubble coalescence and break-up," *Chemical Engineering Science*, vol. 56, no. 21-22, pp. 6359–6365, 2001.

[24] Venneker, J. J. Derksen, and Akker, "Population balance modeling of aerated stirred vessels based on CFD," *Aiche Journal*, vol. 48, no. 4, 2002.

[25] D. Jo and S. T. Revankar, "Investigation of bubble breakup and coalescence in a packed-bed reactor-Part 1: a comparative study of bubble breakup and coalescence models," *International Journal of Multiphase Flow*, vol. 37, no. 9, pp. 995–1002, 2011.

[26] J. Morchain, M. Pigou, and N. Lebaz, "A population balance model for bioreactors combining interdivision time distributions and micromixing concepts," *Biochemical Engineering Journal*, vol. 126, pp. 135–145, 2017.

[27] H. M. Hulburt and S. Katz, "Some problems in particle technology: a statistical mechanical formulation," *Chemical Engineering Science*, vol. 19, no. 8, pp. 555–574, 1964.

[28] X. Luo, Y. Cao, H. Xie, and F. Qin, "Moment method for unsteady flows with heterogeneous condensation," *Computers & Fluids*, vol. 146, no. 26, pp. 51–58, 2017.

[29] R. McGraw, "Description of aerosol dynamics by the quadrature method of moments," *Aerosol Science and Technology*, vol. 27, no. 2, pp. 255–265, 1997.

[30] R. G. Gordon, "Error bounds in equilibrium statistical mechanics," *Journal of Mathematical Physics*, vol. 9, no. 5, pp. 655–663, 1968.

[31] D. L. Marchisio and R. O. Fox, "Computational models for polydisperse particulate and multiphase systems," *Chemical Engineering Progress*, vol. 109, no. 9, p. 55, 2013.

[32] C. Yuan, F. Laurent, and R. O. Fox, "An extended quadrature method of moments for population balance equations," *Aerosol Science*, vol. 51, pp. 0–23, 2012.

[33] S. Aouaouda, M. Chadli, M. Boukhnifer, and H. R. Karimi, "Robust fault tolerant tracking controller design for vehicle dynamics: a descriptor approach," *Mechatronics*, vol. 30, pp. 316–326, 2015.

[34] C. Yuan and R. O. Fox, "Conditional quadrature method of moments for kinetic equations," *Journal of Computational Physics*, vol. 230, no. 22, pp. 8216–8246, 2011.

[35] C. Chalons, F. Laurent, M. Massot, and A. Vié, "Multivariate Gaussian extended quadrature method of moments for turbulent disperse multiphase flow," *Siam Journal on Multiscale Modeling & Simulation*, vol. 15, no. 4, pp. 1553–1558, 2016.

[36] E. I. V. Van den Hengel, N. G. Deen, and J. A. M. Kuipers, "Application of coalescence and breakup models in a discrete bubble model for bubble columns," *Industrial & Engineering Chemistry Research*, vol. 44, no. 14, pp. 5233–5245, 2005.

[37] R. D. Vigil and R. M. Ziff, "On the stability of coagulation-fragmentation population balances," *Journal of Colloid and Interface Science*, vol. 133, no. 1, pp. 257–264, 1989.

[38] J. C. Lamont and D. S. Scott, "An eddy cell model of mass transfer into the surface of a turbulent liquid," *AIChE Journal*, vol. 16, no. 4, 1970.

[39] S. Zhang, Z.-Y. Lv, D. Müller, and G. Wozny, "PBM-CFD investigation of the gas holdup and mass transfer in a lab-scale internal loop airlift reactor," *IEEE Access*, vol. 5, pp. 2711–2719, 2017.

[40] H. Luo and H. F. Svendsen, "Theoretical model for drop and bubble breakup in turbulent dispersions," *AIChE Journal*, vol. 42, no. 5, 1996.

[41] D. L. Marchisio, R. D. Vigil, and R. O. Fox, "Quadrature method of moments for aggregation-breakage processes," *Journal of Colloid and Interface Science*, vol. 258, no. 2, pp. 322–334, 2003.

[42] E. Askari, P. Proulx, and A. Passalacqua, "Modelling of bubbly flow using CFD-PBM solver in OpenFOAM: study of local population balance models and extended quadrature method of moments applications," *ChemEngineering*, vol. 2, no. 1, 2018.

[43] M. Pollack, S. Salenbauch, and D. L. Marchisio, "Bivariate extensions of the Extended Quadrature Method of Moments (EQMOM) to describe coupled droplet evaporation and heat-up," *Journal of Aerosol Science*, vol. 92, pp. 53–69, 2016.

[44] T. Hasse and J. Wang, "Numerical simulations of gas-liquid mass transfer in bubble columns with a CFD-PBM coupled model," *Chemical Engineering Science*, vol. 62, no. 24, pp. 7107–7118, 2007.

[45] T. Hibiki and M. Ishii, "Two-group interfacial area transport equations at bubbly-to-slug flow transition," *Nuclear Engineering and Design*, vol. 202, no. 1, pp. 39–76, 2000.

[46] M. Laakkonen, V. Alopaeus, and J. Aittamaa, "Validation of bubble breakage, coalescence and mass transfer models for gas-liquid dispersion in agitated vessel," *Chemical Engineering Science*, vol. 61, no. 1, pp. 218–228, 2006.

[47] Z. Wu, H. R. Karimi, and C. Dang, "A deterministic annealing neural network algorithm for the minimum concave cost transportation problem," *IEEE Transactions on Neural Networks and Learning Systems*, pp. 1–13, 2019.

[48] Z. Y. Duan, J. B. Hu, and R. K. Zong, "Mass transfer model for SO_2 absorption by NaOH solution in venturi scrubber," *Journal of Tianjin University*, vol. 39, no. 10, pp. 1180–1183, 2006.

[49] R. H. Boll, L. R. Fiais, P. W. Maurer, and W. L. Thompson, "Mean drop size in a full scale venturi scrubber via transmissometer," *Journal of the Air Pollution Control Association*, vol. 24, no. 10, pp. 934–938, 1974.

[50] Y. Wei, J. Qiu, H. R. Karimi, and M. Wang, "Model approximation for two-dimensional Markovian jump systems with state-delays and imperfect mode information," *Multidimensional Systems and Signal Processing*, vol. 26, no. 3, pp. 575–597, 2014.

[51] Z. Naumann and L. Schiller, "A drag coefficient correlation," *V.d.i.zeitung*, vol. 77, no. 1, pp. 51–86, 1935.

[52] M. Xiang, Z. Xiang, and H. R. Karimi, "Asynchronous L1 control of delayed switched positive systems with mode-dependent average dwell time," *Information Sciences*, vol. 278, pp. 703–714, 2014.

[53] Z. Wu, B. Jiang, and H. R. Karimi, "A logarithmic descent direction algorithm for the quadratic knapsack problem," *Applied Mathematics and Computation*, vol. 369, p. 124854, 2019.

[54] N. A. Kazakis, A. A. Mouza, and S. V. Paras, "Experimental study of bubble formation at metal porous spargers: effect of liquid properties and sparger characteristics on the initial bubble size distribution," *Chemical Engineering Journal*, vol. 137, no. 2, pp. 265–281, 2008.

[55] S. Uchida and C. Y. Wen, "Gas absorption by alkaline solutions in a venturi scrubber," *Industrial & Engineering Chemistry Process Design and Development*, vol. 12, no. 4, pp. 437–443, 1973.

[56] G. Bhutani, P. R. Brito-Parada, and J. J. Cilliers, "Polydispersed flow modelling using population balances in an

adaptive mesh finite element framework," *Computers & Chemical Engineering*, vol. 87, pp. 208–225, 2016.

[57] H. Wu, Y. Xu, J. Wang, T. Zhang, and H. Wang, "Study on the similarity of wet gas pressure drop in long-throat Venturi," *Flow Measurement and Instrumentation*, vol. 68, 2019.

[58] X. Zhang, Y. Fu, Z. Li, and Z. Zhao, "The numerical simulation of collapse pressure and boundary of the cavity cloud in venturi," *Chinese Journal of Chemical Engineering*, vol. 17, no. 6, pp. 896–903, 2009.

[59] R. Bannari, F. Kerdouss, B. Selma, A. Bannari, and P. Proulx, "Three-dimensional mathematical modeling of dispersed two-phase flow using class method of population balance in bubble columns," *Computers & Chemical Engineering*, vol. 32, no. 12, pp. 3224–3237, 2008.

[60] B. Selma, R. Bannari, and P. Proulx, "Simulation of bubbly flows: comparison between direct quadrature method of moments (DQMOM) and method of classes (CM)," *Chemical Engineering Science*, vol. 65, no. 6, pp. 1925–1941, 2010.

[61] D. Li, Z. Li, and Z. Gao, "Quadrature-based moment methods for the population balance equation: an algorithm review," *Chinese Journal of Chemical Engineering*, 2018.

[62] A. L. Dale, G. V. Lowry, and E. A. Casman, "Accurate and fast numerical algorithms for tracking particle size distributions during nanoparticle aggregation and dissolution," *Environmental Science Nano*, vol. 4, no. 1, pp. 89–104, 2016.

[63] M. Petitti, M. Vanni, D. L. Marchisio, A. Buffo, and F. Podenzani, "Simulation of coalescence, break-up and mass transfer in a gas-liquid stirred tank with CQMOM," *Chemical Engineering Journal*, vol. 228, pp. 1182–1194, 2013.

[64] A. Buffo, D. L. Marchisio, M. Vanni, and P. Renze, "Simulation of polydisperse multiphase systems using population balances and example application to bubbly flows," *Chemical Engineering Research and Design*, vol. 91, no. 10, pp. 1859–1875, 2013.

Hindawi
Complexity
Volume 2020, Article ID 1974942, 19 pages
https://doi.org/10.1155/2020/1974942

Research Article

Decision and Coordination of Low-Carbon E-Commerce Supply Chain with Government Carbon Subsidies and Fairness Concerns

Qiang Han,[1] **Yuyan Wang**,[1] **Liang Shen**,[2] **and Wenquan Dong**[3,4]

[1]*School of Management Science and Engineering, Shandong University of Finance and Economics, Jinan, Shandong 250014, China*
[2]*School of Public Finance and Taxation, Shandong University of Finance and Economics, Jinan, Shandong 250014, China*
[3]*Institute for a Secure and Sustainable Environment, The University of Tennessee, Knoxville, Tenn 37996, USA*
[4]*Department of Industrial and Systems Engineering, The University of Tennessee, Knoxville, Tenn 37996, USA*

Correspondence should be addressed to Yuyan Wang; wangyuyan1224@126.com

Received 31 May 2020; Revised 16 July 2020; Accepted 30 July 2020; Published 24 August 2020

Academic Editor: Juan Carlos Cortés

More low-carbon products help fight climate change and environmental problems. Governments consider encouraging the manufacturer's initiative of producing low-carbon products by providing subsidies. However, when the manufacturer sells low-carbon products through the e-commerce platform, fairness concerns arise because of the profit difference. So, this paper builds game models to study decision behavior in the low-carbon e-commerce supply chain when the manufacturer receives government carbon subsidies and has fairness concerns. Our findings show that consumers' preference for low-carbon products will be conducive to the operation of the supply chain. So it is necessary to popularize low-carbon products. The effect of government subsidies on supply chain decisions is different from fairness concerns. Government subsidies are positive factors in the supply chain operation, which can stimulate the manufacturer to make low-carbon products as expected and choose the high quality-high price development mode. This will help improve the profit of enterprises in the supply chain but cannot effectively stimulate the e-commerce platform to increase its service level. By contrast, the manufacturer's fairness concerns are negative factors, which make the manufacturer prefer to adopt a low quality-low price development mode to improve their utility. This offsets the positive effect of government subsidies. It turns out that the profit of both node enterprises and the supply chain system has declined. But, fairness concerns are an important way to express the manufacturer's demand. Finally, the joint allocation contract of cost and profit designed by comprehensively considering the effect of government subsidies and fairness concerns can make the supply chain coordinated. However, even as positive factors, only within a specific range do government subsidies help coordinate the supply chain, but not the more, the better.

1. Introduction

With the environmental problems being more and more concerned, low-carbon products that can save energy and reduce carbon emission have gradually become consumption trends, for example, energy-saving light, inverter, and air conditioner. But, producing low-carbon products requires an update of the production process and equipment, which leads to an increase in manufacturers' cost. For encouraging manufacturers to produce low-carbon products, the government generally gives them some carbon subsidies, thereby effectively increasing the production of low-carbon products [1, 2]. In the 2013 home appliance sales of China, energy-saving subsidy policy drove the promotion of more than 32.7 million energy-efficient home appliances, as much as USD 18.9 billion (http://www.chinairn.com/news/20130523/100849491.html).

Since the 1990s, the rapid development of the network technology and express delivery industry has attracted more and more consumers to purchase online. A number of e-commerce platforms (abbreviated as platform in the following if no ambiguity) come into being, for instance, Amazon, JD.com, and Tmall. In 2019, online sales of Black Friday reached USD 7.4 billion, up 19.2 percent from 2018 and setting a new

high (https://www.cnbc.com/2019/11/29/black-friday-online-sales-up-19percent-by-9-am-thanksgiving-sales-hit-record-online.html); total sales of Tmall Double 11 Shopping Festival pulled in USD 38.4 billion from 220 countries and regions worldwide, and 299 merchants have total revenues of over USD 14.3 million each (https://alibabagroup.com/en/news/article?news=p191112). More and more manufacturers sell products through e-commerce platforms, and these manufacturers are mainly small and medium sized. For example, in 2017, more than 20,000 Amazon online sellers across the world exceeded USD 1 million in sales (https://www.marketplacepulse.com/articles/twenty-thousand-amazon-millionaire-sellers).

The e-commerce platform provides manufacturers with new sale channels to sell low-carbon products. Therefore, the platform and low-carbon product manufacturers form a low-carbon e-commerce supply chain. This cooperation seems to be mutually beneficial. However, there are still some discordant factors in the operation process. The e-commerce supply chain is very different from the traditional one that the platform, because of its vast network traffic, becomes the leader. The platform formulates rules for manufacturers' entry and controls the information flow, goods flow, and capital flow. In contrast, manufacturers not only have to pay a specific fixed fee to the platform for entering it but also share the sales profit as a commission with the platform according to an established proportion. In practice, Tmall, JD.com, and Dangdang.com charge their settled manufactures in this way. Moreover, as a shared medium, the platform usually attracts many manufacturers such that it can achieve substantial profit, so sometimes would ignore the manufacturers' interests by using its dominant position. In particular, small- and medium-sized manufacturers are even more affected. For example, during the 6–18 promotion of 2017, many manufacturers have expressed strong dissatisfaction with Tmall and JD.com because these sellers were forced to participate in large-scale discount activities (https://www.chinainternetwatch.com/29999/double-11-2019/). As a result, the decline in status and the gap in profitability in the supply chain has led manufacturers to reexamine their relationship with the platform, which is called fairness concerns. The larger the platform's size, the more significant the income gap, and the stronger the concerns of small- and medium-sized manufacturers in the platform.

This kind of fairness concerns of manufacturers is an instinct response protecting their interests. Then, when they have fairness concerns, how do manufacturers react to the platform, and what impact will they have on the decision of the low-carbon e-commerce supply chain system? When government subsidies and fairness concerns coexist, what will happen to the decision of the supply chain system? When manufacturers have fairness concerns, how could the system coordination be achieved? The current research fruits are still not able to address the above problem well. At present, the research about fairness concern behavior is mainly focused on the traditional offline supply chain [3–5]. Even if the online sale is considered, it is only regarded as one of the distribution channels, which does not reflect the key features of a platform [6–8]. As the leader of a low-carbon e-commerce supply chain, the platform is responsible for providing consumers with logistics, information, and other services besides general services, and consumers demand much more from the platform than from offline sellers. Therefore, the operation of the platform requires costs to maintain, and it is also necessary to take the platform's service cost and service level into account when making decisions. Moreover, manufacturers' carbon subsidies obtained from the government make manufacturers realize the importance of their carbon emission reduction behavior, which will intensify manufacturers' desire for fairness. These are rarely addressed in the existing research.

This paper will study how the low-carbon e-commerce supply chain will make decisions and be coordinated if the manufacturer receives carbon subsidies from the government and has fairness concerns. Our contributions are as follows:

(1) To determine whether the carbon subsidies are effective to promote the low-carbon products by analyzing the effect of the carbon subsidies on the manufacturer's sales price and carbon emission reduction level, the platform's service level, and the profit of the low-carbon e-commerce supply chain.

(2) To explore the transmission mechanisms of the manufacturer's fairness concerns by analyzing the double effects of both carbon subsidies and the manufacturer's fairness concerns on the service level, the sales price, and the profit.

(3) To coordinate the supply chain with government carbon subsidies and fairness concerns by designing the joint allocation contract of cost and profit to eliminate the double marginalization under decentralized decision modes.

The rest of this paper is organized as follows. Literature review is given in Section 2. Some basic work for the models is provided in Section 3. We model four different decision modes in Section 4 and then analyze and compare different decision results in Section 5. In Section 6, the coordination mechanism for the supply chain system is designed. In Section 7, we do the example analysis. In Section 8, we offer concluding comments.

2. Related Literature

This paper mainly involves such three streams of literature: incentive mechanism of government carbon subsidies, supply chain fairness concerns, and supply chain coordination.

2.1. Incentive Mechanism of Government Carbon Subsidies. For protecting our environment, researches about closed-loop supply chain have been conducted [9–11]. As carbon emission reduction is concerned, manufacturers have a direct relation to assume this responsibility and also manage to invest in this area [12]. In fact, economic and environmental benefits can be achieved simultaneously [13], and external factors could do something to guide the

manufactures and the supply chain [14, 15]. Recently, for promoting the production and consumption of low-carbon products, governments of the world are concerned about how the supply chain decision-making will be influenced by different carbon emission reduction measures [16]. Carbon subsidies, often adopted by governments to promote product development, can boost profit growth, increase market demand, and improve the benefits of supply chain members [17]. Currently, carbon subsidies are mainly used in the field of recycling or remanufacturing of electronic products [18]. Li et al. [19] considered the application of carbon subsidy policies in the remanufacturing supply chain and analyzed when and how the government should use carbon subsidies to stimulate enterprises' initiative to reduce carbon emissions. In practice, there are two departments: formal and informal sections, which can recycle electronic products. In order to accelerate the development of the recycling industry, subsidies should be regulated by the government to limit the waste quality to a higher level. If the government subsidies are not sufficient and the waste quality is high, then the informal production sector has a greater competitive advantage [20]. As the subsidy recipient is concerned, the government could subsidize the recycler or remanufacturer and provide subsidies according to the remanufacturers' different service levels, which is helpful to expand the market scale and remanufacturing service level [21].

The carbon subsidy strategy studied in the existing literature is a passive way mainly aiming at the remanufacturing and waste recycling in the traditional supply chain background. However, under the e-commerce environment, the transmission mechanism of government carbon subsidies in the supply chain will be quite different, where the manufacturer directly sells products to consumers on the platform and the low-carbon product manufacturer, as the main contributor to manufacturing low-carbon products can set the product price. Therefore, the government gives carbon subsidies to the low-carbon product manufacturer. After obtaining carbon subsidies, the manufacturer's profit will be raised, and then, this influence will be passed on through the supply chain, which will further affect some decisions of the platform. This means that the existing methodology is no longer applicable. So, from the perspective that the government actively encourages the manufacturer to produce low-carbon products by providing carbon subsidies, this paper introduces carbon emission reduction costs and carbon subsidies into the manufacturer's profit function. Carbon subsidies will be given proportional to the carbon emission level. We aim to drive the production of low-carbon products from the source.

2.2. Supply Chain Fairness Concerns. Besides how much profit they earn, companies or individuals in economic activities will also pay close attention to the profit gap between the trade parties, that is, the fairness of profit allocation [22–24]. At present, the concerns about fairness are particularly reflected in the offline supply chain that maintains long-term partnerships [25–27]. Cui et al. [28] used fairness concerns to express dissatisfaction with the status in the supply chain and explore how the transactions between retailers and manufacturers would be affected, especially by quantity discounts and two-part tariffs. Zhao et al. [29] studied a product and service supply chain and compared its optimal pricing strategy in two cases based on whether fairness concerns of the retailer are considered, finding that if the retailer in the supply chain has fairness concerns, all the enterprises could adopt differentiated service pricing strategies, but the retailer's fairness concerns would do harm to the manufacturer's profit. If both manufacturers and retailers in the supply chain have fairness concerns, retailers' fairness concerns are more likely to result in a narrower supply chain stable area than manufacturers, while manufacturers' fairness concerns can expand the system's stable area [30, 31].

The existing research fruits mainly study the fairness concerns of retailers and manufacturers in the supply chain of ordinary products. The research subject of this paper is the fuse of the e-commerce supply chain and low-carbon supply chain. Manufacturers produce low-carbon products and need to invest in additional R&D costs. The e-commerce platform in the supply chain is the dominant and core enterprise, which puts manufacturers at a disadvantage status in the profit allocation, thereby making manufacturers have fairness concerns. Moreover, fair concerns in this situation have their particularity. On the one hand, the platform could get commissions from numerous small- and medium-sized manufacturers that have settled in it; and on the other hand, manufacturers think that they should get more benefits because of paying for low-carbon production costs and receiving government subsidies. So, even though the manufacturer's profit is no less than what the e-commerce platform can get from this manufacturer, the manufacturer will still have fairness concerns. Thus, the mechanism of how fairness concerns come into being in this paper is different from the existing research fruits.

2.3. Supply Chain Coordination. Classic coordination contracts include sharing revenue contract, buy-back contract, quantity-flexibility contract, wholesale pricing contract, and quantity discount contract [32]. Now, researchers have to add some other factors into the coordination contract, such as environmental, economic, and social dimensions [33–40]. For the two-tier reverse supply chain, Heydari et al. [41] proposed a coordination mechanism combining quantity discounts with increasing fee, adding government subsidies into the contract as incentives so that each member has enough initiative to participate in the coordination process, which favors retailers much more. For a low-carbon supply chain with carbon emission cap-and-trade, Peng et al. [42] combined subsidy on emission reduction with the revenue-sharing contract and then perfectly achieved both the supply chain coordination and the carbon emission reduction.

For the supply chain coordination problems with fairness concerns, many scholars have also designed effective coordination contracts according to practical problems [43–45]. Cui et al. [28] designed the whole price contract and

used this contract to coordinate fairness concerns from retailers only or from both retailers and manufacturers in the supply chain with linear demand. Then, Caliskan-Demiraga et al. [46] extended the linear demand function to the exponential one and found that when retailers have fairness concerns, more relaxed conditions are needed to achieve coordination. Zheng et al. [47] coordinated a closed-loop supply chain by variable-weighted Shapley values, which is better than the traditional Shapley value coordination method when remanufactured goods are accepted by customers at a lower rate.

One supply chain contract cannot apply to all coordination problems, and we need to design them according to the actual ones. The existing literature about supply chain coordination has not considered the existence of both fairness concerns and carbon subsidies. In addition, the difference in the problem addressed here from the existing literature lies in that it is necessary to take four factors into account, that is, the manufacturer's low-carbon cost, the platform's service cost, the commission charged by the platform, and government carbon subsidies, which are critical for achieving coordination. We have to balance the four factors and explore how the coordination condition is influenced by manufacturers' fairness concerns.

Based on the above literature review, the existing research has built a solid base for the related fields; however, there are still research gaps to fill. First, most works studied carbon subsidy strategy for recycling or remanufacturing of electronic products [18–21]; although several studies have investigated supply chains under the governments' carbon subsidy [12, 14, 15], they are not applied to the e-commerce supply chain. Second, fair concerns exist in different backgrounds, but most of them studied that between the retailers and manufacturers in the supply chain of ordinary products [24, 27, 29, 31]; even though there are researches related to online or low-carbon background, they do not consider them together [23, 30]. Third, various coordination contracts have been designed aiming to reduce the carbon emission or protect the environment [32, 36], and some of them have taken government role [41], low-carbon preference [42], or fairness concern [44] into account, but no works addressed the problem with all of them; under the e-commerce background, Wang et al. [48] coordinated the supply chain when the manufacturer has fairness concerns, but no carbon subsidy is considered. So, in this paper, our contributions are to formulate the game model for low-carbon e-commerce supply chain with government carbon subsidies and fairness concerns, exploring the effect of government carbon subsidies and fairness concerns on the supply chain, determining what the manufacturer and the platform will react, achieving the coordination of the supply chain by allocating the carbon subsidies, commission, and the cost as a whole.

3. Preliminaries of Models

We consider a supply chain composed of one e-commerce platform and one small- and medium-sized manufacturer. In this supply chain, the manufacturer is responsible for producing only one low-carbon product, while the platform offers a direct online shop to the manufacturer. Because the fixed fee pays only once when the manufacturer enters the platform, we do not take it into account in the following models.

The platform and the manufacturer are independent, making decisions for maximizing their profit, respectively. They form Stackelberg games. As stated in Section 1, this paper assumes that the platform is the leader with the priority to make decisions, while the manufacturer is the follower. The platform first determines its service level. On obtaining the platform's decision, the manufacturer then determines sales price of the low-carbon product and its carbon emission reduction level.

Some notations are listed in Table 1, which will be used frequently in this paper.

Generally, carbon emission reduction involves more advanced technology and management, so the manufacturer has to spend more extra cost for producing the low-carbon product than general ones. The higher the carbon emission reduction level, the higher the cost. Based on the relation put forward by Nair and Narasimhan [49], the manufacturer's carbon emission reduction cost is as follows:

$$C_m(h) = \frac{th^2}{2}. \tag{1}$$

Because carbon emission reduction is conducive to energy conservation and environmental protection, the government will provide the manufacturer with subsidies to encourage its positive behavior. Suppose the unit emission reduction subsidy received by the manufacturer is $T\,(T > 0)$.

According to Yao and Liu [50], the demanded quantity of low-carbon product depends on its sales price, the manufacturer's carbon emission reduction level, and the platform's service level, which can be formulated as

$$q = D - d_1 p + d_2 s + d_3 h. \tag{2}$$

Suppose D is a large enough constant number. Suppose $d_1 > d_3$, suggesting that the product's price influences consumers much more than its low-carbon level.

Generally, the higher the platform's service level, the more the cost. Based on Shen's research [51], the platform's service cost is functioned as

$$C_e(s) = \frac{ks^2}{2}. \tag{3}$$

Suppose $\rho < p - c$, representing that the commission should be less than the net profit of the product sales.

To make the following analysis hold, we further assume $td_1 < d_3^2 < 2td_1$ and $td_2^2 + kd_3^2 < 2ktd_1$. The former, equivalent to $2d_1 C_m(h) < (d_3 h)^2 < 4d_1 C_m(h)$, means that the influence of the manufacturer's carbon emission reduction level on the demanded quantity of the low-carbon product depends on the carbon emission reduction cost, and the influence is limited, neither too large nor too little, while the latter represents that the sales price has greater influence on the demanded quantity than the combined effect of the manufacturer's carbon emission reduction level and the platform's service level.

Table 1: Mathematical notations.

Notations	Meaning
c	Unit cost for producing the low-carbon product (in dollars)
h	Carbon emission reduction level of the manufacture
p	Sales price of the low-carbon product (in dollars)
q	Market demand for the low-carbon product
s	Service level of the platform
T	Unit government subsidy for the manufacture (in dollars)
ρ	Commission charged by the platform for unit sales of products (in dollars)
t	Carbon emission reduction cost coefficient
D	Maximum quantity demanded of the low-carbon product
d_1	Influence coefficient of the low-carbon product sales price on demand
d_2	Influence coefficient of the platform's service level on demand
d_3	Influence coefficient of the manufacturer's carbon emission reduction level on demand
k	Service cost coefficient

4. Modeling Framework

In this section, we model different decision modes of the e-commerce supply chain according to whether there are government carbon subsidies and manufacturer's fairness concerns or not.

4.1. Model I: Benchmark Model. Starting from the most fundamental case, we build the benchmark model in which the government does not provide any carbon subsidies and the manufacturer does not have fairness concerns. We can also call it the decentralized decision model without government carbon subsidies and manufacturer's fairness concerns. Then, the manufacturer's profit is

$$\pi_m = pq - \rho q - cq - \frac{th^2}{2}. \tag{4}$$

The platform's profit is

$$\pi_e = \rho q - \frac{ks^2}{2}. \tag{5}$$

The supply chain's profit is

$$\pi = pq - cq - \frac{th^2}{2} - \frac{ks^2}{2}. \tag{6}$$

By backward induction, the optimal solution of this model could be achieved as follows.

Theorem 1. *In the benchmark model, the optimal sales price is*

$$p^{b*} = (c+\rho) + d_1 \cdot \left(\frac{td_2}{2td_1 - d_3^2}\right)^2 \cdot \frac{\rho}{k} + \frac{k\left[D - d_1(c+\rho)\right] - \rho d_2^2}{k\left(2td_1 - d_3^2\right)} \cdot t. \tag{7}$$

The optimal carbon emission reduction level is

$$h^{b*} = t \cdot d_1 \cdot d_3 \cdot \frac{\rho}{k} \cdot \left(\frac{d_2}{2td_1 - d_3^2}\right)^2 + d_3 \cdot \frac{k\left[D - d_1(c+\rho)\right] - d_2^2\rho}{k\left(2td_1 - d_3^2\right)}. \tag{8}$$

The optimal service level is

$$s^{b*} = d_2 \cdot \frac{\rho}{k} \cdot \frac{d_3^2 - td_1}{2td_1 - d_3^2}. \tag{9}$$

The manufacturer's optimal profit is

$$\pi_m^{b*} = \frac{t}{2} \cdot \frac{\left[D - d_1(c+\rho)\right]^2}{2td_1 - d_3^2} - \frac{t}{2} \cdot \frac{d_2^4}{2td_1 - d_3^2} \cdot \left(\frac{\rho}{k} \cdot \frac{d_3^2 - td_1}{2td_1 - d_3^2}\right)^2. \tag{10}$$

The platform's optimal profit is

$$\pi_e^{b*} = t\rho d_1 \cdot \frac{D - d_1(c+\rho)}{2td_1 - d_3^2} + \frac{(\rho d_2)^2}{2k} \cdot \left(\frac{d_3^2 - td_1}{2td_1 - d_3^2}\right)^2. \tag{11}$$

The supply chain's optimal profit is

$$\pi^{b*} = t \cdot \frac{\left[D - d_1(c-\rho)\right] \cdot \left[D - d_1(c+\rho)\right]}{2\left(2td_1 - d_3^2\right)} + \frac{(\rho d_2)^2}{2k} \cdot \left(\frac{d_3^2 - td_1}{2td_1 - d_3^2}\right)^2 - \frac{td_2^4}{2} \cdot \left(\frac{\rho}{k}\right)^2 \cdot \frac{1}{2td_1 - d_3^2} \cdot \left(\frac{d_3^2 - td_1}{2td_1 - d_3^2}\right)^2. \tag{12}$$

Proof. See Appendix A. □

4.2. Model II: Decentralized Decision Model with Government Carbon Subsidies and without Manufacturer's Fairness Concerns. Based on the benchmark model, we turn to the case that the government subsidies the manufacturer for its carbon emission reduction behavior and the manufacturer does not have fairness concerns. Then, the manufacturer's profit is

$$\pi_m = pq + Th - \rho q - cq - \frac{th^2}{2}. \tag{13}$$

The platform's profit is

$$\pi_e = \rho q - \frac{ks^2}{2}. \tag{14}$$

The supply chain's profit is

$$\pi = pq + Th - cq - \frac{th^2}{2} - \frac{ks^2}{2}. \tag{15}$$

Similar to the solution process of Theorem 1, we reach the following theorem.

Theorem 2. *In the decentralized decision model with government carbon subsidies, the optimal product sales price is*

$$p^{s*} = (c+\rho) + \frac{\rho d_1}{k} \cdot \left(\frac{td_2}{2td_1 - d_3^2}\right)^2 + \frac{k[Dt + d_3T - td_1(c+\rho)] - \rho t d_2^2}{k\left(2td_1 - d_3^2\right)}. \tag{16}$$

The optimal carbon emission reduction level is

$$h^{s*} = \frac{\rho}{k} \cdot \frac{d_1 d_3}{t} \cdot \left(\frac{td_2}{2td_1 - d_3^2}\right)^2 + \frac{d_3}{k} \cdot \frac{k[(D + 2Td_1)/(d_3 - d_1(c+\rho))] - \rho d_2^2}{2td_1 - d_3^2}. \tag{17}$$

The optimal service level is

$$s^{s*} = d_2 \cdot \frac{\rho}{k} \cdot \frac{d_3^2 - td_1}{2td_1 - d_3^2}. \tag{18}$$

The manufacturer's optimal profit is

$$\pi_m^{s*} = \frac{t \cdot [D - d_1(c+\rho)]^2 + 2d_3T[D - d_1(c+\rho)] + 2d_1T^2}{2\left(2td_1 - d_3^2\right)} - \frac{t}{2} \cdot \frac{d_2^4}{2td_1 - d_3^2} \cdot \left(\frac{\rho}{k} \cdot \frac{d_3^2 - td_1}{2td_1 - d_3^2}\right)^2. \tag{19}$$

The platform's optimal profit is

$$\pi_e^{s*} = d_1 \cdot \frac{t\rho[D - d_1(c+\rho)] + Td_3}{2td_1 - d_3^2} + \frac{(\rho d_2)^2}{2k} \cdot \left(\frac{d_3^2 - td_1}{2td_1 - d_3^2}\right)^2. \tag{20}$$

The supply chain's optimal profit is

$$\pi^{s*} = \frac{t \cdot [D - d_1(c+\rho)][D - d_1c - \rho] + 2T[Td_1 + (D - cd_1)d_3]}{2\left(2td_1 - d_3^2\right)} + \frac{(\rho d_2)^2}{2k} \cdot \left(\frac{d_3^2 - td_1}{2td_1 - d_3^2}\right)^2 - \frac{t}{2} \cdot \frac{d_2^4}{2td_1 - d_3^2} \cdot \left(\frac{\rho}{k} \cdot \frac{d_3^2 - td_1}{2td_1 - d_3^2}\right)^2. \tag{21}$$

By comparing the decision results of model II with model I, we can find the effect of government carbon subsidies on the supply chain decision.

Proposition 1. $p^{b*} < p^{s*}$, $h^{b*} < h^{s*}$, $s^{b*} = s^{s*}$, $\pi_m^{b*} < \pi_m^{s*}$, $\pi_e^{b*} < \pi_e^{s*}$, *and* $\pi^{b*} < \pi^{s*}$.

Proof. See Appendix B. □

Proposition 1 shows that, after the government provides subsidies, product sales price, carbon emission reduction level, the manufacturer's profit, and the platform's profit have all increased. The proof process in Appendix B also suggests that these changes are related to subsidies, which reflects the effectiveness of government subsidies. However, the platform's service level stays the same. On the one hand, since subsidies are directly given to the manufacturer, they have no impact on the platform's service level. On the other hand, if the platform can have its profit increased even without the necessity to improve its service level, it does not have any initiative to make efforts at all. This reflects the shortcoming of government subsidies since they cannot stimulate the platform to improve its sales service.

Government subsidies express their emphasis and recognition on the manufacturer's production of low-carbon products, which can become a guide to social consumption habits. From the consumers' perspective, their low-carbon awareness will also increase, and they will pay much more attention to the low-carbon level of products when making a purchase. Even if the price is higher than nonlow-carbon products, consumers will be more willing to buy. From the perspective of the manufacturer, government subsidies have given it the motivation and responsibility to continue developing low-carbon products, and its low-carbon level has been constantly improved. The modest increase in the price of the product by the manufacturer mainly reflects a differentiating strategy, which is different from previous products and will eventually make itself more profitable.

On January 16, 2017, JD.com and Midea Group signed a USD 2.9 billion comprehensive strategic cooperation agreement (http://news.163.com/17/0117/10/CAVN0MMQ00018AOQ.html). JD.com has witnessed that prices of low-carbon energy-saving products have generally increased by about USD 87.1. Midea Group received government subsidies of USD 0.2 billion in 2017 (http://money.finance.sina.com.cn/corp/view/vCB_AllBulletinDetail.php?stockid=000333&id=4185007) and achieved a year-on-year net profit increase of 17.33% (http://baijiahao.baidu.com/s?id=1596592651173428121&wfr=spider&for=pc). JD.com's full-year net profit in 2017 was USD 0.73 billion, a substantial increase of 140% year-on-year (http://tech.qq.com/a/20180302/030924.html).

4.3. Model III: Decentralized Decision Model with Government Carbon Subsidies and Manufacturer's Fairness Concerns. As mentioned in Introduction, the capital input of carbon emission reduction, the dissatisfaction caused by the platform neglecting its interests, and the support of government's carbon subsidies and other factors will cause the manufacturer's concern over the profit gap between it and the platform, thus creating fairness concerns. Therefore, we bring the manufacturer's fairness concern behavior into our model.

According to Fehr and Schmidt [52] and Katok et al. [53], when having fairness concerns, the manufacturer will take δ times the platform's profit as the reference point. So, we write the manufacturer's utility function as

$$U_m = \pi_m - \theta(\delta\pi_e - \pi_m), \tag{22}$$

where $0 \le \theta \le 1$ denotes the manufacturer's fairness concern coefficient. When θ is closer to 0, it means the manufacturer's fairness concern degree is getting weaker. Otherwise, θ closer to 1 means the manufacturer's fairness concern degree is getting stronger.

Substituting π_m and π_e in U_m, we express the manufacturer's utility function as

$$U_m = (1+\theta)\left(\frac{pq + Th - \rho q - cq - th^2}{2}\right) + \theta\delta\left(\frac{ks^2}{2} - \rho q\right). \tag{23}$$

In this case, the manufacturer's decision is not based on profit, but utility. The manufacturer tries to maximize its utility. By backward induction, we obtain the optimal solution of this model as follows.

Theorem 3. *In the decentralized decision model with government carbon subsidies and manufacturer's fairness concerns, the optimal product sales price is*

$$p^{sf*} = (c+\rho) + \left(d_3^2 - td_1\right)\cdot t\cdot\frac{\rho}{k}\cdot\left(\frac{d_2}{2td_1 - d_3^2}\right)^2 + \frac{t\left[D - d_1(c+\rho)\right] + d_3T}{2td_1 - d_3^2} - \delta\rho\cdot\frac{\theta}{1+\theta}\cdot\frac{d_3^2 - td_1}{2td_1 - d_3^2}. \tag{24}$$

The optimal carbon emission reduction level is

$$h^{sf*} = d_3\cdot\frac{\rho}{k}\cdot\left(d_3^2 - td_1\right)\cdot\left(\frac{d_2}{2td_1 - d_3^2}\right)^2 + \frac{d_3\left[D - d_1(c+\rho)\right] + 2Td_1}{2td_1 - d_3^2} - \frac{d_1d_3\delta\rho}{2td_1 - d_3^2}\cdot\frac{\theta}{1+\theta}. \tag{25}$$

The optimal service level is

$$s^{sf*} = d_2\cdot\frac{\rho}{k}\cdot\frac{d_3^2 - td_1}{2t\beta - d_3^2}. \tag{26}$$

The manufacturer's optimal utility is

$$U_m^{sf*} = T\cdot\frac{d_3\left[(1+\theta)(D - cd_1 - \rho d_1) - \theta d_1\rho\delta\right] + d_1(1+\theta)T}{2td_1 - d_3^2} + \frac{t}{2(1+\theta)}\cdot\frac{\left[(1+\theta)(D - cd_1 - \rho d_1) - \theta d_1\rho\delta\right]^2}{2td_1 - d_3^2} + (\rho d_2)^2\cdot\frac{\delta\theta}{2k}\cdot\left(\frac{d_3^2 - td_1}{2td_1 - d_3^2}\right)^2 - \frac{t\rho^2 d_2^4}{2td_1 - d_3^2}\cdot\frac{1+\theta}{2k^2}\cdot\left(\frac{d_3^2 - td_1}{2td_1 - d_3^2}\right)^2. \tag{27}$$

The platform's optimal profit is

$$\pi_e^{sf*} = \frac{(\rho d_2)^2}{2k}\cdot\left(\frac{d_3^2 - td_1}{2td_1 - d_3^2}\right)^2 + \rho d_1\frac{t\left[D - d_1(c+\rho)\right] + Td_3}{2td_1 - d_3^2} - \frac{\theta}{1+\theta}\cdot\frac{t(1+\delta)(\rho d_1)^2}{2td_1 - d_3^2}. \tag{28}$$

The manufacturer's optimal profit is

$$\pi_m^{sf*} = \frac{\left(t\left[D - d_1(c+\rho)\right]^2/2\right) + Td_3\left[D - d_1(c+\rho)\right] + T^2d_1}{2td_1 - d_3^2} + \rho^2d_2^2\cdot\frac{\delta}{k}\cdot\frac{\theta}{1+\theta}\cdot\left(\frac{d_3^2 - td_1}{2td_1 - d_3^2}\right)^2 - \frac{t\rho^2d_2^4}{2k^2\left(2td_1 - d_3^2\right)}\cdot\left(\frac{d_3^2 - td_1}{2td_1 - d_3^2}\right)^2 - \left(\frac{\theta}{1+\theta}\right)^2\cdot\frac{t\delta^2\rho^2d_1^2}{2\left(2td_1 - d_3^2\right)}. \tag{29}$$

The supply chain's optimal profit is

$$\pi^{sf*} = \frac{t\left[D - d_1(c+\rho)\right]^2 + (d_3 + 2\rho d_1 t)\left[D - d_1(c+\rho)\right] + d_1 T(1+2\rho d_3)}{2\left(2td_1 - d_3^2\right)} + \frac{(\rho d_2)^2}{2k}\cdot\left(1 + 2\delta\cdot\frac{\theta}{1+\theta}\right)\cdot\left(\frac{d_3^2 - td_1}{2td_1 - d_3^2}\right)^2$$
$$- \frac{td_2^2(\rho d_2)^2}{2k^2\left(2td_1 - d_3^2\right)}\cdot\left(\frac{d_3^2 - td_1}{2td_1 - d_3^2}\right)^2 \tag{30}$$
$$- \frac{t}{2}\cdot\frac{\theta}{1+\theta}\cdot\frac{(d_1\rho)^2}{2td_1 - d_3^2}\left[2(1+\delta) + \delta^2\frac{\theta}{1+\theta}\right].$$

Proposition 2. *s^{sf*} is independent of θ, while p^{sf*}, h^{sf*}, π_m^{sf*}, π_e^{sf*}, and π^{sf*} all decrease as θ increases.*

Proof. See Appendix C. □

The manufacturer employs fairness concern behavior to ensure its utility not damaged, with such available means as the product price and the carbon emission reduction level. Dominant in their relationship, the platform is reluctant to adjust its service level to ease up the manufacturer's concerns and will pay the price of reduced profit for this. With fairness concerns increasing, the manufacturer may make decisions irrationally aiming to increase its profit. Therefore, the manufacturer intends to decrease its production cost, no longer exerting effort to improve the low-carbon level of the product. At the same time, the manufacturer reduces the product sales price expecting to increase the sales volume and tries to take the low quality-low price route. As a result, the effect is counterproductive, which eventually leads to the profit decline of the platform, the manufacturer, and the supply chain. Thus, Proposition 2 suggests that the manufacturer's fairness concerns go against the whole supply chain and its members.

In a supply chain system, the manufacturer who pays too much attention to the profit gap and its utility will get the opposite effect. Therefore, during the actual operation, as long as its profit can be increased, it is not necessary to pursue the absolute profit fairness among members. On the one hand, the low-carbon product manufacturer should actively work closely together with the platform, play its role, and keep improving the low-carbon level of products; the platform, on the other hand, should guarantee the service level and customer size and so is the manufacturer's profit.

4.4. Model IV: Centralized Decision Model with Government Carbon Subsidies. Now, we consider the case when the manufacturer and the platform can cooperate to maximize the supply chain's overall profit, which forms a centralized decision mode. Under this mode with government's carbon subsidies, the supply chain's profit is

$$\pi(p,h,s) = (Th + pq) - \left(cq + \frac{th^2}{2} + \frac{ks^2}{2}\right). \tag{31}$$

And, its optimal solution is given below.

Theorem 4. *In the centralized decision model with government carbon subsidies, the optimal product retail price is*

$$p^{c*} = \frac{kt(D + cd_1) + kTd_3 - c\left(td_2^2 + kd_3^2\right)}{2ktd_1 - \left(td_2^2 + kd_3^2\right)}. \tag{32}$$

The optimal carbon emission reduction level is

$$h^{c*} = \frac{kd_3(D - cd_1) + T\left(2kd_1 - d_2^2\right)}{2ktd_1 - \left(td_2^2 + kd_3^2\right)}. \tag{33}$$

The optimal service level is

$$s^{c*} = d_2\cdot\frac{t(D - cd_1) + Td_3}{2ktd_1 - \left(td_2^2 + kd_3^2\right)}. \tag{34}$$

The supply chain's optimal profit is

$$\pi^{c*} = \frac{kt(D - cd_1)^2 + T^2\left(2kd_1 - d_2^2\right) + 2kTd_3(D - cd_1)}{4ktd_1 - 2\left(td_2^2 + kd_3^2\right)}. \tag{35}$$

5. Managerial Analysis

In this section, we show how government carbon subsidies and the manufacturer's fairness concerns would affect the supply chain decisions by comparison of models in Proposition 3 through Proposition 7.

Proposition 3. *$s^{c*} > s^{s*} = s^{sf*}$. Both s^{s*} and s^{sf*} increase with ρ. s^{c*}, s^{s*}, and s^{sf*} increase with d_3.*

Proof. See Appendix D. □

Proposition 3 implies that since the service level is only depended on the platform, it stays the same no matter the low-carbon product manufacturer has fairness concerns or not. As the platform's profit increases, it has more available money to improve the service level. Correspondingly, consumers' preference for low-carbon products helps the rise in service level in all three cases. This inspires the manufacturer that they should try to promote low-carbon products and let consumers favor low-carbon products, which will also drive the platform to improve its service. In this way, the manufacturer, even a follower in the supply chain, still can have effect on the leader to some extent.

Similar to the proof of Proposition 3, we give Propositions 4–6 without extra proofs.

Proposition 4. *$h^{c*} > h^{s*} > h^{sf*}$. Both h^{s*} and h^{sf*} decrease with the increase in ρ, while h^{c*}, h^{s*}, and h^{sf*} increase with d_3.*

Proposition 4 shows that the e-commerce supply chain system has the highest carbon emission reduction level in the centralized decision model, and that when the manufacturer has fairness concerns, its excessive focus on profit allocation has affected the motivation and enthusiasm to reduce carbon emission. As the profit gained by the platform increases, the low-carbon product manufacturer will cut down its carbon emission reduction level due to the decrease in obtained profit. Thus, in order to raise the carbon emission reduction level, the platform should reduce the commission, which will help the sale of low-carbon product. However, as consumers' preference for low-carbon products increases, no matter under the decentralized decision models with or without the manufacturer's fairness concerns, or the centralized decision model, efforts will be made to improve carbon emission reduction levels.

Proposition 5. *$p^{c*} > p^{s*} > p^{sf*}$. Both p^{s*} and p^{sf*} decrease with the increase in ρ while p^{c*}, p^{s*}, and p^{sf*} increase with d_3.*

Proposition 5 expresses that the highest price can be set in the centralized decision model because this mode has both the highest carbon emission level and the highest service level, which can be accepted by consumers. This result reflects the approval by consumers for the cost of the supply chain system to provide high-quality products. Among the three decision models, the manufacturer is most sensitive to the profit when it has fairness concerns. When the manufacturer's profit is affected, it will prefer the low-end development way, not actively improving the carbon emission level, while the platform's service level will not get improved, either, so the manufacturer can only choose the low-price strategy. In the decentralized decision models, with the platform's profit increasing, the manufacturer expects to increase its profit by reducing prices. It will not actually but will reduce the manufacturer's profit. This also exposes the disadvantages of decentralized decision and further discloses the fact that the platform's attempt to obtain profit by collecting too much commission does harm to the supply chain. With the rise in consumers' preference for low-carbon products, it is a good situation for low-carbon sales, which can promote the rise in commodity prices under three decision modes.

Proposition 6. *$\pi^{c*} > \pi^{s*} > \pi^{sf*}$. Both π^{s*} and π^{sf*} decrease with the increase in ρ, while π^{c*}, π^{s*}, and π^{sf*} increase with d_3.*

Proposition 6 tells us that the supply chain's profit is the largest in the centralized decision model, the smallest when the manufacturer has the fairness concerns, and in between when the manufacturer does not have any fairness concerns. This result demonstrates that the manufacturer is more sensitive to profit allocation when having fairness concerns, and its performance in the supply chain is affected. When the platform's profit rises, the supply chain's one will decline in the decentralized decision models (whether with the manufacturer's fairness concerns or not). This relation further reflects the manufacturer's desire to share the profit reasonably. Otherwise, it will adopt a more uncooperative way in the supply chain. As consumers prefer low-carbon products more, the production and sales of low-carbon products are more supported, and then, the supply chain's profit will increase in the end.

Hence, the manufacturer's irrational fairness concerns go against the operation and coordination of the supply chain system. In practice, manufacturers should be guided to give up this irrational behavior and closely cooperate with the operation of the system.

Proposition 7. *U_m^{sf*} increases as θ increases.*

Proof. See Appendix E. □

As stated in Proposition 7, the manufacturer's utility will increase with the fairness concern coefficient. Fairness concerns, in some sense, are thereby proven to have positive effect in the supply chain decision. When the low-carbon product manufacturer focuses on the fairness of profit allocation, the platform will take the manufacturer's needs into account in its decision process after obtaining this information. This guides one way for the weak enterprise in the supply chain how to struggle for its benefit with the strong one.

6. Low-Carbon E-Commerce Supply Chain Coordination Based on Government Carbon Subsidies

It can be seen from the comparison in previous section that the government carbon subsidy mechanism helps increase the supply chain's profit. When government subsidies are applied, the centralized decision is better than other decentralized ones, regardless of with or without the manufacturer's fairness concerns. The centralized decision mode achieves the optimal profit for the system, while decentralized decision modes result in loss of efficiency due to the double marginalization effect. Thus, a specific coordination mechanism is necessary to be applied in this system.

Since cost and benefit are two key factors connecting the manufacture and the platform, we adopt indicators about them as coordination means and design the joint allocation contract of cost and profit to coordinate the system. The idea of this contract is to coordinate the benefits of both sides in this way: the platform adjusts the commission by the manufacturer's sales price and production cost, while the manufacturer pays part of government subsidies to the platform; besides that, the manufacturer and the platform appropriately share the costs for each other.

Under the joint allocation contract of cost and profit, on the one hand, we assume that the platform adjusts the commission to $\overline{\rho}$, pays the proportion $y\,(0 \le y \le 1)$ of the service cost, and leaves the remaining $(1 - y)$ to the manufacturer; on the other hand, we assume that the manufacturer keeps the proportion $z\,(0 \le z \le 1)$ of government subsidies, giving others to the platform, and pays the proportion $x\,(0 \le x \le 1)$ of the low-carbon cost, leaving the remaining $(1 - x)$ to the platform. Then, the profit of the manufacturer is

$$\pi_m^c = (p - \overline{p} - c)q + zTh - x\frac{th^2}{2} - (1 - y)\frac{ks^2}{2}. \tag{36}$$

The profit of the platform is

$$\pi_e^c = \overline{p}q + (1 - z)Th - (1 - x)\frac{th^2}{2} - \frac{yks^2}{2}. \tag{37}$$

Theorem 5. *The joint allocation contract of cost and profit can coordinate the e-commerce supply chain if* $(\overline{p}, x, y, z)$ *satisfies*

$$\begin{cases} \overline{p} = (1 - \phi)(p - c), \\ x = \phi, \\ y = 1 - \phi, \\ z = \phi, \quad (0 < \phi < 1). \end{cases} \tag{38}$$

Proof. See Appendix F. □

When the supply chain achieves coordination, the ratio of the manufacturer's profit to the platform's one is $\phi/(1 - \phi)$. With this, we call ϕ profit allocation coefficient. $\phi\,(0 < \phi < 1)$ reflects the manufacturer's ability to negotiate with the platform. The larger the ϕ is, the more profit the manufacturer could obtain, the less the platform is, and vice versa. So, ϕ cannot be too large or too small. To make the coordination mechanism effective, we analyze its feasible condition as follows:

(1) In model II, the condition for the platform and the manufacturer to agree on the joint allocation contract is that their profit after coordination should not be less than before, respectively. This condition can be formulated as

$$\begin{cases} \pi_m^c \geq \pi_m^{s*}, \\ \pi_e^c \geq \pi_e^{s*}, \end{cases} \tag{39}$$

which is equivalent to

$$\begin{cases} \pi_m^c = \phi\pi_c{}^* \geq \pi_m^{s*}, \\ \pi_e^c = (1 - \phi)\pi_c{}^* \geq \pi_e^{s*}. \end{cases} \tag{40}$$

So, ϕ has to satisfy

$$\frac{\pi_m^{s*}}{\pi_c{}^*} \leq \phi \leq 1 - \frac{\pi_e^{s*}}{\pi_c{}^*}. \tag{41}$$

(2) In model III, two conditions are needed for the platform and the manufacturer to agree on the joint allocation contract. One is that their profit should not decrease after coordination. Another is the manufacturer's utility should not fall because of coordination. This condition can be formulated as

$$\begin{cases} \pi_m^c \geq \pi_m^{s*}, \\ \pi_e^c \geq \pi_e^{s*}, \\ U_m^c \geq U_m^{sf*}, \end{cases} \tag{42}$$

which is equivalent to

$$\begin{cases} \pi_m^c = \phi\pi_c{}^* \geq \pi_m^{sf*}, \\ \pi_e^c = (1 - \phi)\pi_c^* \geq \pi_e^{sf*}, \\ U_m^c = \pi_m^c - \theta\left(\delta\pi_e^c - \pi_m^c\right) = \phi\pi_c^* - \theta\left[\delta(1 - \phi)\pi_c{}^* - \phi\pi_c{}^*\right] \geq \pi_m^{sf*} - \theta\left(\delta\pi_e^{sf*} - \pi_m^{sf*}\right). \end{cases} \tag{43}$$

So, ϕ has to satisfy

$$\frac{\pi_m^{sf*}}{\pi_c{}^*} + \frac{\theta\delta}{\theta(\delta + 1) + 1} \cdot \frac{\pi_c{}^* - \pi^{sf*}}{\pi_c{}^*} \leq \phi \leq \frac{\pi_c{}^* - \pi_e^{sf*}}{\pi_c{}^*}. \tag{44}$$

Since the difference of the lower bound and the upper one of ϕ is

$$\begin{aligned} &\frac{\pi_c{}^* - \pi_e^{sf*}}{\pi_c{}^*} - \left[\frac{\pi_m^{sf*}}{\pi_c{}^*} + \frac{\theta\delta}{\theta(\delta + 1) + 1} \cdot \frac{\pi_c{}^* - \pi^{sf*}}{\pi_c{}^*}\right] \\ &= \frac{\theta + 1}{\theta(\delta + 1) + 1} \cdot \frac{\pi_c{}^* - \pi^{sf*}}{\pi_c{}^*}, \end{aligned} \tag{45}$$

we have the following proposition.

Proposition 8. *The value range of* ϕ *becomes larger as* θ *increases.*

Proposition 8 shows that the manufacturer's fairness concerns are conducive to the coordination of the supply chain so that both the platform and the manufacturer can have much more choice during coordination.

7. Numerical Examples

In the following, we will put the coordination mechanism into practice by an example and analyze how this mechanism is influenced by other factors.

Suppose $c = 200$, $T = 1000$, $D = 10000$, $d_1 = 20$, $d_2 = 2$, $d_3 = 10$, $k = 5$, and $t = 4$, which will be used in this section.

7.1. Effectiveness Verification of the Coordination Mechanism. First, suppose $\rho = 20$, $\theta = 0.1$, and $\delta = 100$. Refer Table 2 for the decision results before the coordination mechanism is applied.

In model II, the coordination mechanism $(\overline{\rho}, x, y, z)$ satisfies

$$\begin{cases} \overline{\rho} = 560.356(1-\phi), \\ x = \phi, \\ y = 1-\phi, \\ z = \phi, \end{cases} \tag{46}$$

where $0.866 \leq \phi \leq 0.943$.

In model III, the coordination mechanism $(\overline{\rho}, x, y, z)$ satisfies

$$\begin{cases} \overline{\rho} = 560.356(1-\phi), \\ x = \phi, \\ y = 1-\phi, \\ z = \phi, \end{cases} \tag{47}$$

where $0.913 \leq \phi \leq 0.956$.

Then, we use ϕ as the independent variable to compare the difference before and after coordination (see Figure 1).

As shown in Figure 1, in these two cases, the joint allocation contract of cost and profit has coordinated the supply chain system and achieved win-win cooperation.

The profit allocation coefficient, ϕ, is the core parameter of the coordination mechanism $(\overline{\rho}, x, y, z)$. In the following three subsections, we will analyze how the coordination mechanism is influenced by other factors of the supply chain system and illustrate this influence through ϕ.

7.2. Influence of ρ on Coordination Mechanism. For the case without fairness concerns, we further suppose $\rho \in [1, 20]$ and then obtain the relation between the bounds of ϕ and ρ in this coordination mechanism, as demonstrated in Figure 2(a). Similarly, for the case with the manufacturer's fairness concerns, after supposing $\theta = 0.1$ and $\delta = 100$, we can also depict this relation, as demonstrated in Figure 2(b).

Figures 2(a) and 2(b) indicate that both the lower bound and the upper one of ϕ are negatively correlated to the commission, no matter whether the manufacturer has fairness concerns or not. As a result, the more commissions the platform collects, the less the manufacturer's profit share, and the more profit proportion the platform gets, which will be more and more beneficial to the platform. At the same time, it is known from Theorem 5 that the carbon emission reduction cost and platform service cost undertaken by the manufacturer will decrease, while the supply chain cost assumed by the platform will rise. This reflects the value of core enterprises of the supply chain. Besides that, as the commission increases, the span between the upper and lower bounds of ϕ becomes larger and larger, which facilitates coordination. This means that as the commission increases, the platform gets more profit, which gives the manufacturer more choices.

7.3. Influence of θ and ρ on Coordination Mechanism. The feasible condition of our joint allocation contract is much more complicated when the manufacturer has fairness concerns because this mechanism will be influenced by θ and δ, besides ρ. Suppose $\rho = 10$ and $\delta = 100$, then Figure 3(a) describes how the bounds of ϕ varies with $\theta \in [0.05, 0.2]$. Moreover, suppose $\rho = 10$ and $\theta = 0.1$, then the relation between the bounds of ϕ and $\delta \in [100, 200]$ is shown in Figure 3(b).

Figures 3(a) and 3(b) show that, in the case with fairness concerns, both the upper and lower bound of ϕ increase with θ or δ, indicating that the manufacturer's fairness concerns play a role in the coordination. In contrast to this, the span between the upper and lower bound of ϕ is shrinking as θ or δ increases, which means fairness concerns of the manufacturer do not contribute to the design of the coordination contract so that the space for the platform and manufacturer to coordinate is getting smaller. The lower bound of ϕ increases rapidly with θ or δ, so fairness concerns can significantly increase the manufacturer's minimum profit. Still, the platform, as the leader in the low-carbon e-commerce supply chain, will also protect its own profit margin. As far as θ and δ are concerned, the influence of former is more prominent; that is to say, the fairness concerns coefficient of the manufacturer has a bigger effect on the coordination mechanism.

7.4. Influence of T on Coordination Mechanism. In this section, suppose $\rho = 10$, $\theta = 0.1$, and $\delta = 100$.

The relation between ϕ and T with or without fairness concerns is shown in Figures 4(a) and 4(b), respectively. Also, Figures 5(a) and 5(b) demonstrate how the span of ϕ between its upper and lower bound changes with T, respectively.

Figures 4(a) and 4(b) tell us that both the upper and lower bounds of ϕ increase with T, which is not related to fairness concerns of the manufacturer. This indicates that government carbon subsidies have a positive effect in the supply chain system, increasing the manufacturer's profit share. However, Figures 5(a) and 5(b) show that the span of ϕ between its upper and lower bound has a trend of rise-fall, which reflects that more government subsidies are not always the better. In the beginning, government subsidies are conducive to supply chain coordination, but when subsidies exceed a certain limit, it does not help coordinate the supply chain system any more. This is because with the continuous increase in ϕ, the manufacturer occupies the more proportion of government subsidies, which leads to unfair allocation. Therefore, the platform will not cooperate as before. Furthermore, the comparison between Figures 5(a) and 5(b) also indicates clearly the manufacturer's fairness

Table 2: Optimal decisions of different decision modes before coordination.

	Price	Carbon emission level	Service level	Profit		
				Manufacturer	Platform	Supply chain
Model II	760.36	1600.89	2.67	2.31×10^6	1.53×10^5	2.46×10^6
Model III	699.75	994.83	2.67	1.40×10^6	1.18×10^5	1.52×10^6
Model IV	798.60	1746.48	239.44	—	—	2.67×10^6

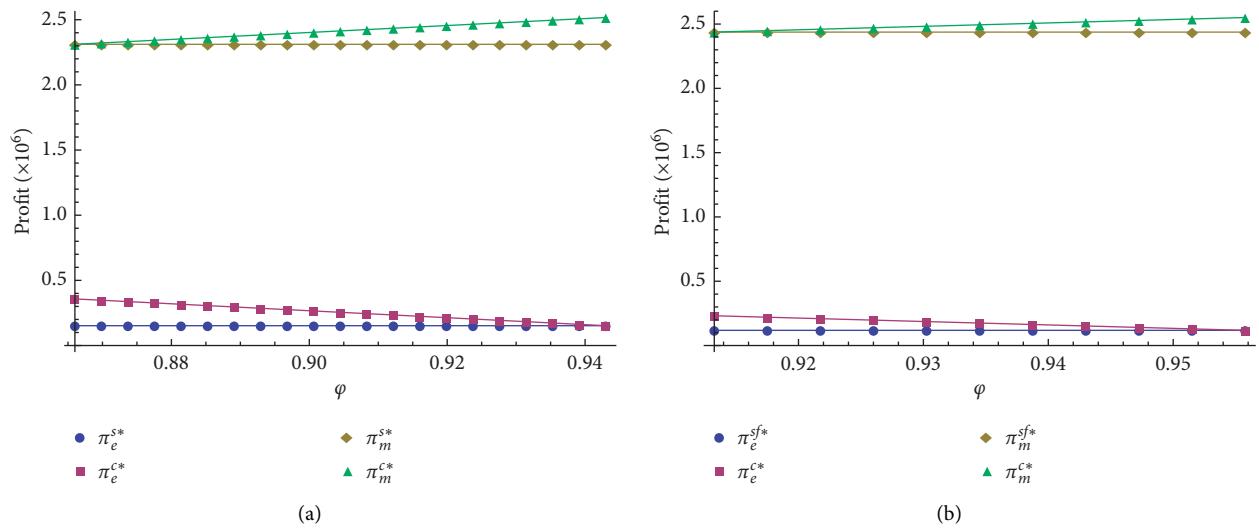

Figure 1: Comparison before and after coordination: (a) without fairness concerns; (b) with fairness concerns.

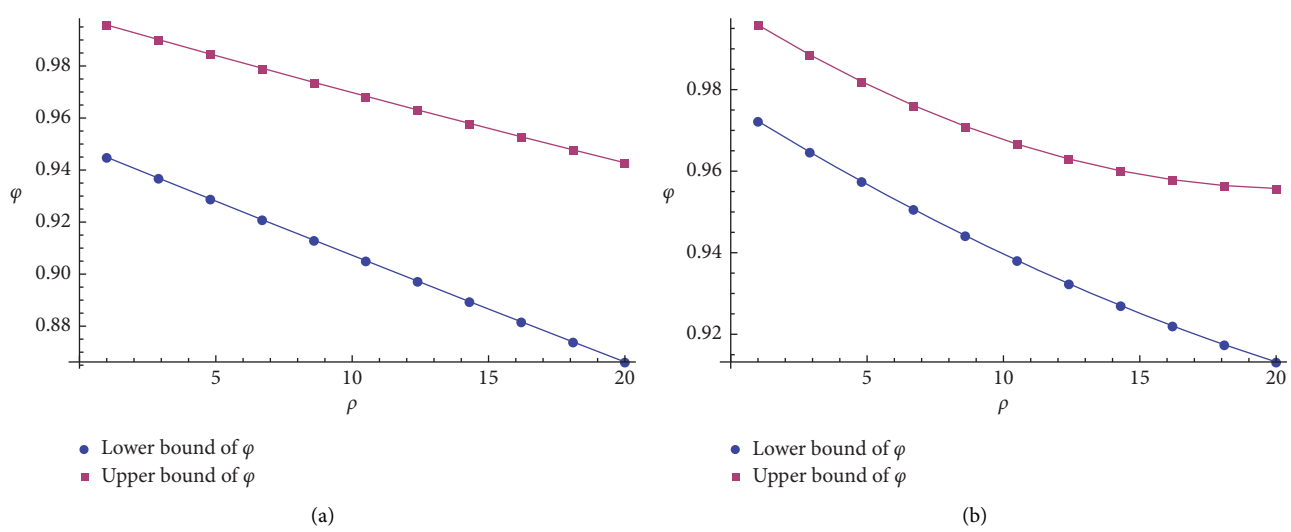

Figure 2: Change in bounds of ϕ with ρ: (a) the case without fairness concerns; (b) the case with fairness concerns.

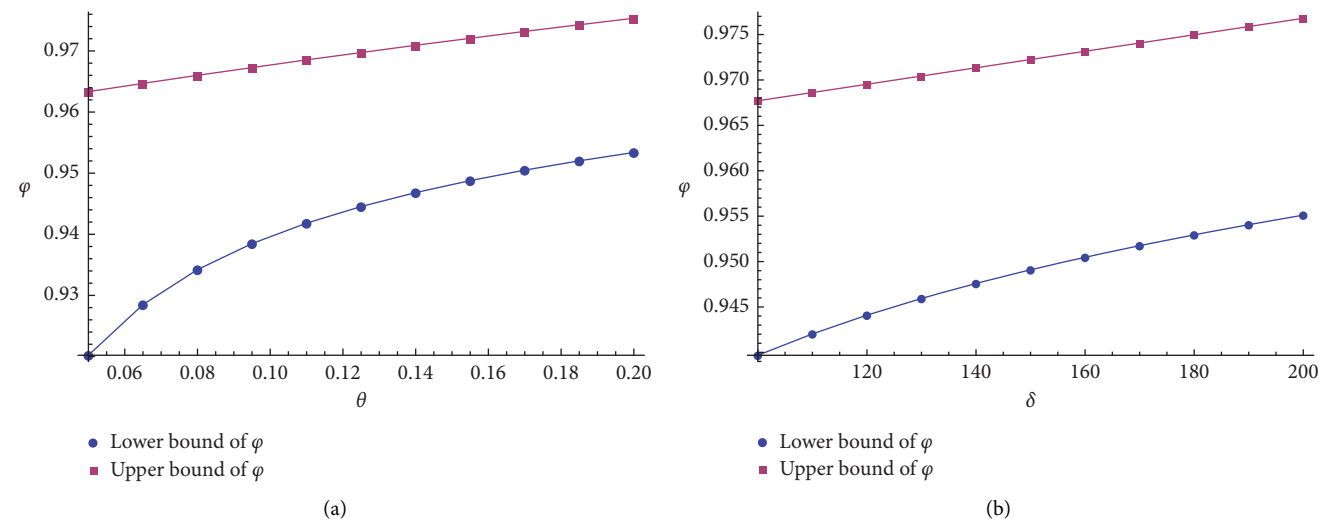

Figure 3: Change in bounds of ϕ in the mode with fairness concerns: (a) change in bounds of ϕ with θ; (b) change in bounds of ϕ with δ.

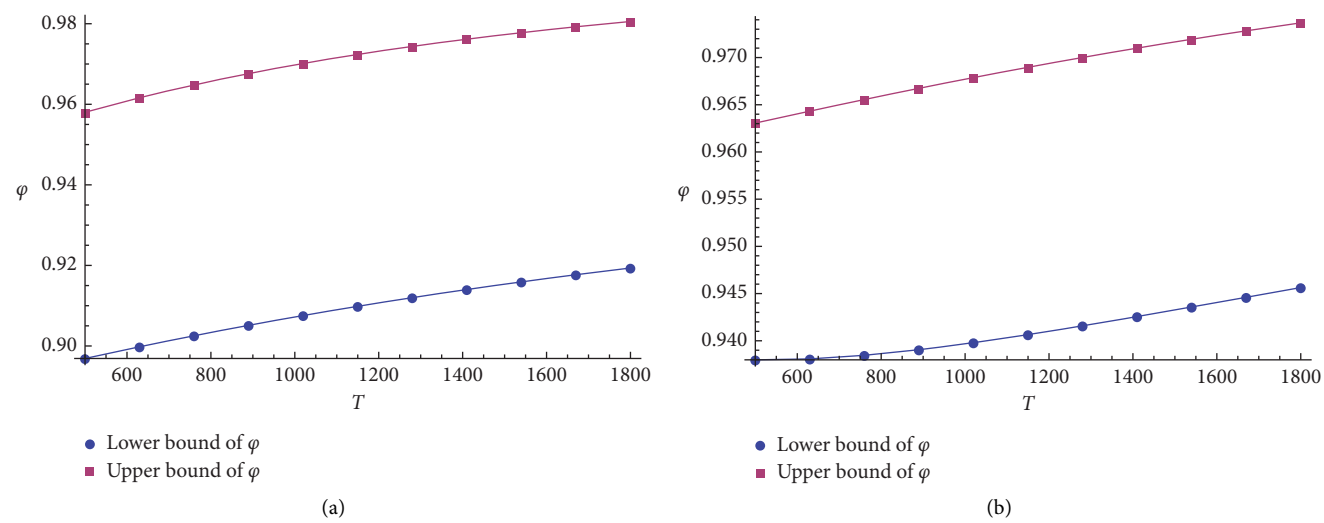

Figure 4: Change in bounds of ϕ with T: (a) case without fairness concerns; (b) case with fairness concerns.

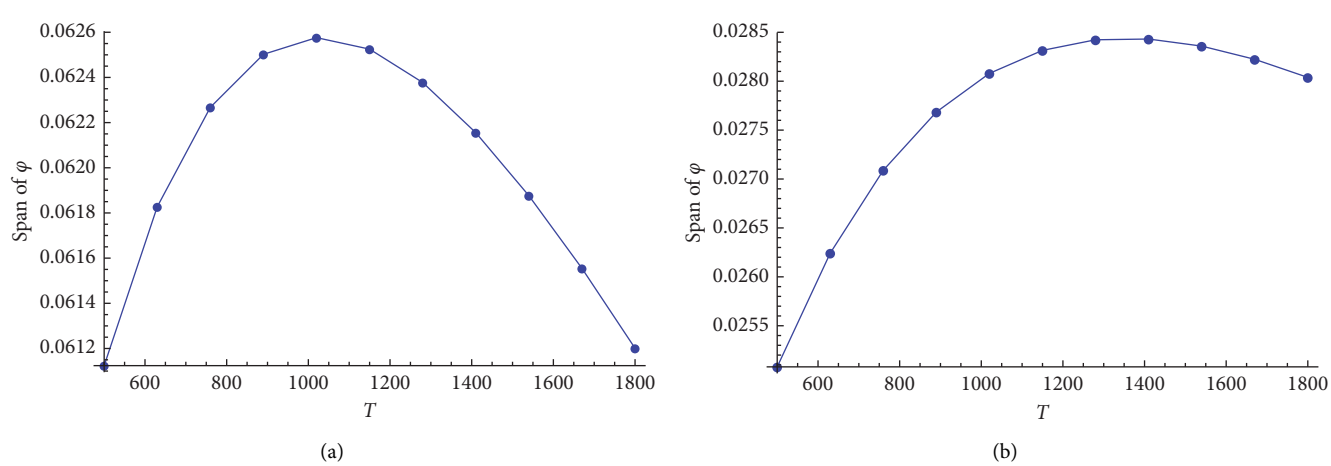

Figure 5: Change in span of ϕ with T: (a) case without fairness concerns; (b) case with fairness concerns.

concerns can push the maximum span of ϕ rightward, which is a decision favorable to itself made by the manufacturer using fairness concerns.

8. Concluding Comments

In this paper, we address the decision and coordination of the e-commerce supply chain system composed of one small- and medium-sized low-carbon product manufacturer and one e-commerce platform. According to whether there are fairness concerns or government subsidies, different decision models are formulated. We reach the optimal decision for each model, design the contract to achieve the coordination of the supply chain system, and use numerical examples to analyze these decision models and the coordination strategy. We also reach the following constructive conclusions.

First, the promotion of low-carbon products will have win-win effects on the environment and economy. On the one hand, we have reached a consensus that carbon emission reduction helps protect the environment. One the other hand, consumers' preference for low-carbon products will be conducive to the operation of the low-carbon e-commerce supply chain. If consumers prefer low-carbon products, the service level, the carbon emission reduction level, the sales price, and the profit of the supply chain will all go up.

Second, government subsidies have positive effects when manufacturers do not have fairness concerns. The government gives some subsidies to low-carbon product manufacturers, which can get benefited obviously. Manufacturers may use the governmental support of carbon subsidies as an attractive feature to attract consumers. As a good result, the product price and carbon emission reduction level can be significantly improved, and this can also lead to the green consumption trend. However, because the platform does not obtain direct subsidies, its service level has not been improved. Yet, the profit improvement of manufacturers from government subsidies can be passed on to the platform.

Third, manufacturers' fairness concerns are an effective way for them to advocate interests. After manufacturers express their fairness concerns, their utility will get better with the increase in the fairness concerns. This means that the platform can receive the fairness concern information released by manufacturers and will consider manufacturers' requirements in the decision process.

Fourth, when manufacturers have fairness concerns, their negative effects will offset the positive effects of government subsidies. Fairness concerns make manufacturers pay too much attention to the profit difference between their own and the platform, which will make them reduce costs and choose to take the low quality-low price shortcut. But, the result of this choice is counterproductive. It significantly affects the benefits of the supply chain, leading to the failure of both manufacturers and the platform. So, as the leader in the supply chain, the platform should properly adjust the commission and share parts of the manufacturer's low-carbon cost. In this way, the manufacturer's fairness concerns can be pacified.

Last, government subsidies are only conducive to supply chain coordination to a specific extent. During the process of coordination, manufacturers give some of the government subsidies to the platform for facilitating centralized decision. However, when government subsidies exceed a specific limit, manufacturers earn too much share. This will lead to the decline of the cooperation from the platform and bring some difficulties to the supply chain coordination.

At present, we only take manufacturers' fairness concerns into account, but in practice, the platform will also have fairness concerns to strive for reasonable profit. Moreover, from the last proposition, we can see that government subsidies are not enough to make the supply chain smoothly coordinated. Therefore, we can consider the full use of carbon tax and other means. Research related to these topics will be further addressed in future studies.

Appendix

A. Proof of Theorem 1

As has been assumed in the model background, in the Stackelberg game, the platform first determines its service level; then, based on the platform's decision, the manufacturer gives the low-carbon product sales price and carbon emission reduction level.

The Hessian matrix of the manufacturer's profit with respect to sales price and carbon emission reduction level is

$$H_m = \begin{bmatrix} \dfrac{\partial^2 \pi_m}{\partial p^2} & \dfrac{\partial^2 \pi_m}{\partial p \partial h} \\ \dfrac{\partial^2 \pi_m}{\partial h \partial p} & \dfrac{\partial^2 \pi_m}{\partial h^2} \end{bmatrix} = \begin{bmatrix} -2d_1 & d_3 \\ d_3 & -t \end{bmatrix}. \tag{A.1}$$

Since $d_3^2 < 2td_1$, H_m is negatively definite.

So, the response function of p and h can be obtained:

$$\begin{aligned} p^{b*} &= \frac{(D + cd_1 + sd_2 + \rho d_1)t - (c+\rho)d_3^2}{2td_1 - d_3^2}, \\ h^{b*} &= \frac{\lambda(D - cd_1 + sd_2 - d_1\rho)}{2td_1 - d_3^2}. \end{aligned} \tag{A.2}$$

After updating equation (5) with these two expressions and solving $d\pi_e/ds = 0$, the authors reach the platform's optimal service level:

$$s^{b*} = d_2 \cdot \frac{\rho}{k} \cdot \frac{d_3^2 - td_1}{2td_1 - d_3^2}. \tag{A.3}$$

After substituting s^{b*} in the expression of p^{b*} and h^{b*}, the authors have the optimal product sales price:

$$p^{b*} = (c+\rho) + d_1 \cdot \frac{\rho}{k} \cdot \left(\frac{td_2}{2td_1 - d_3^2}\right)^2 + t \cdot \frac{k[D - d_1(c+\rho)] - d_2^2\rho}{k\left(2td_1 - d_3^2\right)}. \tag{A.4}$$

And the optimal carbon emission reduction level of the manufacturer

$$h^{b*} = d_1 \cdot \frac{\rho}{k} \cdot \frac{d_3}{t} \cdot \left(\frac{td_2}{2td_1 - d_3^2}\right)^2 + \frac{d_3}{k} \cdot \frac{k[D - d_1(c+\rho)] - d_2^2\rho}{2td_1 - d_3^2}. \tag{A.5}$$

Substituting p^{b*}, h^{b*}, and s^{b*} in equation (5), the authors find the manufacturer's optimal profit is

$$\pi_m^{b*} = t \cdot \frac{[D - d_1(c+\rho)]^2}{2\left(2td_1 - d_3^2\right)} - \frac{td_2^4}{2} \cdot \left(\frac{\rho}{k}\right)^2 \cdot \frac{1}{2td_1 - d_3^2} \cdot \left(\frac{d_3^2 - td_1}{2td_1 - d_3^2}\right)^2. \tag{A.6}$$

The platform's optimal profit is

$$\pi_e^{b*} = t\rho d_1 \cdot \frac{D - d_1(c+\rho)}{2td_1 - d_3^2} + \frac{(\rho d_2)^2}{2k} \cdot \left(\frac{d_3^2 - td_1}{2td_1 - d_3^2}\right)^2. \tag{A.7}$$

The supply chain's optimal profit is

$$\pi^{b*} = t \cdot \frac{[D - d_1(c+\rho)][D - d_1(c-\rho)]}{2\left(2td_1 - d_3^2\right)} + \frac{d_2^2\rho}{2} \cdot \frac{\rho}{k} \cdot \left(\frac{d_3^2 - td_1}{2td_1 - d_3^2}\right)^2 - \frac{td_2^4}{2} \cdot \left(\frac{\rho}{k}\right)^2 \cdot \frac{1}{2td_1 - d_3^2} \cdot \left(\frac{d_3^2 - td_1}{2td_1 - d_3^2}\right)^2. \tag{A.8}$$

B. Proof of Proposition 1

It can be obtained from Theorems 1 and 2 that

$$\begin{aligned}
p^{s*} - p^{b*} &= \frac{Td_3}{2td_1 - d_3^2}, \\
h^{s*} - h^{b*} &= \frac{2Td_1}{2td_1 - d_3^2}, \\
s^{s*} - s^{b*} &= \frac{\rho d_2}{k} \cdot \frac{d_3^2 - td_1}{2td_1 - d_3^2} - \frac{\rho d_2}{k} \cdot \frac{d_3^2 - td_1}{2td_1 - d_3^2} = 0, \\
\pi_m^{s*} - \pi_m^{b*} &= \frac{Td_3[D - d_1(c+\rho)] + T^2 d_1}{2td_1 - d_3^2}, \\
\pi_e^{s*} - \pi_e^{b*} &= \frac{Td_1 d_3}{2td_1 - d_3^2}, \\
\pi^{s*} - \pi^{b*} &= \left(\pi_m^{s*} - \pi_m^{b*}\right) + \left(\pi_e^{s*} - \pi_e^{b*}\right) \\
&= \frac{Td_3[D + d_1 - d_1(c+\rho)] + T^2 d_1}{2td_1 - d_3^2}.
\end{aligned} \tag{B.1}$$

Since $2td_1 > d_3^2$ and D is a large enough number, $p^{b*} < p^{s*}$, $h^{b*} < h^{s*}$, $s^{b*} = s^{s*}$, $\pi_m^{b*} < \pi_m^{s*}$, $\pi_e^{b*} < \pi_e^{s*}$, and $\pi^{b*} < \pi^{s*}$. Proposition 1 holds.

C. Proof of Proposition 2

(1) Because $s^{sf*} = d_2 \cdot (\rho/k) \cdot (d_3^2 - td_1/2td_1 - d_3^2)$, there is no θ in the expression of s^{sf*}. So, s^{sf*} is independent of θ.

(2) Since $(d/d\theta)(\theta/1+\theta) = (1/(1+\theta)^2) > 0$, $(\theta/1+\theta)$ increases with θ.

Thus,

$$p^{sf*} = (c+\rho) + \left(d_3^2 - td_1\right) \cdot \frac{\rho t}{k} \cdot \left(\frac{d_2}{2td_1 - d_3^2}\right)^2 + \frac{[D - d_1(c+\rho)]t + d_3 T}{2td_1 - d_3^2} - \frac{\theta}{1+\theta} \cdot \frac{d_3^2 - td_1}{2td_1 - d_3^2} \cdot \delta\rho, \tag{C.1}$$

decreases with θ.

(3) As $(\theta/1+\theta)$increases with θ,

$$h^{sf*} = d_3 \cdot \frac{\rho}{k} \cdot \left(d_3^2 - td_1\right) \cdot \left(\frac{d_2}{2td_1 - d_3^2}\right)^2 + \frac{d_3[D - d_1(c+\rho)] + 2Td_1}{2td_1 - d_3^2} - \frac{d_1 d_3 \delta\rho}{2td_1 - d_3^2} \cdot \frac{\theta}{1+\theta}, \tag{C.2}$$

decreases with θ.

(4) Let $f(\theta) = (\theta/1+\theta)$, then π_m^{sf*} can be expressed as

$$\pi_m^{sf*} = \frac{td_1^2\rho^2\delta^2}{2\left(2td_1 - d_3^2\right)} f^2 + \frac{\delta\rho^2 d_2^2}{k} \cdot \left(\frac{d_3^2 - td_1}{2td_1 - d_3^2}\right)^2 f + A, \tag{C.3}$$

where A represents the items independent of θ.

So, π_m^{sf*} is a downward parabola with f. If $\theta > 0$, f will be on the right of the symmetry axis of this parabola,

which is the falling part. Therefore, π_m^{sf*} decreases with f. Furthermore, π_m^{sf*} decreases with θ.

(5) As $(\theta/1+\theta)$ increases with θ,

$$\pi_e^{sf*} = \frac{\rho^2 d_2^2}{2k}\cdot\left(\frac{d_3^2 - td_1}{2td_1 - d_3^{22}}\right)^2 + \rho d_1 \frac{t\left[D - d_1(c+\rho)\right] + Td_3}{2td_1 - d_3^2} - \frac{t(1+\delta)(d_1\rho)^2}{2td_1 - d_3^2}\cdot\frac{\theta}{1+\theta}, \tag{C.4}$$

decreases with θ.

(6) Since both π_m^{sf*} and π_e^{sf*} decrease with θ, so does π^{sf*}

D. Proof of Proposition 3

(1) Since $s^{s*} = s^{sf*}$ and s^{c*} is the platform's optimal service level in the centralized decision model, $s^{c*} > s^{s*} = s^{sf*}$:

$$s^{s*} = s^{sf*} = d_2\cdot\frac{\rho}{k}\cdot\frac{d_3^2 - td_1}{2td_1 - d_3^2} = \frac{d_2}{k}\cdot\frac{d_3^2 - td_1}{2td_1 - d_3^2}\cdot\rho \tag{D.1}$$

(2) Thus, s^{s*} and s^{sf*} are direct proportional to ρ. That is to say, both s^{s*} and s^{sf*} increase with ρ.

(3) In the expression of $s^{c*} = d_2\cdot(t(D - cd_1) + Td_3)/(2ktd_1 - (td_2^2 + kd_3^2))$, $td_2(D - cd_1) + Td_2d_3$ increases with d_3 while $2ktd_1 - (td_2^2 + kd_3^2)$ decreases with d_3. Thus, s^{c*} increases with d_3.

Also, $(\mathrm{d}s^{s*}/\mathrm{d}d_3) = (\mathrm{d}s^{sf*}/\mathrm{d}d_3) = d_2\cdot\rho k\cdot((8d_1d_3)/(d_3^2 - 8d_1)^2) > 0$. Therefore, s^{s*} and s^{sf*} increase with d_3. □

E. Proof of Proposition 7

Since

$$\begin{aligned}
U_m^{sf*} &= \frac{(1+\theta)Td_1 + \left[(1+\theta)(D - cd_1 - \rho d_1) - \rho\delta\theta d_1\right]d_3}{2td_1 - d_3^2}\cdot T + \frac{\left[(1+\theta)(D - cd_1 - \rho d_1) - \rho\delta\theta d_1\right]^2}{2(1+\theta)\left(2td_1 - d_3^2\right)}\cdot t + \frac{\delta\theta(\rho d_2)^2}{2k} \\
&\quad\cdot\left(\frac{d_3^2 - td_1}{2td_1 - d_3^2}\right)^2 - \frac{(1+\theta)t\rho^2 d_2^4}{2k^2\left(2td_1 - d_3^2\right)}\cdot\left(\frac{d_3^2 - td_1}{2td_1 - d_3^2}\right)^2, \\
\frac{dU_m^{sf*}}{d\theta} &= \frac{Td_1 + d_3\left[(D - cd_1 - \rho d_1) - d_1\rho\delta\right]}{2td_1 - d_3^2}\cdot T \\
&\quad + \frac{\left[D(1+\theta) - d_1(1+\theta)(\rho + c) - d_1\rho\delta\theta\right]\cdot\left[D(1+\theta) - d_1(1+\theta)(\rho + c) - d_1(\rho\delta\theta + 2\delta)\right]}{2(1+\theta)^2\left(2td_1 - d_3^2\right)}\cdot t + \frac{\delta}{2k}\cdot(\rho d_2)^2 \\
&\quad\cdot\left(\frac{d_3^2 - td_1}{2td_1 - d_3^2}\right)^2 - \frac{t\rho^2 d_2^4}{2k^2\left(2td_1 - d_3^2\right)}\cdot\left(\frac{d_3^2 - td_1}{2td_1 - d_3^2}\right)^2 \\
&= T\cdot\frac{Td_1 + d_3\left[(D - cd_1 - \rho d_1) - d_1\rho\delta\right]}{2td_1 - d_3^2} \\
&\quad + t\cdot\frac{\left[D(1+\theta) - d_1(1+\theta)(\rho + c) - d_1\rho\delta\theta\right]\cdot\left[D(1+\theta) - d_1(1+\theta)(\rho + c) - d_1(\rho\delta\theta + 2\rho\delta)\right]}{2(1+\theta)^2\left(2td_1 - d_3^2\right)} \\
&\quad + \frac{(\rho d_2)^2}{2k}\cdot\frac{k\delta\left(2td_1 - d_3^2\right) - td_2^2}{k\left(2td_1 - d_3^2\right)}\cdot\left(\frac{d_3^2 - td_1}{2td_1 - d_3^2}\right)^2 > T\cdot\frac{Td_1 + d_3\left[(D - cd_1 - \rho d_1) - d_1\rho\delta\right]}{2td_1 - d_3^2} \\
&\quad + t\cdot\frac{\left[D(1+\theta) - d_1(1+\theta)(\rho + c) - d_1\rho\delta\theta\right]\cdot\left[D(1+\theta) - d_1(1+\theta)(\rho + c) - d_1(\rho\delta\theta + 2\rho\delta)\right]}{2(1+\theta)^2\left(2td_1 - d_3^2\right)} \\
&\quad + \frac{(\rho d_2)^2}{2k}\cdot\frac{2ktd_1 - \left(kd_3^2 - td_2^2\right)}{k\left(2td_1 - d_3^2\right)}\cdot\left(\frac{d_3^2 - td_1}{2td_1 - d_3^2}\right)^2 > 0.
\end{aligned} \tag{E.1}$$

Thus, U_m^{sf*} increases as θ increases. □

F. Proof of Theorem 5

In the joint allocation contract of cost and profit, if $(\overline{\rho}, x, y, z)$ satisfies

$$\begin{cases} \overline{\rho} = (1-\phi)(p-c), \\ x = \phi, \\ y = 1-\phi, \\ z = \phi, \quad (0<\phi<1), \end{cases} \tag{F.1}$$

the manufacturer's profit is expressed as

$$\begin{aligned} \pi_m &= \phi(pq-cq) - \phi\frac{th^2}{2} - \phi\frac{ks^2}{2} + \phi Th \\ &= \phi\left[(p-c)q - \frac{th^2}{2}t - \frac{ks^2}{2} + Th\right] = \phi\pi. \end{aligned} \tag{F.2}$$

And the platform's profit is

$$\begin{aligned} \pi_e &= (1-\phi)(pq-cq) - (1-\phi)\frac{th^2}{2} - (1-\phi)\frac{ks^2}{2} \\ &+ (1-\phi)Th = (1-\phi)\left[(p-c)q - \frac{th^2}{2} - \frac{ks^2}{2} + Th\right] = (1-\phi)\pi. \end{aligned} \tag{F.3}$$

Obviously, the profit of the manufacturer and platform is the affine function of that of the supply chain. Therefore, after this contract is applied, the supply chain system must be coordinated. □

Data Availability

The data used to support the findings of this study are included within the article.

Conflicts of Interest

The authors declare that there are no conflicts of interest regarding the publication of this paper.

Acknowledgments

This paper was supported financially by the National Natural Science Foundation of China (71971129 and 71501111), Science and Technology Support Program for Youth Innovation of Colleges and Universities in Shandong Province (2019RWG017), and Philosophy and Social Science Project of Shandong Province (19BJCJ12).

References

[1] X. Zhu, M. Ren, W. Chu, and R. Chiong, "Remanufacturing subsidy or carbon regulation? An alternative toward sustainable production," *Journal of Cleaner Production*, vol. 239, p. 15, Article ID 117988, 2019.

[2] J. Li, W. Du, F. Yang, and G. Hua, "The carbon subsidy analysis in remanufacturing closed-Loop supply chain," *Sustainability*, vol. 6, no. 6, pp. 3861–3877, 2014.

[3] F. Qin, F. Mai, M. J. Fry, and A. S. Raturi, "Supply-chain performance anomalies: fairness concerns under private cost information," *European Journal of Operational Research*, vol. 252, no. 1, pp. 170–182, 2016.

[4] T. Li, J. Xie, X. Zhao, and J. Tang, "On supplier encroachment with retailer's fairness concerns," *Computers & Industrial Engineering*, vol. 98, pp. 499–512, 2016.

[5] P. Jokela and A. Söderman, "Re-examining the link between fairness and commitment in buyer-supplier relationships," *Journal of Purchasing and Supply Management*, vol. 23, no. 4, pp. 268–279, 2017.

[6] J. Xie, L. Liang, L. Liu, and P. Ieromonachou, "Coordination contracts of dual-channel with cooperation advertising in closed-loop supply chains," *International Journal of Production Economics*, vol. 183, pp. 528–538, 2017.

[7] Q. Lu and N. Liu, "Pricing games of mixed conventional and e-commerce distribution channels," *Computers & Industrial Engineering*, vol. 64, no. 1, pp. 122–132, 2013.

[8] Q. Lu and N. Liu, "Effects of e-commerce channel entry in a two-echelon supply chain: a comparative analysis of single- and dual-channel distribution systems," *International Journal of Production Economics*, vol. 165, pp. 100–111, 2015.

[9] Z. Liu, K. W. Li, B.-Y. Li, J. Huang, and J. Tang, "Impact of product-design strategies on the operations of a closed-loop supply chain," *Transportation Research Part E: Logistics and Transportation Review*, vol. 124, pp. 75–91, 2019.

[10] J. Tang, B. Y. Li, K. W. Li, Z. Liu, and J. Huang, "Pricing and warranty decisions in a two-period closed-loop supply chain," *International Journal of Production Research*, vol. 58, no. 6, pp. 1688–1704, 2020.

[11] Y. Su and W. Sun, "Analyzing a closed-loop supply chain considering environmental pollution using the NSGA-II," *IEEE Transactions on Fuzzy Systems*, vol. 27, no. 5, pp. 1066–1074, 2019.

[12] S.-M. Hosseini-Motlagh, S. Ebrahimi, and A. Jokar, "Sustainable supply chain coordination under competition and green effort scheme," *Journal of the Operational Research Society*, vol. 2019, p. 16, Article ID 1671152, 2019.

[13] J. Jian, Y. Guo, L. Jiang, Y. An, and J. Su, "A multi-objective optimization model for green supply chain considering environmental benefits," *Sustainability*, vol. 11, no. 21, p. 5911, 2019.

[14] S.-M. Hosseini-Motlagh, M. Johari, and R. Zirakpourdehkordi, "Grain production management to reduce global warming potential under financial constraints and time value of money using evolutionary game theory," *International Journal of Production Research*, vol. 2020, Article ID 1773562, 22 pages, 2020.

[15] S.-M. Hosseini-Motlagh, M. Nouri-Harzvili, T.-M. Choi, and S. Ebrahimi, "Reverse supply chain systems optimization with dual channel and demand disruptions: sustainability, CSR investment and pricing coordination," *Information Sciences*, vol. 503, pp. 606–634, 2019.

[16] K. Lamba, S. P. Singh, and N. Mishra, "Integrated decisions for supplier selection and lot-sizing considering different carbon emission regulations in big data environment," *Computers & Industrial Engineering*, vol. 128, pp. 1052–1062, 2019.

[17] H. Peng and T. Pang, "Optimal strategies for a three-level contract-farming supply chain with subsidy," *International Journal of Production Economics*, vol. 216, pp. 274–286, 2019.

[18] Z. Li, J. Zhang, Q. Meng, W. Zheng, and J. Du, "Influence of government subsidy on remanufacturing decision under different market models," *Mathematical Problems in Engineering*, vol. 2019, Article ID 9460315, 16 pages, 2019.

[19] J. Li, W. Du, F. Yang, and G. Hua, "The carbon subsidy analysis in remanufacturing closed-loop supply chain," *Sustainability*, vol. 6, no. 6, pp. 3861–3877, 2014.

[20] H. Liu, M. Lei, H. Deng, G. Keong Leong, and T. Huang, "A dual channel, quality-based price competition model for the WEEE recycling market with government subsidy," *Omega*, vol. 59, pp. 290–302, 2016.

[21] L. Deng, W. Li, and Z. Liu, "Different subsidies' impact on equilibrium decision-making of closed-loop supply chain," *Journal of Industrial Engineering and Management*, vol. 7, no. 5, pp. 1061–1075, 2014.

[22] D. Kahneman, J. L. Knetsch, and R. H. Thaler, "Fairness and the assumptions of economics," *Journal of Business*, vol. 59, no. 4, pp. 285–300, 1986.

[23] X. Qin, Q. Su, S. H. Huang, U. J. Wiersma, and M. Liu, "Service quality coordination contracts for online shopping service supply chain with competing service providers: integrating fairness and individual rationality," *Operational Research*, vol. 19, no. 1, pp. 269–296, 2019.

[24] L. Dai, X. Wang, X. Liu, and L. Wei, "Pricing strategies in dual-channel supply chain with a fair caring retailer," *Complexity*, vol. 2019, p. 23, Article ID 1484372, 2019.

[25] Z. Guan, T. Ye, and R. Yin, "Channel coordination under Nash bargaining fairness concerns in differential games of goodwill accumulation," *European Journal of Operational Research*, vol. 285, no. 3, pp. 916–930, 2020.

[26] X.-X. Zheng, Z. Liu, K. W. Li, J. Huang, and J. Chen, "Cooperative game approaches to coordinating a three-echelon closed-loop supply chain with fairness concerns," *International Journal of Production Economics*, vol. 212, pp. 92–110, 2019.

[27] Q. Li and B. Li, "Dual-channel supply chain equilibrium problems regarding retail services and fairness concerns," *Applied Mathematical Modelling*, vol. 40, no. 15-16, pp. 7349–7367, 2016.

[28] T. H. Cui, J. S. Raju, and Z. J. Zhang, "Fairness and channel coordination," *Management Science*, vol. 53, no. 8, pp. 1303–1314, 2007.

[29] D. Zhao, X. Zhang, T. Ren, and H. Fu, "Optimal pricing strategies in a product and service supply chain with extended warranty service competition considering retailer fairness concern," *Mathematical Problems in Engineering*, vol. 2019, p. 15, Article ID 8657463, 2019.

[30] Q. Li, X. Chen, and Y. Huang, "The stability and complexity analysis of a low-carbon supply chain considering fairness concern behavior and sales service," *International Journal of Environmental Research and Public Health*, vol. 16, no. 15, p. 2711, 2019.

[31] Q. Li, Y. Zhang, and Y. Huang, "The complexity analysis in dual-channel supply chain based on fairness concern and different business objectives," *Complexity*, vol. 2018, p. 13, Article ID 4752765, 2018.

[32] Q. Han and Y. Wang, ""Decision and coordination in a low-carbon e-supply chain considering the manufacturer's carbon emission reduction behavior," *Sustainability*, vol. 10, no. 5, pp. 1–23, 2018.

[33] S.-M. Hosseini-Motlagh, M. Nouri-Harzvili, M. Johari, and B. R. Sarker, "Coordinating economic incentives, customer service and pricing decisions in a competitive closed-loop supply chain," *Journal of Cleaner Production*, vol. 255, p. 41, Article ID 120241, 2020.

[34] M. Johari and S.-M. Hosseini-Motlagh, "Coordination of social welfare, collecting, recycling and pricing decisions in a competitive sustainable closed-loop supply chain: a case for lead-acid battery," *Annals of Operations Research*, vol. 2019, Article ID 3292-1, 36 pages, 2019.

[35] M. Johari, S.-M. Hosseini-Motlagh, and M. Nematollahi, "Simultaneous coordination of review period and order-up-to-level in a manufacturer-retailer chain," *Journal of Industrial and Systems Engineering*, vol. 10, pp. 1–17, 2017.

[36] S.-M. Hosseini-Motlagh, M. R. Nematollahi, M. Johari, and T.-M. Choi, "Reverse supply chain systems coordination across multiple links with duopolistic third party collectors," *IEEE Transactions on Systems, Man, and Cybernetics: Systems*, vol. 2019, p. 12, Article ID 2911644, 2019.

[37] S.-M. Hosseini-Motlagh, S. Ebrahimi, and R. Zirakpourdehkordi, "Coordination of dual-function acquisition price and corporate social responsibility in a sustainable closed-loop supply chain," *Journal of Cleaner Production*, vol. 251, p. 28, Article ID 119629, 2020.

[38] S.-M. Hosseini-Motlagh, M. Nematollahi, M. Johari, and B. R. Sarker, "A collaborative model for coordination of monopolistic manufacturer's promotional efforts and competing duopolistic retailers' trade credits," *International Journal of Production Economics*, vol. 204, pp. 108–122, 2018.

[39] M. Johari, S.-M. Hosseini-Motlagh, M. Nematollahi, M. Goh, and J. Ignatius, "Bi-level credit period coordination for periodic review inventory system with price-credit dependent demand under time value of money," *Transportation Research Part E: Logistics and Transportation Review*, vol. 114, pp. 270–291, 2018.

[40] J. Su, C. Li, Q. Zeng, J. Yang, and J. Zhang, "A green closed-loop supply chain coordination mechanism based on third-party recycling," *Sustainability*, vol. 11, no. 19, p. 5335, 2019.

[41] J. Heydari, K. Govindan, and A. Jafari, "Reverse and closed loop supply chain coordination by considering government role," *Transportation Research Part D: Transport and Environment*, vol. 52, pp. 379–398, 2017.

[42] H. Peng, T. Pang, and J. Cong, "Coordination contracts for a supply chain with yield uncertainty and low-carbon preference," *Journal of Cleaner Production*, vol. 205, pp. 291–302, 2018.

[43] T. Nie and S. Du, "Dual-fairness supply chain with quantity discount contracts," *European Journal of Operational Research*, vol. 258, no. 2, pp. 491–500, 2017.

[44] X. Liu, X. Wang, L. Dai, and Y. Pan, "Research on supply chain performance based on retailers' fairness concerns: wholesale prices versus cost sharing of efforts," *PLoS One*, vol. 13, no. 10, Article ID e0204482, 2018.

[45] J. Jian, Y. Zhang, L. Jiang, and J. Su, "Coordination of supply chains with competing manufacturers considering fairness concerns," *Complexity*, vol. 2020, Article ID 4372603, 15 pages, 2020.

[46] O. Caliskan-Demirag, Y. Chen, and J. Li, "Channel coordination under fairness concerns and nonlinear demand," *European Journal of Operational Research*, vol. 207, no. 3, pp. 1321–1326, 2010.

[47] X.-X. Zheng, D.-F. Li, Z. Liu, F. Jia, and J.-B. Sheu, "Coordinating a closed-loop supply chain with fairness concerns through variable-weighted Shapley values," *Transportation Research Part E: Logistics and Transportation Review*, vol. 126, pp. 227–253, 2019.

[48] Y. Wang, Z. Yu, and L. Shen, "Study on the decision-making and coordination of an e-commerce supply chain with manufacturer fairness concerns," *International Journal of Production Research*, vol. 57, no. 9, pp. 2788–2808, 2019.
[49] A. Nair and R. Narasimhan, "Dynamics of competing with quality- and advertising-based goodwill," *European Journal of Operational Research*, vol. 175, no. 1, pp. 462–474, 2006.
[50] D. Yao and J. Liu, "Competitive pricing of mixed retail and e-tail distribution channels," *Omega*, vol. 33, no. 3, pp. 235–247, 2005.
[51] B. Shen, R. Qian, and T.-M. Choi, "Selling luxury fashion online with social influences considerations: demand changes and supply chain coordination," *International Journal of Production Economics*, vol. 185, pp. 89–99, 2017.
[52] E. Fehr and K. M. Schmidt, "A theory of fairness, competition, and cooperation," *The Quarterly Journal of Economics*, vol. 114, no. 3, pp. 817–868, 1999.
[53] E. Katok, T. Olsen, and V. Pavlov, "Wholesale pricing under mild and privately known concerns for fairness," *Production and Operations Management*, vol. 23, no. 2, pp. 285–302, 2014.

Hindawi
Complexity
Volume 2020, Article ID 2960503, 9 pages
https://doi.org/10.1155/2020/2960503

Research Article

Global Stability for a Discrete Space-Time Lotka–Volterra System with Feedback Control

Li Xu [1,2] **and Ruiwen Han** [1]

[1] *School of Science, Tianjin University of Commerce, Tianjin 300134, China*
[2] *School of Mathematics, Tianjin University, Tianjin 300072, China*

Correspondence should be addressed to Li Xu; beifang_xl@163.com

Received 26 May 2020; Revised 11 July 2020; Accepted 27 July 2020; Published 19 August 2020

Academic Editor: Juan Carlos Cortés

In this paper, a discrete space-time Lotka–Volterra model with the periodic boundary conditions and feedback control is proposed. By means of a discrete version of comparison theorem, the boundedness of the nonnegative solution of the system is proved. By the combination of the Volterra-type and quadratic Lyapunov functions, the global asymptomatic stability of the unique positive equilibrium is investigated. Finally, numerical simulations are presented to verify the effectiveness of the main results.

1. Introduction

It is well known that the ecosystem in the real world is often distributed by unpredictable forces or interference factors, such as natural disturbances (floods, fires, disease outbreaks, and droughts), human-caused interference factors (oil spills), and slowly changing long-term stresses (nutrient enrichment), which may result into changes in the biological parameters such as survival rates [1–3]. The presence of the unpredictable forces or interference factors in an ecological system raises the following essential and basic question from the practical interest in ecology: "Can the ecosystem withstand those unpredictable forces which persist for a finite period of time?" The question has motivated the development of some control mechanisms for managing populations to ensure that the interacting species can coexist, such as impulsive control, optimal vibration control, intermittent control, and feedback control. [4–6]. As a basic mechanism by which one can recover stability and move the trajectory towards the desired orbit, the introduction of a feedback control variable is one method that can achieve the objective.

For population dynamical systems with feedback controls, an important and interesting subject is to study the effects of feedback controls to the persistence, permanence, and extinction of species, the stability, and dynamical complexity of systems [7]. There are lots of important and interesting results on stability research for continuous time population dynamical models [8–16]. A necessary condition for sustained concentration oscillations resulting from small perturbations of the steady state is derived from a closure rule using a variation of the direct Lyapunov method on a biochemical feedback system of the Yates-Pardee type [8]. The authors study the dynamical behavior of a continuous reaction-diffusion waterborne pathogen model, such as the existence of positive solutions and its boundedness, the existence of equilibria, local stability, uniform persistence, and global stability [9]. The output feedback stabilization of stochastic feedforward systems with unknown control coefficients and unknown output function using the time-varying technique and backstepping method is achieved [16].

The discrete-time models governed by difference equation are more realistic than the continuous ones when the populations have nonoverlapping generations or the population statistics are compiled from given time intervals and not continuously. Moreover, discrete-time models can also provide efficient computational models of continuous

models for numerical simulations. Therefore, it is reasonable to study discrete-time models governed by difference equations, and there has been some work done on the study of the persistence, permanence, and global stability for various discrete-time nonlinear population systems with feedback when the effect of spatial factors is not considered [5, 7, 17–19]. A weak sufficient condition for the permanence of a nonautonomous discrete single-species system with delays and feedback control is given in the article [7]. A two-species competitive system with feedback controls is considered, in which the global attractivity of a positive periodic solution is obtained, and the existence and uniqueness of the uniformly asymptotically stable almost periodic solution are shown [17, 18]. In reference [19], some sufficient conditions on the permanence and the global stability of the system of a n-species Lotka–Volterra discrete system with delays and feedback control by constructing the suitable discrete type Lyapunov functionals are obtained.

It is a fact that spatial heterogeneity and dispersal play an important role in the dynamics of populations, which has been the subject of much research, both theoretical and experimental, such as the role of dispersal in the maintenance of patchiness or spatial population variation. If the spatial factors are added, more dynamics will occur. The diffusion-driven instability may emerge if the steady-state solution is stable to small spatial perturbations in absence of diffusion, but unstable when diffusion is present [20]. If the diffusion-driven instability should be avoided in some situations, and one may wish recovery stability towards the desired orbit, but the system parameters are not easy to adjust, then some other ways should be adopted to achieve the stabilization aim [21]. There also may exist a situation where the equilibrium of the dynamical model is not the desirable one (or affordable) and a smaller value of the equilibrium is required; then, altering the model structure so as to make the population stabilize at a lower value is necessary [22]. Feedback control will be an effective one and can alter the positions of positive equilibrium or obtain its stability. To the best of our knowledge, there is few work that has been devoted to global properties of the discrete space-time models with feedback control. The robustly asymptotic stability and disturbance attenuation level of the filtering error system for a two-dimensional Roesser models with polytopic uncertainties are discussed [23]. A two-dimensional Fornasini–Marchesini local state-space system is also considered in the article [24]. However, the diffusion terms (discrete Laplace operator) are not directly introduced into the model. There is some work on global stability of discrete diffusion systems [25, 26], in which the positivity, boundedness, and global stability of the equilibria are established, and the discretized models are derived from the corresponding continuous model by nonstandard finite difference, but the Laplace operator has been dealt with. It is a fact that diffusion will produce much richer dynamical behaviors and complexity; how to analyze stability of the discrete diffusion system with feedback control by means of suitable Lyapunov functions is an important problem to solve.

Motivated by above discussions, the main purpose of this paper is to study the global asymptomatic stability of an one-dimensional spatially discrete reaction diffusion Lotka–Volterra model with the periodic boundary conditions and feedback control. So the organization of this paper is as follows. In the Section 2, we formulate the discrete space-time Lotka–Volterra model with feedback control and present some assumptions and preparations which will be essential to our main proofs, and the nonnegativity and boundedness of the solution of the system are proved by means of comparison theorem. Then, global asymptotic stability of the unique positive equilibrium is proved by constructing a combination of the nonnegative Volterra-type and quadratic Lyapunov functions in Section 3. In Section 4, numerical simulations are presented to illustrate the feasibility of our main results. In the last section, brief discussions and conclusions are given.

2. Model and Preliminaries

It is well known that a Lotka–Volterra system can be described in the form of

$$\begin{aligned} x'(t) &= x(t)\left(r_1 - a_{11}x(t) - a_{12}y(t)\right), \\ y'(t) &= y(t)\left(r_2 + a_{21}x(t) - a_{22}y(t)\right), \end{aligned} \tag{1}$$

which is called the predator-prey model. $x(t)$ is the density of prey species, $y(t)$ is the density of predator species, the coefficients a_{11} and a_{22} represent the intraspecific interactions, a_{12} and a_{21} represent the interspecific interactions, and r_1 and r_2 are the intrinsic growth rates of the respective species.

A corresponding discrete model for the system (1) can be derived from [27]:

$$\begin{cases} x_{n+1} = x_n \exp\left(r_1 - a_{11}x_n - a_{12}y_n\right), \\ y_{n+1} = y_n \exp\left(r_2 + a_{21}x_n - a_{22}y_n\right), \end{cases} \tag{2}$$

where $a_{ij}\,(i, j = 1, 2) > 0$. Let $X_n = a_{11}x_n$ and $Y_n = a_{22}y_n$; we have

$$\begin{cases} X_{n+1} = X_n \exp\left(r_1 - X_n - \dfrac{a_{12}}{a_{22}}Y_n\right), \\ Y_{n+1} = Y_n \exp\left(r_2 + \dfrac{a_{21}}{a_{11}}X_n - Y_n\right), \end{cases} \tag{3}$$

$$\text{or} \begin{cases} x_{n+1} = x_n \exp\left(r_1 - x_n - a_{12}y_n\right), \\ y_{n+1} = y_n \exp\left(r_2 + a_{21}x_n - y_n\right). \end{cases}$$

It is believed that the diffusion of individuals can play an important role in determining collective behavior of the population. Space factors can be taken into account in all fundamental aspects of ecological organization, and we can get a one-dimensional discrete reaction-diffusion model as follows:

$$\begin{cases} x_i^{n+1} = x_i^n \exp\left(r_1 - x_i^n - a_{12} y_i^n\right) + D_1 \nabla^2 x_i^n, \\ y_i^{n+1} = y_i^n \exp\left(r_2 + a_{21} x_i^n - y_i^n\right) + D_2 \nabla^2 y_i^n, \end{cases} \tag{4}$$

where $i \in \{1, 2, \ldots, m\} = [1, m]$ and $m, n \in Z^+$ are positive integers and D_1 and D_2 are diffusion parameters.

$$\begin{aligned} \nabla^2 x_i^n &= x_{i+1}^n - 2x_i^n + x_{i-1}^n, \\ \nabla^2 y_i^n &= y_{i+1}^n - 2y_i^n + y_{i-1}^n. \end{aligned} \tag{5}$$

This also indicates the coupling or diffusion from the units or individuals to the left and the right, respectively. The following periodic boundary conditions are considered:

$$\begin{cases} x_0^n = x_m^n,\ x_1^n = x_{m+1}^n, \\ y_0^n = y_m^n,\ y_1^n = y_{m+1}^n. \end{cases} \tag{6}$$

Systems (4)–(6) can exhibit rich dynamic behaviors, and diffusion-driven instability may emerge [28]. As discussed in the introduction part, unpredictable forces or interference factors can be introduced into the forms of feedback control variables, which can contribute significantly to the biological systems by affecting their dynamics and stability. Moreover, structurally modifying existing systems by incorporating variables for defining feedback controls is appropriate for considering the unpredictable forces or interference factors in an ecosystem. So, in the present study, we consider the following one-dimensional discrete space-time Lotka–Volterra model with periodic boundary conditions and feedback control:

$$\begin{cases} x_i^{n+1} = x_i^n \exp\left(r_1 - x_i^n - a_{12} y_i^n - d_1 u_{1i}^n\right) + D_1 \nabla^2 x_i^n, \\ y_i^{n+1} = y_i^n \exp\left(r_2 + a_{21} x_i^n - y_i^n - d_2 u_{2i}^n\right) + D_2 \nabla^2 y_i^n, \\ u_{1i}^{n+1} = (1 - \eta_1) u_{1i}^n + e_1 x_i^n, \\ u_{2i}^{n+1} = (1 - \eta_2) u_{2i}^n + e_2 y_i^n, \end{cases} \tag{7}$$

with the periodic boundary conditions

$$\begin{cases} x_0^n = x_m^n,\ x_1^n = x_{m+1}^n, \\ y_0^n = y_m^n,\ y_1^n = y_{m+1}^n, \end{cases} \tag{8}$$

where $i \in \{1, 2, \ldots, m\} = [1, m]$ and $m, n \in Z^+$ is positive integer, $r_1, r_2, a_{12,} a_{21}, \eta_1, \eta_2, e_1, e_2$ are positive constants, and D_1 and D_2 are diffusion parameters.

$$\begin{aligned} \nabla^2 x_i^n &= x_{i+1}^n - 2x_i^n + x_{i-1}^n, \\ \nabla^2 y_i^n &= y_{i+1}^n - 2y_i^n + y_{i-1}^n. \end{aligned} \tag{9}$$

To the best of our knowledge, no work on global asymptomatic stability of the positive equilibrium of systems (7) and (8) has been done yet.

By simple computation, systems (7) and (8) have a positive equilibrium:

$$E^* = \left(x^*, y^*, u_1^*, u_2^*\right), \tag{10}$$

where

$$\begin{aligned} x^* &= \frac{\eta_1 r_1 \left(\eta_2 + e_2 d_2\right) - \eta_1 \eta_2 a_{12} r_2}{\left(\eta_2 + e_2 d_2\right)\left(\eta_1 + e_1 d_1\right) + a_{12} a_{21} \eta_1 \eta_2}, \\ y^* &= \frac{\eta_2 r_2 \left(\eta_1 + e_1 d_1\right) + \eta_1 \eta_2 a_{21} r_1}{\left(\eta_2 + e_2 d_2\right)\left(\eta_1 + e_1 d_{21}\right) + a_{12} a_{21} \eta_1 \eta_2}, \\ u_1^* &= \frac{e_1}{\eta_1} x^*, \\ u_2^* &= \frac{e_2}{\eta_2} y^*. \end{aligned} \tag{11}$$

If $r_1 \left(\eta_2 + e_2 d_2\right) > \eta_2 a_{12} r_2$, the equilibrium is positive.

To discuss the global asymptomatic stability of the unique positive equilibrium, the following assumptions and preparations are essential.

From the view point of biology, we only need to discuss the positive solution of system (7). So, it is assumed that the initial conditions of (8) are of the form

$$x_i^0 > 0, u_i^0 > 0, \quad i = 1, 2, \ldots, m. \tag{12}$$

For our purpose, we first introduce the following lemma which can be obtained easily by comparison theorem of difference equation.

Lemma 1 (see [29]). *Let $x(n)$ be a nonnegative solution of inequality*

$$x(n+1) \le x(n) \exp\{\alpha - \beta x(n)\}, \quad n \in Z, \tag{13}$$

with $x(0) > 0$ and $\alpha, \beta > 0$; then,

$$\lim_{n \longrightarrow \infty} \sup x(n) \le \frac{\alpha}{\beta}. \tag{14}$$

Lemma 2 (see [30]). *Any solution $x(n)$ of system*

$$x(n+1) = x(n)(1 - \gamma) + \omega(n), \quad n \in Z \tag{15}$$

with $x(0) > 0$ satisfies

$$\lim_{n \longrightarrow \infty} \sup x(n) \le \frac{\operatorname{up} n \in Z \omega(n)}{\gamma}, \tag{16}$$

where $\omega(n)$ is a nonnegative bounded sequence of real numbers and $0 < \gamma < 1$.

Applying the above lemmas, we can obtain the following result.

Theorem 1. *The solution of (7) with initial condition (8) is defined and remains nonnegative and bounded if $e^{r_j} - 2D_j \ge 0$ and $\eta_j < 1$, $j = 1, 2$ hold.*

Proof. From the first equation of system (7), we get

$$\begin{aligned} x_i^{n+1} &= x_i^n \exp\left(r_1 - x_i^n - a_{12} y_i^n - d_1 u_{1i}^n\right) + D_1 \nabla^2 x_i^n \\ &= x_i^n \left(\exp\left(r_1 - x_i^n - a_{12} y_i^n - d_1 u_{1i}^n\right) - 2D_1\right) \\ &\quad + D_1 \left(x_{i+1}^n + x_{i-1}^n\right), \end{aligned} \tag{17}$$

from which it is true that $x_i^n \geq 0$ holds for all n with $x_i^0 > 0, u_i^0 > 0,\ i = 1, 2, \ldots, m$ if $e^{r_1} - 2D_1 \geq 0$ and appropriate parameters a_{12}, d_1 are selected.

Similarly, from the second equation of system (7), we get that $y_i^n \geq 0$ holds for all n with $x_i^0 > 0, u_i^0 > 0,\ i = 1, 2, \ldots, m$, if $e^{r_2} - 2D_2 \geq 0$ and appropriate parameters a_{21}, d_2 are selected.

If $\eta_j \leq 1,\ j = 1, 2, u_{ji}^n \geq 0$ can also hold by means of the third and fourth equations of system (7).

Next, we will show the boundedness of the solutions.

$$\begin{aligned}\sum_{i=1}^{m} x_i^{n+1} &= \sum_{i=1}^{m}\left(x_i^n \exp\left(r_1 - x_i^n - a_{12}y_i^n - d_1u_{1i}^n\right) + D_1\nabla^2 x_i^n\right)\\ &= \sum_{i=1}^{m} x_i^n \exp\left(r_1 - x_i^n - a_{12}y_i^n - d_1u_{1i}^n\right)\\ &\leq \sum_{i=1}^{m} x_i^n \exp\left(r_1 - x_i^n\right).\end{aligned} \tag{18}$$

From Lemma 1, we can obtain

$$\lim_{n\longrightarrow\infty} \sup \sum_{i=1}^{m} x_i^n \leq \sum_{i=1}^{m} r_1 = mr_1. \tag{19}$$

Similarly, we can also obtain

$$\begin{aligned}\sum_{i=1}^{m} y_i^{n+1} &= \sum_{i=1}^{m}\left(y_i^n \exp\left(r_2 + a_{21}x_i^n - y_i^n - d_2u_{2i}^n\right) + D_2\nabla^2 y_i^n\right)\\ &= \sum_{i=1}^{m} y_i^n \exp\left(r2 + a_{21}x_i^n - y_i^n - d_2u_{2i}^n\right)\\ &\leq \sum_{i=1}^{m} y_i^n \exp\left(r_2 + a_{21}M_x - y_i^n\right),\end{aligned} \tag{20}$$

where $M_x = \sup_{n\in Z} x_i^n$. Then,

$$\lim_{n\longrightarrow\infty} \sup \sum_{i=1}^{m} y_i^n \leq \sum_{i=1}^{m}\left(r_2 + a_{21}M_x\right) = m\left(r_2 + a_{21}M_x\right). \tag{21}$$

From Lemma 2, by means of (20) and (21) and $\eta_1, \eta_2 \leq 1$, we can obtain

$$\lim_{n\longrightarrow\infty} \sup u_{1i}^n \leq \frac{e_1M_x}{\eta_1}, \tag{22}$$

$$\lim_{n\longrightarrow\infty} \sup u_{2i}^n \leq \frac{e_2M_y}{\eta_2}, \tag{23}$$

where $M_y = \sup_{n\in Z} y_i^n$. The proof is finished. □

3. Global Stability

In this section, we devote ourselves to studying the global asymptotic stability of the unique positive equilibrium E^*. By using global Lyapunov function, we derive the sufficient conditions under which the positive equilibrium is globally asymptotically stable.

Denote

$$\begin{aligned}&H(1)\colon e^{r_j} - 2D_j \geq 0, \quad j = 1, 2,\\ &H(2)\colon \frac{d_je_j}{2\left(1 - \eta_j\right)} \leq 1, \quad \eta_j \leq 1, j = 1, 2.\end{aligned} \tag{24}$$

Assume $\{x_i^n\}_{i\in[1,m]}^{n\in Z^+}$, $\{y_i^n\}_{i\in[1,m]}^{n\in Z^+}$ are positive solutions of systems (7) and (8); we can establish the following result.

Theorem 2. *Assume $H(1)$ and $H(2)$ hold; the positive equilibrium E^* of systems (7) and (8) is globally asymptotically stable.*

Proof. Let

$$V_1^n = \sum_{i=1}^{m}\left(x_i^n - x^* - x^*\ln\frac{x_i^n}{x^*}\right). \tag{25}$$

Then, we can obtain

$$\begin{aligned}\Delta V_1^n &= V_1^{n+1} - V_1^n\\ &= \sum_{i=1}^{m}\left(x_i^{n+1} - x_i^n - x^*\ln\frac{x_i^{n+1}}{x_i^n}\right)\\ &= \sum_{i=1}^{m}\left(x_i^{n+1} - x_i^n - x^*\frac{x_i^{n+1} - x_i^n}{x_i^n}\right) + o(1)\\ &= \sum_{i=1}^{m}\left(x_i^{n+1} - x_i^n\right)\left(1 - \frac{x^*}{x_i^n}\right) + o(1)\\ &= \sum_{i=1}^{m}\left(1 - \frac{x^*}{x_i^n}\right)\left(x_i^n \exp\left(r_1 - x_i^n - a_{12}y_i^n - d_1u_{1i}^n\right)\right.\\ &\quad \left. + D_1\nabla^2 x_i^n - x_i^n\right) + o(1)\\ &= \sum_{i=1}^{m}\left(1 - \frac{x^*}{x_i^n}\right)\left(x_i^n\left(1 - \left(x_i^n - x^*\right) - a_{12}\left(y_i^n - y^*\right)\right.\right.\\ &\quad \left.\left. - d_1\left(u_{1i}^n - u_1^*\right)\right) + D_1\nabla^2 x_i^n - x_i^n\right)\\ &\quad - D_1\sum_{i=1}^{m} x^*\left(\frac{x_{i+1}^n}{x_i^n} + \frac{x_{i-1}^n}{x_i^n} - 2\right) + o(1) + o(\rho_1)\\ &= -\sum_{i=1}^{m}\left(x_i - x_i^*\right)^2 - a_{12}\sum_{i=1}^{m}\left(x_i^n - x^*\right)\left(y_i^n - y^*\right)\\ &\quad - d_1\sum_{i=1}^{m}\left(x_i^n - x^*\right)\left(u_{1i}^n - u_1^*\right) - D_1x^*\sum_{i=1}^{m-1}\\ &\quad \cdot\left(\sqrt{\frac{x_{i+1}^n}{x_i^n}} - \sqrt{\frac{x_{i-1}^n}{x_i^n}}\right)^2 - D_1x^*\left(\sqrt{\frac{x_m^n}{x_1^n}} - \sqrt{\frac{x_1^n}{x_m^n}}\right)^2\\ &\quad + o(1) + o(\rho_1),\end{aligned} \tag{26}$$

where $\rho_1 = \sqrt{(x_i^n - x^*)^2 + (y_i^n - y^*)^2 + (u_{1i}^n - u_1^*)^2}$.

Let

$$V_2^n = \frac{a_{12}}{a_{21}} \sum_{i=1}^{m} \left(y_i^n - y^* - y^* \ln \frac{y_i^n}{y^*} \right). \tag{27}$$

Then, we can obtain

$$\begin{aligned}
\Delta V_2^n &= V_2^{n+1} - V_2^n \\
&= \frac{a_{12}}{a_{21}} \sum_{i=1}^{m} \left(y_i^{n+1} - y_i^n - y^* \ln \frac{y_i^{n+1}}{y_i^n} \right) \\
&= \frac{a_{12}}{a_{21}} \sum_{i=1}^{m} \left(y_i^{n+1} - y_i^n - y^* \frac{y_i^{n+1} - y_i^n}{y_i^n} \right) + o(1) \\
&= \frac{a_{12}}{a_{21}} \sum_{i=1}^{m} \left(y_i^{n+1} - y_i^n \right) \left(1 - \frac{y^*}{y_i^n} \right) + o(1) \\
&= \frac{a_{12}}{a_{21}} \sum_{i=1}^{m} \left(1 - \frac{y^*}{y_i^n} \right) \left(y_i^n \exp\left(r_2 + a_{21} x_i^n - y_i^n - d_2 u_{2i}^n \right) + D_2 \nabla^2 y_i^n - y_i^n \right) + o(1) \\
&= \frac{a_{12}}{a_{21}} \sum_{i=1}^{m} \left(1 - \frac{y^*}{y_i^n} \right) \left(y_i^n \left(1 - \left(y_i^n - y^* \right) + a_{21} \left(x_i^n - x^* \right) - d_2 \left(u_{2i}^n - u_2^* \right) \right) - y_i^n + D_2 \nabla^2 y_i^n \right) + o(1) + o(\rho_2) \\
&= \frac{a_{12}}{a_{21}} \sum_{i=1}^{m} \left(y_i^n - y^* \right) \left(-\left(y_i^n - y^* \right) + a_{21} \left(x_i^n - x^* \right) - d_2 \left(u_{2i}^n - u_2^* \right) \right) - D_2 \frac{a_{12}}{a_{21}} \sum_{i=1}^{m} y^* \left(\frac{y_{i+1}^n}{y_i^n} + \frac{y_{i-1}^n}{y_i^n} - 2 \right) + o(1) + o(\rho_2) \\
&= -\frac{a_{12}}{a_{21}} \sum_{i=1}^{m} \left(y_i - y_i^* \right)^2 + \sum_{i=1}^{m} a_{12} \left(x_i^n - x^* \right) \left(y_i^n - y^* \right) - \frac{a_{12} d_2}{a_{21}} \sum_{i=1}^{m} \left(y_i^n - y^* \right) \left(u_{2i}^n - u_2^* \right) - D_2 \frac{a_{12}}{a_{21}} \sum_{i=1}^{m-1} \\
&\quad \cdot \left(\sqrt{\frac{y_{i+1}^n}{y_i^n}} - \sqrt{\frac{y_{i-1}^n}{y_i^n}} \right)^2 - D_2 \frac{a_{12}}{a_{21}} \left(\sqrt{\frac{y_m^n}{y_1^n}} - \sqrt{\frac{y_1^n}{y_m^n}} \right)^2 + o(1) + o(\rho_2),
\end{aligned} \tag{28}$$

$$\begin{aligned}
\Delta V_2^n &= V_2^{n+1} - V_2^n \\
&= \frac{a_{12}}{a_{21}} \sum_{i=1}^{m} \left(y_i^{n+1} - y_i^n - y^* \ln \frac{y_i^{n+1}}{y_i^n} \right) \\
&= \frac{a_{12}}{a_{21}} \sum_{i=1}^{m} \left(y_i^{n+1} - y_i^n - y^* \frac{y_i^{n+1} - y_i^n}{y_i^n} \right) + o(1) \\
&= \frac{a_{12}}{a_{21}} \sum_{i=1}^{m} \left(y_i^{n+1} - y_i^n \right) \left(1 - \frac{y^*}{y_i^n} \right) + o(1) \\
&= \frac{a_{12}}{a_{21}} \sum_{i=1}^{m} \left(1 - \frac{y^*}{y_i^n} \right) \left(y_i^n \exp\left(r_2 + a_{21} x_i^n - y_i^n - d_2 u_{2i}^n \right) + D_2 \nabla^2 y_i^n - y_i^n \right) + o(1) \\
&= \frac{a_{12}}{a_{21}} \sum_{i=1}^{m} \left(1 - \frac{y^*}{y_i^n} \right) \left(y_i^n \left(1 - \left(y_i^n - y^* \right) + a_{21} \left(x_i^n - x^* \right) - d_2 \left(u_{2i}^n - u_2^* \right) \right) - y_i^n + D_2 \nabla^2 y_i^n \right) + o(1) + o(\rho_2) \\
&= \frac{a_{12}}{a_{21}} \sum_{i=1}^{m} \left(y_i^n - y^* \right) \left(-\left(y_i^n - y^* \right) + a_{21} \left(x_i^n - x^* \right) - d_2 \left(u_{2i}^n - u_2^* \right) \right) - D_2 \frac{a_{12}}{a_{21}} \sum_{i=1}^{m} y^* \left(\frac{y_{i+1}^n}{y_i^n} + \frac{y_{i-1}^n}{y_i^n} - 2 \right) + o(1) + o(\rho_2) \\
&= -\frac{a_{12}}{a_{21}} \sum_{i=1}^{m} \left(y_i - y_i^* \right)^2 + a_{12} \sum_{i=1}^{m} \left(x_i^n - x^* \right) \left(y_i^n - y^* \right) - \frac{a_{12} d_2}{a_{21}} \sum_{i=1}^{m} \left(y_i^n - y^* \right) \left(u_{2i}^n - u_2^* \right) - D_2 \frac{a_{12}}{a_{21}} \sum_{i=1}^{m-1} \left(\sqrt{\frac{y_{i+1}^n}{y_i^n}} - \sqrt{\frac{y_{i-1}^n}{y_i^n}} \right)^2 \\
&\quad - D_2 \frac{a_{12}}{a_{21}} \left(\sqrt{\frac{y_m^n}{y_1^n}} - \sqrt{\frac{y_1^n}{y_m^n}} \right)^2 + o(1) + o(\rho_2),
\end{aligned} \tag{29}$$

where $\rho_2 = \sqrt{(x_i^n - x^*)^2 + (y_i^n - y^*)^2 + (u_{2i}^n - u_2^*)^2}$.

Let

$$V_3^n = \frac{d_1}{2(1-\eta_1)e_1}(u_{1i}^n - u_1^*)^2. \tag{30}$$

Then, we can obtain

$$\begin{aligned}
\Delta V_3^n &= V_3^{n+1} - V_3^n \\
&= \frac{d_1}{2(1-\eta_1)e_1}\sum_{i=1}^{m}\left(u_{1i}^{n+1} - u_{1i}^n\right)\left(u_{1i}^{n+1} + u_{1i}^n - 2u_1^*\right) \\
&= \frac{d_1}{2(1-\eta_1)e_1}\sum_{i=1}^{m}(-\eta_1 u_{1i}^n + e_1 x_i^n)((2-\eta_1)u_{1i}^n \\
&\quad + e_1 x_i^n - 2u_1^*) \\
&= \frac{d_1}{2(1-\eta_1)e_1}\sum_{i=1}^{m}(-\eta_1(u_{1i}^n - u_1^*) + e_1(x_i^n - x^*)) \\
&\quad \cdot ((2-\eta_1)(u_{1i}^n - u_1^*) + e_1(x_i^n - x^*)) \\
&= -\frac{d_1\eta_1(2-\eta_1)}{2(1-\eta_1)e_1}\sum_{i=1}^{m}(u_{1i}^n - u_1^*)^2 \\
&\quad + \frac{d_1 e_1}{2(1-\eta_1)}\sum_{i=1}^{m}(x_i^n - x^*)^2 + d_1(x_i^n - x^*)(u_{1i}^n - u_1^*).
\end{aligned} \tag{31}$$

Let

$$V_4^n = \frac{d_2 a_{12}}{2(1-\eta_2)e_2 a_{21}}(u_{2i}^n - u_2^*)^2. \tag{32}$$

Then, we can obtain

$$\begin{aligned}
\Delta V_4^n &= V_4^{n+1} - V_4^n \\
&= \frac{d_2 a_{12}}{2(1-\eta_2)e_2 a_{21}}\sum_{i=1}^{m}\left(u_{2i}^{n+1} - u_{2i}^n\right)\left(u_{2i}^{n+1} + u_{2i}^n - 2u_2^*\right) \\
&= \frac{d_2 a_{12}}{2(1-\eta_2)e_2 a_{21}}\sum_{i=1}^{m}(-\eta_2 u_{2i}^n + e_2 y_i^n)((-\eta_2)u_{2i}^n \\
&\quad + e_2 y_i^n - 2u_2^*) \\
&= \frac{d_2 a_{12}}{2(1-\eta_2)e_2 a_{21}}\sum_{i=1}^{m}(-\eta_2(u_{2i}^n - u_2^*) \\
&\quad + e_2(y_i^n - y^*))((2-\eta_2)(u_{2i}^n - u_2^*) + e_2(y_i^n - y^*)) \\
&= -\frac{d_2 a_{12}\eta_2(2-\eta_2)}{2(1-\eta_2)e_2 a_{21}}\sum_{i=1}^{m}(u_{2i}^n - u_2^*)^2 \\
&\quad + \frac{d_2 a_{12} e_2}{2(1-\eta_2)a_{21}}\sum_{i=1}^{m}(y_i^n - y^*)^2 + \frac{a_{12}d_2}{a_{21}} \\
&\quad \cdot (y_i^n - y^*)(u_{2i}^n - u_2^*).
\end{aligned} \tag{33}$$

Let

$$V^n = V_1^n + V_2^n + V_3^n + V_4^n. \tag{34}$$

Then,

$$\begin{aligned}
\Delta V^n &= V^{n+1} - V^n \\
&\le \left(-1 + \frac{d_1 e_1}{2(1-\eta_1)}\right)\sum_{i=1}^{m}(x_i^n - x^*)^2 \\
&\quad + \left(-\frac{a_{12}}{a_{21}} + \frac{d_2 a_{12} e_2}{2(1-\eta_2)a_{21}}\right)\sum_{i=1}^{m}(y_i^n - y^*)^2 \\
&\quad + \frac{d_1\eta_1(\eta_1 - 2)}{2(1-\eta_1)e_1}\sum_{i=1}^{m}(u_{1i}^n - u_1^*)^2 \\
&\quad + \frac{d_2 a_{12}\eta_2(\eta_2 - 2)}{2(1-\eta_2)e_2 a_{21}}\sum_{i=1}^{m}(u_{2i}^n - u_2^*)^2 \\
&\quad - D_1\sum_{i=1}^{m-1}\left(\sqrt{\frac{x_{i+1}^n}{x_i^n}} - \sqrt{\frac{x_{i-1}^n}{x_i^n}}\right)^2 \\
&\quad - D_1\left(\sqrt{\frac{x_m^n}{x_1^n}} - \sqrt{\frac{x_1^n}{x_m^n}}\right)^2 + o(1) + o(\rho_1) \\
&\quad - D_2\frac{a_{12}}{a_{21}}\sum_{i=1}^{m-1}\left(\sqrt{\frac{y_{i+1}^n}{y_i^n}} - \sqrt{\frac{y_{i-1}^n}{y_i^n}}\right)^2 \\
&\quad - D_2\frac{a_{12}}{a_{21}}\left(\sqrt{\frac{y_m^n}{y_1^n}} - \sqrt{\frac{y_1^n}{y_m^n}}\right)^2 + o(1) + o(\rho_2).
\end{aligned} \tag{35}$$

If $(d_1 e_1/2(1-\eta_1)) \le 1$, $(d_2 e_2/2(1-\eta_2)) \le 1$, $(d_1\eta_1(\eta_1 - 2)/2(1-\eta_1)e_1) \le 0$ and $(d_2 a_{12}\eta_2(\eta_2 - 2)/2(1-\eta_2)e_2 a_{21}) \le 0$ or $(d_1 e_1/2(1-\eta_1)) \le 1$, $(d_2 e_2/2(1-\eta_2)) \le 1$, $\eta_1 < 1$ and $\eta_2 < 1$ hold, $\Delta V^n \le 0$. The proof is completed. □

4. Example and Numerical Simulations

In the following example, we will show the feasibility of our main results and discuss the effects of feedback controls. Take $i = 2$ in the system; we obtain a model with feedback controls as follows:

$$\begin{cases}
x_i^{n+1} = x_i^n \exp(r_1 - x_i^n - a_{12}y_i^n - d_1 u_{1i}^n) + D_1\nabla^2 x_i^n, \\
y_i^{n+1} = y_i^n \exp(r_2 + a_{21}x_i^n - y_i^n - d_2 u_{2i}^n) + D_2\nabla^2 y_i^n, \\
u_{1i}^{n+1} = (1-\eta_1)u_{1i}^n + e_1 x_i^n, \\
u_{2i}^{n+1} = (1-\eta_2)u_{2i}^n + e_2 y_i^n, \\
i = 1, 2,
\end{cases} \tag{36}$$

with the periodic boundary conditions

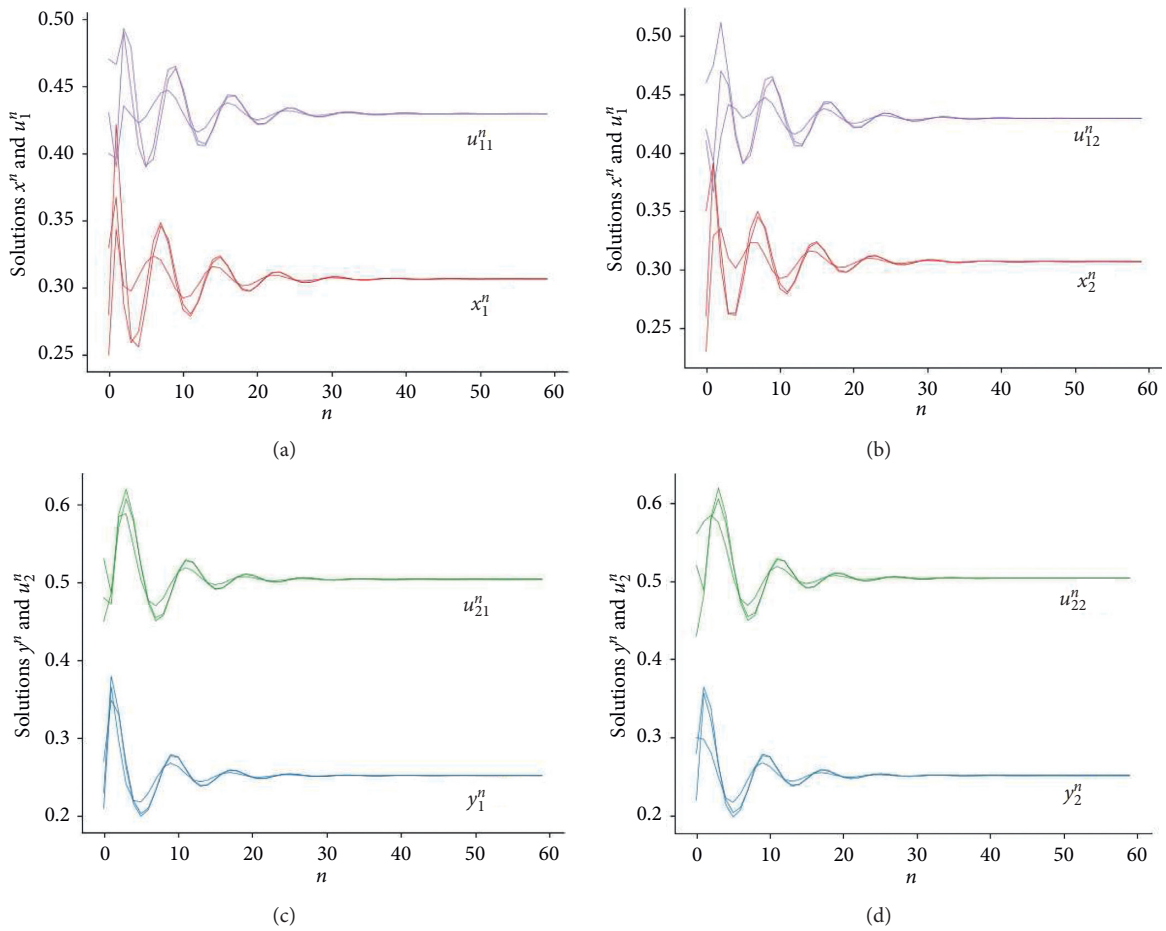

Figure 1: Dynamic behaviors of systems (36) and (37) with three sets of different initial conditions when $r_1 = 1.2$, $r_2 = 1, a_{12} = 0.8, a_{21} = 0.3, e_1 = 0.7, e_2 = 0.6, \eta_1 = 0.5, \eta_2 = 0.6, d_1 = 1, d_2 = 1, D_1 = 0.3$, and $D_2 = 0.4$.

Table 1: Different initial values for $x_1^n, x_2^n, y_1^n, y_2^n, u_{11}^n, u_{12}^n, u_{21}^n, u_{22}^n$.

	x_1^0	x_2^0	y_1^0	y_2^0	u_{11}^0	u_{12}^0	u_{21}^0	u_{22}^0
1	0.22	0.35	0.27	0.22	0.40	0.46	0.45	0.52
2	0.33	0.26	0.23	0.28	0.47	0.42	0.48	0.43
3	0.25	0.23	0.21	0.30	0.43	0.41	0.53	0.56

$$\begin{cases} x_0^n = x_2^n, \\ x_1^n = x_3^n, \\ y_0^n = y_2^n, \\ y_1^n = y_3^n. \end{cases} \tag{37}$$

To illustrate our purposes, the parameter values are chosen as follows (the choice of parameter values is hypothetical with appropriate units and not based on data): $r_1 = 1.2, r_2 = 1, a_{12} = 0.8, a_{21} = 0.3, d_1 = 1, d_2 = 1, D_1 = 0.3, D_2 = 0.4$, $e_1 = 0.7, e_2 = 0.6, \eta_1 = 0.5$, and $\eta_2 = 0.6$; then, there is only a unique positive equilibrium $E^*(x_1^*, x_2^*, y_1^*, y_2^*, u_{11}^*, u_{12}^*, u_{21}^*, u_{22}^*) = (0.3181, 0.3181, 0.5487, 0.5487, 0.4453, 0.4453, 0.5487, 0.5487)$. It is easy to see that the conditions in Theorem 2 are verified. Dynamic behaviors of systems (36) and (37) with the initial conditions are shown in Figure 1, and three sets of different initial conditions are listed in Table 1. The simulations can illustrate the fact that the positive equilibrium is globally asymptotically stable.

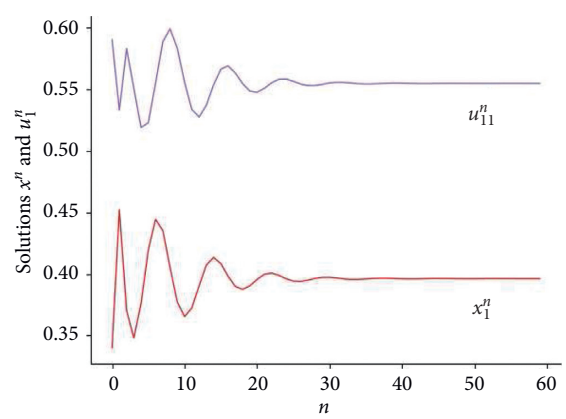

Figure 2: Dynamic behaviors of x_1^n and u_{11}^n for systems (36) and (37) with initial conditions $(0.36, 0.34, 0.36, 0.34, 0.28, 0.31, 0.28, 0.31, 0.59, 0.52, 0.45, 0.54)$ when $d_2 = 0.8$.

To explore clearly the dynamical behavior of systems (36) and (37), we investigate the effect of diffusion parameter d_2 by keeping other parameters of the system fixed. Figure 2 exhibits in detail an interesting situation when

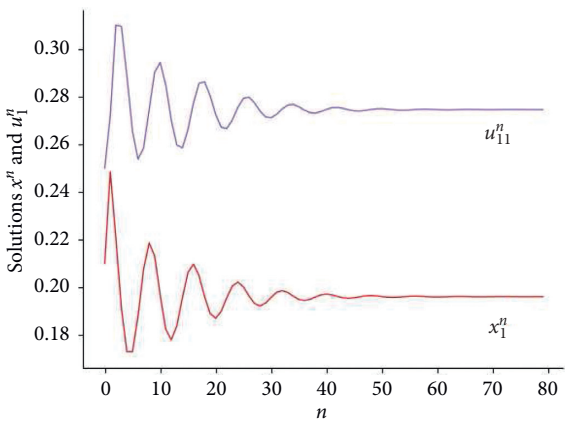

Figure 3: Dynamic behaviors of x_1^n and u_{11}^n for systems (36) and (37) with initial conditions $(0.16, 0.21, 0.16, 0.21, 0.21, 0.26, 0.21, 0.26, 0.25, 0.22, 0.45, 0.50)$ when $d_2 = 1.2$.

$d_2 = 0.8$ ($r_1 = 1.2$, $r_2 = 1$, $a_{12} = 0.8$, $a_{21} = 0.3$, $d_1 = 1$, $D_1 = 0.3$, $D_2 = 0.4$, $e_1 = 0.7, e_2 = 0.6, \eta_1 = 0.5, \eta_2 = 0.6$), in which the solutions converge faster than Figure 1. With the increase of d_2, the solutions converge more slowly, as depicted in Figure 3. For the sake of convenience, only the dynamical behavior of x_1^n and u_{11}^n with a group of initial values is shown in Figures 2 and 3. The simulation results of adjusting feedback control coefficients d_1, e_1, and e_2 are omitted.

5. Conclusions and Discussion

This paper investigates the global asymptomatic stability of the unique positive equilibrium of a discrete diffusion model with the periodic boundary conditions and feedback control. The condition to ensure the nonnegativity and boundedness of the solutions of the discrete model is discussed, and the globally asymptotical stability of the positive equilibrium is proved. Through comparing numerical simulations, we notice that when we improve the feedback control coefficients, the solutions will converge more slowly. It follows that we can adjust the rate of convergence by choosing suitable values of feedback control variables. Such work may also be applied to other discrete diffusion models.

It should be noted that there is only a basic condition obtained to guarantee the existence of positive solution. Judgement sentence $x_i^n, y_i^n, u_{1i}^n, u_{2i}^n \geq 0$ should be added into the simulation programs under the conditions of $e^{r_j} - 2D_j \geq 0$ and $\eta_j \leq 1$, $j = 1, 2$. Further improvements are needed.

In this study, all of the coefficients of the model system are constant; in many situations, they can be assumed to be nonconstant bounded nonnegative sequences such as periodic positive sequences which can reflect the seasonal fluctuations [19]. On the other hand, time delays can have a great influence on species populations. It is worthy to consider the nonautonomous space-time discrete Lotka–Volterra system with feedback control.

Different control schemes, such as switching control, constraint control, and sliding control, can be applied to the system models. Many interesting results can be obtained. Based on the backstepping recursive technique, a neural network-based finite-time control strategy is proposed for a class of non-strict-feedback nonlinear systems [31], and an event-triggered robust fuzzy adaptive prescribed performance finite-time control strategy is proposed for a class of strict-feedback nonlinear systems with external disturbances [32]. How to apply these control schemes on the discrete diffusion models may be worth considering.

It is well known that noise disturbance is unavoidable in real systems, and it has an important effect on the stability of systems. Also, noise can be used to stabilize a given unstable system or to make a system even more stable when the system is already stable which reveals that the stochastic feedback control can stabilize and destabilize the deterministic systems [33, 34]. Therefore, it will be interesting and challenging to investigate stabilization or destabilization of nonlinear discrete space-time systems by stochastic feedback control in our future work.

Data Availability

No data were used to support this study.

Conflicts of Interest

The authors declare that they have no conflicts of interest.

Acknowledgments

This research was supported by the Applied Study Program (grant nos. 171006901B, 60204, and WH18012).

References

[1] J. Xu and Z. Teng, "Permanence for a nonautonomous discrete single-species system with delays and feedback control," *Applied Mathematics Letters*, vol. 23, no. 9, pp. 949–954, 2010.

[2] O. S. Board, *An Ecosystem Services Approach to Assessing the Impacts of the Deepwater Horizon Oil Spill in the Gulf of Mexico*, National Academies Press, Washington, DC, USA, 2013.

[3] V. Tiwari, J. P. Tripathi, R. K. Upadhyay, Y.-P. Wu, J.-S. Wang, and G.-Q. Sun, "Predator-prey interaction system with mutually interfering predator: role of feedback control," *Applied Mathematical Modelling*, vol. 87, pp. 222–244, 2020.

[4] X. Li, X. Yang, and T. Huang, "Persistence of delayed cooperative models: impulsive control method," *Applied Mathematics and Computation*, vol. 342, pp. 130–146, 2019.

[5] T. Luo, "Stabilization of multi-group models with multiple dispersal and stochastic perturbation via feedback control based on discrete-time state observations," *Applied Mathematics and Computation*, vol. 354, pp. 396–410, 2019.

[6] W. Qin, X. Tan, M. Tosato, and X. Liu, "Threshold control strategy for a non-smooth Filippov ecosystem with group defense," *Applied Mathematics and Computation*, vol. 362, Article ID 124532, 2019.

[7] J. Xu, Z. Teng, and H. Jiang, "Permanence and global attractivity for discrete nonautonomous two-species lotka-volterra competitive system with delays and feedback controls," *Periodica Mathematica Hungarica*, vol. 63, no. 1, pp. 19–45, 2011.

[8] C. Walter, "Stability of controlled biological systems," *Journal of Theoretical Biology*, vol. 23, no. 1, pp. 23–38, 1969.

[9] P. Wang, Z. Zhao, and W. Li, "Global stability analysis for discrete-time coupled systems with both time delay and multiple dispersal and its application," *Neurocomputing*, vol. 244, pp. 42–52, 2017.

[10] Y. Kuang, "Global stability in delay differential systems without dominating instantaneous negative feedbacks," *Journal of Differential Equations*, vol. 119, no. 2, pp. 503–532, 1995.

[11] Y. Yan and E.-O. N. Ekaka-a, "Stabilizing a mathematical model of population system," *Journal of the Franklin Institute*, vol. 348, no. 10, pp. 2744–2758, 2011.

[12] Y. Muroya, "Global stability of a delayed nonlinear lotka-volterra system with feedback controls and patch structure," *Applied Mathematics and Computation*, vol. 239, pp. 60–73, 2014.

[13] J. L. Liu and W. C. Zhao, "Dynamic analysis of stochastic lotka–volterra predator-prey model with discrete delays and feedback control," *Complexity*, vol. 2019, p. 15, Article ID 4873290, 2019.

[14] Q. Zhu and H. Wang, "Output feedback stabilization of stochastic feedforward systems with unknown control coefficients and unknown output function," *Automatica*, vol. 87, pp. 166–175, 2018.

[15] Q. Zhu, "Stabilization of stochastic nonlinear delay systems with exogenous disturbances and the event-triggered feedback control," *IEEE Transactions on Automatic Control*, vol. 64, no. 9, pp. 3764–3771, 2019.

[16] K. Kiss and É. Gyurkovics, "LMI approach to global stability analysis of stochastic delayed lotka-volterra models," *Applied Mathematics Letters*, vol. 104, pp. 106227: 1–6, 2020.

[17] X. Chen and C. Fengde, "Stable periodic solution of a discrete periodic lotka-volterra competition system with a feedback control," *Applied Mathematics and Computation*, vol. 181, no. 2, pp. 1446–1454, 2006.

[18] C. Niu and X. Chen, "Almost periodic sequence solutions of a discrete lotka-volterra competitive system with feedback control," *Nonlinear Analysis: Real World Applications*, vol. 10, no. 5, pp. 3152–3161, 2009.

[19] X. Liao, S. Zhou, and Y. Chen, "Permanence and global stability in a discrete n-species competition system with feedback controls," *Nonlinear Analysis: Real World Applications*, vol. 9, no. 4, pp. 1661–1671, 2008.

[20] A. M. Turing, "The chemical basis of morphogenesis," *Philo-Sophical Transactions of the Royal Society B: Biological Sciences*, vol. 237, no. 641, pp. 37–72, 1952.

[21] K. Gopalsamy and P. X. Weng, "Feedback regulation of logistic growth," *International Journal of Mathematics and Mathematical Sciences*, vol. 16, no. 1, pp. 177–192, 1993.

[22] L. Xu, S. S. Lou, P. Q. Xu, and G. Zhang, "Feedback control and parameter invasion for a discrete competitive lotka–volterra system," *Discrete Dynamics in Nature and Society*, vol. 2018, p. 8, Article ID 7473208, 2018.

[23] X. W. Li and H. J. Gao, "Robust finite frequency H_∞filtering for uncertain 2-D roesser systems," *Automatica*, vol. 48, pp. 1163–1170, 2012.

[24] X. W. Li, H. J. Gao, and C. H. Wang, "Generalized kalman–yakubovich–popov lemma for 2-D FM LSS model," *IEEE Transaction on Automatic Control*, vol. 57, no. 12, pp. 3090–3193, 2012.

[25] J. Zhou, Y. Yang, and T. Zhang, "Global dynamics of a reaction-diffusion waterborne pathogen model with general incidence rate," *Journal of Mathematical Analysis and Applications*, vol. 466, no. 1, pp. 835–859, 2018.

[26] Y. Yang and J. Zhou, "Global stability of a discrete virus dynamics model with diffusion and general infection function," *International Journal of Computer Mathematics*, vol. 96, no. 9, pp. 1752–1762, 2019.

[27] P. Liu and S. N. Elaydi, "Discrete competitive and cooperative models of lotka-volterra type," *Journal of Computational Analysis and Applications*, vol. 3, no. 1, pp. 53–73, 2001.

[28] L. L. Meng and Y. T. Han, "Bifurcation, chaos, and pattern formation for the discrete predator-prey reaction-diffusion model," *Discrete Dynamics in Nature and Society*, vol. 2019, p. 9, Article ID 9592878, 2019.

[29] R. M. May and G. F. Oster, "Bifurcations and dynamic complexity in simple ecological models," *The American Naturalist*, vol. 110, no. 974, pp. 573–599, 1976.

[30] Z. Zhou and X. Zou, "Stable periodic solutions in a discrete periodic logistic equation," *Applied Mathematics Letters*, vol. 16, no. 2, pp. 165–171, 2003.

[31] K. K. Sun, J. B. Qiu, H. R. Karimi, and H. J. Gao, "A novel finite-time control for nonstrict feedback saturated nonlinear systems with tracking error constraint," *IEEE Transactions on Systems, Man, and Cybernetics: Systems*, pp. 1–12, 2020.

[32] K. K. Sun, J. B. Qiu, H. R. Karimi, and Y. L. Fu, "Event-triggered robust fuzzy adaptive finite-time control of nonlinear systems with prescribed performance," *IEEE Transactions on Fuzzy Systems*, 2020.

[33] X. Mao, "Almost sure exponential stabilization by discrete-time stochastic feedback control," *IEEE Transactions on Automatic Control*, vol. 61, no. 6, pp. 1619–1624, 2016.

[34] Q. Zhu and T. Huang, "Stability analysis for a class of stochastic delay nonlinear systems driven by G-Brownian motion," *Systems & Control Letters*, vol. 140, Article ID 104699, 9 pages, 2020.

Hindawi
Complexity
Volume 2020, Article ID 1976584, 12 pages
https://doi.org/10.1155/2020/1976584

Research Article

Independent Control of Temperature and Humidity in Air Conditioners by Using Fuzzy Sliding Mode Approach

Lijian Yang,[1,2] Ziyang Li,[1,2] Zhengtian Wu,[1,2] Mingyang Xie,[3] Baoping Jiang,[1,2] and Baochuan Fu[1,2]

[1]*School of Electronic and Information Engineering, Suzhou University of Science and Technology, Suzhou, China*
[2]*Suzhou Institute of Smart City, Suzhou University of Science and Technology, Suzhou, China*
[3]*College of Automation Engineering, Nanjing University of Aeronautics & Astronautics, Nanjing, China*

Correspondence should be addressed to Zhengtian Wu; wzht8@mail.usts.edu.cn and Baochuan Fu; fubc@163.com

Received 17 June 2020; Accepted 18 July 2020; Published 4 August 2020

Academic Editor: Quanxin Zhu

This paper proposes a sliding mode control (SMC) strategy to solve the problem of independent control of temperature and humidity in air conditioners; the complexity increases due to the need to make full use of the wind side for cooling. First, dynamics of indoor temperature and humidity are determined based on mathematical models. Second, in order to reduce the chattering effect of SMC and coordinate indoor conditions to satisfy people's needs, the independent control of temperature and humidity is realized via a novel fuzzy sliding mode control strategy based on reaching laws. Finally, simulation results are provided to verify the effectiveness of the proposed method.

1. Introduction

In traditional central air-conditioning control systems, temperature is typically the controlled parameter and multiloop PID control method is commonly adopted. However, achieving desired control performance is difficult with the aid of traditional PID controllers due to a variety of reasons, for instance, nonlinearity and time-varying effects in temperature variation and complexity in establishing mathematical models [1]. In addition to the complexity of parameter setting methods, conventional PID controller parameters often have poor system performance and poor adaptability to the controlled process. Therefore, ordinary PID control is difficult to meet the control requirements in the central air-conditioning system.

Compared with the conventional air-conditioning system, the temperature- and humidity-independent control system uses high-temperature cold source, solution humidity control, and other technologies to ensure energy saving. Lazzarin and Castellotti studied a self-regenerating solution dehumidification system driven by a heat pump, which was applied to supermarket to verify its energy efficiency by simulating year-round outdoor working conditions [2]. Hao designed a cooling radiant roof, rotary dehumidification, and displacement ventilation air conditioner system. The system can effectively save electrical energy, significantly improve the indoor environment quality, and increase comfort [3]. Although the advantages of independent temperature and humidity controlled air-conditioning systems are obvious, there are still some problems in the actual operation process. For example, if the temperature- and humidity-independent control system needs to make full use of the free cooling on the wind side during the transition season, the exhaust fan needs to be configured, which increases the complexity of the system [4]. Compared with traditional air-conditioning systems, the installation of temperature- and humidity-independent control air-conditioning is more stringent, complicated, and costly.

During air-conditioning control, the fuzzy control strategy is more efficient than the PID control because the former can adjust the room temperature under partial load operation and flow rate of cooling water in cooling coil shows satisfactory oscillation response; however, given that

the fuzzy approach lacks systemicity, the disadvantages of using fuzzy control method alone in air-conditioning systems are instability and poor robustness in the fuzzy process [5, 6]. In [7–9], a genetic algorithm-based PID controller and self-tuning PID-type fuzzy adaptive controller were designed to simulate the temperature of central air-conditioning systems. These two methods can meet the needs of central air-conditioning temperature control system; the experimental results show that the cooling effect is better. For the problem of parameter/structure uncertainty and input dead zone of nonlinear system, an adaptive control method based on neural network is designed to ensure the stability and robustness of the system [10, 11]. The articles [12–15] study the feedback control problem of stochastic nonlinear systems and have made a lot of contributions to the backstepping between controllers and the system stability proof. In order to compensate the interference or unmeasured state of the system, the articles [16, 17] give a new form of reduced-order K-filters. These control methods and anti-interference methods are also applicable to air-conditioning systems with large lags and numerous interference.

Sliding mode control (SMC) was proposed by Emelyanov et al. in the 1950s. Itkin et al. subsequently summarized and developed SMC theory [18]. Later, sliding mode control was widely used in robotics and aviation [19]. Given that the sliding motion is designed to be independent of system parameters and disturbances, therefore, SMC models have the good properties of strong robustness, fast response, and easy implementation. These characteristics can be optimized in the central air-conditioning system and compensate for the shortcomings of conventional PID controllers. In addition, it has witnessed many researches in the related field; for example, a class of discrete-time interval type-2 fuzzy systems were studied in [20]. In [21], the problem of sliding mode control for semi-Markov switching systems with quantized measurement in finite-time level was investigated. When system state trajectory reached the sliding mode surface, the exclusive occurrence of sliding motion on the sliding surface toward the equilibrium point is impossible due to switching signals. Several studies have shown that the fuzzy SMC can suppress chattering effect by linearizing discontinuous signals. The fuzzy sliding mode approach reduces the influence of switching control and remarkably reduces the chattering effect [22]. In terms of application, the fuzzy SMC approach was applied to stochastic systems with (semi)Markov switching parameters which have been developed in [23–25]. In [26, 27], the fuzzy SMC was proposed for nonlinear descriptor systems. Therefore, this paper proposes fuzzy rules in the design of sliding mode parameters and reduction of chattering phenomenon of SMC to ensure the accurate control of indoor temperature and humidity.

Different from the traditional control method, the robust and fast response characteristics of the fuzzy sliding mode control adopted in this paper are more suitable for the air-conditioning system with large lags and numerous interference. Meanwhile, the contribution of this study is to propose fuzzy rules in the design of sliding mode controller for independent control of indoor temperature and humidity to solve the problem of increased complexity due to the configuration of the exhaust fan. Compared with the conventional PID control and fuzzy PID control methods, the proposed fuzzy SMC strategy achieves faster adjustment response, smaller overshoot, higher accuracy, and better control effect. At the same time, it ensures that the indoor carbon dioxide concentration is at a normal level. However, this air-conditioning system is mainly suitable for the case where the room model data is known. The design method of the stochastic delay feedback control and the stability controller for the discrete-time half-Markov jump linear system with bounded residence time used in [28–30] will be of a great help for the future work of expanding to random cases.

2. Mathematical Modeling of Indoor Environment

The independent control of temperature and humidity in the air-conditioning system adjusts the volume of fresh air supply of the dehumidification system and the volume of return air supply of the temperature control system to meet people's requirements for indoor environment comfort [31]. The system is illustrated in Figure 1.

This study considers an office building environment with the following assumptions [32]: (1) the office building is considered as a closed-loop system. (2) The air pressure in the building remains unchanged. (3) The indoor air diffusion is good and the room temperature can be measured using a temperature sensor. (4) The effect of humidity on room temperature is unclear.

2.1. Dynamic Response of Temperature. Given that the independent control of temperature and humidity in the air-conditioning system uses fresh air in the dehumidification system to remove indoor residual humidity, CO_2, and odors such that to ensure indoor air quality, the dynamic response modeling of room temperature must only consider the room's sensible heat [33].

The heat energy balance in an air-conditioning system is expressed as follows [34, 35]:

$$\dot{Q}_s t = Q_r(t) + Q_w(t) - Q_d(t), \tag{1}$$

where $Q_r(t)$ is the heat provided by the air-conditioning supply air; $Q_s t$ is the sensible heat; $Q_d(t)$ is the outflow heat; and $Q_w(t)$ is the heat dissipation.

The room sensible heat change can be described as follows [28]:

$$\dot{Q}_s t = \rho V C_1 T_i, \tag{2}$$

where ρ is the indoor air density, (kg/m^3); V is the room volume, m^3; C_1 is the specific heat capacity of indoor air, J/(Kg $*$ K); and T_i is the room temperature.

The relationship between the sensible heat provided by the air-conditioning system to the room and the air output can be expressed as follows [28]:

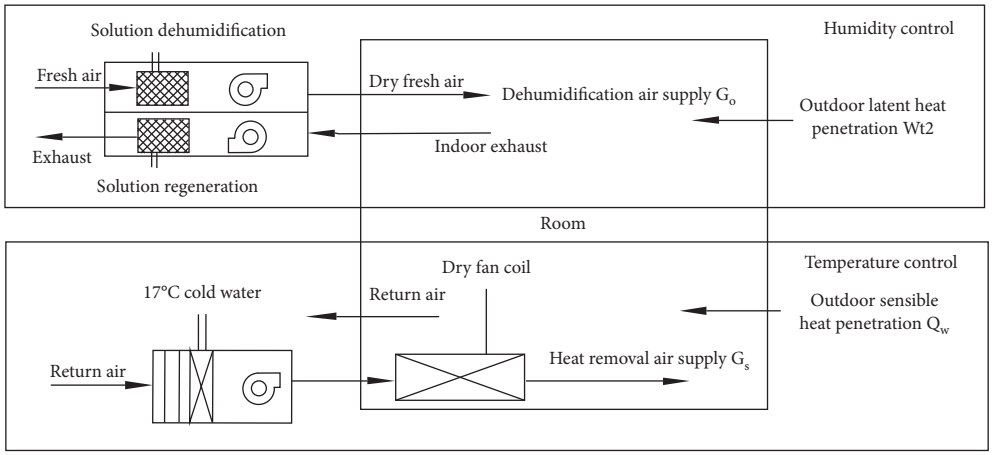

Figure 1: Air-conditioning system diagram.

$$Q_r(t) = \rho C_1 G_s(t) T_s(t), \tag{3}$$

where $G_s(t)$ is the volume of air supplied, m^3, and $T_s(t)$ is the air temperature of the sensible heat dry fan coil, °C.

For rooms that use temperature and humidity as variables to control the air-conditioning system independently, the main factors that affect the indoor temperature response are listed as follows: sensible heat flowing out of the room and heat dissipation of the room [36]. Heat dissipation of the room includes the following parts: (1) instantaneous sensible cooling load due to the indoor and outdoor temperature difference and direct heat dissipation from the indoor heat source. (2) Heat dissipation caused by the radiation of sunlight through the window.

Heat dissipation of the room $Q_w(t)$ is expressed as follows [37]:

$$Q_w(t) = \frac{F\lambda}{\delta}\left(T_o(t) - T_i(t)\right) + \alpha_i\left(T_o(t) - T_i(t)\right) + \sigma, \tag{4}$$

where F is the wall area, m^2; λ is the thermal conductivity of the wall material layer; δ is the thickness of the wall material layer, m; T_o is the outdoor ambient temperature; α_i is the heat transfer coefficient of composite heat transfer surface of the inner wall of the glass window; and σ is the heat generated by the solar radiation of the glass window in the room.

The sensible heat flowing out of the room is primarily the heat taken away by return air. Given that the office building is assumed to be a closed-loop system, the return air volume can be calculated according to the supply air volume of the temperature control system as follows [29]:

$$Q_d(t) = \rho C_1 G_s(t) T_i(t). \tag{5}$$

Substituting (2)–(5) into (1),

$$\begin{aligned}\rho V C_1 \dot{T}_i &= \rho C_1 G_s(t) T_s(t) + \frac{F\lambda}{\delta}\left(T_o(t) - T_i(t)\right) \\ &\quad + \alpha_i\left(T_o(t) - T_i(t)\right) + \sigma - \rho C_1 G_s(t) T_i(t).\end{aligned} \tag{6}$$

2.2. Dynamic Response of Humidity. The dehumidification system of the air conditioner with independent control of temperature and humidity adopts the full fresh air system. The humidity control system bears all the latent heat load of the building by sending dry fresh air with moisture content lower than the interior designed state. Under the assumptions that the office building is a closed-loop system and the pressure in the building remains unchanged, mass conservation of air humidity can be calculated as follows [38]:

$$M_n \dot{d}_n(t) = G_o(t)\left(d_s(t) - d_n(t)\right) + W_h(t), \tag{7}$$

where M_n is the total mass of air in the building, g; $d_n(t)$ is the moisture content of the air in the building, g/kg; $d_s(t)$ is the moisture content of the air supply of the air conditioner, g/kg; $G_o(t)$ is the exhaust volume of the dehumidification system, g/h; and $W_h(t)$ is the indoor humidity load, g/h.

Hence, determining the total indoor wet load W_h is important. The building's moisture production primarily comes from people indoors, water surface, plants, and the amount of moisture from infiltrating air [39]. Given that this paper considers an office place, the main indoor moisture load involves the number of people that dissipates moisture and the amount of moisture dissipated by fresh air penetration [40].

The wet load of personnel in the office building based on the adults is calculated as follows [32]:

$$W_{t1}(t) = 0.278 n \varnothing g * 10^{-6}, \tag{8}$$

where n is the number of indoor personnel, $\varnothing$ is the personnel cluster coefficient, and g is the amount of moisture dissipated by the adults, g/h.

Conventional air-conditioning systems only considered the wet load caused by fresh air penetration in winter but ignored the insignificant wet load generated by fresh air penetration in summer. By comparison, dry air is responsible for dehumidification in air-conditioning systems with independent temperature and humidity control although its dehumidification capacity is limited. Therefore, large humidity load caused by outdoor fresh air penetration

must be considered. The wet load due to fresh air penetration can be calculated as follows [33]:

$$W_{t2}(t) = L\rho\left(d_o(t) - d_n(t)\right), \tag{9}$$

where L is the infiltration air volume m^3 and d_o is the outdoor air moisture content.

Substituting (8) and (9) into (7) leads to

$$\begin{aligned} M_n\dot{d}_n(t) &= G_o(t)\left(d_s(t) - d_n(t)\right) \\ &\quad + 0.278n\varnothing g * 10^{-6} + L\rho\left(d_o(t) - d_n(t)\right). \end{aligned} \tag{10}$$

2.3. Estimate of Indoor CO_2 *Concentration.* The latent heat control system in the air conditioner with independent control of temperature and humidity uses full fresh air input to ensure that the predicted air concentration in the office space will remain fresh. The relationship between the indoor concentration and the air volume of the air conditioner in the absence of people is expressed as follows:

$$V\dot{C} = C_{\text{out}}V_v(t) + Q_p - \left(V_v(t) + L\right)C, \tag{11}$$

where C is the indoor CO_2 concentration; Q_p is the pollutant emission rate; and V_v is the room mechanical ventilation (m^3/h). Given that the room is considered a closed-loop system, the mechanical ventilation volume is equal to the input air volume of the latent heat control system, that is, $V_v(t) = (G_o(t)/\rho)$.

According to the actual situation of the office building, the amount of indoor CO_2 concentration is calculated from 8 am to 6 pm. Indoor persons are in the normal office state. The extremely light activity state estimates that the average amount of CO_2 concentration is 18 L/(person $*$ h).

Therefore, the indoor CO_2 concentration prediction model is expressed as follows:

$$V\dot{C} = C_{\text{out}}V_v(t) + Q_p + 18n - \left(V_v(t) + L\right)C, \tag{12}$$

where n is the number of people in the office.

3. Design of Sliding Mode Controller

Define that $x_1 = T_s - T_i$, $u_1 = G_s(T_s - T_i) = G_s x_1$, and $x_2 = d_s - d_n, u_2 = G_o(d_s - d_n)$ are the state variables. Given that the supplied air temperature T_s and the supplied air moisture content d_s are unchanged, $\dot{T}_i = -\dot{x}_1$ and $\dot{d}_n = -\dot{x}_2$.

3.1. Temperature Controller. The state equation of the temperature response in the room can be expressed as follows:

$$\rho VC_1\dot{x}_1 = -\rho C_1 u_1 - \frac{F\lambda}{\delta}\left(T_o - T_s + x_1\right) - \alpha_i\left(T_o - T_s + x_1\right) - \sigma. \tag{13}$$

Define x_{d1} as the error between the supplied air temperature of the terminal device and the ideal indoor temperature T_d; that is, if $x_{d1} = T_s - T_d$, then $e_1 = x_1 - x_{d1}$.

The integral sliding surface can reduce the steady-state error of the system, weaken the chattering, and enhance the stability of the temperature controller. Therefore, the integral sliding mode surface function is defined as follows:

If $s = e_1 + k\int e_1 \mathrm{d}t$, then

$$\begin{aligned} \dot{s} = \dot{e}_1 + ke_1 = \dot{x}_1 + ke_1 &= -\frac{u_1}{V} - \frac{(F\lambda + \alpha_i\delta)x_1}{\rho VC_1\delta} \\ &\quad - \frac{(F\lambda + \alpha_i\delta)(T_o - T_s)}{\rho VC_1\delta} - \frac{\sigma}{\rho VC_1} + ke. \end{aligned} \tag{14}$$

When the system state trajectories reached onto the sliding surface, $\dot{s} = 0$ is satisfied and the sliding mode accessibility condition ensures that the motion point at any position in the state space reaches the switching surface within a limited time and the trajectory of approaching movement is unlimited. Therefore, the approach law can effectively improve the dynamic quality of the approach movement. Therefore, the following reaching law of the power function is selected:

$$\dot{s} = -k_1|s|^a \operatorname{sgn}(s), \quad k > 0,\ 0 < a < 1. \tag{15}$$

Given that $\lim_{s\longrightarrow 0^+}\dot{s} = \lim_{s\longrightarrow 0^+} = k_1|s|^a\operatorname{sgn}(s) < 0$ and $\lim_{s\longrightarrow 0^-}\dot{s} = \lim_{s\longrightarrow 0^-} = k_1|s|^a\operatorname{sgn}(s) > 0$, the power reaching law guarantees the existence of the sliding mode and the global arrival condition.

Therefore, we can obtain the following formula based on (14) and (15):

$$\begin{aligned} \dot{s} &= -\frac{u_1}{V} - \frac{(F\lambda + \alpha_i\delta)x_1}{\rho VC_1\delta} - \frac{(F\lambda + \alpha_i\delta)(T_o - T_s)}{\rho VC_1\delta} \\ &\quad - \frac{\sigma}{\rho VC_1} + ke_1 = -k_1|s|^a\operatorname{sgn}(s). \end{aligned} \tag{16}$$

Thus, the following sliding mode controller based on the power reaching law is obtained:

$$\begin{aligned} u_1 &= -\frac{(F\lambda + \alpha_i\delta)x_1}{\rho VC_1\delta} - \frac{(F\lambda + \alpha_i\delta)(T_o - T_s)}{\rho VC_1\delta} \\ &\quad - \frac{\sigma}{\rho C_1} + \left(ke_1 + k_1|s|^a\operatorname{sgn}(s)\right)V. \end{aligned} \tag{17}$$

Define the following Lyapunov function, $V(s) = (1/2s^2)$:

$$\begin{aligned} \dot{V}(s) &= s\dot{s} = \left(\dot{e} + ke_1\right)s \\ &= \left(-\frac{u_1}{V} - \frac{(F\lambda + \alpha_i\delta)x_1}{\rho VC_1\delta} - \frac{(F\lambda + \alpha_i\delta)(T_o - T_s)}{\rho VC_1\delta}\right. \\ &\quad \left. - \frac{\sigma}{\rho C_1} + ke_1\right)s. \end{aligned} \tag{18}$$

Substituting that (17) is substituted into the available $\dot{V}(s) = -k_1|s|^a\operatorname{sgn}(s)s$ since $k_1 > 0$ and $0 < a < 1$, it obtains $\dot{V}(s) < 0$. Therefore, the dehumidification system is stable.

3.2. Humidity Controller. Equation (10) presents that the state equation of the temperature response in the room can be expressed as follows:

$$M_n \dot{x}_2 = -u_2 - 0.278 n \varnothing g * 10^{-6} - L\rho\left(d_o - d_s + x_2\right). \tag{19}$$

Define x_{d2} as the error between the supplied air humidity of the latent heat removal terminal device and the ideal indoor humidity d_l; that is, $x_{d2} = d_s - d_l$ and $e_2 = x_2 - x_{d2}$.

Selecting sliding surface function which is $s = e_2 + k_3 \int e_2 \mathrm{d}t$, then

$$\begin{aligned} \dot{s} &= \dot{e}_2 + k_3 e_2 \\ &= -\frac{-u_2 - 0.278 n \varnothing g * 10^{-6} - L\rho\left(d_o - d_s + x_2\right)}{M_n} + k_3 e_2. \end{aligned} \tag{20}$$

The selected exponential approach law is

$$\dot{s} = -k_2 s - \varepsilon \operatorname{sgn}(s), \quad k_2 > 0,\ \varepsilon > 0. \tag{21}$$

If $\lim_{s \to 0^+} \dot{s} = \lim_{s \to 0^+} = -k_2 s - \varepsilon \operatorname{sgn}(s) < 0$ and $\lim_{s \to 0^-} \dot{s} = \lim_{s \to 0^-} = -k_2 s - \varepsilon \operatorname{sgn}(s) > 0$, then power reaching law achieves the condition of sliding motion and global reachability.

Furthermore we can obtain the following formula based on (20) and (21):

$$\begin{aligned} \dot{s} &= \frac{-u_2 - 0.278 n \varnothing g * 10^{-6} - L\rho\left(d_o - d_s + x_2\right)}{M_n} + k_3 e_2 \\ &= -k_2 s - \varepsilon \operatorname{sgn}(s). \end{aligned} \tag{22}$$

Hence, $u_2 = -M_n(-k_2 s - \varepsilon \operatorname{sgn}(s) - k_3 e_2) - L\rho(d_o - d_s + x_2) - 0.278 n \varnothing g * 10^{-6}$.

Select the following Lyapunov function: $V(s) = (1/2s^2)$.

Then, $\dot{V}(s) = s\dot{s} = ((-u_2 - 0.278 n \varnothing g * 10^{-6} - L\rho(d_o - d_s + x_2)/M_n) + k_3 e_2)s = s\,(-k_2 s - \varepsilon \operatorname{sgn}(s)) = -k_2 s^2 - s\varepsilon \operatorname{sgn}(s)$.

Because $k_2 > 0$, $\varepsilon > 0$, $\dot{V}(s) < 0$, the system is stable.

4. Design of Fuzzy Sliding Mode Controller

In this paper, approach laws $\dot{s} = -k_1 |s|^a \operatorname{sgn}(s)$ and $\dot{s} = -k_2 s - \varepsilon \operatorname{sgn}(s)$ are selected, in which k_1, k_2, and ε are appropriate parameters to be selected to ensure that the system state trajectories reach to sliding surface rapidly and suppress chattering. Thus, this paper proposes fuzzy SMC based on reaching laws. The use of fuzzy control instead of traditional control solves the chattering problem of the air-conditioning system while improving the dynamic quality of the system and ensuring the good robustness of the system.

4.1. Parameter Fuzzification. This study designs a two-dimensional fuzzy controller to meet the requirements for a stable air-conditioning system under the conditions of temperature parameter changes and interference effects during the operation of the air conditioner. The input signal of fuzzy law is the temperature error e and its derivative (d_e/d_t). The output signal is the reaching law parameters ε, k_1, and k_2. The fuzzy subsets of input and output variables are {NB, NM, NS, ZO, PS, PM, PB} and quantified in the (−1, 1) area. The membership function is selected as a symmetric triangular function, and each value of the fuzzy subset has the same range width [41].

4.2. Fuzzy Rules. According to the principle of SMC, the parameters of the reaching law k_1, k_2, and ε determine the fuzzy rules, as shown in Tables 1–3, respectively.

4.3. Fuzzy Reasoning. This paper uses the center of gravity method to complete deblurring. The output result after deblurring is presented as follows:

$$x_0 = \frac{\sum_{i=1}^{n} x_i u_c(x_i)}{\sum_{i=1}^{n} x_i}, \tag{23}$$

where x_0 is the output result after defuzzification, x_i is the output variable, and $u_c(x_i)$ is the membership function corresponding to x_i.

5. Simulation Analysis

This study uses MATLAB/Simulink to establish the simulation model of the central air-conditioning system. Fuzzy sliding mode control and traditional PID control methods are used to compare and verify the correctness and feasibility of the proposed strategy.

Assuming that the room has a length, width, and height of 16, 10, and 4 m, respectively, the indoor air density, indoor air specific heat capacity, coefficient of thermal conductivity of wall materials, and thickness of the wall material are $\rho = 1.204$ kg/m^3, $C = 1.003$ J/(Kg ∗ K), $\lambda = 0.58$ W/(mK), and $\delta = 0.5$ m, respectively. Figure 2 illustrates the heat generated by sunlight radiating through the glass in the room.

The indoor temperature is set to 25°C, and the input of outdoor temperature and humidity changes according to the data collected in Suzhou in July, as shown in Figures 3 and 4.

Assuming that the initial indoor ambient temperature is 26°C and the moisture content is 13 g/kg, the enthalpy chart demonstrates that the air moisture content is 12 g/kg when the temperature is set to 25°C and the optimum indoor relative humidity is 60%. Therefore, the ideal air moisture content is 12 g/kg.

The comparison of indoor temperature and humidity responses under the sliding mode and the PID control strategies are illustrated in Figures 5 and 6, respectively.

The air volume input of indoor temperature and humidity control under the sliding mode and PID control strategies is compared and illustrated in Figures 7 and 8, respectively.

Figures 5–8 demonstrate that the air conditioner system with independent control of temperature and humidity using the fuzzy SMC strategy can achieve the set temperature

Table 1: Fuzzy rule with parameter k_1.

e_1	$\dot{e}_1$						
	NB	NM	NS	ZO	PS	PM	PB
NB	PB	PB	PM	PS	PS	ZO	ZO
NM	PB	PB	PM	PS	PS	ZO	NS
NS	PM	PM	PM	ZO	ZO	NS	NS
ZO	PM	PM	PS	NS	NS	NM	NM
PS	PS	PS	ZO	NS	NS	NM	NM
PM	PS	ZO	NS	NM	NM	NM	NB
PB	ZO	ZO	NM	NM	NM	NB	NB

Table 2: Fuzzy rule with parameter k_2.

e_2	$\dot{e}_2$						
	NB	NM	NS	ZO	PS	PM	PB
NB	NB	NB	NM	NM	NS	ZO	ZO
NM	NB	NB	NM	NS	NS	ZO	ZO
NS	NB	NM	NS	NS	ZO	PS	PS
ZO	NM	NM	NS	ZO	PS	PM	PM
PS	NM	NS	ZO	PS	PS	PM	PB
PM	ZO	ZO	PS	PS	PM	PB	PB
PB	ZO	ZO	PS	PM	PM	PB	PB

Table 3: Fuzzy rule with parameter ε.

e_2	$\dot{e}_2$						
	NB	NM	NS	ZO	PS	PM	PB
NB	NB	NB	NM	NM	NS	ZO	ZO
NM	NB	NB	NM	NS	NS	ZO	PS
NS	NB	NM	NS	NS	ZO	PS	PS
ZO	NM	NS	NS	ZO	PS	PM	PM
PS	NM	NS	ZO	PS	PM	PM	PB
PM	NS	ZO	PS	PS	PM	PB	PB
PB	ZO	ZO	PS	PM	PM	PB	PB

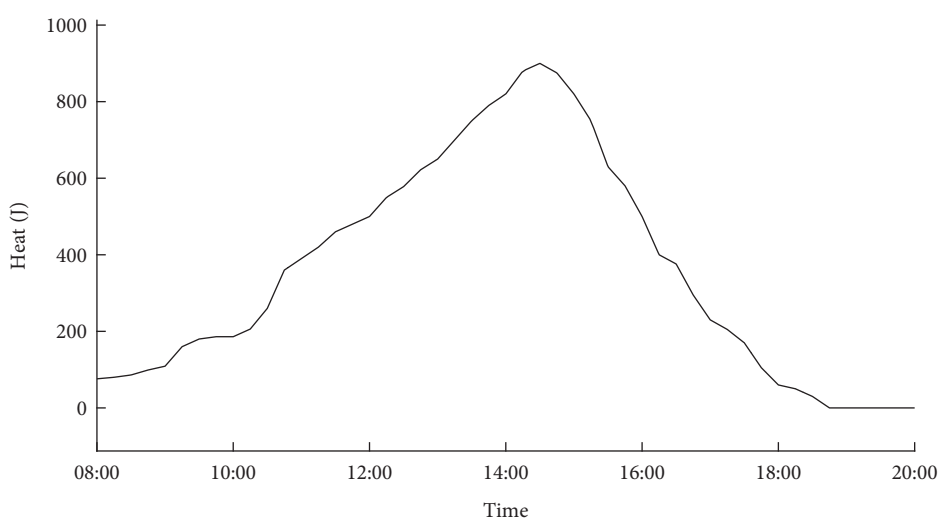

Figure 2: Heat from solar radiation.

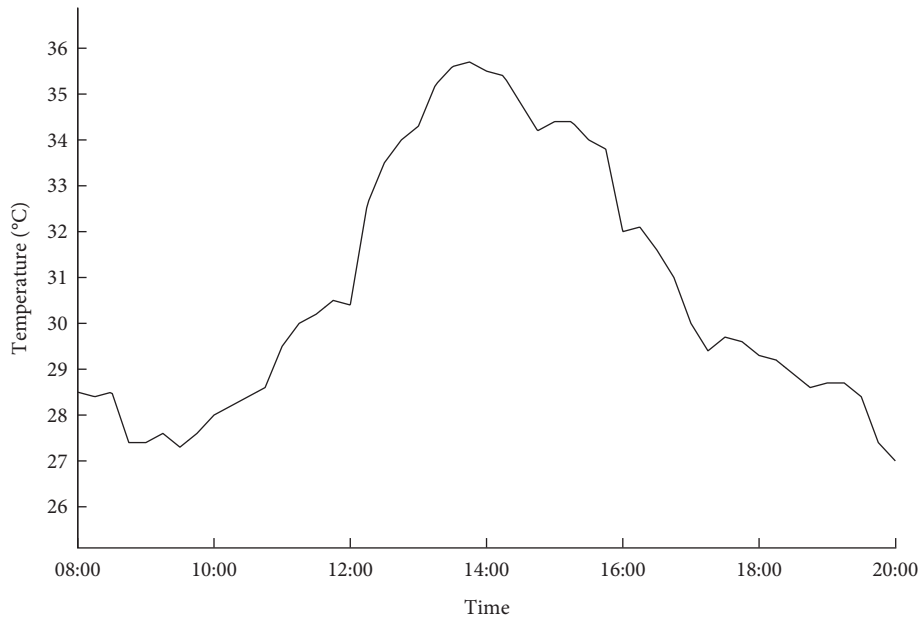

Figure 3: Outdoor temperature change.

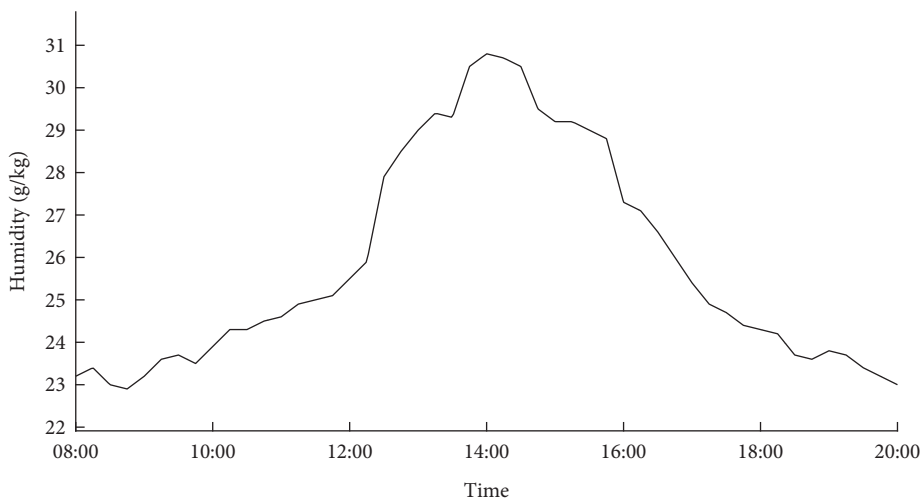

Figure 4: Outdoor humidity change.

and humidity faster when the input air volume is only slightly different compared with the PID control. Meanwhile, it can be seen in Figures 5 and 6 that, compared with the air-conditioning system under PID control, the fuzzy sliding mode control strategy has minimal vibration at the preset humidity and temperature. From the data derived from the figure, it can be seen that the indoor temperature reaches the expected temperature time under fuzzy sliding mode control, fuzzy PID, and PID strategies: 7.668 min, 9.630 min, and 11.256 min, and the temperature overshoots are 0.0939, 0.3095, and 0.3789. The time for indoor humidity to reach the expected humidity is 11.256 min, 17.148 min, and 18.954 min. The humidity overshoot is 0.1145, 0.2284, and 0.3272.

So, you can get the following result.

Theorem 1. *The temperature error of the fuzzy sliding mode control strategy is only 30% and 24% of the other two methods.*

Theorem 2. *The humidity error of the fuzzy sliding mode control strategy is 50% and 35% of the other two methods.*

Theorem 3. *Compared with the traditional PID control technique, the higher accuracy of the SMC strategy ensures that the indoor environment is maintained at the desired level and meets the comfort requirements of the human body.*

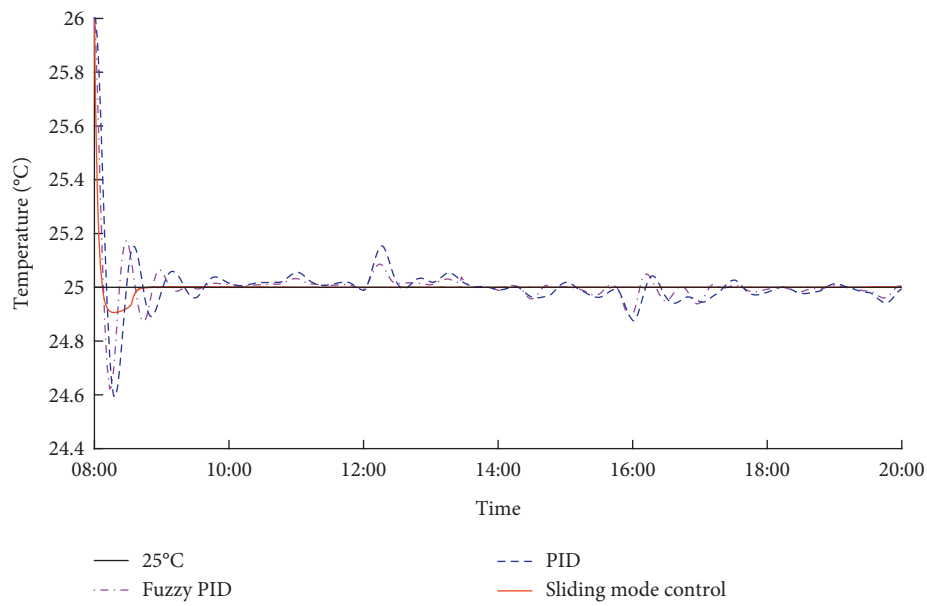

Figure 5: Indoor temperature response.

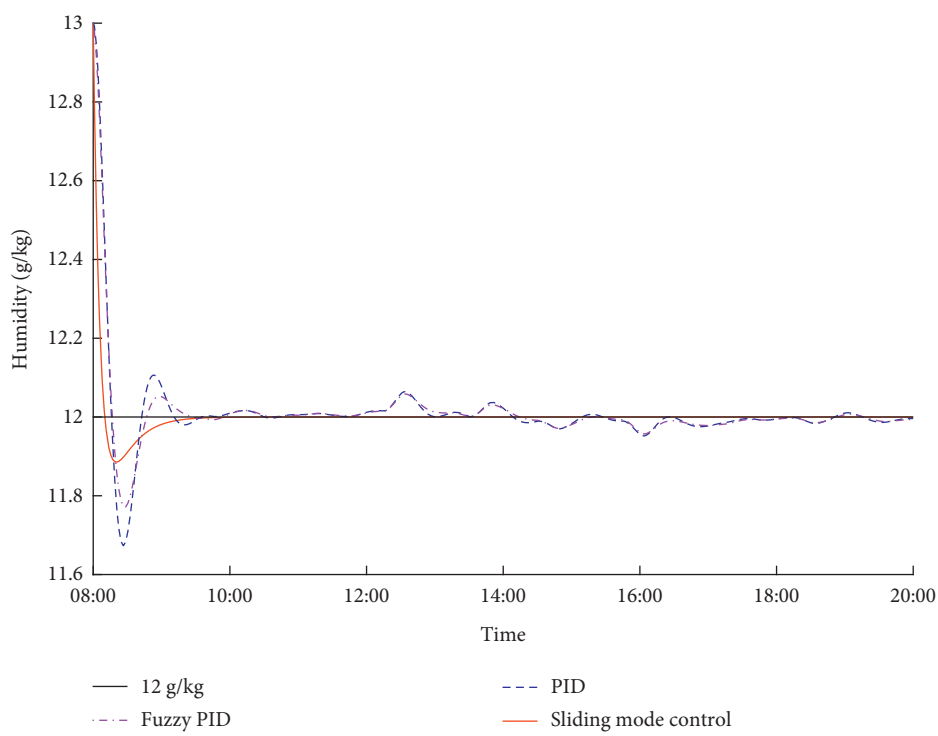

Figure 6: Indoor humidity response.

Under the above circumstances, assuming that 10 people are inside the office, the fresh air input can be used to estimate the CO_2 concentration in the indoor air within a day with the office CO_2 concentration accounting for 0.045% of the air at 8:00. The simulation results are illustrated in Figure 9.

Figure 9 shows that the air conditioner with independent control of temperature and humidity using the fuzzy SMC can ensure a maximum indoor CO_2 concentration of 0.1% [42], which belongs to fresh air and meets the requirements of human comfort.

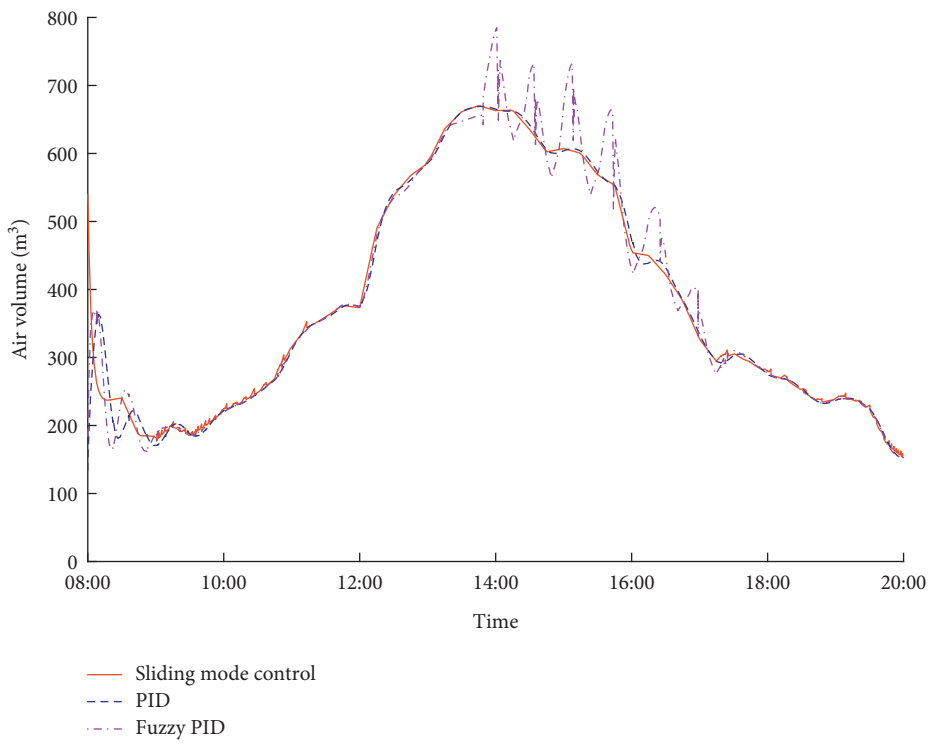

Figure 7: Temperature control input air volume.

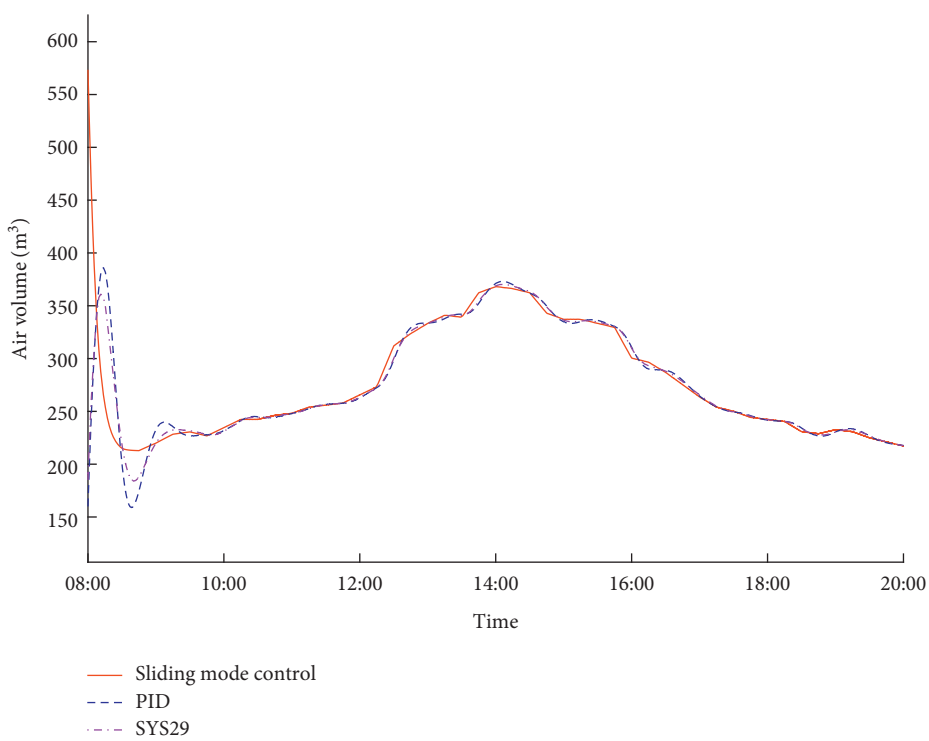

Figure 8: Humidity control input air volume.

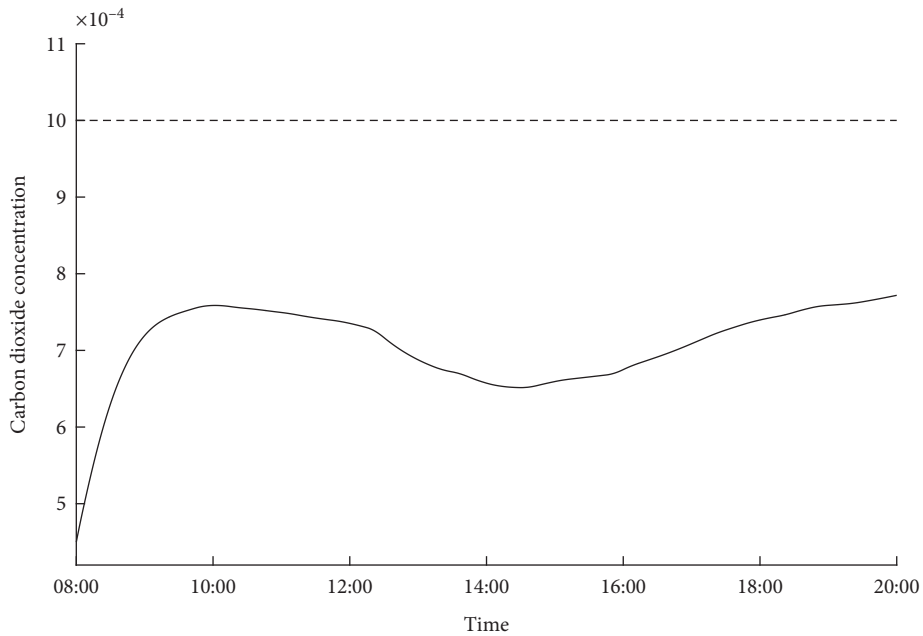

Figure 9: CO_2 content assessment.

6. Conclusion

This paper proposes a fuzzy sliding mode approach for the independent control of temperature and humidity in air-conditioning systems. By analyzing the indoor environmental effect, mathematical models for room temperature, humidity, and CO_2 concentration are developed. Compared with the traditional PID method, the simulation results show that the fuzzy-rules-based SMC achieves better dynamic performance. However, the proposed method is only applicable to the temperature- and humidity-independent control air-conditioning system in solution dehumidification mode. If the rotor dehumidification is used, it may lead to a large deviation in temperature control due to the coupling of heat and humidity. It is expected that the following research can overcome the temperature and humidity coupling of the air conditioner happening. The results of this study can provide practical guidance for engineering applications.

Data Availability

The data of outdoor temperature and humidity changes in this paper are measured by the author. The data used to support the findings of this study are available from the corresponding author upon request.

Conflicts of Interest

The authors declare that they have no conflicts of interest.

Acknowledgments

This work was supported in part by the NSFC under Grant nos. 61803279, 11871366, and 61672371, the Qing Lan Project of Jiangsu, the China Postdoctoral Science Foundation under Grant no. 2020M671596, the Open Project Funding from Anhui Province Key Laboratory of Intelligent Building and Building Energy Saving, Anhui Jianzhu University, under Grant no. IBBE2018KX02ZD, the Natural Science Foundation of the Jiangsu Higher Education Institutions of China under Grant no. 18KJB460026, the Suzhou Science and Technology Foundation under Grant no. SYG201813, and the Jiangsu Province Graduate Practice Innovation Program under Grant no. SJCX19_0844.

References

[1] M. Castilla, J. D. Álvarez, J. E. Normey-Rico, and F. Rodríguez, "Thermal comfort control using a non-linear MPC strategy: a real case of study in a bioclimatic building," *Journal of Process Control*, vol. 24, no. 6, pp. 703–713, 2014.

[2] R. M. Lazzarin and F. Castellotti, "A new heat pump desiccant dehumidifier for supermarket application," *Energy and Buildings*, vol. 39, no. 1, pp. 59–65, 2007.

[3] X. L. Hao, G. Q. Zhang, Y. M. Chen, S. Zou, and D. J. Moschandreas, "A combined system of chilled ceiling, displacement ventilation and desiccant dehumidification," *Building and Environment*, vol. 42, no. 9, pp. 3298–3308, 2007.

[4] P. Zhang, S. Cao, L. Wu, and J. Lv, "Status and development of temperature and humidity independent control air conditioning system," *Shanghai Energy Saving*, vol. 10, pp. 583–587, 2017.

[5] A. Abdel Hamid, S. F. Rezeka, and A. M. Saleh, "Fuzzy logic control of air-conditioning system in residential buildings," *Alexandria Engineering Journal*, vol. 54, no. 3, pp. 395–403, 2015.

[6] S. A. Shahnawaz, M. M. Shah, H. Novia, and H. Abd Rahman, "Fuzzy logic based energy saving technique for a central air conditioning system," *Energy and Buildings*, vol. 32, no. 7, pp. 1222–1234, 2007.

[7] G. Li, "Fuzzy PID research on the temperature control system of central air conditioning based on genetic algorithms,"

Information Technology Journal, vol. 12, no. 24, pp. 8313–8317, 2013.

[8] S. Soyguder, M. Karakose, and H. Alli, "Design and simulation of self-tuning PID-type fuzzy adaptive control for an expert HVAC system," *Expert Systems with Applications*, vol. 36, no. 3, pp. 4566–4573, 2009.

[9] F. Ascione, N. Bianco, C. De Stasio, G. M. Mauro, and G. P. Vanoli, "Simulation-based model predictive control by the multi-objective optimization of building energy performance and thermal comfort," *Energy and Buildings*, vol. 111, pp. 131–144, 2016.

[10] T. Yang, N. Sun, H. Chen, and Y. Fang, "Neural network-based adaptive antiswing control of an underactuated ship-mounted crane with roll motions and input dead zones," *IEEE Transactions on Neural Networks and Learning Systems*, vol. 31, no. 3, pp. 901–914, 2020.

[11] N. Sun, D. Liang, Y. Wu, Y. Chen, Y. Qin, and Y. Fang, "Adaptive control for pneumatic artifificial muscle systems with parametric uncertainties and unidirectional input constraints," *IEEE Transactions on Industrial Informatics*, vol. 16, no. 2, pp. 969–979, 2019.

[12] W. Hu, Q. Zhu, and H. R. Karimi, "Some improved Razumikhin stability criteria for impulsive stochastic delay differential systems," *IEEE Transactions on Automatic Control*, vol. 64, no. 12, pp. 5207–5213, 2019.

[13] H. Wang and Q. Zhu, "Global stabilization of stochastic nonlinear systems via $C1$ and $C{\infty }$ controllers," *IEEE Transactions on Automatic Control*, vol. 62, no. 11, pp. 5880–5887, 2017.

[14] Q. Zhu and H. Wang, "Output feedback stabilization of stochastic feedforward systems with unknown control coefficients and unknown output function," *Automatica*, vol. 87, pp. 166–175, 2018.

[15] Q. Zhu, "Stabilization of stochastic nonlinear delay systems with exogenous disturbances and the event-triggered feedback control," *IEEE Transactions on Automatic Control*, vol. 64, no. 9, pp. 3764–3771, 2019.

[16] H. Wang and Q. Zhu, "Adaptive output feedback control of stochastic nonholonomic systems with nonlinear parameterization," *Automatica*, vol. 98, pp. 247–255, 2018.

[17] W. Hu and Q. Zhu, "Stability analysis of impulsive stochastic delayed differential systems with unbounded delays," *Systems & Control Letters*, vol. 136, Article ID 104606, 2020.

[18] V. Utkin, "Variable structure systems with sliding modes," *IEEE Transactions on Automatic Control*, vol. 22, no. 2, pp. 212–222, 1977.

[19] J. Liu, Z. Wu, J. Yu, and M. Tan, "Sliding mode fuzzy control-based path-following control for a dolphin robot," *Science China Information Sciences*, vol. 61, no. 2, pp. 240–242, 2018.

[20] Z. Zhang, Y. Niu, and H. R. Karimi, "Sliding mode control of interval type-2 fuzzy systems under round-robin scheduling protocol," *IEEE Transactions on Systems, Man, and Cybernetics Systems*, pp. 1–11, 2019.

[21] W. Qi, G. Zong, and H. R. Karimi, "Finite-time observer-based sliding mode control for quantized semi-Markov switching systems with application," *IEEE Transactions on Industrial Informatics*, vol. 16, no. 2, pp. 1259–1271, 2020.

[22] Q. P. Ha, Q. H. Nguyen, D. C. Rye, and H. F. Durrant-Whyte, "Fuzzy sliding-mode controllers with applications," *IEEE Transactions on Industrial Electronics*, vol. 48, no. 1, pp. 38–46, 2001.

[23] B. Jiang, H. R. Karimi, Y. Kao, and C. Gao, "A novel robust fuzzy integral sliding mode control for nonlinear semi-markovian jump T-S fuzzy systems," *IEEE Transactions on Fuzzy Systems*, vol. 26, no. 6, pp. 3594–3604, 2018.

[24] B. Jiang, H. R. Karimi, Y. Kao, and C. Gao, "Adaptive control of nonlinear semi-Markovian jump T-S fuzzy systems with immeasurable premise variables via sliding mode observer," *IEEE Transactions on Cybernetics*, vol. 50, no. 2, pp. 810–820, 2018.

[25] H. R. Karimi, "A sliding mode approach to H ∞ synchronization of master-slave time-delay systems with Markovian jumping parameters and nonlinear uncertainties," *Journal of the Franklin Institute*, vol. 349, no. 4, pp. 1480–1496, 2012.

[26] Y. Wang, H. R. Karimi, H. Shen, Z. Fang, and M. Liu, "Fuzzy-model-based sliding mode control of nonlinear descriptor systems," *IEEE Transactions on Cybernetics*, vol. 49, no. 9, pp. 3409–3419, 2019.

[27] Z. Wu, B. Jiang, and Y. Kao, "Finite-time H ∞ filtering for Itô stochastic Markovian jump systems with distributed time-varying delays based on optimisation algorithm," *IET Control Theory & Applications*, vol. 13, no. 5, pp. 702–710, 2019.

[28] Q. Zhu and T. Huang, "Stability analysis for a class of stochastic delay nonlinear systems driven by G-Brownian motion," *Systems & Control Letters*, vol. 140, Article ID 104699, 2020.

[29] B. Wang and Q. Zhu, "Stability analysis of semi-Markov switched stochastic systems," *Automatica*, vol. 94, pp. 72–80, 2018.

[30] B. Wang and Q. Zhu, "Stability analysis of discrete-time semi-Markov jump linear systems," *IEEE Transactions on Automatic Control*, p. 1, 2020.

[31] X. Jin, H. Ren, and X. Xiao, "Prediction-based online optimal control of outdoor air of multi-zone VAV air conditioning systems," *Energy and Buildings*, vol. 37, no. 9, pp. 939–944, 2005.

[32] Y. Zhu, X. Jin, Z. Du, and X. Fan, "Control and energy simulation of variable refrigerant flow air conditioning system combined with outdoor air processing unit," *Applied Thermal Engineering*, vol. 64, no. 2, pp. 385–395, 2014.

[33] X. Xiao, C. Liang, C. Tao, and L. Tong, "Simulation and analysis of a novel cascade double cooling source temperature and humidity independent control air-conditioning system," *IOP Conference Series: Earth and Environmental Science*, vol. 242, Article ID 022068, 2019.

[34] R. Whalley and A. Abdul-Ameer, "Heating, ventilation and air conditioning system modelling," *Building and Environment*, vol. 46, no. 3, pp. 643–656, 2011.

[35] P. D. Morosan, R. Bourdais, D. Dumur, and J. Buisson, "Building temperature regulation using a distributed model predictive control," *Energy and Buildings*, vol. 42, no. 9, pp. 1445–1452, 2010.

[36] A. Afram and F. Janabi-Sharifi, "Theory and applications of HVAC control systems-a review of model predictive control (MPC)," *Building and Environment*, vol. 72, pp. 343–355, 2014.

[37] G. Ulpiani, S. Summa, and C. Di Perna, "Sunspace coupling with hyper-insulated buildings: investigation of the benefits of heat recovery via controlled mechanical ventilation," *Solar Energy*, vol. 181, pp. 17–26, 2019.

[38] R. E. L. Diasty, P. Fazio, and I. Budaiwi, "Modelling of indoor air humidity, the dynamic behavior within an enclosure," *Energy and Building*, vol. 19, pp. 61–63, 1992.

[39] X. Chen, Q. Wang, and J. Srebric, "Model predictive control for indoor thermal comfort and energy optimization using occupant feedback," *Energy and Buildings*, vol. 102, pp. 357–369, 2015.

[40] S. Yang, M. P. Wan, B. F. Ng et al., "A state-space thermal model incorporating humidity and thermal comfort for

model predictive control in buildings," *Energy and Buildings*, vol. 170, pp. 25–39, 2018.

[41] M. Mahmoud, M. A. Mohamed, S. E. Mohamed, F. S. Sabry, and F. G. Fayez, "An adaptive neuro-fuzzy sliding mode controller for MIMO systems with disturbance," *Chinese Journal of Chemical Engineering*, vol. 25, pp. 463–476, 2017.

[42] GB/T18883-2002: Indoor Air Quality Standards.

Hindawi
Complexity
Volume 2020, Article ID 6549410, 14 pages
https://doi.org/10.1155/2020/6549410

Research Article

Learning-Based Dark and Blurred Underwater Image Restoration

Yifeng Xu,[1,2] Huigang Wang,[1] Garth Douglas Cooper,[1] Shaowei Rong,[1] and Weitao Sun[1]

[1]*School of Marine Science and Technology, Northwestern Polytechnical University, Xi'an, Shaanxi 710072, China*
[2]*Jinhua Polytechnic, Jinhua, Zhejiang 321017, China*

Correspondence should be addressed to Huigang Wang; wanghg74@nwpu.edu.cn

Received 24 May 2020; Revised 26 June 2020; Accepted 7 July 2020; Published 1 August 2020

Guest Editor: Hamid Reza Karimi

Underwater image processing is a difficult subtopic in the field of computer vision due to the complex underwater environment. Since the light is absorbed and scattered, underwater images have many distortions such as underexposure, blurriness, and color cast. The poor quality hinders subsequent processing such as image classification, object detection, or segmentation. In this paper, we propose a method to collect underwater image pairs by placing two tanks in front of the camera. Due to the high-quality training data, the proposed restoration algorithm based on deep learning achieves inspiring results for underwater images taken in a low-light environment. The proposed method solves two of the most challenging problems for underwater image: darkness and fuzziness. The experimental results show that the proposed method surpasses most other methods.

1. Introduction

Recently, developing, exploring, and protecting the ocean's resources have received significant attention from the international community. Following the recent development of sea research, the autonomous underwater vehicles (AUVs) and remotely operated vehicles (ROVs) have been widely used as the carrier of various sensing devices. Sonars and vision camera are two kinds of major perception equipment to detect and recognize objects in underwater environments. In general, sonar is suitable for long-range detection and generates low-resolution image. However, these vision sensors are used for short-range and high-resolution identification.

The underwater imaging model could help us better understand underwater optical propagation. The diagram of light transmission in underwater is shown in Figure 1. The optical sensor receives three types of light which are shown as three different arrow symbols. The first solid arrow represents the direct of transmission of the light from the subject without the obstruction and scattering of particles. The second kind of light is the forward scattering light which is reflected from the objects and scattered by particles. The third kind of light is background scattering light which comes from the background light and is reflected by the suspended particles. According to the model, the imaging process of underwater images can be represented as the linear superposition of three components [1], shown as follows:

$$E_r = E_d + E_f + E_b, \tag{1}$$

where E_r represents the total received light. E_d, E_f, and E_b represent the direct transmission light, the forward scattering light, and the background scattering light, respectively. The background scattering light comes from all scattered light of the suspended particles except the objects. This kind of light blurs the visual effect and reduces the clarity of underwater images. If the object is close to the camera, the forward scattering light should have very little value in the direction of the camera. In this situation, the component E_f often is ignored for easier analysis of the model [2], so (1) can be shortened as follows:

$$E_r = E_d + E_b. \tag{2}$$

Due to light absorption and scattering in an underwater environment, the underwater images generally have the following problems: low contrast and brightness, blurry details, color distortion, and bright specks. In addition, the dark environment is also encountered in the period of deep-

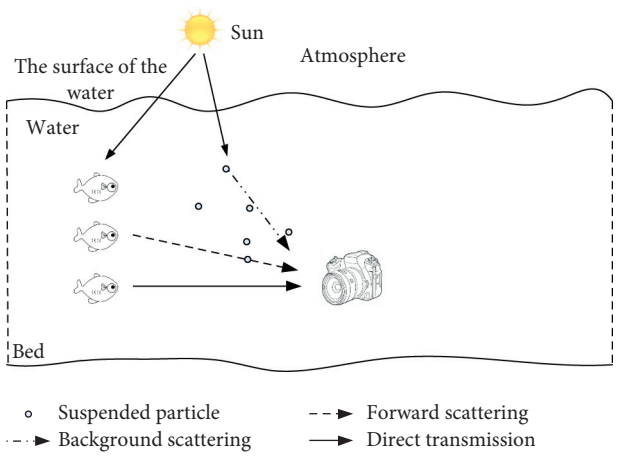

Figure 1: Diagram of light transmission in underwater.

sea exploration and complex environmental detection. The camera flash also can be used to increase light in the environment; however, it is still necessary that the restoration algorithms are highly capable in an underwater dark environment when the flash is not available. The case can be divided into three primary factors: (1) The flash is not allowed on certain occasions such as the detection of certain sea creatures or passive detection of underwater intrusion. (2) The flash could be ineffective in complex surroundings. For example, the light from the flash could be blocked by the complicated structure of bridge bases, ports, and sea wrecks. (3) The battery's power limits the flash exposure range. Even when the flash is turned on, there are larger areas away from the areas illuminated by flash. The above issues mentioned in a special submerged scene are urgently needed to be addressed. In this paper, we mainly focus on restoring the dark and blurred underwater images.

The methods related to image restoration can be divided into traditional methods and "modern" data-driven techniques. The former type of method includes the model-based and the model-free methods, detailed in Section 2. The latter method utilizes big data to learn the model and mainly uses machine learning techniques to complete the task. Deep learning methods are an important technique in machine learning. Deep learning methods have made rapid progress since 2012 in various computer vision tasks. There are three components that can vastly improve deep learning methods: big data, improved networks, and powerful hardware. Big data provides not only adequate data for training but also a standard answer (Ground Truth) to the algorithms. In other words, deep learning methods "peek" at the ground truth while traditional methods go without it.

The contributions of this paper are summarized as follows:

(1) The image pairs (the dark and blurred underwater images and the corresponding normal exposure and clear images) are collected and provided to a neural network. We use a new method to collect the image pairs (the dark and blurred underwater images and the corresponding normal exposure and clear images). In particular, the objects are placed in the air, and the light passes through both air and water to the camera to simulate the underwater environment. The collecting method is proved to be effective to generate the underwater images in theory and practice

(2) The proposed algorithm restores the images captured in the extremely dark and blurred underwater environment. The restoration results are beyond most underwater enhancement and restoration methods.

The rest of this paper is organized as follows. Related work about underwater restoration is proposed in Section 2. The new framework of the neural network is shown in Section 3. Detailed experimental results are shown in Section 4. Several problems which need to be further studied are proposed in Section 5. The paper concludes with Section 6.

2. Related Work

The restoration of dark underwater images has been extensively studied in huge works of literature. In this section, we provide a short review of related work. In our research, we only consider that the underwater image restoration relies on a single image. The categories of single underwater image restoration are shown in Figure 2. The algorithms can be divided into two categories: traditional methods and machine learning methods [3].

Traditional methods include image enhancement and restoration and aim at improving the image quality which can be performed in both spatial and frequency domains [4]. The former is often a subjective process, a heuristic procedure designed to improve low-quality images, and without degradation model. On the other hand, the latter formulates an objective criterion and attempts to reconstruct a degraded image by using the prior knowledge of the degradation. In other words, it models the degradation procedure and applies the inverse process to recover the ideal image. The model is called the underwater image formation model (IFM) in the underwater scene. Image enhancement is equivalent to a blind operation, while image restoration tries to model the reverse procedure of the degradation. The difference between image enhancement and image restoration is listed in Table 1.

Early studies of underwater IFM-free methods directly used the corresponding methods that were used out of the water. Later methods are designed according to the distinguishing features found underwater, such as haze, color cast, and low contrast. The IFM-free methods can be divided into two categories: spatial-domain [5, 6] and transform-domain methods [7–9].

The methods based on spatial domain complete a redistribution about intensity histogram by expanding gray levels. It works in different color models such as Red-Green-Blue (RBG), Hue-Saturation-Intensity (HSI), and Hue-Saturation-Value (HSV). The color models can also be divided into single-color model (SCM) and multiple-color model (MCM) by class number of color models. The typical SCM-based image enhancement methods, Histogram Equalization (HE) [10], Contrast Limited Adaptive

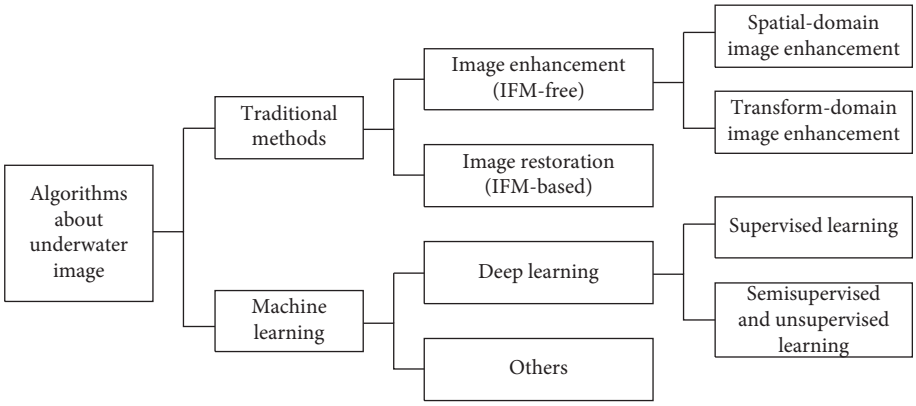

Figure 2: Categories of the quality improvement algorithms about single underwater image.

Table 1: The key difference between image enhancement and image restoration.

Criterion	Enhancement	Restoration
Result evaluation	Objective	Subjective
Modeling of degradation	No	Yes
Use of prior knowledge	No	Yes

Histogram Equalization (CLAHE) [11], and Generalized Unsharp Masking (GUM) [12], work in RGB color model. Many researchers such as Torres-Méndez et al. [13], Iqbal et al. [14], and Huang et al. [15] proposed MCM-based image enhancement. For example, Torres-Méndez et al. [13] and Iqbal et al. [14] used Markov Random Field (MRF) and Integrated Colour Model (ICM) to describe the correlation procedure of distortion. Huang et al. [15] proposed the relative global histogram stretching (RGHS) strategy in RGB and CIE-Lab color models.

An image can be explained in frequency domain. The high-frequency component in an image usually indicates the edge region where the brightness value or color value of the pixels have sudden change, whereas the low-frequency component indicates the flat and large area. In order to achieve a higher-quality image, the high-frequency component needs more data, while the low-frequency component does not require as much data. Firstly, the transform-domain image enhancement methods convert the spatial domain image into the frequency domain through the conversion methods of the spatial-transform domain such as the Fourier Transform [16]. Secondly, the quality of underwater images can be improved by increasing the high-frequency component and suppressing the low-frequency component, synchronously. In 2010, Prabhakar et al. [17] used a homomorphic filter, an anisotropic filter, and an adaptive wavelet subband threshold to correct nonuniform illumination and smooth and denoise the image. In 2016, Amjad et al. presented the wavelet-based fusion method [18] to improve the low-quality issue of underwater images. In 2017, Vasamsetti et al. proposed a wavelet-based perspective technique [19] for underwater images, which performed the discrete wavelet transform (DWT) [20] on the RGB channels to generate two decomposition levels and reconstruct the grayscale images.

The image formation model-based (IFM-based) method is one of the traditional methods. It analyzes the underwater imaging mechanism and law of light propagation in water then constructs a physical model to restore high-quality images. Considering the optical properties, different prior-based methods are used for underwater image restoration. These methods include dark channel prior (DCP) [21], underwater dark channel prior (UDCP) [22], red channel prior (RCP) [23], and blurriness and light prior [24]. According to the priors, the background light (BL) and transmission map (TM) can be derived and entered into the IFM model for image restoration.

In recent years, many researchers have explored machine learning technology to improve the quality of the underwater images. Support Vector Machines (SVM) [25], one of the machine learning methods, was mostly used in underwater image object detection [26]. The deterministic annealing algorithm [27, 28] is developed based on Lyapunov's functional method. It can be used in the learning of network parameters. During the past few decades, deep learning has achieved rapid development.

Deep learning works well by using convolutional neural networks (CNNs) [29, 30] or generative adversarial networks (GANs) [31] by backpropagation training [32]. The model in deep learning is unlike the physical model in the image restoration. The methods based on deep learning are neither image enhancement nor image restoration. Depending on the various models, deep learning can be divided into several categories. Sun et al. [33] suggested the pixel-to-pixel (P2P) network to enhance underwater images. The encoder part is composed of three convolutional layers, while the decoder is three deconvolutional layers. Underwater generative adversarial network (UGAN) [34] is proposed to improve the underwater image quality. The discriminator of UGAN is Wasserstein GAN with gradient penalty (WGANGP) [35] to soft constraint on the output. For solving the limitation of underwater images, Anwar et al. [36] proposed an end-to-end model UWCNN trained by the synthetic image. To take advantage of the popular dense connections, residual network, and multiscale network, the

multiscale dense block (MSDB) algorithm [37] is proposed to enhance the underwater images. Not only the single-branch network, but also the multibranch network is designed to learn the different features of the same input. For example, UIE-Net [38] is composed of three subnetworks. In general, deep learning is divided into two classes: supervised learning and semisupervised/unsupervised learning. Mainstream technology in the two learning methods is CNN and GAN, respectively.

3. Method

3.1. Procedure Pipeline of Dark and Blurred Underwater Image. The pipelines based on the traditional methods and deep learning can be used to process the dark and blurred underwater images, as shown in Figure 3. The dark environment is defined as a 100-fold reduction in exposure amount to normal exposure in our study. The blurred underwater environment is made by adding a little milk powder. The traditional methods are divided into the single algorithm and the cascading algorithms, shown as the upper subimage surrounded by the dotted box.

The traditional pipeline using a single algorithm works well on the normal-light underwater images, shown in line A of Figure 3. However, it has less consideration for the low-light environment, often having poor performance in low-light underwater environments.

The second type of traditional method cascades multiple low-level vision processing procedures, shown in line B of Figure 3. The first step is luminosity scaling of the dark images. The images taken by the Nikon D700 made in Japan are RAW-format images with 14 bits. The maximum brightness value of the images is 2^{14}, 16384. Experiments show that the brightness values of the pixels are less than 50 in the underexposure 100 times environment. The procedure of luminosity scaling can be written as $(v_x/v_{\max}) \times 16384$, where v_x represents the brightness value of a pixel and $v_{\max}$ represents the max brightness value of all pixels. The simple luminosity scaling initially solves the issue of underexposure, but simultaneously amplifies the noise while amplifying the information. For denoising the amplified noise, the next step noise reduction is immediately behind luminosity scaling. Considering the fact that BM3D [39] is a classic noise reduction algorithm, we select it as a baseline in the step of denoising. After brightness enhancement and noise reduction, the last step is underwater image enhancement and restoration.

The third type of traditional method is also a cascade method, but it uses a single method to accomplish both brightness enhancement and denoising, shown in line C of Figure 3. Recently, many algorithms were proposed to recover the low-light images while keeping a high SNR, such as the Robust Retinex Model algorithm [40], LIME [41], etc. Because LIME is a simple yet effective low-light image enhancement (LIME) method, we select LIME as the baseline in our study. The principle of LIME is that firstly the illumination value of each pixel is estimated individually by calculating the maximum value in RGB channels. Further, the initial illumination map is refined by imposing a structure prior to it. Finally, the enhancement can be achieved by the constructed illumination map.

Unlike the traditional methods without ground truth images, a general deep learning neural network must train the data before the test phase, shown in the bottom of the pipelines figure. The deep learning method includes the training phase (line D_1) and the test phase (line D_2). Data in the training phase is taken in the atmosphere by placed tanks in front of the camera, while data in the test phase is taken from the water. The details about the procedure of collecting data are described in the next section. In our work, the deep learning convolutional neural network [42] is proposed for dark and blurred underwater images. Specifically, a network similar to U-net [43] is used for processing, inspired by the recent algorithms [43, 44].

The structure of the proposed deep learning network is shown in Figure 4. The raw images are entered into the input of the network, and the restored images are output.

In the network, block 1 includes three layers: two convolutional layers abbreviated as conv2d(32, [3, 3]) and max pooling2d. The parameter "32, [3, 3]" in convolutional layers represents that output array size is 32 and convolutional kernel size is 3×3. The blocks from the 2nd to the 8th, respectively, include two conv2d(64, [3, 3]) and max pooling2d, two conv2d(128, [3, 3]) and max pooling2d, two conv2d(256, [3, 3]) and max pooling2d, two conv2d(512, [3, 3]), two conv2d(256, [3, 3]), two conv2d(128, [3, 3]), and two conv2d(64, [3, 3]). Block 9 includes two conv2d(32, [3, 3]) and conv2d(12, [1, 1]) layers.

The U-net network belongs to autoencoder neural networks [45, 46], which are trained to attempt to map the input to the output. The autoencoder network is divided into two parts: an encoder function $h = F(x)$ and a decoder function $G(h)$ which generates the reconstruction, respectively, shown as the left and the right parts of Figure 4. The skip connection shown as the blue arrow in Figure 4 transfers weight, avoiding gradient disappearance.

The algorithm is an offline one; it is necessary to provide the computational complexity analysis. Computational complexity is a concept that focuses on the amount of computing resources for particular kinds of tasks. Each operation of deep learning requires a lot of computing resources. For convolutional layer, each input feature has a $F_w * F_h$ convolutional kernel, and output feature has a $W_{\text{cout}} * H_{\text{cout}}$ convolutional kernel. At the same time, the number of input and output features is defined as N_{in} and N_{cout}, respectively. If multiplication and addition are required for each element, all operations of the convolution layer can be calculated as $2 * N_{\text{in}} * N_{\text{cout}} * F_w * F_h * W_{\text{cout}} * H_{\text{cout}}$. For ReLU activation layer, there is only one compare operation in each cell. So, the operation number of ReLU is N_{cout}. For pooling layer, each filter has the size of $P_w * P_h$, and output is N_{pout} images which have the size of $W_{\text{pout}} * H_{\text{pout}}$. The operation number of pooling layer can be calculated as $P_w * P_w * W_{\text{pout}} * H_{\text{pout}} * N_{\text{pout}}$.

3.2. Procedure of Collecting Data. The deep learning portion is divided into three methods: full supervision, semi-supervision, and unsupervised methods according to whether

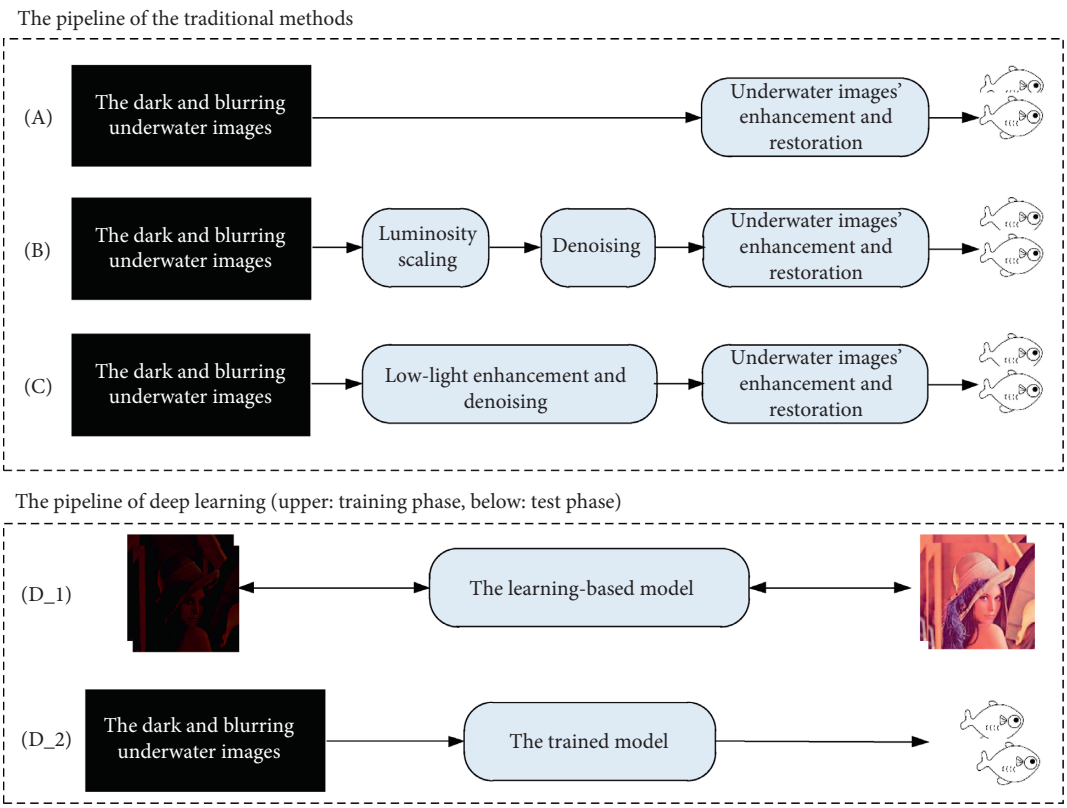

Figure 3: The pipelines are based on traditional methods and deep learning. The input test images are taken in dark and blurred water. The goal of the algorithm is to generate the respective high-quality clear images. The top subimage surrounded by the dotted box represents traditional methods, including the pipeline only using an underwater image enhance/restoration algorithm (line A) and the cascade algorithms (line B and line C). The bottom subimage represents an end-to-end algorithm based on deep learning including the training phase (line D_1) and the test phase (line D_2).

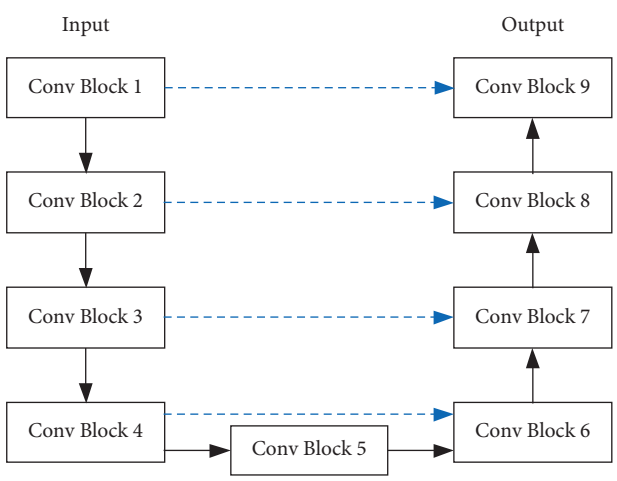

Figure 4: The structure of the deep learning network. The array of input data is a 4-dimensional data converted from the original RAW image. The convolutional block is abbreviated as "Conv Block," which represents a convolutional block including 2D convolutional layers and a pooling layer. The blue dotted arrow represents copy and crop operations.

the data is labeled. In our research, we consider the underwater image restoration as a supervised learning task, in which the data label must be given in the training phase.

A label is not just the name of the image but has varied concepts in different computer vision areas. For example, a label is a number that represents the ID of a category in an image classification task. It is the location of the objects in the object detection task. It indicates whether each pixel belongs to a category in image segmentation. In the image restoration, the label is the high-quality image corresponding to the low-quality image.

The training phase and test phase are shown as the bottom of Figure 3. The training data in the training phase (line D_1) have two parts: the low-light and blurred images (left) and the Ground Truth images (right). The Ground Truth represented by the clear Lena image is the label of the left dark images. Because our method uses the label data, the method is considered a full supervision method. Two kinds of images before and after restoration must be the same size, preferably aligned pixel by pixel. The learning-based model can learn the map relation between the two kinds of training data using BP algorithm [47]. The trained model is produced through the training phase, shown in line D_1. In the test phase (line D_2), the low-light images are input into the trained model, and then the normal-light images are generated by the model.

The test and training data are best derived from the same probability distribution to ensure the effectiveness of the algorithm. Specifically, test data is taken from an extremely

dark and blurred underwater environment; training data needs to be collected from the same or similar environment. However, it is well known that the collection of underwater images requires high computational cost. It hinders the application of deep learning methods in underwater image processing. In Section 2, several methods about collecting underwater images are discussed. We propose a method to collect underwater images, as shown in Figure 5.

In scene 1, the camera is fixed on the tripod, and a glass tank filled with clear water is placed on the table. The glass tank has a high grade of transparency, and the water is clear. The images taken in scene 1 are considered as the ground truth in our research. Then, the first tank is moved; the second tank is placed on the same location as the first tank. In other words, the only difference between scene 1 and scene 2 is the replacement of the tank. The second tank is filled with water mixed with suspended particles. The milk powder is added into the clear water in order to simulate the suspended particles. In scene 2, we capture dark images by adjusting the camera parameter, for example, reduction of the exposure time, closing the aperture, and reduction of the ISO value. Thus, we can collect the low-quality underwater images in scene 2.

The bottom subimage in Figure 5 demoes the light refraction transmission, which follows Snell's law expressed as follows: $(\sin\theta_1/\sin\theta_2) = (I_{r1}/I_{r2})$, where θ_1 and θ_2 are the angle of incidence and I_r is an abbreviation for the indices of refraction. The equation states that for a given pair of media, the ratio of $\sin\theta_1$ and $\sin\theta_2$ is equal to the ration of the indices of refraction in the respective media. The indices of refraction are about 1, 1.33, and 1.5 in the following media: atmosphere, water, and glass, respectively. The indices of refraction of the water are larger than those of the atmosphere. Considering that the thickness of the glass is much smaller than the width of the water in the bottom of Figure 5, the refractive effect of the glass is ignored. According to the refractive law, the camera has a larger angle of view when the light passes through a tank filled with water. If we remove the tank in scene 1, the camera directly takes a picture in the clear air. In this case, we can actually get higher-quality label data (Ground Truth), but the angle of view should shrink. So, the images from scene 1 and scene 2 have different shooting regions, and the two images from the image pairs cannot be aligned pixel by pixel. The summary is as follows; we can collect the image pairs from the two scenes.

3.3. Scattering Models

3.3.1. Atmospheric Scattering Model. For an image shot in a scattering medium, only a part of the light from the object reaches the camera due to the absorption and scattering effects. Similar to (2), the atmospheric scattering model [48, 49] can be written as

$$U(x) = I(x)T(x) + B(1 - T(x)), \tag{3}$$

where x denotes the pixel coordinates, $U(x)$ is the captured image, $I(x)$ is a clear image, B is the global atmospheric light, and $T(x)$ is the transmission proportion of light passing through the object to the camera. When the media is homogenous, $T(x)$ can be written in an exponential decay term as follows:

$$T(x) = e^{-\beta d(x)}, \tag{4}$$

where β represents the atmospheric attenuation coefficient and $d(x)$ is the distance from the object to the camera. In the atmospheric scattering model, attenuation is independent of wavelengths. Since underwater images usually have a blurred appearance, the atmospheric scattering model can be used to describe the degradation the underwater image.

3.3.2. Underwater Scattering Model [4, 50]. Similar to the atmosphere scattering model, the underwater image imaging model can be written as

$$U_\lambda(x) = I_\lambda(x)T_\lambda(x) + B_\lambda(1 - T_\lambda(x)), \tag{5}$$

where λ presents the wavelength of the light. The main difference between the models about the underwater and the air environments is the effect of the wavelength parameters. The attenuation of varying wavelengths needs to be calculated separately in (5), because light with varying wavelengths has varying attenuation levels in an underwater environment. Experiments show that the light with about 500 nm wavelength (blue-green color) has the smallest attenuation coefficient [51]. Thus, the underwater images have a more blue-green color. In our research, the object is close to the camera, so the effect of the wavelength is ignored.

Similar to the equation in the atmosphere, the transmission ration in underwater environments can be written as

$$T_\lambda(x) = e^{-\beta_\lambda d(x)}. \tag{6}$$

It can be also written as

$$T_\lambda(x) = \frac{E_\lambda(x, d(x))}{E_\lambda(x, 0)} = N_\lambda(d(x)), \tag{7}$$

where $E_\lambda(x, d(x))$ is the strength of light after the transmission of $d(x)$ distance, $E_\lambda(x, 0)$ is the energy of light in the original location before transmission, and $N_\lambda(d(x))$ is the normalized residual energy.

3.3.3. Mixed Scattering Model in Underwater and Atmosphere. Two different media are between the object and the camera, as shown in Figure 6; the scattering model is defined as a mixed scattering model. If the tank is removed between the camera and the object, the mixed scattering model is converted to atmospheric scattering model. Similarly, the atmosphere media is removed; in other words, if the object is placed in the water, then the model should be converted to an underwater scattering model.

The mixed mode is expressed as

$$U(x) = I(x)T_{\text{air}}(x)T_\lambda(x) + B_\lambda(1 - T_\lambda(x)), \tag{8}$$

where $T_{\text{air}}(x)$ is the light transmittance ratio in air, $T_\lambda(x)$ is the transmittance ratio in water with suspended particles, and B_λ is the global background light in the tank. Because

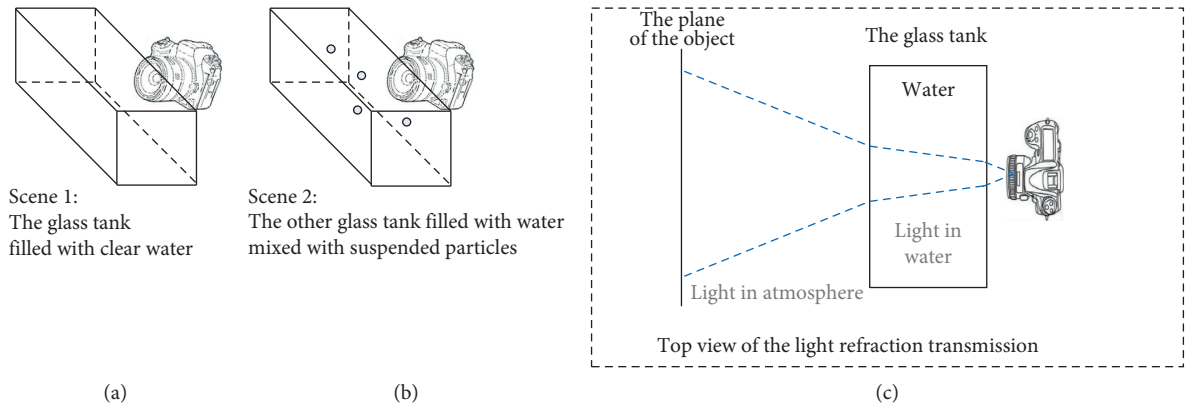

Figure 5: The experimental schematics of collecting images. The subimage in the upper-left corner shows the experimental equipment to collect the ground truth. The subimage in the upper-right corner shows the equipment to collect the underwater images to be restored. The bottom subimage surrounded by a dashed box represents a top view of the experimental equipment.

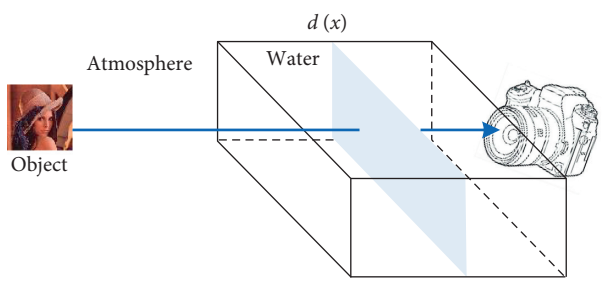

Figure 6: Mixed scattering model used to describe both media underwater and atmosphere. The path of light propagation is from the object to the camera, shown with the blue line. The tank is filled with water and particles.

clear air can be approximated to contain fewer particles, $T_{\text{air}}(x)$ approximately set to 1 and B_λ is close to B_{air}. Additionally, because the particles in air are fewer than those in water, the parameter $T_\lambda(x)$ can be ignored. By the above analysis, the mixed model can be expressed as

$$U(x) \approx I(x)T_\lambda(x) + B_\lambda(1 - T_\lambda(x)). \tag{9}$$

Comparing (9) with (5), we can find that if the light passes through two media (air and water), objects placed in the air are equivalent to being placed in water. Taking advantage of this law, the objects are placed in air to simulate the scene of the objects in water in the experimental part of our research.

3.4. Formulation as an Image Restoration Task. To recover the clear image $I(x)$, the traditional underwater image restoration methods estimate not only $I(x)$ but also homogenous global background light B and the medium energy ratio $T(x)$ from an underwater image $U(x)$, shown in the equation $U(x) = I(x)T(x) + B(1 - T(x))$ (3). The estimating process can be divided into two main steps. After the first step of estimating B and b, the latent image I is reconstructed by inverting the underwater formation model.

Unlike the previous conventional methods, the methods based on deep learning directly estimate the latent image I without calculating the global background light and the medium energy ratio. Instead of estimating parameters, deep learning methods compute the residual information between the target latent image and the underwater image in a data-driven and end-to-end manner. We use maximum a posteriori estimator (MAP estimator) to explain the restoration procedure from $I(x)$ to $U(x)$, written in a nonlinear function $U(x) = f(I(x))$. The function can be further shortened as $U = f(I)$.

According to the Bayes rule, the maximization over the probability distribution of the posterior can be written as

$$p(I \mid U) = p(U \mid I)\frac{p(I)}{p(U)}, \tag{10}$$

where $p(U \mid I)$ is the likelihood of observing U given I, and $p(I)$ is the prior on the latent image. Having a uniform distribution $p(U)$ on the observations, the maximization of the posterior can be written as

$$I_{\text{MAP}} = \arg\max_I p(I \mid U) = \arg\max_I [p(U \mid I)p(I)]. \tag{11}$$

In (11), because U is a determined value, $p(U)$ is a fixed value and omitted. Further, (11) can be converted by minimizing the log likelihood as

$$\begin{aligned} I_{\mathrm{MAP}} &= \arg\max_{I} p(I \mid U) \\ &= \arg\min_{I} [-\log p(U \mid I) - \log p(I)] \\ &= \arg\min_{I} \left[|U - f(I)|^2 + \alpha \Psi(I) \right], \end{aligned} \tag{12}$$

where the first item $\log p(U \mid I)$ is log-probability term similar with the maximum likelihood method, $\log p(I)$ is a priori probability influencing the results, $|U - f(I)|^2$ term enforces the observations to be faithful to the degraded image, and $\alpha\Psi(I)$ is the regularization prior term.

4. Experiments

Three factors including big data, subtle algorithms, and hardware for parallel computing have led to significant progress in the deep learning approach. The high cost of collecting underwater images causes the scarcity of the data in underwater restoration algorithms. We designed the corresponding experimental scene for collecting training and test data, shown in Figure 7, based on the theoretical analysis in the section "The Procedure of Collecting Data" of the approach chapter.

In the training phase, two kinds of data are collected in scene 1 and scene 2 as shown in Figure 5. Figure 7(a) shows the scene 1 for collecting the Ground Truth images in the training phase. A variety of methods are adopted to make the quality of the images better. A Wi-Fi controller is used to take a photo remotely by the app "qDslrDashboard." Polarized lenses are mounted in front of the lens to eliminate the reflection light of the glass. The tripods and tables are fixed steadily. After collecting the GT data, the first tank filled with clear water is removed and the second tank filled with the slightly muddy water is placed in the same location. We adjust the camera parameter to take the corresponding low-exposure images.

In the training phase, the distance between the tank and the camera is only about 2 cm, while the corresponding distance of the test phase is longer than 45 cm. The different focus objects cause different distances in two phases. In the training phase, the camera focuses on the object away from the tank. However, the camera focused on the object in the tank in the test phase. The closest focus distance for the lens is 45 cm, so the camera must be placed at least 45 cm away. The training pictures picked randomly from the training data including about 50 pictures are shown in Figure 8. We can see that the images taken in dark environments are noisy and blurry.

The scene of the test phase is shown in Figure 7(b); several black cloths are used to obtain better test images. Firstly, the top of the tank is covered by a black cloth to avoid direct sunlight on the top. Secondly, the back of the tank is sheltered by a black cloth to make sure the scene has a black background. Thirdly, a big black cloth is placed behind the camera to prevent the rear light from shining on the tank and reflecting back to the camera. In the test phase, only one tank with slightly muddy water is provided, and the camera is adjusted to take the low-exposure images.

Based on the recent advances in underwater low-light image processing algorithms, the comparative experiments are divided into four categories, respectively, shown in lines A, B, C, and D.

Line A in Figure 3 describes the pipeline that the underwater low-light images are processed directly by underwater enhancement and restoration algorithms. The comparative results using different underwater algorithms are shown in Figure 9.

It can be seen from Figure 9 that single processing underwater enhancement and restoration algorithms cannot effectively process the underwater images taken in a dark environment. The results by single underwater algorithms are too dark except for the column E. The result of column E has abnormal bright spots and rough texture on a smooth surface. Our algorithm achieves the closest effect to the Ground Truth.

Objective IQA methods are used to measure the results. The classical FR methods peak signal-to-noise ratio (PSNR) and structural similarity index [56] (SSIM index) are selected in our quantitative analysis as full-reference methods. The higher the value of the two FR methods, the better the image quality. Other IQA methods selected in the analysis are IL-NIQE [57] and NIQE [58]. IL-NIQE uses a feature-enriched completely blind image quality evaluator. NIQE makes a completely blind image quality analyzer and is also one of the NR methods.

The results of objective IQA methods between our algorithm and underwater enhancement and restoration algorithms are shown in Table 2. The results show that our algorithm works better than the other algorithms.

The second image processing pipeline is shown in line B of Figure 3. This pipeline cascades the following three steps: luminosity scaling, denoising, and underwater processing algorithm. The first two steps are abbreviated as "S + D." In the experiment, the classic BM3D [39] is selected in the denoising step. The results of the pipeline are shown in Figure 10.

All cascading pipelines obtain the results with normal exposure relative to the single underwater algorithm. We consider that the normal exposure benefits from the step of luminosity scaling. The images of column C are fuzzier than our algorithm. The results of other algorithms, such as columns E, F, and G, cannot restore dark areas well. The results of objective IQA methods are shown in Table 3.

The 3rd kind of image processing pipeline is shown in line C of Figure 3. The pipeline cascades low-light enhancement algorithm LIME [41] and underwater images processing algorithm. The results of algorithms and the objective IQA methods are shown in Figure 11 and Table 4. In Figure 11, our algorithm exceeds all LIME + underwater enhancement and restoration algorithms. The column D (LIME + GBdehazingRCorrection) has the same effect in terms of color and brightness recovery. In the aspect of objective IQA methods, our algorithm exceeds all of the LIME + underwater enhancement and restoration algorithms.

The pipeline based on deep learning is shown in line D of Figure 3. In the field of computer vision, most of the

(a) (b)

Figure 7: The experimental scenes for collecting the training and test data. The left image (a) and the right image (b) show the scene of shooting the ground truth images in the training phase and test images.

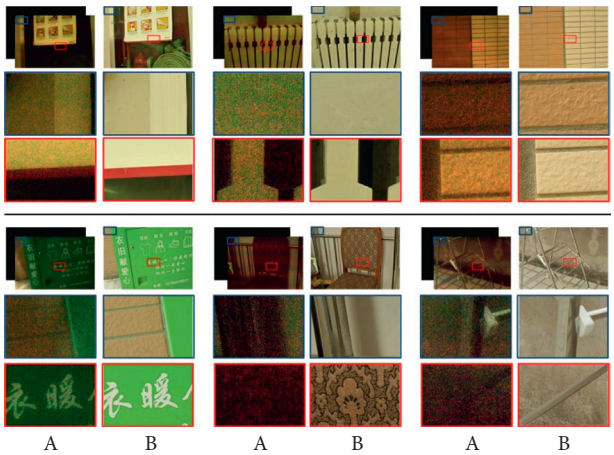

Figure 8: The training images randomly picked from the training set. The first and fourth lines show the images of the original size, and the subsequent two lines are the corresponding magnified images. The pictures of column A are the dark and fuzzy pictures taken in a low-light environment. Because the original pictures are dark and invisible, we used Ubuntu software for brightness adjustment. The pictures of column B are the corresponding clear images.

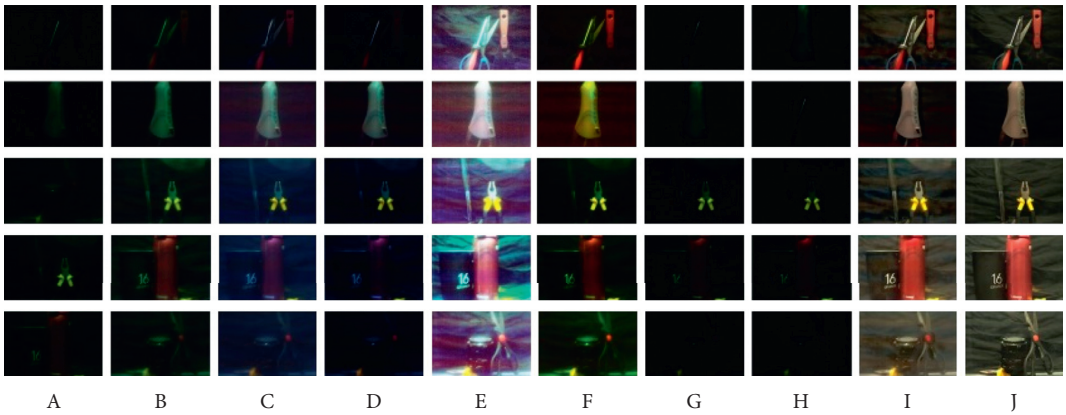

Figure 9: The testing comparison between our algorithm and underwater enhancement and restoration algorithms. The columns from A to J, respectively, mean the results: original image, by CLAHE [11], by Gamma Correction (GC) [3, 52], by ICM [14], by Rayleigh Distribution [53], by UCM [54], by RoWS [55], by UDCP [22], by our algorithm, and the reference image.

Table 2: The test results of objective IQA methods between our algorithm and underwater enhancement and restoration algorithms.

Image ID	Assessment methods	Original image	CLAHE	GC	ICM	Rayleigh Distribution	UCM	RoWS	UDCP	Ours	Ground Truth
100600	PSNR	15.39	16.826	18.110	16.059	9.813	19.071	14.924	14.925	**27.036**	Inf
100600	SSIM	0.121	0.448	0.574	0.250	0.183	0.426	0.012	0.011	**0.840**	1
100600	IL-NIQE	85.737	92.681	85.937	82.378	53.607	76.323	157.962	154.894	**39.235**	28.716
100600	NIQE	14.473	8.559	8.652	8.687	8.810	8.862	20.830	20.901	**5.756**	5.1267
100602	PSNR	15.839	18.815	19.633	16.740	10.495	17.191	15.169	14.727	**24.579**	Inf
100602	SSIM	0.280	0.624	0.646	0.412	0.246	0.358	0.117	0.030	**0.842**	1
100602	IL-NIQE	83.133	84.796	84.337	72.221	62.313	72.443	85.413	87.961	**32.961**	34.990
100602	NIQE	7.467	8.458	8.490	8.360	10.198	8.131	7.731	8.021	**5.9664**	6.849
100603	PSNR	11.717	13.872	14.803	12.363	12.292	12.952	11.353	11.290	**23.613**	Inf
100603	SSIM	0.205	0.505	0.605	0.349	0.375	0.277	0.089	0.077	**0.867**	1
100603	IL-NIQE	80.893	80.292	68.379	65.774	45.447	64.708	80.856	84.260	**37.503**	33.236
100603	NIQE	7.310	7.176	7.296	7.504	9.025	7.085	7.339	7.186	**5.622**	4.641
100605	PSNR	11.633	13.156	14.822	12.173	11.956	14.140	10.985	11.023	**22.167**	Inf
100605	SSIM	0.134	0.352	0.512	0.237	0.279	0.357	0.007	0.017	**0.770**	1.00
100605	IL-NIQE	113.811	96.737	106.721	100.244	62.865	85.374	112.699	105.880	**51.919**	28.02
100605	NIQE	9.979	9.278	9.248	9.533	9.931	9.300	12.789	10.492	**5.4618**	4.944

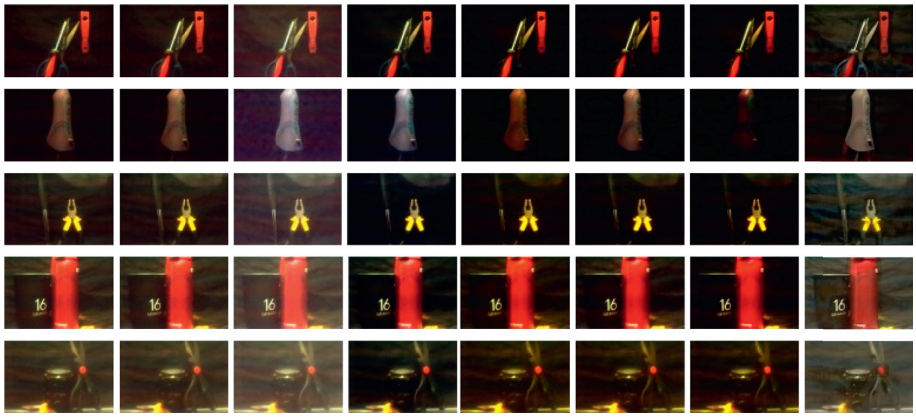

(A) (B) (C) (D) (E) (F) (G) (H) ours

Figure 10: The testing comparison between our algorithm and S + D + underwater enhancement and restoration algorithms. The columns from A to G, respectively, mean the pipeline: luminosity scaling (A), luminosity scaling + denoising algorithm (B), S + D + GC (C), S + D + ICM (D), by S + D + DCP (E), S + D + RoWS (F), S_D_UDCP (G), and our algorithm (H).

Table 3: The test results of objective IQA methods between our algorithm and S + D + underwater enhancement and restoration algorithms.

Image ID	Assessment methods	(A)	(B)	(C)	(D)	(E)	(F)	(G)	(H) ours
100600	PSNR	13.271	13.360	15.058	12.287	11.253	11.273	11.265	**27.036**
100600	SSIM	0.371	0.434	0.556	0.297	0.094	0.095	0.094	**0.840**
100600	IL-NIQE	59.899	50.375	47.866	49.569	77.211	75.689	74.244	**39.235**
100600	NIQE	6.442	6.952	5.757	6.376	6.458	6.500	6.470	**5.756**
100602	PSNR	13.825	13.974	15.241	12.233	11.900	11.702	11.416	**24.579**
100602	SSIM	0.426	0.520	0.571	0.338	0.243	0.210	0.171	**0.842**
100602	IL-NIQE	63.870	50.368	50.735	47.969	56.586	65.474	68.118	**32.961**
100602	NIQE	6.271	7.019	5.766	6.312	6.453	6.175	6.727	**5.9664**
100603	PSNR	13.088	13.221	12.941	12.010	11.733	12.104	11.132	**23.613**
100603	SSIM	0.432	0.521	0.516	0.356	0.288	0.373	0.211	**0.867**
100603	IL-NIQE	63.646	39.312	39.850	39.882	43.502	40.647	42.096	**37.503**
100603	NIQE	5.988	6.281	5.621	5.679	5.867	5.693	5.998	**5.622**
100605	PSNR	21.213	22.223	17.194	17.472	16.744	16.845	15.717	**22.167**
100605	SSIM	0.617	0.744	0.690	0.577	0.524	0.537	0.452	**0.770**
100605	IL-NIQE	85.565	67.611	66.661	67.624	68.777	65.319	70.876	**51.919**
100605	NIQE	7.207	6.815	6.130	5.906	6.278	6.314	6.433	**5.4618**

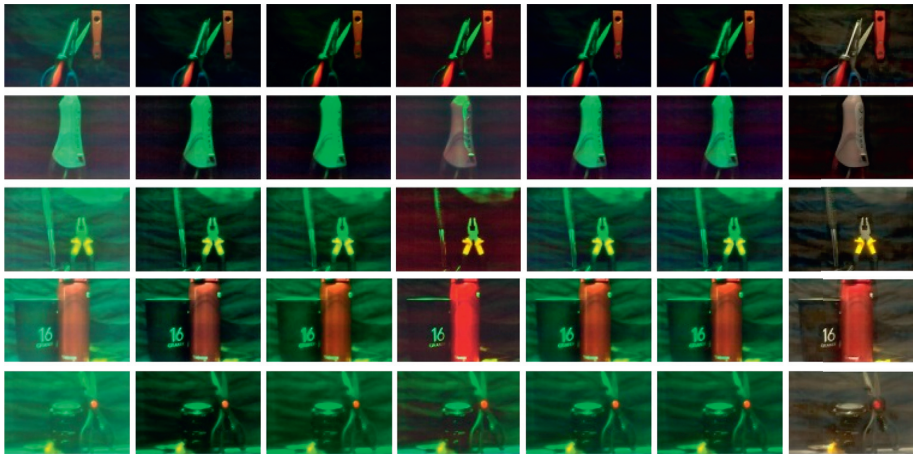

(A) (B) (C) (D) (E) (F) (G) ours

Figure 11: The testing results between our algorithm and other algorithms. The columns from A to H, respectively, represent the algorithms: LIME + GC (A), LIME + ICM (B), LIME + DCP [21] (C), by LIME + GBdehazingRCorrection (D), by LIME + RoWS (E), by LIME + UDCP (F), and by our algorithm (G).

Table 4: The test results of objective IQA methods between our algorithm and LIME + underwater enhancement and restoration algorithms.

Image ID	Assessment methods	(A)	(B)	(C)	(D)	(E)	(F)	(H) ours
100600	PSNR	17.558	21.831	19.104	22.417	20.759	20.914	**27.036**
100600	SSIM	0.532	0.697	0.445	0.717	0.578	0.592	**0.840**
100600	IL-NIQE	68.850	61.838	68.343	66.967	61.455	60.936	**39.235**
100600	NIQE	7.200	6.909	6.814	7.166	6.131	6.135	**5.756**
100602	PSNR	12.693	20.232	18.472	20.502	18.872	18.844	**24.579**
100602	SSIM	0.423	0.671	0.541	0.622	0.551	0.544	**0.842**
100602	IL-NIQE	69.912	59.435	60.962	69.759	61.744	61.317	**32.961**
100602	NIQE	7.283	8.054	6.885	6.832	7.036	6.952	**5.9664**
100603	PSNR	14.584	18.765	17.148	20.580	18.396	18.012	**23.613**
100603	SSIM	0.562	0.690	0.584	0.701	0.628	0.617	**0.867**
100603	IL-NIQE	64.945	59.374	54.171	65.780	51.560	47.943	**37.503**
100603	NIQE	6.503	6.711	6.360	6.946	6.484	6.455	**5.622**
100605	PSNR	15.408	16.461	15.450	19.119	17.667	17.406	**22.167**
100605	SSIM	0.531	0.569	0.483	0.629	0.576	0.568	**0.770**
100605	IL-NIQE	91.358	81.761	81.389	85.474	78.275	73.778	**51.919**
100605	NIQE	7.819	7.652	6.863	6.792	8.183	7.738	**5.4618**

current deep learning methods are applied to aerial pictures. There are also some deep learning methods used in underwater image recovery, but few deep learning methods can be applied to blurring and dark underwater images. Deep underwater image enhancement [36] is selected as a comparison algorithm. The results of restoration and objective IQA methods are shown in Figure 12 and Table 5. It can be seen that columns B, E, and F show whiteness, column A has low clarity and color cast, columns D, E, and F cannot restore the background, and column C has rough particles on the smooth surfaces. Because underwater image characteristics are more complex than aerial images, many algorithms have not enough robustness. The test results of objective IQA methods show that our algorithm exceeds all deep underwater image enhancement algorithms.

4.1. Implementation Details. In all of our experiments, we used $L1$ loss and the Adam optimizer [59]. We only trained the network with the use of a Nikon D700 camera. The initial learning rate was set to 0.0001. The initial learning rate decreased according to the cosine function. The weight decay was set to 0.00001 and dampened to 0. According to the practical effect of the experiment, the training epoch is set between 3000 and 5000. Our implementation was based on Torch which is one of the deep learning platforms.

5. Discussion

In this work, we shared a new method for collecting images that can be used for future research of machine learning. With the help of a high-quality dataset, our algorithm achieves inspiring results in the restoration of the extremely low-light underwater images.

In future, we should try to improve our work with the following points. (1) The improved U-net networks can be used to improve performance. (2) The generalization performance of the method still needs to be studied, for

(A) (B) (C) (D) (E) (F) (G) ours

Figure 12: The testing comparison between our algorithm and the method based on deep learning. The columns from A to H, respectively, represent S + D + type 1 UWCNN model (A), S + D + type 7 model (B), S + D + type I (C), S + D + type III (D), by type7 from original image (E), type 9 model (F), and by our algorithm (G).

Table 5: The test results of objective IQA methods between our algorithm and deep underwater image enhancement.

Image ID	Assessment methods	(A)	(B)	(C)	(D)	(E)	(F)	(G) ours
100600	PSNR	20.947	22.403	23.485	22.829	19.190	18.724	**27.036**
100600	SSIM	0.646	0.781	0.780	0.783	0.744	0.741	**0.840**
100600	IL-NIQE	58.020	48.487	54.521	59.034	81.410	72.060	**39.235**
100600	NIQE	7.334	6.732	6.903	7.652	10.062	12.704	**5.756**
100602	PSNR	21.935	16.091	24.409	21.828	9.366	18.593	**24.579**
100602	SSIM	0.757	0.655	0.813	0.749	0.470	0.736	**0.842**
100602	IL-NIQE	66.381	50.995	62.061	62.318	68.022	51.325	**32.961**
100602	NIQE	7.331	7.222	6.996	7.698	6.899	6.638	**5.9664**
100603	PSNR	17.440	20.641	18.465	17.364	12.476	16.236	**23.613**
100603	SSIM	0.643	0.807	0.736	0.651	0.615	0.761	**0.867**
100603	IL-NIQE	47.975	44.817	45.509	53.039	94.663	68.420	**37.503**
100603	NIQE	6.812	7.003	6.410	7.104	7.584	5.852	**5.622**
100605	PSNR	16.170	20.454	18.611	16.791	17.272	16.095	**22.167**
100605	SSIM	0.551	0.696	0.671	0.607	0.638	0.640	**0.770**
100605	IL-NIQE	71.732	44.950	58.549	73.383	100.597	95.610	**51.919**
100605	NIQE	6.848	6.373	6.163	7.693	8.905	8.598	**5.4618**

example, different depth and different turbidity. (3) Experimental equipment for underwater image acquisition can be extended from water tank to pool.

Our research has important theoretical value for the underwater robot, surveillance, and many more areas.

6. Conclusions

To see in dark and blurred underwater environments, we propose a new method of collecting underwater image pairs by two tanks filled with different-turbidity water and different-environment light. Experiments show that our approach in the collection underwater image is simple and highly effective. We demonstrate the efficacy of our algorithm in blurred and dark underwater image restoration by supervised learning. The experiment shows that this approach can achieve inspiring results.

Data Availability

The data used to support the findings of this study are available from the corresponding author upon request.

Conflicts of Interest

The authors declare that there are no conflicts of interest regarding the publication of this paper.

Authors' Contributions

All authors contributed to the paper. Huigang Wang carried out project administration; Yifeng Xu carried out conceptualization and methodology, investigation, and writing; Garth Douglas Cooper carried out review and editing; Shaowei Rong carried out data curation; and Weitao Sun carried out software.

Acknowledgments

This research was funded by the National Science Foundation of China (Grant no. 61571369). It was also funded by Zhejiang Provincial Natural Science Foundation (ZJNSF) (Grant no. LY18F010018) and by the 111 Project under Grant no. B18041.

References

[1] J. S. Jaffe, "Computer modeling and the design of optimal underwater imaging systems," *IEEE Journal of Oceanic Engineering*, vol. 15, no. 2, pp. 101–111, 1990.

[2] E. Trucco and A. T. Olmos-Antillon, "Self-tuning underwater image restoration," *IEEE Journal of Oceanic Engineering*, vol. 31, no. 2, pp. 511–519, 2006.

[3] Y. Wang, W. Song, G. Fortino, L. Z. Qi, W. Zhang, and A. Liotta, "An experimental-based review of image enhancement and image restoration methods for underwater imaging," *IEEE Access*, vol. 7, 2019.

[4] D. Akkaynak and T. Treibitz, "A revised underwater image formation model," in *Proceedings of the IEEE Computer Society Conference on Computer Vision and Pattern Recognition*, Salt Lake City, UT, USA, June 2018.

[5] C. O. Ancuti and C. Ancuti, "Single image dehazing by multi-scale fusion," *IEEE Transactions on Image Processing*, vol. 28, no. 2, 2013.

[6] C. O. Ancuti, C. Ancuti, C. De Vleeschouwer, and P. Bekaert, "Color balance and fusion for underwater image enhancement," *IEEE Transactions on Image Processing*, vol. 27, no. 1, 2018.

[7] S. Wang, J. Zheng, H. M. Hu, and B. Li, "Naturalness preserved enhancement algorithm for non-uniform illumination images," *IEEE Transactions on Image Processing*, vol. 22, no. 9, 2013.

[8] J. Y. Chiang, Y. C. Chen, and Y. F. Chen, "Underwater image enhancement: using wavelength compensation and image dehazing (WCID)," in *Lecture Notes in Computer Science (including Subseries Lecture Notes in Artificial Intelligence and Lecture Notes in Bioinformatics)*, Springer, Berlin, Germany, 2011.

[9] K. Gu, G. Zhai, X. Yang, W. Zhang, and C. W. Chen, "Automatic contrast enhancement technology with saliency preservation," *IEEE Transactions on Circuits and Systems for Video Technology*, vol. 25, no. 9, 2015.

[10] R. Hummel, "Image enhancement by histogram transformation," *Computer Graphics and Image Processing*, vol. 6, no. 2, 1977.

[11] K. Zuiderveld, "Contrast limited adaptive histogram equalization," in *Graphics Gems*, Elsevier, Amsterdam, Netherlands, 1994.

[12] G. Deng, "A generalized unsharp masking algorithm," *IEEE Transactions on Image Processing*, vol. 20, no. 5, 2011.

[13] L. A. Torres-Méndez and G. Dudek, "Color correction of underwater images for aquatic robot inspection," in *Lecture Notes in Computer Science (including Subseries Lecture Notes in Artificial Intelligence and Lecture Notes in Bioinformatics)*, Springer, Berlin, Germany, 2005.

[14] K. Iqbal, R. A. Salam, A. Osman, and A. Z. Talib, "Underwater image enhancement using an integrated colour model," *IAENG International Journal of Computer Science*, vol. 34, no. 2, 2007.

[15] D. Huang, Y. Wang, W. Song, J. Sequeira, and S. Mavromatis, "Shallow-water image enhancement using relative global histogram stretching based on adaptive parameter acquisition," in *Lecture Notes in Computer Science (including Subseries Lecture Notes in Artificial Intelligence and Lecture Notes in Bioinformatics)*, Springer, Berlin, Germany, 2018.

[16] R. N. Bracewell, "The Fourier Transform and Its Applications," vol. 31999, McGraw-Hill, New York, NY, USA, 1986.

[17] C. J. Prabhakar and P. U. Praveen Kumar, "Underwater image denoising using adaptive wavelet subband thresholding," in *Proceedings of the 2010 International Conference on Signal and Image Processing, ICSIP 2010*, Chennai, India, December 2010.

[18] A. Khan, S. S. A. Ali, A. S. Malik, A. Anwer, and F. Meriaudeau, "Underwater image enhancement by wavelet based fusion," in *Proceedings of the USYS 2016 - 2016 IEEE 6th International Conference on Underwater System Technology: Theory and Applications*, Penang, Malaysia, December 2017.

[19] S. Vasamsetti, N. Mittal, B. C. Neelapu, and H. K. Sardana, "Wavelet based perspective on variational enhancement technique for underwater imagery," *Ocean Engineering*, vol. 141, 2017.

[20] M. J. Shensa, "The discrete wavelet transform: wedding the À trous and mallat algorithms," *IEEE Transactions on Signal Processing*, vol. 40, no. 10, 1992.

[21] K. He, J. Sun, and X. Tang, "Single image haze removal using dark channel prior," *IEEE Transactions on Pattern Analysis and Machine Intelligence*, vol. 33, no. 12, 2011.

[22] P. Drews Jr., E. Do Nascimento, F. Moraes, S. Botelho, and M. Campos, "Transmission estimation in underwater single images," in *Proceedings of the IEEE International Conference on Computer Vision*, Sydney, Australia, December 2013.

[23] A. Galdran, D. Pardo, A. Picón, and A. Alvarez-Gila, "Automatic Red-Channel underwater image restoration," *Journal of Visual Communication and Image Representation*, vol. 26, 2015.

[24] Y. T. Peng and P. C. Cosman, "Underwater image restoration based on image blurriness and light absorption," *IEEE Transactions on Image Processing*, vol. 26, no. 4, 2017.

[25] M. D. Wilson, "Support vector machines," in *Encyclopedia of Ecology*, Elsevier, Amsterdam, Netherlands, 2008.

[26] V. Mitra, C. J. Wang, and S. Banerjee, "Lidar detection of underwater objects using a neuro-SVM-based architecture," *IEEE Transactions on Neural Networks*, vol. 17, no. 3, 2006.

[27] Z. Wu, H. R. Karimi, and C. Dang, "A deterministic annealing neural network algorithm for the minimum concave cost transportation problem," in *Proceedings of the IEEE Transactions on Neural Networks and Learning Systems*, 2019.

[28] Z. Wu, B. Jiang, and H. R. Karimi, "A logarithmic descent direction algorithm for the quadratic knapsack problem," *Applied Mathematics and Computation*, vol. 369, 2020.

[29] Y. Lecun, Y. Bengio, and G. Hinton, "Deep learning," *Nature*, vol. 521, 2015.

[30] A. Krizhevsky, I. Sutskever, and H. E. Geoffrey, "ImageNet classification with deep convolutional neural networks," *Advances in Neural Information Processing Systems*, vol. 25, pp. 1–9, 2012.

[31] I. Goodfellow, J. Pouget-Abadie, and M. Mirza, "Generative adversarial networks," pp. 1–9, 2014.

[32] A. Waibel, T. Hanazawa, G. Hinton, K. Shikano, and K. J. Lang, "Phoneme recognition using time-delay neural networks," *IEEE Transactions on Acoustics, Speech, and Signal Processing*, vol. 37, 1989.

[33] X. Sun, L. Liu, Q. Li, J. Dong, E. Lima, and R. Yin, "Deep pixel-to-pixel network for underwater image enhancement and restoration," *IET Image Process*, vol. 13, no. 2, 2019.

[34] C. Fabbri, M. J. Islam, and J. Sattar, "Enhancing underwater imagery using generative adversarial networks," in

Proceedings of the IEEE International Conference on Robotics and Automation, Brisbane, Australia, May 2018.

[35] I. Gulrajani, F. Ahmed, M. Arjovsky, V. Dumoulin, and A. Courville, "Improved training of wasserstein GANs," pp. 1–19, 2017, http://arxiv.org/abs/1704.00028.

[36] S. Anwar, C. Li, and F. Porikli, "Deep underwater image enhancement," 2018, http://arxiv.org/abs/1807.03528.

[37] Y. Guo, H. Li, and P. Zhuang, "Underwater image enhancement using a multiscale dense generative adversarial network," *IEEE Journal of Oceanic Engineering*, vol. 35, no. 3, pp. 862–870, 2019.

[38] Y. Wang, J. Zhang, Y. Cao, and Z. Wang, "A deep CNN method for underwater image enhancement," in *Proceedings of the International Conference on Image Processing, ICIP*, Beijing, China, September 2018.

[39] K. Dabov, A. Foi, V. Katkovnik, and K. Egiazarian, "Image denoising by sparse 3-D transform-domain collaborative filtering," *IEEE Transactions on Image Processing*, vol. 16, no. 8, 2007.

[40] M. Li, J. Liu, W. Yang, X. Sun, and Z. Guo, "Structure-revealing low-light image enhancement via Robust Retinex model," *IEEE Transactions on Image Processing*, vol. 27, no. 6, 2018.

[41] X. Guo, Y. Li, and H. Ling, "LIME: low-light image enhancement via illumination map estimation," *IEEE Transactions on Image Processing*, vol. 26, no. 2, 2017.

[42] Y. LeCun, B. Boser, J. S. Denker et al., "Backpropagation applied to handwritten zip code recognition," *Neural Computation*, vol. 1, no. 4, pp. 541–551, 1989.

[43] O. Ronneberger, P. Fischer, and T. Brox, *U-Net: Convolutional Networks for Biomedical Image Segmentation*, pp. 234–241, Miccai, Callao District, Peru, 2015.

[44] C. Chen, Q. Chen, J. Xu, and V. Koltun, "Learning to see in the dark," in *Proceedings of the IEEE Computer Society Conference on Computer Vision and Pattern Recognition*, Salt Lake City, UT, USA, June 2018.

[45] Y. Le Cun and F. Fogelman-Soulié, "Modèles connexionnistes de l'apprentissage," *Intellectica. Revue de l'Association pour la Recherche Cognitive*, vol. 2, no. 1, 1987.

[46] G. E. Hinton and R. S. Zemel, "Autoencoders, minimum description length and helmholtz free energy," *Advances in Neural Information Processing Systems*, vol. 6, no. 3, 1994.

[47] D. E. Rumelhart, G. E. Hinton, and R. J. Williams, "Learning representations by back-propagating errors," *Nature*, vol. 323, no. 6088, 1986.

[48] H. Israël, F. Kasten, H. Israël, and F. Kasten, "KOSCHMIEDERs theorie der horizontalen sichtweite," in *Die Sichtweite im Nebel und die Möglichkeiten ihrer künstlichen Beeinflussung*, Springer, Berlin, Germany, 1959.

[49] S. G. Narasimhan and S. K. Nayar, "Chromatic framework for vision in bad weather," in *Proceedings of the IEEE Computer Society Conference on Computer Vision and Pattern Recognition*, Hilton Head Island, SC, USA, June 2000.

[50] W. Hou, "A simple underwater imaging model," *Optics Letters*, vol. 34, no. 17, 2009.

[51] D. Berman, T. Treibitz, and S. Avidan, "Diving into haze-lines: color restoration of underwater images," in *British Machine Vision Conference*, BMVC, London, UK, 2017.

[52] S. C. Huang, F. C. Cheng, and Y. S. Chiu, "Efficient contrast enhancement using adaptive gamma correction with weighting distribution," *IEEE Transactions on Image Processing*, vol. 22, no. 3, 2013.

[53] A. S. Abdul Ghani and N. A. Mat Isa, "Underwater image quality enhancement through composition of dual-intensity images and rayleigh-stretching," *Springerplus*, vol. 3, no. 1, 2014.

[54] K. Iqbal, M. Odetayo, A. James, R. A. Salam, and A. Z. H. Talib, "Enhancing the low quality images using unsupervised colour correction method," in *Proceedings of the IEEE International Conference on Systems, Man and Cybernetics*, Istanbul, Turkey, October 2010.

[55] L. Chao and M. Wang, "Removal of water scattering," in *Proceedings of the ICCET 2010 - 2010 International Conference on Computer Engineering and Technology, Proceedings*, Chengdu, China, April 2010.

[56] Z. Wang, A. C. Bovik, H. R. Sheikh, and E. P. Simoncelli, "Image quality assessment: from error visibility to structural similarity," *IEEE Transactions on Image Processing*, vol. 13, no. 4, 2004.

[57] L. Zhang, L. Zhang, and A. C. Bovik, "A feature-enriched completely blind image quality evaluator," *IEEE Transactions on Image Processing*, vol. 24, no. 8, 2015.

[58] A. Mittal, R. Soundararajan, and A. C. Bovik, "Making a "completely blind" image quality analyzer," *IEEE Signal Processing Letters*, vol. 20, no. 3, 2013.

[59] D. P. Kingma and J. L. Ba, "Adam: a method for stochastic optimization," in *Proceedings of the 3rd international conference on learning representations, ICLR 2015-Conference Track Proceedings*, San Diego, CA, USA, May 2015.

Hindawi
Complexity
Volume 2020, Article ID 9427102, 13 pages
https://doi.org/10.1155/2020/9427102

Research Article

Prediction of Air Quality Based on Hybrid Grey Double Exponential Smoothing Model

Zhicun Xu, Meng Dun, and Lifeng Wu

School of Management Engineering and Business, Hebei University of Engineering, Handan 056038, China

Correspondence should be addressed to Lifeng Wu; wlf6666@126.com

Received 6 June 2020; Accepted 6 July 2020; Published 26 July 2020

Guest Editor: Xiaodi Li

To predict the concentration of air pollutants accurately, conformable fractional accumulation grey double exponential smoothing and adjacent accumulation grey double exponential smoothing are proposed, respectively. A hybrid model with conformable fractional accumulation and adjacent accumulation is proposed to further improve the prediction accuracy. The hybrid model is applied to the prediction of AQI, $PM_{2.5}$, and PM_{10}. Compared with the traditional double exponential smoothing model, the new model has a higher prediction accuracy.

1. Introduction

Air quality pollution can induce a variety of respiratory diseases and seriously endanger human health. Therefore, environmental pollution is highly valued. A series of policies to deal with environmental issues have also been proposed, such as the "Air Pollution Prevention and Control Action Plan" and "Notice of Winning the Three-Year Plan of Action to Defend the Blue Sky." With the vigorous control of the country, the air pollution problem has gradually improved. In order to have a better air level, it is necessary to continue to study air quality issues. Due to the promulgation of the new air quality standards, there are less available data on air quality under the new standards. Grey system theory provides an opportunity for accurate prediction of air quality due to its characteristics of "less data" and "poor information." Since Professor Deng published the first grey system paper "The control problems of grey systems" in "Systems & Control Letters" in 1982, this paper symbolizes the advent of the discipline of grey systems theory [1]. Since the emergence of the grey system theory, it has been widely used in various fields, such as construction demand [2], evaluating the interaction between cryptocurrencies [3], traffic-related emissions [4], energy consumption [5], environmental protection investment [6], medicine and health [7], and missile development cost [8]. With the development of grey system theory, different scholars have improved and expanded the grey system theory in terms of cumulative generation methods, parameters, and background values. For example, a grey multivariable convolution model with new information priority accumulation is proposed by Wu and Zhang [9]. Conformable fractional accumulation is proposed by Ma et al. [10]. Nonhomogenous discrete grey model with fractional-order accumulation is proposed by Wu et al. [11]. The error feedback is used to optimize the fractional accumulation grey model to predict per capita power generation by Yang and Xue [12]. Original condition, power exponent, and background value are optimized by Lu et al. The optimized nonlinear grey Bernoulli model is applied for traffic flow prediction [13]. Luo et al. used particle swarm optimization to optimize parameters and proposed a discrete grey polynomial model DGPM (1, 1, N) with new information priority accumulation, which effectively improved the prediction accuracy [14]. Xiong et al. proposed a new GM (1, 1) model to predict China's energy consumption and production based on the optimized original condition [15]. In order to enhance the forecasting accuracy of the traditional grey model, the grey model with the fractional Hausdorff derivative is proposed by Chen et al. [16]. All the above scholars have improved and optimized the grey model, but they are all a single model, and there is no hybrid prediction model.

The hybrid prediction method was first proposed by Bates and Granger [17]. Due to its applicability and high accuracy, it has received much attention. In predictive competitions, M-series competitions are very authoritative. The $M4$ competition is based on the previous three sessions of $M1$, $M2$, and $M3$. An important conclusion drawn from the $M4$ competition is that hybrid prediction can improve the calculation accuracy [18]. A hybrid approach for obtaining optimal cutting conditions during turning of commercially pure titanium (CP-TI) grade 2 was proposed by Khan and Maity [19]. This approach can generate adequate dimensional accuracy. The purpose of a hybrid model is to make up for the shortcomings of individual errors. For example, Zhu et al. believed that the existing prediction methods could not fully reflect the information of the pollution index sequence, so they proposed two hybrid models and conducted an empirical study taking Xingtai City as an example [20]. Gulia et al. combined the deterministic-based models with suitable statistical distribution models to predict the entire range of pollutant concentration distribution [21]. A hybrid model was established by Lai et al. from the perspective of air quality pollution sources. As emissions from pollution sources decrease, $PM_{2.5}$ would also decrease [22]. Smyl proposed the combination of exponential smoothing and neural networks to predict time series [23]. Sharma et al. combined online sequential extreme learning machines with empirical pattern decomposition algorithms to predict hourly air quality [24]. Wu and Lin considered air pollution factors, such as $PM_{2.5}$, PM_{10}, SO_2, CO, NO_2, and O_3. Wavelet decomposition, variational mode decomposition improved by sample entropy, and long-term memory neural network were used to predict air quality index [25]. The above scholars used various hybrid models to evaluate and predict air quality but did not involve the field of grey system. This paper introduces the grey accumulation operator into the statistical model. Then, the grey double exponential smooth hybrid forecasting model is proposed. The conformable fractional accumulation proposed by Ma and the adjacent accumulation will be introduced to grey double exponential smoothing, respectively, in this paper. Finally, the two grey double exponential smoothing prediction results are hybridized for prediction using the coefficient of variability. The validity of the model was verified by applying the hybrid model for the air quality prediction in Chongqing and Foshan.

This article is divided into four parts: Section 2 introduces the conformable fractional accumulation grey double exponential smoothing (CFES), adjacent accumulation grey double exponential smoothing (AAES), and hybrid model. Section 3 uses Nanchong as an example to predict AQI through CFES and AAES, respectively. Then, CFES and AAES are compared with the traditional grey double exponential smoothing (ES). In order to obtain better prediction results, the grey double exponential smoothing model of the two accumulation methods is used to make a hybrid prediction with the variation coefficient. Finally, this paper compares the hybrid model with ES. Section 4 is a summary of the full paper.

2. Grey Double Exponential Smoothing Model

CFES and AAES differ from ES in that grey exponential smoothing contains accumulation operators. The following model will explain in detail.

Assume that $X^{(0)} = \{x^{(0)}(1), x^{(0)}(2), x^{(0)}(3), \ldots, x^{(0)}(n-1), x^{(0)}(n)\}$ is a nonnegative time series. $x^{(r)}(k) = \sum_{i=1}^{k} (x^{(0)}(i)/i^{[r]-r})$ $(i = 1, 2, \ldots, k)$ is the conformable fractional accumulation generating operator of order r, $r \in (0, 1]$. In special cases, r takes 1 as the traditional grey first-order accumulation, and the accumulation operator is $x^{(1)}(k) = \sum_{i=1}^{k} x^{(0)}(i)$ [26]. So $X^{(r)} = \{x^{(r)}(1), x^{(r)}(2), x^{(r)}(3), \ldots, x^{(r)}(n-1), x^{(r)}(n)\}$ can be deduced that the r-order accumulation sequence of $X^{(0)}$ is

$$\left[x^{(r)}(1), x^{(r)}(2), x^{(r)}(3), \cdots, x^{(r)}(k-1), x^{(r)}(k)\right] = \left[x^{(0)}(1), x^{(0)}(2), x^{(0)}(3), \cdots, x^{(0)}(k-1), x^{(0)}(k)\right] \cdot \begin{bmatrix} 1 & 1 & 1 & \cdots & 1 & 1 \\ 0 & \frac{1}{2^{[r]-r}} & \frac{1}{2^{[r]-r}} & \cdots & \frac{1}{2^{[r]-r}} & \frac{1}{2^{[r]-r}} \\ 0 & 0 & \frac{1}{3^{[r]-r}} & \cdots & \frac{1}{3^{[r]-r}} & \frac{1}{3^{[r]-r}} \\ \vdots & \vdots & \vdots & & \vdots & \vdots \\ 0 & 0 & 0 & \cdots & \frac{1}{(k-1)^{[r]-r}} & \frac{1}{(k-1)^{[r]-r}} \\ 0 & 0 & 0 & \cdots & 0 & \frac{1}{(k)^{[r]-r}} \end{bmatrix}. \tag{1}$$

Equations (2)(5) are derived from [27, 28].

CFES based on the $X^{(r)}$ sequence is

$$S^{(1)}(k) = \alpha x^{(r)}(k) + (1-\alpha)S^{(1)}(k-1), \tag{2}$$

$$S^{(2)}(k) = \alpha S^{(1)}(k) + (1-\alpha)S^{(2)}(k-1). \tag{3}$$

$S^{(1)}(k)$ is the grey single exponential smoothing value of the k period, and $S^{(2)}(k)$ is the grey double exponential smoothing value of the k period.

$$a_k = 2S^{(1)}(k) - S^{(2)}(k), \tag{4}$$

$$b_k = \frac{\alpha}{1-\alpha}\left[S^{(1)}(k) - S^{(2)}(k)\right]. \tag{5}$$

The fitting formula is

$$\hat{x}^{(r)}(k) = a_k + b_k. \tag{6}$$

The prediction formula is

$$\hat{x}^{(r)}(k) = a_k + mb_k, \tag{7}$$

where m is the out-of-sample size.

Finally, we transform the $\hat{x}^{(r)}(k)$ back to the $\hat{x}^{(0)}(k)$:

$$\hat{x}^{(0)}(k) = k^{(1-r)}\left(\hat{x}^{(r)}(k) - \hat{x}^{(r)}(k-1)\right). \tag{8}$$

The original sequence of $X^{(r)}$ is $\hat{x}^{(0)}(i) = k^{(1-r)}(\hat{x}^{(r)}(i) - \hat{x}^{(r)}(i-1))$ $(i = 2, 3, \ldots, k)$.

Furthermore, the original sequence can be also expressed in the form of a matrix as follows:

$$\begin{aligned}
&\left[\hat{x}^{(0)}(1), \hat{x}^{(0)}(2), \hat{x}^{(0)}(3), \ldots, \hat{x}^{(0)}(k-1), \hat{x}^{(0)}(k)\right] \\
&= \left[\hat{x}^{(r)}(1), \hat{x}^{(r)}(2), \hat{x}^{(r)}(3), \ldots, \hat{x}^{(r)}(k-1), \hat{x}^{(r)}(k)\right]
\begin{bmatrix}
1 & -2^{(1-r)} & \cdots & 0 & 0 \\
0 & 2^{(1-r)} & \cdots & 0 & 0 \\
\vdots & \vdots & & \vdots & \vdots \\
0 & 0 & \cdots & -(k-1)^{(1-r)} & 0 \\
0 & 0 & \cdots & (k-1)^{(1-r)} & -k^{(1-r)} \\
0 & 0 & \cdots & 0 & k^{(1-r)}
\end{bmatrix} \\
&= \left[a_1 + b_1, a_2 + b_2, \ldots, a_k + b_k\right]
\begin{bmatrix}
1 & -2^{(1-r)} & \cdots & 0 & 0 \\
0 & 2^{(1-r)} & \cdots & 0 & 0 \\
\vdots & \vdots & & \vdots & \vdots \\
0 & 0 & \cdots & -(k-1)^{(1-r)} & 0 \\
0 & 0 & \cdots & (k-1)^{(1-r)} & -k^{(1-r)} \\
0 & 0 & \cdots & 0 & k^{(1-r)}
\end{bmatrix}.
\end{aligned} \tag{9}$$

The prediction reduction formula is

$$\begin{aligned}
&\left[\hat{x}^{(0)}(1), \hat{x}^{(0)}(2), \ldots, \hat{x}^{(0)}(k), \ldots \hat{x}^{(0)}(k+m)\right] \\
&= \left[a_1 + b_1, a_2 + b_2, \ldots, a_k + b_k, a_k + 2b_k, \ldots, a_k + mb_k\right]
\begin{bmatrix}
1 & -2^{(1-r)} & \cdots & 0 \\
0 & 2^{(1-r)} & \cdots & 0 \\
\vdots & \vdots & & \vdots \\
0 & 0 & \cdots & -(k+m)^{(1-r)} \\
0 & 0 & \cdots & (k+m)^{(1-r)}
\end{bmatrix}.
\end{aligned} \tag{10}$$

The above is the calculation method of the CFES. The difference between the AAES and the CFES is the accumulated method.

Assume that $X^{(0)} = \{x^{(0)}(1), x^{(0)}(2), x^{(0)}(3), \ldots, x^{(0)}(n-1), x^{(0)}(n)\}$ is a nonnegative time series:

$$\begin{aligned}
x^{(1)}(1) &= x^{(0)}(1), \\
x^{(1)}(i) &= \lambda x^{(0)}(i-1) + x^{(0)}(i), \\
&(i = 2, 3, \ldots, n),
\end{aligned} \tag{11}$$

where $\lambda \in (-1, 1)$ is a parameter accumulated nearby, and its purpose is to adjust the weight between old and new

information. After accumulation, we can obtain $X^{(1)} = \{x^{(1)}(1), x^{(1)}(2), x^{(1)}(3), \ldots, x^{(1)}(n-1), x^{(1)}(n)\}$, and the accumulation sequence of $X^{(0)}$ can be expressed as follows:

$$\begin{aligned}&\left[x^{(1)}(1), x^{(1)}(2), x^{(1)}(3), \ldots, x^{(1)}(n-1), x^{(1)}(n)\right]\\&= \left[x^{(0)}(1), x^{(0)}(2), x^{(0)}(3), \ldots, x^{(0)}(n-1), x^{(0)}(n)\right]\begin{bmatrix} 1 & \lambda & 0 & \cdots & 0 & 0\\ 0 & 1 & \lambda & \cdots & 0 & 0\\ 0 & 0 & 1 & \cdots & 0 & 0\\ \vdots & \vdots & \vdots & & \vdots & \vdots\\ 0 & 0 & 0 & \cdots & \lambda & 0\\ 0 & 0 & 0 & \cdots & 1 & \lambda\\ 0 & 0 & 0 & \cdots & 0 & 1 \end{bmatrix}.\end{aligned} \tag{12}$$

Then, we use $X^{(1)}$ for traditional double exponential smoothing. Finally, equation (13) is used to transform the prediction value to original sequence:

$$\widehat{x}^{(0)}(k) = \widehat{x}^{(1)}(k) - \lambda\widehat{x}^{(0)}(k-1). \tag{13}$$

So the original sequence of $X^{(0)}$ can be also expressed as follows:

$$\begin{aligned}&\left[\widehat{x}^{(0)}(1), \widehat{x}^{(0)}(2), \widehat{x}^{(0)}(3), \ldots, \widehat{x}^{(0)}(k)\right]\\&= \left[\widehat{x}^{(r)}(1), \widehat{x}^{(r)}(2), \widehat{x}^{(r)}(3), \ldots, \widehat{x}^{(r)}(k-1), \widehat{x}^{(r)}(k)\right]\begin{bmatrix} 1 & -\lambda & \lambda^2 & \ldots & (-1)^{(n-1)}\lambda^{(n-1)}\\ 0 & 1 & -\lambda & \ldots & (-1)^{(n-1)}\lambda^{(n-2)}\\ 0 & 0 & 1 & \ldots & (-1)^{(n-1)}\lambda^{(n-3)}\\ \vdots & \vdots & \vdots & & \vdots\\ 0 & 0 & 0 & \ldots & \lambda^2\\ 0 & 0 & 0 & \ldots & -\lambda\\ 0 & 0 & 0 & \ldots & 1 \end{bmatrix}\\&= \left[a_1 + b_1, a_2 + b_2, \cdots, a_n + b_n\right]\begin{bmatrix} 1 & -\lambda & \lambda^2 & \ldots & (-1)^{(n-1)}\lambda^{(n-1)}\\ 0 & 1 & -\lambda & \ldots & (-1)^{(n-1)}\lambda^{(n-2)}\\ 0 & 0 & 1 & \ldots & (-1)^{(n-1)}\lambda^{(n-3)}\\ \vdots & \vdots & \vdots & & \vdots\\ 0 & 0 & 0 & \ldots & \lambda^2\\ 0 & 0 & 0 & \ldots & -\lambda\\ 0 & 0 & 0 & \ldots & 1 \end{bmatrix}.\end{aligned} \tag{14}$$

The prediction values can be shown in the following formula.

When

$$\begin{aligned} k=1,\quad & \hat{x}^{(0)}(1)=\hat{x}^{(1)}(1),\\ k=2,\quad & \hat{x}^{(0)}(2)=\hat{x}^{(1)}(2)-\lambda\hat{x}^{(0)}(1)\\ & \quad =\hat{x}^{(1)}(2)-\lambda\hat{x}^{(1)}(1),\\ k=3,\quad & \hat{x}^{(0)}(3)=\hat{x}^{(1)}(3)-\lambda\hat{x}^{(0)}(2)\\ & \quad =\hat{x}^{(1)}(3)-\lambda\left[\hat{x}^{(1)}(2)-\lambda\hat{x}^{(1)}(1)\right]\\ & \quad =\hat{x}^{(1)}(3)-\lambda\hat{x}^{(1)}(2)+\lambda^2\hat{x}^{(1)}(1). \end{aligned} \tag{15}$$

Without loss of generality,

$$\begin{aligned} k=4,\quad & \hat{x}^{(0)}(4)=\hat{x}^{(1)}(4)-\lambda\hat{x}^{(0)}(2)\\ & =\hat{x}^{(1)}(4)-\lambda\left[\hat{x}^{(1)}(3)-\lambda\hat{x}^{(1)}(2)+\lambda^2\hat{x}^{(1)}(1)\right]\\ & =\hat{x}^{(1)}(4)-\lambda\hat{x}^{(1)}(3)+-\lambda^2\hat{x}^{(1)}(2)-\lambda^3\hat{x}^{(1)}(1). \end{aligned} \tag{16}$$

If n is an even number, then

$$\begin{aligned} \hat{x}^{(0)}(n-1)&=\hat{x}^{(1)}(n-1)-\lambda\hat{x}^{(0)}(n-2)\\ &=\hat{x}^{(1)}(n-1)-\lambda\hat{x}^{(0)}(n-2)+\cdots\\ &\quad+\lambda^{(n-3)}\hat{x}^{(1)}(2)-\lambda^{(n-2)}\hat{x}^{(1)}(1),\\ \hat{x}^{(0)}(n)&=\hat{x}^{(1)}(n)-\lambda\hat{x}^{(1)}(n-1)+\cdots\\ &\quad+\lambda^{(n-2)}\hat{x}^{(1)}(2)-\lambda^{(n-1)}\hat{x}^{(1)}(1). \end{aligned} \tag{17}$$

If n is an odd number, then

$$\begin{aligned} \hat{x}^{(0)}(n-1)&=\hat{x}^{(1)}(n-1)-\lambda\hat{x}^{(1)}(n-2)\\ &=\hat{x}^{(1)}(n-1)-\lambda\hat{x}^{(1)}(n-2)+\cdots\\ &\quad+\lambda^{(n-3)}\hat{x}^{(1)}(2)-\lambda^{(n-2)}\hat{x}^{(1)}(1),\\ \hat{x}^{(0)}(n)&=\hat{x}^{(1)}(n)-\lambda\hat{x}^{(1)}(n-1)\\ &\quad+\cdots-\lambda^{(n-2)}\hat{x}^{(1)}(2)-\lambda^{(n-1)}\hat{x}^{(1)}(1). \end{aligned} \tag{18}$$

When the prediction of a single model is completed, CFES and AAES are hybridized with the variation coefficient to determine the weight. The hybrid formula is shown in equations (19)(24). Suppose there are m single prediction models, and each original sequence has n data; then, the matrix formed by the sequence values $x_{ij}^{(0)}$ of a single prediction model is $X_{ij}^{(0)}$:

$$\mathrm{X}_{ij}^{(0)}=\begin{bmatrix} x_{11}^{(0)} & \cdots & x_{1n}^{(0)}\\ \vdots & \ddots & \vdots\\ x_{m1}^{(0)} & \cdots & x_{mn}^{(0)} \end{bmatrix},\quad i=1,2,\ldots,m;\ j=1,2,\ldots,n. \tag{19}$$

The mean of the individual sequence prediction is

$$\overline{x}_i^{(0)}=\frac{1}{n}\sum_{i=1}^{n}x_{ij}^{(0)}. \tag{20}$$

The standard deviation of the single prediction series is

$$S_i=\sqrt{\frac{1}{n}\sum_{j=1}^{n}\left(x_{ij}^{(0)}-\overline{x}_i^{(0)}\right)^2}. \tag{21}$$

The variation coefficient of the single method is

$$V_i=\frac{S_i}{\overline{x}_i^{(0)}},\quad i=1,2,\ldots,m. \tag{22}$$

We can obtain the weight of the hybrid model is

$$w_i=\frac{V_i}{\sum_{i=1}^{m}V_i}. \tag{23}$$

We can hybridize the individual forecasting sequences from the obtained weights:

$$Y=\sum_{i=1}^{m}w_iy_j. \tag{24}$$

In this paper, CFES and AAES are used to compare with ES, respectively. Then, the two models are hybridized with the variation coefficient to compare with ES again to prove that the cumulative grey double exponential smoothing has a better prediction effect. This article uses MAPE as the prediction criterion, as shown in following equation:

$$\mathrm{MAPE}=\frac{1}{n}\sum_{k=1}^{n}\frac{\left|x^{(0)}(k)-\hat{x}^{(0)}(k)\right|}{x^{(0)}(k)}. \tag{25}$$

3. Application of Grey Double Exponential Smoothing in Air Quality Prediction

This part will use data to verify the validity of CFES, AAES, and hybrid model, respectively. The data in this article come from https://www.aqistudy.cn/historydata/.

3.1. Application of CFES in Air Quality Prediction. The whale algorithm is proposed by Mirjalili and Lewis [29]. The algorithm mimics the social behavior of humpback whales, and it is inspired by the bubble-net hunting strategy. The whale algorithm is used to search for the smallest fitting error in this paper. The original sequence is $X^{(0)}=\{51,78,90,83,72,80,84,94,133,109\}$. The conformable fractional order is $r=0.5563$, and the smoothing coefficient $\alpha=0.5032$. Then, $X^{(0.5563)}=\{51,108.35,163.63,208.50,243.75,279.88,315.31,352.67,402.85,442.09\}$. For convenience of calculation, the first value of the original sequence is used as the original value of the single exponential smoothing value and the double exponential smoothing value, respectively. Equations (2) and (3) are used to calculate $S^{(1)}(k)$ and $S^{(2)}(k)$. The results are shown as follows:

$$\begin{aligned} S^{(1)}(k)&=\{51,79.86,122.02,165.54,204.90,242.64,279.21,\\ &\quad 316.18,359.79,401.21\},\\ S^{(2)}(k)&=\{51,65.52,93.95,129.98,167.68,205.40,242.55,\\ &\quad 279.60,319.96,360.85\}. \end{aligned} \tag{26}$$

We can obtain a_k and b_k by equations (4) and (5):

$$\begin{aligned} a_k &= \{51, 94.20, 150.08, 201.10, 242.12, 279.87, \\ &\quad 315.87, 352.76, 399.63, 441.57\}, \\ b_k &= \{0, 14.52, 28.43, 36.03, 37.70, 37.72, 37.14, \\ &\quad 37.06, 40.36, 40.89\}. \end{aligned} \tag{27}$$

So $a_n = 441.57$ and $b_n = 40.89x^{(0.5563)}(k) = \{51, 108.72, 178.51, 237.12, 279.82, 317.59, 353.01, 389.81, 439.99, 482.46, 523.35, 564.24, 605.13\}$ The data of December 1–10, 2019 were used to predict the AQI concentration value of December 11–13. The final prediction is

$$\begin{aligned} x^{(0)}(k) &= \{51, 78.51, 113.62, 108.42, 87.20, 83.62, \\ &\quad 84.00, 92.58, 133.00, 117.97, 118.48, 123.14, 127.60\}. \end{aligned} \tag{28}$$

The prediction results between ES and CFES are shown in Table 1. In Table 1, in order to facilitate the comparison of the prediction accuracy of the two models, the smoothing coefficient between ES and CFES takes the same value $\alpha = 0.5032$. As can be seen in Table 1, the prediction error of ES is 18.82%, and the prediction error of CFES is 8.08%. It can be seen that CFES makes the prediction error significantly lower.

3.2. Application of AAES in Air Quality Prediction. The original sequence is $X^{(0)} = \{51, 78, 90, 83, 72, 80, 84, 94, 133, 109\}$. The whale algorithm is used to search for the smallest fitting error. The adjacent accumulation is $\lambda = -0.3863$, and the smoothing coefficient $\alpha = 0.4995$. The sequence $X^{(1)} = \{51, 58.30, 59.87, 48.23, 39.94, 52.19, 53.10, 61.55, 96.69, 57.62\}$ is obtained by adjacent accumulation. We can get $S^{(1)}(k)$ and $S^{(2)}(k)$ by equations (2) and (3):

$$\begin{aligned} S^{(1)} &= \{51, 54.65, 57.25, 52.75, 46.35, 49.26, 51.18, 56.36, 76.50, 67.07\}, \\ S^{(2)} &= \{51, 52.82, 55.04, 53.89, 50.12, 49.70, 50.44, 53.39, 64.94, 66.00\}, \end{aligned} \tag{29}$$

where a_k and b_k can be obtained by equations (4) and (5):

$$\begin{aligned} a_k &= \{51, 56.47, 59.47, 51.60, 42.57, 48.83, 51.92, 59.32, 88.07, 68.14\}, \\ b_k &= \{0, 1.82, 2.21, -1.14, -3.77, -0.43, 0.74, 2.96, 11.54, 1.07\}. \end{aligned} \tag{30}$$

So $a_n = 68.14$ and $b_n = 1.07$.

$$\begin{aligned} x^{(1)}(k) &= \{51, 58.29, 61.69, 50.46, 38.81, 48.40, 52.66, \\ &\quad 62.28, 99.61, 69.21, 70.27, 71.34, 72.41\}. \end{aligned} \tag{31}$$

The final prediction is

$$\begin{aligned} \hat{x}^{(0)}(k) &= \{51, 77.99, 91.82, 85.93, 72.00, 76.22, 82.10, \\ &\quad 94.00, 135.92, 121.71, 117.29, 116.65, 117.47\}. \end{aligned} \tag{32}$$

Table 1: Comparison of CFES and ES prediction results.

Date	Actual value	ES	CFES
11-Dec	102	128.95	118.48
12-Dec	118	135.39	123.14
13-Dec	123	141.83	127.60
MAPE		18.82%	8.08%

As can be seen in Figure 1, the fitted value and predicted value of the AAES are closer to the actual value. The fitting error and forecasting error of AAES are 2.64% and 6.88%, respectively. The fitting error and forecasting error of ES are 4.94% and 18.93%. It can be seen that AAES has a higher prediction accuracy than ES.

Forecasting AQI in Nanchong demonstrated that the grey double exponential smoothing with conformable fractional accumulation and adjacent accumulation can improve the prediction effect. It is proved that the grey double exponential smoothing with accumulation mode is meaningful. In order to obtain a more accurate prediction effect, a hybrid prediction model is proposed.

3.3. Application of Hybrid Model in Air Quality Prediction

Case 1. Forecasting AQI, $PM_{2.5}$, and PM_{10} in Chongqing.

Compared with ES, the grey exponential smoothing with the accumulation operator has improved the prediction accuracy to a certain extent, but individual prediction values sometimes have large errors. The conformable fractional accumulation is the principle of old information first, and adjacent accumulation is the principle of new information first. In order to make the model more applicable, a hybrid model is used to balance new information with old information to make up for the shortcomings of a single model.

Table 2 shows the original data of Chongqing AQI, $PM_{2.5}$, and PM_{10} in December 2019. Chongqing is foggy and is known as "fog Chongqing." The annual average foggy day in Chongqing is 104 days. The average annual foggy day in London, England, which is known as the world 's foggy city, is only 94 days. Therefore, it is necessary to study Chongqing air quality.

This section uses AQI as an example to elaborate the model. In the ES model, the fitting error is minimal when $\alpha = 0.4$.

We can obtain

$$\begin{aligned} S^{(1)} &= \{46, 54.40, 62.64, 75.18, 78.71, 77.23, 77.14, \\ &\quad 89.08, 105.05, 113.83\}, \\ S^{(2)} &= \{46, 49.36, 54.67, 62.88, 69.21, 72.42, \\ &\quad 74.30, 80.22, 90.15, 99.62\}, \end{aligned} \tag{33}$$

by

$$\begin{aligned} S^{(1)}(k) &= 0.4 \times X^{(0)}(k) + 0.6 \times S^{(1)}(k-1), \\ S^{(2)}(k) &= 0.4 \times S^{(1)}(k) + 0.6 \times S^{(2)}(k-1). \end{aligned} \tag{34}$$

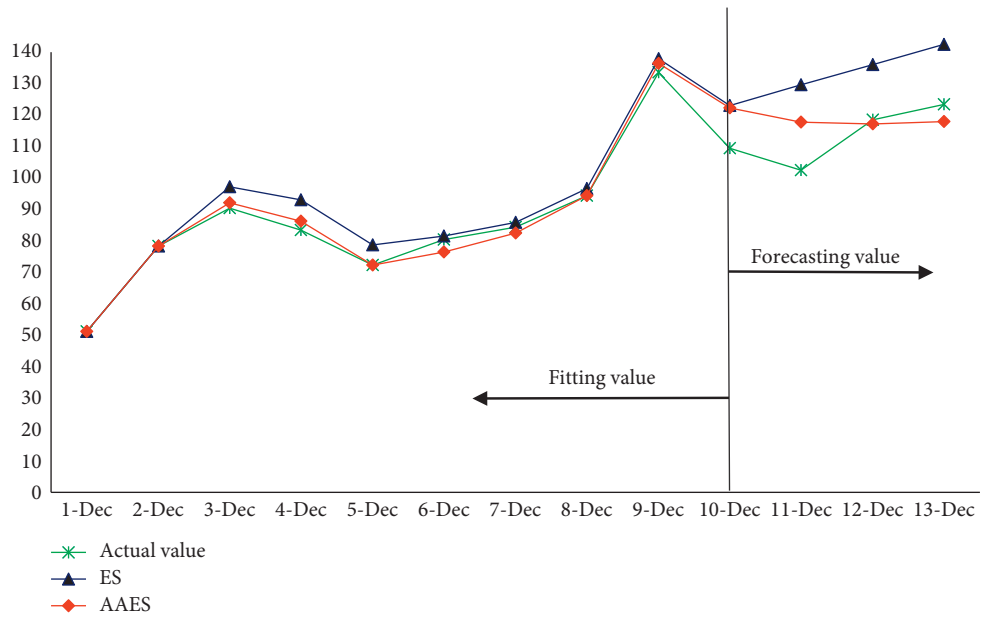

Figure 1: Comparison of AAES and ES forecasting results.

Table 2: The original data of Chongqing AQI, $PM_{2.5}$, and PM_{10} in December 2019.

Date	AQI	$PM_{2.5}$	PM_{10}
1-Dec	46	32	46
2-Dec	67	46	75
3-Dec	75	55	86
4-Dec	94	70	105
5-Dec	84	62	88
6-Dec	75	55	84
7-Dec	77	56	84
8-Dec	107	80	121
9-Dec	129	98	138
10-Dec	127	96	137
11-Dec	135	103	142
12-Dec	143	109	146
13-Dec	145	111	156

We can obtain

$$\begin{aligned} a_k &= \{46, 59.44, 70.61, 87.49, 88.21, 82.04, \\ &\quad 79.97, 97.95, 119.95, 128.04\}, \\ b_k &= \{0, 3.36, 5.31, 8.20, 6.33, 3.21, 1.89, 5.91, 9.93, 9.47\}, \end{aligned} \tag{35}$$

by

$$\begin{aligned} a_k &= 2S^{(1)}(k) - S^{(2)}(k), \\ b_k &= 0.67 \times \left(S^{(1)} - S^{(2)}\right). \end{aligned} \tag{36}$$

So $a_n = 128.04$ and $b_n = 9.47$.

The forecasting result of ES can be obtained as follows:

$$\begin{aligned} \hat{x}^{(0)}(k) &= \{46, 62.80, 75.92, 95.70, 94.54, 85.24, 81.85, \\ &\quad 103.86, 129.88, 137.51, 146.98, 156.45, 165.93\}. \end{aligned} \tag{37}$$

When the conformable fractional grey double exponential smoothing takes $r = 0.5385$ and $\alpha = 0.5$,

$$\begin{aligned} \hat{x}^{(0.5385)}(k) &= \{46, 67, 95.20, 115.41, 103.66, 84.44, 77.00, \\ &\quad 103.36, 131.79, 135.14, 124.60, 129.70, 134.58\}. \end{aligned} \tag{38}$$

When the adjacent accumulation grey double exponential smoothing takes $\lambda = -0.4540$ and $\alpha = 0.5122$,

$$\begin{aligned} \hat{x}^{(1)}(k) &= \{46, 67, 74.99, 94.00, 87.20, 75.04, 73.96, \\ &\quad 105.14, 135.54, 138.98, 144.96, 152.08, 159.72\}, \end{aligned} \tag{39}$$

where $\hat{x}^{(0.5385)}(k)$ obtained by CFES and $\hat{x}^{(1)}(k)$ obtained by AAES are combined using the variation coefficient. A matrix $X_{ij}^{(0)}$ composed of the sequence values $x_{ij}^{(0)}$ of a single prediction model obtained by two accumulation methods is

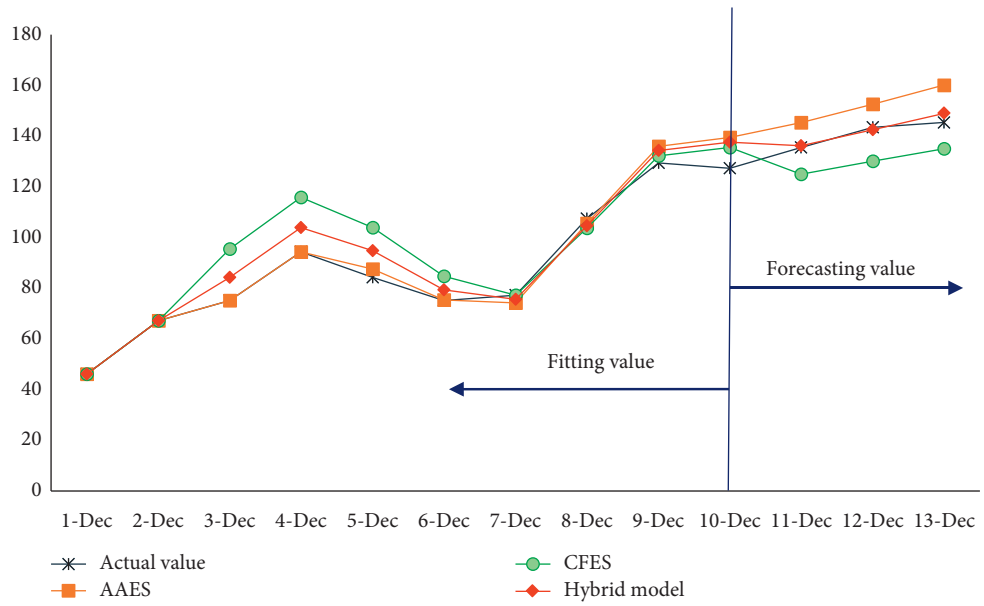

Figure 2: Prediction results of AQI concentration in four models.

Table 3: The forecasting results of $PM_{2.5}$ concentration.

Date Parameter	CFES $\alpha = 0.5$, $r = 0.5216$	AAES $\alpha = 0.5041$, $\lambda = -0.4905$	Hybrid model $w_c = 0.45, w_A = 0.55$	ES $\alpha = 0.4$
1-Dec	32	32	32	32
2-Dec	46.00	45.99	45.99	43.20
3-Dec	68.96	54.58	61.03	54.88
4-Dec	85.78	70.00	77.07	71.10
5-Dec	77.01	64.78	70.27	70.37
6-Dec	62.26	55.27	58.40	63.16
7-Dec	56.00	53.64	54.70	60.06
8-Dec	77.06	77.93	77.54	70.50
9-Dec	100.27	102.52	101.51	98.57
10-Dec	102.71	105.38	104.18	104.47
MAPE	9.83%	2.69%	5.81%	5.60%
11-Dec	93.85	109.91	102.71	112.01
12-Dec	97.84	115.27	107.45	119.56
13-Dec	101.66	121.03	112.34	127.10
MAPE	9.18%	7.16%	0.97%	10.98%

$$X_{ij}^{(0)} = \begin{bmatrix} 46 & 67 & 74.99 & 94.00 & 87.20 & 75.04 & 73.96 & 105.14 & 135.54 & 138.98 & 144.96 & 152.08 & 159.72 \\ 46 & 67 & 95.20 & 115.41 & 103.66 & 84.44 & 77.00 & 103.36 & 131.79 & 135.14 & 124.60 & 129.70 & 134.58 \end{bmatrix}. \tag{40}$$

We can get $\overline{x}_{ij}^{(0)} = \begin{bmatrix} 104.20 \\ 103.68 \end{bmatrix}$, $S_i = \begin{bmatrix} 32.80 \\ 26.15 \end{bmatrix}$, $V_i = \begin{bmatrix} 0.31 \\ 0.25 \end{bmatrix}$, and $w_i = \begin{bmatrix} 0.56 \\ 0.44 \end{bmatrix}$ by equations (11)(14).

So the final fitting values and forecasting values can be obtained by w_i:

$$Y = \{46 \quad 67 \quad 83.98 \quad 103.53 \quad 94.52 \quad 79.22 \quad 75.31 \quad 104.35 \quad 133.87 \quad 137.27 \quad 135.90 \quad 142.12 \quad 148.83\}. \tag{41}$$

As can be seen from Figure 2, the fitting error of CFES is large and the deviation from the true value is higher, but the fitting of the AAES model to the actual value is higher. After combining the two models of CFES and AAES, the curve fitting effect of the hybrid model is significantly better than the CFES model. Judging from the prediction results, the

Table 4: The forecasting results of PM_{10} concentration.

Date Parameter	CFES $\alpha = 0.5000$, $r = 0.5488$	AAES $\alpha = 0.4588$, $\lambda = -0.5153$	Hybrid model $w_c = 0.46$, $w_A = 0.54$	ES $\alpha = 0.5$
1-Dec	46	46	46	46
2-Dec	75.00	74.56	74.76	75.00
3-Dec	108.51	87.18	96.90	93.25
4-Dec	129.48	105.00	116.15	115.00
5-Dec	109.94	93.05	100.74	100.94
6-Dec	92.84	84.00	88.03	90.19
7-Dec	84.00	80.93	82.33	85.95
8-Dec	116.88	114.41	115.53	121.41
9-Dec	142.03	141.09	141.52	147.17
10-Dec	145.09	147.28	146.28	150.32
MAPE	9.72%	2.65%	5.87%	5.90%
11-Dec	135.48	154.40	145.78	161.09
12-Dec	140.90	162.00	152.39	171.87
13-Dec	146.08	169.84	159.02	182.64
MAPE	4.82%	9.52%	2.99%	16.08%

Table 5: The forecasting results of AQI concentration.

Date Parameter	Actual value —	CFES $\alpha = 0.5174$, $r = 0.4383$	AAES $\alpha = 0.4605$, $\lambda = 0.1814$	Hybrid model $w_c = 0.3943$, $w_A = 0.6057$
1-Dec	63	63	63	63
2-Dec	44	45.53	44.60	44.97
3-Dec	56	70.75	53.66	60.40
4-Dec	58	74.14	58.00	64.36
5-Dec	54	64.60	55.69	59.21
6-Dec	58	61.53	58.33	59.59
7-Dec	57	57.05	58.11	57.69
8-Dec	67	64.71	67.02	66.11
9-Dec	100	100.00	100.00	100.00
10-Dec	108	115.69	116.97	116.46
MAPE	—	9.40%	1.95%	4.38%
11-Dec	111	97.46	126.93	115.31
12-Dec	112	102.35	138.16	124.04
13-Dec	118	107.05	149.16	132.56
MAPE	—	10.03%	21.37%	8.99%

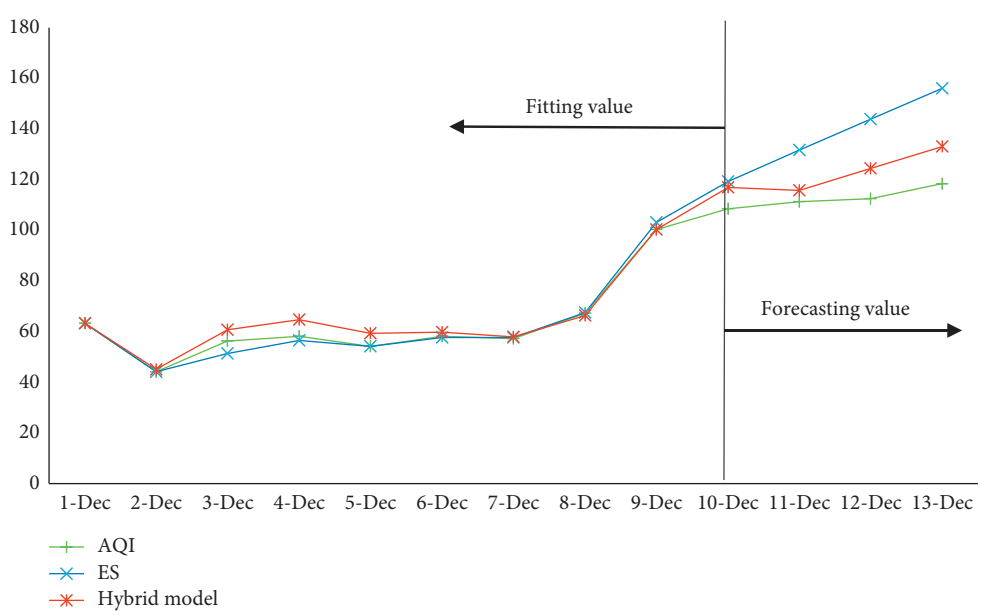

Figure 3: Compared forecasting results between hybrid model and ES.

Table 6: The forecasting results of $PM_{2.5}$ concentration.

Date Parameter	Actual value —	CFES $\alpha = 0.5029$, $r = 0.3760$	AAES $\alpha = 0.4573$, $\lambda = 0.4571$	Hybrid model $w_c = 0.4057$, $w_A = 0.5943$
1-Dec	35	35	35	35
2-Dec	19	19.11	19.00	19.04
3-Dec	29	35.21	28.77	31.38
4-Dec	32	40.67	32.00	35.52
5-Dec	26	32.97	28.58	30.36
6-Dec	30	32.03	30.18	30.93
7-Dec	34	34.33	34.51	34.44
8-Dec	33	33.00	34.65	33.98
9-Dec	51	49.94	50.86	50.49
10-Dec	66	69.03	69.36	69.23
MAPE	—	9.03%	2.32%	4.95%
11-Dec	66	53.80	70.86	63.94
12-Dec	67	56.80	80.13	70.67
13-Dec	78	59.71	85.85	75.25
MAPE	—	19.05%	12.34%	4.04%

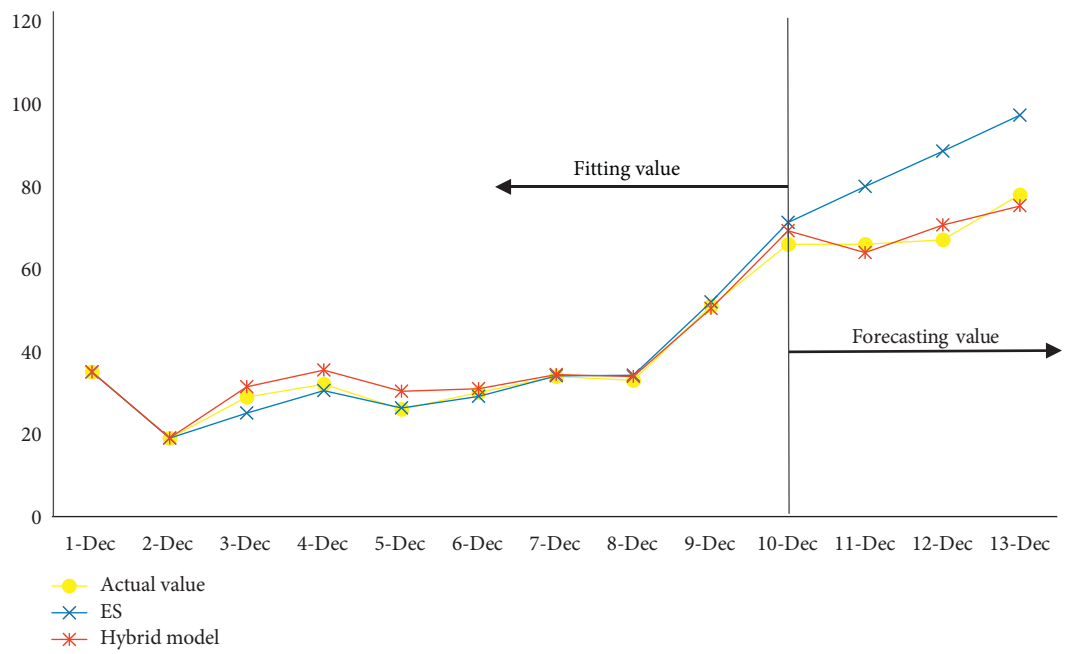

Figure 4: Compared forecasting results between hybrid model and ES in $PM_{2.5}$.

predicted value polyline of the combined model is closer to the actual value polyline, so it can explain the superiority of the hybrid model compared to the single model.

Table 3 is the $PM_{2.5}$ concentration values predicted by ES, CFES, AAES, and hybrid model. The smoothing coefficients and parameters of CFES and AAES are obtained by using the whale algorithm in Matlab R2014b. The prediction error obtained by the hybrid model in Table 3 is 0.97%, which is far lower than the traditional double exponential smoothing prediction error of 10.98%, so the hybrid model has better prediction performance.

Table 4 shows the predicted concentrations of PM_{10} under the four models. In $PM_{2.5}$ concentration prediction, the single prediction error of CFES is relatively large. In PM_{10} concentration prediction, the single prediction error of AAES is relatively large. The hybrid model makes up for the lack of single errors, integrates ES new information and old information first, and improves prediction accuracy. Comparing the hybrid model with ES, the prediction error of ES is significantly higher than the prediction error of the hybrid model, so the hybrid model has more advantages.

The above content uses Chongqing as an example to explain the grey double exponential smoothing. The following content further verifies the model with Foshan, and the calculation process is the same, so it will not be repeated.

Case 2. Forecasting AQI, $PM_{2.5}$, and PM_{10} in Foshan

Foshan is located in the central and southern part of Guangdong Province, China. It is an important part of the Pearl River Delta economic circle. While vigorously

Table 7: The forecasting results of PM_{10} concentration.

Date Parameter	Actual value —	CFES $\alpha = 0.5000$, $r = 0.5837$	AAES $\alpha = 0.5037$, $\lambda = 0.2386$	Hybrid model $w_c = 0.3632$, $w_A = 0.6368$
1-Dec	75	75	75	75
2-Dec	44	44.00	43.90	43.94
3-Dec	61	74.02	57.77	63.67
4-Dec	66	83.19	66.00	72.24
5-Dec	58	72.08	60.22	64.52
6-Dec	65	71.21	65.22	67.40
7-Dec	63	66.22	64.40	65.06
8-Dec	60	59.99	60.81	60.51
9-Dec	97	94.36	97.00	96.04
10-Dec	120	126.12	129.08	128.01
MAPE	—	9.42%	2.08%	4.07%
11-Dec	122	95.41	138.30	122.73
12-Dec	126	98.93	152.98	133.35
13-Dec	154	102.28	166.35	143.08
MAPE	—	25.62%	14.26%	4.51%

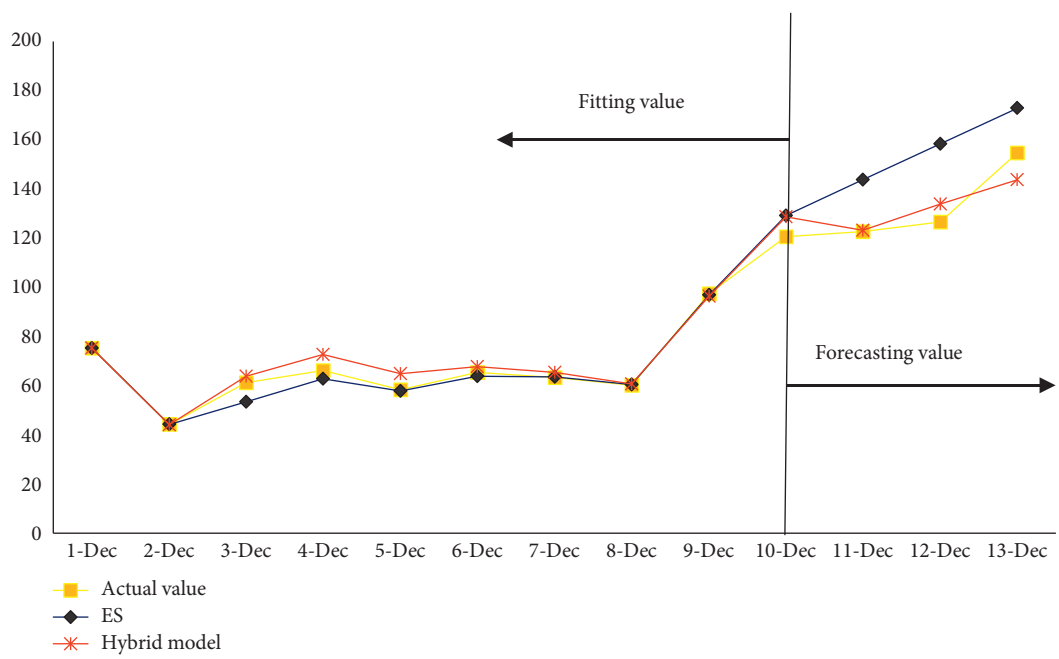

Figure 5: Compared forecasting results between hybrid model and ES in PM_{10}.

developing the economy, the country is also actively addressing air pollution. Compared with the air quality in December 2013, air quality has improved significantly in 2019. With the increasing pursuit in a better life, a high-quality atmospheric environment has received more attention. This section uses Foshan as an example to predict the three air quality indicators of AQI, $PM_{2.5}$, and PM_{10}.

Table 5 shows the prediction results of the AQI in Foshan City. The optimal parameters of CFES $\alpha = 0.5174$ and $r = 0.4383$ and the optimal parameters of AAES $\alpha = 0.4605$ and $\lambda = 0.1814$ are obtained from the whale algorithm search. The two sets of prediction results obtained based on the optimal parameters were used to make a fixed weight combination prediction using the variation coefficient. The CFES weight was 0.3943, and the AAES weight was 0.6057. It can be seen from Table 3 that the prediction error of the single model has exceeded 10% and is no longer suitable for single prediction, but the prediction error of CFES is only more than 0.03% of the MAPE standard, so a hybrid prediction can be considered. The hybrid fitting error is 4.38%, and the prediction error is 8.99%. Therefore, compared with the single model, the hybrid model can improve the prediction accuracy.

When using ES to predict AQI, the smoothing coefficient is determined to be 0.5 based on the minimum fitting error. The comparison between ES and the hybrid prediction results is shown in Figure 3. The fitting error of ES is 2.66%, the fitting error of the hybrid model is 4.38%, and the fitting error of the two models is far below 10%, while the

prediction error of the two models is quite different, and the fitting error of ES is 25.92%, more than 10%, so it can be said that the combination model is meaningful.

It can be seen in Table 6 that the prediction error of CFES is 19.05%, the prediction error of AAES is 12.34%, the hybrid prediction error is 4.04%, and the prediction accuracy has been greatly improved. Compare the hybrid prediction result with the ES. As shown in Figure 4, the predicted polyline of the hybrid model is closer to the actual value of $PM_{2.5}$.

Table 7 is similar to Table 6, and Figure 5 is similar to Figure 4. The hybrid model is superior to the single model. In general, when the error of the single model is greater than or close to 10%, to obtain a higher fitting accuracy, a hybrid model can be used. In the above charts, the superiority of the hybrid model can be verified. The new information-first principle of adjacent accumulation and the old information-first principle of conformable fractional-order accumulation are fused in this paper to obtain a higher prediction accuracy. Therefore, the proposed hybrid model has certain practical significance.

4. Conclusion

The conformable fractional accumulation proposed by Ma is the old information first principle, and the adjacent accumulation is the new information-first principle. In this paper, the conformable fractional order and adjacent are added to the double exponential smoothing model, respectively. Taking the AQI of Nanchong in December 2019 as an example, two sets of grey exponential smoothing models are used to obtain two sets of sequences. In order to facilitate the comparison of model priorities, the conformable fractional smoothing coefficient is the same as the traditional double exponential smoothing coefficient, proving that CFES is better than ES. Under the condition that adjacent cumulative grey double exponential smoothing and traditional double exponential smoothing have the same smoothing coefficient, AAES is also better than ES. Therefore, it is proved that the exponential smoothing model with accumulation is better than the ES.

CFES and AAES models have their advantages and disadvantages in general. Generally speaking, the prediction accuracy of CFES is better than the fitting accuracy, while the fitting accuracy of AAES is better than its own prediction accuracy. Considering the two situations, in order to get more good results, this paper uses a combination of the variation coefficient of the CFES and AAES to obtain a fixed weighted combination of predicted values. From the case of this article, it can be seen that the hybrid prediction result is significantly better than the prediction result using the single grey double exponential smoothing model. Comparing the hybrid results with the prediction results of ES, it is also verified that the hybrid model is better than ES.

In general, from the perspective of predicting air quality, it is of practical significance to put two new grey accumulation methods of conformable fractional accumulation and adjacent accumulation into the exponential smoothing model and their hybrid model, respectively. In future work, we can combine these two new accumulation methods with Holt–Winters model for further research.

Data Availability

The data that support the findings of this study are openly available at https://www.aqistudy.cn/historydata/. The creator is Jie Wang, air data are available after December 2013, the title is air quality historical data query, and copyright is owned by aqistudy.cn.

Conflicts of Interest

The authors declare that they have no conflicts of interest.

Acknowledgments

The relevant researches are supported by the National Natural Science Foundation of China (no.71871084), the Excellent Young Scientist Foundation of Hebei Education Department (no. SLRC2019001), and the Project of High-Level Talent in Hebei Province.

References

[1] S. Liu and Y. Yang, "Advances in grey system research (2004-2014)," *Journal of Nanjing University of Aeronautics & Astronautics*, vol. 47, no. 1, pp. 1–18, 2015.

[2] Y. Tan, C. Langston, M. Wu, and J. J. Ochoa, "Grey Forecasting of Construction Demand in Hong Kong over the Next Ten Years," *International Journal of Construction Management*, vol. 15, no. 3, pp. 219–228, 2015.

[3] P. Gatabazi, J. C. Mba, E. Pindza, and C. Labuschagne, "Grey Lotka-Volterra models with application to cryptocurrencies adoption," *Chaos, Solitons & Fractals*, vol. 122, pp. 47–57, 2019.

[4] M. Xie, L. Wu, B. Li, and Z. Li, "A novel hybrid multivariate nonlinear grey model for forecasting the traffic-related emissions," *Applied Mathematical Modelling*, vol. 77, no. 2, pp. 1242–1254, 2020.

[5] Z.-X. Wang, L.-Y. He, and H.-H. Zheng, "Forecasting the residential solar energy consumption of the United States," *Energy*, vol. 178, pp. 610–623, 2019.

[6] L. Wu and Z. Xu, "Analyzing the air quality of Beijing, Tianjin, and Shijiazhuang using grey Verhulst model," *Air Quality, Atmosphere & Health*, vol. 12, pp. 1419–1426, 2019.

[7] C. Zhang, L. Duan, H. Liu et al., "Analysis of patients'attitudes towards medical service prices in different regions based on grey relational theory," *Grey Systems: Theory and Application*, vol. 9, no. 2, pp. 143–154, 2019.

[8] L. Wu, Yu Liang, and Z. Wen, "GM (0, *N*) model for its application on forecasting the development cost of complicated equipment," *Chinese Journal of Management Science*, vol. 27, pp. 203–207, 2019.

[9] L. Wu and Z. Zhang, "Grey multivariable convolution model with new information priority accumulation," *Applied Mathematical Modelling*, vol. 62, pp. 595–604, 2018.

[10] X. Ma, W. Wu, B. Zeng, Y. Wang, and X. Wu, "The conformable fractional grey system model," *ISA Transactions*, vol. 96, pp. 255–271, 2020.

[11] L.-F. Wu, S.-F. Liu, W. Cui, D.-L. Liu, and T.-X. Yao, "Non-homogenous discrete grey model with fractional-order

accumulation," *Neural Computing and Applications*, vol. 25, no. 5, pp. 1215–1221, 2014.

[12] Y. Yang and D. Xue, "Continuous fractional-order grey model and electricity prediction research based on the observation error feedback," *Energy*, vol. 115, pp. 722–733, 2016.

[13] J. Lu, W. Xie, H. Zhou, and A. Zhang, "An optimized nonlinear grey Bernoulli model and its applications," *Neurocomputing*, vol. 177, pp. 206–214, 2016.

[14] D. Luo, M. Ambreen, A. Latif, and X. Wang, "Forecasting Pakistan's electricity based on improved discrete grey polynomial model," *Grey Systems: Theory and Application*, vol. 10, no. 2, pp. 215–230, 2020.

[15] P.-p. Xiong, Y.-g. Dang, T.-x. Yao, and Z.-x. Wang, "Optimal modeling and forecasting of the energy consumption and production in China," *Energy*, vol. 77, pp. 623–634, 2014.

[16] Y. Chen, W. Lifeng, L. Lianyi, and Z. Kai, "Fractional Hausdorff grey model and its properties," *Chaos, Solitons & Fractals*, vol. 138, p. 109915, 2020.

[17] J. M. Bates and C. W. J. Granger, "The combination of forecasts," *OR*, vol. 20, no. 4, pp. 451–468, 1969.

[18] S. Makridakis, E. Spiliotis, and V. Assimakopoulos, "The M4 Competition: 100,000 time series and 61 forecasting methods," *International Journal of Forecasting*, vol. 36, no. 1, pp. 54–74, 2020.

[19] A. Khan and K. Maity, "Estimation of optimal cutting conditions during machining of CP-Ti grade 2 in fuzzy-VIKOR context," *Grey Systems: Theory and Application*, vol. 10, no. 3, pp. 293–310, 2020.

[20] S. Zhu, X. Lian, H. Liu, J. Hu, Y. Wang, and J. Che, "Daily air quality index forecasting with hybrid models: a case in China," *Environmental Pollution*, vol. 231, pp. 1232–1244, 2017.

[21] S. Gulia, S. M. S. Nagendra, and M. Khare, "A system based approach to develop hybrid model predicting extreme urban NO x and PM 2.5 concentrations," *Transportation Research Part D: Transport and Environment*, vol. 56, pp. 141–154, 2017.

[22] H.-C. Lai, H.-W. Ma, C.-R. Chen, M.-C. Hsiao, and B.-H. Pan, "Design and application of a hybrid assessment of air quality models for the source apportionment of PM2.5," *Atmospheric Environment*, vol. 212, pp. 116–127, 2019.

[23] S. Smyl, "A hybrid method of exponential smoothing and recurrent neural networks for time series forecasting," *International Journal of Forecasting*, vol. 36, no. 1, pp. 75–85, 2020.

[24] E. Sharma, R. C. Deo, R. Prasad et al., "A hybrid air quality early-warning framework: an hourly forecasting model with online sequential extreme learning machines and empirical mode decomposition algorithms," *Science of the Total Environment*, vol. 709, pp. 1–23, 2020.

[25] Q. Wu and H. Lin, "A novel optimal-hybrid model for daily air quality index prediction considering air pollutant factors," *Science of the Total Environment*, vol. 683, pp. 808–821, 2019.

[26] S. Liu, Y. Yang, and L. Wu, *Grey System Theory and its Applications*, Science Press, Beijing, China, 7th edition, 2014.

[27] L. Wu and N. Zhang, *Fractional Grey Model and its Application in Equipment Cost Estimation*, Science Press, Beijing, China, 2017.

[28] L. Wu, S. Liu, and Y. Yang, "Grey double exponential smoothing model and its application on pig price forecasting in China," *Applied Soft Computing*, vol. 39, pp. 117–123, 2016.

[29] S. Mirjalili and A. Lewis, "The whale optimization algorithm," *Advances in Engineering Software*, vol. 95, pp. 51–67, 2016.

Hindawi
Complexity
Volume 2020, Article ID 7652648, 13 pages
https://doi.org/10.1155/2020/7652648

Research Article

New Controllability Results of Fractional Nonlocal Semilinear Evolution Systems with Finite Delay

Daliang Zhao [1] **and Juan Mao** [2]

[1] *School of Mathematics and Statistics, Shandong Normal University, Jinan 250014, China*
[2] *Department of Basic Courses, Shandong Polytechnic, Jinan 250104, China*

Correspondence should be addressed to Daliang Zhao; dlzhao928@sdnu.edu.cn

Received 9 May 2020; Accepted 19 June 2020; Published 13 July 2020

Academic Editor: Quanxin Zhu

In the present paper, sufficient conditions ensuring the complete controllability for a class of semilinear fractional nonlocal evolution systems with finite delay in Banach spaces are derived. The new results are obtained under a weaker definition of complete controllability we introduced, and then the Lipschitz continuity and other growth conditions for the nonlinearity and nonlocal item are not required in comparison with the existing literatures. In addition, an appropriate complete space and a corresponding time delay item are introduced to conquer the difficulties caused by time delay. Our main tools are properties of resolvent operators, theory of measure of noncompactness, and Mönch fixed point theorem.

1. Introduction

In recent decades, various research studies on fractional differential systems are growing vigorously, which are chiefly due to the enormous scope and extensive applications of fractional calculus theory in mathematics, biology, physics, economics, and engineering science [1–9].

As we all know, time delay effects exist widely in various fields such as communication security, weather predicting, and population dynamics. The difficulties in the study of these fields lie in the time lag effect for the systems caused by the delay. One can see [10–20], for further details. It should be noted that, in the case of research on fractional delay evolution systems, it is still in the initial stage. On the contrary, fractional calculus has also been applied to controllability issues in recent years. As one of the most important notions in control theory of mathematics, controllability has significant influence on the fields of control and engineering. We point out that complete controllability of infinite dimensional systems with noncompact semigroup is an important research direction, and there have been many outstanding achievements in this regard such as [21–26]. For more details of other research results on control theory, please refer to [27–40] and the reference therein.

As we have seen, there is scarcely any results on complete controllability of fractional nonlocal evolution equations with delay in Banach spaces, except [21, 23, 24]. However, the Lipschitz and certain growth conditions on nonlocal item and nonlinearity are still necessary for [21]. In [23], the authors supposed the nonlinear function and nonlocal item to be Lipschitz continuous and the semigroup generated by the considered system to be compact. In [24], nonlinear function was imposed some growth conditions, and the resolvent operator used to define the mild solution was compact. However, it is a little pity that these suppositions are usually difficult to be made to work in numerous specific applications. In fact, many excellent achievements concerning complete controllability of various nonlinear differential systems, such as those in Debbouche and Baleanu, [11], Nirmala et al. [22], and Wang and Zhou [25], have been derived during recent years. However, the limitation also lies in that the nonlinear functions here are all provided with the Lipschitz continuity or other growth assumptions. In

addition, the compactness or other assumptions of C_0 semigroup actually prevents us from studying complete controllability in the infinite dimensional space.

The current paper, inspired by the aforementioned analyses, is to address the complete controllability of the following fractional nonlocal semilinear evolution equations with finite delay in Banach spaces:

$$\begin{cases} D^q u(t) = Au(t) + f(t, u(t), u_t) + B\mu(t), & \text{a.e.} t \in I := [0, T], \\ u(t) + M(t, u) = \phi(t), & t \in [-r, 0], \end{cases} \tag{1}$$

where D^q denotes the Caputo derivative of order $q \in (0,1)$. $u\colon I \longrightarrow X$, $\mu \in L^2(I, U)$, and $B\colon U \longrightarrow X$ is a bounded linear operator, where X and U are Banach spaces. $A\colon \mathscr{D} \subset X \longrightarrow X$ is a closed linear unbounded operator on X with dense domain $\mathscr{D}$. $\phi(t) \in C([-r, 0], X)$. f and M are given functions satisfying certain appropriate conditions that will be given later.

The proposed fractional evolution system (1) here, which generalizes the case of integral (first) order differential equations studied in [41] about the complete controllability, has more extensive and valid applications in contrast to the abovementioned literatures [11, 21–25] as follows. First of all, under the new concept of complete controllability we drew into, that is, a weaker definition of complete controllability than the existing notion, the nonlinear function and nonlocal item here are only allowed to be continuous instead of other restrictions such as Lipschitz continuity and certain growth conditions. Secondly, compactness of the C_0 semigroup and the resolvent operator used to define the mild solution for system (1) is no longer needed. Last but not the least, obstacles in the estimation of Kuratowski measures of noncompactness caused by time delay have been conquered in a new complete space with corresponding defined delay function.

An outline of the current paper is as follows. Some essential preparations are made in Section 2. In Section 3, we derive a sufficient condition on complete controllability for the addressed systems. In Section 4, we give an example to illustrate the obtained new results.

2. Preliminaries

Let $C(I, X)$ be the space of continuous functions from I into X provided with the supreme norm $\|\cdot\|_{C(I,X)}$. Similarly, $C([-r, T], X)$ denotes the Banach space of continuous functions from $[-r, T]$ to X with the usual supreme norm. If $T = 0$, we denote the norm of this space simply by $\|\cdot\|_r$. The domain $\mathscr{D}$ is endowed with the graph norm $\|u\|_{\mathscr{D}} = \|u\| + \|Au\|$, where $\|\cdot\|$ denotes the norm of Banach space X. For $q \in (0,1)$, $C^q(I, X)$ stands for the space of all the continuous functions from I into X equipped with the norm $\|u\|_{C^q(I,X)} = \|u\|_{C(I,X)} + [|u|]_{C^q(I,X)}$, where $[|u|]_{C^q(I,X)} = \sup_{t,s \in I, t \neq s} \|u(t) - u(s)\| / (t-s)^q$. Throughout this paper, $\mathscr{L}(X, Y)$ denotes the space of bounded linear operators from X into Banach space Y provided with the operator norm $\|\cdot\|_{\mathscr{L}(X,Y)}$.

In order to conquer the inconveniences caused by time delay in the study of complete controllability, for each $u \in C(I, X)$, $t \in I$, and the function $\phi(t)$ in (1), we draw into the function u_t defined by

$$u_t(\theta) = \begin{cases} u(t+\theta), & t + \theta \geq 0, \\ \phi(t+\theta), & t + \theta \leq 0, \end{cases} \tag{2}$$

for each $\theta \in [-r, 0]$. Simple check indicates $x_t \in L([-r, 0], X)$, where $L([-r, 0], X)$ stands for a complete integrable space consists of integrable functions from $[-r, 0]$ into X.

Remark 1. Under the function u_t defined in (2) in complete space $L([-r, 0], X)$, we can get over the difficulties caused by time delay in the process of estimating Kuratowski measures of noncompactness (for details, please see Lemmas 4 and 5).

Next, we list the well-known definitions as follows.

Definition 1 (see [5]). The fractional integral with order $q > 0$ for a function $u\colon (0, +\infty) \longrightarrow R$ can be defined as

$$I_{0^+}^q u(t) = \frac{1}{\Gamma(q)} \int_0^t (t-s)^{q-1} u(s) \mathrm{d}s, \tag{3}$$

provided that the right-side integral is pointwise defined on $[0, +\infty)$.

Definition 2 (see [5]). The Caputo fractional derivative with order $q > 0$ for a function $u\colon (0, +\infty) \longrightarrow R$ is written as

$$D_{0^+}^q u(t) = \frac{1}{\Gamma(n-q)} \int_0^t \frac{u^{(n)}(s)}{(t-s)^{q-n+1}} \mathrm{d}s, \tag{4}$$

where $n = [q] + 1$, provided the right-side integral is pointwise defined on $[0, +\infty)$.

Definition 3 (see [42]). The bounded linear operator $\{\mathfrak{J}(t)\}_{t \geq 0} \subset \mathscr{L}(X)$ on X is defined as a resolvent operator of the following integral equation:

$$u(t) = \int_0^t \sigma(t-s) Au(s) \mathrm{d}s, \quad t \geq 0, \tag{5}$$

where scalar kernel $\sigma \in L^1_{loc}(R^+)$ and $\sigma \equiv 0$, provided that it satisfies

(i) $\mathfrak{J}(t)$ is strongly continuous, $\mathfrak{J}(0) = I$

(ii) $\mathfrak{J}(t)$ commutes with A, that is, $\mathfrak{J}(t)\mathscr{D} \subset \mathscr{D}$, and $A\mathfrak{J}(t)u = \mathfrak{J}(t)Au$ for each $u \in \mathscr{D}$ and each $t \geq 0$

(iii) $\mathfrak{J}(t)u = u + \int_0^t \sigma(t-s) A\mathfrak{J}(s)u \mathrm{d}s$, for all $u \in \mathscr{D}$, $t \geq 0$

Definition 4 (see [42]). Suppose $\mathfrak{J}(\cdot)u \in W^{1,1}_{loc}(R^+, X)$ for each $u \in \mathscr{D}$, and there exists a function $\varphi \in L^1_{loc}(R^+)$, which satisfy

$$\|\dot{\mathfrak{J}}(t)u\| \leq \varphi(t) \|u\|_{\mathscr{D}}, \quad \text{a.e. on } R^+, \forall u \in \mathscr{D}. \tag{6}$$

Then, we call $\mathfrak{J}(t)$ a differentiable resolvent operator of (5).

Next, we focus on the following equation:

$$u(t) = g(t) + \int_0^t \sigma(t-s)Au(s)\mathrm{d}s, \quad t \in I, \tag{7}$$

where $g \in L^1(I, X)$, and list the definition of mild solution of (7) as below on the basis of literature [42].

Definition 5. We call $u \in C(I, X)$ a mild solution for (7) if $\int_0^t \sigma(t-s)u(s)\mathrm{d}s \in \mathscr{D}$, which satisfies

$$u(t) = g(t) + A\int_0^t \sigma(t-s)u(s)\mathrm{d}s, \tag{8}$$

for each $t \in I$.

Taking advantage of properties of the differentiable resolvent operator, we present the equivalent definition of mild solution for (7).

Lemma 1 (see [42]). *Assume that $\mathfrak{I}(t)$ is a differentiable resolvent operator for (7) and $g \in C(I, \mathscr{D})$. Then,*

$$u(t) = \int_0^t \dot{\mathfrak{I}}(t-s)g(s)\mathrm{d}s + g(t), \quad t \in I, \tag{9}$$

is a mild solution of (7).

Before going further, we now recall below a few relevant properties of Kuratowski measures of noncompactness, which will play a critical role in our next proof of complete controllability. For further details, please see [43].

Lemma 2. *Let X be a Banach space and $\gamma(\cdot)$ be the Kuratowski measures of noncompactness which is given by $\gamma(\Omega) = \inf\{\delta > 0\colon \Omega = \cup_{i=1}^k \Omega_i \text{with } diam(\Omega_i) \le \delta, \quad i = 1, 2, \ldots, k\}$ for a bounded subset Ω in X.*

(I) Let D_1, D_2 be bounded sets of X and $\lambda \in R$. Then,

(i) $\gamma(D_1) = 0 \Longleftrightarrow D_1$ is relatively compact
(ii) $\gamma(\lambda D_1) = |\lambda|\gamma(D_1)$
(iii) $\gamma(D_1 + D_2) \le \gamma(D_1) + \gamma(D_2)$

(II) Assume that $D = \{u_n\}$ is a countable set of strongly measurable functions from I into Banach space X, and there exists a function $\psi \in L^1(I)$ such that $\|u_n(t)\| \le \psi(t)$, a.e. $t \in I, n = 1, 2, \ldots$, then $\gamma(D(t))$ is integrable on I, which satisfies

$$\gamma\left(\left\{\int_I u_n(t)\mathrm{d}t\colon n \in N\right\}\right) \le 2\int_I \gamma(D(t))\mathrm{d}t. \tag{10}$$

For the convenience of expression, the Kuratowski measures of noncompactness of a bounded subset in spaces X, $C(I, X)$ and $L([-r, 0], X)$ are all written as $\gamma(\cdot)$, on the premise of no confusion.

Lemma 3 (Mönch). *If there is a closed and convex set $D \subset X$, where X is a Banach space, $u_0 \in D$, and suppose that $A\colon D \longrightarrow D$ is continuous and satisfies $C \subset D$ countable, $C \subset \overline{co}(\{u_0\} \cup A(C)) \Longrightarrow C$ is relatively compact. Then, A has a fixed point in D.*

To end this section, we give the following useful lemmas.

Lemma 4. *Assume that u_n converges to u_0 in $C(I, X)$ as $n \longrightarrow +\infty$. Then, $(u_n)_t$ converges to $(u_0)_t$ in $L([-r, 0], X)$ for every $t \in I$ as $n \longrightarrow +\infty$.*

Proof. Based on the definition in (2), we know

$$\left\|(u_n)_t - (u_0)_t\right\|_{L[-r,0]} = \begin{cases} \int_0^t \left\|u_n(s) - u_0(s)\right\| ds, & t \le r, \\ \int_{t-r}^t \left\|u_n(s) - u_0(s)\right\| ds, & t \ge r, \end{cases} \tag{11}$$

which implies that

$$\left\|(u_n)_t - (u_0)_t\right\|_{L[-r,0]} \le r\left\|u_n - u_0\right\|_{C(I,X)}, \quad \forall t \in I. \tag{12}$$

This completes the proof. □

From the definition of Kuratowski measures of noncompactness in Lemma 2, we can infer the following lemma.

Lemma 5. *Let $D = \{u_n\}_{n=1}^\infty$ be any bounded countable sequence in $C(I, X)$. Then, for each $t \in I$, one has*

$$\gamma(D_t) \le r\gamma(D), \tag{13}$$

where $D_t = \{(u_n)_t\}_{n=1}^\infty$.

3. Main Results

In the sequel, we assume that A admits a differentiable resolvent operator $\{\mathfrak{I}(t)\}_{t\ge0}$ on X. Based on Definition 5 and the Riemann–Liouville standard fractional integral, the mild solution of system (1) can be defined as follows.

Definition 6. For each $\mu \in L^2(I, U)$, a function $u \in C(J, X)$ is said to be a mild solution of the considered system (1) on J, if $\int_0^t (t-s)^{q-1}u(s)\mathrm{d}s \in \mathscr{D}$ for any $t \in [0, T^*]$ and

$$u(t) = \begin{cases} \phi(0) - M(0, u) + \dfrac{1}{\Gamma(q)}A\displaystyle\int_0^t \dfrac{u(s)}{(t-s)^{1-q}}ds + \dfrac{1}{\Gamma(q)}\displaystyle\int_0^t \dfrac{f(s, u(s), u_s) + B\mu(s)}{(t-s)^{1-q}}\mathrm{d}s, & t \in [0, T^*], \\ \phi(t) - M(t, u), & t \in [-r, 0], \end{cases} \tag{14}$$

where $J = [-r, T^*], T^* \in (0, T]$.

Definition 7 (complete controllability). We shall call system (1) is completely controllable on $I = [0,T]$, if for each initial function $\phi(t) \in C([-r,0],X)$ and $u_1 \in X$, there exist a corresponding control $\mu \in L^2(I,U)$ and a real number $T^* \in (0,T]$ such that the mild solution u of (1) on $J = [-r,T^*]$ satisfies $u(T^*) = u_1$.

Remark 2. In comparison with the existing notion in [11, 21, 22, 25, 41], in which T^* is equal to T, our concept in which $T^* \in (0,T]$ is weaker can be regarded as an extension of the present notion of complete controllability.

Before presenting and proving the main results, we firstly list the hypotheses as below:

(H1) $f \in C(I \times X \times L([-r,0],X),\mathscr{D})$, $\phi(0) \in \mathscr{D}$ and satisfies

(i) f maps bounded sets in $I \times X \times L([-r,0],X)$ into bounded sets in $\mathscr{D}$.

(ii) There exist a constant $q_1 \in (0,q)$ and a function $m \in L^{(1/q_1)}(I,R^+)$ such that, for any bounded subsets $D_1 \subset X, D_2 \subset L([-r,0],X)$

$$\gamma(f(t,D_1,D_2)) \le m(t)(\gamma(D_1)+\gamma(D_2)), \quad t \in I. \tag{15}$$

(H2) (i) The linear operator B: $L^2(I,U) \longrightarrow L^1(I,\mathscr{D})$ is bounded, and there exists a constant $N_1 > 0$ satisfying $\|B\|_{\mathscr{L}(U,\mathscr{D})} \le N_1$.

(ii) Linear operators $\mathfrak{R}(t), t \in I$, denoted by $\mathfrak{R}(\cdot)$ from $L^2(I,U)$ to X are defined as

$$\mathfrak{R}(t)\mu = \Pi_B(t,\mu) + \int_0^t \dot{\mathfrak{J}}(t-s)\Pi_B(s,\mu)\mathrm{d}s, \quad t \in I, \tag{16}$$

where $\Pi_B(t,\mu) = 1/\Gamma(q)\int_0^t (t-s)^{q-1}B\mu(s)\mathrm{d}s$ has invertible operators $\mathfrak{R}^{-1}(\cdot)$ taking values in $L^2(I,U)/\ker\mathfrak{R}(\cdot)$, which satisfy, for some constant $N_2 > 0$, $\sup\|\mathfrak{R}^{-1}(\cdot)\|_{\mathscr{L}(X,L^2(I,U)/\ker\mathfrak{R}(\cdot))} \le N_2$, and there is a constant $q_2 \in (0,q)$ and a function $p \in L^{(1/q_2)}(I,R^+)$ satisfying

$$\gamma\left(\mathfrak{R}^{-1}(\cdot)(D)(s)\right) \le p(s)\gamma(D), \quad s \in I, \tag{17}$$

for any bounded subset $D \subset X$.

(H3) (i) For every $t \in [-r,0]$, $M(t,\cdot)$: $C([-r,T],X) \longrightarrow X$ is a strict k-set contraction and for every $u \in C([-r,T],X)$, $M(t,u)$ is continuous with respect to each $t \in [-r,0]$.

(ii) $M(0,\cdot)$: $C([-r,T],X) \longrightarrow \mathscr{D}$ and there exists a positive constant G such that $\|M(0,u)\|_{\mathscr{D}} \le G$ for every $u \in C([-r,T],X)$.

(H4) The following estimation is valid:

$$kM\left(1+2\|\varphi\|_{L^1(I)}\right) < 1, \tag{18}$$

where

$$M = 1 + \frac{2N_1L\left(1+2\|\varphi\|_{L^1(I)}\right)}{\Gamma(q)},$$
$$L = T^{q-q_2}\left(\frac{1-q_2}{q-q_2}\right)^{1-q_2}\|p\|_{L^{(1/q_2)}}, \tag{19}$$

and φ is the function mentioned in Definition 4.

In the following, let R_0 be a fixed constant satisfying $R_0 > (\|\phi(0)\|_{\mathscr{D}} + G)(1+\|\varphi\|_{L^1(I)}) := N_0$. From (H1), take

$$M_0 = \sup\left\{\|f(t,u,v)\|_{\mathscr{D}}: \|u\|_{C(I,X)} \le R_0, \|v\|_{L[-r,0]} \le r(\|\phi\|_r + R_0), \quad t \in I\right\}. \tag{20}$$

For simplicity, let

$$\Pi(t,u,\mu) = \frac{1}{\Gamma(q)}\int_0^t (t-s)^{q-1}f(s,u(s),u_s)\mathrm{d}s + \frac{1}{\Gamma(q)}\int_0^t (t-s)^{q-1}B\mu(s)\mathrm{d}s, \tag{21}$$

and set

$$\lambda = \frac{2(r+1)}{\Gamma(q)}\left(\frac{1-q_1}{q-q_1}\right)^{1-q_1}\|m\|_{L^{(1/q_1)}}. \tag{22}$$

By means of conditions (H2) and (H4), for any $u(\cdot) \in C(I,X)$ and any $u_1 \in X$, $t \in I$, define a feedback control function

$$\mu_u(t) := \mathfrak{R}^{-1}(T^*)\Big(u_1 - \phi(0) + M(0,u) - \Pi_f(T^*,u) - \int_0^{T^*}\dot{\mathfrak{J}}(T^*-s)\big(\phi(0) - M(0,u) + \Pi_f(s,u)\big)\mathrm{d}s\Big)(t), \tag{23}$$

where

$$T^* = \min\left\{T, \left(\frac{(R_0-N_0)\Gamma(q+1)}{(M_0+N_1M_1)(1+\|\varphi\|_{L^1(I)})}\right)^{(1/q)}, \left(\frac{1-kM(1+2\|\varphi\|_{L^1(I)})}{\lambda M(1+2\|\varphi\|_{L^1(I)})}\right)^{(1/q)}\right\}, \tag{24}$$

$$M_1 = N_2\left((1+\|\varphi\|_{L^1(I)})\left(\|\phi(0)\|_{\mathscr{D}} + G + \frac{M_0T^q}{\Gamma(q+1)}\right) + \|u_1\|\right), \tag{25}$$

$$\Pi_f(t,u) = \frac{1}{\Gamma(q)}\int_0^t (t-s)^{q-1}f(s,u(s),u_s)\mathrm{d}s. \tag{26}$$

Denote

$$\Omega = \left\{u \in C(J,X): \|u\|_{C([0,T^*],X)} \le R_0, \sup_{t\in[0,T^*]}\|u_t\|_{L[-r,0]} \le r(\|\phi\|_r + R_0 0); u(t) = \phi(t) - M(t,u), t \in [-r,0],\right\}, \tag{27}$$

then Ω is clearly a closed convex set in $C(J,X)$. From Lemma 1, we thus define an operator $\Psi\colon C(J,X) \longrightarrow C(J,X)$ which is given by

$$(\Psi u)(t) = \begin{cases} \phi(0) - M(0,u) + \Pi(t,u,\mu_u) + \int_0^t \dot{\mathfrak{J}}(t-s)\left(\phi(0) - M(0,u) + \Pi(s,u,\mu_u)\right)\mathrm{d}s, & t \in [0,T^*], \\ \phi(t) - M(t,u), & t \in [-r,0]. \end{cases} \tag{28}$$

For the purpose of simplifying our next proof processes, we give the following conclusions.

Lemma 6. *Assume $f(\cdot,u(\cdot),u_\cdot) \in C(I \times X \times L([-r,0],X),X)$ and $\mu(\cdot) \in L^2(I,U)$. Then, $\Pi(\cdot,u,\mu) \in C^q(I,X)$, and*

$$[|\Pi(\cdot,u,\mu)|]_{C^q} \le \frac{2}{q}\left(\left\|f(\cdot,u(\cdot),u_\cdot)\right\|_{C(I,X)} + \|B\|_{\mathscr{L}(U,X)}\|\mu(\cdot)\|_{L^2}\right). \tag{29}$$

Proof. For $t \in [0,T)$ and $h > 0$ such that $t + h \in I$, we have

$$\begin{aligned} &\|\Pi(t+h,u,\mu) - \Pi(t,u,\mu)\| \\ &\le \int_0^t \left((t-s)^{q-1} - (t+h-s)^{q-1}\right)\left(\left\|f(s,u(s),u_s)\right\| + \|B\mu(s)\|\right)\mathrm{d}s \\ &\quad + \int_t^{t+h} (t+h-s)^{q-1}\left(\left\|f(s,u(s),u_s)\right\| + \|B\mu(s)\|\right)\mathrm{d}s \\ &\le \left(\frac{t^q - (t+h)^q + h^q}{q} + \frac{h^q}{q}\right)\left(\left\|f(\cdot,u(\cdot),u_\cdot)\right\|_{C(I,X)} + \|B\|_{\mathscr{L}(U,X)}\|\mu(\cdot)\|_{L^2}\right) \\ &\le \frac{2h^q}{q}\left(\left\|f(\cdot,u(\cdot),u_\cdot)\right\|_{C(I,X)} + \|B\|_{\mathscr{L}(U,X)}\|\mu(\cdot)\|_{L^2}\right), \end{aligned} \tag{30}$$

which implies that $[|\Pi(\cdot,u,\mu)|]_{C^q} \le (2/q)(\|f(\cdot,u(\cdot),u_\cdot)\|_{C(I,X)} + \|B\|_{\mathscr{L}(U,X)}\|\mu(\cdot)\|_{L^2})$ and $\Pi(\cdot,u,\mu) \in C^q(I,X)$. The conclusion follows. □

Lemma 7. *Assume that conditions (H1) (i) and (H2)–(H4) hold. Then, the operator $\Psi\colon \Omega \longrightarrow \Omega$ is equicontinuous on J.*

Proof. Firstly, we prove that $\Psi(\Omega) \subseteq \Omega$. In view of assumptions (H1) (i), (H2), and (H3) (ii), we can derive

$$\begin{aligned} \left\|\mu_u(t)\right\| &\le N_2\left(\left\|u_1\right\| + \|\phi(0)\|_{\mathscr{D}} + G + \int_0^{T^*} \varphi(T^*-s)\left(\|\phi(0)\|_{\mathscr{D}} + G\right)\mathrm{d}s\right) \\ &\quad + \frac{N_2}{\Gamma(q)}\left(\int_0^{T^*} (T^*-s)^{q-1}\left\|f(s,u(s),u_s)\right\|_{\mathscr{D}}\mathrm{d}s + \int_0^{T^*} \varphi(T^*-s)\left(\int_0^s (s-\eta)^{q-1}\left\|f(\eta,u(\eta),u_\eta)\right\|_{\mathscr{D}}d\eta\right)\mathrm{d}s\right) \\ &\le N_2\left(\left\|u_1\right\| + \|\phi(0)\|_{\mathscr{D}} + G + \|\varphi\|_{L^1(I)}\left(\|\phi(0)\|_{\mathscr{D}} + G\right)\right) + N_2\left(\frac{M_0T^q}{\Gamma(q+1)} + \|\varphi\|_{L^1(I)}\frac{M_0T^q}{\Gamma(q+1)}\right) \\ &\le N_2\left(\left(\|\varphi\|_{L^1(I)} + 1\right)\left(\|\phi(0)\|_{\mathscr{D}} + G + \frac{M_0T^q}{\Gamma(q+1)}\right) + \left\|u_1\right\|\right) = M_1, \quad t \in I. \end{aligned} \tag{31}$$

Observing (H2), for any $u \in \Omega$ and $t \in [0, T^*]$, we deduce

$$\begin{aligned}\left\|\Pi(t,u,\mu_u)\right\|_{\mathscr{D}} &\le \frac{1}{\Gamma(q)}\int_0^t (t-s)^{q-1}\left\|f(s,u(s),u_s)\right\|_{\mathscr{D}}\mathrm{d}s + \frac{1}{\Gamma(q)}\int_0^t (t-s)^{q-1}\left\|B\mu_u(s)\right\|_{\mathscr{D}}\mathrm{d}s \\ &\le \frac{M_0T^{*q}}{\Gamma(q+1)} + \frac{N_1M_1T^{*q}}{\Gamma(q+1)} = \frac{(M_0+N_1M_1)T^{*q}}{\Gamma(q+1)}.\end{aligned} \tag{32}$$

Then, this together with (24) indicates

$$\begin{aligned}&\|(\Psi u)(t)\| \\ &\le \|\phi(0)\|_{\mathscr{D}} + \|M(0,u)\|_{\mathscr{D}} + \left\|\Pi(t,u,\mu_u)\right\|_{\mathscr{D}} + \int_0^t \varphi(t-s)\left(\|\phi(0)\|_{\mathscr{D}} + \|M(0,u)\|_{\mathscr{D}} + \left\|\Pi(s,u,\mu_u)\right\|_{\mathscr{D}}\right)\mathrm{d}s \\ &\le \|\phi(0)\|_{\mathscr{D}} + G + \frac{(M_0+N_1M_1)T^{*q}}{\Gamma(q+1)} + \|\varphi\|_{L^1(I)}\left(\|\phi(0)\|_{\mathscr{D}} + G + \frac{(M_0+N_1M_1)T^{*q}}{\Gamma(q+1)}\right) \\ &\le \left(\|\phi(0)\|_{\mathscr{D}} + G\right)\left(\|\varphi\|_{L^1(I)} + 1\right) + \frac{(M_0+N_1M_1)\left(\|\varphi\|_{L^1(I)}+1\right)}{\Gamma(q+1)}T^{*q} \le R_0.\end{aligned} \tag{33}$$

On the contrary,

$$\begin{aligned}\left\|(\Psi u)_t\right\|_{L[-r,0]} &= \int_{-r}^0 \left\|(\Psi u)_t(\theta)\right\|\mathrm{d}\theta \\ &= \begin{cases} \displaystyle\int_{t-r}^0 \|\phi(s)\|\mathrm{d}s + \int_0^t \|(\Psi u)(s)\|\mathrm{d}s, & t \le r, \\ \displaystyle\int_{t-r}^t \|(\Psi u)(s)\|\mathrm{d}s, & t \ge r, \end{cases}\end{aligned} \tag{34}$$

which infers that

$$\left\|(\Psi u)_t\right\|_{L[-r,0]} \le r\|\phi\|_r + r\|\Psi u\|_{C([0,t],X)}. \tag{35}$$

Therefore, we can obtain

$$\sup_{t\in[0,T^*]}\left\|(\Psi u)_t\right\|_{L[-r,0]} \le r\left(\|\phi\|_r + R_0\right). \tag{36}$$

It is obvious that $(\Psi u)(t) = \phi(t) - M(t,u)$ for any $u \in \Omega, t \in [-r, 0]$. Then, we conclude that $\Psi(\Omega) \subseteq \Omega$.

Next, we shall demonstrate that $\Psi\colon \Omega \longrightarrow \Omega$ is equicontinuous on J. For arbitrary $u \in \Omega$ and $\tau_1, \tau_2 \in J = [-r, T^*]$ with $\tau_1 < \tau_2$, we present the following discussions.

(i) If $0 \le \tau_1 < \tau_2 \le T^*$, then

$$\begin{aligned}(\Psi u)(\tau_2) - (\Psi u)(\tau_1) &= \Pi(\tau_2,u,\mu_u) - \Pi(\tau_1,u,\mu_u) \\ &\quad + \int_0^{\tau_2}\dot{\mathfrak{J}}(\tau_2-s)(\phi(0)-M(0,u))\mathrm{d}s - \int_0^{\tau_1}\dot{\mathfrak{J}}(\tau_1-s)(\phi(0)-M(0,u))\mathrm{d}s \\ &\quad + \int_0^{\tau_2}\dot{\mathfrak{J}}(\tau_2-s)\Pi(s,u,\mu_u)\mathrm{d}s - \int_0^{\tau_1}\dot{\mathfrak{J}}(\tau_1-s)\Pi(s,u,\mu_u)\mathrm{d}s.\end{aligned} \tag{37}$$

Clearly,

$$\left\|(\Psi u)(\tau_2) - (\Psi u)(\tau_1)\right\| \le \left\|\mathscr{B}_1\right\| + \left\|\mathscr{B}_2\right\| + \left\|\mathscr{B}_3\right\|, \tag{38}$$

where

$$\begin{aligned}
\mathscr{B}_1 &= \Pi(\tau_2, u, \mu_u) - \Pi(\tau_1, u, \mu_u),\\
\mathscr{B}_2 &= \int_0^{\tau_2} \dot{\mathfrak{J}}(\tau_2 - s)(\phi(0) - M(0,u))\mathrm{d}s - \int_0^{\tau_1} \dot{\mathfrak{J}}(\tau_1 - s)(\phi(0) - M(0,u))\mathrm{d}s,\\
\mathscr{B}_3 &= \int_0^{\tau_2} \dot{\mathfrak{J}}(\tau_2 - s)\Pi(s, u, \mu_u)\mathrm{d}s - \int_0^{\tau_1} \dot{\mathfrak{J}}(\tau_1 - s)\Pi(s, u, \mu_u)\mathrm{d}s.
\end{aligned} \tag{39}$$

Next, we shall show that $\|\mathscr{B}_i\| \longrightarrow 0$ is independent of $u \in \Omega$ as $|\tau_1 - \tau_2| \longrightarrow 0$, $i = 1, 2, 3$. In fact, with regard to $\mathscr{B}_1$, we derive

$$\begin{aligned}
&\|\mathscr{B}_1\|\\
&\le \left\| \int_0^{\tau_2} (\tau_2 - s)^{q-1} f(s, u(s), u_s)\mathrm{d}s - \int_0^{\tau_1} (\tau_1 - s)^{q-1} f(s, u(s), u_s)\mathrm{d}s \right\| + \left\| \int_0^{\tau_2} (\tau_2 - s)^{q-1} B\mu_u(s)\mathrm{d}s - \int_0^{\tau_1} (\tau_1 - s)^{q-1} B\mu_u(s)\mathrm{d}s \right\|\\
&\le \int_0^{\tau_1} \left[(\tau_1 - s)^{q-1} - (\tau_2 - s)^{q-1} \right] \|f(s, u(s), u_s)\|_{\mathscr{D}} \mathrm{d}s + \int_{\tau_1}^{\tau_2} (\tau_2 - s)^{q-1} \|f(s, u(s), u_s)\|_{\mathscr{D}} \mathrm{d}s\\
&\quad + \int_0^{\tau_1} \left[(\tau_1 - s)^{q-1} - (\tau_2 - s)^{q-1} \right] \|B\mu_u(s)\|_{\mathscr{D}} \mathrm{d}s + \int_{\tau_1}^{\tau_2} (\tau_2 - s)^{q-1} \|B\mu_u(s)\|_{\mathscr{D}} \mathrm{d}s\\
&\le \frac{M_0}{q}\left(\tau_1^q - \tau_2^q + (\tau_2 - \tau_1)^q\right) + \frac{M_0}{q}(\tau_2 - \tau_1)^q + \frac{N_1 M_1}{q}\left(\tau_1^q - \tau_2^q + (\tau_2 - \tau_1)^q\right) + \frac{N_1 M_1}{q}(\tau_2 - \tau_1)^q \longrightarrow 0, \text{as } |\tau_1 - \tau_2| \longrightarrow 0.
\end{aligned} \tag{40}$$

Notice that

$$\begin{aligned}
\mathscr{B}_2 &= \int_0^{\tau_2} \dot{\mathfrak{J}}(\tau_2 - s)(\phi(0) - M(0,u))\mathrm{d}s - \int_0^{\tau_1} \dot{\mathfrak{J}}(\tau_1 - s)(\phi(0) - M(0,u))\mathrm{d}s\\
&= \int_0^{\tau_2 - \tau_1} \dot{\mathfrak{J}}(\tau_2 - s)(\phi(0) - M(0,u))\mathrm{d}s + \int_{\tau_2 - \tau_1}^{\tau_2} \dot{\mathfrak{J}}(\tau_2 - s)(\phi(0) - M(0,u))\mathrm{d}s - \int_0^{\tau_1} \dot{\mathfrak{J}}(\tau_1 - s)(\phi(0) - M(0,u))\mathrm{d}s\\
&= \int_0^{\tau_2 - \tau_1} \dot{\mathfrak{J}}(\tau_2 - s)(\phi(0) - M(0,u))\mathrm{d}s.
\end{aligned} \tag{41}$$

According to Definition 4, we deduce

$$\begin{aligned}
\|\mathscr{B}_2\| &\le \left(\|\phi(0)\|_{\mathscr{D}} + \|M(0,u)\|_{\mathscr{D}}\right) \int_0^{\tau_2 - \tau_1} \varphi(\tau_2 - s)\mathrm{d}s\\
&\le \left(\|\phi(0)\|_{\mathscr{D}} + G\right) \int_{\tau_1}^{\tau_2} \varphi(s)\mathrm{d}s \longrightarrow 0, \text{as } |\tau_1 - \tau_2| \longrightarrow 0.
\end{aligned} \tag{42}$$

From the proof process of Lemma 6 and (32), it follows that

$$\begin{aligned}
\|\mathscr{B}_3\| &= \left\| \int_0^{\tau_2} \dot{\mathfrak{I}}(\tau_2 - s)\Pi(s,u,\mu_u)\mathrm{d}s - \int_0^{\tau_1} \dot{\mathfrak{I}}(\tau_1 - s)\Pi(s,u,\mu_u)\mathrm{d}s \right\| \\
&\le \left\| \int_0^{\tau_2-\tau_1} \dot{\mathfrak{I}}(\tau_2 - s)\Pi(s,u,\mu_u)\mathrm{d}s + \int_{\tau_2-\tau_1}^{\tau_2} \dot{\mathfrak{I}}(\tau_2 - s)\Pi(s,u,\mu_u)\mathrm{d}s - \int_0^{\tau_1} \dot{\mathfrak{I}}(\tau_1 - s)\Pi(s,u,\mu_u)\mathrm{d}s \right\| \\
&\le \left\| \int_0^{\tau_2-\tau_1} \dot{\mathfrak{I}}(\tau_2 - s)\Pi(s,u,\mu_u)\mathrm{d}s + \int_0^{\tau_1} \dot{\mathfrak{I}}(s)\Pi(\tau_2 - s,u,\mu_u)\mathrm{d}s - \int_0^{\tau_1} \dot{\mathfrak{I}}(s)\Pi(\tau_1 - s,u,\mu_u)\mathrm{d}s \right\| \\
&\le \int_0^{\tau_2-\tau_1} \varphi(\tau_2 - s)\|\Pi(s,u,\mu_u)\|_{\mathscr{D}}\mathrm{d}s + \int_0^{\tau_1} \varphi(s)\|\Pi(\tau_2 - s,u,\mu_u) - \Pi(\tau_1 - s,u,\mu_u)\|_{\mathscr{D}}\mathrm{d}s \\
&\le \int_{\tau_1}^{\tau_2} \varphi(s)\mathrm{d}s \cdot \frac{(M_0 + N_1M_1)T^{*q}}{\Gamma(q+1)} + \int_0^{\tau_1} \varphi(s)\mathrm{d}s \cdot \frac{2(M_0 + N_1M_1)}{q}(\tau_2 - \tau_1)^q \longrightarrow 0, \text{as } |\tau_1 - \tau_2| \longrightarrow 0.
\end{aligned} \tag{43}$$

(ii) If $-r \le \tau_1 < \tau_2 \le 0$, then from the continuity of $\phi(\cdot)$ and (H3) (i), one has

$$\begin{aligned}
\|(\Psi u)(\tau_2) - (\Psi u)(\tau_1)\| &= \|\phi(\tau_2) - \phi(\tau_1) - (M(\tau_2,u) - M(\tau_1,u))\| \\
&\le \|\phi(\tau_2) - \phi(\tau_1)\| + \|M(\tau_2,u) - M(\tau_1,u)\| \longrightarrow 0, \text{as } |\tau_1 - \tau_2| \longrightarrow 0.
\end{aligned} \tag{44}$$

(iii) If $-r \le \tau_1 < 0 < \tau_2 \le T^*$, then

$$\begin{aligned}
&\|(\Psi u)(\tau_2) - (\Psi u)(\tau_1)\| \\
&\le \|(\Psi u)(\tau_2) - (\Psi u)(0)\| + \|(\Psi u)(0) - (\Psi u)(\tau_1)\| \\
&\le \left\| \Pi(\tau_2,u,\mu_u) + \int_0^{\tau_2} \dot{\mathfrak{I}}(\tau_2 - s)(\phi(0) - M(0,u) + \Pi(s,u,\mu_u))\mathrm{d}s \right\| + \|(\phi(0) - M(0,u)) - \phi(\tau_1) - M(\tau_1,u)\| \\
&\le \frac{M_0 + N_1M_1}{\Gamma(q+1)}\tau_2^q + \left(\|\phi(0)\|_{\mathscr{D}} + \|M(0,u)\|_{\mathscr{D}} + \|\Pi(s,u,\mu_u)\|_{\mathscr{D}}\right)\int_0^{\tau_2} \varphi(\tau_2 - s)\mathrm{d}s + \|\phi(0) - \phi(\tau_1)\| + \|M(0,u) - M(\tau_1,u)\| \\
&\le \frac{M_0 + N_1M_1}{\Gamma(q+1)}\tau_2^q + \left(\|\phi(0)\|_{\mathscr{D}} + G + \frac{M_0 + N_1M_1}{\Gamma(q+1)}T^q\right)\int_0^{\tau_2} \varphi(s)\mathrm{d}s + \|\phi(0) - \phi(\tau_1)\| + \|M(0,u) - M(\tau_1,u)\| \\
&\quad \longrightarrow 0, \text{as } |\tau_1 - \tau_2| \longrightarrow 0.
\end{aligned} \tag{45}$$

Thus, it implies that $\|(\Psi u)(\tau_2) - (\Psi u)(\tau_1)\| \longrightarrow 0$, as $|\tau_1 - \tau_2| \longrightarrow 0$, for all $u \in \Omega$. Consequently, $\Psi\colon \Omega \longrightarrow \Omega$ is equicontinuous on J. □

Lemma 8. *Let conditions (H1) (i), (H2), (H3) (i), and (H4) be satisfied. Then, the operator $\Psi\colon \Omega \longrightarrow \Omega$ is continuous.*

Proof. It follows from Lemma 7 that $\Psi(\Omega) \subseteq \Omega$. Next, we show that Ψ is continuous. Let $\{v_n\}$ be a sequence such that $v_n \longrightarrow v$ in Ω as $n \longrightarrow \infty$.

In view of condition (H1) (i) and Lebesgue dominated convergence theorem, we have

$$\int_0^t (t-s)^{q-1}\|f(s,v_n(s),(v_n)_s) - f(s,v(s),v_s)\|_{\mathscr{D}}\mathrm{d}s \longrightarrow 0, \quad \forall t \in [0,T^*], \text{as } n \longrightarrow +\infty. \tag{46}$$

Therefore, this together with the continuity of $M(0,\cdot)$ implies

$$\begin{aligned}
&\left\|B\mu_{v_n}(s)-B\mu_v(s)\right\|_{\mathscr{D}}\\
&\le N_1N_2\Big[\left\|M(0,v_n)-M(0,v)\right\|_{\mathscr{D}}+\left\|\Pi_f(T^*,v_n)-\Pi_f(T^*,v)\right\|_{\mathscr{D}}\\
&\quad+\int_0^{T^*}\varphi(T^*-s)\left\|M(0,v_n)-M(0,v)\right\|_{\mathscr{D}}+\left\|\Pi_f(s,v_n)-\Pi_f(s,v)\right\|_{\mathscr{D}}\mathrm{d}s\Big]\\
&\le N_1N_2\Big[\left\|M(0,v_n)-M(0,v)\right\|_{\mathscr{D}}+\int_0^{T^*}(T^*-s)^{q-1}\left\|f(s,v_n(s),(v_n)_s)-f(s,v(s),v_s)\right\|_{\mathscr{D}}\mathrm{d}s\\
&\quad+\int_0^{T^*}\varphi(T^*-s)\Big(\left\|M(0,v_n)-M(0,v)\right\|_{\mathscr{D}}+\int_0^s(s-\eta)^{q-1}\left\|f\big(\eta,v_n(\eta),(v_n)_\eta\big)-f\big(\eta,v(\eta),v_\eta\big)\right\|_{\mathscr{D}}\mathrm{d}\eta\Big)\mathrm{d}s\Big]\\
&\longrightarrow 0,\ \text{as}\ n\longrightarrow+\infty.
\end{aligned}\tag{47}$$

Consequently, for each $t\in[0,T^*]$, we have

$$\begin{aligned}
&\left\|(\Psi v_n)(t)-(\Psi v)(t)\right\|\\
&\le\left\|\Pi\big(t,v_n,\mu_{v_n}\big)-\Pi(t,v,\mu_v)\right\|_{\mathscr{D}}+\int_0^t\left\|\dot{\mathfrak{J}}(t-s)\big(\Pi\big(s,v_n,\mu_{v_n}\big)-\Pi(s,v,\mu_v)\big)\right\|\mathrm{d}s\\
&\le\int_0^t\int_0^t(t-s)^{q-1}\left\|f(s,v_n(s),(v_n)_s)-f(s,v(s),v_s)_{\mathscr{D}}\right\|\mathrm{d}s+\int_0^t(t-s)^{q-1}\left\|B\mu_{v_n}(s)-B\mu_v(s)\right\|_{\mathscr{D}}\mathrm{d}s\\
&\quad+\int_0^t\varphi(t-s)\Big(\int_0^s(s-\eta)^{q-1}\left\|f\big(\eta,v_n(\eta),(v_n)_\eta\big)-f\big(\eta,v(\eta),v_\eta\big)\right\|_{\mathscr{D}}\mathrm{d}\eta\Big)\mathrm{d}s\\
&\quad+\int_0^t\varphi(t-s)\Big(\int_0^s(s-\eta)^{q-1}\left\|B\mu_{v_n}(\eta)-B\mu_v(\eta)\right\|_{\mathscr{D}}\mathrm{d}\eta\Big)\longrightarrow 0,\ \text{as}\ n\longrightarrow+\infty.
\end{aligned}\tag{48}$$

From the analogous proof of equicontinuous for operator Ψ in Lemma 7 and the well-known Ascoli–Arzelà theorem, it is not difficult to obtain $\|\Psi v_n-\Psi v\|_{C(J,X)}\longrightarrow 0$, as $n\longrightarrow+\infty$, i.e., Ψ is continuous on Ω. This completes the proof. □

We present now our main results of this paper.

Theorem 1. *If assumptions (H1)–(H4) hold, then the fractional evolution (1) is completely controllable on I.*

Proof. Consider the operator Ψ defined as (28). In view of Lemma 1, it is enough to prove that when using the control μ_u, the operator Ψ has a fixed point $u(\cdot)$ which is exactly a mild solution of (1) on J. From the verified fact $u(T^*)=(\Psi u)(T^*)=u_1$, it follows that the control μ_u steers system (1) from the initial function ϕ to u_1 in finite time T^*. The complete controllability on I of system (1) is thus proved. To this end, we shall take advantage of Mönch fixed point theorem. The continuity of operator Ψ: $\Omega\longrightarrow\Omega$ is given by Lemma 8. In the next step, we demonstrate that Mönch's condition holds for operator Ψ: $\Omega\longrightarrow\Omega$.

Let $B=\overline{co}\,\Psi(\Omega)$. It is not difficult to check that $\Psi(B)\subseteq B$. Assume that bounded set $D_0\subset B$ is countable and $D_0\subset\overline{co}(\{u_0\}\cup\Psi(D_0))$, and we shall prove that $\gamma(D_0)=0$. From Lemma 7, it is easy to derive that $\Psi(D_0)$ is equicontinuous on J. Notice that $D_0\subset\overline{co}(\{u_0\}\cup\Psi(D_0))$, so D_0 is also equicontinuous on J.

For any $u\in D_0$, let

$$(\Psi u)(t)=\begin{cases}(\Psi_1u)(t)+(\Psi_2u)(t), & t\in[0,T^*],\\ \phi(t)-M(t,u), & t\in[-r,0],\end{cases}\tag{49}$$

where

$$\begin{aligned}
(\Psi_1u)(t)&=\phi(0)-M(0,u)+\Pi(t,u,\mu_u),\\
(\Psi_2u)(t)&=\int_0^t\dot{\mathfrak{J}}(t-s)(\phi(0)-M(0,u)+\Pi(s,u,\mu_u))\mathrm{d}s.
\end{aligned}\tag{50}$$

No loss of generality, suppose $D_0=\{w_n\}_{n=1}^{\infty}$. From hypothesis (H1) (ii) and Lemma 5, for any $s\in I$, it follows that

$$\begin{aligned}
\gamma(\{f(s,w_n(s),(w_n)_s)\})&\le m(s)((\gamma(\{w_n(s)\}))+\gamma(\{(w_n)_s\}))\\
&\le m(s)((\gamma(\{w_n(s)\}))+r\gamma(\{w_n\}))\\
&\le m(s)(\gamma(D_0(s))+r\gamma(D_0))\\
&\le m(s)(r+1)\gamma(D_0).
\end{aligned}\tag{51}$$

Then, this indicates from Lemma 2 and Hölder inequality that

$$\begin{aligned}
\gamma\left(\left\{\Pi_f(t,w_n)\right\}\right) &= \gamma\left(\left\{\frac{1}{\Gamma(q)}\int_0^t (t-s)^{q-1} f(s,w_n(s),(w_n)_s)\mathrm{d}s\right\}\right)\\
&\le \frac{2}{\Gamma(q)}\left(\int_0^t (t-s)^{q-1}\gamma\left(\left\{f(s,w_n(s),(w_n)_s)\right\}\right)\mathrm{d}s\right)\\
&\le \frac{2(r+1)}{\Gamma(q)}\int_0^t (t-s)^{q-1} m(s)\mathrm{d}s\cdot\gamma\left(\left\{w_n\right\}\right)\\
&\le \frac{2(r+1)}{\Gamma(q)}\left(\int_0^t \left[(t-s)^{q-1}\right]^{(1/1-q_1)}\mathrm{d}s\right)^{1-q_1}\left(\int_0^t m(s)^{(1/q_1)}\mathrm{d}s\right)^{q_1}\cdot\gamma\left(\left\{w_n\right\}\right)\\
&\le \frac{2(r+1)}{\Gamma(q)}\left(\frac{1-q_1}{q-q_1}\right)^{1-q_1} t^{q-q_1}\|m\|_{L^{(1/q_1)}}\cdot\gamma\left(\left\{w_n\right\}\right)\\
&\le \lambda T^{*q}\gamma(D_0), \quad t\in[0,T^*],
\end{aligned} \tag{52}$$

which together with Lemma 2, (H2) (ii), and (H3) (i) implies

$$\begin{aligned}
&\gamma\left(\left\{\mu_{w_n}(s)\right\}\right)\\
&\quad\le p(s)\left(\gamma\left(\left\{M(0,w_n)\right\}\right)+\gamma\left(\left\{\Pi_f(T^*,w_n)\right\}\right)+2\int_0^{T^*}\varphi(T^*-s)\left(\gamma\left(\left\{M(0,w_n)\right\}\right)+\gamma\left(\left\{\Pi_f(s,w_n)\right\}\right)\right)\mathrm{d}s\right)\\
&\quad\le p(s)\left(k\gamma\{w_n\}+\lambda T^{*q}\gamma\left(\left\{w_n\right\}\right)+2\|\varphi\|_{L^1(I)}\left(k\gamma\{w_n\}+\lambda T^{*q}\gamma\left(\left\{w_n\right\}\right)\right)\right)\\
&\quad\le p(s)\left(k+\lambda T^{*q}\right)\left(1+2\|\varphi\|_{L^1(I)}\right)\gamma(D_0), \quad s\in[0,T^*].
\end{aligned} \tag{53}$$

Thus, by using Hölder inequality again, one has

$$\begin{aligned}
\gamma\left(\left\{\Pi_B\left(t,\mu_{w_n}\right)\right\}\right) &\le \frac{2N_1}{\Gamma(q)}\int_0^t (t-s)^{q-1}\gamma\left(\left\{\mu_{w_n}(s)\right\}\right)\mathrm{d}s\\
&\le \frac{2N_1\left(k+\lambda T^{*q}\right)\left(1+2\|\varphi\|_{L^1(I)}\right)}{\Gamma(q)}\int_0^t (t-s)^{q-1}p(s)\mathrm{d}s\gamma(D_0)\\
&\le \frac{2N_1L\left(k+\lambda T^{*q}\right)\left(1+2\|\varphi\|_{L^1(I)}\right)}{\Gamma(q)}\gamma(D_0), \quad t\in[0,T^*].
\end{aligned} \tag{54}$$

Consequently, from the abovementioned, we can derive

$$\begin{aligned}
\gamma\left(\Psi_1(D_0)(t)\right) &\le \gamma\left(\left\{M(0,w_n)\right\}\right)+\gamma\left(\left\{\Pi_f(t,w_n)\right\}\right)+\gamma\left(\left\{\Pi_B\left(t,\mu_{w_n}\right)\right\}\right)\\
&\le k\gamma(D_0)+\lambda T^{*q}\gamma(D_0)+\frac{2N_1L\left(k+\lambda T^{*q}\right)\left(1+2\|\varphi\|_{L^1(I)}\right)}{\Gamma(q)}\gamma(D_0)\\
&\le \left(k+\lambda T^{*q}\right)\left(1+\frac{2N_1L\left(1+2\|\varphi\|_{L^1(I)}\right)}{\Gamma(q)}\right)\gamma(D_0)\\
&\le \left(\lambda MT^{*q}+kM\right)\gamma(D_0).
\end{aligned} \tag{55}$$

For $t \in [0, T^*]$, also in view of Lemma 2, one obtains

$$\begin{aligned}\gamma(\Psi_2(D_0)(t)) &= \gamma\left(\left\{\int_0^t \dot{\mathfrak{J}}(t-s)\left(\phi(0) - M(0, w_n) + \Pi\left(s, w_n, \mu_{w_n}\right)\right)\mathrm{d}s\right\}\right) \\ &\le 2\int_0^t \gamma\left(\left\{\dot{\mathfrak{J}}(t-s)\left(\phi(0) - M(0, w_n) + \Pi\left(s, w_n, \mu_{w_n}\right)\right)\right\}\right)\mathrm{d}s \\ &\le 2\int_0^t \varphi(t-s)\gamma(\Psi_1(D_0)(s))\mathrm{d}s \\ &\le 2\|\varphi\|_{L^1(I)}(\lambda M T^{*q} + kM)\gamma(D_0).\end{aligned} \tag{56}$$

Then, by (55) and (56), we can infer

$$\begin{aligned}\gamma(\Psi(D_0)(t)) &\le \gamma(\Psi_1(D_0)(t)) + \gamma(\Psi_2(D_0)(t)) \\ &\le (\lambda M T^{*q} + kM)\gamma(D_0) \\ &\quad + 2\|\varphi\|_{L^1(I)}(\lambda M T^{*q} + kM)\gamma(D_0) \\ &\le \left(\lambda M\left(1 + 2\|\varphi\|_{L^1(I)}\right)T^{*q} \right. \\ &\quad \left. + kM\left(1 + 2\|\varphi\|_{L^1(I)}\right)\right)\gamma(D_0), \quad t \in [0, T^*].\end{aligned} \tag{57}$$

Besides, for $t \in [-r, 0]$, we have from (H3) (i) that

$$\begin{aligned}\gamma(\Psi(D_0)(t)) &\le \gamma(\{\phi(t) - M(t, w_n)\}) \\ &\le \gamma(\{M(t, w_n)\}) \le k\gamma(\{w_n\}) < \gamma(D_0).\end{aligned} \tag{58}$$

On the contrary, from the equicontinuity of $\Psi(D_0)$ on J, it follows that

$$\gamma(\Psi(D_0)) = \max_{t\in J} \gamma((\Psi D_0)(t)). \tag{59}$$

Consequently, by (24) and (57)–(59), one can derive

$$\gamma(D_0) \le \gamma(\overline{co}(\{u_0\} \cup \Psi(D_0))) \le \gamma(\Psi(D_0)) < \gamma(D_0), \tag{60}$$

which deduces $\gamma(D_0) = 0$. Due to Lemma 2 (I) (i), we know that D_0 is relatively compact. Then, from Lemma 3, Ψ has at least one fixed point $u \in B$. This shows that the complete controllability on I for system (1) is valid. The proof is now completed. □

Remark 3. (i) Different from some papers [21, 25, 44] utilizing the definition of mild solution by probability density functions which are initially presented by El-Borai [3], the way of making use of differentiable resolvent operators to define mild solution in this paper can avoid the complexity of definitions and properties related to the probability density functions and its associated characteristic solution operators; sometimes, the limitation of fractional order q lying in (0, 1) due to the probability density functions can be extricated. (ii) In a comparative way, nonlocal item in this paper has better application effect in physics. In practical applications, it may be given by $M(t, u) = \sum_{i=1}^{k} c_i u(\tau_i + t)$, $t \in [-r, 0]$, where $c_i (i = 1, 2, \ldots, k)$ is a given constant and $0 < \tau_1 < \tau_2 < \cdots < \tau_n \le T$. At time $t = 0$, we have $M(0, u) = \sum_{i=1}^{k} c_i u(\tau_i)$, which is exactly the case in [44].

4. An Example

As an application of our abstract results, we consider the following fractional partial differential nonlocal evolution equations with delay of the form:

$$\begin{cases} \dfrac{\partial^{(1/3)}}{\partial t^{(1/3)}} u(t, \tau) = \dfrac{\partial}{\partial \tau} u(t, \tau) + \dfrac{\vartheta(t) u_t(\tau)}{2 + |u_t(\tau)|} + \displaystyle\int_{-r}^{t} \eta(t-s) u(s, \tau) ds + \delta(\tau)\mu(t, \tau), & (t, \tau) \in [0, T] \times (0, \pi), \\ u(t, 0) = u(t, \pi) = 0, & t \in [0, T], \\ u(t, \tau) + \displaystyle\sum_{i=1}^{l} m_i \sin\left(u\left(c_i + t, \tau\right)\right) = \phi(t, \tau), & (t, \tau) \in [-r, 0] \times [0, \pi], 0 < c_1 < c_2 < \cdots < c_l < T, \end{cases} \tag{61}$$

where $\vartheta \in C([0, T], R)$, $\eta \in L((-r, T + r), R)$, δ denotes the characteristic function of some subinterval $D \subset [0, \pi]$, $\mu \in C([0, T] \times [0, \pi], R)$ and satisfies $\mu(t, 0) = \mu(t, \pi) = 0$ for $t \in [0, T]$. m_i is a fixed constant for $i = 1, 2, \ldots, l$ satisfying $\sum_{i=1}^{l} |m_i| < 1$. $\phi \in C([-r, 0] \times [0, \pi], X)$, which satisfies $\phi(t, 0) = \phi(t, \pi) = 0$ for $t \in [-r, 0]$, $X = C([0, \pi], R)$, and $\mathscr{D} = \{u \in X: u' \in X, u(0) = u(\pi) = 0\}$, $Au = u'$ for $u \in \mathscr{D}$. Thus, A is an infinitesimal generator of a noncompact semigroup $\{T(t): t \ge 0\}$ which is given by $T(t)u(s) = u(t + s)$ for $u \in X$. Let

$$
\begin{aligned}
D^{(1/3)}u(t)(\tau) &= \frac{\partial^{(1/3)}}{\partial t^{(1/3)}}u(t,\tau),\\
f(t,u(t),u_t)(\tau) &= \frac{\vartheta(t)u_t(\tau)}{2+|u_t(\tau)|}+\int_{-r}^{t}\eta(t-s)u(s,\tau)ds,\\
u(t)(\tau) &= u(t,\tau),\\
B\mu(t)(\tau) &= \delta(\tau)\mu(t,\tau),\\
\phi(t)(\tau) &= \phi(t,\tau),\\
M(t,u)(\tau) &= \sum_{i=1}^{l} m_i \sin\left(u\left(c_i+t,\tau\right)\right),\\
\sum_{i=1}^{l}|m_i| &< 1, \quad 0<c_1<c_2<\cdots<c_l<T.
\end{aligned}
\tag{62}
$$

Under these assumptions, partial system (61) can be regarded as a control problem of the abstract form:

$$
\begin{cases}
D^q u(t) = Au(t)+f(t,u(t),u_t)+B\mu(t), & a.e.t\in I:=[0,T],\\
u(t)+M(t,u)=\phi(t), & t\in[-r,0].
\end{cases}
\tag{63}
$$

For any $t\in[-r,0]$ and for any bounded set $D\subset C([-r,T],X)$, we have that $\gamma(M(t,D))\leq \sum_{i=1}^{l}|m_i|\gamma(D)<\gamma(D)$, which indicates that $M(t,\cdot)$: $C([-r,T],X)\longrightarrow X$ is a strict k-set contraction with $k=\sum_{i=1}^{l}|m_i|<1$. In addition, it is not difficult to verify that f, B, and M satisfy other assumptions of Theorem 1. Thus, system (61) is completely controllable on $[0,T]$.

5. Conclusions

In this work, complete controllability of a class of semilinear fractional nonlocal evolution systems with finite delay in Banach spaces is investigated by using properties of resolvent operators, theory of measure of noncompactness, and Mönch fixed point theorem. Under a weaker concept of complete controllability and a proper complete space we introduced, the controllability results of the addressed system are obtained without Lipschitz continuity and other growth conditions imposed on the nonlinearity and nonlocal item. In fact, the nonlinear function is only supposed to be continuous. Then, we improve and generalize some analogous results of fractional evolution systems such as [11, 21–25].

Data Availability

No data were used to support this study.

Conflicts of Interest

The author declares that there are no conflicts of interest.

Acknowledgments

This research was supported by the National Natural Science Foundation of China under Grant 61873150 and a project of Shandong Province Higher Educational Science and Technology Program of China under Grant J18KA233 hosted by the author Daliang Zhao.

References

[1] P. Chen, X. Zhang, and Y. Li, "Existence and approximate controllability of fractional evolution equations with nonlocal conditions via resolvent operators," *Fractional Calculus and Applied Analysis*, vol. 23, no. 1, pp. 268–291, 2020.

[2] P. Chen, X. Zhang, and Y. Li, "Cauchy problem for fractional non-autonomous evolution equations," *Banach Journal of Mathematical Analysis*, vol. 14, no. 2, pp. 559–584, 2020.

[3] M. M. El-Borai, "Some probability densities and fundamental solutions of fractional evolution equations," *Chaos, Solitons & Fractals*, vol. 14, no. 3, pp. 433–440, 2002.

[4] K. S. Miller and B. Ross, *An Introduction to the Fractional Calculus and Fractional Differential Equations*, A Wiley-Interscience Publication, John Wiley, Sons, Inc., New York, NY, USA, 1993.

[5] I. Podlubny, *Fractional Differential Equations, Mathematics in Science and Engineering*, Academic Press, New York, NY, USA, 1999.

[6] T. Qi, Y. Liu, and Y. Cui, "Existence of solutions for a class of coupled fractional differential systems with nonlocal boundary conditions," *Journal of Function Spaces*, vol. 2017, Article ID 6703860, 9 pages, 2017.

[7] Y. Tian and S. Zhao, "Existence of solutions for perturbed fractional equations with two competing weighted nonlinear terms," *Boundary Value Problems*, vol. 2018, no. 1, p. 154, 2018.

[8] Y. Tian, "Some results on the eigenvalue problem for a fractional elliptic equation," *Boundary Value Problems*, vol. 2019, no. 1, p. 13, 2019.

[9] Y. Wang, Y. Liu, and Y. Cui, "Infinitely many solutions for impulsive fractional boundary value problem with p-Laplacian," *Boundary Value Problems*, vol. 2018, no. 1, p. 94, 2018.

[10] H. Cheng and R. Yuan, "Stability of traveling wave fronts for nonlocal diffusion equation with delayed nonlocal response," *Taiwanese Journal of Mathematics*, vol. 20, no. 4, pp. 801–822, 2016.

[11] A. Debbouche and D. Baleanu, "Controllability of fractional evolution nonlocal impulsive quasilinear delay integro-differential systems," *Computers & Mathematics with Applications*, vol. 62, no. 3, pp. 1442–1450, 2011.

[12] W. Hu, Q. Zhu, and H. R. Karimi, "Some improved razumikhin stability criteria for impulsive stochastic delay differential systems," *IEEE Transactions on Automatic Control*, vol. 64, no. 12, pp. 5207–5213, 2019.

[13] X. Li, X. Fu, and R. Rakkiyappan, "Delay-dependent stability analysis for a class of dynamical systems with leakage delay and nonlinear perturbations," *Applied Mathematics and Computation*, vol. 226, pp. 10–19, 2014.

[14] X. Li, J. Shen, and R. Rakkiyappan, "Persistent impulsive effects on stability of functional differential equations with finite or infinite delay," *Applied Mathematics and Computation*, vol. 329, pp. 14–22, 2018.

[15] Y. Liu, Y. Zheng, H. Li, F. E. Alsaadi, and B. Ahmad, "Control design for output tracking of delayed Boolean control

networks," *Journal of Computational and Applied Mathematics*, vol. 327, pp. 188–195, 2018.

[16] I. Stamova, T. Stamov, and X. Li, "Global exponential stability of a class of impulsive cellular neural networks with supremums," *International Journal of Adaptive Control and Signal Processing*, vol. 28, no. 11, pp. 1227–1239, 2014.

[17] D. Yang, X. Li, J. Shen, and Z. Zhou, "State-dependent switching control of delayed switched systems with stable and unstable modes," *Mathematical Methods in the Applied Sciences*, vol. 41, no. 16, pp. 6968–6983, 2018.

[18] Q. Zhu, "Stability analysis of stochastic delay differential equations with Lévy noise," *Systems & Control Letters*, vol. 118, pp. 62–68, 2018.

[19] Q. Zhu, "Stabilization of stochastic nonlinear delay systems with exogenous disturbances and the event-triggered feedback control," *IEEE Transactions on Automatic Control*, vol. 64, no. 9, pp. 3764–3771, 2019.

[20] Q. Zhu and T. Huang, "Stability analysis for a class of stochastic delay nonlinear systems driven by G-Brownian motion," *Systems & Control Letters*, vol. 140, Article ID 104699, 2020.

[21] J. Du, W. Jiang, D. Pang, and A. U. K. Niazi, "Controllability for a new class of fractional neutral integro-differential evolution equations with infinite delay and nonlocal conditions," *Advances in Difference Equations*, vol. 139, pp. 1–22, 2017.

[22] R. J. Nirmala, K. Balachandran, L. Rodríguez-Germa, and J. J. Trujillo, "Controllability of nonlinear fractional delay dynamical systems," *Reports on Mathematical Physics*, vol. 77, no. 1, pp. 87–104, 2016.

[23] Z. Tai, "Controllability of fractional impulsive neutral integrodifferential systems with a nonlocal Cauchy condition in Banach spaces," *Applied Mathematics Letters*, vol. 24, no. 12, pp. 2158–2161, 2011.

[24] Z. Tai and S. Lun, "On controllability of fractional impulsive neutral infinite delay evolution integrodifferential systems in Banach spaces," *Applied Mathematics Letters*, vol. 25, no. 2, pp. 104–110, 2012.

[25] J. Wang and Y. Zhou, "Complete controllability of fractional evolution systems," *Communications in Nonlinear Science and Numerical Simulation*, vol. 17, no. 11, pp. 4346–4355, 2012.

[26] D. Zhao, Y. Liu, and X. Li, "Controllability for a class of semilinear fractional evolution systems via resolvent operators," *Communications on Pure & Applied Analysis*, vol. 18, no. 1, pp. 455–478, 2019.

[27] X. Ding, H. Li, Q. Yang, Y. Zhou, A. Alsaedi, and F. E. Alsaadi, "Stochastic stability and stabilization of n -person random evolutionary Boolean games," *Applied Mathematics and Computation*, vol. 306, pp. 1–12, 2017.

[28] F.-F. Jin and B.-Z. Guo, "Performance boundary output tracking for one-dimensional heat equation with boundary unmatched disturbance," *Automatica*, vol. 96, pp. 1–10, 2018.

[29] P. Li, X. Li, and J. Cao, "Input-to-state stability of nonlinear switched systems via lyapunov method involving indefinite derivative," *Complexity*, vol. 2018, Article ID 8701219, 8 pages, 2018.

[30] H. Li, X. Xu, and X. Ding, "Finite-time stability analysis of stochastic switched boolean networks with impulsive effect," *Applied Mathematics and Computation*, vol. 347, pp. 557–565, 2019.

[31] X. Li, X. Yang, and T. Huang, "Persistence of delayed cooperative models: impulsive control method," *Applied Mathematics and Computation*, vol. 342, pp. 130–146, 2019.

[32] S. Liang, G. Zhao, H. Li, and X. Ding, "Structural stability analysis of gene regulatory networks modeled by Boolean networks," *Mathematical Methods in the Applied Sciences*, vol. 42, no. 7, pp. 2221–2230, 2019.

[33] J. Liu and X. Li, "Impulsive stabilization of high-order nonlinear retarded differential equations," *Applications of Mathematics*, vol. 58, no. 3, pp. 347–367, 2013.

[34] Y. Liu and D. O'Regan, "Controllability of impulsive functional differential systems with nonlocal conditions," *Electronic Journal of Differential Equations*, vol. 2013, p. 194, 2013.

[35] X. Xu, H. Li, Y. Li, and F. E. Alsaadi, "Output tracking control of Boolean control networks with impulsive effects," *Mathematical Methods in the Applied Sciences*, vol. 41, no. 4, pp. 1554–1564, 2018.

[36] X. Xu, Y. Liu, H. Li, and F. E. Alsaadi, "Robust set stabilization of Boolean control networks with impulsive effects," *Nonlinear Analysis: Modelling and Control*, vol. 23, no. 4, pp. 553–567, 2018.

[37] X. Xu, Y. Liu, H. Li, and F. E. Alsaadi, "Synchronization of switched Boolean networks with impulsive effects," *International Journal of Biomathematics*, vol. 11, no. 6, Article ID 1850080, 2018.

[38] X. Zhang, X. Li, and X. Han, "Design of hybrid controller for synchronization control of Chen chaotic system," *The Journal of Nonlinear Sciences and Applications*, vol. 10, no. 6, pp. 3320–3327, 2017.

[39] G. Zhao, Y. Wang, and H. Li, "A matrix approach to modeling and optimization for dynamic games with random entrance," *Applied Mathematics and Computation*, vol. 290, pp. 9–20, 2016.

[40] Z. Zhou and N. N. Yan, "A survey of numerical methods for convection-diffusion optimal control problems," *Journal of Numerical Mathematics*, vol. 22, no. 1, pp. 61–85, 2014.

[41] S. Ji, G. Li, and M. Wang, "Controllability of impulsive differential systems with nonlocal conditions," *Applied Mathematics and Computation*, vol. 217, no. 16, pp. 6981–6989, 2011.

[42] J. Prüss, "Evolutionary integral equations and applications," in *Monographs in Mathematics*, vol. 87Basel, Switzerland, Birkhäuser Verlag, 1993.

[43] D. Guo, V. Lakshmikantham, and X. Liu, *Nonlinear Integral Equations in Abstract Spaces*, Kluwer Academic Publishers, Dordrecht, Netherlands, 1996.

[44] J. Liang and H. Yang, "Controllability of fractional integro-differential evolution equations with nonlocal conditions," *Applied Mathematics and Computation*, vol. 254, pp. 20–29, 2015.